REDESIGN AND CHARACTERISATION OF THE NOSE WHEEL FORK OF A LIGHT AIRCRAFT FOR PRODUCTION IN Ti6Al4V(ELI) THROUGH LASER POWDER BED FUSION

by

LEHLOHONOLO FRANCIS MONAHENG

A thesis submitted in fulfilment of the requirements for the degree:

DOCTOR OF ENGINEERING IN MECHANICAL ENGINEERING

in the

Department of Mechanical and Mechatronics Engineering

Faculty of Engineering, Built Environment and Information Technology

at

Central University of Technology, Free State

Promoter: Prof. W. B. du Preez, PhD, Pr Sci Nat

Co-promoter: Prof. C. Polese, PhD

BLOEMFONTEIN, FREE STATE, SOUTH AFRICA

SEPTEMBER 2024

© Central University of Technology, Free State

Central University of
Technology, Free State

DECLARATION OF INDEPENDENT WORK

DECLARATION WITH REGARD TO INDEPENDENT WORK

I, **LEHLOHONOLO FRANCIS MONAHENG**, identity number **#############** and student number **#########**, do hereby declare that this research project submitted to Central University of Technology, Free State for the Degree **DOCTOR OF ENGINEERING IN MECHANICAL ENGINEERING**, is my own independent work; and complies with the Code of Academic Integrity, as well as other relevant policies, procedures, rules and regulations of Central University of Technology, Free State; and has not been submitted before to any institution by myself of any other person in fulfilment (or partial fulfilment) of the requirements for the attainment of any qualification.

12 September 2024

SIGNATURE OF STUDENT DATE

© Central University of Technology, Free State

ABSTRACT

In agreement with the AHRLAC company (currently known as Paramount Aerospace Industries), the nose wheel fork of the AHRLAC, which was conventionally machined in 7050 aluminium alloy, was selected for this study. A technique of topology optimisation, aligned with design for additive manufacturing (TO-DfAM), was applied to redesign the nose wheel fork. This was done to obtain a lightweight component without compromising the required strength and to allow the use of laser powder bed fusion (L-PBF) for the production of the nose wheel fork in Ti6Al4V(ELI). The redesigned Ti6Al4V(ELI) nose wheel fork was 20% lighter than the fork produced through conventional machining from 7050 aluminium alloy.

For the current research, the dimensions of the component were adjusted to a size which allowed the production of the prototype scaled-down nose wheel fork in Ti6Al4V(ELI) in the available EOSINT M290 direct metal laser sintering (DMLS) system. The prototype nose wheel fork, together with standard test specimens built in the same machine process parameters, were submitted to a two-phase heat treatment. This heat treatment consisted of a stress-relieving heat treatment at 650 °C for 3 hours, which was followed by high-temperature annealing at 950 °C for 2 hours. Subsequently, the built and heat-treated test specimens were characterised through porosity assessment, dimensional accuracy determination and surface roughness testing.

Standard tests were done according to the respective ASTM standards to determine the mechanical and fatigue properties of the DMLS Ti6Al4V(ELI) test specimens. To confirm the integrity of the building process, tensile test specimens, built along the deposition direction, were tested following ASTM E8. Other properties included tensile strength, impact toughness, fracture toughness (K_{IC}), fatigue crack growth rate (FCGR) and high cycle fatigue (HCF). For impact toughness determination, two sets of specimens were tested, one set had a V-notch printed and the other V-notches were created using electrical discharge machining (EDM). Before testing these specimens based on the ASTM E23 standard, they were conditioned to a temperature of -50 °C. The K_{IC} and FCGR were determined in accordance with the ASTM E399 and ASTM E647 standards, respectively. To determine the impact of

© Central University of Technology, Free State

surface roughness on the fatigue properties of the alloy, HCF specimens with as-built surface roughness were subjected to tension-tension fatigue testing in compliance with the ATSM E466 standard.

Subsequently, the operational performance of the DMLS Ti6Al4V(ELI) scaled-down nose wheel fork, also with as-built surface roughness, was experimentally tested using a unique test jig designed to allow static and fatigue loading. Initially, the nose wheel fork was tested under maximum static loads along the X- and Y-axes that were set 24% higher than the design loads required by the General Aviation (GA) Code of Federal Regulations (CFR). The results of this test were used to validate the finite element analysis (FEA) executed to model the performance of the component. Secondly, the component was tested under cyclic loading along the X- and Y-axes to investigate its fatigue performance. These cyclic loads were also 24% higher than the accepted design load. All loads were applied at a frequency of 3 Hz with a fully reversed (stress ratio R = -1) fatigue loading as the baseline. The microstructure near the crack regions and the analysis of the fracture surfaces of the scaled-down nose wheel fork were analysed to confirm the failure mechanisms.

The average impact toughness of 26 J which was measured for both the as-built and wire-cut V-notch Charpy impact test specimens, was 8% higher than the impact energy required by the aviation industry. When comparing the FCGR results obtained in the current study with the one reported in literature, higher crack growth resistance was observed. These were attributed to the heat-treatment post-process that was executed. The fatigue strengths of 190 MPa and 225 MPa recorded for the standard DMLS Ti6Al4V(ELI) HCF test specimens with as-built surface roughness that were built in, and perpendicular to, the plane of the build platform, respectively, were 50% lower than those of machined test specimens. This confirmed the negative impact of the surface roughness obtained with the DMLS process.

The DMLS Ti6Al4V(ELI) scaled-down nose wheel fork withstood static loading without any plastic deformation. It resisted more than 100 000 cycles during the first X-loading of 6 000 N, however, failure was observed after 15 000 cycles in an area predicted to have high cycle fatigue under Z-loading. These results illustrated that the inherent surface roughness on the DMLS Ti6Al4V(ELI) scaled-down nose wheel

© Central University of Technology, Free State

fork, due to the staircase effect and partially melted powder particles on the surface, was detrimental to the fatigue life of the component.

The current study was a unique first attempt to redesign and characterise a mission-critical structural component of an actual aircraft for production in Ti6Al4V(ELI) through DMLS technology and assess its compliance with the performance requirements of the component. It was confirmed that a digital design method that includes FEA can be used to design a unique intricately shaped DMLS Ti6Al4V(ELI) nose wheel fork, provided experimentally determined mechanical properties, fatigue properties and inherent surface roughness were integrated into the model. Based on static and fatigue performance testing, as well as standardised destructive and non-destructive testing, the potential to produce a dimensionally accurate full-scale nose wheel fork of the AHRLAC in Ti6Al4V(ELI) through DMLS was confirmed. Improved fatigue performance of a full-scale DMLS Ti6Al4V(ELI) nose wheel fork can be obtained through surface finishing.

© Central University of Technology, Free State

RESEARCH OUTPUTS

A summary of the main research outputs originating from this work is provided in this section. Other outputs are provided in Appendixes A and B.

Peer-reviewed journal articles:

- L. F. Monaheng, W. B. Du Preez and C. Polese, "Towards qualification in the aviation industry: Impact toughness of Ti6Al4V(ELI) specimens produced through laser powder bed fusion followed by two-stage heat treatment", *Metals (Basel)*, vol. 11, no. 1736, pp. 1–12, 2021, https://doi.org/10.3390/met11111736

- H. P. Miya, W. B. du Preez and L. F. Monaheng, "High cycle fatigue performance of Ti6Al4V(ELI) specimens produced with inherent laser powder bed fusion surface roughness", *South African Journal of Industrial Engineering*, vol. 32, no. 3, pp. 248–257, 2021, https://doi:10.7166/32-3-2659

- L. F. Monaheng, W. B. du Preez and C. Polese, "Failure analysis of a landing gear nose wheel fork produced in Ti6Al4V(ELI) through selective laser melting", *Engineering Failure Analysis*, p. 107548, 2023, https://doi:10.1016/j.engfailanal.2023.107548.

Peer-reviewed international conference papers:

- L. F. Monaheng, W. B. du Preez, N. Kotze and M. Vermeulen, "Topology optimisation of an aircraft nose-wheel fork for production in Ti6Al4V by the Aeroswift high-speed laser powder bed fusion machine", *14th World Conference on Titanium*, MATEC Web of Conferences, vol. 321, 03103, 2019, Nantes, France, Europe, https://doi.org/10.1051/matecconf/202032103013

- L. F. Monaheng, W. B. du Preez, and C. Polese, "Selective laser melting process chain for development of a Ti6Al4V(ELI) nose wheel fork of a light aircraft", *15th World Conference on Titanium*, 2023, Edinburgh, Scotland, United Kingdom.

Conference and workshop presentations:

- L. F. Monaheng, W. B. du Preez, and C. Polese, "Towards qualification: Fatigue crack growth rate of Ti6Al4V(ELI) specimens produced through Direct Metal Laser Sintering", Virtual conference: The ASTM International

© Central University of Technology, Free State

Conference on Additive Manufacturing (ASTM ICAM - 2021), Anaheim, California, United States.

- L. F. Monaheng, W. B. du Preez, and C. Polese, “Failure analysis of a landing gear nose wheel fork produced in Ti6Al4V(ELI) through selective laser melting”, Virtual conference: The 9th International Conference on Engineering Failure Analysis (ICEFA 2022), 2022, Shanghai, China, Asia.

- L. F. Monaheng, W. B. du Preez, C. Polese, “Failure analysis of a landing gear nose wheel fork produced in Ti6Al4V(ELI) through selective laser melting”, 25th Annual Research Seminar of FEBIT at CUT, Free State, 15 November 2022. 3rd Best Presentation Award.

- L. F. Monaheng, W. B. du Preez, and C. Polese, “The performance of the scaled-down landing gear nose wheel fork produced in Ti6Al4V(ELI) through L-PBF”, The Aeronautical Society of South Africa Conference (AeSSA 2023), CSIR International Convention Centre, Pretoria.

© Central University of Technology, Free State

ACKNOWLEDGEMENTS

Glory to the Almighty God for permitting me a life and energy to complete my study. Many thanks to my promoter Prof. Willie du Preez for his priceless support and guidance throughout my study. My sincere gratitude to my co-promoter Prof. Claudia Polese for her constant technical support in my studies.

I acknowledge and thank Altair, SIMTEQ and FEAS for availing the SolidThinking Inspire software, MSC software and Abaqus plus FE-Safe, respectively. This software added significant value to the design for additive manufacturing of the nose wheel fork of the light aircraft.

My deepest thanks to the Centre for Rapid Prototyping and Manufacturing (CRPM) of the Faculty of Engineering, Built Environment and Information Technology, Central University of Technology, Free State (CUT) for allowing the additive manufacturing facilities to produce, heat treat and analyse the microstructure of the test specimens and scaled-down nose wheel fork. With the same breath, thanks to the Product Development Technology Station (PDTS) of CUT for the development of the test jig used to test the nose wheel fork. My sincere gratitude to Mr Emmanuel Zungu from the CUT Library for the uninterrupted supply of technical articles and books even during the COVID-19 pandemic.

I take this opportunity to thank the Mechanical Testing Laboratory of the CSIR for providing facilities to perform tensile, fracture toughness, fatigue crack growth rate and high cycle fatigue tests. I also thank CSIR for machining the scaled-down nose wheel fork bores to size. As for testing of impact toughness specimens, thanks to the SecMet subsidiary of MegChem Holdings (Pty) Ltd. I also wish to thank Necsa for allowing access to the facilities to determine the porosity in the Ti6Al4V(ELI) specimen built through SLM. The author acknowledges the Department of Geology at the University of the Free State (UFS) for providing the scanning electron microscope (SEM) for analysis of the fracture surfaces of the impact and fatigue specimens.

My deepest gratitude to the Centre for Asset Integrity Management (C-AIM) in the Department of Mechanical and Aeronautical Engineering of the University of Pretoria (UP) for availing facilities to perform static and fatigue testing of the scaled-

© Central University of Technology, Free State

down nose wheel fork. Without such tests, the design of the Ti6Al4V(ELI) nose wheel fork produced through L-PBF would have no significant value. The author acknowledges the TANDM test and measurement for supplying the strain gauges and their accessories.

The author also expresses sincere gratitude to the following departments for their financial support: The South African Department of Science and Innovation through the Collaborative Program in Additive Manufacturing, contract No.: CSIR-NLC-CPAM-18-MOA-CUT-01 and contract No.: CSIR-NLC-CPAM-21-MOA-CUT-01. The Department of Higher Education and Training (DHET), University Capacity Development Grant (UCDG) 2021, Research Grants and Scholarships Committee of Central University of Technology, Free State. Financial support from the Chair in Innovation and Commercialisation of Additive Manufacturing is also gratefully acknowledged. Finally, thanks to the employee study staff tuition support of CUT.

DEDICATIONS

This doctoral thesis is dedicated to my lovely wife Limakatso Innocentia Monaheng, my son Kamohelo Charity Monaheng, my daughter Relebohile Monaheng, my late grandmother Malehola Annatleta Monaheng, and other fellow researchers in the field of finite element analysis applied in design for additive manufacturing.

© Central University of Technology, Free State

TABLE OF CONTENTS

© Central University of Technology, Free State

© Central University of Technology, Free State

© Central University of Technology, Free State

5. CHAPTER 5: MECHANICAL AND FATIGUE PROPERTIES OF L-PBF TI6AL4V(ELI) SPECIMENS 125

6. CHAPTER 6: PERFORMANCE OF THE L-PBF Ti6Al4V(ELI) NOSE WHEEL FORK 149

© Central University of Technology, Free State

© Central University of Technology, Free State

© Central University of Technology, Free State

LIST OF FIGURES

© Central University of Technology, Free State

© Central University of Technology, Free State

© Central University of Technology, Free State

© Central University of Technology, Free State

© Central University of Technology, Free State

© Central University of Technology, Free State

© Central University of Technology, Free State

© Central University of Technology, Free State

LIST OF TABLES

© Central University of Technology, Free State

© Central University of Technology, Free State

LIST OF SYMBOLS AND ABBREVIATIONS

1D	One-Dimensional
2D	Two-Dimensional
3D	Three-Dimensional
AHRLAC	Advanced High-performance Reconnaissance Light Aircraft
AM	Additive Manufacturing
ASTM	American Society for Testing and Materials
BCC	Body-Centered Cubic
BTF	Buy-to-Fly
CAD	Computer-Aided Design
CAGR	Compound Annual Growth Rate
CFR	Code of Federal Regulations
CG	Centre of Gravity
CMM	Coordinate Measuring Machine
CNC	Computer Numerical Controlled
CUT	Central University of Technology, Free State
DfAM	Design for Additive Manufacturing
EASA	European Union Aviation Safety Agency
EDM	Electrical Discharge Machining
ELI	Extra Low Interstitial
FAA	Federal Aviation Administration
FCGR	Fatigue Crack Growth Rate
FEA	Finite Element Analysis
GA	General Aviation
GF	Gauge Factor
HCP	Hexagonal-Closed Packed
HD	Horizontal Direction
HIP	Hot Isostatic Pressing
HS-SLM	High-speed Selective Laser Melting
HTA	High Temperature Annealing
K_{IC}	Fracture Toughness
LD	Longitudinal Direction
L-PBF	Laser Powder Bed Fusion
MAM	Metal Additive Manufacturing
MMA	Method of Moving Asymptotes
SA	South Africa
SEM	Scanning Electron Microscopy
SIMP	Solid Isotropic Material with Penalisation
SD	Standard Deviation
SG	Strain Gauge
SLM	Selective Laser Melting
SLP	Sequential Linear Programming
SQP	Sequential Quadratic Programming
Tet-10	Ten-node Tetrahedron
TO	Topology Optimisation
USD	United State Dollar
UTS	Ultimate Tensile Strength

RBE	Rigid Body Elements
α’ phase	Martensitic Alpha Phase
β phase	Beta Phase

© Central University of Technology, Free State

CHAPTER 1: INTRODUCTION

1.1. Background

The military aviation market was projected to increase at a compound annual growth rate (CAGR) of 7.37% from 52.17 billion USD in 2023 to 74.44 billion USD by 2028 [1]. Armed war and internal security were stated to be the contributing factors to this global demand for defence aircraft. The 2022-2028 forecast CAGR percentage of the military aviation market for various regions is shown in Figure 1.1.

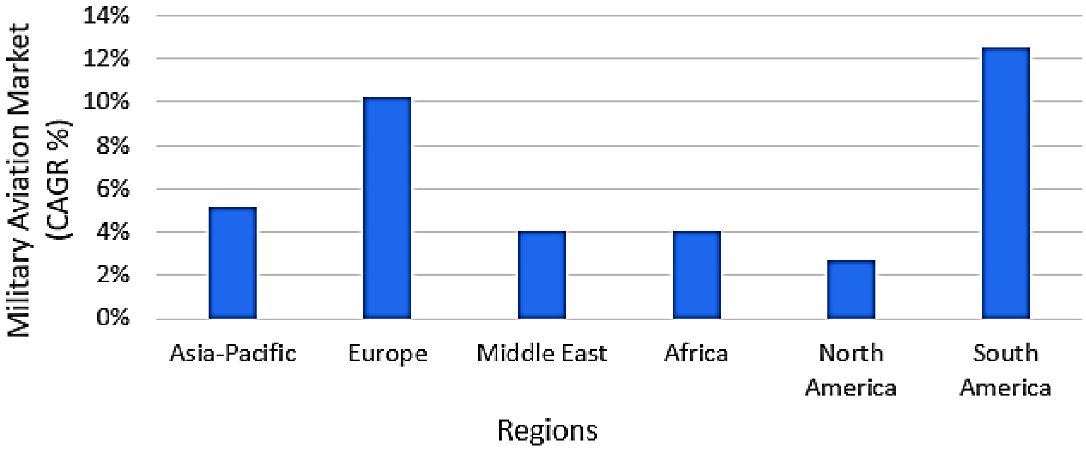

Figure 1.1: The projected CAGR % of the military aviation market for different regions for 2022-2028 [1]

This increasing demand for military aircraft is expected to accelerate the application of new manufacturing technologies. Additive manufacturing (AM), as a rapidly growing technology for the fabrication of end products, has the potential to be accepted in the aerospace industry. The strategic nature of this technology for production has been widely accepted by various countries such as the United States and Germany. It is actively promoted by companies such as Airbus, Boeing and General Electric [2].

The current study entails the redesign and characterisation of the landing gear nose wheel fork of a light aircraft for production in Ti6Al4V (extra-low interstitial (ELI)) through laser powder bed fusion (L-PBF). It was initiated in response to the South African Additive Manufacturing Strategy with a priority focus area of identifying and

© Central University of Technology, Free State

selecting opportunities that can contribute towards South Africa’s socio-economics essentials [3]. The production of aerospace parts through AM was among the high priority opportunities. Subsequently, the qualification of the AM parts for the aerospace and military markets, based on current customer and collaboration agreements with the original equipment manufacturer (OEM), was set out as one of the focus areas. Development of new AM systems focus area aligned with the current study, especially with the development of the Aeroswift high-speed selective laser melting (HS-SLM) system. This system, with a maximum build volume of 0.6 m x 0.6 m x 2 m, allows the production of large parts such as the nose wheel fork at a rate that is ten times faster than competitive commercial L-PBF systems [4].

The expressed intention of the South African producer of the Advanced High-Performance Reconnaissance Light Aircraft (AHRLAC) to consider replacing the conventional manufacturing of some aircraft components with AM parts provided the opportunity for this study. However, the defects still associated with L-PBF, such as inherent surface roughness and porosity, complicate the certification of L-PBF parts for structural applications, because these have a detrimental effect on the fatigue performance of components. Therefore, the aviation industry has not yet accepted L-PBF as manufacturing technology for parts that experience high dynamic loading during normal operation. For such acceptance by the aviation industry, compliance of the mechanical and fatigue properties of L-PBF components with international standards must be demonstrated.

The AHRLAC is a twin-person cockpit military aircraft driven by a single pusher propeller engine. It was designed by the SA engineering company Aerosud and manufactured by the Paramount Group and its partners in AHRLAC Holdings [5]. Currently, the manufacturer of the AHRLAC is Paramount Aerospace Industries Proprietary Limited, which is a part of Paramount Aerospace and Technology Group [6]. In its production strategy, Paramount Aerospace Industries sought to explore AM for the production of aircraft components [6]. Through metal additive manufacturing (MAM), particularly L-PBF, an excellent buy-to-fly (BTF) ratio can be obtained [7]. For example, the unsustainable BTF ratio of 20:1 is not unusual for the production of complex-shaped parts in the aerospace industry through conventional

© Central University of Technology, Free State

manufacturing methods (milling, forging, turning and drilling), which can be improved to 3:1 if L-PBF could be used [8]. An agreement was reached in 2018 between the Central University of Technology, Free State (CUT) and the Aerospace Development Corporation to investigate the feasibility of manufacturing a nose wheel fork of the AHRLAC through L-PBF, see Appendix C. In Figure 1.2, an image of the AHRLAC and various components of the landing gear nose wheel assembly are shown.

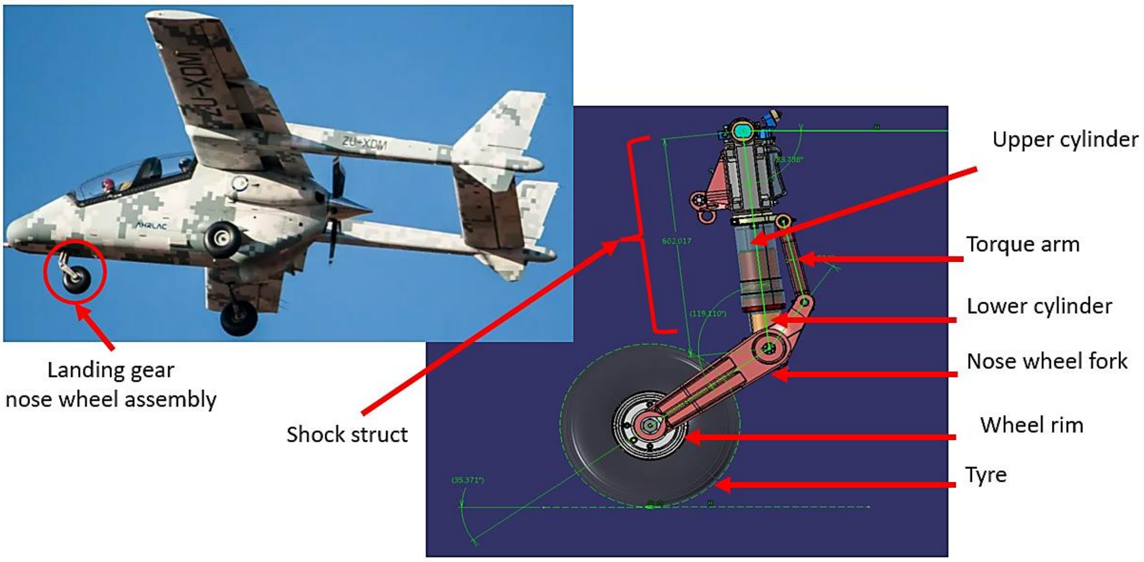

Figure 1.2: An image of the AHRLAC indicating the landing gear nose wheel assembly and its various components [9]

As a critical subsystem of an aircraft, the landing gear serves as a link between the ground and the aircraft fuselage. It is designed to safely handle the ground operations such as taxiing, take-off and landing. Its nose wheel fork, as the main structural part, is traditionally fabricated from aluminium-based alloy. For the AHRLAC, the nose wheel fork was machined from 7050 aluminium alloy mainly through computer numerical controlled (CNC) milling and drilling. In various studies, several landing gear failure cases were recorded [10][11]. In the case of [11], the main failure was due to fatigue occurring mainly in the steel components and corrosion-related problems in the aluminium alloys, with very few overloading failures noted. Franco *et al.* [12] analysed the nose wheel fork of a military transport aircraft for fatigue fracture. They found that the initial crack growth in the nose wheel fork, produced from aluminium by CNC milling, was due to fatigue. The stress raisers around the bolt holes, which acted as the supporting connections on the topside of the aluminium nose wheel fork, were also reported as a cause of fatigue failure [10]. Subsequently, it was concluded that the areas in which fatigue failure originated were subjected to cyclic stress that initiated and propagated cracks in the fork.

The potential fabrication of various parts of an aircraft through L-PBF in titanium alloys has been attractive due to the good mechanical and fatigue properties of the Ti6Al4V(ELI) alloy [13][14]. The global market for titanium alloys, which was impacted negatively by the COVID-19 pandemic, started recovering in 2021 and it is anticipated to reach a CAGR of over 7% by 2028 [15]. As the most widely used titanium alloy in the aircraft sector, Ti6Al4V(ELI) has excellent properties, such as high strength, low density, high fracture toughness and good corrosion resistance [16]. It has distinct strength at higher temperatures of up to 400 °C, unlike the strength of aluminium alloys which diminishes with an increase in temperature [17]. Above a temperature of 150 °C to 300 °C, the strength of aluminium alloys can reduce from 250 MPa to 90 MPa [18]. This ranks titanium alloys highly for the replacement of steel and aluminium-base alloys for application in aircraft engines, fan blades, airframes and fasteners [19]. Moreover, titanium is selected for the production of aircraft parts due to its potential to act as a strategic economic driver in developing countries such as South Africa (SA) [20]; consequently, fulfilling the beneficiation strategies for the mineral industry in SA, which promotes titanium value-added products instead of only exporting the raw material [21].

The digital design process could provide a solution to the aerospace industry for the design of structural components with a good strength-to-weight ratio [22]. Topology optimisation (TO) during the redesign of existing aircraft parts for production through AM is a computational tool for achieving the required solution [23]. Through TO, the requirement to remove material from a design domain, while ensuring that the final component strength remains acceptable, can be achieved [24]. This often results in a complex-shaped component that is impractical to produce through conventional manufacturing methods, but quite feasible through AM [25]. The TO technique has

© Central University of Technology, Free State

been applied in the aviation industry for the optimisation of various components such as aircraft brackets, wings and struts [26][27][28]. Chengwei *et al.* [29], demonstrated the inclusion of TO in the design procedure through a redesign of a structural part of a landing gear named the low drag, whereas Wu *et al*. [30] optimised a landing gear strut under fatigue constraints. A landing gear strut was also designed using TO in an attempt to produce it through AM by Cain [31]. Niutta *et al*. [32], explored the significance of AM defects on the fatigue performance of a topologically optimised aircraft component. However, the fatigue performance of a landing gear structural component produced through AM, particularly an L-PBF component designed by using the TO process and fabricated in Ti6Al4V(ELI), is still to be investigated.

Design for additive manufacturing (DfAM) is defined as the practice of designing and optimising a product together with its production system to reduce development time and cost while increasing the end-product performance and profitability [33]. The design goals and manufacturing constraints, such as user and market needs, material, process, assembly, and disassembly methods, are considered during the design process [34]. Consideration of multiple aesthetic, functional and manufacturing requirements is essential to transform a computer-aided design (CAD) model into an end product free from design and manufacturing defects at the first attempt. However, implementation of such a procedure is still challenging [35] since DfAM knowledge, tools, rules, processes and methodologies are insufficiently understood. Irrespective of the recent advancement of AM, which broadens the application from the fabrication of prototypes to the production of functional parts, tight geometric tolerance and strict surface integrity required in the aircraft industry are not achievable [36]. This limits the penetration of DfAM in industries such as the aerospace industry [37], holds back the rapid use of AM for the production of end-use parts [38], especially the mission-critical components and prevents the designer from fully benefiting from AM [39].

The rapid development of DfAM-supporting software, such as Simufact Additive for prediction of AM processes and SolidThinking Inspire for TO, has been promoting the use of AM technology [39]. However, validation of these software packages is necessary because they are based on finite element analysis (FEA) principles, which imply that the accuracy of a predicted variable depends on the input data such as the CAD model, mesh, loads and constraints [40]. If the input data is inaccurate the predicted results will be inaccurate [41].

Apart from the design-related aspects, defects in L-PBF parts, such as internal porosity and surface roughness, have a detrimental impact on the fatigue properties of Ti6Al4V(ELI) parts, because they form material discontinuities, which can cause initiation of fatigue fracture [42]. Pores in L-PBF parts can be due to porous metal powder, entrapment of gasses in the molten material, lack of fusion and the presence of unmelted powder particles between the layers [43]. Lack-of-fusion pores have the largest pore size compared to pores created by other sources and its random distribution results in low fatigue resistance, as well as large scatter in fatigue life [44]. Another factor impacting the fatigue properties of L-PBF parts is residual stress induced in the built parts due to the high temperature gradients involved in the L-PBF build process [45]. In parts produced through L-PBF, the resulting surface stresses are usually tensile [46]. Tensile residual stresses in the surfaces of components can support crack initiation during cyclic loading. However, pores can be reduced, if not removed, by hot isostatic pressing (HIP) and residual stress can be removed completely by stress-relieving heat treatment [47][48]. The inherent surface roughness of L-PBF Ti6Al4V(ELI) components is challenging to remove evenly across a large volume component with a complex shape. It was found that only 20% of this can be reduced through chemical etching [49].

Stringent aerospace standards are limiting the rapid growth of L-PBF applications in the aircraft industry. The qualification challenges for the production of aircraft parts through L-PBF were presented in several studies [50][51][52]. Aviation authorities such as the Federal Aviation Administration (FAA) and the European Aviation Safety Agency (EASA), are the approving bodies for aircraft components and certify the manufacturing technology used [53]. The main challenge faced by designers is to establish the material data needed for a design since it is compulsory to demonstrate that an aircraft part meets all requirements through performance testing and analytical calculations [50]. Another proposed compliance method is

© Central University of Technology, Free State

known as Certification by Analysis (CbA), which is a simulation method used to generate results for certification compliance that have conventionally been obtained through physical flight tests or ground-based testing [54]. Normally, an accepted material database of titanium alloys is used for designing landing gear, but for the production of a landing gear component through an emerging manufacturing process such as L-PBF, data for a specific product is often not available [55].

1.2. Problem statement

As discussed, the demand for a manufacturing process that could lead to reduced material wastage, machine operation and cost of production of high-quality, lightweight and structurally sound metal parts of aircraft, has resulted in extensive research on introducing L-PBF of Ti6Al4V as manufacturing technology in the aviation industry. However, the lack of proven design methodology for L-PBF processes and well-established DfAM knowledge, tools, rules and processes, are impeding the acceptance in the aviation industry. Therefore, a study on the redesign, including TO, for manufacture through L-PBF of a Ti6Al4V(ELI) component that would comply with aviation standards and specifications, while being cost effective and lighter in weight than the existing conventionally produced part, was needed. The required output of such a study would be data on the properties of the selected component that would contribute towards its qualification. For this, the AHRLAC nose wheel fork was selected. Redesign of the nose wheel fork had to, as far as practicable, avoid points of stress concentration where localised fluctuating stress above the fatigue limit would be likely to occur in normal service. The method of fabrication used should produce a consistently sound nose wheel fork. In addition, the suitability and durability of the material had to meet the approved specifications to ensure that the component would have the desired mechanical properties. Lastly, the operational performance of the fork, which would be directly related to its design, had to be established through non-destructive and destructive testing techniques.

1.3. Aim of the study

The study was aimed at developing guidelines for the DfAM approach and redesign of an optimised nose wheel fork of a light aircraft for production in Ti6Al4V(ELI) through L-PBF. The component would have to be characterised to demonstrate compliance with aircraft standards and requirements. Data required on the suitability and durability of the L-PBF Ti6Al4V(ELI) component had to be collected. The research was expected to contribute towards the acceptance by the aviation industry of L-PBF as a manufacturing process for structural components.

1.4. Objectives of the study

- To confirm the reliability of the L-PBF process by determining the microstructural, mechanical and fatigue properties of the Ti6Al4V(ELI) test specimens.
- To redesign and build a scaled-down prototype L-PBF Ti6Al4V(ELI) nose wheel fork.
- To evaluate the performance of the scaled-down prototype nose wheel fork through mechanical and fatigue testing under simulated operational load conditions.
- To assess all results and draw conclusions on the prospects of designing and producing components through L-PBF which would be suitable for structural aircraft applications.

1.5. Original contribution:

The conventionally manufactured nose wheel fork of the AHRLAC was redesigned and produced in Ti6Al4V(ELI) through L-PBF to deliver a novel topology optimised component. From the performance test results of the prototype scaled-down nose wheel fork, an assessment was made regarding the potential for producing qualified structural aircraft components through L-PBF in Ti6Al4V(ELI).

© Central University of Technology, Free State

The study provides researchers in the AM field with valuable insight into the performance and failure mechanism of the L-PBF Ti6Al4V(ELI) scaled-down nose wheel fork of the light aircraft for comparison with failure mechanisms of components manufactured using traditional processes. Through this output, the research makes a valuable contribution towards the qualification of metal AM for the production of structural aircraft components.

1.6. Delimitation of the study

Although the eventual purpose remains the production of the full-scale nose wheel fork in the Aeroswift HS-SLM machine, the current study was limited to research on a scaled-down Ti6Al4V(ELI) nose wheel fork that was produced through direct metal laser sintering (DMLS). This was due to the fact that the Aeroswift machine had to undergo major maintenance after malfunctioning of its laser unit during the initial trial production of the full-scale nose wheel fork. Maintenance took a year and a half to be completed and did not allow the full-scale component to be manufactured in the residence period of this D Eng study.

1.7. Layout of the thesis

The first chapter provides the background, problem statement, aims and objectives of the study as well as its original contribution and the delimitation of the study. A literature review, including a theoretical framework of the most important concepts of the study, is presented in Chapter 2. In Chapter 3, the research methodology is presented. The characteristics of the designed L-PBF Ti6Al4V(ELI) nose wheel fork of the AHRLAC are presented in Chapter 4. This chapter deals with the load paths necessary for optimal design, based on the safety factor, as well as the obtained geometric accuracy, porosity and surface roughness of the L-PBF Ti6Al4V(ELI) scaled-down nose wheel fork. In Chapter 5, the results of the standard test specimens are presented to accumulate data necessary for qualification of L-PBF as the technology for production of the Ti6Al4V(ELI) nose wheel fork. This includes tensile, impact toughness, fracture toughness, FCGR and HCF properties of the L-

PBF Ti6Al4V(ELI) specimens. Subsequently, Chapter 6 presents the performance of the L-PBF Ti6Al4V(ELI) scaled-down nose wheel fork under static and dynamic experimental loading conditions. The microstructure and fractography of the tested L-PBF Ti6Al4V(ELI) scaled-down nose wheel fork are also presented in Chapters 5 and 6. Discussions of the results are presented in Chapter 7. Finally, in Chapter 8 conclusions and recommendations drawn about the capability of L-PBF for production of Ti6Al4V(ELI) mission-critical structural aircraft components are presented. Figure 1.3 shows the layout of the thesis.

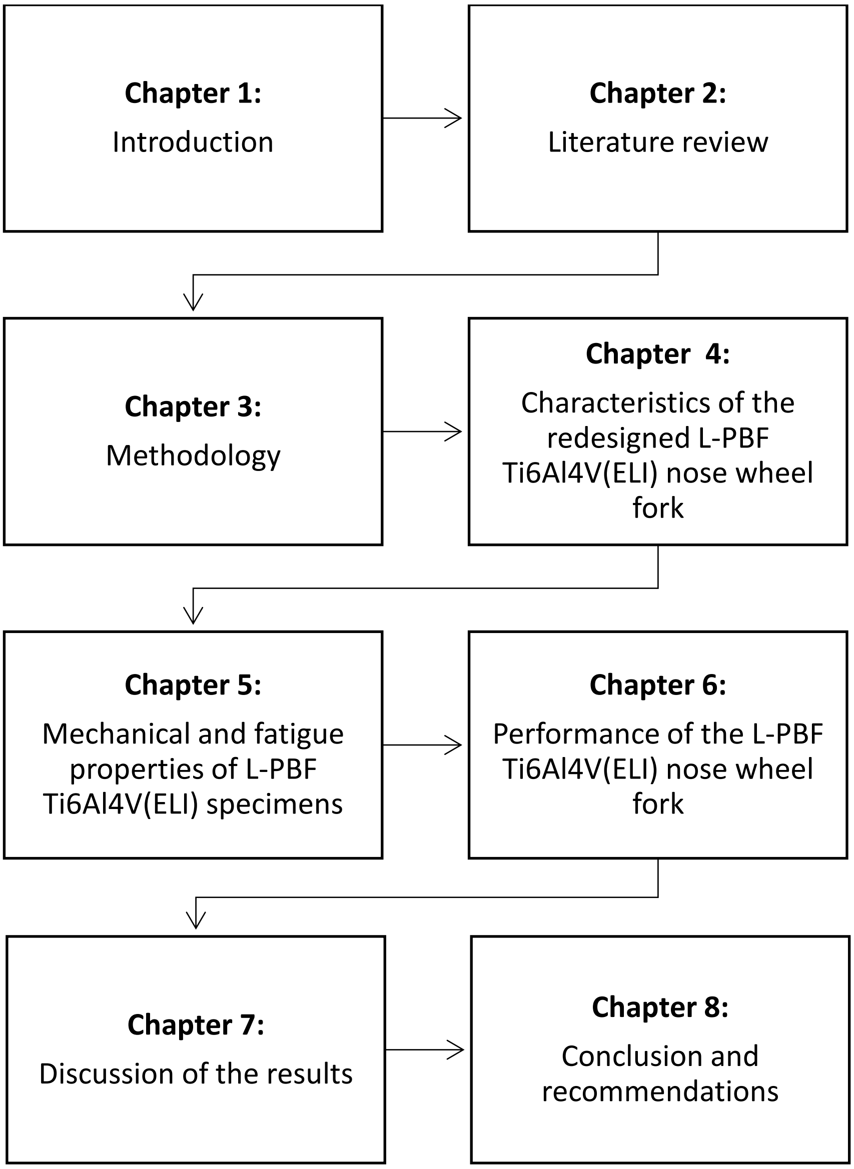

Figure 1.3: The layout of the thesis

© Central University of Technology, Free State

CHAPTER 2: LITERATURE REVIEW

2.1. Introduction

In this chapter, the structural features of the landing gear that determine the load experienced by the nose wheel fork, are discussed. It starts with the configuration of the landing gear, particularly the tricycle and its components, and ends with the fundamental formulation of forces. This is guided by the General Aviation (GA) Code of Federal Regulations (CFR) for the application of landing gear 14 CFR 23.471 to 23.511 [56]. Subsequently, the structural optimisation procedure that is commonly applied during DfAM is presented. Discussions of TO, followed by FEA, fatigue simulation and experimental validation of numerical models are described. Thereafter, the obtainable quality of Ti6Al4V(ELI) components produced through L-PBF is discussed. This includes the geometric accuracy, microstructure and its effect on the mechanical properties, as well as the fatigue properties. Moreover, the mechanical and fatigue properties of L-PBF Ti6Al4V(ELI), captured experimentally and available in literature, are discussed. Mechanical properties involved tensile strength, impact toughness and fracture toughness, whereas the fatigue properties include low and high cycle fatigue as well as the fatigue crack growth rate (FCGR). These data would confirm the readiness of L-PBF for the production of mission-critical components of an aircraft in Ti6Al4V(ELI) [57]. Finally, a summary of the insights gained from the literature review presented in this chapter is provided.

2.2. The structure of the landing gear

2.2.1. Landing gear configuration

Designing a retractable landing gear, the kinematics of the landing gear mechanism and the space claimed inside the airframe are challenging. Even once the configuration of the landing gear has been resolved, other design issues are still not trivial [57]. In Figure 2.1, the commonly used landing gear configurations of light aircraft are shown.

© Central University of Technology, Free State

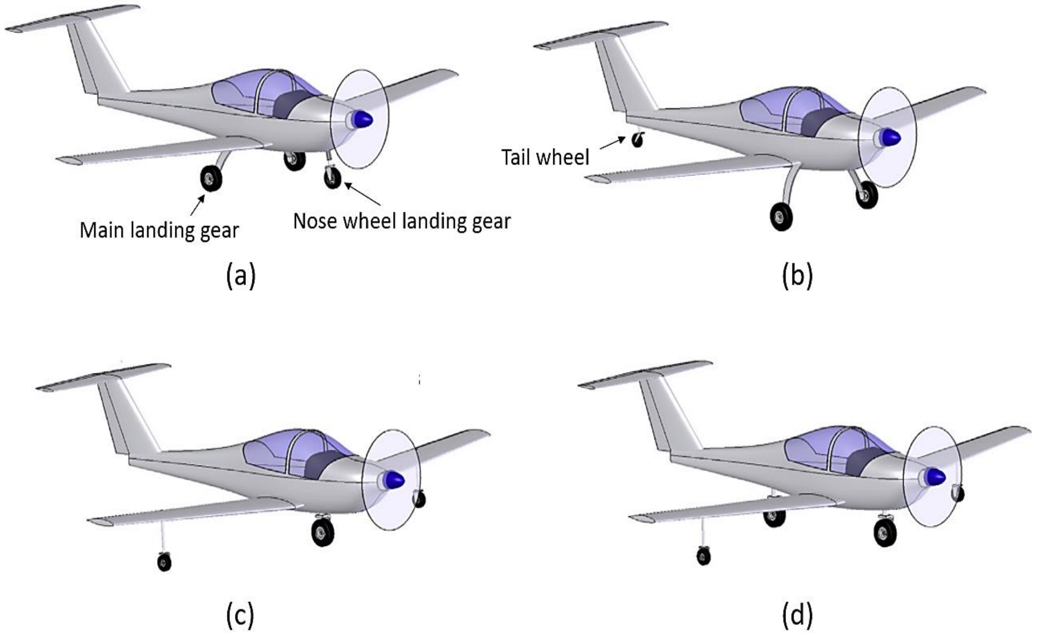

Figure 2.1: The common configurations of the landing gear of light aircraft: (a) tricycle, (b) taildragger, (c) monowheel with outrigger, and (d) tandem with outrigger [57]

A total of 95.5% of current aircraft use tricycle and taildragger configurations. Alternative configurations are considered if the common one does not fit the purpose [57]. In the AHRLAC, the tricycle landing gear configuration is used. For a successful design of the tricycle landing gear configuration, the position of the nose wheel, aircraft ground clearance, tyres and tyre inflation pressure, as well as landing impact and braking, must be considered. The nose wheel must be positioned with respect to the centre of gravity (CG) to avoid ground looping and overturning [57]. The nose wheel gear must carry a balanced load since a highly loaded nose wheel fork results in high resistance to the rotation of the aeroplane during take-off. On the other hand, a light-loaded nose wheel landing gear promotes unwanted impact forces and makes the steering of the aircraft harder due to the reduced ground friction. This promotes bouncing on the ground. Diagrams used to identify the wheel positions of the tricycle landing gear are shown in Figure 2.2.

© Central University of Technology, Free State

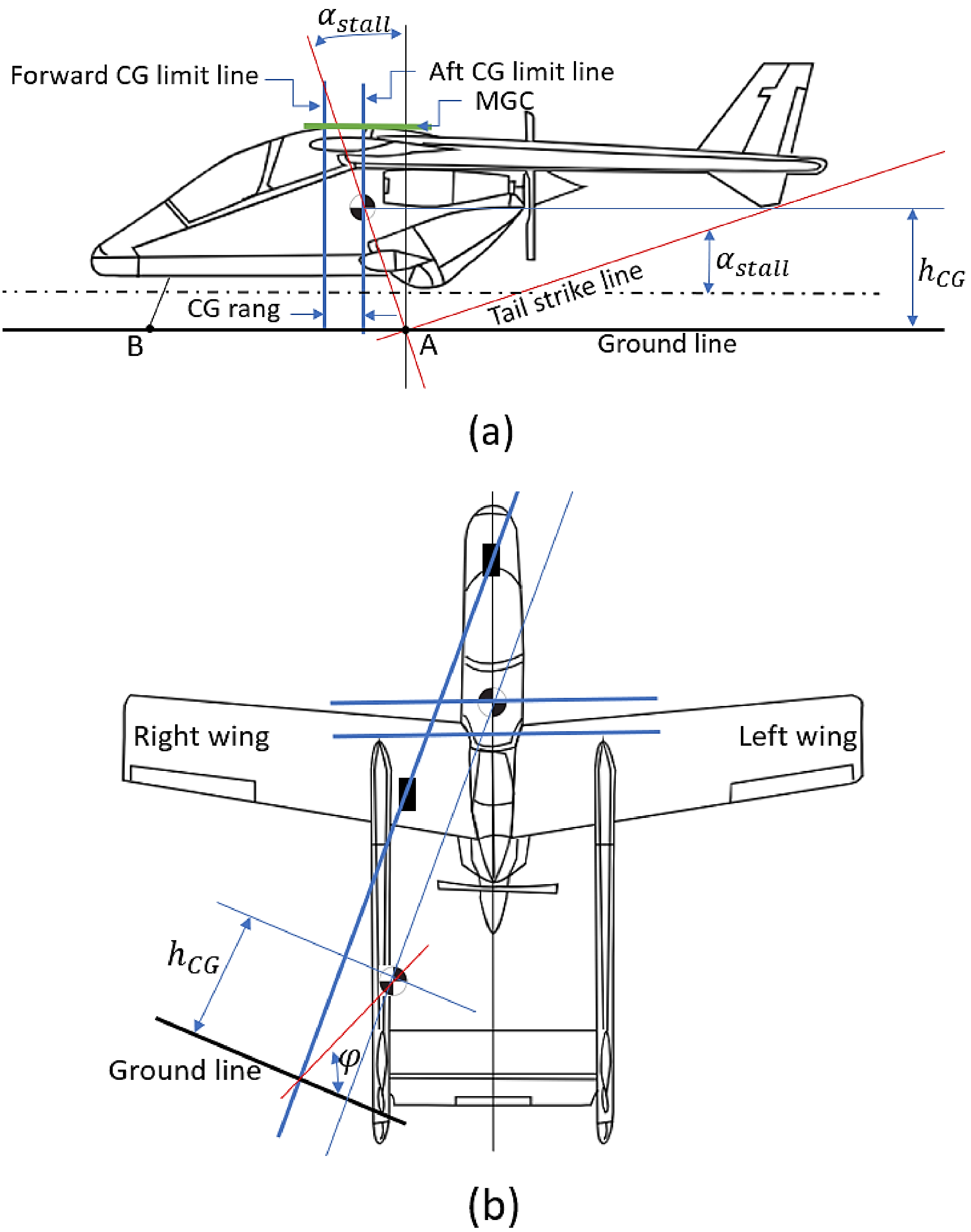

Figure 2.2: Diagrams used to identify the wheel positions of the tricycle landing gear, (a) side view, and (b) top view of the aircraft

During the positioning of the aircraft wheels, the CG must first be located. Thereafter, the forward and aft CG limit must be determined and plotted on the side of the aircraft, as shown in Figure 2.2 (a). The tail strike line is then created

© Central University of Technology, Free State

from the lowest tip of the aircraft tail and is recommended to be at a stall angle (α_{stall}) of 15° to avoid a tail crash during take-off. Thereafter, a normal line to the tail strike, which passes through CG is constructed to identify the position of the main landing gear tyre, see point A in Figure 2.2 (a). Thus, the nose wheel landing gear is allocated no more than 20% of the aircraft weight when the CG is at the forward limit, and no less than 10% when the CG is at the aft limit. Point B in Figure 2.2 (a) represents the contact between the nose wheel tyre and the ground. Finally, angle φ in Figure 2.2 (b) is recommended to be less than 63° for land-based aircraft to avoid overturning [57]. If φ is larger, the wheel track and wheelbase must be increased, while the height of the landing gear is reduced.

2.2.2. Tyres, tyre inflation and wheels

The weight of the aircraft, the number of tyres and the bearing capability of the airfield that the aircraft should be operated on are the contributing factors to the selected inflation pressure. The load rating of the main gear tyre depends on the maximum gross weight and the CG location of the aircraft. This rating should allow a 25% increase in gross weight. The nose wheel of a light aircraft such as the AHRLAC uses type III tyres as designated by the Tire and Rim Association (TRA) technical standardising body of the USA [58]. The inflation pressure of this tyre should be based on the allowable dynamic loads. This should be equal to 1.4 times the static maximum vertical load. In Figure 2.3 (a), the important dimensions of the tricycle landing gear system are shown. This figure also demonstrates the caster angle (∅) commonly used in light aircraft for steering nose wheel landing gear.

© Central University of Technology, Free State

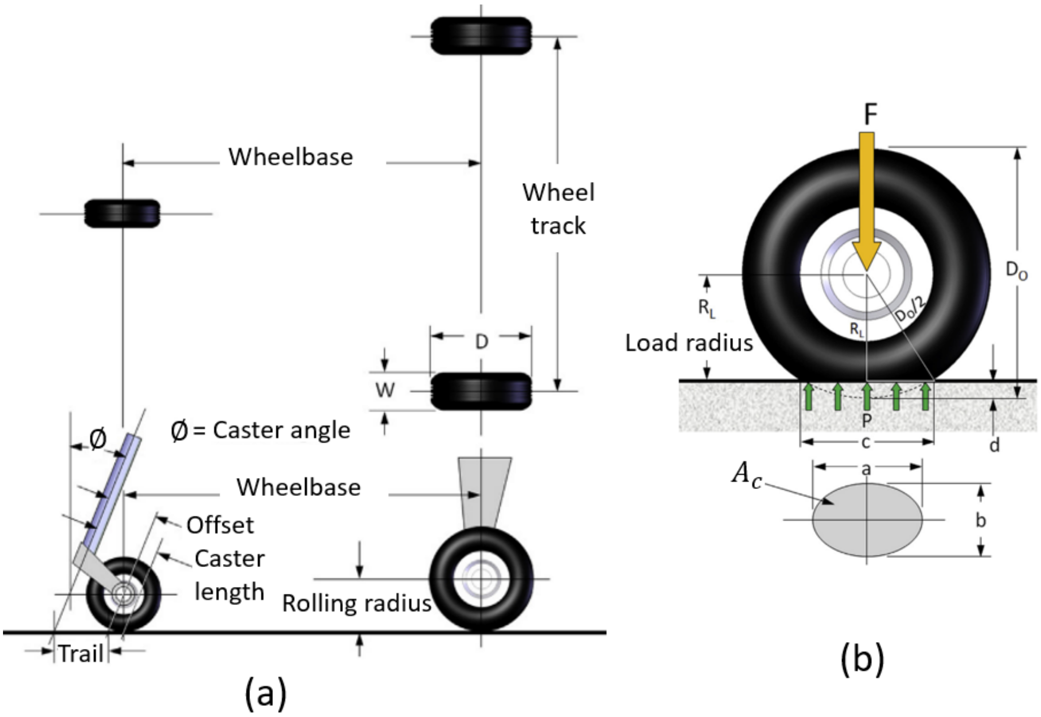

Figure 2.3: (a) Geometric dimensions of the tricycle landing gear, and (b) tyre footprint [59]

The tyre in contact with the ground resembles an ellipse on the surface of the ground because it flattens slightly as the weight (F) of the aircraft is applied. This phenomenon is illustrated in Figure 2.3 (b). The average pressure (P) generated on the contact area (A_c) amounts to:

$$\boldsymbol{P} = \frac{F}{A_c} = \frac{4F}{\pi \cdot a \cdot b} \tag{2.1}$$

Aluminium alloy wheels that were fabricated through a forging process are recommended [58]. These wheels can carry high landing loads from the point when the tyre touches the ground until the aircraft comes to a stop [60]. Such ground loads are distributed through the entire elements of the landing gear assembly, which includes the nose wheel fork.

2.2.3. Ground loads and constraints of the landing gear

A landing gear of an aircraft must handle various ground load scenarios such as landing on main gear only, side impact landing, three-point landing, high speed

© Central University of Technology, Free State

taxiing, brake roll, etc. [61]. As a result, very high load magnitudes are experienced by the landing gear. In general aviation, the impact loads are normally absorbed using leaf-spring, rubber doughnuts, rubber bungees, coiled steel springs or oleo-pneumatic shock absorbers [59]. The complexity and efficiency of these damping systems are illustrated in Figure 2.4 (a to d) and (e to h), respectively. The efficiency is represented by the stiffness constant (K_s), which relates the applied load with the deflection.

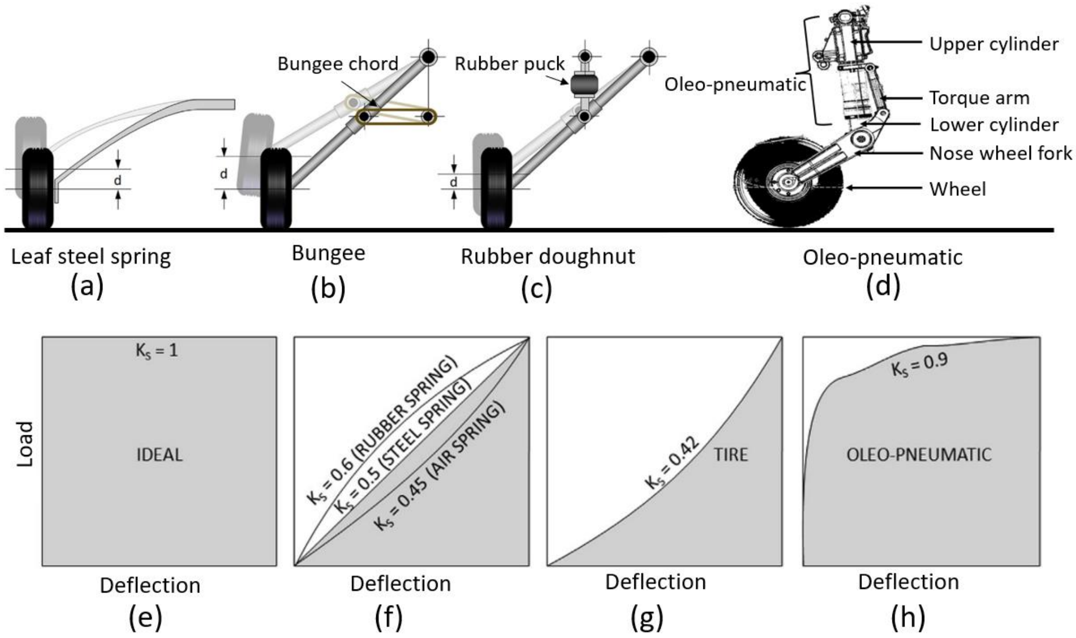

Figure 2.4: The complexity of various shock absorber systems (a) leaf steel spring, (b) bungee, (c) rubber doughnut, and (d) oleo-pneumatic as well as the efficiency of (e) an ideal system (no deflection when load is applied), (f) rubber, steel and air spring system, (g) rubber puck of doughnut and (h) oleo-pneumatic [59]

Various shock struts dissipate impact energy differently due to its K_s. For example, shock struts with high K_s resist deflection and can carry a higher impact load than other systems with low factor. The oleo-pneumatic system is the most efficient damping system to dissipate the impact energy of an aircraft during landing. However, this is the heaviest and most complex to construct dashpot compared to other systems, which provides an opportunity to optimise its structural components, such as the nose wheel fork.

The loads and constraints are primary inputs during structural optimisation. Figure 2.5 shows the loads and boundary conditions of a tricycle landing gear configuration which is fitted with the oleo-pneumatic shock absorber. The symbols R_N, and R_M, represent the vertical reaction forces on the nose and main landing gear wheels, respectively. R_{Nx}, and R_{Mx} represent the horizontal reaction forces also on the nose and main landing gear wheels, respectively. The symbols M_W, W, L_W, T, and L_{HT} represent pitching moment, total weight of the aircraft through the CG, wing lift, thrust and horizontal tail lift. Finally, the symbols x_N, x_M, x_W, L_{HT}, h_{CG} and y_T stand for the distances between the CG and the nose wheel reaction force, main landing gear reaction force, wing lift, horizontal tail lift, ground and the thrust line of action, respectively [57].

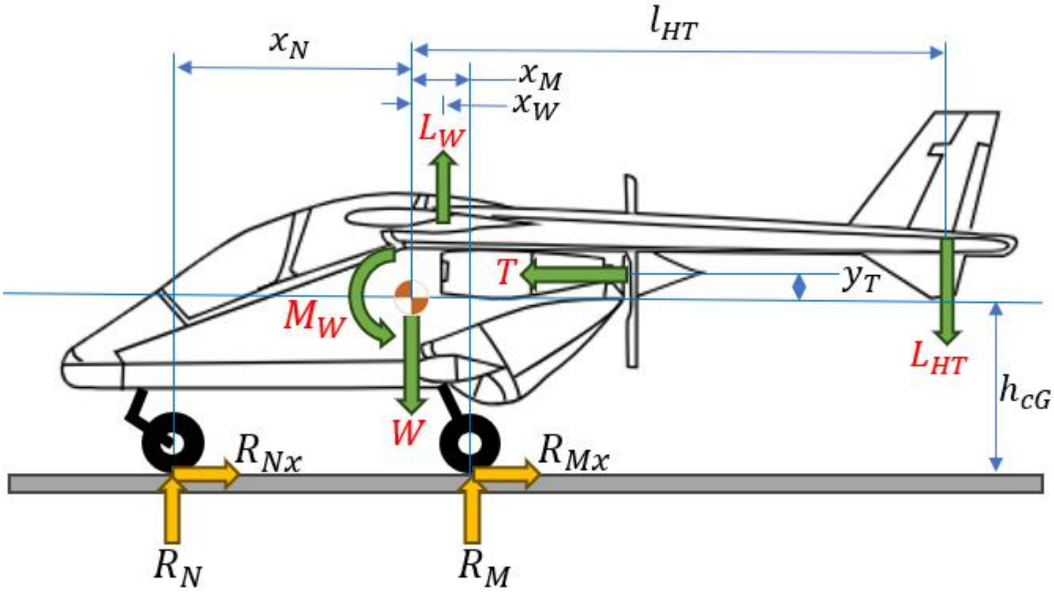

Figure 2.5: A diagram of the balanced forces when the tricycle aircraft has reached a constant speed on the runway [57]

The forces in the diagram are in a balanced state when the aircraft is moving at a constant speed. The set of equations presented in this section is based only on the forces experienced by the nose wheel fork, since the current study is based on redesigning the nose wheel fork for production in Ti6Al4V(ELI) through L-PBF. The sum of the horizontal reaction forces acting on the aircraft nose and main landing gear are presented as:

© Central University of Technology, Free State

$$\boldsymbol{R_{Nx} + R_{Mx} = \mu(R_N + R_M)} \qquad (2.2)$$

where μ is the coefficient of friction between the tyre and the ground surface.

The sum of the vertical forces (in the Z-direction) is given by:

$$\boldsymbol{\sum F_z = 0 \ \rightarrow R_N + R_M + L_W - W - L_{HT} = 0} \qquad (2.3)$$

By taking a moment about the CG such that the nose pitch-up moments are positive, Equation 2.4 is obtained.

$$\sum M_{CG} = 0 \quad \rightarrow$$

$$\boldsymbol{-T \cdot y_T + R_N \cdot x_N - R_M \cdot x_M - L_W \cdot x_W + L_{HT} \cdot l_{HT} - \mu(R_N + R_M) \cdot h_{CG} + M_W = 0} \qquad (2.4)$$

By integrating Equation 2.3 into 2.4 to replace R_M and rearranging it to obtain the reaction force (R_N), equation 2.5 is obtained. This represents the reaction force of the nose wheel when the aircraft is moving at constant speed.

$$\boldsymbol{R_N = \frac{T \cdot y_T + (W + L_{HT} - L_W) \cdot (x_M - \mu h_{CG}) + L_W \cdot x_W - L_{HT} \cdot l_{HT} - M_W}{x_N + x_M - 2\mu \cdot h_{CG}}} \qquad (2.5)$$

The reaction force of the nose wheel when the aircraft is in the static position is given by:

$$\boldsymbol{R_N = \frac{W \cdot x_M}{x_N + x_m}} \qquad (2.6)$$

In addition, the brakes must handle the load associated with stopping the aircraft after landing, aborted take-off and keeping the aircraft at rest during full engine power, thereby allowing the aircraft to be steered via differential braking. Two commonly used brake systems are drum and disc brake systems. The drum brake system is the best solution for retractable landing gear, because it resides in the wheel, leading to the reduction of space occupied by the landing gear assembly in the airframe. However, the disc brake system provides superior performance, is easier to maintain and is lighter compared to the drum brake

© Central University of Technology, Free State

system. Nonetheless, the 14 CFR 23.735 requires the brakes to absorb the kinetic energy (E_k) defined by Equation 2.7.

$$\boldsymbol{E_k} = \frac{\mathbf{1}}{\mathbf{2}}\mathbf{m} \cdot \boldsymbol{V_{S0}^2} \quad \rightarrow \frac{\boldsymbol{E_k}}{\boldsymbol{N}} = \frac{\frac{\boldsymbol{W}}{\mathbf{2} \cdot \boldsymbol{g}}(\mathbf{1.688} \cdot \boldsymbol{V_{s0}})^2}{\boldsymbol{N}} = \frac{\mathbf{0.0433}\boldsymbol{W} \cdot \boldsymbol{V_{S0}^2}}{\boldsymbol{N}} \tag{2.7}$$

where, V_{s0} and N denote the stalling speed in the landing configuration and the number of wheel brakes, respectively. Therefore, the braking force (F_B) at time t is expressed by Equation 2.8.

$$\boldsymbol{F_B} = \frac{\mathbf{2} \cdot \boldsymbol{E_k}}{\boldsymbol{V_{s0}} \cdot \boldsymbol{t}} \tag{2.8}$$

2.3. Structural optimisation

2.3.1. Fundamentals of structural optimisation

Structural optimisation is a process of reducing material without compromising the required strength of a component. The process is based on a mathematical formulation which considers three basic geometric design parameters, namely size, shape and topology. To formulate the structural optimisation problem, an objective function, structural design domain and state variables are introduced [62]. The objective function (f) is subjected to its associated design and state variables to drive the optimisation to a required solution. In the process, material is selectively removed from the design domain to obtain a new design which is light in weight.

Performance requirements may include maximising the stiffness-to-weight ratio or maximising displacement, as well as the combination of the two for a given set of loads and boundary conditions [63]. The design variable or constraint (x) represents the geometry of a given design or a structural component. Furthermore, the state variable or constraint (y) represents the structural response, which includes stress, strain or displacement and depends on the design variable, resulting in $y(x)$. Consequently, the structural optimisation problem takes the form of a nested and simultaneous formulation:

$$\textbf{\textit{Structural optimisation}}\begin{cases} \underset{\boldsymbol{x}}{\min} & \boldsymbol{f}(\boldsymbol{x},\boldsymbol{y}(\boldsymbol{x})) \\ \textbf{\textit{Subject to}} & \begin{cases} \textbf{\textit{design constrain x}} \\ \textbf{\textit{state constraint y(x)}} \\ \textbf{\textit{equilibrium constraint}} \end{cases} \end{cases} \tag{2.9}$$

The state constraint is introduced as a state function $g(y)$, for example, a displacement in a certain direction. This function can be incorporated in optimisation as a constraint and formulated as $g(y) \leq 0$. In the case where load is applied on a structure, a specific magnitude of displacement $u(x)$ will be experienced by the structure in a certain direction. This is expressed by a linear equilibrium constraint shown in Equation 2.10.

$$\boldsymbol{u}(\boldsymbol{x}) = \boldsymbol{K}(\boldsymbol{x})^{-\mathbf{1}} \cdot \boldsymbol{f}(\boldsymbol{x}) \tag{2.10}$$

where K is a global stiffness matrix and $f(x)$ represents a global load vector. Therefore, optimisation can be expressed in the formulation given in Equation 2.11, where the equilibrium constraint is dependent on the state function formulation.

$$\textbf{Structural optimisation}\begin{cases} \underset{\boldsymbol{x}}{\min} & \boldsymbol{f}(\boldsymbol{x}) \\ \textbf{\textit{Subject to}} & \{\boldsymbol{g}(\boldsymbol{u}(\boldsymbol{x})) \leq \mathbf{0} \end{cases} \tag{2.11}$$

The structural optimisation in Equation 2.11 is achieved by solving a derivative of f and g with respect to x.

2.3.2. Topology optimisation

The concept of topology optimisation (TO) has been in existence for more than 150 years with the initial optimisation formulation work of Maxwell [64]. Following this initial work, was the derivation of the optimality criteria for lightweight layout of trusses that was published in 1904 by Michell [65]. Since then, TO has been extensively studied, leading to the development of various algorithms that are based on numerical modelling. These algorithms include Solid Isotropic Material with Penalisation (SIMP), method of moving asymptotes (MMA), sequential linear programming (SLP) and sequential quadratic programming (SQP).

SIMP is widely used as it is the most suitable algorithm for the FEA platform. This technique is based on seeking an optimal design (Ω_{mat}), which would be contained in the available design domain (Ω) [66]. It is concentrated on the placement of material points in an available design domain to arrive at an optimal design. The available design domain is partitioned into void and solid elements by finite element discretisation. In this case, the design variable x is represented by the density vector (ρ) containing elemental densities (ρ_e). Consequently, the local stiffness tensor ($E(\rho)$) is formulated by incorporating ρ and the component of stiffness (E^0) as shown in Equation 2.12:

$$\boldsymbol{E}(\boldsymbol{\rho}) = \boldsymbol{\rho}\boldsymbol{E}^{\mathbf{0}} \qquad (2.12)$$

The elemental densities in the design variable are applied using Equation 2.13 [25].

$$\boldsymbol{\rho_e} = \begin{cases} \mathbf{1} & \textbf{if } \boldsymbol{e} \,\boldsymbol{\epsilon}\, \Omega_{\boldsymbol{mat}} \\ \mathbf{0} & \textbf{if } \boldsymbol{e} \,\boldsymbol{\epsilon}\, \Omega \backslash \Omega_{\boldsymbol{mat}} \end{cases} \qquad (2.13)$$

The integer is formulated as a continuous function of density taking values between 0 and 1, with $\rho_e = 1$ for filled elements and $\rho_e = 0$ for voids in a discrete element design domain. Additionally, the volume constraint is employed, as shown in equation 2.14, where V is the volume of the initial design domain.

$$\int_{\Omega} \boldsymbol{\rho} \boldsymbol{d}\Omega = \boldsymbol{Vol}\,(\Omega_{\boldsymbol{mat}}) \leq \boldsymbol{V} \qquad (2.14)$$

Based on the above-mentioned, a gradient-based solution strategy for optimisation is introduced. In this method, a SIMP interpolation procedure is mostly used. Therefore, the density function is written in Equation 2.15 as:

$$\boldsymbol{E} = \boldsymbol{\rho}^{\boldsymbol{p}}\boldsymbol{E}^{\mathbf{0}},\ \boldsymbol{\rho\epsilon}\ [\boldsymbol{\rho_{min}}, \mathbf{1}],\ \boldsymbol{p} > \mathbf{1} \qquad (2.15)$$

© Central University of Technology, Free State

where, p is the penalising factor that penalises elements with intermediate density to approach 0 or 1, and ρ_{min} represents the lower density value limit to avoid singularities. Importantly, penalisation is achieved without any explicit penalisation scheme. Moreover, materials with a Poisson's ratio of 0.3 are recommended to have $p \geq 3$ [62].

When the manufacturing constraint is incorporated in the TO process, the optimisation function which uses the SIMP interpolation method should be written as [63]:

$$\textbf{Structural optimisation} \begin{cases} \min\limits_{\boldsymbol{x}} & \boldsymbol{f(\rho)} \\ \boldsymbol{Subject\ to} & \begin{cases} \boldsymbol{0 \leq \rho \leq 1} \\ \boldsymbol{g(u(x)) \leq 0} \\ \boldsymbol{Manufacturing\ constraints} \end{cases} \end{cases} \tag{2.16}$$

Consequently, two objectives can be set up, namely minimising compliance $C(\rho)$ or volume $V(\rho)$. Minimising compliance is reached by maximising the positive property of the structure, which is global stiffness. The compliance is equivalent to the strain energy of the finite element solution, which results in higher stiffness when it is minimised. Compliance is expressed by Equation 2.17.

$$\boldsymbol{C(\rho) = F \cdot u} \tag{2.17}$$

where $\boldsymbol{F}$ represents the applied external force used to solve the equilibrium Equation 2.18:

$$\boldsymbol{K(\rho) \cdot u = F} \tag{2.18}$$

The global stiffness matrix $K(\rho)$ is expressed in terms of the elemental stiffness matrix ($\boldsymbol{K_e^0}$) and is given by Equation 2.19 [62]:

$$\boldsymbol{K(\rho)} = \sum_{\boldsymbol{e=1}}^{\boldsymbol{nel}} \boldsymbol{\rho_e^p \cdot K_e^0} \tag{2.19}$$

On the other hand, when minimising volume, Equation 2.20 is used, where $\boldsymbol{V(\rho)}$ and $\boldsymbol{V_e^0}$ represent final and initial volume, respectively.

© Central University of Technology, Free State

$$V(\boldsymbol{\rho}) = \sum_{e=1}^{nel} \rho_e^p \cdot V_e^0 \tag{2.20}$$

When multiple load cases are considered for the optimisation, the objective can be formulated as a scalar formulation of objective functions using weights (w), where specific load cases are specified with index k and M is the total number of load cases [62].

$$\boldsymbol{f} = \sum_{k=1}^{M} \boldsymbol{f}_k \cdot \boldsymbol{w}_k \tag{2.21}$$

It is important to note that different manufacturing constraints result in different designs. In the case of AM, different designs are obtained from the same design domain by altering the build orientation. For example, a design domain constraint, as shown in Figure 2.6, can result in different optimal designs by altering the build orientation only.

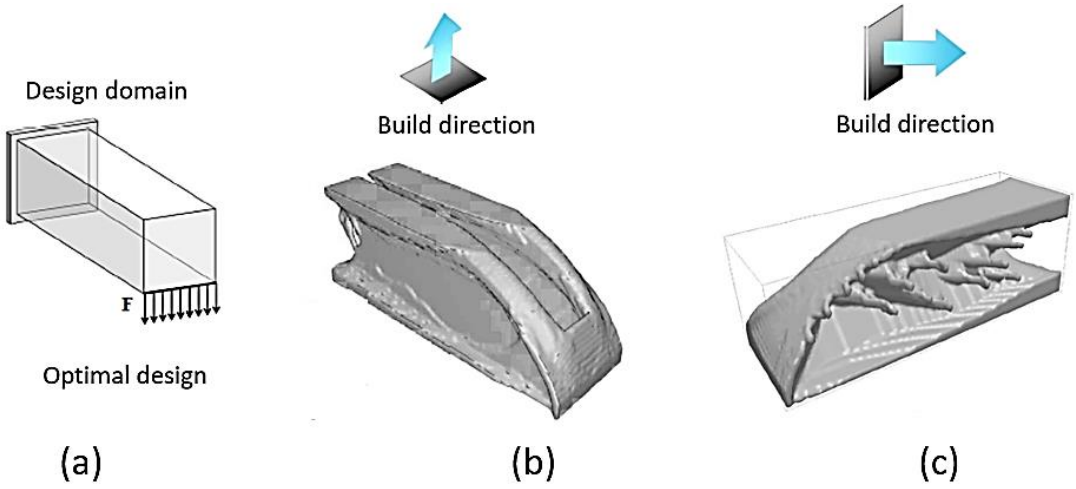

Figure 2.6: An illustration of the topology optimisation process with different AM constraints, (a) design domain, (b) AM constraint set parallel to build direction, and (c) AM constraint set perpendicular to build direction [67]

2.3.3. Finite element analysis

Finite element analysis (FEA) is a computational numerical method used to solve a general continuum problem [68]. In general, FEA begins with the discretisation

© Central University of Technology, Free State

of the continuum problem which is referred to as the division of a region into finite elements. A discretisation is formed by a number of elements and nodes, material properties, coordinates of nodal points, connectivity array of finite elements, array of element types, array for the description of displacement boundary conditions and array for the description of distributed and concentrated loads. During this process, the pre-processor program is used to generate the finite element mesh for the whole system [41]. The element types are shown in Figure 2.7 together with their typical applications.

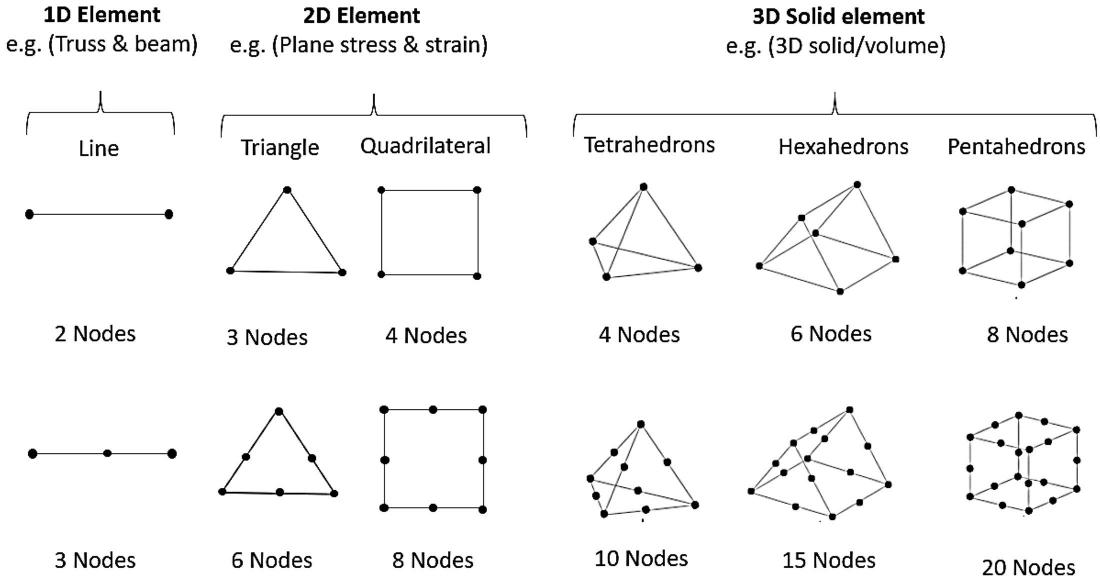

Figure 2.7: Different types of finite elements and their typical applications [69]

In FEA, 1D elements are used to approximate beams and trusses, since they have translation and rotation (only beams) functions. 2D elements, on the other hand, are typical for surface elements used to solve 2D problems. They consider linear approximations of translation displacements of u(x,y) and v(x,y). For a complex shape solid body, 3D elements are used to discretise a volume. These elements account for three unknown translation functions such as u(x,y,z), v(x,y,z) and w(x,y,z). The discretisation in FEA allows the polynomial interpolation function to be written in the general Equation 2.22 [70].

$$\boldsymbol{f(x) = a_n x^n + a_{n-1} x^{n-1} + \cdots + a_2 x^2 + a_1 x + a_0} \qquad (2.22)$$

where a is the real number, n is the degree of $f(x)$ and x is a variable of function f.

For the analysis of solid mechanics (or 3D mesh), such as the topologically optimised Ti6Al4V(ELI) nose wheel fork for fabrication using L-PBF, the second complete polynomial (ten-node tetrahedron or Tet-10 as it is called in programming), which is also known as a quadratic tetrahedron, is commonly used. This is because it behaves significantly better than other polynomials such as a four-node (linear) tetrahedron. In Figure 2.8 an illustration of Tet-10 elements is shown.

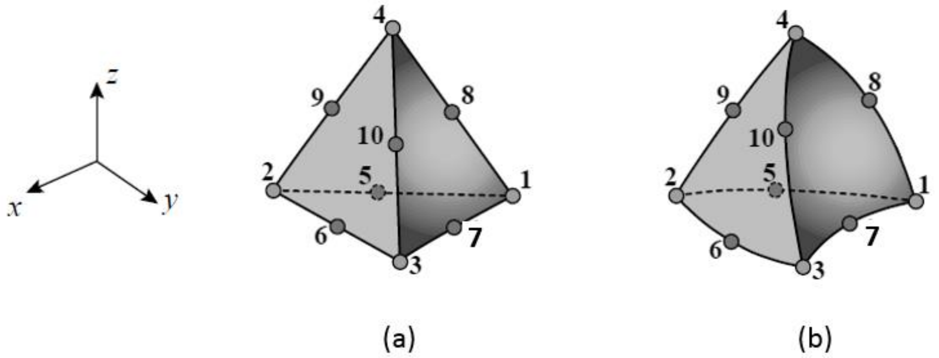

Figure 2.8: The quadratic tetrahedron (ten-node element), (a) elements with side corner nodes, midpoints nodes and planar faces; (b) elements with side corner nodes, midpoints nodes and curved faces [71]

The Tet-10 elements consist of four corner nodes labelled 1 through 4 as shown in Figure 2.8. Nodes 7, 8 and 10 are placed on sides 1–3, 1–4 and 3–4, respectively. These elements can have curved sides and faces as represented in Figure 2.8 (b). The shape function for a 1D quadratic element exemplified in Figure 2.9 with three nodes and stretch of the element (ξ), is discussed for better understanding.

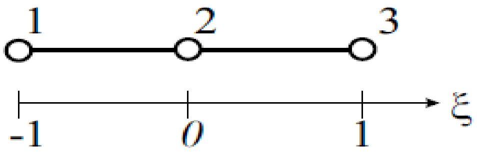

Figure 2.9: The local coordinate system (-1 ≤ ξ ≤ 1) of 1D quadratic element

© Central University of Technology, Free State

Any field inside an element is signified by a shape function given by Equation 2.23. It should be noted that at a node the approximated shape function should be equal to its nodal values.

$$\boldsymbol{u(\xi) = \sum N_i\, u_i, \qquad i = 1, 2, 3} \tag{2.23}$$

where N_i signifies an unknown function termed a shape function. For instant $u(-1) = u_1$, $u(0) = u_2$, $u(1) = u_3$.

The shape function can be a quadratic polynomial with three coefficients and three shape functions (N_1) [41]. These result from three nodes of the element in Figure 2.9.

$$\boldsymbol{N_1 = \alpha_1 + \alpha_2\xi + \alpha_3\xi^2} \tag{2.24}$$

where α_i represents unknown coefficients which are defined from the system of the several equivalences, which include $N_1(-1) = \alpha_1 - \alpha_2 + \alpha_3 = 1$, $N_2(0) = \alpha_1 = 0$, and $N_3(1) = \alpha_1 + \alpha_2 + \alpha_3 = 1$. The solutions are as follows: $\alpha_1 = 0$, $\alpha_2 = -\frac{1}{2}$, $\alpha_3 = \frac{1}{2}$. This leads to a first shape function (N_1) as:

$$\boldsymbol{N_1 = -\frac{1}{2}\xi(1 - \xi)} \tag{2.25}$$

Likewise, shape functions N_2 and N_3 are indicated in Equations 2.26 and 2.27, respectively.

$$\boldsymbol{N_2 = 1 - \xi^2} \tag{2.26}$$

$$\boldsymbol{N_3 = \frac{1}{2}\xi(1 + \xi)} \tag{2.27}$$

In Figure 2.10, the effect of the shape functions 1, 2 and 3 are illustrated.

© Central University of Technology, Free State

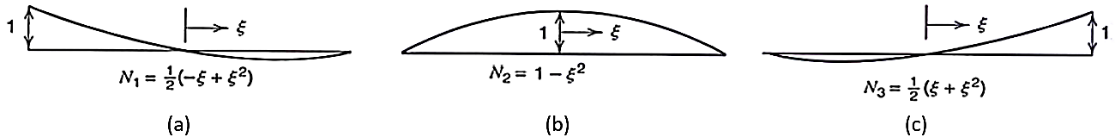

Figure 2.10: An illustration of the effect of the quadratic element shape functions N1, N2 and N3 [71]

The calculation of the stiffness of elements (k^e) is compulsory in FEA. For simplicity, consider that a uniaxial bar shown in Figure 2.11 is subjected to forces F_1 and F_2 on its ends.

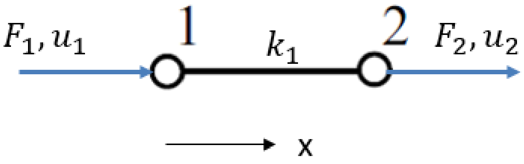

Figure 2.11: A single element representing a uniaxial bar

The stiffness matrix of the bar when modelled using a single element is given by:

$$\boldsymbol{k_1} = \frac{\boldsymbol{AE}}{\boldsymbol{L}} \tag{2.28}$$

In this case, the spring effect of the material of the element is equivalent to the Young's modulus (E) and the bar's length and cross-sectional area, represented by L and A, respectively. Therefore, the forces F_1 and F_2 can be related to displacement u_1 and u_2 by Equations 2.29 and 2.30.

$$\boldsymbol{F_1} = \boldsymbol{k_1}(\boldsymbol{u_1} - \boldsymbol{u_2}) \tag{2.29}$$

$$\boldsymbol{F_2} = \boldsymbol{k_1}(-\boldsymbol{u_1} + \boldsymbol{u_2}) \tag{2.30}$$

The matrix computation of Equations 2.29 and 2.30 is shown in Equation 2.31.

$$\left\{\frac{F_1}{F_2}\right\} = \begin{bmatrix} \boldsymbol{k_1} - & \boldsymbol{k_1} \\ -\boldsymbol{k_1} & \boldsymbol{k_1} \end{bmatrix} \left\{\frac{u_1}{u_2}\right\} \tag{2.31}$$

© Central University of Technology, Free State

A simplified form of Equation 2.31 is shown in Equation 2.32.

$$\{\boldsymbol{F}\} = [\boldsymbol{k}^e]\boldsymbol{u} \tag{2.32}$$

To satisfy compulsory analysis conditions, the sum of forces and moments must equal zero. The compatibility of deformation (strain-displacement relation) must be established by removing discontinuities in the deformable continuous body. Constitutive relations such as stress-strain relations must also be established. Hooke's law can then be used to relate linear stress (σ) and strain (ε), see Equation 2.33.

$$\boldsymbol{\sigma} = \boldsymbol{E}\{\boldsymbol{\varepsilon}\} \tag{2.33}$$

Furthermore, the stress and strain tensors can be written as:

$$\{\boldsymbol{\sigma}\} = \begin{bmatrix} \boldsymbol{\sigma_x} & \boldsymbol{\tau_{xy}} & \boldsymbol{\tau_{xz}} \\ \boldsymbol{\tau_{yx}} & \boldsymbol{\sigma_y} & \boldsymbol{\tau_{yz}} \\ \boldsymbol{\tau_{zx}} & \boldsymbol{\tau_{zy}} & \boldsymbol{\sigma_z} \end{bmatrix} = \begin{bmatrix} \boldsymbol{\sigma_x} & \boldsymbol{0} & \boldsymbol{0} \\ \boldsymbol{0} & \boldsymbol{\sigma_y} & \boldsymbol{0} \\ \boldsymbol{0} & \boldsymbol{0} & \boldsymbol{\sigma_z} \end{bmatrix} \tag{2.34}$$

$$\{\boldsymbol{\varepsilon}\} = \begin{bmatrix} \boldsymbol{\varepsilon_x} & \boldsymbol{\gamma_{xy}} & \boldsymbol{\gamma_{xz}} \\ \boldsymbol{\gamma_{yx}} & \boldsymbol{\varepsilon_y} & \boldsymbol{\gamma_{yz}} \\ \boldsymbol{\gamma_{zx}} & \boldsymbol{\gamma_{zy}} & \boldsymbol{\varepsilon_z} \end{bmatrix} = \begin{bmatrix} \boldsymbol{\varepsilon_x} & \boldsymbol{0} & \boldsymbol{0} \\ \boldsymbol{0} & \boldsymbol{\varepsilon_y} & \boldsymbol{0} \\ \boldsymbol{0} & \boldsymbol{0} & \boldsymbol{\varepsilon_z} \end{bmatrix} \tag{2.35}$$

where, τ and γ represent shear stress and shear strain, respectively.

For multiple elements used to represent a part as shown in Figure 2.12, a solution for the whole system is obtained by assembling elemental equations.

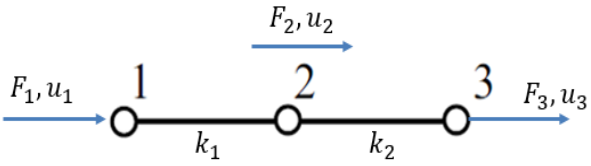

Figure 2.12: Assembly of elements for better representation of part

© Central University of Technology, Free State

The sum of the nodal forces equals the total force experienced by the system. Therefore, the equation of the global system is:

$$\begin{Bmatrix} F_1 \\ F_2 \\ F_3 \end{Bmatrix} = \begin{bmatrix} k_1 & -k_1 & 0 \\ -k_1 & k_1 + k_2 & -k_2 \\ 0 & -k_2 & k_2 \end{bmatrix} \begin{Bmatrix} u_1 \\ u_2 \\ u_3 \end{Bmatrix} \qquad (2.36)$$

The constraints must be established to solve the global equation. For example, fixing one end of the element assembly, as shown in Figure 2.13, will result in zero displacement $u_1 = 0$. Consequently, the global equation will be written as in Equation 2.37.

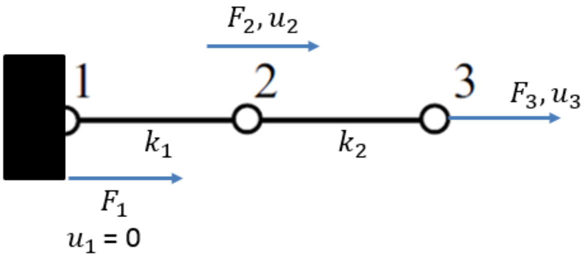

Figure 2.13: An assembly of elements with an illustration of constraint

$$\begin{Bmatrix} F_1 \\ F_2 \\ F_3 \end{Bmatrix} = \begin{bmatrix} k_1 & -k_1 & 0 \\ -k_1 & k_1 + k_2 & -k_2 \\ 0 & -k_2 & k_2 \end{bmatrix} \begin{Bmatrix} 0 \\ u_2 \\ u_3 \end{Bmatrix} \qquad (2.37)$$

Then:

$$[K] = \begin{bmatrix} k_1 + k_2 & -k_2 \\ -k_2 & k_2 \end{bmatrix} \qquad (2.38)$$

Finally, the force for each node can be calculated using Equations 2.39 through 2.41.

$$F_1 = -k_1 u_2 \qquad (2.39)$$

$$F_2 = k_1 u_2 + k_2 u_2 - k_2 u_3 \qquad (2.40)$$

$$F_3 = k_2 u_3 - k_2 u_2 \qquad (2.41)$$

© Central University of Technology, Free State

In the FEA software, finite element solutions for the displacement, deformations, stresses, reaction forces and other state variables, such as temperature in a 3D solid body subjected to load and boundary conditions, are obtained by using Equation 2.42.

$$\int_{S} \boldsymbol{t}\cdot d\boldsymbol{S} = \int_{V} \boldsymbol{F}\cdot d\boldsymbol{V} \tag{2.42}$$

Here V stands for the volume occupied by the part of the body in the configuration and S denotes the surface bounding the volume. The symbols t and F represent force per unit of current area and force at any point within the volume (force per unit of a current volume), respectively. For nonlinear analysis, the solution is obtained following Equation 2.43.

$$\boldsymbol{F}^{\boldsymbol{N}}(\boldsymbol{u}^{\boldsymbol{M}}) = \boldsymbol{0} \tag{2.43}$$

where the number of variables in the problem is denoted by (N), F^N is the force on the component conjugated to the N^{th} and u^M is the value of the M^{th} variable.

During nonlinear FEA, the solution is obtained by incrementing time in the load versus time function. The three sources of nonlinearity in the structural mechanics simulation are material, boundary and geometric nonlinearities. Material nonlinearity is the most relevant in the current study and it is defined by inputting elastic and plastic properties, as well as the density of the material, in the ABAQUS/Standard software. Thereafter, ABAQUS uses the Newton-Raphson method to obtain the solution [72]. This method is based on the principle that if the initial estimate of the solution (root) of the function $f(x) = 0$ is x_i, the second root at the point x_{i+1} will be obtained where the tangent line at $f(x)$ crosses the x-axis, as shown in Figure 2.14 [73]. This can be repeated until the solution within desirable tolerance is obtained.

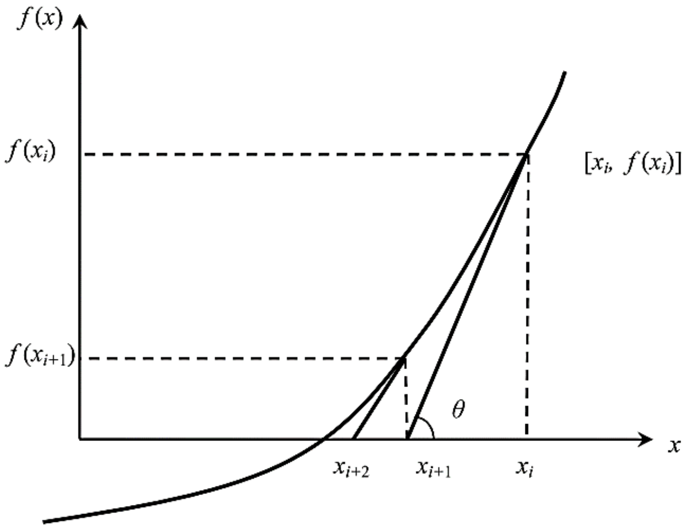

Figure 2.14: An illustration of the Newton-Raphson method [73]

2.3.4. *Fatigue simulation*

The fatigue life of a structure can be calculated using a stress- or strain-based method *[74]*. When FEA is used, material properties, component geometry and loading history are used to calculate displacements from which stress and strain values are extracted for fatigue life computation. In the current study, the stress-based method of determining the fatigue life of the nose wheel fork was followed. In Figure 2.15 a schematic illustration of the method used to determine the fatigue life is shown.

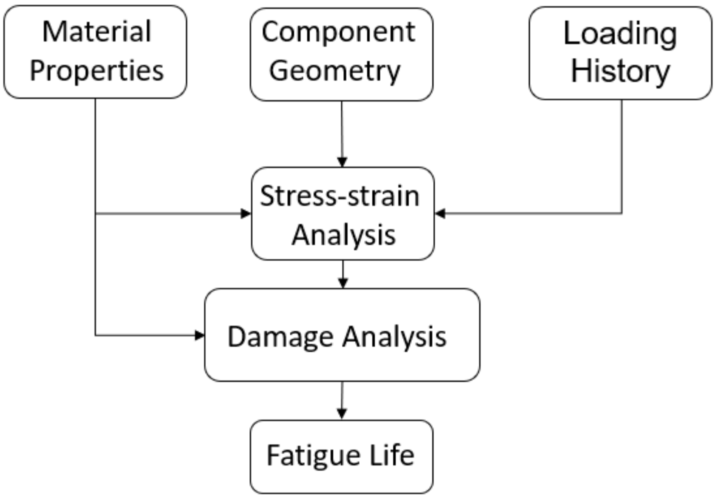

Figure 2.15: A diagram for fatigue life determination

Several approximations of material fatigue properties have been proposed. These include simple approximation, four points correction, universal slopes, method of Socie *et al*. Seeger's (uniform material method), Roessle and Fatemi [75]. The uniform material method of approximating material fatigue properties was published by Baumel and Seeger for plain carbon and low to medium alloy steel, as well as aluminium and titanium alloys [75]. They have experimentally shown that a uniform material method generally gives satisfactory agreement with the measured material properties.

The principal stresses (σ_1 and σ_2) are commonly used for the prediction of the fatigue life of a component under uniaxial cyclic stress. Such stress can be calculated using Equation 2.44.

$$\sigma_{1,2} = \left(\frac{\sigma_x+\sigma_y}{2}\right) \pm \sqrt{\left(\frac{\sigma_x-\sigma_y}{2}\right)^2 + \tau_{xy}^2} \qquad (2.44)$$

where, σ_x and σ_y represent components of stress in the X- and Y-direction and τ_{xy} stand for shear stress along the XY-plane. However, for a ductile material under multiaxial cyclic stress, as shown in Figure 2.16, the combined effect of the stress must be computed using the von Mises criterion.

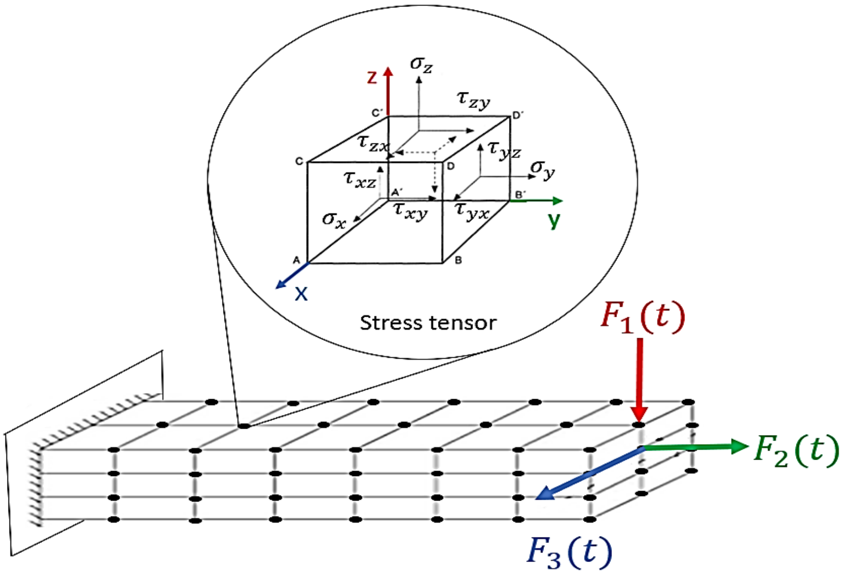

Figure 2.16: Typical fatigue model with illustration of a nodal stress tensor and components of stress [76]

© Central University of Technology, Free State

The von Mises stress amplitude (σ_a) can be calculated using Equation 2.45.

$$\sigma_a = \frac{\mathbf{1}}{\sqrt{\mathbf{2}}}\sqrt{\left(\boldsymbol{\sigma_x} - \boldsymbol{\sigma_y}\right)^2 + \left(\boldsymbol{\sigma_y} - \boldsymbol{\sigma_z}\right)^2 + (\boldsymbol{\sigma_z} - \boldsymbol{\sigma_x})^2 + \mathbf{6}(\boldsymbol{\tau_{xy}}^2 + \boldsymbol{\tau_{yz}}^2 + \boldsymbol{\tau_{zx}}^2)} \qquad (2.45)$$

In the fe-safe software, the von Mises stress amplitude is incorporated within the Manson-McKnight algorithm [77]. This algorithm is recommended in the aerospace sector and is based on a signed von Mises mean stress. Therefore, the Manson-McKnight mean stress (σ_m) is expressed as a product of the von Mises yield criterion and the sign of the first stress tensor invariant ($I_1 = \sigma_{xm} + \sigma_{ym} + \sigma_{zm}$) of a mean stress tensor, see Equation 2.46.

$$\sigma_m = \frac{\mathbf{1}}{\sqrt{\mathbf{2}}}\sqrt{\left(\boldsymbol{\sigma_x} - \boldsymbol{\sigma_y}\right)^2 + \left(\boldsymbol{\sigma_y} - \boldsymbol{\sigma_z}\right)^2 + (\boldsymbol{\sigma_z} - \boldsymbol{\sigma_x})^2 + \mathbf{6}\left(\boldsymbol{\tau_{xy}}^2 + \boldsymbol{\tau_{yz}}^2 + \boldsymbol{\tau_{zx}}^2\right)} \cdot (\mathrm{sign} \cdot I_1) \quad (2.46)$$

The stresses σ_a and σ_m are used to calculate the damage of each potential cycle for every stress tensor in the stress history. Therefore, two limitations can be considered. If $\sigma_m < 0$, the stress ratio $(R) < -1$, then $R = -1$ is used, which results in limiting the reduction in damage attributed to the compressive cycles. Secondly, if the $\sigma_a > \sigma_y$, where σ_y is the 0.2% yield stress of the material, an adjustment is made to cycles that are partly compressive $R < 0$, resulting in cycle amplitudes corrected as if they were fully tensile [77]. In the current study, load amplitudes were based on the provided load cases, scaled down for the prototype, and increased by 24%. The increased loads were applied since the baseline fatigue loading of $R = \ -1$ was used. In other words, more than 20% loads were applied while the mean stress was at minimum. The resulting spectra were less severe than the real ones, which are the ones dominating the design. If the part failed prematurely under these baseline spectra, an erroneous design would immediately be identified.

For an object loaded in a sequence shown in Figure 2.17, its cumulative damage (D_f) is expressed by the sum of the ratio of the number of the applied cycles (n_i) to the number of cycles to failure (N_f), see Equation 2.47 [78].

© Central University of Technology, Free State

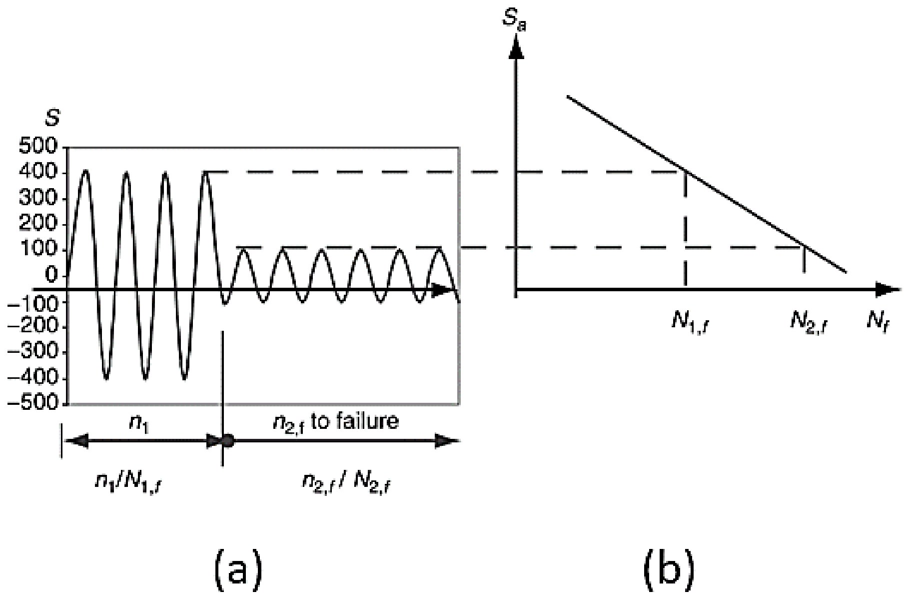

Figure 2.17: An illustration of a loading sequence (a) relates number of applied cycles to number of cycles to failure, (b) relates the applied stress to the number of cycles to failure [79]

$$\boldsymbol{D_f} = \sum \frac{\boldsymbol{n_i}}{\boldsymbol{N_f}} = \frac{n_1}{N_1} + \frac{n_2}{N_2} \dots \qquad (2.47)$$

By following Miner’s hypothesis, the so-called Palmgren-Miner hypothesis failure is expected to occur when D_f reaches unit [79]. This results in Equation 2.48 for fatigue life (L_f) computation.

$$\boldsymbol{L_f} = \frac{\boldsymbol{1}}{\boldsymbol{D_f}} \qquad (2.48)$$

To predict the fatigue life in hours, the factor L_f is multiplied by the number of hours a part took to fail. All this can be calculated using the fe-safe software.

2.3.5. Experimental validation of numerical model

To establish confidence in numerical modelling used to design a critical component of an aircraft, such as the nose wheel fork, experimental validation must be carried out. An available technique used to validate FEA is strain gauge

© Central University of Technology, Free State

measurement, optical sensing as applied in a digital image correlation system and photostress technology [80][81]. Optical sensing offers a full-field measurement of a component, while a strain gauge provides the strain at a single point. However, strain gauges tend to provide more accurate measurements compared to the other techniques [82]. A strain gauge is made from a wire with a specific resistance (R) in ohms, resistivity (ρ) of the wire material, length (L) and cross-sectional area (A). Therefore, the resistance of the strain gauge shown in Figure 2.17 can be calculated as:

$$\boldsymbol{R} = \boldsymbol{\rho}\left(\frac{\boldsymbol{L}}{\boldsymbol{A}}\right) \tag{2.49}$$

To measure a strain for validating the FEA results, a strain gauge is bonded onto the surface of a part. When a force is applied on the part, as shown in Figure 2.18, the length of the material changes, with a corresponding change in the length of the strain gauge. This results in a change in the resistance of the gauge, as given by Equation 2.47.

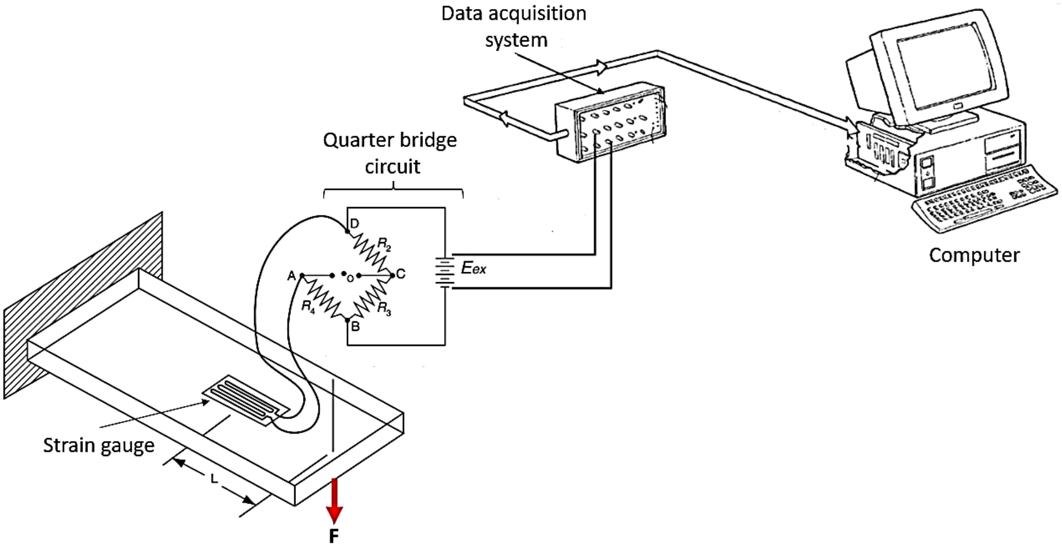

Figure 2.18: An illustration of a strain gauge measurement system [79]

The change in resistance (ΔR) is detected by the quarter bridge circuit and measured as a specific change of voltage in the data acquisition system. By applying the gauge factor (GF) as given by Equation 2.50, the strain (ε) value is obtained [83].

$$\boldsymbol{\varepsilon} = \frac{\Delta R}{GF \cdot R} \qquad (2.50)$$

Strain values measured through the strain gauges during experimental testing are then compared with the strains calculated through FEA. The accepted percentage of deviation is recommended to be ≤ 10%.

2.4. Metal additive manufacturing

2.4.1. Laser powder bed fusion

The ASTM standard F2792-12a defines AM as “the process of joining materials to make objects from 3D model data, usually layer upon layer, as opposed to subtractive manufacturing methodologies” [84]. This standard defines Powder Bed Fusion (PBF) as one of the categories of metal AM processes [84]. L-PBF is a PBF technology that uses a laser beam as the power source to selectively melt layers of metal powder to form 3D objects [84]. It is also known as selective laser melting (SLM) and can be used to produce solid structural components of an aircraft with complex shapes, while reducing material wastage and obtaining material properties comparable to conventionally produced casting parts [85]. Direct metal laser sintering (DMLS) is a tradename used by the machine supplier EOS GmbH [86]. In Figure 2.19 the L-PBF process is illustrated with a detailed view of the melt pool.

© Central University of Technology, Free State

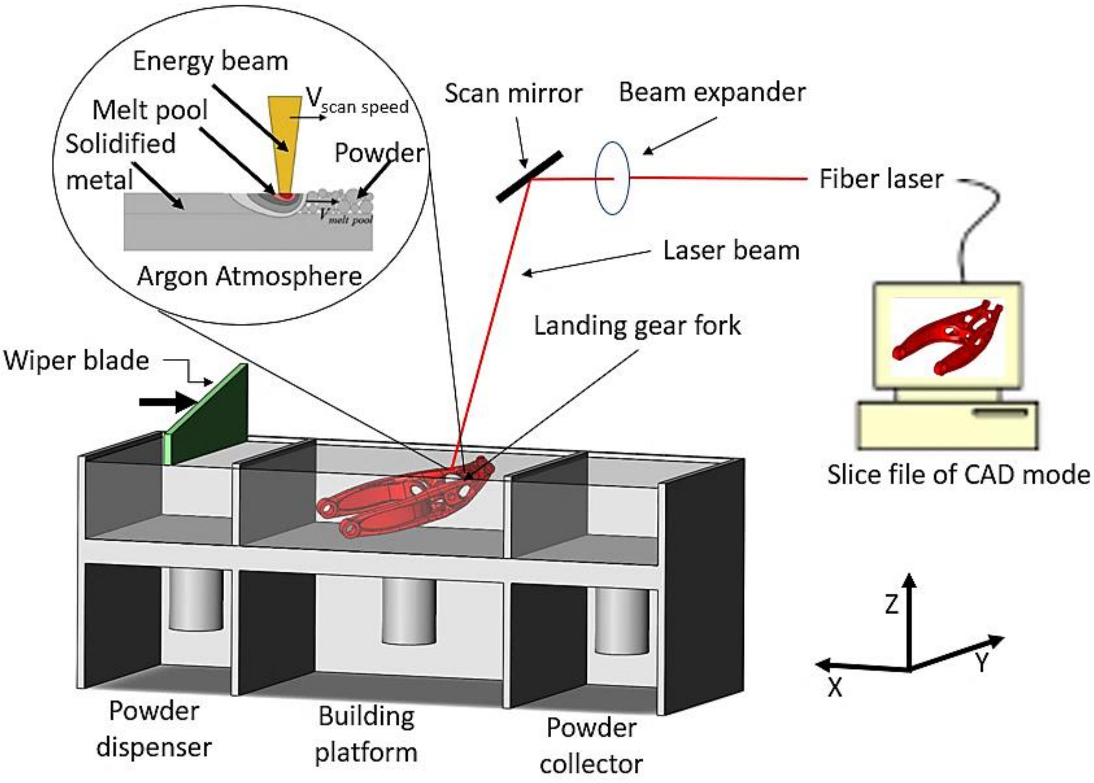

Figure 2.19: An illustration of the L-PBF process and detailed view of the melt pool (modified from [87][88])

During L-PBF, the laser beam is controlled based on the data in a 2D slice of the 3D CAD model which has been converted into an STL file, to follow the contours of a single layer and eventually, layer upon layer, build a component. For titanium alloys, this process takes place in an argon gas atmosphere. A layer of metal powder, such as Ti6Al4V(ELI), is evenly distributed on a substrate on the build platform by the wiper or recoater blade. Thereafter, the laser beam selectively fuses the particles of metallic powder into a solid layer, based on the information in the 2D slice of the CAD model. The build platform moves down by the thickness of a powder layer and another layer of powder is distributed over the building platform and selectively fused onto the existing layer. Each laser energy exposure penetrates into the preceding layer in order to form a proper metallic bond between the current and previous layers [89][90]. This implies that the melt pool depth (D) must be greater than at least one layer thickness (t) as illustrated in Figure 2.20.

© Central University of Technology, Free State

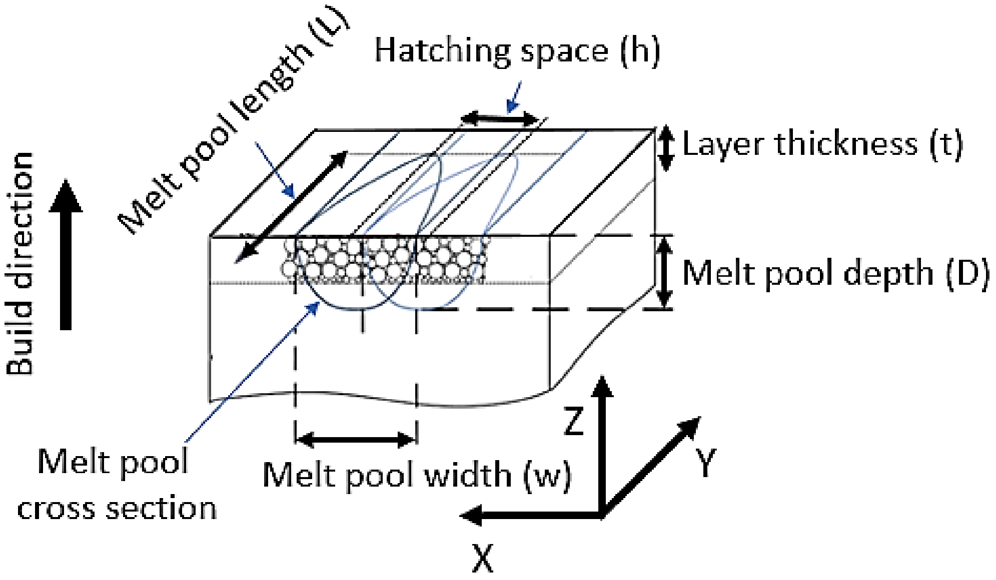

Figure 2.20: A schematic illustration of the melt pool, width-to-hatching space, depth-to-layer thickness of L-PBF [91]

During the L-PBF building process, the scanning direction is rotated between successive layers by 67° to obtain identical mechanical properties in the horizontal direction of a component. With careful choice of the process parameters melt pool width (w), hatch spacing (h), melt pool depth (D), layer thickness (t), laser power (P), scanning speed (V) and beam diameter (d), a fully dense part can be built by L-PBF from Ti6Al4V(ELI) alloy [92]. From Equation 2.51 the volumetric energy density *(E)* in (J/m^3) used in the L-PBF process can be determined. The maximum process parameters of the commercial EOSINT M280 and M290 L-PBF machines are tabulated in Table 2.1.

$$\boldsymbol{E} = \frac{\boldsymbol{P}}{\boldsymbol{V.h.t}} \qquad (2.51)$$

Table 2.1: Specified EOSINT M280 and M290 L-PBF machine parameters [93][94]

System	Build volume (mm^3)	Laser power (W)	Beam diameter (μm)	Scan speed (mm/s)
M290	250 x 250 x 325	400	100	7 000
M280	250 x 250 x 325	200 or 400	100-500	7 000

© Central University of Technology, Free State

The building volume stated in Table 2.1 conforms to the printing of the scaled-down nose wheel fork. The optimal parameters provided by the machine supplier, which included laser power, beam diameter, layer thickness and scanning speed of 170 W, 80 µm, 30 µm and 1 400 mm/s, respectively were accepted in the current study.

2.4.2. Porosity in L-PBF

Porosity in L-PBF deteriorates the quality of a part and can be formed through various mechanisms [95]. Different types of mechanisms that develop pores are lack of fusion, lack of melt pool penetration and gas entrapment. The lack-of-fusion pores are formed due to the low laser energy needed to fully melt all powder particles and result in unmelted or partially melted particles in the final part [96][97]. When the melt pool of the current deposited track does not overlap adequately with the previous consolidated layer, this results in a lack of penetration pores. During L-PBF, gas trapped inside powder particles can be released, leading to spherical pores, commonly known as gas pores. Moreover, the various process parameters of L-PBF have a direct impact on the density of the built part. Typical examples are shown in Table 2.2.

Table 2.2: The L-PBF process parameters that affect the part density

Laser power (W)	Scanning speed (mm/s)	Layer thickness (µm)	Hatch spacing (µm)	Relative density (%)	Ref
60	150	30	100	92.58	[95]
77.5	150	30	100	99.98	
200	600	30	-	99.8	[98]

The post-process heat treatment also affects the porosity of the L-PBF Ti6Al4V(ELI) parts. As-built L-PBF Ti6Al4V(ELI) has a density of 99.8%. After each stress release of 650 ℃ for 2 hours and two-stage anneal (first anneal at 910 ℃ followed by water quench and anneal at 800 ℃ followed by furnace cool, both for 2 hours), a density of 99.7% was recorded [98]. Finally, the hot isostatic press diminishes porosity completely, resulting in 100% dense L-PBF Ti6Al4V(ELI) parts [98].

© Central University of Technology, Free State

2.4.3. *Geometric accuracy and surface roughness*

Distortion of a part manufactured by L-PBF leads to an unwanted geometric deviation that could affect the assembly parameters and the functional characteristics of the product. There are two forms of deviation from the designed geometry, namely stochastic and systematic [99]. Stochastic deviation occurs due to varying environmental conditions, material fluctuations, tribology and changing thermo-mechanical boundary conditions, whereas systematic deviation is related to identifiable causes and possesses unique and unidirectional characteristics. One of the systematic deviations is the difference between the surface geometry of the end product and that of the 3D CAD model [100]. There are several reasons why the geometric accuracy of parts built through L-PBF must still be investigated. Firstly, to evaluate a part as fit-for-purpose, for example, to determine if a shaft will fit in the hole of a part. Secondly, to allow assembly of complex components, especially if they were manufactured by different supplier companies. Thirdly, to establish the quality control of parts to avoid unnecessary material wastage by getting a part right the first time. The latter would automatically improve energy efficiency since reduced rework of the manufacturing process results in less energy required for the production of the end product [101].

A voxel-based volumetric representation of a part is a computational method that can be used to determine the geometric deviation [102]. In this method, the manufacturability of the L-PBF part can be evaluated by importing a CAD model of the part into a software package and predicting the geometric deviation upfront in the design process to guide DfAM practice [103]. For example, with Simufact Additive®, the build orientation, L-PBF building process, and post-process heat treatment before and after removal of the support structure of the L-PBF part can be simulated, and the geometric deviation can be determined [102][104].

A coordinate measuring machine (CMM) with tactile, optical, or X-ray sensing capability, can be used to measure the geometric deviation of built parts [105][106]. The applicable method is selected based on the complexity of the part. With an optical CMM, large amounts of data can be accumulated at a rate faster than the tactile CMM. These types of optical sensors are classified into two

© Central University of Technology, Free State

groups, active and passive. The active sensor offers better measurement, accuracy and speed [107]. Therefore, active optical sensors are commonly used for measuring metal parts produced through AM [106]. The accuracy of active optical sensors is classified into five categories. These are interferometry and confocal, conoscopic holography, laser triangulation, time-of-flight phase-based and pulse-based [107]. The triangulation (laser and light projection) active optical CMM, with an accuracy ranging from 10 to 100 μm, is more appropriate for the measurement of freeform parts used in aeroplanes [108]. These measurement systems are widely used in the metrology of metal AM parts and are selected by considering several factors, which include L-PBF part surface roughness, typical part size, measurement accuracy required, as well as practical matters such as commercial availability and cost [109]. Consequently, optical CMM triangulation was used in the current study.

To manufacture a product complying with the required geometric accuracy, several stages in the complex L-PBF process chain from CAD to the end product have to be quality controlled [110]. This includes the challenge of conveying the design complexity to the manufacturing planner, since its geometric tolerance standards are not as well established as those that are widely available for traditional manufacturing methods [111][112]. L-PBF capabilities such as the production of complex, freeform internal and external features amplify this challenge [113][114].

The initial geometric deviation between the built part and CAD starts from the creation of a discrete mesh, usually in STL format, during the transfer of CAD data into the L-PBF system [115]. Additionally, each layer is 2D and the 3D object is obtained by joining individual layers of a metal alloy, such as Ti6Al4V(ELI) layer upon a layer, resulting in a staircase or stair stepping effect on the contoured surfaces of the end product [115][116]. This stair stepping effect is more profound on the inclined and curved surface and its size (S) depends on the layer thickness (t) and inclination angle (θ), as illustrated in Figure 2.21 [117].

© Central University of Technology, Free State

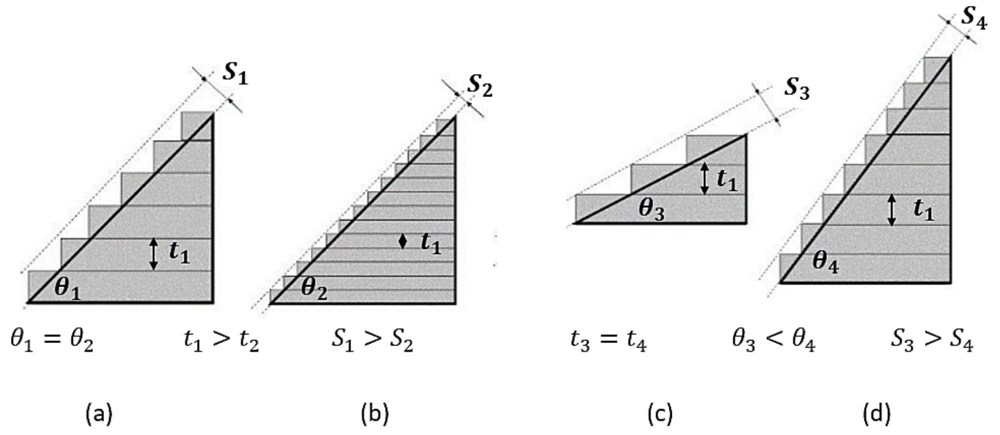

Figure 2.21: An illustration of the effect of layer thickness and the angle of inclination on the size of the stair stepping effect. Figures (a) and (b) represent equal inclination angles, while (c) and (d) denote equal layer thickness [117]

For a similar inclination angle, it is expected that the size of the stair stepping effect diminishes with a decrease in the layer thickness. Contrary to this, the size of the stair stepping decreases with an increase in the inclination angle when the layer thickness is kept constant [118]. This staircase effect results in relatively high surface roughness on the Ti6Al4V(ELI) parts built through L-PBF and is challenging to remove evenly across a large volume component with a complex shape. Chemical etching can only improve the surface roughness by 20% [49]. During this process, a component is submerged in a solution of hydrofluoric and nitric acid, known as Kroll's reagent for a given time. This removes Ti6Al4V(ELI) powder particles that adhere to the surfaces of a part and improves the surface roughness [49].

Published studies on geometric deviation during L-PBF focus on topics such as the compensation for dimensional deviation resulting from the geometric approximation errors due to the translation of data from a parametric CAD model to an STL file format [110][119][120][121]. The thermal shrinkage behaviour in L-PBF Ti6Al4V(ELI) parts causes a dimensional variation of the product shape and a warpage effect, which results in shape deflection along the build direction and is among the investigated topics [122]. It was demonstrated that shrinkage is caused by the solidification of the material and takes place in three forms. In

Figure 2.22, the three shrinkages of an L-PBF part that result from solidification are shown.

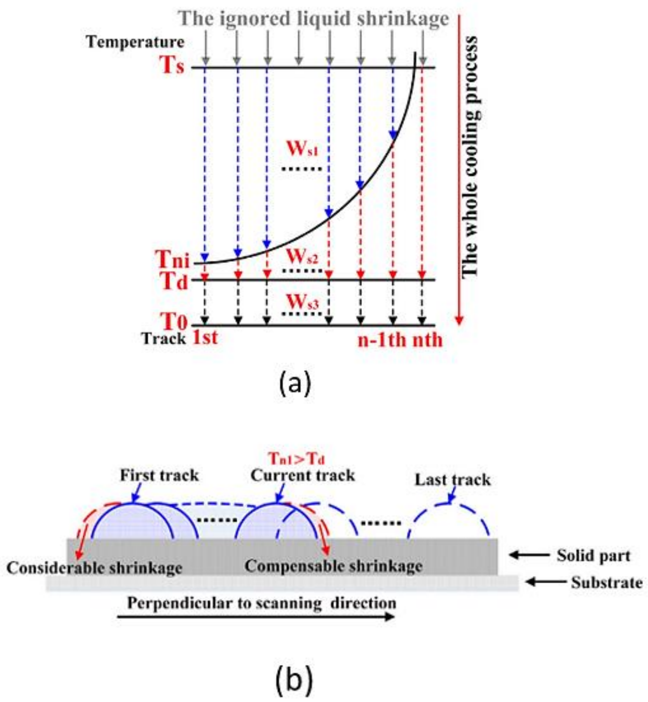

(a)

(b)

Figure 2.22: Schematic representation of the solidification shrinkage (W_s), (a) illustrates temperature versus number of tracks, and (b) shows shrinkage phenomenal when the $T_{ni} > T_d$ [122]

The first shrinkage (W_{s1}) is due to the cooling from solidus temperature (T_s) to ith temperature of the track among the whole nth tracks. The second shrinkage (W_{s2}) results from cooling of nth temperature to holding temperature (T_d), while the third shrinkage (W_{s3}) occurs when cooling is from T_d to the ambient temperature (T_0) [122]. These analytical formulation models contribute to the development of DfAM rules [123]. Nonetheless, there are limited studies on modelling the geometric deviation that would result from L-PBF post-processes of large parts such as aircraft undercarriage components produced in titanium alloys through L-PBF. Therefore, the geometric deviation analysis of the scaled-down nose wheel fork produced in Ti6Al4V(ELI) through L-PBF was carried out in this study.

© Central University of Technology, Free State

2.4.4. *Microstructure of L-PBF of Ti6Al4V(ELI) parts*

Pure titanium (Ti) exists in two main elemental crystal structures that are the hexagonal closed-packed (HCP) α phase and the body-centered cubic (BCC) β phase. In the absence of alloying elements, Ti can exist in the β phase only at high temperature, whereas below the β transus temperature of 882.5 °C Ti exists in the α phase [124]. In Figure 2.23, the HCP and BCC phases of pure Ti are shown.

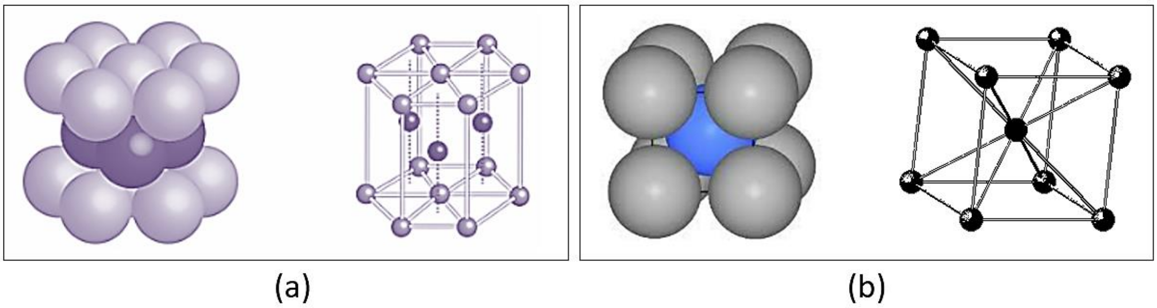

Figure 2.23: The crystal structures of pure titanium: (a) the HCP α phase and (b) the BCC β phase that exists above 882.5 °C [125]

Pure Ti is in the HCP crystal structure at room temperature but can be produced in a range of possible microstructures when adding alloying elements. Titanium alloys are commonly classified into five groups, which are alpha, near-alpha, alpha plus beta, near beta and beta. In Figure 2.24, the effects of the common alloying elements on the microstructure of the Ti are shown.

© Central University of Technology, Free State

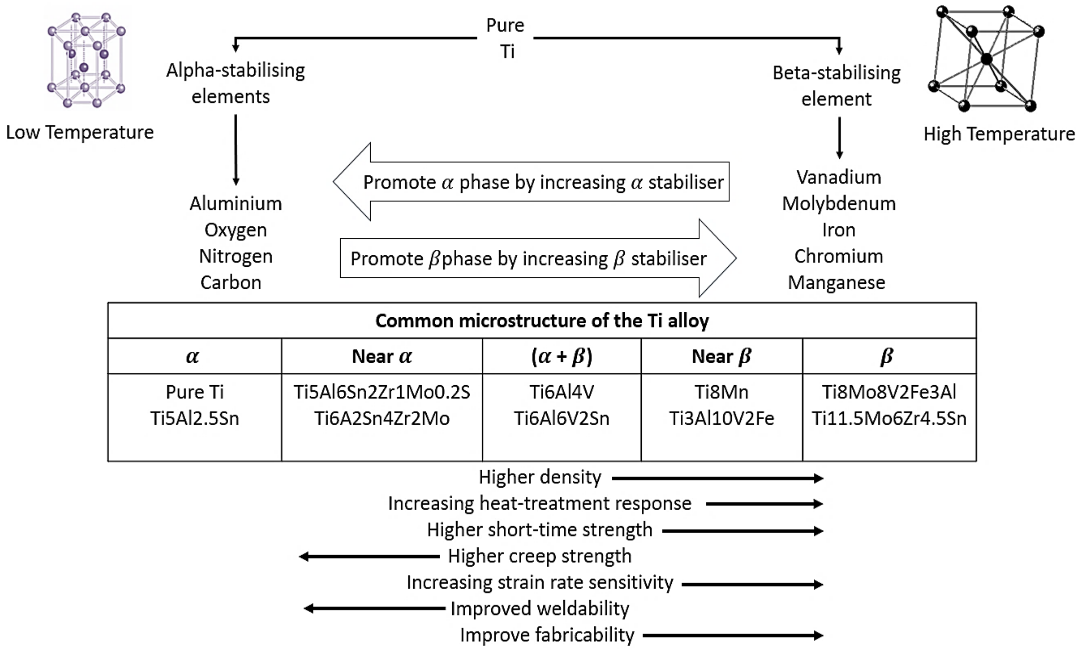

Common microstructure of the Ti alloy				
α	**Near** α	$(\alpha+\beta)$	**Near** β	β
Pure Ti Ti5Al2.5Sn	Ti5Al6Sn2Zr1Mo0.2S Ti6A2Sn4Zr2Mo	Ti6Al4V Ti6Al6V2Sn	Ti8Mn Ti3Al10V2Fe	Ti8Mo8V2Fe3Al Ti11.5Mo6Zr4.5Sn

Figure 2.24: Effects of alloying elements on the Ti microstructure [124]

The Ti6Al4V alloy is a corrosion-resistant (α + β) alloy that contains 6 wt.% aluminium and 4 wt.% vanadium as α and β stabilisers, respectively. The thermal history and cooling rate experienced by Ti6Al4V controls the α/β transformation and the resultant ratio of α and β phase in the alloy [126]. When Ti6Al4V is cooled at a low rate from the β phase, α phase nucleates below the beta transus temperature of 995 °C [127]. As the alloy temperature decreases, α platelets are formed in six non-parallel crystallographic planes in a given β grain, as illustrated in Figure 2.25(a) and (b) [124]. Subsequently, α plates grow in the close-packed planes of the β grain (Figure 2.25 (c)). During further cooling, the α plates thicken slowly in directions perpendicular to the planes, while rapidly growing in size along these planes, to eventually form the lath structure shown in Figure 2.25 (d).

© Central University of Technology, Free State

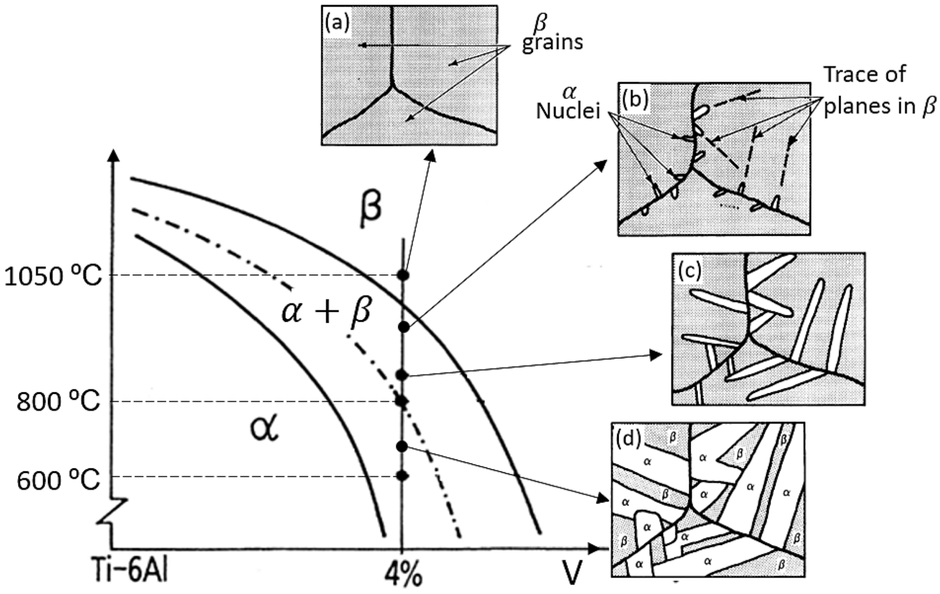

Figure 2.25: Phase diagram of Ti6Al4V [124] [128]

Alloys with controlled interstitial element levels have improved fracture toughness and ductility [124]. They are designated by ELI, for example Ti6Al4V(ELI). The microstructure of this alloy has a direct impact on its mechanical properties [13]. It is commonly used in the aerospace industry for the production of aircraft structural parts due to its balanced strength-to-weight ratio, good fatigue crack growth rate and fracture toughness. These excellent mechanical properties of Ti6Al4V(ELI) have stimulated research on the application of this alloy for the production of structural parts through L-PBF technology [129]. For application in L-PBF the alloy must be in the form of powder with a spherical morphology. Scanning electron microscopy (SEM) is one of the techniques that can be used to analyse the particle morphology and size distribution of metal powder. Typical Ti6Al4V(ELI) powder particle morphology and size distribution are shown in Figure 2.26.

© Central University of Technology, Free State

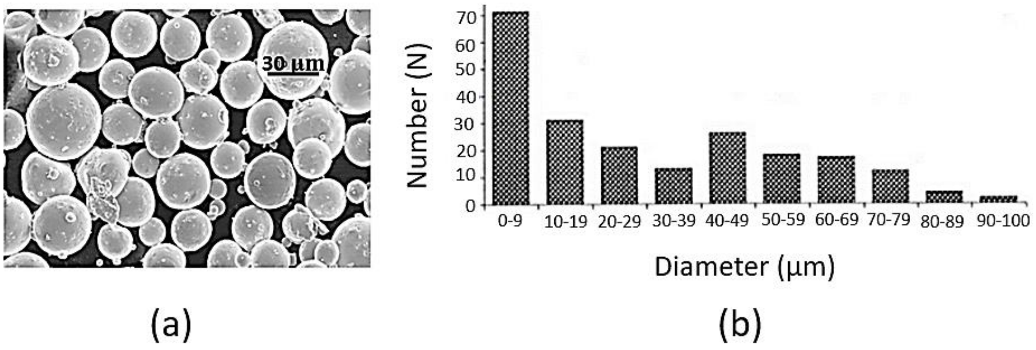

Figure 2.26: The Ti6AL4V(ELI) powder particles (a) SEM image and (b) size distribution [130]

As-built Ti6Al4V(ELI) components produced by L-PBF comprise of an α' martensitic microstructure consisting of acicular (needle-shaped) α phase in prior β grains [131] [132]. The microstructure resulting from stress-relieving heat treatment consists of α' martensite embedded in more stable $\alpha + \beta$ phase, with hardly any change to the grain size and morphology. After high temperature annealing (HTA) and furnace cooling, Ti6Al4V(ELI) consists of laths of α phase in an $\alpha + \beta$ matrix, and the prior β grain boundaries diminish with increase of the temperature [47]. At a temperature of 950 ℃, the α laths become slender and shorter due to the transformation of α to β phase which occurs at the transus temperature, and the β grain boundaries are completely diminished [128]. In Figure 2.27, the typical microstructure of Ti6Al4V(ELI) specimens produced through L-PBF are shown in two different planes (X-Y and Z-X). Images (a)–(b) are for as-built (AB), (c)–(d) for stress-relieved (SR) at 650 ℃ for 3 hours, (e)–(f) for HTA at 950 ℃ for 2 hours. After each heat treatment the specimens were furnace-cooled.

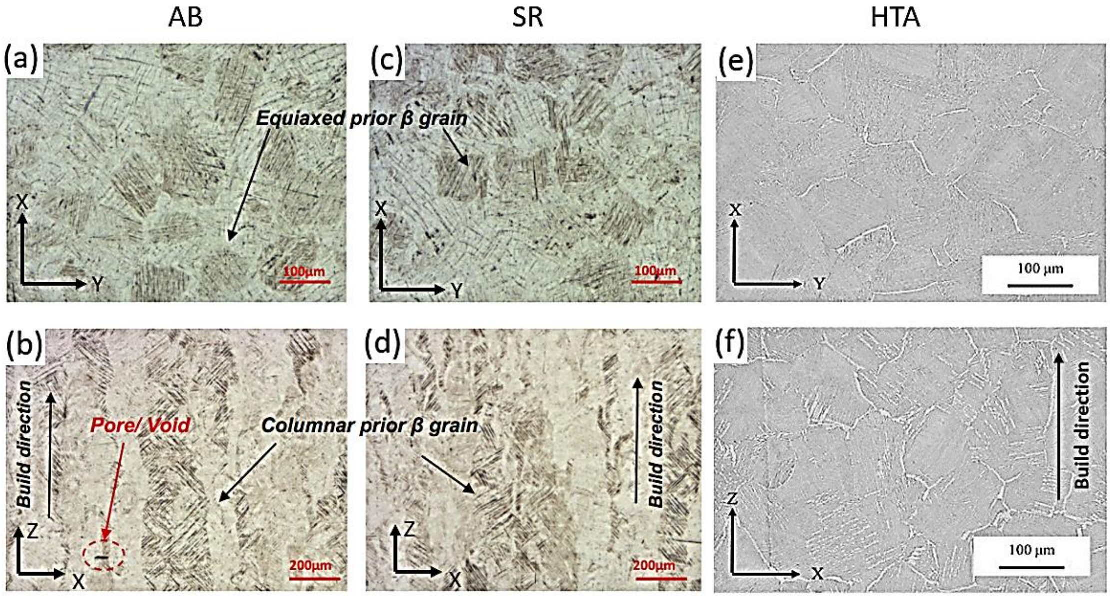

Figure 2.27: Microstructure of Ti6Al4V(ELI) specimens built by L-PBF in the X-Y and Z-X planes. Images (a) and (b) are for AB, (c) and (d) for SR, (e) and (f) for HTA [133][127]

2.4.5. Effect of microstructure on mechanical and fatigue properties

The rapid cooling rate of the Ti6Al4V(ELI) layers which is intrinsic in the L-PBF process limits the growth of the α phase resulting in high ultimate tensile strength (UTS) and yield strength ($\sigma_{Y0.2}$). In a study by Yan *et al.* [109], an as-built Ti6Al4V(ELI) component produced through L-PBF exhibited a UTS and $\sigma_{Y0.2}$ of 1 241 MPa and 1 065 MPa, respectively. However, it recorded a very low elongation (EL) of 6% due to the presence of metastable α' martensite in its $\alpha + \beta$ microstructure [127].

Due to the α to β transformation of the L-PBF Ti6Al4V(ELI) alloy, the microstructure and mechanical properties, such as tensile strength and ductility, of this alloy can be custom-made through heat treatment [134]. For example, Becker *et al.* [41] reported the tensile strength of as-built Ti6Al4V(ELI) components as 1 155 MPa, which can be altered to 1 230 MPa, 914 MPa, and 871 MPa after stress relieving, recrystallisation annealing, and two-stage heat treatment, respectively [47]. This was attributed to the removal of the residual stresses and alteration of the microstructures that were formed when acicular α' martensite transformed into $\alpha + \beta$ microstructure during heat treatment [48].

© Central University of Technology, Free State

Van Zyl *et al.* [45] found that during stress relieving at a temperature of 650 ℃ for 3 hours, the unwanted residual stresses were completely removed, resulting in α' martensite embedded in a more stable $\alpha + \beta$ phase microstructure. As described in section 2.4.3, an HTA at a temperature of 950 ℃ for a few hours, followed by a slow cooling rate promotes the growth of α phase leading to larger α phase laths in an $\alpha + \beta$ matrix microstructure, which delivers improved material ductility.

2.5. Determination of mechanical and fatigue properties

2.5.1. Tensile mechanical properties

The mechanical properties of a Ti6Al4V(ELI) structural part of an aircraft built through L-PBF must be tested and fully understood when a new design and manufacturing method of a specific aircraft part, such as the nose wheel fork, is proposed. Tensile testing of L-PBF Ti6Al4V(ELI) test specimens should be performed based on the ASTM E8/E8M standard test method [135]. In previous studies, several specimens were built in different build orientations on the platform of the L-PBF machine to evaluate the effect of the build orientation on the tensile properties of the part [136][137]. The standard specimen is normally machined and the gauge length surface is polished to have a smooth surface. Therefore, there is a limited number of studies on the effect of the as-built surface roughness on the tensile properties of Ti6Al4V(ELI) built using L-PBF. In Table 2.3, the tensile properties of Ti6Al4V(ELI) built through L-PBF, obtained from literature, are provided. These properties include the conditions of the specimens, build direction, UTS, yield stress and elongation (El) percentage. It should be noted that the stress relieving (SR) specimens had higher UTS and $\boldsymbol{\sigma_{y0.2}}$, but lower El% as compared to the specimens that were submitted to HTA. However, the HTA specimens had comparable tensile properties to those of the wrought, forged and as-cast specimens. The build direction in Table 2.3 is defined as follows. For L-PBF: LD: longitudinal direction (load applied parallel to the building direction), HD: horizontal direction (load applied perpendicular to the building direction). For the wrought material, the LD and HD relate to the direction in which

© Central University of Technology, Free State

the Ti6Al4V(ELI) plate was rolled. In Figure 2.28, the build or rolling direction, as well as the direction of the applied force, are illustrated.

Table 2.3: Tensile properties of Ti6Al4V(ELI) test specimens built through L-PBF as compared to wrought, forged and cast specimens

Process	**Conditions**	**Build direction**	**UTS (MPa)**	**$\sigma_{y0.2}$ (MPa)**	**El (%)**	**Ref**
L-PBF	AB, not machined	Longitudinal direction (LD)	1040–1062	664–802	10.3 ± 0.7	[138]
	AB, not machined	Horizontal direction (HD)	1035 ± 29	910 ± 9.9	3.3 ± 0.79	[139]
	AB, machined	LD	1155 ± 3	986 ± 6	10.8 ± 0.5	[140]
	AB, machined	LD	1166 ± 25	962 ± 47	1.7 ± 0.3	[141]
	AB, machined	HD	1211 ± 31	1100 ±12	6.5 ± 0.6	
	AB, machined	HD	1421 ± 12	1273 ± 53	3.2 ± 0.5	[142]
	AB, machined	LD	1265 ± 5	1098 ± 2	9.4 ± 0.5	[134]
	SR, machined	LD	1170 ± 6	1098 ± 5	10.9 ± 0.8	
	SR, machined	LD	1052 ± 11	937 ± 9	9.6 ± 0.9	[143]
	SR, machined	HD	1067 ± 18	966 ± 14	9.8 ± 3.3	
	SR, machined followed by HTA (950 ℃/2h/FC)	LD	909 ± 11	765 ± 5	14.92 ± 1.7	[136]
		HD	931 ± 11	848 ± 5	14.8 ± 1.7	
	SR, not machined. followed by HTA (950 ℃/2h/FC)	LD	892 ± 26	779 ± 40	15.8 ± 0.9	[144]
		HD	943.1 ± 26	856 ± 40	16 ± 0.9	
	HTA (730 ℃/2h/AC) then machined	LD	1000 ± 53	900 ± 101	19 ± 0.8	[141]
		HD	1046 ± 6	965 ± 16	9.5 ± 10	
	HTA (950 ℃/1h/WQ) then machined	LD	1040 ± 4	925 ± 14	7.5 ± 14	[141]
		HD	1036 ± 30	944 ± 8	8.5 ± 1	
	HTA (1050 ℃/1h/WQ then machined)	LD	951 ± 55	836 ± 64	7.9 ± 2	[141]
		HD	1019 ± 11	913 ± 7	8.9 ± 1	

Process	Conditions	Build Direction	UTS (MPa)	$\sigma_{y0.2}$ MPa)	El (%)	Ref
L-PBF	HTA (800 ℃/2h/AC)	-	1073 ± 9	1010 ± 11	17.1 ± 1	[145]
	HTA (950 ℃/2h/AC)	-	984 ± 5	893 ± 3	14.2 ± 1.5	
	HTA (1050 ℃/1h/AC)	-	988 ± 8	869 ± 4	13.3 ± 0.7	
	HTA (1200 ℃/1h/AC)	-	988 ± 8	878 ± 7	11.3 ± 1.3	
	HTA (1050 ℃/1h/WQ, followed by 990 ℃/0.5h/AC)	-	962 ± 12	838 ± 6	12 ± 0.1	
	HTA (850 ℃/2h/FC)	-	1004 ± 6	955 ± 6	12.8 ± 1.4	[146]
	HTA (850 ℃/5h/FC)	-	965 ± 20	909 ± 24	Premature failure	
	HTA (1015 ℃/0.5h/ AC, followed by 843 ℃/2h/FC	-	874 ± 23	801 ± 20	13.5 ± 1	
	HTA (1020 ℃/2h/FC)	-	840 ± 27	760 ± 19	14.1 ± 3	
	HTA (705 ℃/3h/FC)	-	1082 ± 34	1026 ± 35	9.1 ± 2	
	HTA (940 ℃/1h/AC, followed by 650 ℃/2h/AC	-	948 ± 27	899 ± 27	13.6 ± 0.3	
	HTA (1015 ℃/0.5h/ AC, followed by 730 ℃/2h/AC)	-	902 ± 19	822 ± 25	12.7 ± 0.6	
	ASTM F2924-14	-		825	10	[147]
Wrought	-	LD	942 ± 8	836 ± 9	12.5 ± 1.2	[142]
	-	HD	933 ± 7	832 ± 10	13.0 ± 1.5	
Forged	Mill annealed	-	1006 ± 10	960 ± 10	18.37 ± 0.9	[146]
As cast	-	-	980	865	13.5	

*FC, WQ, and AC, represents furnace cooled, water quenched, and air cooled.

© Central University of Technology, Free State

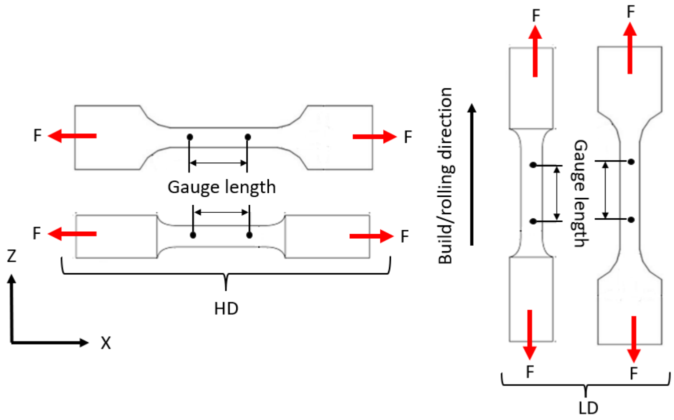

Figure 2.28: Definition of the test specimen orientation with regard to the L-PBF building or the rolling direction and application of the force F during testing

The ability of the Ti6Al4V(ELI) alloy to be extensively plastically deformed without fracture is important when designing a structural aircraft part such as a nose wheel fork. When a cylindrical tensile test specimen, with an original length of (L_o) and a cross-sectional area of (A_o) is subjected to a uniaxial tensile force (F), it increases its length and reduces its diameter. This phenomenon is described by the Poisson's ratio (v), expressed by Equation 2.52.

$$\boldsymbol{v} = \frac{\varepsilon_{lateral}}{\varepsilon_{longitudinal}} \tag{2.52}$$

where $\boldsymbol{\varepsilon_{lateral}}$ and $\boldsymbol{\varepsilon_{longitudinal}}$ represent the lateral and longitudinal strain, respectively.

The engineering stress (σ_e) experienced by the specimen is expressed by Equation 2.53.

$$\boldsymbol{\sigma_e} = \frac{\boldsymbol{F}}{\boldsymbol{A_o}} \tag{2.53}$$

The engineering strain (ε_e) is defined as the change in length ($\Delta \boldsymbol{L}$) per the original length, see Equation 2.54.

$$\boldsymbol{\varepsilon_e} = \frac{\Delta \boldsymbol{L}}{\boldsymbol{L_o}} \tag{2.54}$$

The true stress (σ_t) and strain (ε_t), which are needed during the numerical modelling of components that experience high deformation, can be derived from the measured engineering stress-strain data. The true stress can be obtained by dividing an applied force by the instantaneous area (A) of a specimen, as in Equation 2.55.

$$\boldsymbol{\sigma_t = \frac{F}{A}} \tag{2.55}$$

By assuming constant stress, the AL is equal to A_oL_o. However, after necking has started, this assumption is not valid. But A and σ_t, can be obtained using Equation 2.56 and 2.57, respectively.

$$\boldsymbol{A = \frac{A_oL_o}{L}} \tag{2.56}$$

$$\boldsymbol{\sigma_t = \frac{F}{A} = \frac{FL}{A_oL_o} = \frac{F}{A_o}(1+\varepsilon_e) = \sigma_e(1+\varepsilon_e)} \tag{2.57}$$

The true strain is calculated from the small increments δL in the instantaneous gauge length using Equation 2.58.

$$\boldsymbol{\varepsilon_t = \int_{L_0}^{L}\frac{\delta L}{L} = \ln\left(\frac{L}{L_0}\right) = \ln(1+\varepsilon_e)} \tag{2.58}$$

The relationship between stress and strain is given by the monotonic tensile test plots shown in Figure 2.29.

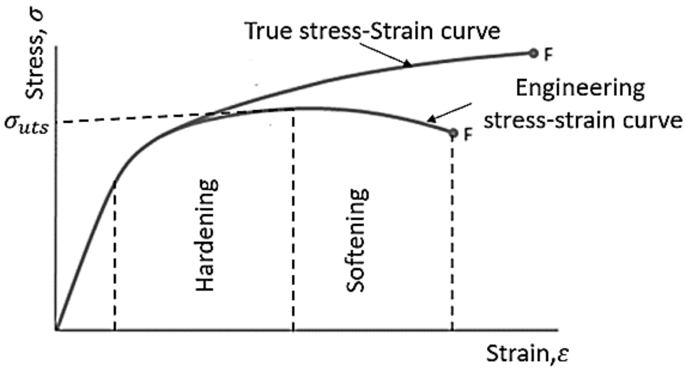

Figure 2.29: Stress-strain curve for engineering and true stress-strain curve

The true stress-strain curve always increases while the engineering stress-strain curve decreases after necking of the specimen. In the first region of the stress-strain plot, the metal is deformed elastically. If the applied load on the specimen is removed, the specimen will return to its original dimension. The second region of the stress-strain plot illustrates the plastic deformation of the specimen. By computing the slope of the stress-strain curve, the elastic modulus is obtained. This material property is computed by Equation 2.59 from the measured engineering stress-strain data.

$$\boldsymbol{E = \sigma_e \varepsilon_e} \tag{2.59}$$

On the other hand, the plastic strain $\boldsymbol{\varepsilon_p}$ experienced by the specimen is given by:

$$\boldsymbol{\varepsilon_p = \varepsilon_t - \varepsilon_y = \left(\frac{\sigma}{k}\right)^{1/n}} \tag{2.60}$$

where n and k represent the strain hardening exponent and strain coefficient, respectively, and $\boldsymbol{\varepsilon_y}$ is the strain at the yield point of the material.

In the case where a structure or an element has two or three dimensions, the stress will also have 2D or 3D components of stress. As shown in Figure 2.30, in the Cartesian coordinate system, if the stress is arranged into x, y, and z components, the Cauchy stress tensor can be determined with Equation 2.61:

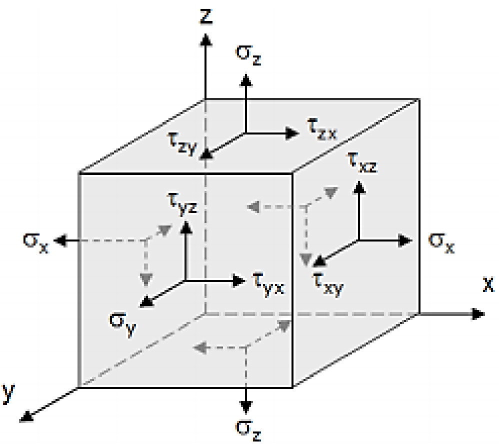

Figure 2.30: Components of the stress tensor in a Cartesian coordinate system for a 3D element [148]

© Central University of Technology, Free State

$$\boldsymbol{\sigma} = \begin{bmatrix} \sigma_{xx} & \sigma_{xy} & \sigma_{xz} \\ \sigma_{yx} & \sigma_{yy} & \sigma_{yz} \\ \sigma_{zx} & \sigma_{zy} & \sigma_{zz} \end{bmatrix} = \begin{bmatrix} \sigma_{xx} & \tau_{xy} & \tau_{xz} \\ \tau_{yx} & \sigma_{yy} & \tau_{yz} \\ \tau_{zx} & \tau_{zy} & \sigma_{zz} \end{bmatrix} \qquad (2.61)$$

Stresses σ_{xx}, σ_{yy} and σ_{zz} are the applied stress components and $\tau_{xy}, \tau_{xz}, \tau_{yx}, \tau_{yz}, \tau_{zx}$ and τ_{zy} are the shear stress components. To distinguish these stresses the first subscript represents the plane in which the stress is applied to the component, as indicated in Figure 2.30, whereas the second subscript stands for the direction of the stress component. The strain components can also be represented in a similar way.

2.5.2. *Impact toughness*

Toughness is a measure of the amount of energy a material can absorb before fracture [125]. It is typically measured through a Charpy impact test at a specific temperature with a specimen prepared to have a specific geometry and dimensions. The V-notch specimen geometry is normally used and the impact test procedure is performed, based on the ASTM E23 standard [149]. In Figure 2.31, a Charpy impact test apparatus is illustrated.

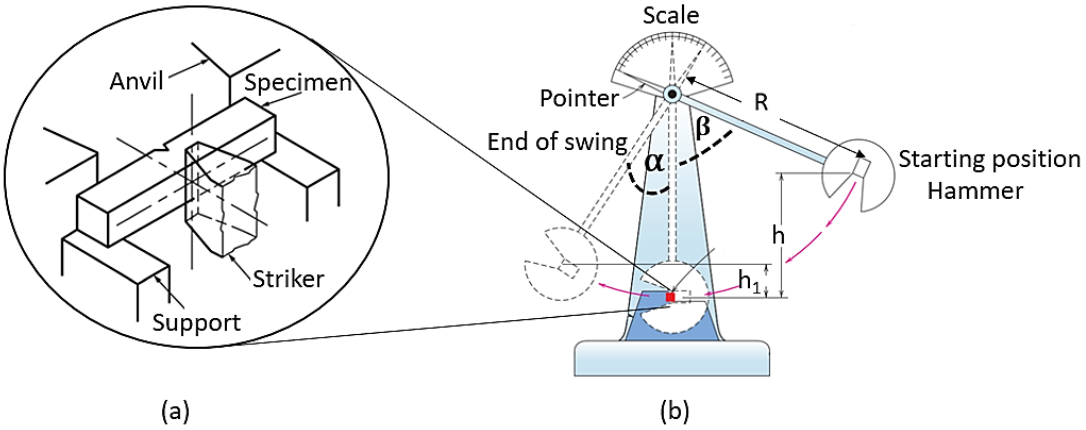

Figure 2.31: Illustration of the impact toughness test, (a) Charpy impact toughness specimen arrangement [149], (b) impact toughness apparatus [125]

During Charpy impact toughness testing, the specimen, placed against the anvil and on the support, as shown in Figure 2.31(a), is ruptured by the impact force of the striker. The striker (hammer) impacts the specimen through a single

© Central University of Technology, Free State

swinging movement, as illustrated in Figure 2.31(b). The falling and rising angles of the pendulum hammer are denoted β and α, respectively. At the starting position of the height of the hammer is $h = R - Rcos\beta$ and at the end of the swing position is $h_1 = R - R\cos\alpha$. Equations 2.62 and 2.63 give the initial and final potential energy of the pendulum, respectively, where R is the pendulum radius.

$$\boldsymbol{E_i = mgR(1 - \cos\beta)} \tag{2.62}$$

$$\boldsymbol{E_f = mgR(1 - \cos\alpha)} \tag{2.63}$$

Equation 2.64b gives the energy (E_{ab}) absorbed by the specimen:

$$\boldsymbol{E_{ab} = mgh(\cos\beta - \cos\alpha)} \tag{2.64}$$

All specimens fracture at the V-notch because it acts as a stress concentration region. The impact toughness of Ti6Al4V specimens built through L-PBF is influenced by factors such as test temperature, build orientation, build parameters and heat treatment, as found in the following studies.

The ductile-to-brittle transition of metals can be determined using the Charpy impact test. Low temperatures, high stress rates and fast loading rates may all cause a ductile material to fail in a brittle manner. This transition is influenced by factors such as alloy composition, heat treatment and manufacturing processes. For example, in Figure 2.32 the impact energy versus temperature plots of as-built L-PBF Ti6A4V(ELI) specimens in two different orientations of the V-notch are shown.

© Central University of Technology, Free State

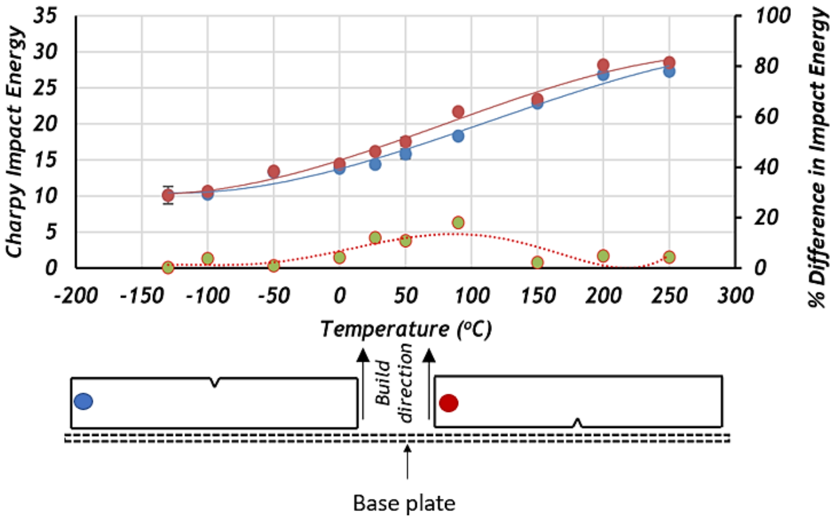

Figure 2.32: Plots of the impact energy versus temperature of L-PBF Ti6Al4V(ELI) specimens built at two different orientations of the V-notch with regard to the base plate [150]

From Figure 2.32 it is clear that the impact toughness of Ti6Al4V(ELI) test specimens built by L-PBF varied with the orientation of the specimen. Specimens built with the V-notch facing the base plate had better impact toughness values than those that were produced with the V-notch facing upward (away from the base plate) over most of the temperature range of -30 to +250 ℃ [150]. In a study by Louw [151], it was found that for Ti6Al4V components built by high-speed SLM, high laser power resulted in an improved value of the impact toughness compared to ones built at low laser power. In Table 2.4, the impact toughness values of L-PBF Ti6Al4V(ELI) specimens, built in different machines and submitted to different heat treatments, are tabulated.

Table 2.4: Impact toughness values of Ti6Al4V(ELI) specimens built by L-PBF

Materials and references	**L-PBF machine type**	**Testing environment**	**Specimen conditions**	**Impact energy (J)**
Ti6Al4V(ELI) [150]	EOSINT M280	-50 °C	As-built	13.3
Ti6Al4V(ELI) [133]			SR at 650 °C for 3 h	14.9
Ti6Al4V [152]	SLM	Ambient	As-built	6.0
			SR at 650 °C for 3 h	7.3
Ti6Al4V(ELI) [151]	HS-SLM (high laser power)	Ambient	Annealed at 940 °C for 1 hand SR at 650 °C for 2h	8-10
	HS-SLM (low laser power)	Ambient	Annealed at 940 °C for 1 hand SR at 650 °C for 2h	6

© Central University of Technology, Free State

The stress-relieving heat treatment of 650 °C for 3 hours improved the impact toughness by more than 10%, as illustrated in Table 2.4. Contrary to this, a reduction in impact toughness was recorded when a temperature of 730 °C was used for stress relieving. Clearly, an appropriate heat treatment improves the impact toughness of the L-PBF Ti6Al4V(ELI) alloy.

2.5.3. Fracture toughness

Metal fracture starts in an area where the stress concentration is the highest, such as at a sharp edge or a crack. When designing aircraft components that experience high stress during their operation it is crucial to have a design criterion that integrates the effect of stress concentration. The stress intensity factor (K_I) is used to express the combination of the effect of the stress at the crack tip and the crack length (a) and is given by Equation 2.65.

$$\boldsymbol{K_I = Y\sigma\sqrt{\pi a}} \tag{2.65}$$

where Y and σ represent the dimensional geometric constant, and the applied stress, respectively. For the specific mode of fracture, a specific stress intensity can be determined. In Figure 2.33 different modes of fracture are illustrated.

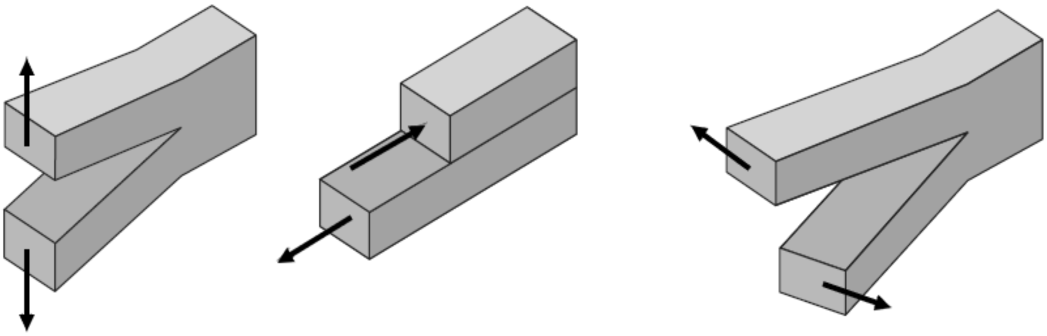

(a) Mode I (b) Mode II (c) Mode III

Figure 2.33: Schematic illustration of fracture modes in fracture mechanics [153]

The critical value of the stress-intensity factor that causes the failure of the component is called fracture toughness (K_{IC}). The K_{IC} of metals, including

© Central University of Technology, Free State

Ti6Al4V(ELI), is determined under predominantly linear-elastic, plane-strain conditions using a pre-cracked test specimen of specific dimensions. It is computed using Equation 2.66 for mode I and has a unit of (MPa$\sqrt{m}$), where σ_f represents stress at the point of fracture.

$$\boldsymbol{K_{IC} = Y\sigma_f\sqrt{\pi a}} \tag{2.66}$$

The K_{IC} test has several purposes in research and development, service evaluation and specification of acceptance and manufacturing quality control. In the current study, the K_{IC} test was carried out to establish quantitatively the service performance of the nose wheel fork produced through L-PBF, with a particular focus on the effect of the heat treatment on the K_{IC} of the Ti6Al4V(ELI) component.

Fracture toughness specimens are commonly prepared according to the ASTM E399 standard [154]. All specimens must be tested in the heat treated and environmentally conditioned state (e.g., room temperature of 20 °C). To obtain valid fracture toughness results, the specimen ligament size (W - a) must not be less than 2.5 $\left(\frac{K_{IC}}{\sigma_y}\right)^2$ where $\sigma_{y0.2}$ is the 0,2% offset yield stress. The compact test specimen orientation and fracture toughness testing system are indicated in Figure 2.34. Here, W is the specimen width, a is the crack length, B is the specimen thickness and H represents the distance between the intersection of the crack notch tip and the top or the bottom edge of the specimen.

© Central University of Technology, Free State

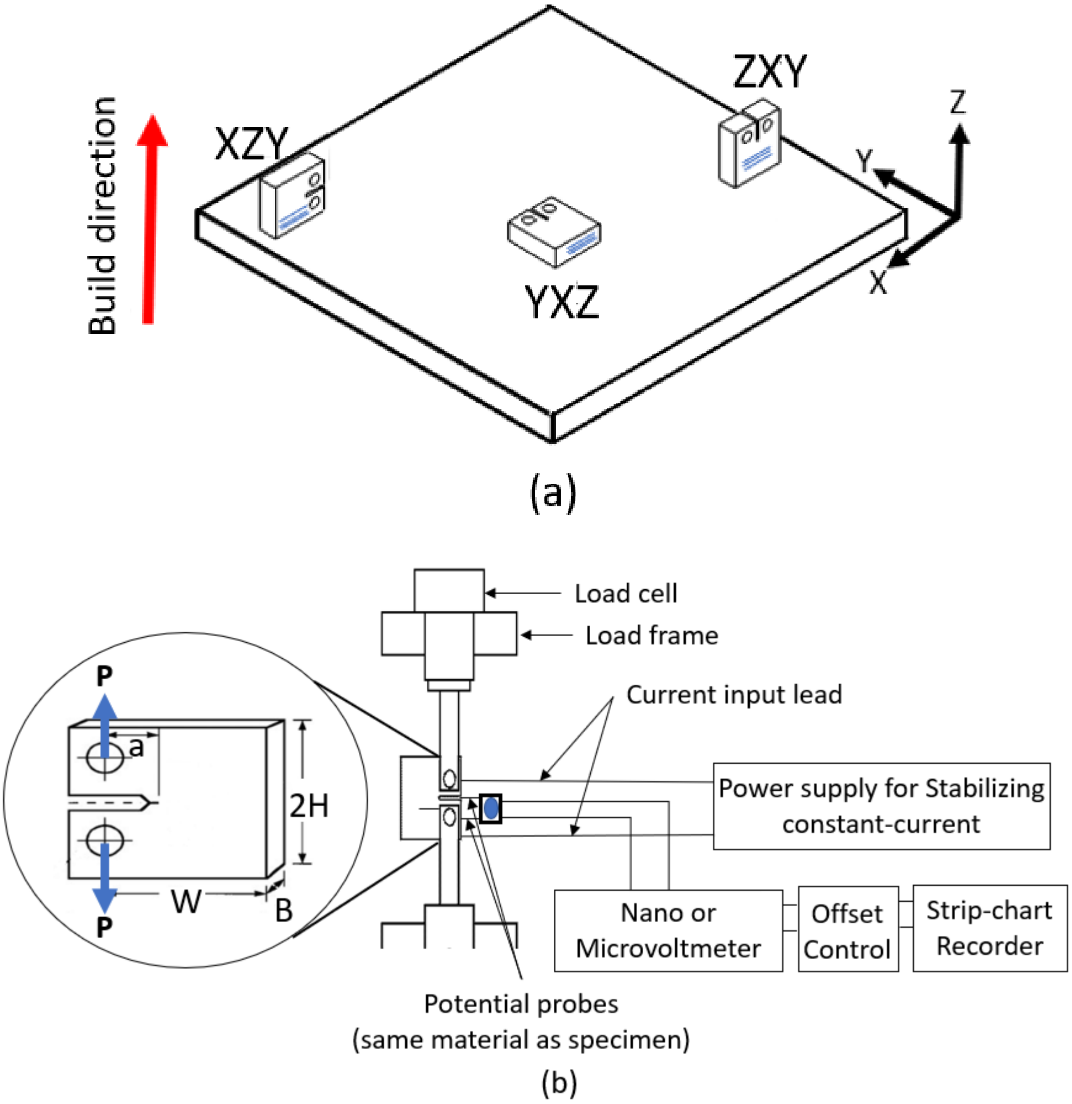

Figure 2.34: Orientation of compact test specimens (a) on the L-PBF build platform and (b) in the fracture toughness testing system

To correctly determine K_{IC} from the recorded data, it is necessary to calculate a conditional fracture toughness (K_Q), and then to determine whether the results are consistent with the size and yield strength of the specimen. Figure 2.35 shows typical recorded force-displacement plots that are used in this calculation.

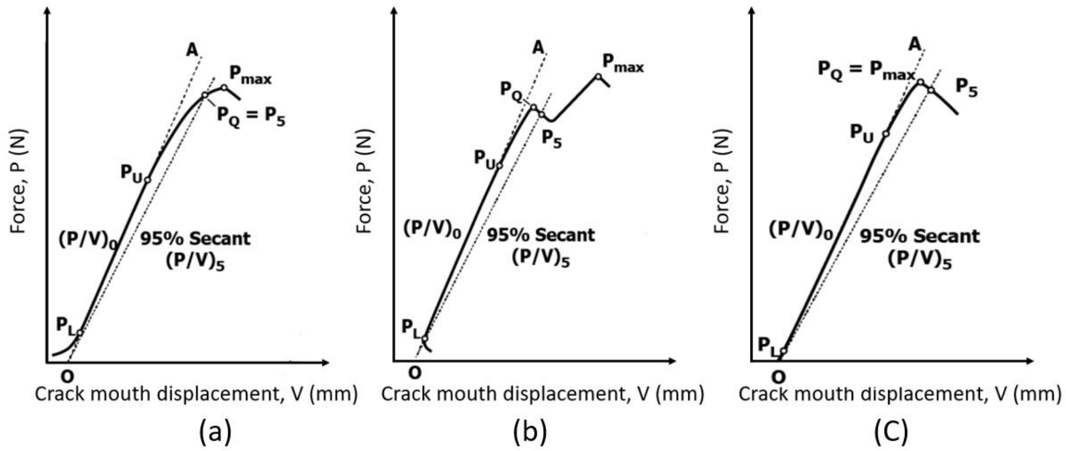

(a) (b) (C)

Figure 2.35: Schematic illustration of different types of force-displacement recorded: (a) Type I, (b) Type II and (c) Type III [155]

A conditional value P_Q is determined by the secant line OP_5 through the origin O of the test record with a slope $\left({}^{P}/_{V}\right)_5$, which is 95% of $\left({}^{P}/_{V}\right)_o$ where, $\left({}^{P}/_{V}\right)_o$ represents the slope of the tangent OA to the initial linear portion of the graph between the lower bound force (P_L) and the upper bound (P_U). Point O does not necessarily lie on the intersection of the force-displacement axes and $P_Q = P_5$ if the force at every point on the graph that precedes P_5 is lower than P_5. However, if there is a maximum force preceding P_5 which exceeds it, as shown in Figure 2.35 (b) and (c), this maximum force (P_{max}) = P_Q. Furthermore, if the P_{max}/P_Q does not exceed 1.10, then the test is valid and K_{IC} can be calculated using Equation 2.67. On the other hand, if the P_{max}/P_Q exceeds 1.10, then the test is invalid for the determination of K_{IC}. In this case the K_Q is reported as result.

$$\boldsymbol{K_Q} = \frac{\mathrm{P}}{\sqrt{BB_N}\sqrt{W}} \boldsymbol{f}\left(\frac{a}{W}\right) \tag{2.67}$$

where:

$$\boldsymbol{f}\left(\frac{a}{W}\right) = \frac{\left(2+\frac{a}{W}\right)\left[0.886+4.64\frac{a}{W} - 13.32\left(\frac{a}{W}\right)^2 + 14.72\left(\frac{a}{W}\right)^3 - 5.6\left(\frac{a}{W}\right)^4\right]}{\left(1-\frac{a}{W}\right)^{3/2}} \tag{2.68}$$

© Central University of Technology, Free State

and B_N is the thickness of the specimen measured between the roots of the side groove as shown in Figure 2.36. These side grooves are created at the edge of the specimens's crack to connect the displacement gauge.

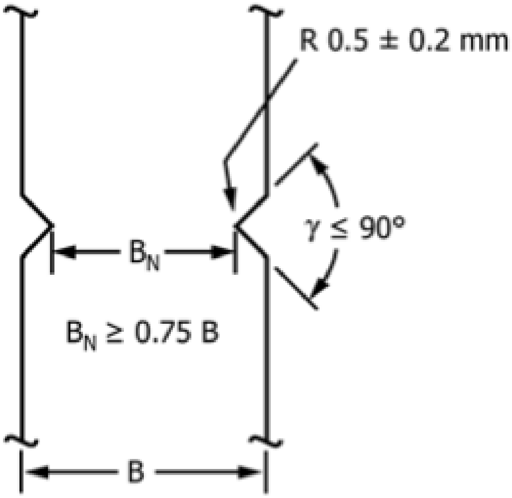

Figure 2.36: An illustration of B_N on the CT specimens [155]

Another important aspect to be considered is the calculation of the value $2.5\left(K_Q/\sigma_{ys}\right)^2$. If $2.5\left(K_Q/\sigma_{ys}\right)^2 < (W - a)$ of the specimen, then $K_Q = K_{IC}$, provided that all other validity requirements are met. Finally, larger specimens will have to be used for determination of K_{IC} if the required validity requirements are not met. In Table 2.5, the fracture toughnesses of L-PBF-produced Ti6Al4V(ELI) that were determined in published studies, are tabulated.

Table 2.5: Fracture toughness of the Ti6Al4V(ELI) components produced through L-PBF in comparison with other fabrication methods

Process	Orientation	Conditions	K_Q (MPa·m$^{0.5}$)	K_{IC} (MPa·m$^{0.5}$)	Ref
L-PBF / SLM	XZY	AB		23 ± 1	[156]
	YXZ			28 ± 2	
	ZXY			16 ± 1	
	XZY	SR, at 650 ℃ for 4 hours		30 ± 1	
	YXZ			28 ± 2	
	ZXY			31 ± 2	
	∥ to deposition	HTA, at 920 ℃ for 0.5h	106	-	[157]
	⊥ to deposition		77	-	

© Central University of Technology, Free State

Process	Orientation	Conditions	K_Q	K_{IC}	Ref
			(MPa·m$^{0.5}$)	(MPa·m$^{0.5}$)	
	XZY	HTA, at 910 ℃ for 8h		82	[43]
	YXZ				
	ZXY				
	XZY	HTA, at 890 ℃ for 2h		49	[156]
	YXZ			41	
	ZXY			49	
Wrought	-	Annealed		52	[124]
Cast	-	As-cast		107	
		Annealed		103	
		HIP		109	

The K_{IC} values of the specimens that were submitted to HTA were higher than those of the as-built and stress relieved ones, but were comparable to those of the wrought specimens. Finally, HTA specimens had comparable K_{IC} regardless of the build orientation.

2.5.4. Fatigue crack propagation rate

The existence of cracks or flaws on the surface of a component acts as stress concentration regions and results in low fatigue life. The fatigue crack growth rate (FCGR), which is represented by ($\frac{da}{dN}$), varies with the crack length (a) and applied cyclic stress (σ), as per expression 2.69.

$$\left(\frac{da}{dN}\right) \propto f(\sigma, a) \tag{2.69}$$

For determining the FCGR, compact-type specimens, which are fabricated according to the ASTM E647, are used [158]. When the effect of the build orientation on the FCGR is investigated, Ti6Al4V(ELI) compact specimens are built through L-PBF in different orientations [159][160]. The increase in the crack length of the compact-type specimen under constant-amplitude cyclic stress is plotted against the number of stress cycles. In Figure 2.37, the quantitative plots of crack length versus the number of stress cycles for three different orientations of Ti6Al4V(ELI) specimens built through L-PBF are shown.

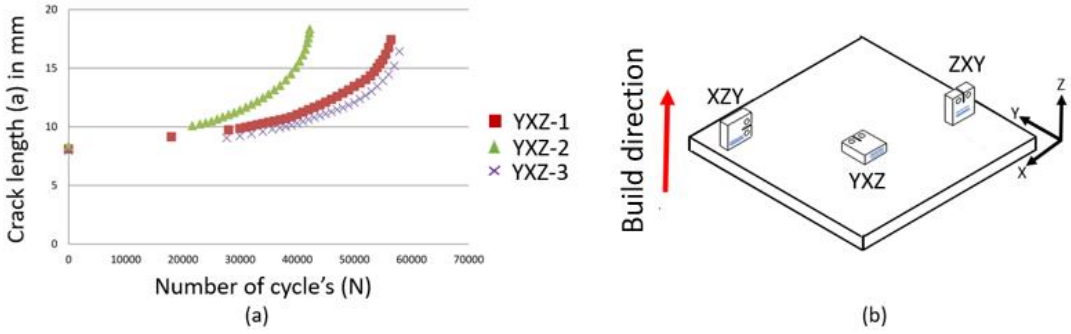

Figure 2.37: Illustration of a plot of crack length versus the number of stress cycles of Ti6Al4V(ELI) compact-type specimen built through L-PBF [161]

The FCGR of an alloy can be expressed as the stress-intensity factor range (ΔK) for constant-amplitude fatigue stress and is given by Equation 2.70, the Paris equation [162].

$$\frac{da}{dN} = C\Delta K^{m} \qquad (2.70)$$

where, C and m represent constants that are functions of the material, environment, frequency, temperature and stress ratio.

In most cases, the crack propagation rate experimentation is based on mode one of fracture mechanics defined in section 2.6.3. Therefore, the stress-intensity factor range can be calculated by the modified equations given here:

$$K_{max} = \sigma_{max}\sqrt{\pi a} \qquad (2.71)$$

$$K_{min} = \sigma_{min}\sqrt{\pi a} \qquad (2.72)$$

$$\Delta K = \sigma_{range}\sqrt{\pi a} \qquad (2.73)$$

The stress-intensity factor is not defined for compressive stress. Therefore, the value of K_{min} is taken as zero. Additionally, if there is a geometric correction factor or the stress-intensity factor range, Equation 2.74 is used.

$$\Delta \boldsymbol{K} = \boldsymbol{Y}\boldsymbol{\sigma}_{range}\sqrt{\boldsymbol{\pi a}} \qquad (2.74)$$

The FCGR as a function of the stress-intensity factor range is governed by Equation 2.70. If the logarithm is taken on both sides of Equation 2.70, Equations 2.75 and 2.76 are obtained.

$$\boldsymbol{log}\frac{\boldsymbol{da}}{\boldsymbol{dN}} = \boldsymbol{log}(\boldsymbol{C}\Delta\boldsymbol{K}^{\boldsymbol{m}}) \qquad (2.75)$$

$$\boldsymbol{log}\frac{\boldsymbol{da}}{\boldsymbol{dN}} = \mathbf{m}\boldsymbol{log}\,\boldsymbol{\Delta K} + \boldsymbol{logC} \qquad (2.76)$$

In Figure 2.38, a typical plot of the log FCGR versus the log ΔK is shown.

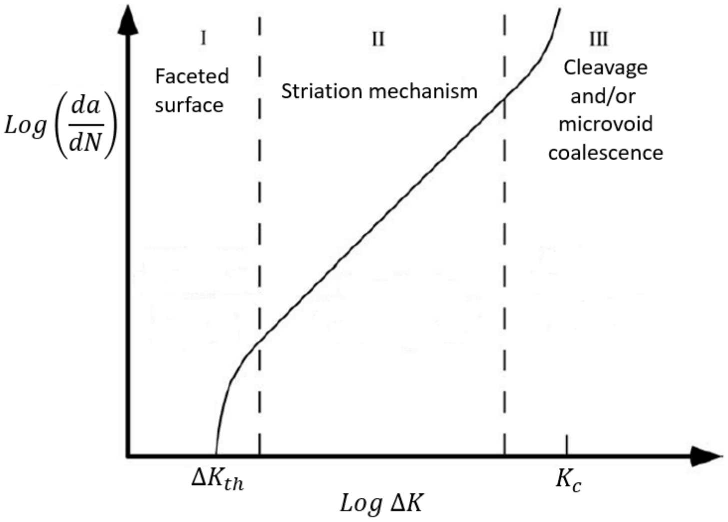

Figure 2.38: A plot of log FCGR versus log ΔK [153]

A FCGR versus ΔK plot is divided into three regions, which are Region I, the slow crack growth or threshold region, Region II, stable crack growth, which is known as the Paris region, and Region III, the fast fracture (rapid-unstable crack growth) region [153]. The limiting value of ΔK, below which there is no measurable crack growth is called the stress-intensity factor range threshold ΔK_{th}. Below this threshold, no crack growth should occur, and for Region II, the FCGR usually varies from 2.5 to 6. In recent studies, the effects of the L-PBF inherent residual stresses on the FCGR of SLM of Ti6Al4V in as-built and stress-relieved

© Central University of Technology, Free State

conditions have been investigated [156][157] [163][164][165][166]. In Table 2.6, the FCGR properties of Ti6Al4V(ELI) test specimens produced through L-PBF from some of these sources are tabulated.

Table 2.6: Fatigue crack growth rate properties of L-PBF of Ti6Al4V(ELI) test specimens from recent literature

Orientation	**Machine**	**Annealing (°C)**	ΔK_{th} **(MPa·m$^{0.5}$)**	C	m	**Ref**
Parallel to build deposition	EOSINT M280	920 for 0.5h	8.0		3.9	[157]
Perpendicular build to deposition			8.1		3.5	
XZY	EOSINT M280	910 for 8h	2.7	1.87e-11	3.51	[43]
YXZ			3.5	1.87e-11		
ZXY			2.7	1.87e-11		
XZY	SLM	890 for 2h		2.58e-11	2.94	[156]
YXZ				2.04e-12	3.83	
ZXY				1.71e-11	3.11	

The data presented in Table 2.6 depicts similar FCGR properties (C and m), regardless of the annealing soaking period, build orientation and L-PBF system. However, there is a significant difference in ΔK_{th} that resulted from annealing for different soaking periods.

2.5.5. Fatigue strength

Two methods can be used to determine the fatigue strength of a component. If the part experiences a measurable plastic deformation, a strain life method is considered. Otherwise, in the absence of plastic deformation, as anticipated for the design of aircraft components such as a nose wheel fork, a stress life method is a more appropriate approach. The stress-life method, commonly known as the SN fatigue approach, is appropriate for a long-life situation where the strength of the material and the nominal stress control fatigue life. Additionally, the stress concentration region of the tested structure remains elastic. Several loading modes such as fully reversed, repeated and random stress cycles, are used to determine fatigue strength. In Figure 2.39, different fatigue loading modes are illustrated.

© Central University of Technology, Free State

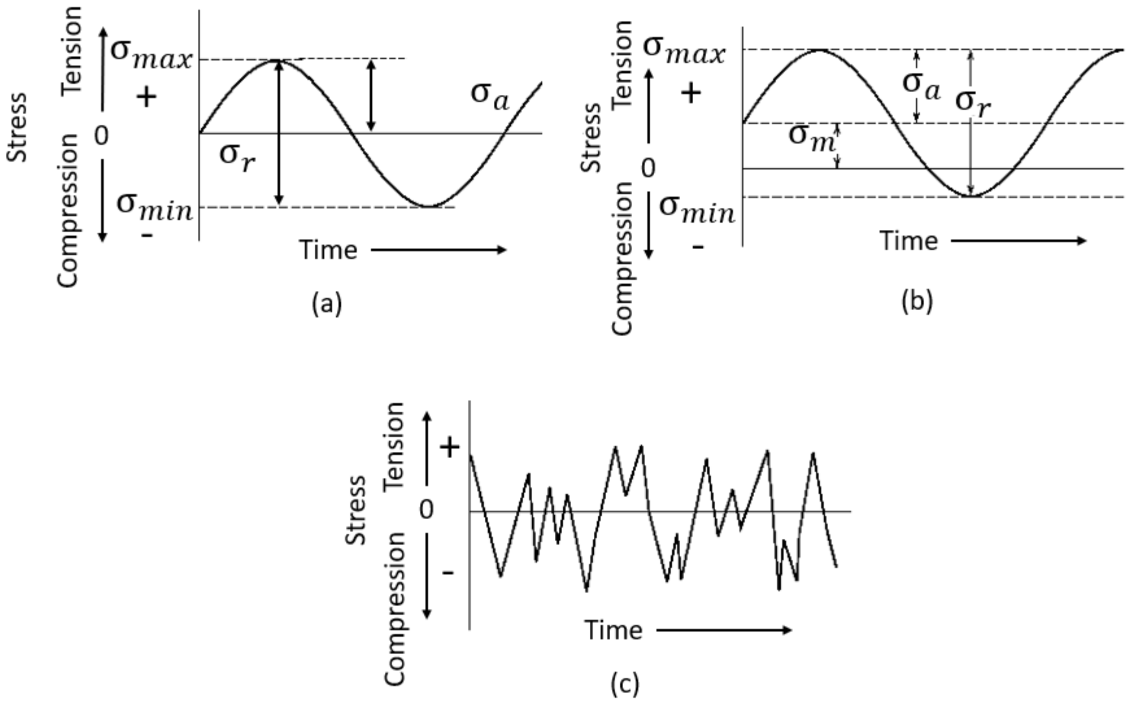

Figure 2.39: Graphical illustration of fatigue loading modes: (a) fully reversed stress cycle, (b) repeated stress cycle, and (c) random stress cycle [125]

For a completely reversed stress cycle, the compression stress equals the tensile stress, but in the opposite direction. Thus, the stress ratio (R) is equal to -1. In the repeated stress cycle the maximum (σ_{max}) and minimum (σ_{min}) stresses are not equal, resulting in R < 0. Finally, the random fatigue mode is a complicated stress cycle, which could be encountered by aircraft components such as the wings and landing gear [167]. The fluctuating stress cycles (Figure 2.39(a) and (b)) are characterised by a number of parameters. These parameters are computed using Equations 2.77 to 2.80.

$$\boldsymbol{\Delta\sigma} = \boldsymbol{\sigma_{max}} - \boldsymbol{\sigma_{min}} \tag{2.77}$$

$$\boldsymbol{\sigma_a} = \frac{\boldsymbol{\sigma_{max} - \sigma_{min}}}{\mathbf{2}} \tag{2.78}$$

$$\boldsymbol{\sigma_m} = \frac{\boldsymbol{\sigma_{max} + \sigma_{min}}}{\mathbf{2}} \tag{2.79}$$

$$\boldsymbol{R} = \frac{\sigma_{min}}{\sigma_{max}} \tag{2.80}$$

where $\Delta\sigma$, is the stress range, σ_a the alternating stress amplitude, and σ_m is the mean stress.

There are two types of equipment used to determine the fatigue strength of metal. If the load is applied along the longitudinal axis of the specimen, the test is known as an axial loading fatigue test. Alternatively, it is named a rotation-bending test if the specimen experiences a bending load while it is rotated. A schematic diagram of the axial fatigue and the rotation-bending fatigue testing configurations are shown in Figure 2.40 (a) and (b), respectively.

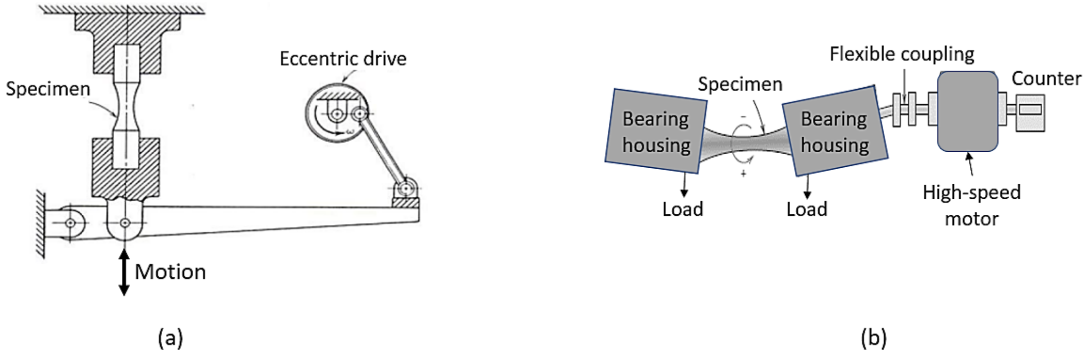

Figure 2.40: Schematic illustration of the configurations used to determine the fatigue strength of metals (a) axial loading fatigue test and (b) rotation-bending fatigue test [125]

The further discussion here deals with the axial fatigue test because it was used in the current study. During the axial fatigue test a cylindrical fatigue specimen, prepared as explained in ASTM E466-15, is used [168]. A minimum number of 8 to 12 specimens are commonly used to determine the SN curve, since there is a considerable amount of scattering in the fatigue results. The SN curve shown in Figure 2.41(a) is used to illustrate the typical relationship between the stress amplitude and the number of cycles to failure of a metal that exhibits a fatigue limit. Low cycle fatigue results from high amplitude, low frequency cyclic stress, whereas high cycle fatigue is due to low amplitude, high frequency cyclic stress. Figure 2.41(b) shows the SN curve of L-PBF Ti6Al4V(ELI) specimens that were machined and polished. The SN curve of the Ti6Al4V(ELI) becomes horizontal at a certain limiting stress known as the fatigue strength of the alloy. Below the fatigue strength, the material is assumed to have an infinite number of cycles without failure.

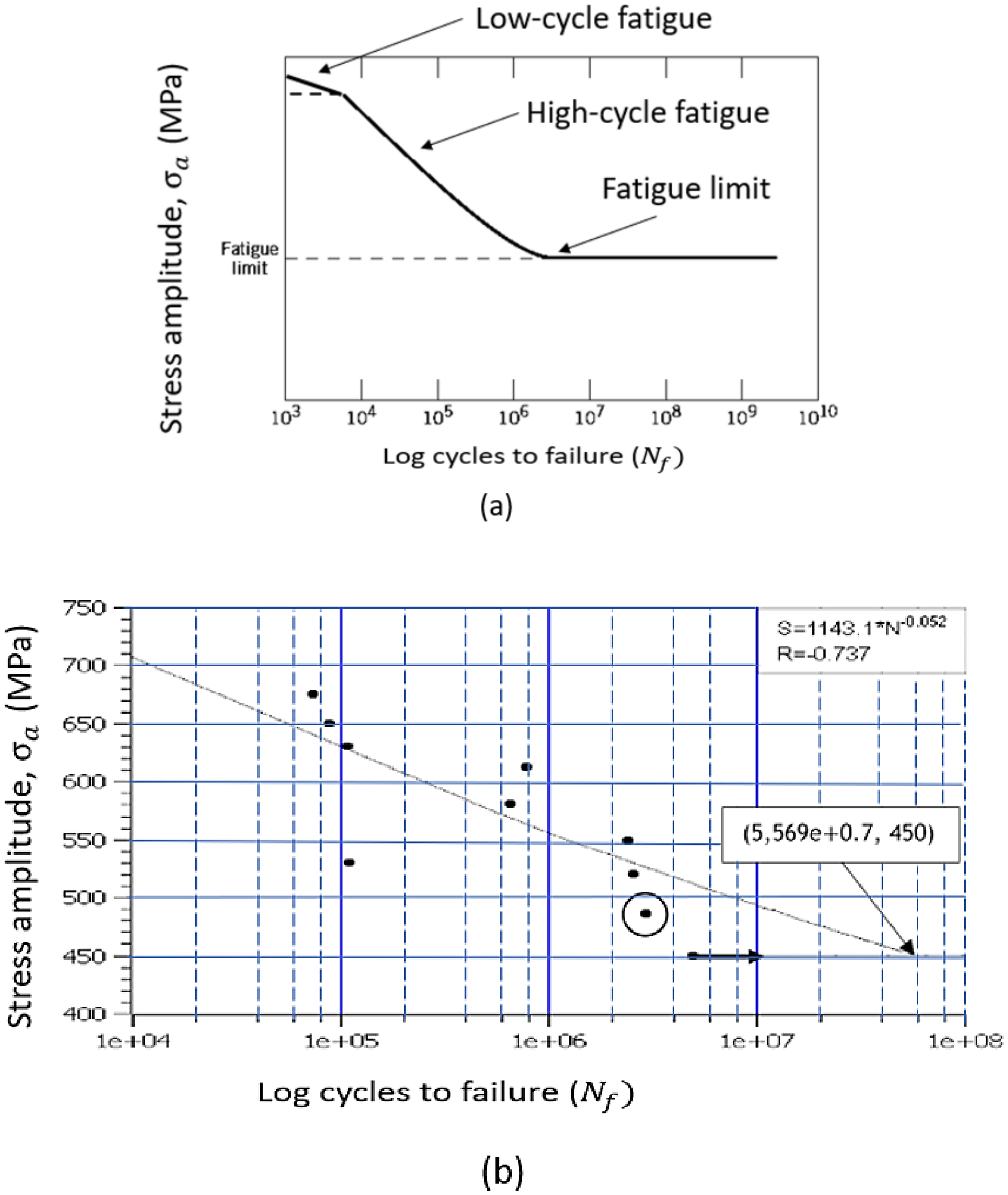

Figure 2.41: An illustration of the relationship between stress amplitude and the number of cycles to failure: (a) a typical SN curve [125] and (b) SN curve of polished Ti6Al4V(ELI) specimens produced through L-PBF [136]

© Central University of Technology, Free State

The relationship between the alternating stress amplitude (σ_a) and the number of cycles to failure is described by the Basquin equation, here given as Equation 2.81 for high cycle fatigue.

$$\boldsymbol{\sigma_a = \sigma'_f\,(2N_f)^b} \tag{2.81}$$

where σ'_f represents the fatigue strength coefficient, which is defined as the stress intercept in the stress versus the number of cycles to failure ($2N_f$). The slope of the SN curve b represents the fatigue strength exponent (Basquin's exponent), which varies for most materials between -0.05 and -0.12 [169]. A smaller value of b results in a longer fatigue life. In Table 2.7, the high cycle fatigue properties of specimens produced in a L-PBF and the Aeroswift machine, are tabulated.

Table 2.7: The fatigue strength of the polished Ti6Al4V(ELI) specimens produced through L-PBF and tested at the stress ratio of 0.1

Process	Conditions	Orientation	Fatigue strength (MPa)	Ref
L-PBF	as-built	45° to the manufacturing plane	210	[170]
	SR at 650 °C for 3 h		500	
	HTA at 950 °C, FC	X	450	[136]
		Y	450	
		Z	486	
Aeroswift (HS-SLM)	HTA at 950 °C, FC	X	450	[137]
		Z	350	

As illustrated in Table 2.7 the fatigue strength of the as-built specimens was the lowest when compared to the SR and HTA. A combination of SR and build orientation of 45° resulted in high fatigue strength of 500 MPa, whereas the HTA resulted in the same fatigue strength for the X- and Y-orientation and higher fatigue strength for the Z-build orientation. However, specimens built along the Z-axis in the Aeroswift system were reported to have lower fatigue strength as compared to X-specimens.

© Central University of Technology, Free State

Fatigue failure is usually recognised from the appearance of the fracture surface. It occurs in three stages, as shown schematically in Figure 2.42. These include crack origin, slow crack zone and fast fracture.

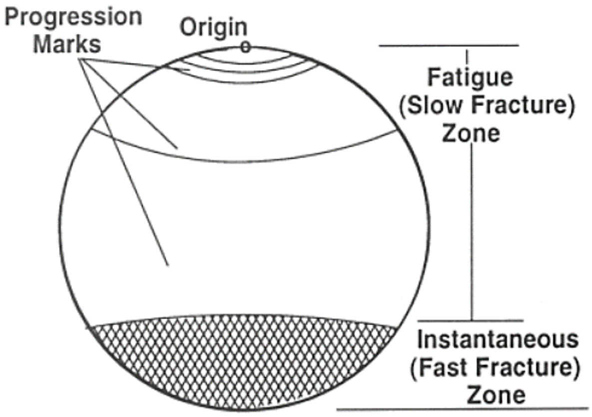

Figure 2.42: A schematic representation of macroscopic surface features of fatigue failure on a metallic specimen [171]

Cracks originate on the surface of specimens due to plastic deformation which resulted from slip-band and manufacturing defects. Low stress overload usually results in single crack initiation, while multiple crack origins indicate high applied stress or high stress concentration. Such multiple crack origins are separated by the ratchet marks, see Figure 2.43. For example, the stress concentration in Ti6Al4V(ELI) produced through L-PBF could be due to high surface roughness resulting from staircase effects and gas entrapment pores [172].

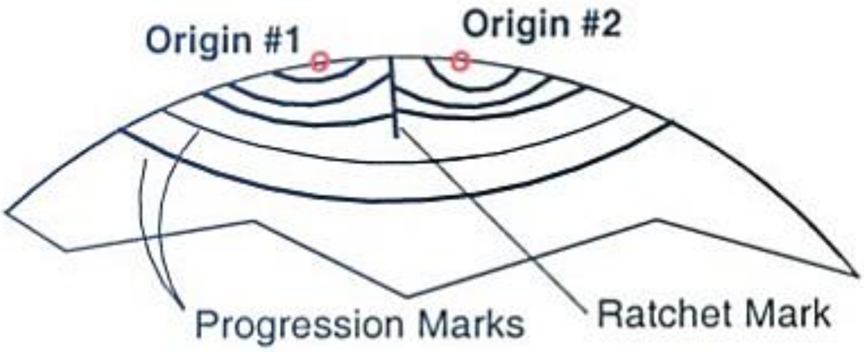

Figure 2.43: An illustration of ratchet marks which are located next to the crack origin

The plane of maximum stress that causes the fatigue failure is usually perpendicular to the fatigue zone. The crack propagates slowly across the fatigue slow fracture zone. Variations in load that occur during this crack propagation create progression marks (beach marks) in this slow crack growth zone. These marks demonstrate how the cross load changed and the individual stress cycles. Under high magnification, fatigue striations can also show each stress cycle experienced by a specimen. When the crack reaches the point where the remaining material cannot carry the load, an instantaneous fracture occurs, resulting in a fast fracture zone. This overload zone is frequently observed as macroscopically brittle.

2.6. Performance testing of L-PBF Ti6Al4V aircraft parts

The 14 Code of Federal Regulations (CFR) performance testing requirements set out by the FAA are:

CFR 23.603: "The suitability and durability of the material of a part that could adversely affect safety must meet the approved specifications that ensure they have the strength and other properties assumed in the design data" [56]. The specimen performance tests include microstructure analysis, static mechanical properties, impact, and fatigue testing.

CFR 23.605: "The method of fabrication used must produce the consistently sound structure." [56] For the L-PBF process, where fusion and/or heat treatment need to be controlled to reach the required structure, the process must be performed under the approved process specifications.

CFR 23.621 requires that non-destructive testing (NDT) techniques must be used to inspect the quality of the component. According to this regulation, each component that could preclude continued safe flight and landing of the aeroplane or result in serious injury to occupants must be inspected. These inspections must be done by using approved NDT techniques, such as radiographic imaging, and either magnetic particle or penetrant methods [56]. Computer tomography (CT) scanning is widely used for its capability to detect fine-scale porosity, surface

© Central University of Technology, Free State

roughness and material density [173]. This includes inspection of complex geometry produced from Ti6Al4V by L-PBF.

The performance integrity of a component is directly related to its design. The design requirement regulations CFR 23.613 and 23.627 state that the structure must be designed as far as practicable, to avoid points of stress concentration where variable stresses above the fatigue limit are likely to occur in normal service [56]. This would be particularly relevant when designing the nose wheel fork for production in Ti6Al4V(ELI) through L-PBF.

2.7. Summary

Through the literature review, the following insights were gained:

The position of the nose wheel of a light aircraft in a tricycle configuration is a key aspect in designing a landing gear nose wheel fork. A well-positioned nose wheel provides a balanced load distribution on the landing gear. A light load nose wheel landing gear promotes unwanted impact forces since it promotes bouncing on the ground, whereas the high loaded gear resists rotation of the aircraft during take-off. This must be carefully considered when determining the load that is carried by the landing gear nose wheel fork. Braking after landing also induces significant loads on the nose wheel fork. Therefore, various load cases must be considered when redesigning the nose wheel fork.

TO during DfAM allows multiple load cases to be set when generating the optimal design by maximising stiffness, while reducing the weight of the part. An optimal design can be evaluated for failure through experimentally validated FEA. This can be accurately done by applying strain gauge measurement. Finally, validated FEA results can be used to predict the fatigue life of an optimally designed component.

The L-PBF compatible Ti6Al4V(ELI) alloy, commonly used for production of the aircraft components due to its good mechanical and dynamic properties, can be optimised through heat treatment by altering its microstructure. If TO-DfAM could

© Central University of Technology, Free State

be employed to redesign and produce the Ti6Al4V(ELI) nose wheel fork through L-PBF, an optimal design with a balanced specific weight can be obtained.

The literature study discussed in the current chapter reveals important aspects for consideration during production of a qualified nose wheel fork of a light aircraft in Ti6Al4V(ELI) through L-PBF and assessment of its performance. The first aspect is based on evaluation of the L-PBF Ti6Al4V(ELI) quality through NDT. It includes geometric deviation evaluation, porosity testing and surface roughness measurement. These must be followed by the production of various Ti6Al4V(ELI) standard test specimens built with inherent defects of the L-PBF and testing them to investigate their tensile strength, fatigue strength, impact toughness, fracture toughness and FCGR. Subsequently, assess the static and fatigue performance of the L-PBF Ti6Al4V(ELI) nose wheel fork that was built with the inherent defects. Thereafter, evaluation of the microstructure and fracture mechanism of the L-PBF of Ti6Al4V(ELI) components must be carried out. Finally, an in-depth analysis of the test results must be done to draw a conclusion on the use of the L-PBF of Ti6Al4V(ELI) as a technology for the production of mission-critical components of an aircraft.

© Central University of Technology, Free State

CHAPTER 3: METHODOLOGY

3.1. Introduction

In Figures 3.1 and 3.2, a diagrammatic outline of the research methodology followed in Phases 1 and 2 of this study is given.

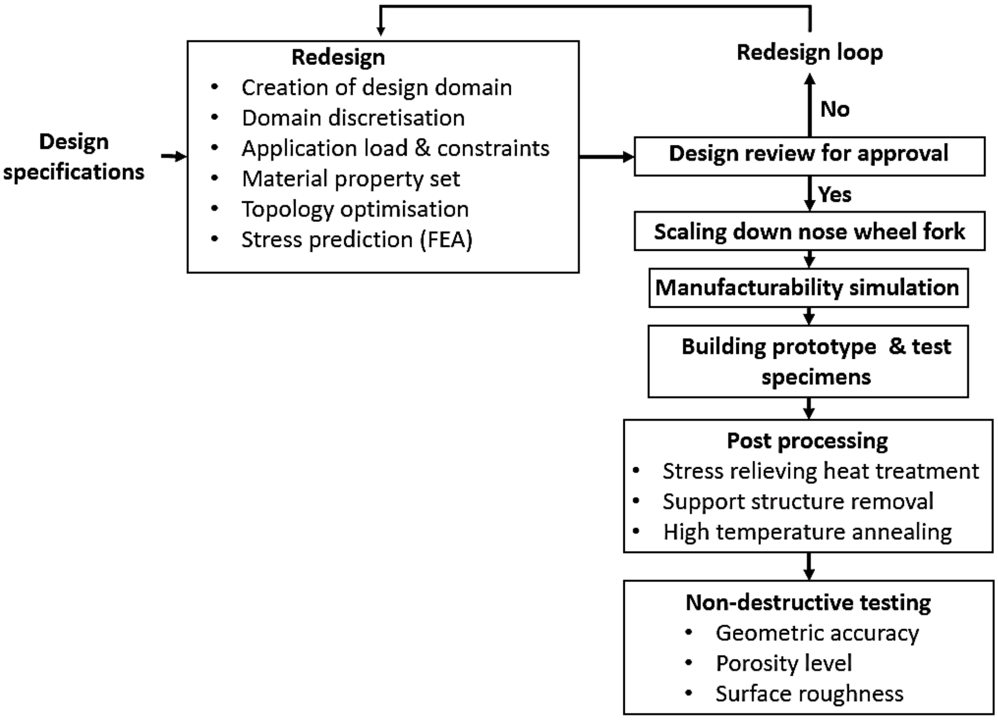

Figure 3.1: A diagrammatic outline of Phase 1 of the research methodology

Phase 1 of the methodology included three main stages which are design specifications, redesign of the nose wheel fork and design approval. These stages are described in detail in sections 3.2, 3.3 and 3.4 of Chapter 3. The redesign of the nose wheel fork as second stage of phase 1 consists of six steps such as creation of the design domain, design domain discretisation, load and constraints, material properties, topology optimisation and stress prediction. In sections 3.3.1 through 3.3.6, detailed descriptions of these steps are presented. It is important to note that the redesign of the component integrated TO and FEA to obtain a design with a balanced strength-to-weight ratio (specific strength) and stresses experienced by the nose wheel fork, respectively.

© Central University of Technology, Free State

The additional stages of Phase 1 are scaling down of the nose wheel fork, manufacturability simulation, building of the prototype and standard test specimens, post processing and non-destructive testing. The approved design was scaled down to obtain the experimental prototype. Thereafter, a manufacturability simulation of the prototype was performed to improve building orientation and minimise distortion. After the specimens and nose wheel fork were fabricated from Ti6Al4V(ELI) powder through L-PBF, post-processing was performed to relieve residual stresses and improve the mechanical properties through HTA. Phase 1 ended with NDT of the prototype to determine the geometric accuracy, porosity level and surface roughness. These tests were done to investigate the effect of the defects of the L-PBF on the performance of the Ti6Al4V(ELI) nose wheel fork. The detailed description of these additional stages of Phase 1 is presented in sections 3.5 through 3.9. The second phase of the methodology was carried out once the first phase was complete. In Figure 3.2, this methodology Phase is illustrated.

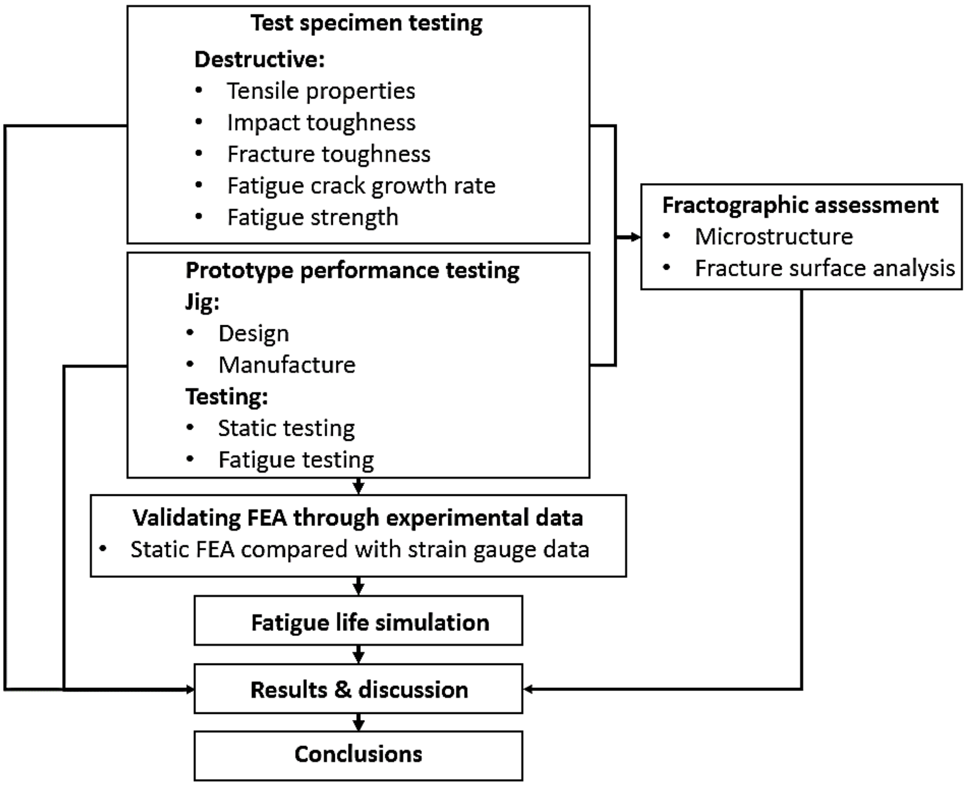

Figure 3.2: A diagrammatic outline of Phase 2 of the research methodology

Phase 2 of the research methodology applied in the current study have 4 main stages which are destructive testing of standard test specimens, metallographic preparation, preparation of specimens for fractography and performance testing of the prototype. These stages are presented in detail through sections 3.10 to 3.13 and summarised here. Phase 2 of the research methodology began with destructive testing of specimens. Tensile tests were done to confirm the building quality of L-PBF, whereas impact tests were performed to obtain the impact toughness of Ti6Al4V(ELI) under low temperature, and fracture toughness tests were run to investigate the fracture resistance of L-PBF Ti6Al4V(ELI) components in the presence of cracks. Furthermore, the FCGR and fatigue strength were investigated. Thereafter, the scaled-down nose wheel fork was tested under static and fatigue loading. The static results were used for strain gauge validation of the FEA model. This experimentally validated FEA was used for fatigue predictions of the scaled-down nose wheel fork. Microstructure and fractographic evaluations were also performed to confirm the cause of failure of the L-PBF Ti6Al4V(ELI) nose wheel fork. These were followed by the presentation and discussion of results. Finally, conclusions on the feasibility of producing the nose wheel fork of an aircraft in Ti6Al4V through L-PBF technology were drawn.

3.2. Design specifications

The AHRLAC company, which is currently operating as Paramount Aerospace Industries, provided the design specifications for the redesign of the nose wheel fork. These included load cases experienced by the AHRLAC nose wheel fork during landing and ground operation, the design domain, as well as assembly and boundary conditions that must be adhered to for the new design to be approved. In Figure 3.3(a), an image of the AHRLAC is shown to illustrate its landing gear configuration. During the maximum landing case, as indicated in the loading configuration in Figure 3.3(b), X, Y and Z forces are applied concurrently through the wheel axle of the nose wheel fork. For the ground static load case, the Y and Z forces are applied at the same time on the wheel axle through a

© Central University of Technology, Free State

wheel radius distance of 175.26 mm, see Figure 3.3(c). In the jacking load case in Figure 3.3(d), Z load is applied at the pivoting point of the nose wheel fork.

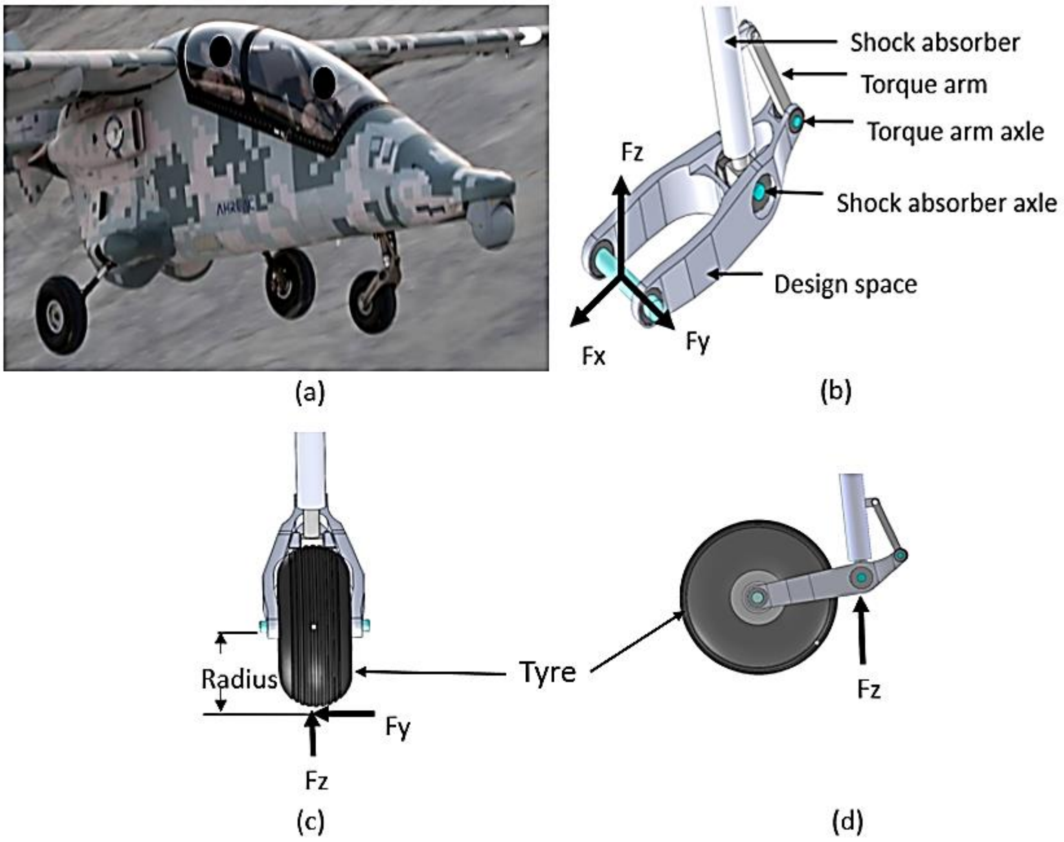

Figure 3.3: (a) the AHRLAC landing gear configuration, (b) maximum landing case, (c) ground static load case, and (d) jacking load case

There was a total of 16 load cases for consideration during the redesign of the AHRLAC nose wheel fork for production in Ti6Al4V(ELI) through L-PBF. The highest load cases were the maximum landing and ground static loading. In Table 3.1, the various load cases provided by Paramount Aerospace Industries are tabulated. These load cases were based on the FAR guidelines.

Table 3.1: Load cases of the AHRLAC provided by Paramount Aerospace Industries

Load cases	**Applied forces**		
	F_X (N)	**F_Y (N)**	**F_Z (N)**
Maximum landing	13 960	8 395	20 711
Ground static (Wheel radius = 175.26 mm)	0	9 910	14 347
Minimum landing	-10 012	8 395	0
Towing load	9 223	7 987	5 330

© Central University of Technology, Free State

Load cases	Applied forces		
	F_X (N)	F_Y (N)	F_Z (N)
Jacking	0	0	8 000
3 Point landing	5 494	0	6 868
Braked roll	761	0	7 609
Shock absorber test	11 328	0	14 160
Supplementary condition A	9 912	0	14 160
Supplementary condition B	-5 664	0	14 160
Supplementary condition C	0	0	12 660
Limit drop test	6 696	850	8 370
Level landing	6 459	0	15 585
High speed	2 156	0	2 695
Maximum spin up landing	10 124	0	12 655
Wheel spring back landing	-10 124	0	0

3.3. Redesign of the nose wheel fork

The redesign of the nose wheel fork for production in Ti6Al4V(ELI) through L-PBF was carried out by following six steps. These are: (i) design domain creation, (ii) domain discretisation, (iii) application of loads and constraints, (iv) compilation of the material property set, (v) topology optimisation and (vi) prediction of the stress. When the predicted stress experienced by the nose wheel fork was more than the strength of L-PBF Ti6Al4V(ELI) specimen, the redesign iterations were followed. Otherwise, when the safety factor was 1.5 or more the design was approved. These redesign iterations resulted in multiple design concepts. In section 4.2 of Chapter 4, different design concepts and the best optimal design concept are presented. The 2018 MSC Patran-Nastran® and 2018.2 version of Altair SolidThinking Inspire® software packages were used to redesign the Ti6Al4V(ELI) nose wheel fork for production through L-PBF. These packages were selected due to their availabilities and financial constraints. The objective was to minimise mass by maximising the stiffness to obtain a Ti6Al4V(ELI) nose wheel fork which would be light in weight compared to the Al 7050 fork without compromising the strength. This optimisation was strictly based on the design specifications provided by Paramount Aerospace Industries.

© Central University of Technology, Free State

3.3.1. Design domain

The CAD model of the design domain was derived from the full-scale CAD model of the actual nose wheel fork of the AHRLAC shown in Figure 3.4(a) and (c). The volume of the design domain was made larger by 452×10^{-6} m^3 than the actual fork to ensure enough design freedom, where the original volume was 2.921×10^{-3} m^3. The bushes were separated from the design domain using the SolidThinking Inspire® partition tool. Additionally, the top contour on the design domain, as well as the dimensions of the wheel, shock strut and torque arm bushes, were kept the same as in the actual fork to ensure zero interference between the optimal design of the nose wheel fork and other parts of the aircraft. In Figure 3.4(b) and (d), the images of the design domain with bushes are shown.

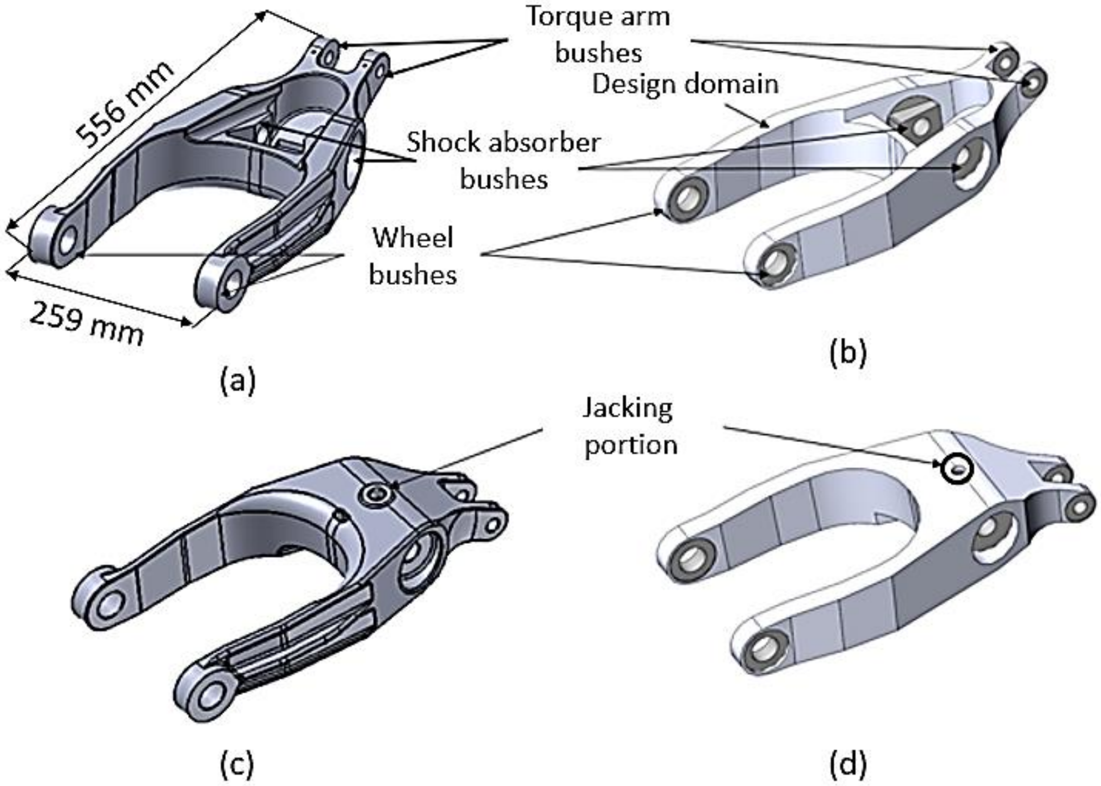

Figure 3.4: CAD model of the nose wheel fork (a) top view of the actual fork, (b) top view of design domain, (c) bottom view of the actual fork, and (d) bottom view of the design domain CAD model

© Central University of Technology, Free State

3.3.2. *Design domain discretisation*

The mesh generation in SolidThinking Inspire® is automated (null user dependent). This software automatically carries out meshing according to the specified element length, which was 6 mm in the current study. Thereafter, rigid body element (flexible connectors) was created on the design domain bushes to allow the realistic application of loads and boundary conditions.

In the MSC Patran® software, a quadratic hexahedral mesh, which is recommended for TO, was created using the MSC Apex® software. The global element length was set to 6 mm. Thereafter, the design domain of the nose wheel fork with mesh was imported into the Patran software to create beam elements to represent the wheel, shock struts, and torque arm axles. To transfer loads, rigid body elements (RBE) were used to connect each beam element to the meshed design domain of the nose wheel fork. In Figure 3.5(a) and (b) the discrete CAD model from SolidThinking Inspire® and Patran® are illustrated.

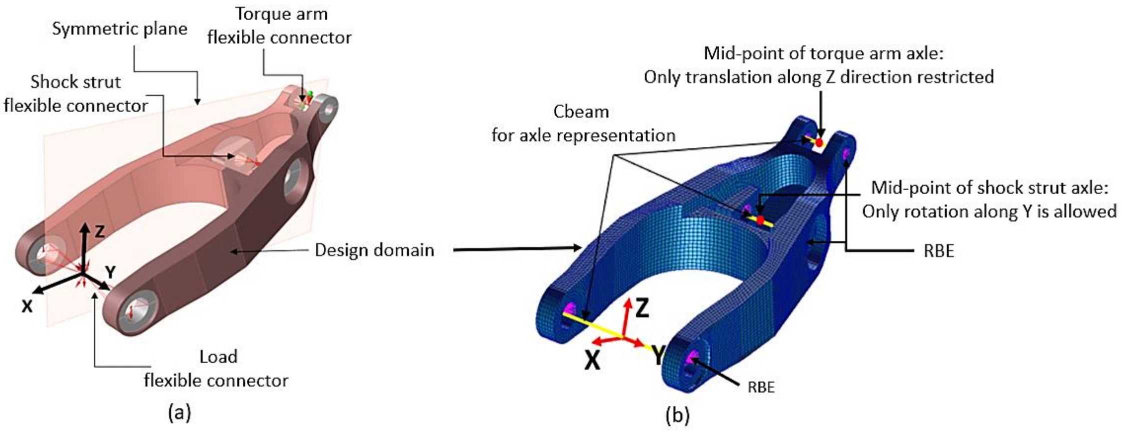

Figure 3.5: Illustration of the discretisation of the AHRLAC nose wheel fork design domain CAD model in (a) SolidThinking Inspire® and (b) Patran®

In Figure 3.5, the plane ZX was created to generate symmetry on either side of the nose wheel fork during TO. The line connecting bushes on both sides of plane ZX represent the shafts. In the Inspire® and Patran® software, these were referred to as the connectors and beam elements, respectively.

© Central University of Technology, Free State

3.3.3. Loads and constraints

All load cases and boundary conditions of the AHRLAC, which are given in Table 3.1, were set in the discrete design domain. For all load cases except the jacking load case, forces were applied on the design domain through the wheel axle. For the ground static load case, forces were applied at a distance of 175.25 mm and the jacking load was applied at the jacking area shown in 3.3(d). For each load case, the mid-node of the beam passing through the torque arm bushes was restricted to translate in the Z direction only, whereas the mid-node of the shock absorber beam was allowed to rotate about the Y axis. Finally, the shape control, symmetric about the Z-X plane, was also set in the design domain.

3.3.4. Material properties

The nose wheel fork of the AHRLAC, which was produced from wrought Al 7050 alloy and had a weight of 8.23 kg, was redesigned using TO for production in Ti6Al4V(ELI) through L-PBF. Table 3.2 gives the material properties of Ti6Al4V(ELI) used in the redesign of the AHRLAC nose wheel fork and the properties of the Al 7050 that was used to produce the nose wheel fork through conventional milling processes.

Table 3.2: Material properties of the Ti6Al4V(ELI) alloy used in the redesign of the AHRLAC nose wheel fork compared to the Al 7050 properties used during conventional manufacturing

Material	Elastic modulus (GPa)	Poisson's ratio	Density (kg/m^3)	UTS MPa	$\sigma_{y0.2}$ (MPa)	Ref
Ti6Al4V(ELI)	110	0.31	4 429	909	765	[136]
AA 7050	75	0.33	2 700	515	455	[174]

From Table 3.2 it is clear that the tensile properties of the Ti6Al4A(ELI) are higher than those of the AA 7050. However, the density of the AA 7050 is lower than that of the Ti6Al4V(ELI). Therefore, to use Ti6Al4V(ELI) for production of a lightweight part of the aircraft, a balanced strength-to-weight ratio had to be obtained.

© Central University of Technology, Free State

3.3.5. *Topology optimisation*

The elements that experienced low stress in the nose wheel fork design domain were removed to obtain the optimal geometry, whereas elements that experienced high stress were kept in the design domain. The process resulted in a complex geometry which is commonly called the load path. In the SolidThinking Inspire® and Patran® software the penalisation of the elemental density that allows the removal of low-stress elements was carried out in the OptiStruct and Nastran solver, respectively. Once the load path was determined, a smooth CAD model was generated to create the optimal design.

The geometric smoothing of the Patran® software resulted in a part with less material to connect the symmetric half of the optimal nose wheel fork. This limited the geometric stiffness in the longitudinal middle region of the fork. The part also consisted of partially sharp edges which could lead to high-stress concentration regions. To convert the Patran® geometry into an acceptable nose wheel fork, SolidWorks® was used. Alternatively, the PolyNurb function of the SolidThinking Inspire® software allowed the creation of a novel and complex geometrically shaped nose wheel fork which was accepted as the final optimal design. In section 4.2 of Chapter 4, a detailed description of the various concepts and the selected optimal concept of the nose wheel fork are presented.

3.3.6. *Stress prediction*

FEA was used to predict the stress experienced by the optimal nose wheel fork. For this purpose, the Patran-Nastran® software was used. Firstly, the smooth optimal nose wheel fork CAD model created from the SolidThinking Inspire® software was imported into the Patran-Nastran® software. Thereafter, a quadratic tetrahedral solid mesh with a global element size of 6 mm was generated on the optimal nose wheel fork. Loads and constraints were set, as explained in section 3.3.3. The maximum displacement, von Mises stress and safety factor experienced by the optimal nose wheel fork were computed for all load cases. In section 4.3, the predicted results for the nose wheel fork are presented.

© Central University of Technology, Free State

3.4. Design approval

The optimal design of the AHRLAC nose wheel fork was evaluated against the provided specifications. The design was accepted based on the maximum distortion energy theory, which is known as the von Mises safety criteria. If the calculated von Mises stress of the nose wheel fork was not acceptable, the design domain or the load path had to be altered. Once the stresses in the fork were found to be satisfactory, obtaining a safety factor of 1.5 or more, the optimal design of the nose wheel fork was accepted.

3.5. Scaling down nose wheel fork

The dimensions of the optimal AHRLAC nose wheel fork were reduced by a constant scale factor of 0.4 to create an experimental prototype that could be manufactured using the EOS M290 L-PBF system with a building volume of 250 x 250 x 325 mm. This resulted in a uniform load scaling factor of 16%, which was determined using the theory of similarity [175]. The detailed description of the approved design of the nose wheel fork for production in Ti6Al4V(ELI) through L-PBF and the FEA results obtained are discussed in Chapter 4.

3.6. Experimental prototype manufacturability

The scaled-down nose wheel fork as an experimental prototype was evaluated for manufacturability. This was done to identify the best build orientation to limit fork distortion during L-PBF. Version 4.1 of the Simufact Additive® software was used to predict the building orientation and distortion that could result from the L-PBF manufacturing process of the Ti6Al4V(ELI) nose wheel fork. Firstly, the machine parameters of the EOSINT M290 L-PBF system were set. The most important parameter was the laser power of 170 W because it is the optimal parameter used at the CRPM [176] and was used to build the nose wheel fork and test specimens. This was followed by the auto-generation of the support structure using the Materialise Magics coding which is incorporated in the

© Central University of Technology, Free State

Simufact Additive® software. Thereafter, the building orientation was selected and set. The Simufact Additive® orientation assistance was used to determine the best building orientation. Out of 10 possible orientations of the scaled-down nose wheel fork provided by the software, one orientation was selected as presented in detail in Chapter 4. The simulated process sequence included: building the nose wheel fork using L-PBF, stress-relieving heat treatment at 650 °C for a soaking time of 3 hours, cutting off the support structure from the building base plate, support structure removal from the fork and HTA heat treatment at 950 °C for a soaking time of 2 hours. The build orientation and manufacturability predicted results, such as geometric deviation and residual stress, are presented in sections 4.4 and 4.5.1 of Chapter 4, respectively.

3.7. Building of prototype and test specimens

A Ti6Al4V(ELI) powder that was supplied by TLS Technik GmbH & Co Spezialpulver KG (Bitterfeld-Wolfen, Germany) was used to build the prototype (scaled-down nose wheel fork) and all test specimens. This spherical powder had a particle size distribution of less than 45 μm. In Table 3.3, the chemical composition of the Ti6Al4V(ELI) powder is shown and compared with ASTM F3001-14 [177].

Table 3.3: Chemical composition of the supplied Ti6Al4V(ELI) powder and the composition required in the ASTM F3001-14 standard

Materials	**Titanium (Ti)**	**Aluminium (Al)**	**Vanadium (V)**	**Iron (Fe), max**	**Oxygen (O), max**	**Nitrogen (N), max**
TLS powder [29]	90.30%	5.56%	4.02%	0.23%	0.12%	0.04%
ASTM F3001-14 [177]	Balance	5.5–6.5%	3.5–4.5%	0.25%	0.13%	0.05%

As shown in Table 3.3, the chemical composition of the powder used in the current study complied with the composition specified in ASTM F3001-14.

The new version of the L-PBF at the time, the EOSINT M290 system (EOS GmbH, Germany) was selected for production of the experimental prototype (scaled-down nose wheel fork) and three cylindrical test bars on the same

© Central University of Technology, Free State

substrate. This was done using a machine parameter set provided by the supplier. These bars were machined to create standard tensile test witness specimens to confirm the quality of the build process. In Figure 3.6(a) and (b), the L-PBF Ti6Al4V(ELI) scaled-down nose wheel fork on the base plate with the support structure and the component with the support structures removed, respectively, are shown. The pin support structures were necessary to increase the surface area of the normal support structures, which resulted in high reaction forces required to anchor the fork on the base plate during L-PBF. Such pin support structures have a cone-like shape with a diameter of 2 mm and 4 mm on the side of the fork and base plate, respectively. In Figure 3.6(c) and (d), the positions of the pin support structures are illustrated.

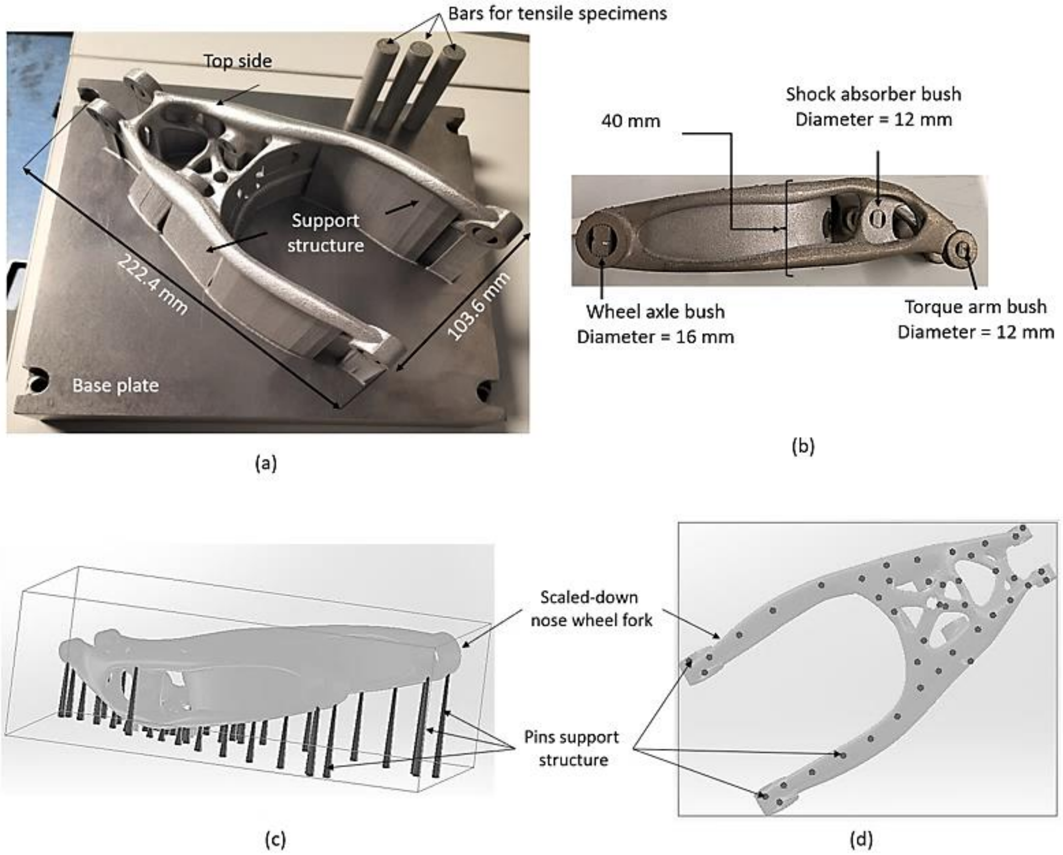

(a) (b)

(c) (d)

Figure 3.6: Images of (a) the L-PBF Ti6Al4V(ELI) scaled-down nose wheel fork with the cylindrical bars for machining standards tensile test specimens, (b) dimensions on the side view of the nose wheel fork, and (c)–(d) positions of the pin support structures

© Central University of Technology, Free State

On a separate build platform, 9 tensile and 21 high cycle fatigue (HCF) test specimens were built from Ti6Al4V(ELI) powder through L-PBF, such that they retained the as-built surface roughness. On the same platform, a set of 9 Charpy impact toughness test specimens was built with a V-notch, while another set of 9 specimens was built without a V-notch, because the V-notch was machined using an EDM wire cutter. On the last build platform, 9 fracture toughness and 9 fatigue crack growth rate (FCGR) Ti6Al4V(ELI) test specimens were built and polished before testing. At that time, the available L-PBF machine was the EOSINT M280 (EOS GmbH, Germany). The parameter set provided by the supplier was used to build all specimens. The build orientation of the tensile, impact toughness, fracture toughness (K_{IC}), FCGR and HCF test specimens are illustrated in Figure 3.7.

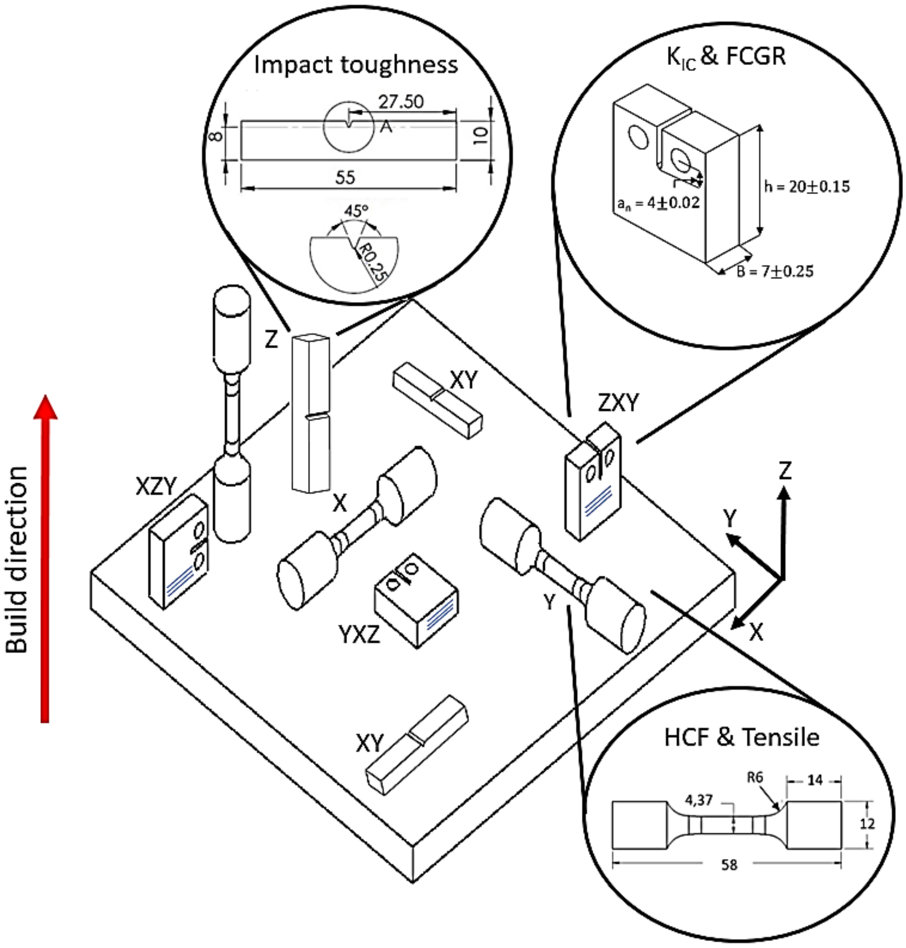

Figure 3.7: Illustration of the build orientation of the tensile, HCF, impact toughness, fracture toughness, and FCGR test specimens

© Central University of Technology, Free State

Triplicate impact toughness specimens were built in each of three directions (XY, YX and Z). For each of the K_{IC} and FCGR test specimens, the 3 specimens were built in the XZY-, YXZ- and ZXY-orientations. For the tensile and HCF test specimens, 3 and 7 specimens were built in each of the X-, Y-, and Z-directions, respectively. For the X- and Y-specimens, the support structure and pins were necessary to anchor the specimens on the building platform during the L-PBF process. These pins were created outside the specimen's gauge length, as shown in Figure 3.8. The Z-specimens had to be built using the block support structure to minimise the vibration as the recoater blade distributed powder particles. The block support structures had no direct contact with the gauge length of the Z-specimens, as shown in the magnified image of Figure 3.8.

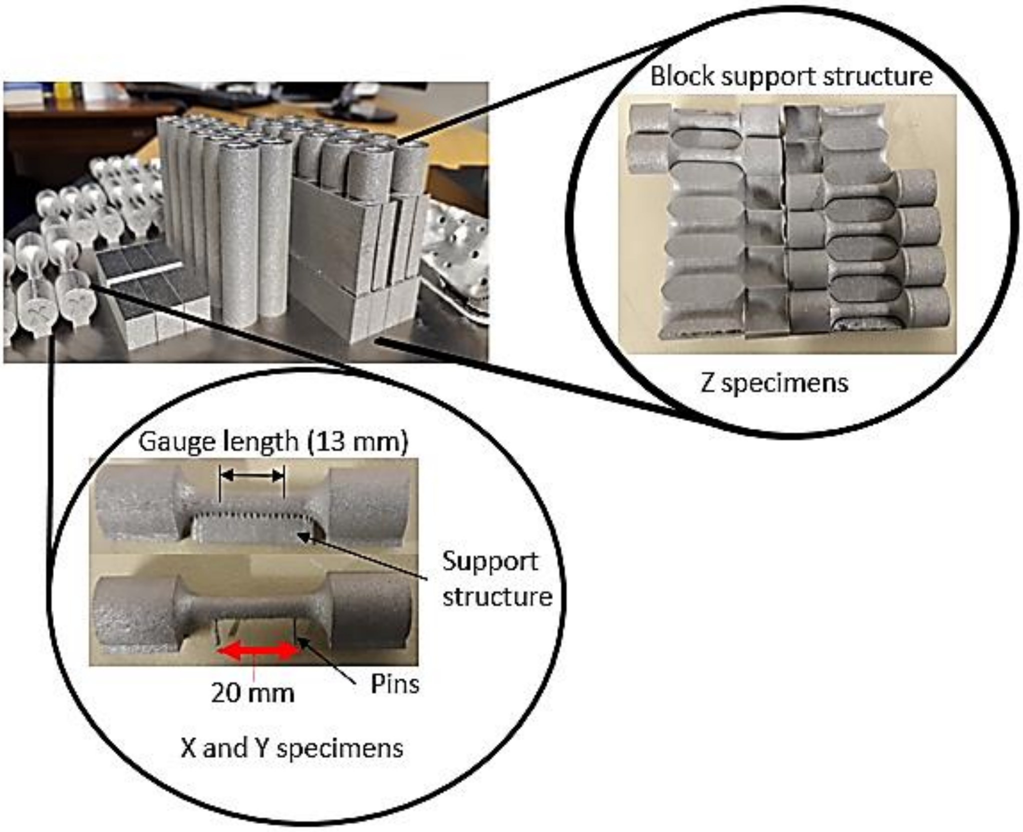

Figure 3.8: A detailed view of the tensile and HCF specimens built from Ti6Al4V(ELI) through EOSINT M280

© Central University of Technology, Free State

3.8. L-PBF post-processing

The L-PBF Ti6Al4V(ELI) scaled-down nose wheel fork and all specimens were submitted to a two-stage heat treatment. In Figure 3.9, the two-stage heat treatment used for treating the scaled-down nose wheel fork and all specimens in a vacuum furnace is shown.

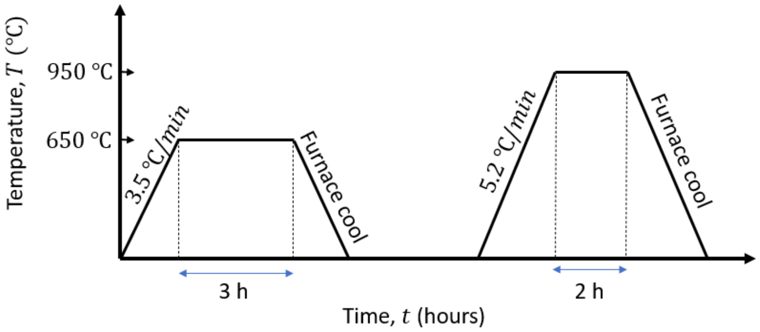

Figure 3.9: Two-stage heat treatment used for treating the L-PBF Ti6Al4V(ELI) scaled-down nose wheel fork and all specimens in a vacuum furnace

While the scaled-down nose wheel fork and test specimens were still secured on the base plate by the support structure, they were heated to 650 ^{o}C at a rate of 3.6 ^{o}C/min and soaked at that temperature for 3 hours, followed by furnace cooling to room temperature. Thereafter, the scaled-down nose wheel fork and test specimens were cut from the base plate through EDM wire cutting and the support structures were manually removed from them. Subsequently, the scaled-down nose wheel fork and all the test specimens were annealed by heating to 950 ^{o}C at a rate of 5.2 ^{o}C/min, soaked at that temperature for 2 hours, followed by furnace cooling to room temperature.

3.9. Non-destructive testing of prototype

The quality of the L-PBF Ti6Al4V(ELI) scaled-down nose wheel fork built as the experimental prototype was evaluated using NDT, which included determining the geometric accuracy, porosity of representative test specimens and surface roughness measurements.

© Central University of Technology, Free State

3.9.1. *Geometric accuracy*

The dimensional accuracy of the L-PBF Ti6Al4V(ELI) scaled-down nose wheel fork was measured through triangulation with a Kreon (Kreon GmbH Deutschland, Germany) 3D scanning CMM shown in Figure 3.10. This instrument had a maximum laser scanning speed of 600 points per second and data was captured over a length of 10 cm at an accuracy of 40 μm.

Figure 3.10: An illustration of the Kreon scanning system used to measure deviation on the L-PBF Ti6Al4V(ELI) nose wheel fork during Scan A

To determine the deviation resulting from the post-process heat treatments, two scans were performed. Scan A was done after L-PBF, followed by stress-relieving heat treatment and support structure removal, whereas Scan B was performed after subsequent HTA. During the scanning process, the scaled-down nose wheel fork was virtually sectioned, and the scan data was auto-aligned on the CAD model to compute the geometric deviation using the Geomagic® software [179].

© Central University of Technology, Free State

A total of 22 points were selected for geometric deviation analyses, as shown in Figure 3.11. At each location point (1 to 22), the difference in millimetres between the CAD data and the measured data was recorded at a tolerance of ± 0.1 mm.

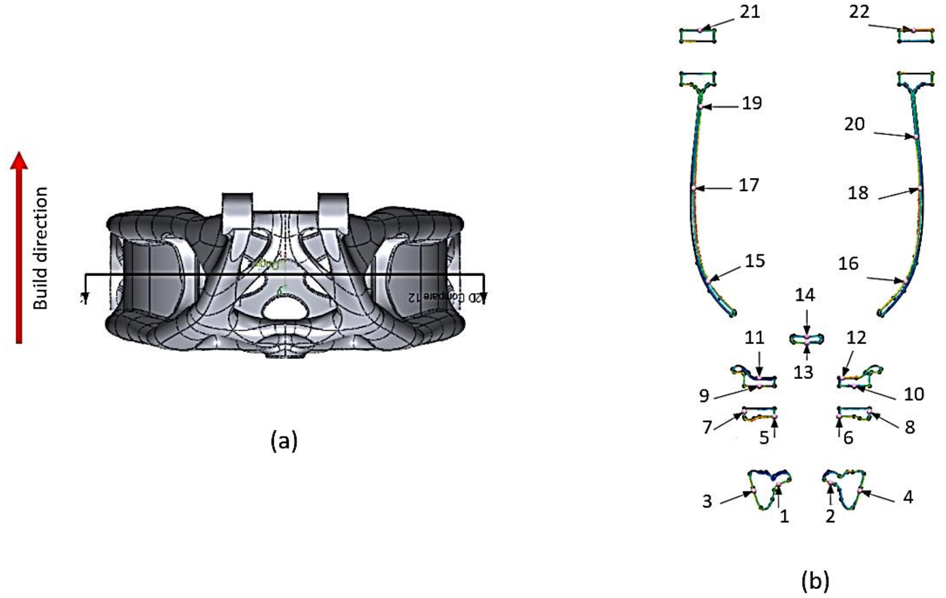

(a)

(b)

Figure 3.11: (a) Virtual Section 1 of the scaled-down nose wheel fork for geometric deviation determination, (b) positions of the 22 points used during Scan A and Scan B. The measurement planes of the mid area were perpendicular to the build direction

Subsequently, the torque arm, shock absorber strut, and wheel axel bushes of the nose wheel fork were virtually sectioned in planes parallel to the L-PBF build direction. This represented Section 2 with the deviation data points measured in these planes. Points 1 to 15 were measured for both Scans A and B to compare the geometric deviation. In Figure 3.12, the 15 points of Section 2 are illustrated.

© Central University of Technology, Free State

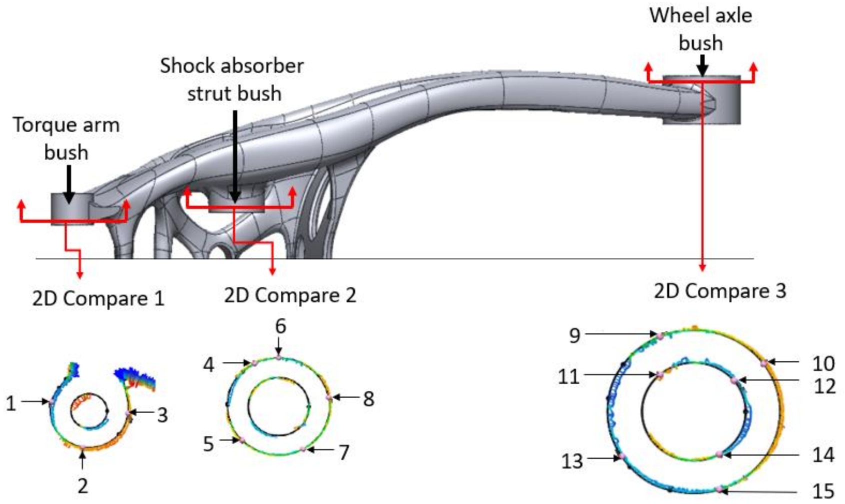

Figure 3.12: Illustration of the data points in Section 2 of the nosewheel fork. The measurement planes of the bushes were parallel to the build direction

Finally, to determine how significant the differences between Scan A and Scan B were, a statistical significance F-test was performed for a significance level of 5%. For this, the F-distribution table in Appendix D was used to determine the statistical critical value. On the other hand, the geometric deviation results obtained from this experimental procedure are presented in section 4.5.2 of Chapter 4 and Appendix E.

3.9.2. Porosity

Three Ti6Al4V(ELI) specimens built through the EOSINT M280 L-PBF machine along the X-, Y-, and Z-directions were used for porosity determination. The specimens had a length and diameter of 13 mm and 4.37 mm, respectively. A Nikon XTH 225 ST X-ray micro-computed tomography (Micro-CT) system (Nikon Corporation, Japan) was used for this determination. The test parameters were: scanning resolution of 8.2 µm, current of 200 µA, accelerating potential voltage of 185 kV, exposure period of 4 s per projection, and a total of 2 000 projections per specimen. Porosity levels detected are presented in section 4.5.3.

© Central University of Technology, Free State

3.9.3. Surface roughness

A ZEISS Smartzoom 5 microscope (Carl Zeiss, Germany), equipped with D5x/0.3 FWD 30 mm objective, was used to capture high resolution digital images of the surface areas where the scaled-down nose wheel fork failed during performance testing. This was done to qualitatively characterise the surface roughness of the L-PBF Ti6Al4V(ELI) nose wheel fork. In sections 4.5.4 and 6.2.4 of Chapters 4 and 6 respectively, the surface roughness of the L-PBF Ti6Al4V(ELI) scaled-down nose wheel fork is shown.

The surface roughness of the Ti6Al4V(ELI) scale-down nose wheel fork produced through L-PBF was also measured. The Surftest SJ-210 tester (Mitutoyo Corporation, Japan) was used to measure the R_a surface roughness values on the scale-down nose wheel fork. To characterise the surface roughness on the sides of the nose wheel fork where the Surftest could not reach, additional measurements were taken on a test specimen that had been built with the fork. The measurements were carried out over a length of 5 mm at a speed of 0.5 mm/s. Three surface roughness measurements were taken on each side of the test specimen along two directions, as shown in Figure 3.13, and the average R_a values were calculated.

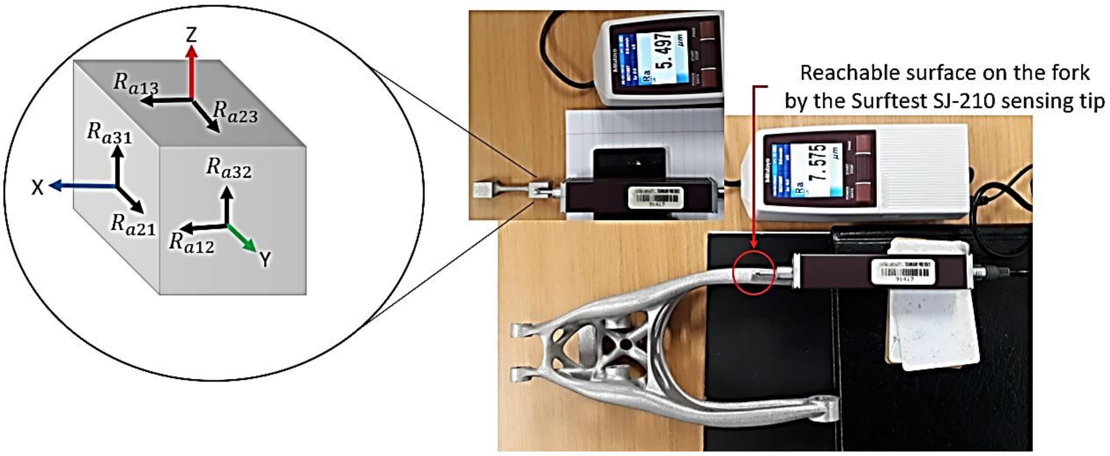

Figure 3.13: Illustration of the surface roughness measurement setup on the specimen and the scaled-down nose wheel fork

The magnified image in Figure 3.13 shows the orientations considered for the measurement of the R_a values on the test specimen. The first digit of the subscript of the R_a value indicates the direction of the measurement and corresponds to the X, Y and Z coordinate system: subscript 1 corresponds to X, 2 to Y and 3 to Z. The second digit represents the plane in which the measurements were taken. Take note that the Z-direction was along the build direction of the L-PBF machine. Therefore, the XY-plane was perpendicular to the build direction and represented the top view of the specimens and the scaled-down nose wheel fork, whereas the ZX- and ZY-planes represented the two side views of the specimen, which were parallel to the build direction. The R_a values of the build direction are presented in section 4.5.4.

3.10. Destructive testing of standard test specimens

3.10.1. Tensile strength

The tensile testing of the Ti6Al4V(ELI) specimens was performed according to ASTM E8. The witness tensile test specimens were tested using a 30 kN Model 43 MTS® Criterion™ tensile testing machine (MTS, Eden Prairie, US), whereas the other tensile test specimens were tested on a 30 kN Instron 1342 servo-hydraulic testing machine (Instron, Norwood, US). The tensile properties of both sets of tensile test specimens are presented and discussed in section 5.3.1 of Chapter 5.

3.10.2. Impact toughness

Determination of the Charpy impact toughness of the L-PBF Ti6Al4V(ELI) specimens was done according to the ASTM E23 standard. An Instron 450MP2-J1 system (Instron, Norwood, US) with a maximum capacity of 300 J was used for these tests. All specimens were conditioned to a temperature of -50℃ by immersing them in ethanol solution followed by liquid nitrogen before testing. The resulting impact toughness values are presented in section 5.3.2.

© Central University of Technology, Free State

3.10.3. *Fracture toughness and fatigue crack growth rate*

The 30 kN Instron 1342 servo-hydraulic testing machine (Instron, Norwood, US) was used to perform the K_{IC} and FCGR tests following ASTM E399 and E647, respectively. In Table 3.4, the pre-crack termination values and testing conditions are given. The pre-cracking was done under a constant stress intensity range (ΔK) and the FCGR tests were performed under constant load while decreasing ΔK.

Table 3.4: The pre-crack termination values and test conditions

Pre-crack termination values	
Final crack length (a_p)	6 mm
Stress intensity range (ΔK)	11 MPa·m$^{0.5}$
Force ratio	0.1
Cycle waveform	Sinusoidal

FCGR test conditions	
Environment and relative humidity	Air, 35 ~ 60%
Temperature	20 ± 5 °C
Measurement interval of crack length (a)	0.25 mm
Force frequency	15 Hz
Force ratio	0.1
Waveform	Sinusoidal
Initial stress-intensity range (ΔK_i)	11 MPa·m$^{0.5}$
Force	2 kN

The results of the fracture toughness and FCGR are presented in sections 5.3.3 and 5.4.1 of Chapter 5, respectively.

3.10.4. *High cycle fatigue*

A tension-tension fatigue test was performed on each L-PBF Ti6Al4V(ELI) specimen built in the X-, Y- and Z-orientations, following the ASTM E466 standard. A 50 kN Instron 1432 axial servo hydraulic machine (Instron, Norwood, US) was used for these HCF tests at a frequency of 10 Hz and a stress ratio R = 0.1. These axial force-controlled tests were performed at an environmental temperature of 20 ± 2 ℃. The run-out number of cycles (N) to failure was set at 5 million.

© Central University of Technology, Free State

The Z-specimens were first tested for HCF at an initial maximum stress of 450 MPa which was reduced till the fatigue strength was obtained. This initial stress was informed by the fatigue strength obtained by Malefane *et al.* [136] during a study on HCF properties of annealed Ti6Al4V(ELI) L-PBF specimens that were machined and polished. A similar strategy was adopted for the X- and Y-specimens but at an initial maximum stress of 360 MPa, which was 20% less than the initial stress applied when testing the Z-specimens. The stresses were also reduced when performing HCF of the X- and Y-specimens until the fatigue limit/endurance was obtained. In Table 3.5, the stresses applied during HCF testing are tabulated and detailed results are presented in Chapter 5, section 5.4.2.

Table 3.5: The stresses applied during HCF testing of L-PBF Ti6Al4V(ELI) specimens built in various orientations

Z-specimens loading		**X-specimens loading**		**Y-specimens loading**	
Specimen ID	**Max stress (MPa)**	**Specimen ID**	**Max stress (MPa)**	**Specimen ID**	**Max stress (MPa)**
Z4	450	X4	360	Y4	360
Z5	418	X5	300	Y5	300
Z6	360	X9	270	Y9	270
Z10	300	X6	230	Y8	250
Z7	270	X7	210	Y6	230
Z9	250	X10	200	Y10	200
Z8	225	X8	190	Y7	190

3.11. Metallographic preparation

Metallographic investigations were carried out to determine the microstructures of the Ti6Al4V(ELI) L-PBF specimens and the scaled-down nose wheel fork. Representative samples for microstructural evaluation were cut from the impact toughness specimens. Specimens in the XY-, ZX-, and ZY-planes were studied using a ZEISS Axio Observer optical microscope (Zeiss, Oberkochen, Germany). These specimens were mounted in MultiFast phenolic resin and ground by using 46 μm waterproof SiC grinding discs. Next, they were mechanically polished on a Struers Tegramin-25 machine (Struers LLC, Cleveland, OH, US), using DiaMaxx Poly 9 and 3 μm diamond suspensions. To complete the metallographic preparation, etching was done on all specimens using Kroll’s reagent. The

© Central University of Technology, Free State

microstructure observed from the representative test specimens and the nose wheel fork are shown and discussed in sections 5.2 and 6.2.3, respectively.

3.12. Preparation of specimens for fractography

For the investigation of the failure mechanism, fractography was performed on the Ti6Al4V(ELI) L-PBF impact toughness, FCGR and HCF test specimens and a fractured part of the scaled-down nose wheel fork. A Jeol JSM-6610 (Jeol, Peabody, MA, USA) SEM was used for these studies. All samples were washed in an ethanol solution in an ultrasonic bath before placing them in the SEM sample chamber. The fracture modes of the fractured FCGR and HCF test specimens and the nose wheel fork were investigated. For each FCGR specimen built in the XZY-, YXZ-, and ZXY-orientation, the fracture surface characteristics were studied. The fracture features of the X-, Y- and Z-HCF test specimens were characterised. Apart from these, the effects of the 3D-printed and wire-cut V-notches on the fracture surfaces of the Charpy impact toughness specimens were determined. The effect of the build orientation on the fracture surface was also investigated. The percentage shear fracture of the specimens with 3D-printed and wire-cut V-notches was determined based on the ASTM E23-18 standard. In sections 5.3.2, 5.3.3, 5.4.1 and 5.4.2 the fracture surface of the impact toughness, fracture toughness, FCGR and HCF specimens are shown and discussed. The fracture surface of the nose wheel fork is presented in section 6.2.4.

3.13. Performance testing of prototype

The performance testing of Ti6Al4V(ELI) L-PBF scaled-down nose wheel fork as the experimental prototype began with the design and manufacturing of the custom testing jig. This was followed by the installation of strain gauges on the prototype and the assembly of the fork on the test jig. Such assembly was done on the isolation bed to eliminate external forces. Thereafter, static and fatigue testing were performed. The static test results were used to validate the FEA model which was used for fatigue life prediction of the Ti6Al4V(ELI) L-PBF

© Central University of Technology, Free State

scaled-down nose wheel fork. Finally, the predicted fatigue life of the fork was compared with the experimental life endured by the nose wheel fork. All test was executed at the University of Pretoria (UP) Mechanical Engineering Heavy Machine Laboratory. The UP laboratory was selected for its unique facilities for dynamic testing of structural components under simulated operational conditions for various applications. The results of the performance testing of the L-PBF Ti6Al4V(ELI) are presented in Chapter 6.

3.13.1. Design and manufacturing of test jig

A customised experimental test jig was designed and fabricated from high-strength steel. Such steel had UTS, yield strength and elongation of 925 MPa, 650 MPa and 13%, respectively. This test jig allowed the application of the static and fatigue loads without any energy absorption system, meaning the full applied total loads were experienced by the scaled-down nose wheel fork. The designed and manufactured test jig for performance testing of the L-PBF Ti6Al4V(ELI) scaled-down nose wheel fork is shown in Figure 3.14.

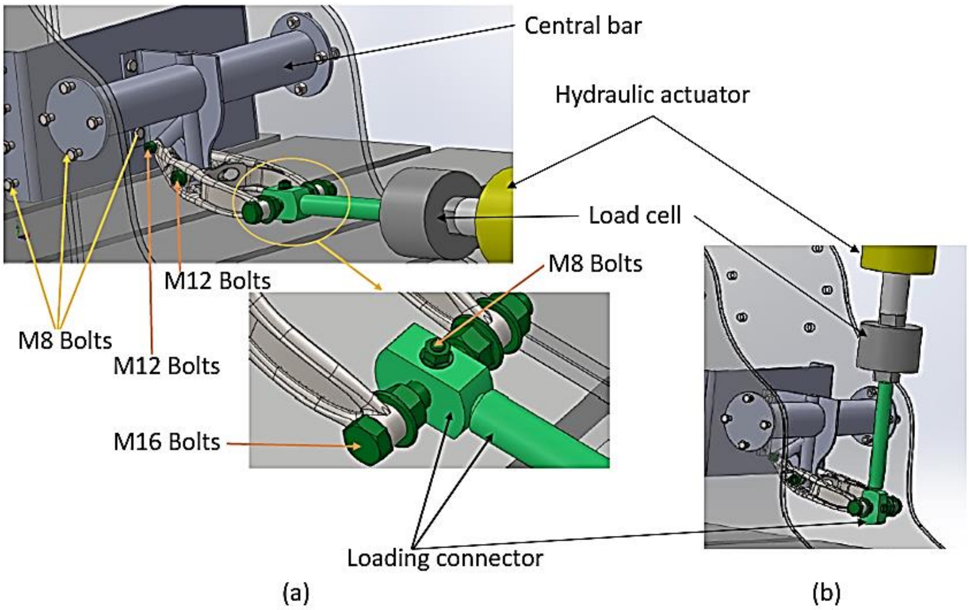

© Central University of Technology, Free State

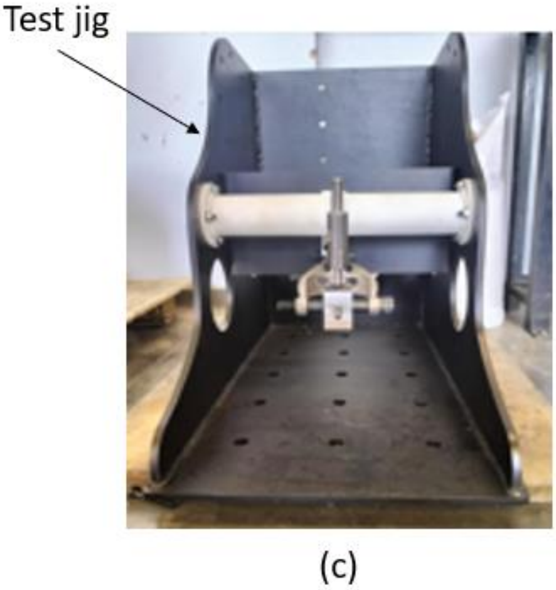

Figure 3.14: Illustration of the designed and manufactured test jig (a) for assembly of fork during X-load case testing, (b) for assembly of the fork during Z-load case testing and (c) shows manufactured test jig

The central bar of the test jig holds the nose wheel fork in a similar orientation as in the AHRLAC during the actual landing operation. The torque arm and shock strut bushes of the fork are connected to the test jig by M12 high-strength steel bolts, whereas the wheel bushes were linked to the loading connector. On the other end of the loading connector, a load cell which measures the amount of load applied on the fork was connected and coupled to the hydraulic actuator. A detailed description of the test jig was presented by Miya *et al.* [180].

3.11.2. Installation of strain gauges

Two single grid strain gauges (6/350 LY4) (SG1 and SG2) and two rosette strain gauges (3/120 RY8) (SG3 and SG4) were bonded on the selected areas of the nose wheel fork anticipated to experience high strain values. These areas of high strain were predicted as defined in section 3.11.4 and the results are presented in Chapter 6. The positions of the strain gauges are shown in Figure 3.15(a) and (b).

© Central University of Technology, Free State

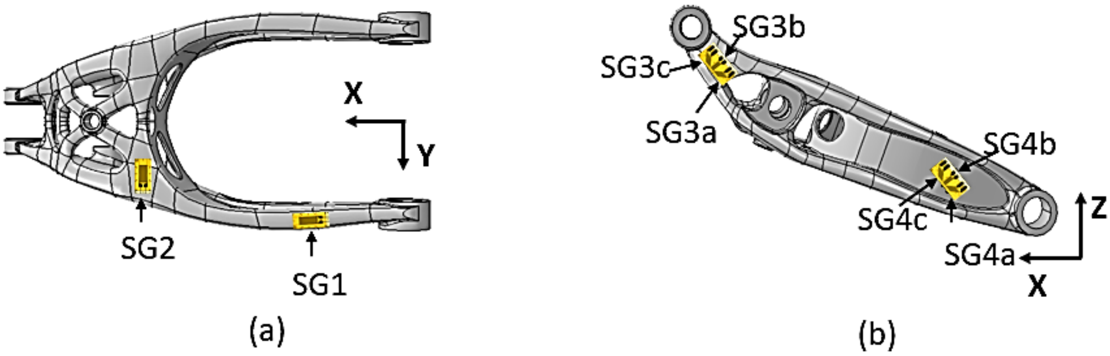

Figure 3.15: Positions of the strain gauge on the nose wheel fork (a) single strain gauges and (b) rosette strain gauges

The first step when installing strain gauges was to remove any grease, oil and organic contaminants on the surface of the nose wheel fork using Hottinger Baldwin Messtechnik (HBM) reinigungsmittel (RMS1) spray. This chemical consists of a mixture of acetone and isopropanol. Thereafter, areas of the L-PBF Ti6Al4V(ELI) nose wheel fork identified for strain gauge installation were abraded using silicon-carbide paper of 80, 180 and 320 grit size, one after another. This resulted in the surface roughness being conducive to proper bonding of the strain gauge. Moreover, the RMS1 was sprayed on the areas of the strain gauge on the fork and wiped with a single stroke of a new towel several times until the towel appeared clean after a single wipe. The strain gauge was placed on adhesive tape with its sensing grid facing upwards. Thereafter, a final wipe was done with a towel after spraying RMS1 spray on an area of a strain gauge. Subsequently, a single small drop of HBM strain gauge adhesive (Z70) was dropped on the gauge area of the L-PBF Ti6Al4V(ELI) nose wheel fork. Immediately after that, a strain gauge was placed on the nose wheel fork with its sensing grid facing the fork. This was followed by the application of uniform thumb pressure on the gauge for fifteen minutes. Finally, the adhesive was allowed to completely cure for 30 minutes before the adhesive tape was removed and three wire conductors were connected.

© Central University of Technology, Free State

3.11.3. *Testing of experimental prototype*

All strain gauges that were bonded on the fork and load cell were connected to the Quantum X Universal Amplifier (MX840 8 channel), which was directly coupled to the Quantum X data recorder (CX 22W). Connection of the strain gauges was done through the quarter bridge circuits (SCM-SG350) and (SCM-SG120) for strain gauge (6/350 LY4) and (3/120 RY8), respectively. These were done through a three-wire configuration. In Table 3.6, the technical specifications of the strain gauges, quarter bridge circuit and the load cell are stated.

Table 3.6: The technical specifications of strain gauge, quarter bridge circuit and load cell

Strain gauges	
Resistance (R) for single grid gauge	350 Ohm ± 0.3%
Resistance (R) for rosetted strain gauge	120 Ohm ± 0.3%
Gauge factor (SG)	2.03 ± 1.0 %
Transverse sensitivity	-0.4 %
Quarter bridge circuit	
SG connection	Quarter bridge, three wire
Bridge excitation	DC 50V; AC 2.5V
Operation temperature range	-20 ^oC …± 65 ^oC
Storage temperature range	-40 ^oC …± 75 ^oC
Cable length to the quarter bridge, max	30 m
Impact 6 ms	350 g
Zero error with 2 m cable to strain gauge	0.2 mV/V
Universal low-profile load cell	
Load capacity	1 ton
Temperature effect on output	0.001%
Temperature effect on zero signal	0.001%
Combined error	0.03%
Input resistance	350 ± 1%
Recommended excitation	5-15 V

The scaled-down nose wheel fork as the experimental prototype was tested under the extreme loads provided by Paramount Aerospace Industries (see Table 3.1), as adjusted for the prototype dimensions. As explained previously, the prototype had the inherent surface roughness of parts produced through L-PBF. The selected experimental loads were the components of the maximum landing load case acting along the X- and Z- directions. In each load case, the fork was fixed through the torque arm and shock absorber strut bushes by high-strength

© Central University of Technology, Free State

steel bolts of 12 mm diameter. For all loads cases, the application of loads was through the wheel shaft as illustrated in Figure 3.16.

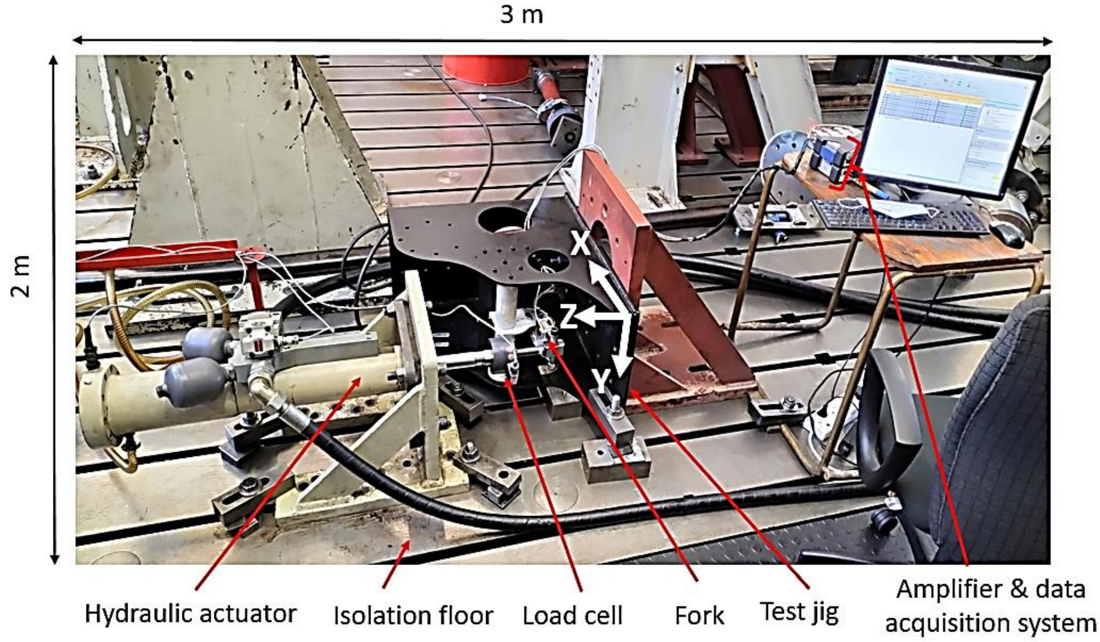

Figure 3:16: An experimental set-up for static and fatigue testing

The maximum landing loads were set at 24% higher than the design load acceptable for designs that comply with the FAR. To measure strain values necessary for the validation of the FEA, static tests were performed using five equal load divisions of the Z-load case. Such equal load divisions are shown in Table 3.7. During the application of each load division, a load was applied along the Z-direction and kept for 10 seconds, before it was applied in an opposite direction following the same sequence. In section 6.2.1 of Chapter 6, the experimental static results of the L-PBF Ti6Al4V(ELI) scaled-down nose wheel fork are presented.

Table 3.7: An equal load division of the Z-load case applied during static testing of the L-PBF Ti6Al4V(ELI) scaled-down nose wheel fork

Load divisions	Vertically upwards load (N)	Vertically downwards load (N)
1	8 300	-8 300
2	6 640	-6 640
3	4 980	-4 980
4	3 320	-3 320
5	1 660	-1 660

Fatigue tests were performed in a force-controlled mode. Separate constant amplitude spectra in the X- and Z-directions, based on the extreme landing loads and fully reversed (stress ratio R = -1), were adopted and used as baseline. The resulting spectra were expected to be less severe than the actual operational ones for positive X- and Z-loads, which were the loading conditions dominating the design. If the part failed prematurely under these baseline spectra, a substandard design would immediately be identified. Firstly, a constant maximum load of 6 000 N was applied in the X-direction, followed by inspection of cracks after 100 000 cycles using a 996 PB red dye penetrant. Thereafter, a fatigue load of 8 300 N was applied in the Z-direction. In each load case, a frequency of 3 Hz was adopted. The experimental fatigue results of the L-PBF Ti6Al4V(ELI) scaled-down nose wheel fork are presented in section 6.2.2 of Chapter 6.

3.11.4. Validation of finite element analysis

To validate FEA through experimental data, the FEA with input parameters resembling the experimental test conditions was performed. For the FEA, the Abaqus® software 2020 version was used to compute stress and strain values of the L-PBF Ti6Al4V(ELI) scaled-down nose wheel fork. Quadratic tetrahedron elements were used to discretise the CAD model of the nose wheel fork. A plasticity material model with isotropic hardening was used, introducing data experimentally obtained from Ti6Al4V(ELI) specimens with L-PBF as-built surface roughness, namely the elastic modulus, Poisson’s ratio and plastic stress–strain values [144]. Constraints were applied to the torque arm, shock strut and wheel bushes. The torque arm bushes were restricted to only rotate around the Y-direction with only a radial constraint on both internal cylindrical surfaces and a constraint in the Y-direction on four annular surfaces shown in Figure 3.17(b). The shock strut bushes were only allowed to rotate around the Y-direction, using only a radial constraint on both internal cylindrical surfaces, and a constraint in the Y-direction on the two red highlighted annular surfaces. The wheel bushes were constrained only in the Y-direction on the four annular surfaces indicated in Figure 3.17(b).

© Central University of Technology, Free State

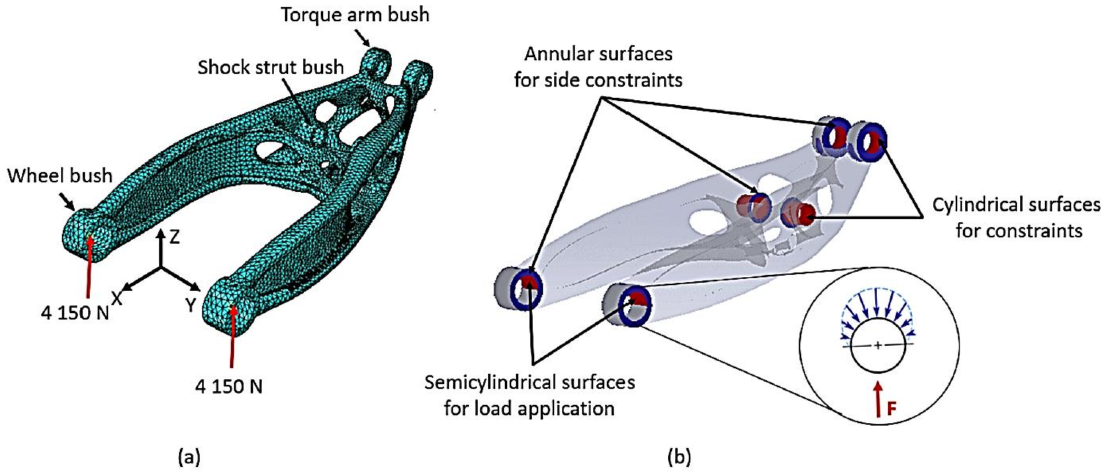

Figure 3.17: Illustration of (a) discretised CAD model of the nose wheel fork and (b) surfaces where loads and constraints were applied during FEA of the Z-load case

The maximum Z-load of 8 300 N was divided into five equal partitions and applied on the nose wheel fork together with boundary conditions which represented the experimental setup. As in the experimental test, the force on the nose wheel fork was applied on a semicylindrical surface of the wheel bushes to approximate a bearing load condition. The nodal strain results recorded from the FEA model and corresponded to the surface areas of the strain gauges on the experimental prototype were compared by computing the deviation percentage. In Figure 3.18, an illustration of the strain gauge on the L-PBF Ti6Al4V(ELI) scaled-down nose wheel fork and partitioning of strain gauge area on the FEA model for the validation process are shown.

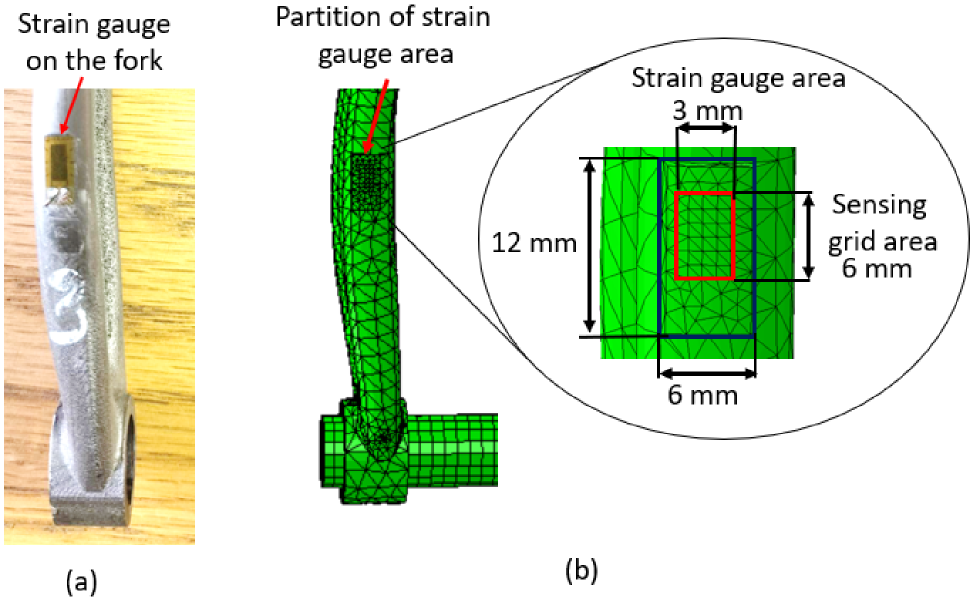

Figure 3.18: (a) Illustration of the strain gauge on L-PBF Ti6Al4V(ELI) scaled-down nose wheel fork single grid strain gauge mounted on fork and (b) partitioning of strain gauge area on the FEA model

For each static load division applied, the surface nodal strain gauge values that were simulated to be experienced by the nose wheel fork were recorded. These strain gauge values were along the longitudinal direction of the gauge and averaged to obtain a single value for comparison with the measured value. Thereafter, the percentage deviations between the FEA and measured strain values were computed for each static load division. Validation results are presented in section 6.4 of Chapter 6.

3.11.5.Fatigue failure simulation

The experimentally validated FEA model was imported into the fe-safe software for stress-based fatigue failure simulations [181]. To compensate for the inherent surface roughness resulting from the L-PBF process, the stress versus the number of cycles-to-failure data of the Ti6Al4V(ELI) standard fatigue specimens, tested at an R value of 0.1 and with an as-built surface roughness, was used as input in the fatigue simulations [144]. The uniform material method of approximating fatigue material properties was used. This commonly used method

© Central University of Technology, Free State

has been reported to be more appropriate for aluminium and titanium alloys [75]. Tensile data necessary for approximating fatigue material properties were also obtained from L-PBF Ti6Al4V(ELI) standard test specimens with as-built surface roughness [144]. In Table 3.6, the material fatigue properties resulting from the uniform material approximation method are tabulated.

Table 3.8: Ti6Al4V(ELI) material fatigue properties resulting from the uniform material approximation method [75].

$\sigma'_f = 1.67\sigma_{uts}$	ε'_f	b	c	n'	$K' = 1.61\sigma_{uts}$
1 486.3	0.35	–0.095	–0.69	0.11	1 432.9

The fatigue simulations for separate X- and Z-loads were performed using a stress ratio of R = -1, as in the experimental tests. Finally, the number of cycles to failure for the maximum X- and Z-load cases were computed and compared with the experimental results. In section 6.5 of Chapter 6, the simulated fatigue results are presented.

3.12. Summary

In this chapter, the procedure for the redesign of the nose wheel fork of the AHRLAC for production in Ti6Al4V(ELI) through L-PBF was presented. This demonstrated the integration of the TO technique in the redesign process. The fabrication procedure of the scaled-down nose wheel fork, together with the standard tensile, impact toughness, fracture toughness, FCGR and HCF test specimens through L-PBF, were also presented. This was followed by the description of the NDT procedures for characterising the Ti6Al4V(ELI) component produced through L-PBF. The testing procedure for all standard test specimens followed by performance testing of L-PBF Ti6Al4V(ELI) scaled-down nose wheel fork was also discussed. These were followed by a description of the preparation of metallographic specimens and specimens for fractographic analysis. Moreover, the procedure for experimental validation of the FEA model for static performance testing of the scaled-down nose wheel fork was outlined. Finally, the methodology for performing fatigue simulation which can be compared with experimental tests was described.

© Central University of Technology, Free State

CHAPTER 4: CHARACTERISTICS OF THE REDESIGNED L-PBF Ti6Al4V(ELI) NOSE WHEEL FORK

Some of the material contained in Chapter 4 was published in the following peer-reviewed paper:

- L. F. Monaheng, W. B. du Preez, N. Kotze, and M. Vermeulen, “Topology optimisation of an aircraft nose-wheel fork for production in Ti6Al4V by the Aeroswift high-speed laser powder bed fusion machine,” *14th World Conference on Titanium*, MATEC Web of Conferences, vol. 321, 03013, 2020, https://doi.org/10.1051/matecconf/202032103013

4.1. Introduction

In this chapter, the characteristics of the redesigned scaled-down nose wheel fork are presented and discussed. Initially, the topology optimised design of the nose wheel fork is presented and discussed. This includes consideration of the FEA results of the mechanical properties of the design. An analysis of the relationship between the orientation of the redesigned component on the L-PBF build platform and the preferred properties is presented as well as the selection that was made. This is followed by a presentation and discussion of the geometrical and physical characteristics of the Ti6Al4V(ELI) scaled-down nose wheel fork produced through L-PBF.

4.2. Optimal nose wheel fork

The redesign of the nose wheel fork for production in Ti6Al4V(ELI) was described in sections 3.3.1 through 3.3.6 of Chapter 3. In this section, the optimal design of the nose wheel fork is presented. The load paths obtained through the MSC Patran-Nastran and Altair SolidThinking Inspire® TO suites are presented in Figure 4.1(a)–(c) and (b)–(d), respectively. The different views of the load paths are shown to demonstrate the similarities and differences between the design generated from the MSC and Altair TO software. These load paths illustrate the elements which experience high load. The top and bottom boundary elements carry more load; therefore, they were not removed from the design domain. Conversely, the elements which experience low levels of stress were removed from the design domain, as seen for both the MSC and Altair optimal load paths.

© Central University of Technology, Free State

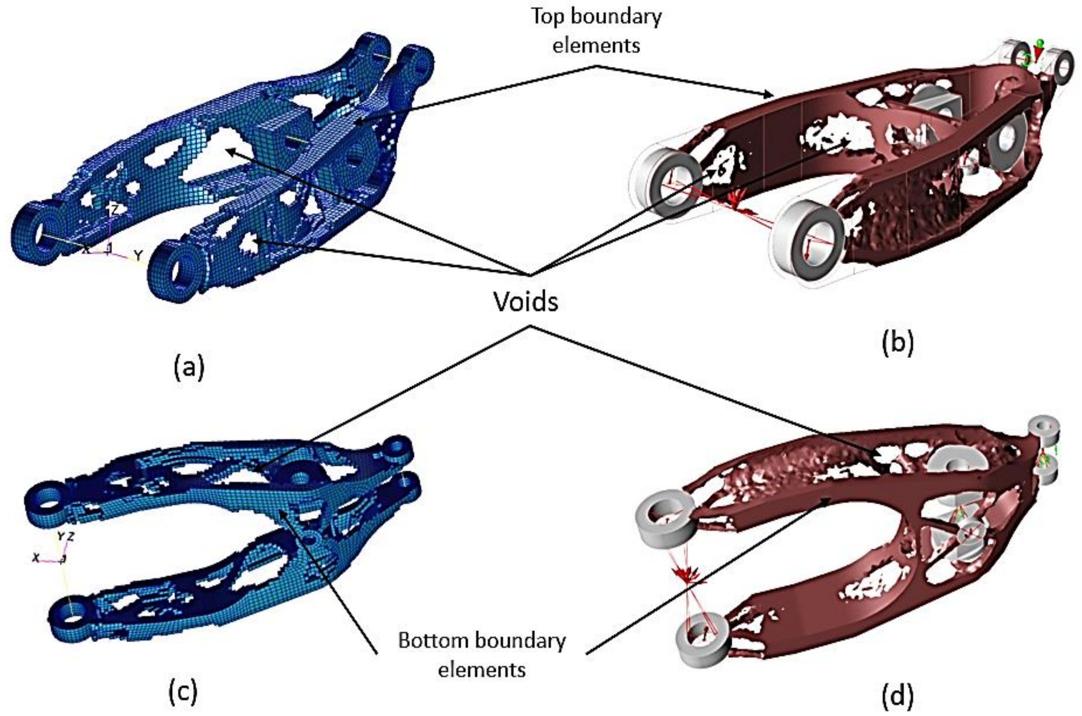

Figure 4.1: Various views of the optimised nose wheel fork load path, (a) and (c) resulted from the MSC Patran-Nastran (b) and (d) from the Altair SolidThinking Inspire® software

The Patran-Nastran load path consists of the truss-like element between the wheel and shock strut bushes, whereas that of the SolidThinking Inspire® has thin shell elements. This variation was attributed to the different meshing strategies performed by the software and resulted in a number of conceptual designs for the nose wheel fork, as shown in Figure 4.2.

© Central University of Technology, Free State

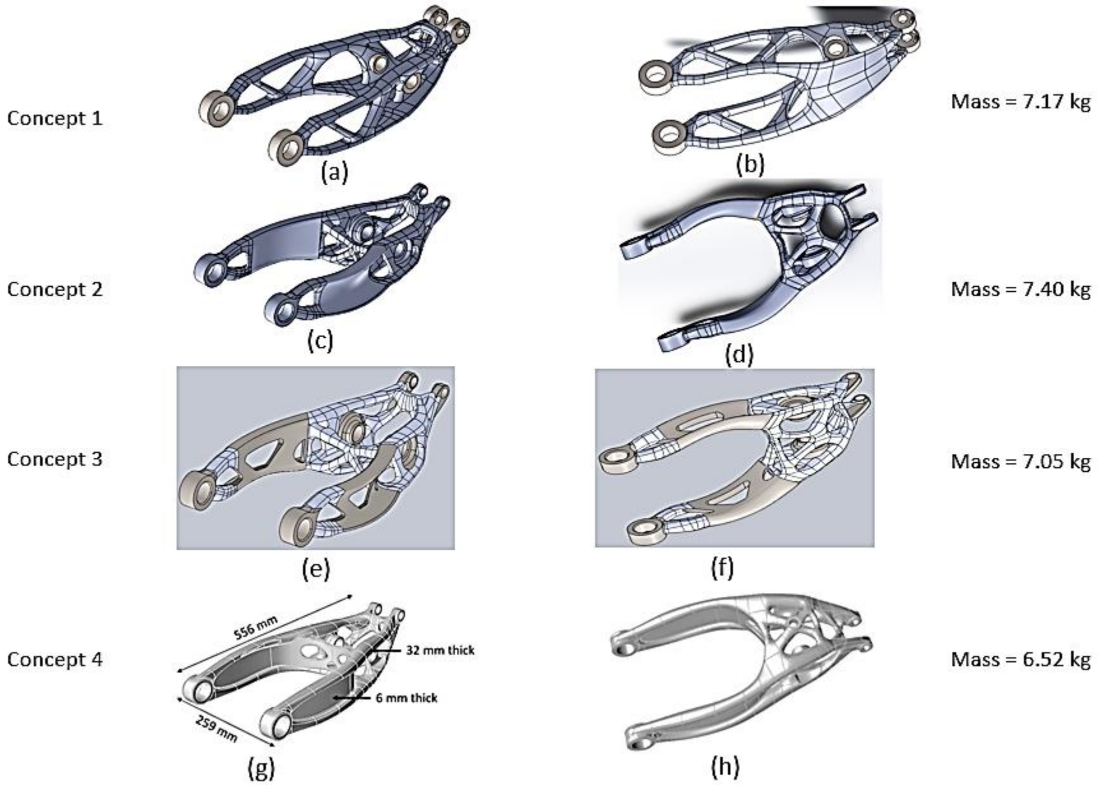

Figure 4.2: Various conceptual designs of the AHRLAC nose wheel fork generated from the load paths

The safety factors obtained from all concepts of the Ti6Al4V(ELI) nose wheel fork for production through L-PBF were more than 1.5, whereas the mass savings were different. Concepts 1, 2, 3 and 4 have mass savings of 13%, 10%, 10% and 20% respectively. These were compared with the actual nose wheel fork of the AHRLAC that was produced from Al 7050 through conventional milling and had a mass of 8.23 kg. Therefore, concept 4 was selected as the best optimal design.

The cross-sectional view of the top and bottom bar of the best optimal design nose wheel fork consists of a solid elliptical-like shape, see Figure 4.3(a). These bars are supported by 6 mm thick web in between, resembling an I-beam-like structure. Towards the torque bushes, it consists of a complex cross-sectional shape shown in Figure 4.3(b).

© Central University of Technology, Free State

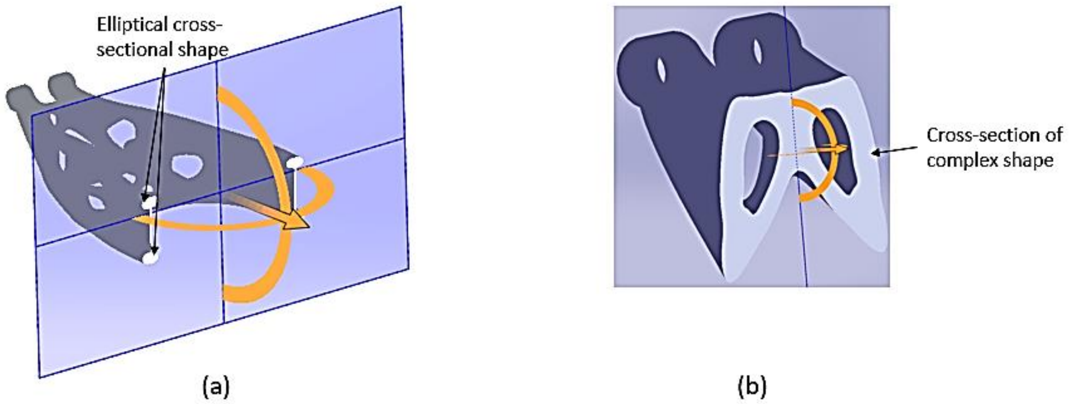

Figure 4.3: An illustration of the cross-sectional view of the best optimal design of the nose wheel fork, (a) shows the I-beam-like configuration, and (b) the region close to the torque arm bushes

4.3. FEA results of the selected concept

The results of the FEA procedure that was described in section 3.3.6 are presented in the current section. For each load case provided by Paramount Aerospace Industries, a representative displacement, stress and safety factor experienced by the best optimal nose wheel fork (Concept 4) were calculated. These computed variables and their relative applied loads are presented in Table 4.1.

Table 4.1: The applied loads, total displacement, von Mises stress, and safety factor of the best optimal nose wheel fork (Concept 4)

Load Cases	**Applied loads** F_X **(N)**	F_Y **(N)**	F_Z **(N)**	**U (mm)**	**Stress von Mises (MPa)**	**Safety factor**
Maximum landing	13 960	8 395	20 711	13.20	510	1.5
Ground static	0	9 910	14 347	12.20	426	1.8
Minimum landing	-10 012	8 395	0	6.38	252	3.1
Towing load	9 223	7 987	5 330	6.48	256	3.0
Jacking	0	0	8 000	2.47	150	5.2
3 Point landing	5 494	0	6 868	2.65	163	4.8
Braked roll	761	0	7 609	2.42	147	5.3
Shock absorber test	11 328	0	14 160	5.46	336	2.3
Supplementary condition A	9 912	0	14 160	5.32	327	2.4
Supplementary condition B	-5 664	0	14 160	3.83	230	3.4

© Central University of Technology, Free State

	Applied loads					
Load Cases	**F_X (N)**	**F_Y (N)**	**F_Z (N)**	**U (mm)**	**Stress von Mises (MPa)**	**Safety factor**
Supplementary condition C	0	0	12 660	3.91	237	3.3
Limit drop test	6 696	850	8 370	3.29	195	4.0
Level landing	6 459	0	15 585	5.43	332	2.4
High speed taxing	2 156	0	2 695	1.04	63.9	12.2
Maximum spin up landing	10 124	0	12 655	4.88	300	2.6
Wheel spring back landing	-10 124	0	0	1.01	68.6	11.4

Table 4.1 illustrates that the stress experienced by the best optimal nose wheel fork was directly proportional to the displacement for different load cases. This behaviour was expected since the stress is proportional to strain when the elastic modulus is kept constant, or the material behaves elastically. Moreover, the lower the stress experienced by the optimal nose wheel fork the higher the safety factor. The maximum landing and high-speed taxiing load cases recorded the maximum and the minimum safety factors, respectively, whereas the stresses experienced during the maximum landing and the ground static cases were found to be the highest load cases. In Figure 4.4(a) and (b) the graphical values of maximum von Mises stress and the corresponding displacement are shown. Similarly, Figure 4.4(c) and (d) illustrate the stress experienced during the ground static load case with its respective displacement. The region between the torque arm and the shock strut bushes of the best optimal nose wheel fork, experienced higher stress as compared to the area between the shock strut and the wheel bushes, when the maximum load case was applied. This was due to the flexible movement occurring between shock strut and wheel bushes as illustrated in Figure 4.4(b). For the ground static load case, a twisting deformation was depicted, whereas the stress distribution was un-symmetric about the ZX-plane, see Figure 4.4(c) and (d).

© Central University of Technology, Free State

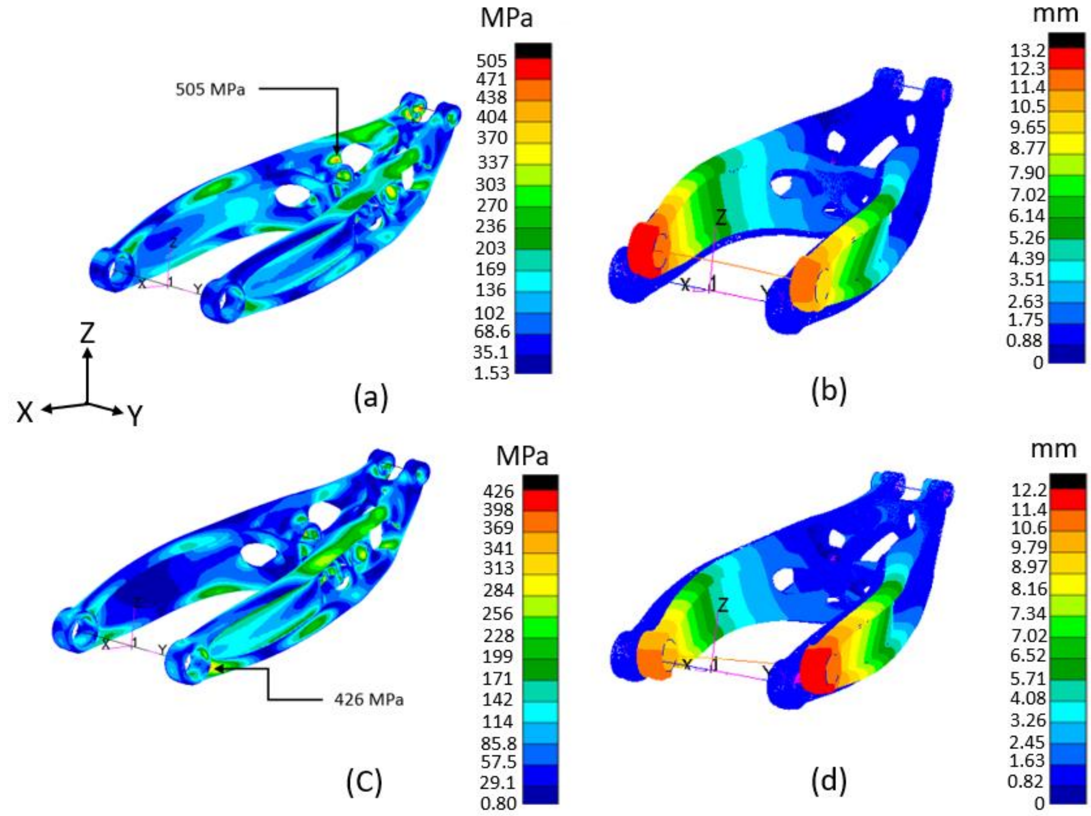

Figure 4.4: The von Mises stress and displacement for maximum load case (a)–(b) and ground static load case (c)–(d)

The maximum von Mises stress calculated for the maximum and ground static load cases were 505 MPa and 426 MPa, respectively. When following the design requirement regulations stated in CFR 23.613 and 23.627 these stress values were relatively high since the fatigue strength of L-PBF Ti6Al4V(ELI) specimens that were submitted to HTA was reported to be 450 MPa [56] [136]. The maximum displacement for these same load cases were 13.2 mm and 12.2 mm. Nonetheless, the best optimal nose wheel fork was accepted for fabrication from Ti6Al4V(ELI) through the L-PBF system since the safety factor was 1.5 and had the highest mass saving when compared with other concepts. First, the experimental prototype was generated from the best optimal nose wheel fork by applying a constant scale factor, as was explained in section 3.5.

4.4. Experimental prototype build orientation.

The selected build orientation of the scaled-down nose wheel fork is presented in this section. First, other possible build orientations are presented. In Table 4.2, such possible build orientations of the scaled-down nose wheel fork, together with their related support structures and predicted distortions obtained during the building process, are shown.

Table 4.2: Various build orientations of the scaled-down nose wheel fork versus the resulting distortion

Building orientation and support structures	**Distortion (mm)**
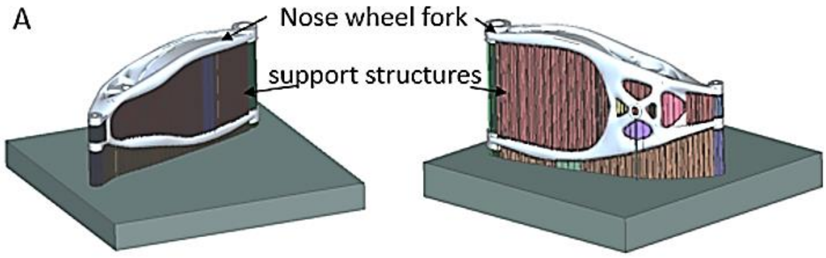	1.06–1.58
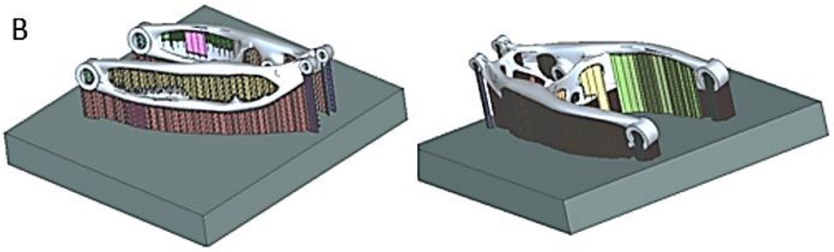	4.45–1.52
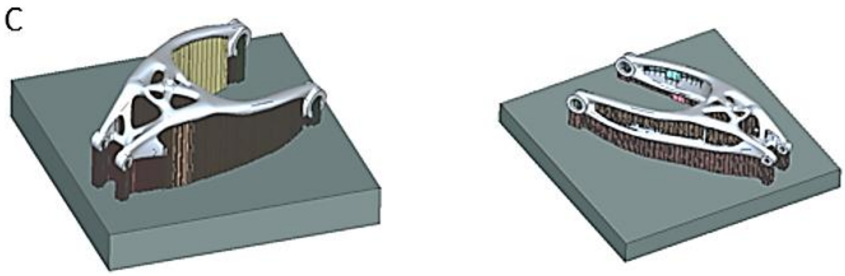	1.23–1.43

Three simulated building orientations that were considered (orientations A, B and C, indicated in Table 4.2) of scaled-down nose wheel forks recorded comparable distortions. Orientation B was selected based on simplicity to remove the support

© Central University of Technology, Free State

structure and cut it from the base plate. Most importantly, reducing the building time would improve energy efficiency, since lower building height results in lower energy required for the production of the scaled-down nose wheel fork.

4.5. Physical characteristics of the prototype

4.5.1. Predicted geometric deviation

The manufacturability simulation method that was presented in section 3.9.1 included a procedure that was followed during the investigation of a geometric deviation between L-PBF Ti6Al4V(ELI) and the CAD model. The simulated geometric deviation distributions of the scaled-down nose wheel fork for Scan A and Scan B are presented in Figures 4.5 (a)–(b) and (c)–(d), respectively. Scan A prediction of geometric deviation was done after L-PBF, stress-relieving plus support structure removal, whereas Scan B was done subsequent to HTA heat treatment. The negative values of the spectrum represent contraction, whereas positive values represent expansion of the scale-down nose wheel fork.

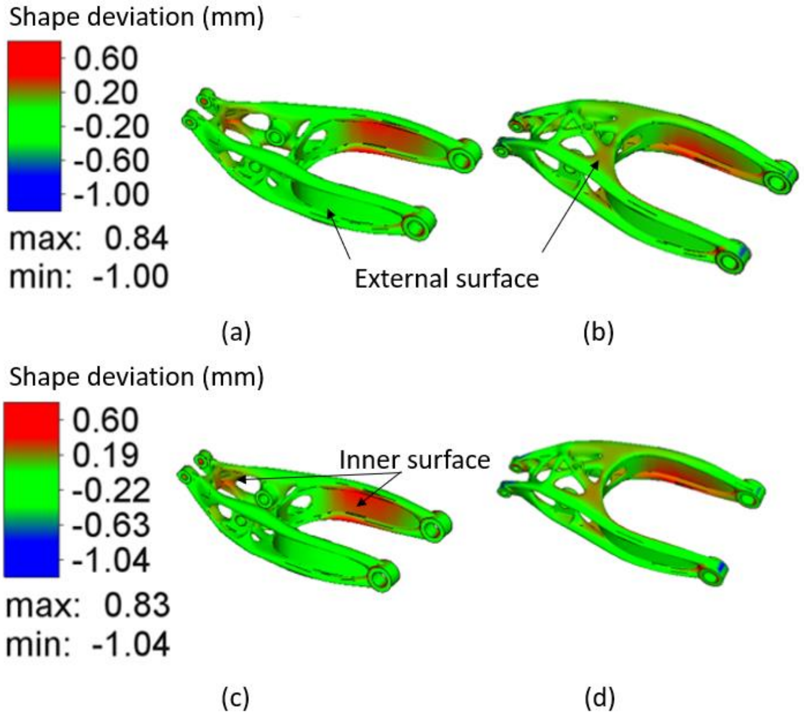

Figure 4:5: The spectrum mapping of the predicted geometric deviation of (a)–(b) Scan A and (c)–(d) Scan B

© Central University of Technology, Free State

The predicted geometric deviation of the scaled-down nose wheel fork for both Scan A and Scan B was within 0.84 mm to -1.04 mm. Thick portions of the nose wheel fork were predicted to have higher manufacturing accuracy than the thin sections with a minimal deviation of -0.2 mm. Furthermore, the highest contraction value was observed on the lower surface of the wheel axle bush, which was oriented such that it was the closest surface to the base plate. This was attributed to the conduction heat transfer mechanism during the L-PBF process [136]. Moreover, the inner surface of the scaled-down nose wheel fork experienced higher expansion than the external surface. This was attributed to the lower heat dissipation rate in the inner surface of the scale-down nose fork as compared to the external surface [136].

The geometric deviation for the selected build orientation was due to the residual stress presented in Figure 4.6. The maximum and minimum value of residual stress of 300 MPa and 5.57 MPa was predicted on the inner and external surfaces of the scaled-down nose wheel fork, respectively. This corresponded to the higher expansion observed on the inner surface than on the external surface in Figure 4.5. These high residual stresses in the inner surface were attributed to higher heat input generated through a convection process [182].

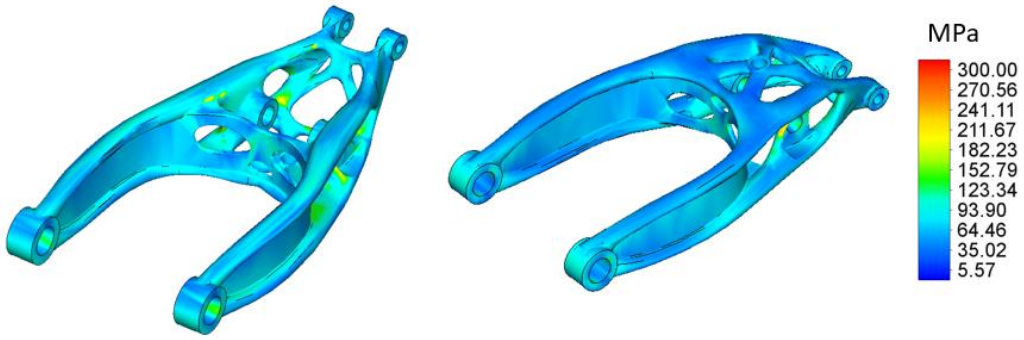

Figure 4:6: Predicted residual stress on the L-PBF Ti6Al4V(ELI) scaled-down nose wheel fork

To minimise distortion and warpage, which resulted from residual stresses, the scaled-down nose wheel fork was built with multiple pins and a traditional support structure. Details on the building of the L-PBF Ti6Al4V(ELI) scaled-down nose wheel fork as the experimental prototype and post-processes were presented in sections 3.7 and 3.8, respectively.

© Central University of Technology, Free State

4.5.2. *Measured geometric deviation*

Similar to the simulation of the scaled-down nose wheel fork geometric deviation, the scanned image of the scaled-down nose wheel fork was also superimposed on the CAD model to obtain a comprehensive view of the shape deviation resulting from post-processes in the L-PBF process chain. A detailed procedure followed during the experimental investigation of the geometric deviation was presented in section 3.9.1, while in Figure 4.7, the geometric deviations of the scaled-down nose wheel fork for Scan A and Scan B are presented.

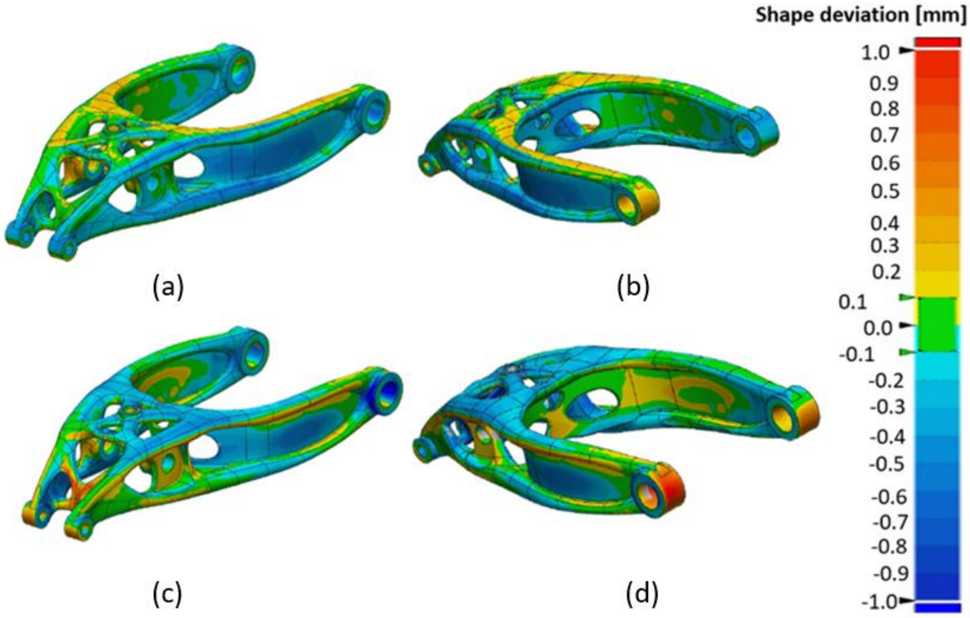

Figure 4:7: The spectrum mapping of the digitally scanned geometric deviation of (a)–(b) Scan A and (c)–(d) Scan B

The recorded maximum and minimum geometric deviations in the scaled-down nose wheel fork for both Scan A and Scan B were 0.40 mm and -0.80 mm, respectively. Moreover, the bottom surface of the fork after Scan A depicted a shape deviation of about 0.3 mm to 0.4 mm, whereas after Scan B the same surface recorded -0.2 mm to -0.3 mm. In addition, the experimentally measured data also confirmed expansion on the inner surface of the scaled-down nose wheel fork. For example, the inner surface of Scan A depicted no deviation, while the inner surface of Scan B showed a deviation of 0.3. Clearly, the distribution of the measured geometric deviation on Scan A and Scan B was different. This

© Central University of Technology, Free State

suggested that the HTA affected the geometric accuracy of the scaled-down nose wheel fork.

To determine how significant the difference between Scan A and Scan B was, a statistical significance F-test was performed. Two sections of the scaled-down nose wheel fork were selected for the significance test. The data measured in Section 1 (mid-area) and Section 2 (bushes) of the scaled-down nose wheel fork for Scan A and Scan B are shown in Table 4.3.

Table 4.3: Variation data between scanned values and the CAD geometry of the scaled-down nose wheel fork for sections 1 and 2

Section 1: Measurements perpendicular to build direction		
Point ID	**Scan A (mm)**	**Scan B (mm)**
1	0.255	0.198
2	0.04	0.361
3	0.288	0.348
4	0.218	0.216
5	0.036	0.35
6	0.516	0.269
7	0.022	0.167
8	0.286	0.185
9	0.402	0.311
10	0.24	0.187
11	0.799	0.513
12	0.285	0.221
13	0.046	0.064
14	0.353	0.177
15	0.32	0.155
16	0.017	0.277
17	0.369	0.483
18	0.467	0.509
19	0.027	0.224
20	0.01	0.028
21	0.329	0.535
22	0.388	1.009

Section 2: Measurements parallel to build direction		
Point ID	**Scan A (mm)**	**Scan B (mm)**
1	0.514	0.275
2	0.395	0.294
3	0.464	0.390
4	0.071	0.103
5	0.150	0.131
6	0.181	0.364
7	0.123	0.541
8	0.185	0.202
9	0.080	0.131
10	0.432	1.077
11	0.355	0.573
12	0.222	1.306
13	0.303	1.275
14	0.198	0.316
15	0.351	0.566

© Central University of Technology, Free State

The data point identification (point ID) in Table 4.3 corresponds with the geometric points in Figures 3.11 and 3.12. The minimum and maximum deviation values measured from positions 1 to 22 of virtual Section 1 of the scaled-down nose wheel fork were 0.010 mm and 0.799 mm for Scan A, whereas 0.028 mm and 1.009 mm were measured during Scan B. For Section 2, the minimum and maximum deviation values measured on the various points were 0.071 mm and 0.514 mm from Scan A, while in Scan B 0.103 mm and 1.306 mm were measured. These results suggest that some regions of the scaled-down nose wheel fork were built more accurately than others. Moreover, when comparing values of Scan A and Scan B there was a variation in deviation values.

The geometric dimensional deviation distributions of the scaled-down nose wheel fork for Scan A and Scan B, as reported in Section 1 and Section 2 data points stated in Table 4.3, are presented in Figure 4.8.

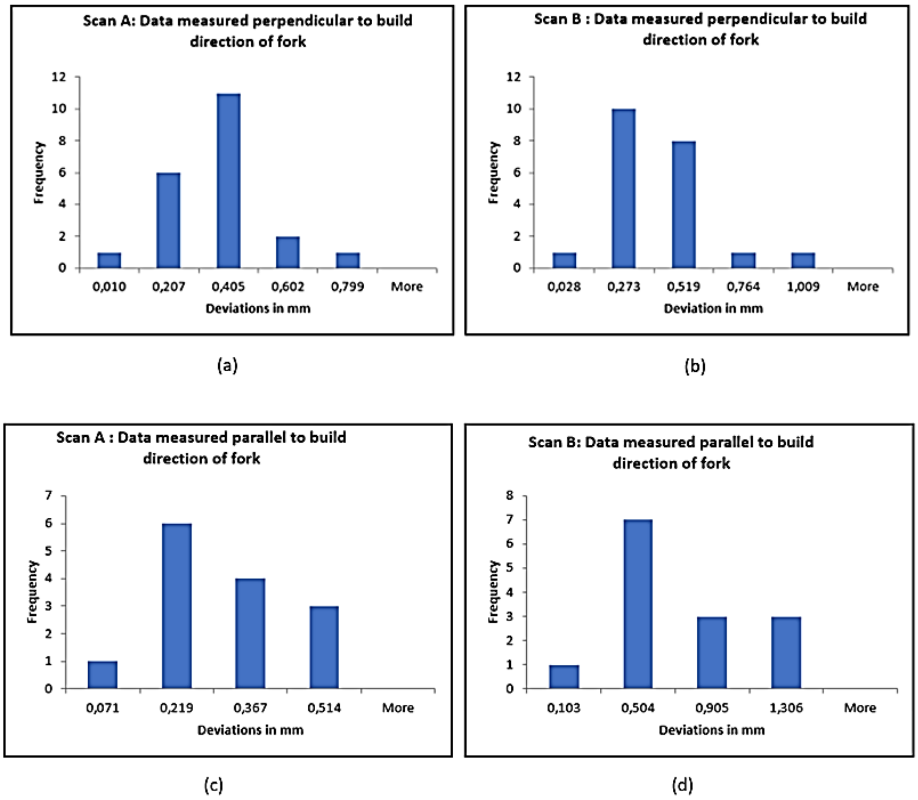

(a) (b)

(c) (d)

Figure 4:8: (a)–(b) measurement distribution obtained from the data in Section 1 (a) Scan A, (b) Scan B, as well as (c)–(d) representing data from Section 2 for Scan A and Scan B

© Central University of Technology, Free State

The distribution (range) of the Section 1 data that represents the deviation between the CAD model and the measured values is presented in Figure 4.8 (a)-(b) for Scan A and Scan B and were 0.789 mm and 0.981 mm, respectively. In this case, the interquartile range was 0.324 mm for Scan A and 0.173 mm for Scan B. Moreover, the mean and median of Scan A were 0.259 mm and 0.286 mm, respectively, while for Scan B they were 0.309 mm and 0.246 mm, respectively. These differences in the mean and median values proved that the data distributions shown in the histograms in Figure 4.8 were skewed to the right. Therefore, the median was the main measure of data centrality and the statistical F-test was performed as presented in section 3.9.1 of Chapter 3.

In Table 4.4, the statistical F-test results of the deviation data measured at the solid mid-area (Section 1) and bushes (Section 2) of the scaled-down nose wheel fork are presented.

Table 4.4: The statistical F-test results of the solid mid-area (Section 1) and bushes (Section 2) of the scaled-down nose wheel fork for Scan A and Scan B

F-test results measured on Section 1: (The mid-portion of the nose wheel fork)			**F-test results measured on Section 2: (The bushes of the nose wheel fork)**		
	Scan A	**Scan B**		**Scan A**	**Scan B**
Mean	0.26 mm	0.31 mm	Mean	0.27 mm	0.50 mm
Variance	0.04 mm	0.04 mm	Variance	0.02 mm	0.16 mm
Number of samples	22	22	Number of samples	15	15
Degrees of freedom	21	21	Degrees of freedom	14	14
F Calculated	1.20		F Calculated	7.87	
F Critical	2.08		F Critical	2.48	

For Section 1, the calculated F-value was found to be less than the critical F-value obtained from the F-distribution table reported in Appendix 1, indicating that there is no significant deviation between Scan A and Scan B. However, the Section 2 data showed significant variation between Scan A and Scan B. This illustrates that various portions of the scaled-down nose wheel fork produced through L-PBF experienced different geometric deviations after the HTA post-process. Moreover, the build orientation can be a contributing factor, since the deviation recorded at a plane perpendicular to the layer deposition direction was found to be less than that found along the layer deposition direction. To gain

© Central University of Technology, Free State

dimensional accuracy on important portions of the scale-down nose wheel fork, such as on the bushes, machining was necessary since the L-PBF as-build surface roughness will negatively impact the required tolerance during axle shaft assembly. Similar results were obtained from the simulation and the experimental measurements of the scale-down nose wheel fork. It was observed from both simulation and experimental data that most portions of the scaled-down nose wheel fork can be built within a geometric deviation of 0.2 mm after two-stage heat treatment. The maximum deviation recorded was less than 1.27 mm. Similar measurement accuracy was reported by Rokicki *et al.* [106]. Therefore, L-PBF technology can be used to produce an accurate scale-down nose wheel fork.

4.5.3. Porosity

The percentage porosity level of the representative specimens of the L-PBF TI6Al4V(ELI) scaled-down nose wheel fork that were built along X-, Y- and Z-directions is tabulated in Table 4.5. In section 3.9.2 of Chapter 3, the procedure followed to scan specimens for pores at a resolution of 8.2 µm was described.

Table 4.5: The percentage porosity of the L-PBF Ti6Al4V(ELI) witness specimens that represent the scaled-down nose wheel fork

Specimen ID	Porosity (%)
X1	0.0029
Y1	0.0033
Z1	0.0011

The recorded low level of porosity indicated a good bond between the grains of the EOSINT M280 Ti6Al4V(ELI) build specimens. This was also confirmed by the absence of lack-of-fusion pores. In Figure 4.9, the top view of Micro-focus X-ray images of the L-PBF Ti6Al4V(ELI) specimens built along X-, Y- and Z-directions are shown.

© Central University of Technology, Free State

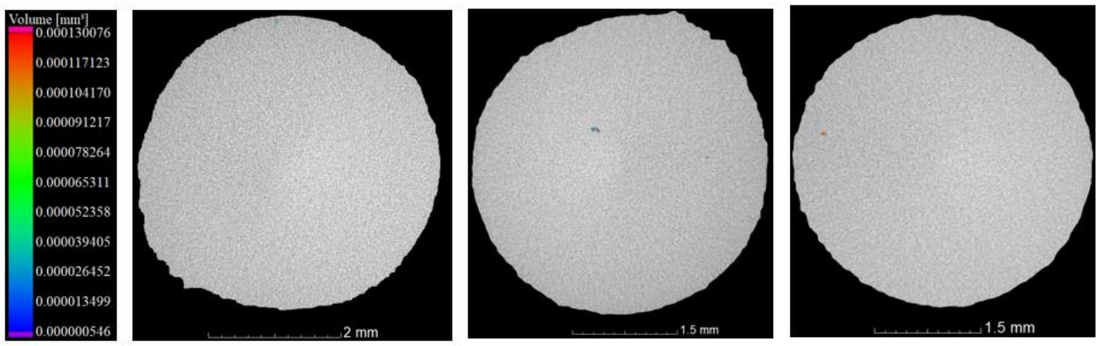

(a) (b) (c)

Figure 4:9: The Micro-focus X-ray images illustrating the absence of lack-of-fusion pore on L-PBF Ti6Al4V(ELI) specimens built along X-, Y- and Z-directions in images (a), (b) and (c), respectively.

The lack of melt pool penetration and gas entrapment were also not depicted on L-PBF Ti6Al4V(ELI) specimens suggesting that the EOSINT M280 machine can build Ti6Al4V(ELI) specimens at a very low level of porosity defects. This was attributed to the L-PBF machine parameters and two-stage heat treatment performed on the specimens that represent the Ti6Al4V(ELI) scaled-down nose wheel fork. It has been reported that specimens built through the EOSINT M270 system result in a porosity level of 0.005%, which is 40% more than the porosity level detected in the current study [183]. Therefore, it can be projected that the EOSINT M290 that was used to build the scaled-down nose wheel fork could result in an even better porosity level.

4.5.4. Surface roughness

In section 3.7.3, the procedure followed to measure the surface roughness was explained. Although the surface roughness of the as-built Ti6Al4V(ELI) scaled-down nose wheel fork produced through L-PBF differed from that of the CAD model, this had an insignificant impact on the geometric deviation. The top surface of the nose wheel fork, produced in different orientations compared to the specimen had a surface roughness of 7.395 µm. This value was 60% higher and 40% lower than the lowest and the highest surface roughness measured on the

© Central University of Technology, Free State

specimens, respectively. In Table 4.6, the surface roughnesses of a Ti6Al4V(ELI) specimen produced through L-PBF are shown.

Table 4.6: The as-built surface roughnesses of the Ti6Al4V(ELI) specimen produced through L-PBF

			ZY-plane			
		R_{a31} (µm)			**R_{a21} (µm)**	
R_a Values	12.75	11.32	14.02	11.13	12.39	12.58
Average		12.69			12.03	
			ZX-plane			
		R_{a12} (µm)			**R_{a32} (µm)**	
R_a Values	11.86	11.47	10.79	12.05	11.88	15.67
Average		11.37			13.20	
			XY-plane			
		R_{a13} (µm)			**R_{a23} (µm)**	
R_a Values	3.96	4.87	5.76	4.46	4.69	4.05
Average		4.86			4.40	

When comparing various planes of the specimen, the XY-plane had a lower surface roughness than the ZY- and the ZX-planes. This confirms that variation in orientation has a significant effect on the surface roughness. In Figure 4.10, the variation in the surface roughness in relation to the built orientation is illustrated.

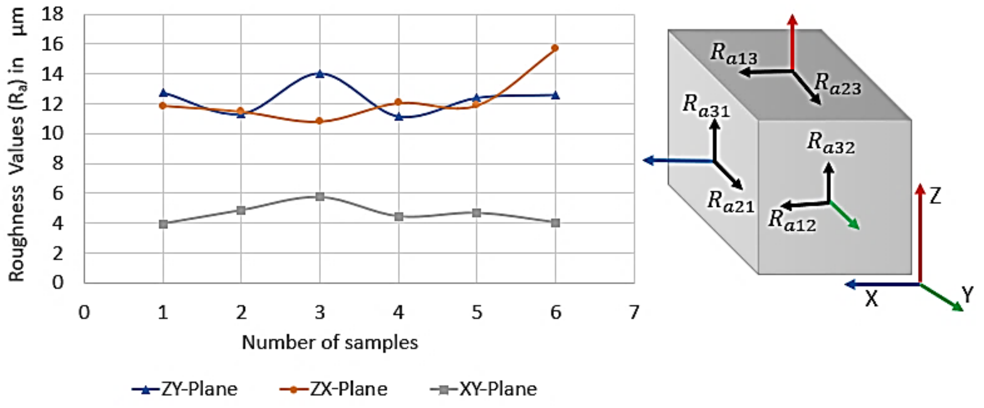

Figure 4:10: An illustration of the variation in surface roughness in relation to the built orientation

The surface roughness of L-PBF Ti6Al4V(ELI) specimens oriented in ZY- and ZX-planes were comparable, whereas there was a significant variation compared to the XY-plane. The surface roughness measured on the XY-plane of the L-PBF Ti6Al4V(ELI) scaled-down nose wheel fork ranged between the ZY- and XY-R_a

© Central University of Technology, Free State

values measured from the specimens. The high R_a value measured on the scaled-down nose wheel fork was attributed not only to the attachment of unmelted powder particles on the surface but also to the staircase effect resulting from a L-PBF Ti6Al4V(ELI) nose wheel fork complex geometry. In Figure 4.11, micro-images of various surfaces of the L-PBF Ti6Al4V(ELI) nose wheel fork are shown.

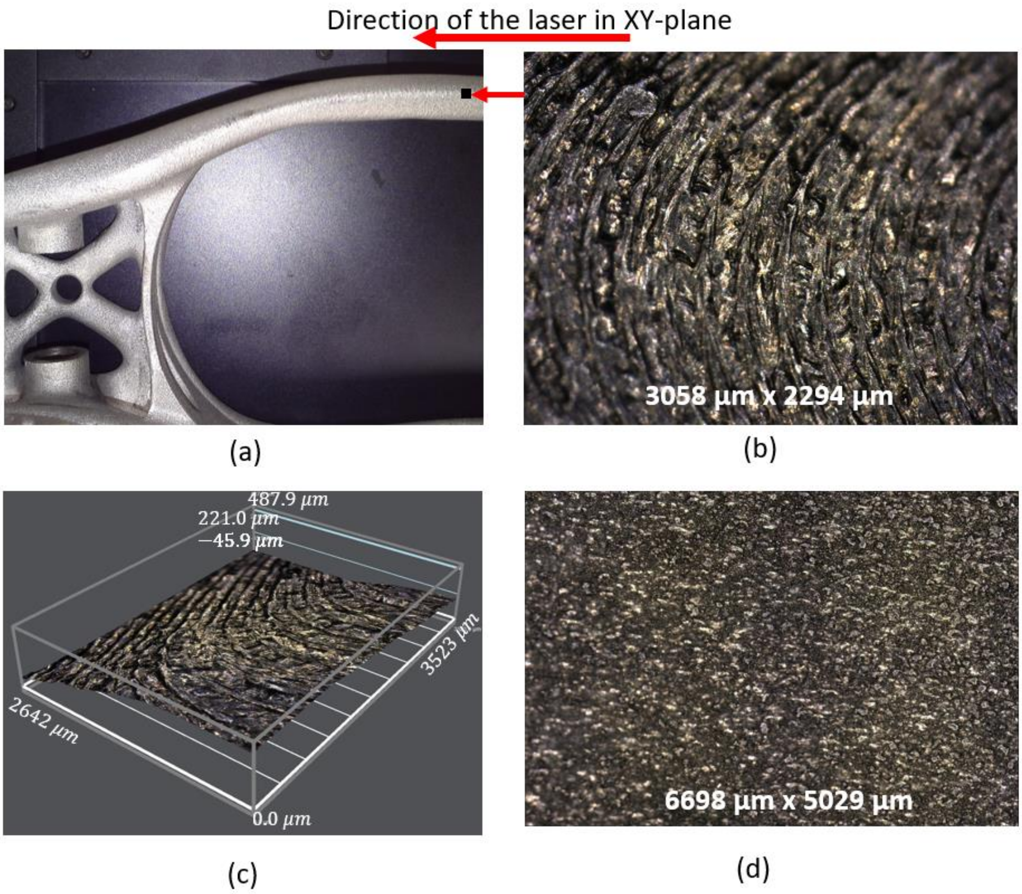

Figure 4:11: The micro image of the L-PBF Ti6Al4V(ELI) nose wheel fork for illustration of the surface roughness on: (a) overview top view image of the fork, (b) 2D high-magnification top view, (c) 3D view of the magnified top view and (d) 2D high-magnification of the side view

The high magnification of the top view of the L-PBF Ti6Al4V(ELI) scaled-down nose wheel fork depicted higher surface roughness than the side view, as shown in Figure 4.11(a) and (d), respectively. In Figure 4.11(c), the 3D micro-image clearly demonstrates that the surface where the image was taken was not flat. Therefore, the high surface roughness was due to the staircase effect. In section

© Central University of Technology, Free State

2.4.3 of Chapter 2, the creation of the staircase effect during the manufacturing of Ti6Al4V(ELI) components through L-PBF was described.

4.6. Summary

Various conceptual designs of the nose wheel fork of the AHRLAC were considered and the best concepts were presented in this chapter. The selected design for production in Ti6Al4V(ELI) through L-PBF has a mass saving of 20% which is higher than other conceptual designs when compared with the actual Al 7050 nose wheel fork. The FEA results of the nose wheel fork under different load cases confirmed a safety factor of more than 1.5, acceptable maximum stress and displacement. This was followed by the selection of the best built orientation of the experimental prototype, namely the scaled-down nose wheel fork. Such orientations were selected based on the simplicity of cutting off the fork from the base plate, removal of the support structure and, most importantly, reducing the building time.

The characteristics of the scaled-down nose wheel fork which reveals the structural integrity were presented. These include dimensional accuracy, porosity and surface roughness of the scaled-down nose wheel fork that was produced in Ti6Al4V(ELI) through L-PBF. The Ti6Al4V(ELI) scaled-down nose wheel fork can be built through L-PBF with a geometric accuracy of 0.2 mm after two-stage heat treatment. However, in some regions of the fork such as bushes, machining should be carried out to gain dimensional accuracy. Moreover, the scaled-down nose wheel fork was projected to have a good density of 99.997% since the representative specimens resulted in a porosity of 0.0033%. However, it has high surface roughness due to partially melted powder particles on its surface, which is even higher in the region where the support structures were removed. This surface roughness varies with the build orientation and ranges between 4.4 µm and 16 µm.

© Central University of Technology, Free State

CHAPTER 5: MECHANICAL AND FATIGUE PROPERTIES OF L-PBF TI6AL4V(ELI) SPECIMENS

Some of the material contained in Chapter 5 was published in the following peer-reviewed publications:

- L. F. Monaheng, W. B. du Preez, and C. Polese, “Towards qualification in the aviation industry: Impact toughness of Ti6Al4V(ELI) specimens produced through laser powder bed fusion followed by two-stage heat treatment,” *Metals (Basel).*, vol. 11, no. 1736, pp. 1–12, 2021, https://doi.org/10.3390/met11111736

- H. P. Miya, W. B. du Preez, and L. F. Monaheng, “High cycle fatigue performance of Ti6Al4V(ELI) specimens produced with inherent laser powder bed fusion surface roughness,” *South African Journal of Industrial Engineering.*, vol. 32, no. 3, pp. 248–257, 2021, https://doi:10.7166/32-3-2659

- L. F. Monaheng, W. B. du Preez, and C. Polese, “Selective laser melting process chain for development of a Ti6Al4V(ELI) nose wheel fork of a light aircraft,” 15th World Conference on Titanium, Edinburgh International Conference Centre, 12–16 June 2023.

5.1. Introduction

In this chapter, microstructure, mechanical and fatigue properties of the L-PBF Ti6Al4V(ELI) specimens produced using the same machine parameters and heat treatment as that of the nose wheel fork are presented. Consequently, the properties discussed in this chapter confirm the quality and integrity of the L-PBF Ti6Al4V nose wheel fork. The mechanical properties consist of the tensile, impact and fracture toughness, whereas the fatigue properties involve the FCGR and the HCF properties. Note that in each description of the impact toughness, fracture toughness, FCGR and HCF, the fractography of the specimens is also presented.

5.2. Microstructure

Microstructures of Ti6Al4V(ELI) components produced through L-PBF can be altered through heat treatment and are directly related to mechanical properties. A previous study by Lütjering showed that a reduced tensile strength and an increased ductility result from coarsened α phase and large colony size [33]. A very fine acicular (needle-like) microstructure was reported for the as-built Ti6Al4V(ELI) specimens, which resulted from the inherited rapid cooling of the material during L-PBF [146]. Such specimens had a high yield strength and UTS of 1 110 MPa and 1 267 MPa, respectively, but had a low elongation of 7.28%.

© Central University of Technology, Free State

As for the impact toughness of the as-built Ti6Al4V(ELI) L-PBF specimens, an impact toughness of 13.3 was reported [150]. The microstructure obtained in the current study is shown in Figure 5.1 for various planes XY, ZY and ZX, according to the coordinate system shown in Figure 3.7. These microstructures were obtained after the two-stage heat treatment presented in section 3.8. They consist of acicular α and a small amount of β. Importantly, various planes of the specimens have similar microstructure. The starting of the α globalisation was also observed as indicated with arrows.

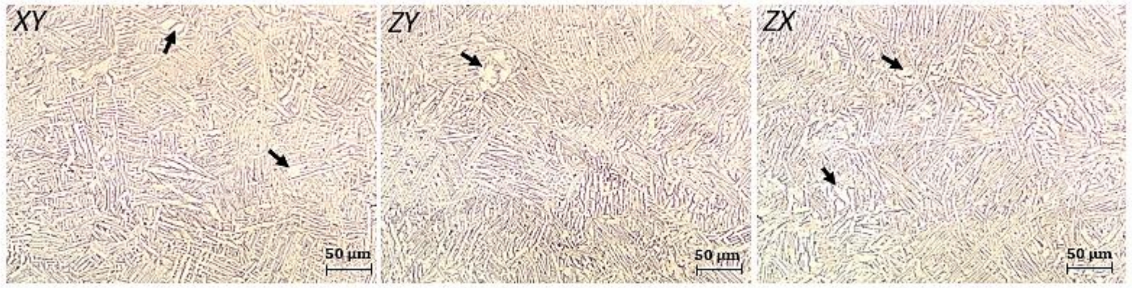

Figure 5:1: Microstructure of two-stage heat-treated Ti6Al4V(ELI) specimens built through L-PBF in various planes XY, ZY, and ZX. The arrows indicate globalised $\boldsymbol{\alpha}$ grains (light) where $\boldsymbol{\beta}$ is indicated by dark marks

These microstructures are comparable to two-stage heat-treated (950 ℃, air cooled, followed by 700 ℃ and furnace cooled) Ti6Al4V(ELI) specimens reported by Becker *et al*., which have a tensile strength of 871 MPa and a percentage elongation of 11.5% [47].

5.3. Mechanical properties

5.3.1. Tensile properties

In Table 5.1, the tensile properties of the triplicate L-PBF Ti6Al4V(ELI) specimens built along each of the X-, Y-, and Z-orientations, and subsequently submitted to two-stage heat treatment discussed in section 3.8 are presented. Testing of the procedure of the tensile test specimens was described in section 3.10.1.

Table 5.1: Tensile properties of the Ti6Al4V(ELI) specimens built through L-PBF, followed by two-stage heat treatment

Specimen orientations	**Elastic modulus (GPa)**	**Yield strength (σ_{ys}) (Offset 0.2%) (MPa)**	**UTS (MPa)**	**Elongation (%)**
ASTM F3001-14				
	-	**795**	**860**	**10**
Witness specimens built with the nose wheel fork				
Z1	121.17	848.49	935.30	20.86
Z2	120.52	842.14	932.80	20.00
Z3	120.77	844.11	935.60	21.62
Mean	**120.82**	**844.91**	**934.60**	**20.83**
SD	**0.331**	**3.25**	**1.50**	**0.810**
Results from the current study				
X1	116.30	860.42	948.13	16.50
X2	113.90	852.44	939.65	15.50
X3	115.00	853.73	941.53	15.05
Mean	**115.10**	**855.53**	**943.10**	**15.68**
SD	**1.162**	**4.285**	**4.450**	**0.472**
Y1	118.10	863.94	947.64	13.25
Y2	120.80	860.75	943.50	14.70
Y3	114.60	856.71	941.14	15.05
Mean	**114.69**	**860.47**	**941.14**	**14.33**
SD	**3.089**	**3.625**	**3.289**	**0.954**
Z1	110.00	774.78	888.52	15.75
Z2	109.50	780.48	894.81	15.60
Z3	108.50	781.33	891.61	16.15
Mean	**109.30**	**778.86**	**891.65**	**15.83**
SD	**0.796**	**3.562**	**3.146**	**0.284**

*SD represents standard deviation

In Figure 5.2, a graphical representation of the tensile properties of the Ti6Al4V(ELI) L-PBF specimens is shown.

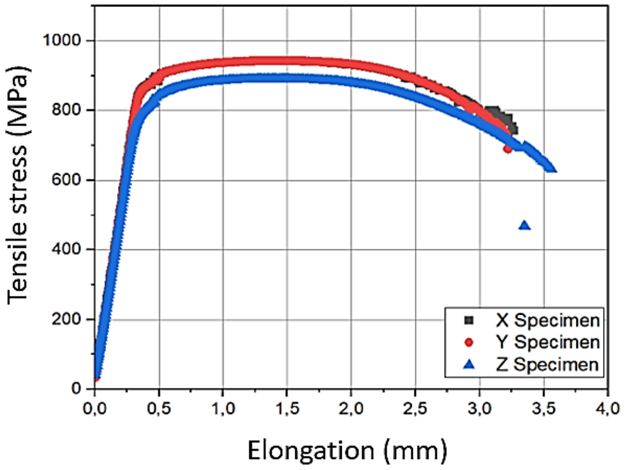

Figure 5:2: The plot of tensile stress versus elongation for the specimens built aligned with the X-, Y- and Z-axes

© Central University of Technology, Free State

The highest elastic modulus, yield strength, and ultimate tensile strength were recorded on the Ti6Al4V(ELI) specimens built aligned with the X- and Y-axes, whereas the Z-specimens had the lowest tensile properties. These results conform to the ASTM F3001-14 indicating good build quality was executed. In addition, they were equivalent to those found in a previous study on Ti6Al4V(ELI) specimens produced by L-PBF and heat treated similarly, but that were machined from bars to obtain the specified test specimen geometry [31]. These results are comparable with the mechanical properties of wrought Ti6Al4V(ELI) [185]. Importantly, the lowest recorded yield strength, UTS, and elongation reported in Table 5.1 are still comparable with the tensile properties of 780 MPa, 860 Mpa and 15%, respectively, required in the aircraft industry [186].

5.3.2. Impact Toughness

It is clear from Table 5.2 that the impact toughness of specimens with wire-cut V-notches is higher than that of 3D-printed V-notches for all orientations. The XY-3D-printed V-notch specimens absorbed 20% less impact energy compared to the similar wire-cut V-notch specimens, see Table 5.2. For both the YX- and Z-3D-printed V-notch specimens, the toughness was 3.5% lower compared to the similar wire-cut V-notch specimens. These specimens were tested as prescribed in section 3.8.2 of Chapter 3.

Table 5.2: Charpy impact toughness in Joule per square centimetre for the 3D-printed and wire-cut V-notch Ti6Al4V(ELI) specimens built in three orthogonal directions

V-Notch	**Build orientations**	**Charpy impact toughness (J/cm²)**						
		Values			**Min**	**Max**	**Mean**	**SD**
3D printed	XY	33	34	33	33	34	33	0.7
	YX	35	35	34	34	35	35	0.7
	Z	36	38	39	36	39	38	1.3
Wire cut	XY	40	41	43	40	43	41	1.3
	YX	35	36	38	35	38	36	1.3
	Z	38	38	40	38	40	38	1.4

The dispersion of the impact toughness dataset, relative to the mean values determined through standard deviation analysis, is illustrated in Figure 5.3.

© Central University of Technology, Free State

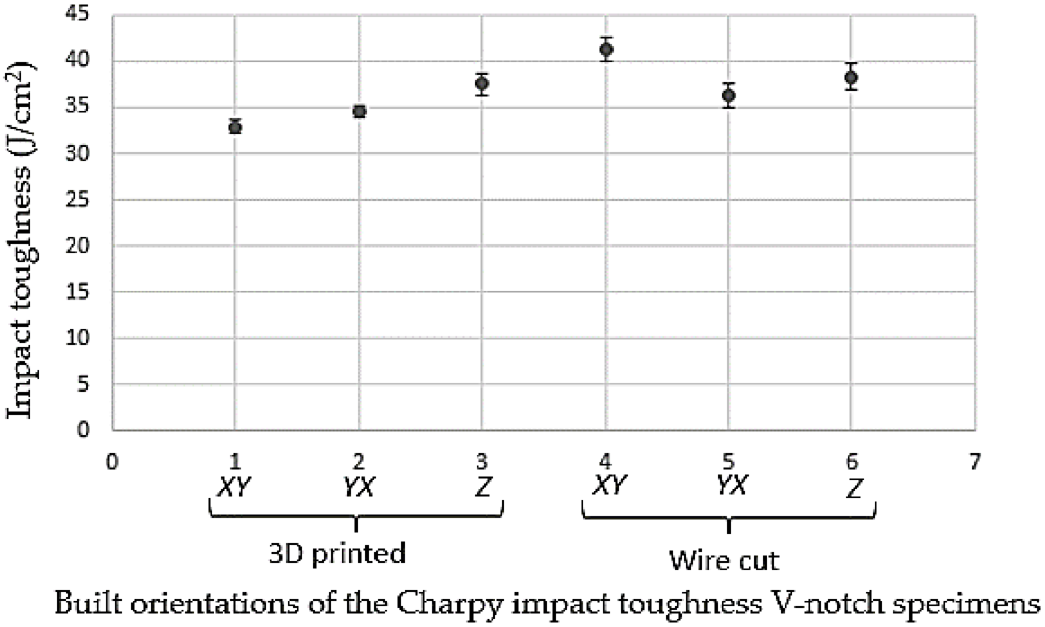

Figure 5:3: An illustration of the impact toughness dispersion concerning the built orientations of the 3D-printed and wire-cut V-notch specimens

Specimens with 3D-printed V-notch were compared with wire-cut V-notch. In general, the impact toughness of the 3D-printed specimens was found to be lower than that of the wire cut specimens for all build orientations. Dispersion of the XY- and YX-specimen with a 3D-printed notch falls outside that of the wire-cut notch, suggesting a significant difference in the impact toughness. As for specimens built in the Z orientation, comparable results were obtained between the 3D-printed and wire cut specimens. As shown in Table 5.2, the lowest recorded value of impact energy in this study, for both 3D-printed and wire-cut V-notch Ti6Al4V(ELI) specimens, was 26 J, which is 8% more than the impact energy required in the aviation industry [186]. When comparing these results with the impact energy values of as-built L-PBF Ti6Al4V(ELI) specimens available in the literature, more than 45% improvement was achieved [150], and for the stress-relieved and heat-treated specimens, more than 40% improvement was recorded [133] (see the data given in Table 2.4).

The Ti6Al4V(ELI) Charpy specimens produced through L-PBF and submitted to two-stage heat treatment showed four distinct fracture modes when subjected to

© Central University of Technology, Free State

the impact load. These fracture modes were investigated as prescribed in section 3.12 of Chapter 3. They correspond to other high-strength metals including 12CrMoV steel [187][188]. In Figure 5.4, the fracture zones of the Charpy specimens with wire-cut and 3D-printed V-notches are shown for various orientations. I in image (a) represents the crack initiation zone, II is for the zone of crack growth (unstable fracture), III is for shear lips, and IV is for precritical growth (final fracture). Images (a), (b) and (c) are for wire-cut V-notches and (d), (e) as well as (f) are for Charpy specimens with 3D-printed notches.

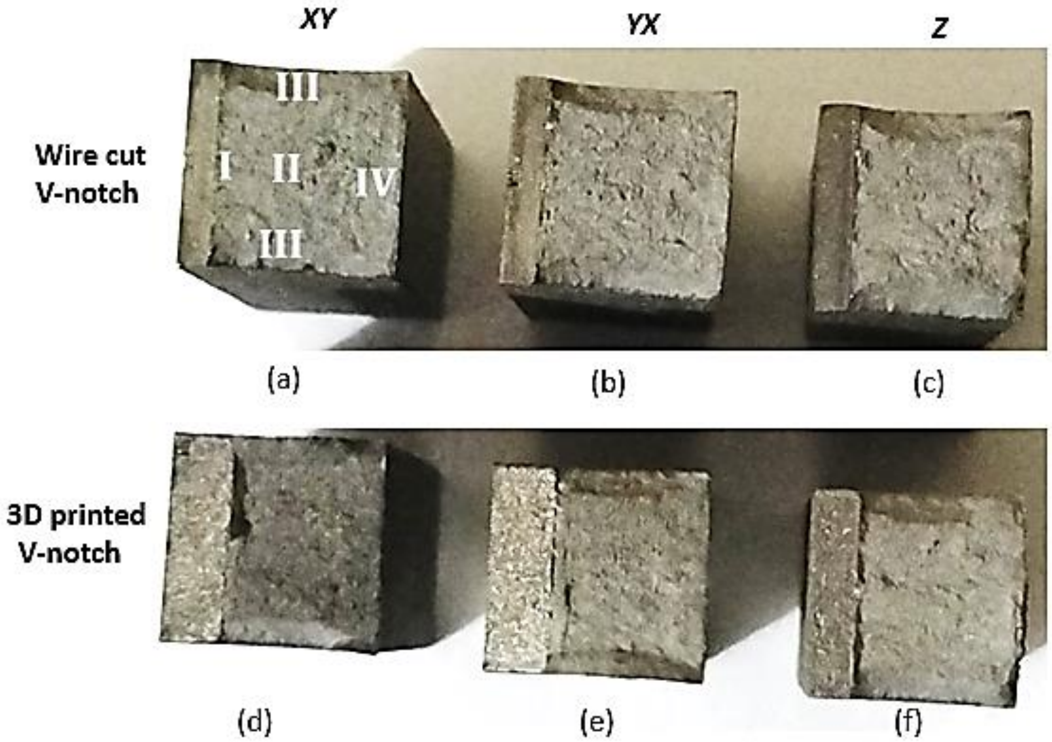

Figure 5:4: An illustration of the fracture zones of the Ti6Al4V(ELI) Charpy impact toughness specimens for the various orientations of the wire-cut and 3D-printed V-notches. **I, II , III, and IV** in image (a) represents the crack initiation, crack growth, shear lips, and final fracture, respectively. Images (a–c) are for wire-cut V-notches and (d, e) as well as (f) are for Charpy specimens with 3D-printed notches

A zone of mesoscopic scale is formed in the tip of the notch after impact due to the development of localised plastic deformation (zone I), followed by the propagation of macro defects, which result from the formation of a plastic hinge (zone II). Thereafter, the shear lips were formed, as shown in Figure 5.4 (zone III), as the material deforms due to shear stress. Finally, a region of rotational-

© Central University of Technology, Free State

shear deformation was formed as a result of a high-speed development of fracture that leads to final fracture (zone IV).

Secondary SEM images of a Charpy impact toughness specimen shown in Figure 5.4(a) reveal four distinct fracture modes. In Figure 5.5(b)–(e), detailed features of each fracture mode are illustrated.

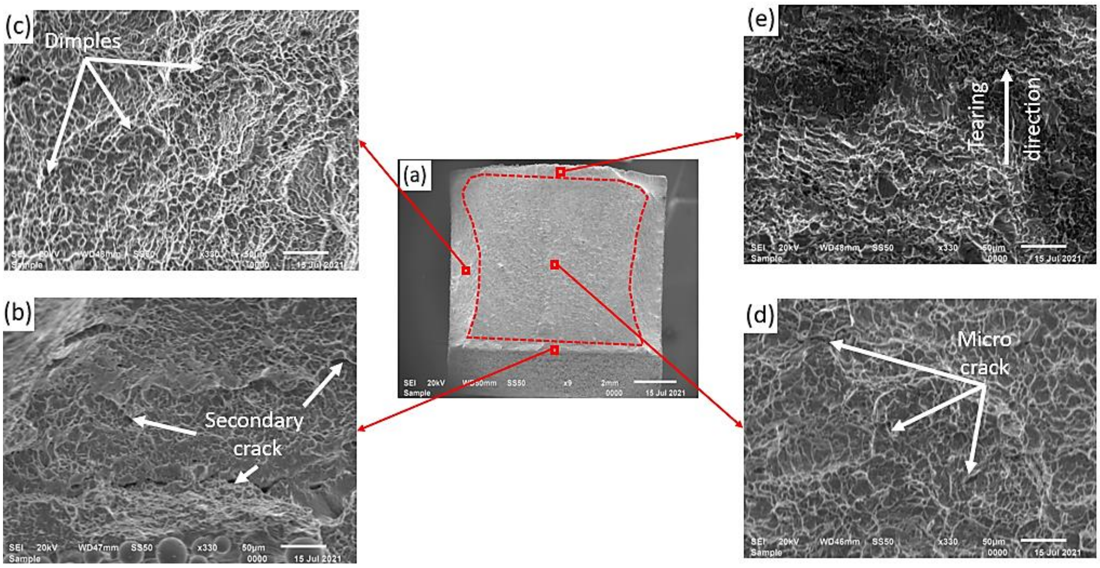

Figure 5:5: (a) SEM SE images of the fracture surface of a Z-specimen with 3D-printed V-notch, (b) crack initiation zone, (c) shear-lip region (d) unstable fracture and (e) final fracture

The crack initiation zone in Figure 6.5(a) of the Z-specimen with 3D-printed V-notch contained a secondary crack, while the unstable zone had multiple micro-cracks as illustrated in Figure 5.5(d). Dimples were observed in the shear-lip region shown in Figure 5.5(c) and flat facets surrounded by dimples with clear tear directionality were observed in the final fracture shown in Figure 5.5(e).

In all specimens, fractures initiated from the root of the notch due to stress concentration and secondary cracks were depicted, as shown in Figures 5.5(b) and 5.6 (XY1, YX1, and Z1). This secondary crack nucleation ability of the annealed Ti6Al4V(ELI) impact toughness samples near the notch arose from the ductility of the material. The impact energy was dissipated by the creation and movement of dislocations in the crystal lattices of the structure near the crack tip [35]. As a result, the specimens absorbed the high-impact energy and a fibrous fracture surface was observed in the crack initiation region.

© Central University of Technology, Free State

As a crack propagated through an unstable fracture region, a fracture surface with dimples, micro-cracks and pores was depicted, as can be seen in Figures 5.5(d) and 5.6 (XY2, YX2, and Z2). At the sides of the specimens, material ruptured due to shear stress set up by the applied load at about 45° with respect to the normal stress, resulting in a fibrous surface that is associated with plastic deformation, and formed a shear lip. This phenomenon occurs when the shear stress exceeds the shear strength of the material, as stated by the ASTM E23-18 standard [149]. The shear areas, as a percentage of the total fracture surface of 3D-printed and wire-cut V-notch specimens, were 40% and 30%, respectively. However, both types of specimens had tortuous fracture surfaces with dimples in the shear-lip region. The final fracture occurred microseconds later with evidence of flat-faced fracture surrounded by dimples, pointing towards a mixed fracture mode (ductile and brittle fracture).

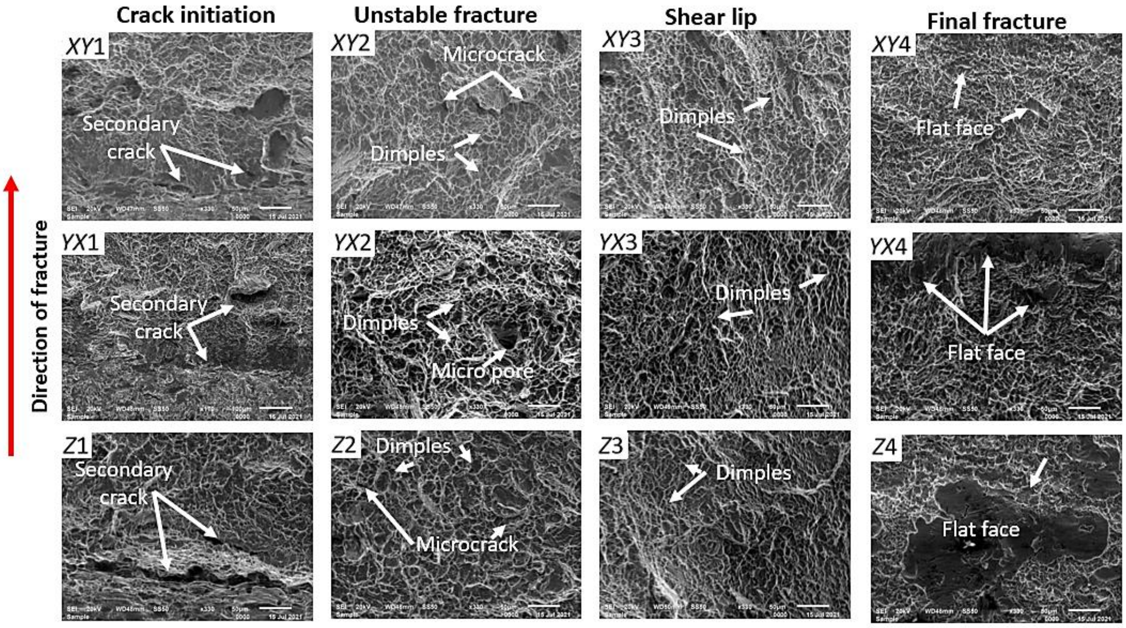

Figure 5:6: Fracture surfaces of the various regions of fracture for the Charpy impact toughness specimens built with different orientations (XY, YX, and Z)

As seen in Table 5.2, the surface roughness in the root of the 3D-printed V-notch significantly reduced the impact toughness compared to the impact toughness value of the wire-cut V-notch. This variation in the impact toughness value is attributed to a conspicuous variation between 3D-printed and wire-cut V-notch

© Central University of Technology, Free State

specimens observed by comparing Figure 5.5(b) with Figure 5.6(Z1). The 3D-printed V-notch contained unmelted powder particles in the notch region resulting in an uneven surface that acted as a stress raiser, whereas the wire-cut V-notch had a smooth surface.

5.3.3. Conditional Fracture toughness

The value of the conditional fracture toughness (K_Q) properties of triplicate Ti6Al4V(ELI) specimens, produced through L-PBF in three orientations (XZY, YXZ, and ZXY) and subsequently submitted to two-stage heat treatment, are given in Table 5.3. A detailed testing procedure for these specimens was provided in Chapter 3, section 3.8.3. It is important to note that the test was done at a temperature of 20 ℃ and the fracture toughness (K_{IC}) could not be obtained because its determination criteria stated in ASTM E399 were not attained [155]. For example, the P_{max}/P_Q was more than 1.1 and the loading rate $(\Delta K/dt)$ was not within the 0.55 MPa·m$^{0.5}$ and 2.75 MPa·m$^{0.5}$.

Table 5.3: The average values of the conditional fracture toughness (KQ) of the L-PBF Ti6Al4V(ELI) triplicate specimens

Specimens	**XZY**			**YXZ**			**ZXY**		
	1	**2**	**3**	**1**	**2**	**3**	**1**	**2**	**3**
P_Q (kN)	7.08	7.01	7.18	7.93	7.64	7.65	7.51	7.54	7.51
P_{max}/P_Q	1.27	1.34	1.34	1.28	1.24	1.29	1.24	1.29	1.29
$\Delta K/dt$	3.30	2.81	2.70	2.69	2.50	2.75	2.70	2.66	2.70
B (mm)	6.62	6.35	6.65	7.06	7.01	6.99	6.61	6.59	6.54
a (mm)	10.47	10.36	10.32	10.17	10.16	10.22	10.03	10.28	10.12
W (mm)	19.74	19.79	19.89	19.87	19.79	19.81	19.81	20.14	19.99
K_Q (MPa·m$^{0.5}$)	80.98	77.98	78.42	80.14	78.06	78.91	79.46	80.46	80.02
		79.13			**79.04**			**79.98**	
SD		**1.32**			**0.85**			**0.41**	

*P_Q = Force determined by the secant line (OP_5) from the origin that has slope of 95%, see Figure 2.34). P_{max} = maximum load sustained by the specimen. $\Delta K/dt$ = loading rate. B = thickness of the specimen. W = width of the specimen. a = crack size. These can be found in the ASTM E399 [155]

Similar K_Q values were measured for all orientations of the specimens. As supported by previous studies, these isotropic K_Q values were due to similar microstructures in various planes as shown in Figure 5.1. Isotropic fracture

© Central University of Technology, Free State

toughness was also reported by Macallister *et al.* for specimens annealed at a high temperature of 910 °C for 8 hours [43]. Contrary to this, Cain *et al.* [156] reported for specimens heat treated at 890 °C for 2 hours, a similar value of K_{IC} between XZY and ZXY specimens, whereas a lower value of fracture toughness was reported for the YXZ specimens. Kumar and Ramamurty [157] also obtained anisotropic values of fracture toughness for Ti6Al4V(ELI) specimens heat treated at a temperature of 920 °C for 0.5 hours, see Table 2.4.

The results from the current study (Table 5.3) and those from literature (Table 2.4) suggest that an increased soaking period at high temperature resulted in isotropic fracture toughness values for L-PBF Ti6Al4V(ELI) parts built in different orientations. Furthermore, the data in Table 5.3 illustrated that for Ti6Al4V(ELI) specimens built by L-PBF and followed by two-stage heat treatment, the fracture toughness had improved by approximately 20% when compared with the wrought $(\alpha + \beta)$ Ti6Al4V(ELI) alloy with equiaxed microstructure reported in [124]. The wrought $(\alpha + \beta)$ Ti6Al4V(ELI) with equiaxed microstructure had fracture toughness of 66 MPa·m$^{0.5}$ which could be altered to 91 MPa·m$^{0.5}$ after annealing heat treatment.

The investigation methodology of the fracture regions was stated in section 3.10.3. Fracture surfaces of the Ti6Al4V(ELI) fracture toughness specimens produced through L-PBF and submitted to the two-stage heat treatment, showed four distinct fracture regions after testing. These are crack initiation, crack propagation, shear-lip formation and final fracture, as shown in Figure 5.7. For all the specimens built in the three orientations, the fracture regions were similar. This was attributed to a similar microstructure that resulted from HTA. The same features of fractured regions were reported in previous studies [157][165].

© Central University of Technology, Free State

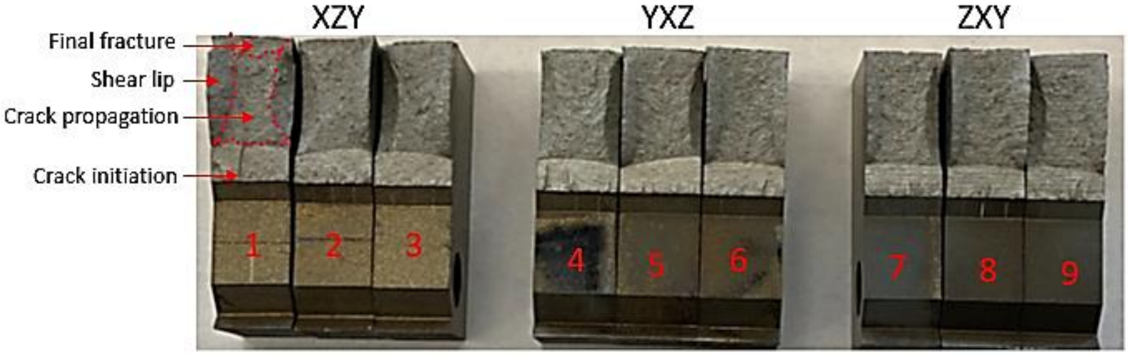

Figure 5:7: Fracture surfaces of the Ti6Al4V(ELI) fracture toughness specimens produced through L-PBF in various build orientations, followed by two-stage heat treatment

As a specimen experienced tensile loading, the Ti6Al4V(ELI) developed plastic strain when the yield strength was exceeded in the region near the crack tip. The metal at the free surface deformed in a lateral direction, forming a 45^{o} shear lip at both ends of the crack. This is typical ductile metal behaviour and confirms the ductile characteristic of the Ti6Al4V(ELI) produced through L-PBF and followed by two-stage heat treatment. The central area of the specimen was restricted to deform laterally by the surrounding material, resulting in zero strain perpendicular to both the loading axis and the crack propagation direction. Ultimately, the specimen experienced fracture stress and then a rapid final fracture occurred. This fracture mechanism of the two-stage heat-treated Ti6Al4V(ELI) that was produced by L-PBF was also found by Cain *et al.* [156].

5.4. Fatigue properties

5.4.1. Fatigue crack growth rate

The values of FCGR ($^{da}/_{dN}$) properties of triplicate Ti6Al4V(ELI) specimens, produced through L-PBF in three orientations (XZY, YXZ, and ZXY) and subsequently submitted to two-stage heat treatment, are given in Table 5.4. These specimens were built, heat treated and tested as defined in 3.7, 3.8 and 3.10.3, respectively. The ΔK_{th} is the fatigue crack growth threshold that signifies the critical value of ΔK below which crack growth will not occur.

© Central University of Technology, Free State

Table 5.4: FCGR properties of the Ti6Al4V(ELI) specimens, built through L-PBF and followed by two-stage heat treatment

Specimen orientations	**ΔK_{th}**	**ΔK_{th}**	**Coefficients**	
	(1E-08) (MPa·m$^{0.5}$)	**(1E-07) (MPa·m$^{0.5}$)**	**C (1E-08)**	**m**
XZY4	0.653	1.465	3.37	2.85
XZY5	0.661	1.477	3.328	2.86
XZY6	0.761	1.661	2.24	2.95
Mean	**0.692**	**1.534**	**2.963**	**2.89**
SD	**0.049**	**0.090**	**0.523**	**0.045**
YXZ4	0.569	1.288	4.98	2.76
YXZ5	0.463	1.111	7.64	2.65
YXZ6	0.504	1.183	6.36	2.70
Mean	**0.512**	**1.194**	**6.327**	**2.70**
SD	**0.044**	**0.073**	**1.086**	**0.045**
ZXY4	0.539	1.261	5.33	2.71
ZXY5	0.552	1.325	4.55	2.80
ZXY6	0.577	1.325	4.59	2.77
Mean	**0.556**	**1.304**	**4.823**	**2.76**
SD	**0.016**	**0.030**	**0.359**	**0.037**

*The threshold crack growth rate in mm/cycle 10^{-4}~10^{-3} throughout all specimens.

The FCGR of the Ti6Al4V(ELI) specimens produced by L-PBF in various orientations in the current study depicted an improvement of this property compared to the previous studies given in Table 2.5. For example, the slope (m value) of the FCGR versus ΔK based on the current results is lower than the values reported in the previous studies for all specimen build orientations. Therefore, the two-stage heat treatment performed in the current study improves the FCG resistance of the Ti6Al4V(ELI) produced through L-PBF compared to the work presented in Table 2.5.

In Figures 5.8, 5.9 and 5.10, the graphs of FCGR versus the ΔK for XZY4, YXZ4 and ZXY4 are presented. The slopes of all curves are comparable, confirming isotropic FCGR properties. These were attributed to the two-stage heat treatment performed, which also yielded similar microstructure on various build orientations. However, the critical crack length of 16 mm of the Ti6Al4V(ELI) specimens built in various orientations occurred at different numbers of cycles, see Figure 5.11. This has also been reported in previous literature [165].

© Central University of Technology, Free State

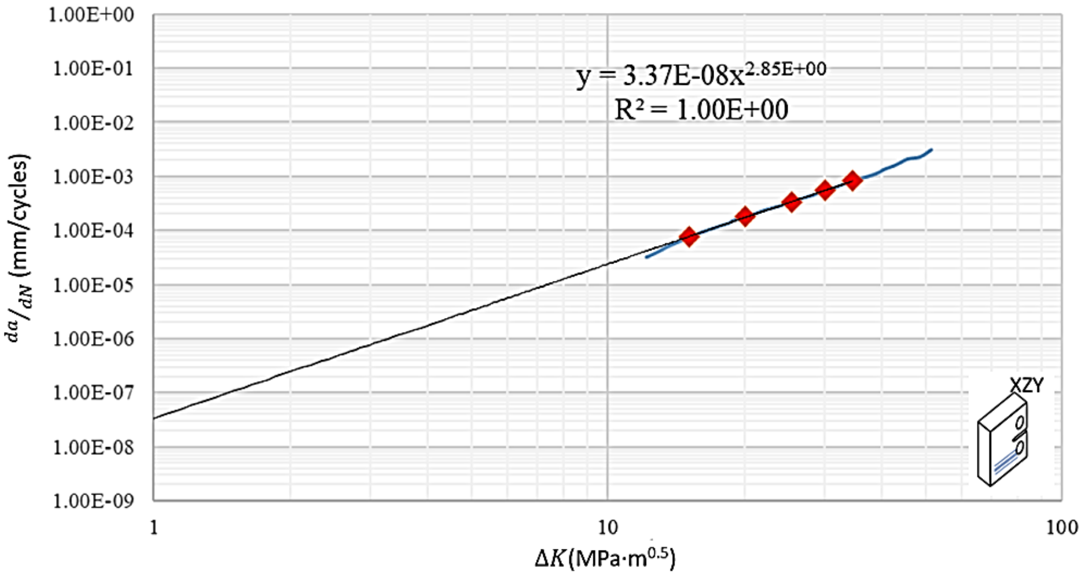

Figure 5:8: A plot of FCGR vs stress-intensity factor range of the XZY-specimen

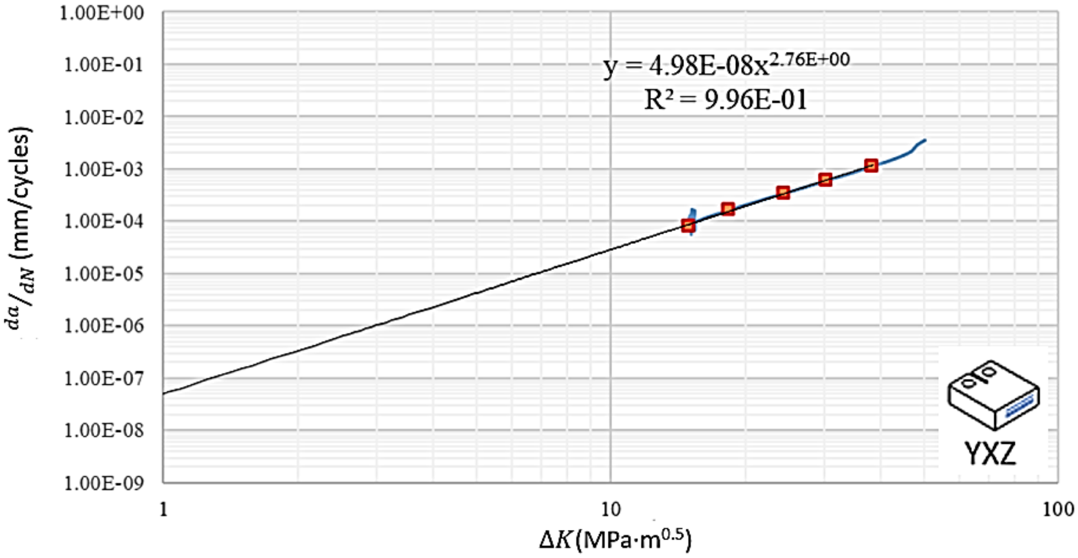

Figure 5:9: A plot of FCGR vs stress-intensity factor range of the YXZ-specimen

© Central University of Technology, Free State

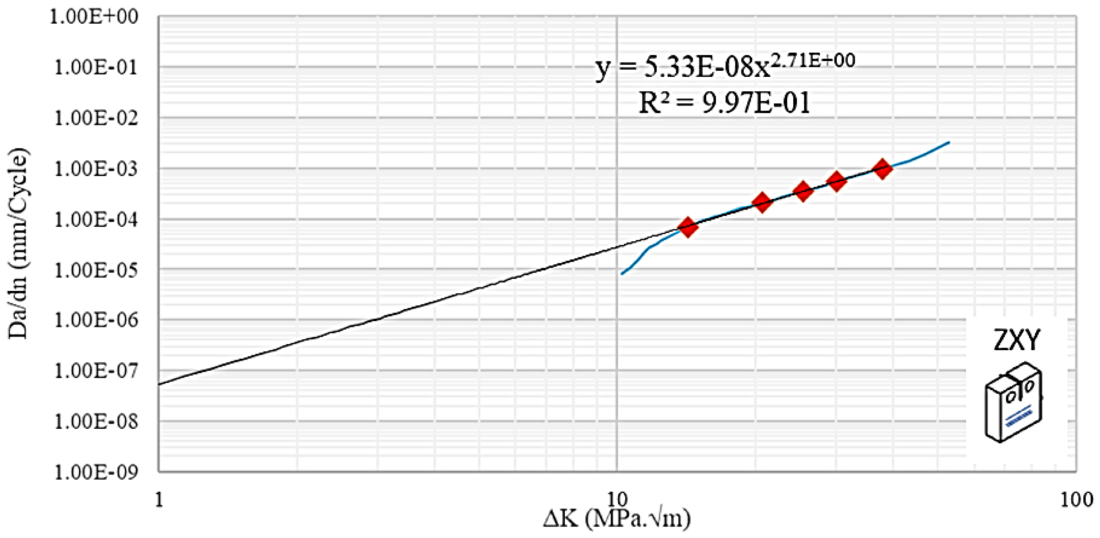

Figure 5:10: A plot of FCGR vs stress-intensity factor range of the ZXY-specimen

The critical crack length was determined for the Ti6Al4V(ELI) specimens under cyclic load, as indicated in Figure 5.11.

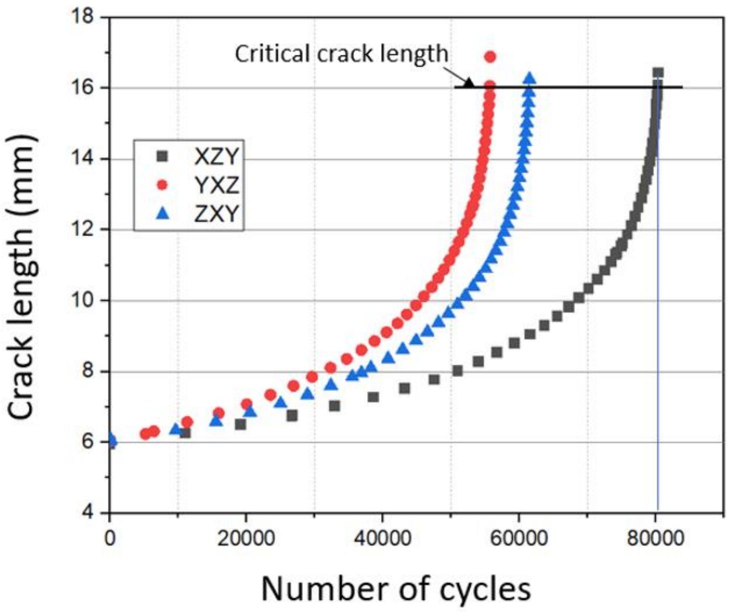

Figure 5:11: The crack length plot versus number of cycles to failure of the various Ti6Al4V(ELI) specimens built in XZY-, YXZ-, and ZXY-orientations

Ti6Al4V(ELI) specimens built through L-PBF, followed by a two-stage heat treatment, depicted very slow crack growth during the initial stage of crack

© Central University of Technology, Free State

propagation. As the crack length increased, the growth rate (da/dN) increased. This was due to the increase of ΔK at the crack tip. ΔK increased directly proportional to the crack length, leading to rapidly increasing crack propagation. The specimens in the YXZ-orientation reached the critical crack length at the lowest number of cycles. In these specimens, cracks propagated until they reached the critical size of about 16 mm after $\sim$ 55 000 cycles, followed by final fracture, whereas specimens ZXY and XZY reached the critical size of 16 mm at 60 000 and 80 000 cycles, respectively.

The SEM images shown in Figures 5.12, 5.13 and 5.14 represent the fracture surfaces of the Ti6Al4V(ELI) FCGR test specimens built through L-PBF, followed by two-stage heat treatment. In all SEM images, the crack propagation direction is from the top to the bottom of the images, as illustrated by the red arrow.

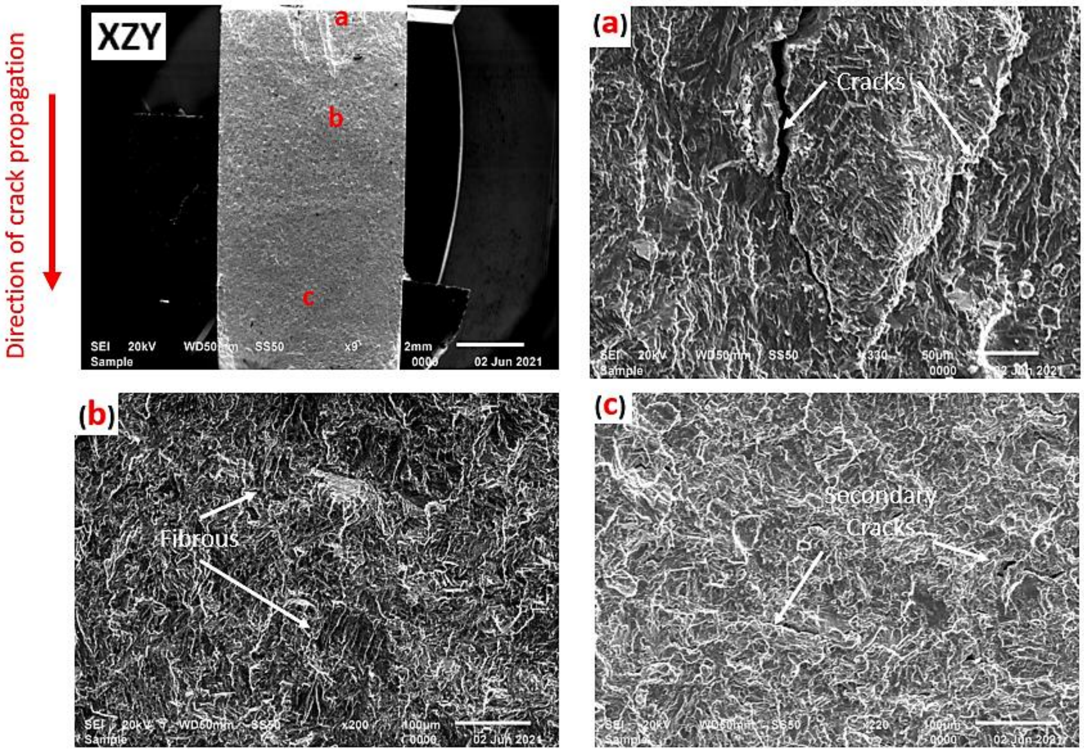

Figure 5:12. Representative SEM images of the fracture surfaces of XZY FCGR specimens indicating the (a) crack initiation section, (b) crack propagation area, and (c) final fracture region

© Central University of Technology, Free State

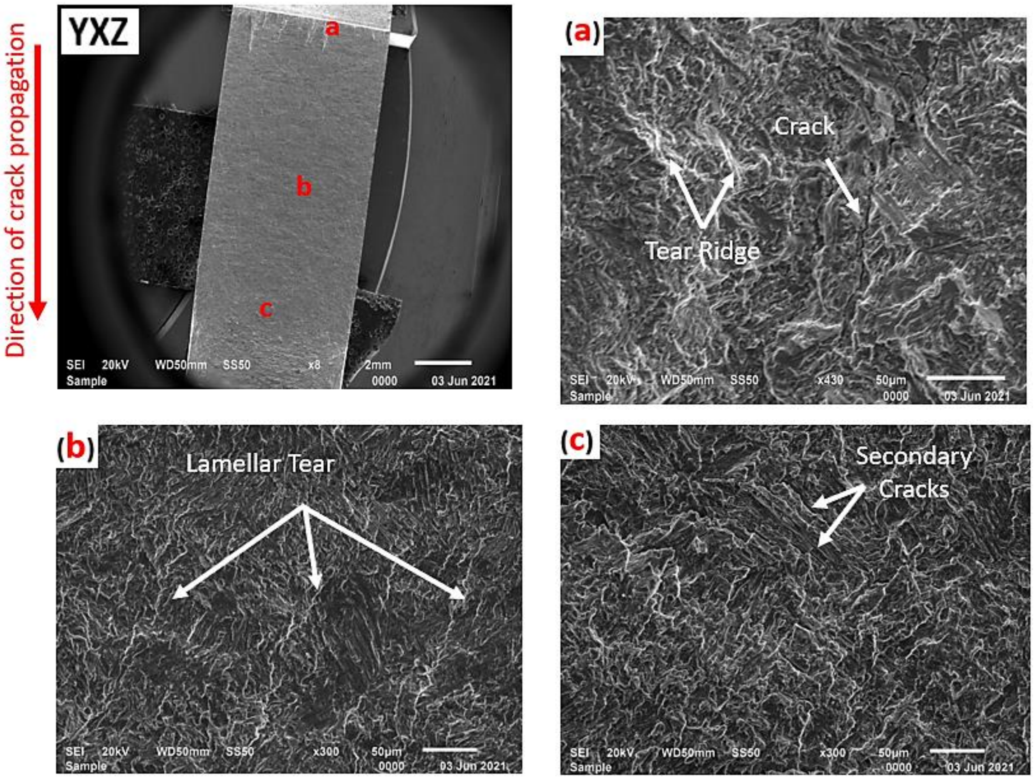

Figure 5:13. Representative SEM images of the fracture surfaces of YXZ FCGR specimens indicating the (a) crack initiation section, (b) crack propagation area, and (c) final fracture region

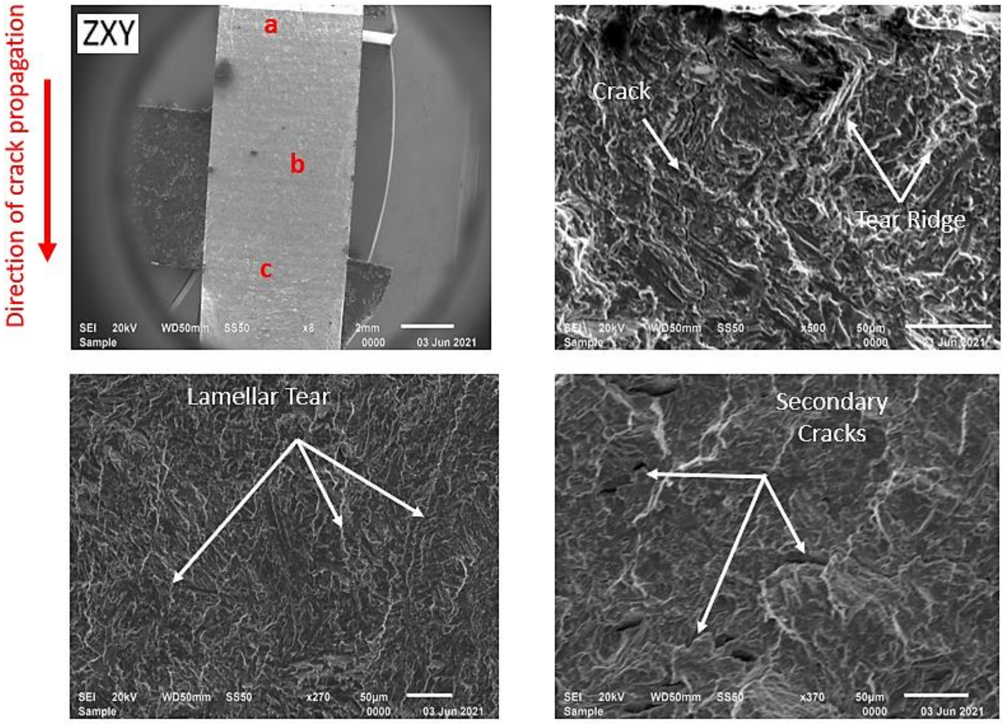

Figure 5:14. Representative SEM images of the fracture surfaces of ZXY FCGR specimens indicating the (a) crack initiation section, (b) crack propagation area, and (c) final fracture region

© Central University of Technology, Free State

The crack initiation regions consisted of tear ridges forming river-like patterns. Dimples, as well as some inter-lamellar tears, were observed in the crack propagation areas of the specimens. In the final fracture area, secondary cracks were observed, which were found to be approximately perpendicular to the primary crack plane. This behaviour was also observed by Wu *et al.* [190]. In general, the fracture surfaces of all specimens consisted of tortuous surfaces indicative of strong metallurgical bonds between the L-PBF layers. This was also reported in a previous study on the fracture toughness and FCGR of heat-treated Ti6Al4V specimens built through L-PBF [28].

5.4.2. High cycle fatigue

The number of cycles to failure determined from the HCF specimen tests is presented in Tables 5.5, 5.6 and 5.7 for L-PBF Ti6Al4V(ELI) specimens built along Z-, X- and Y-orientation, respectively. These specimens were built, heat treated and tested as defined in 3.7, 3.8 and 3.10.4.

Table 5.5: Number of cycles to failure (N) for the HCF Z-specimens

Z-specimens loading		
Specimen ID	**Max stress (MPa)**	**N (Cycles)**
Z4	450	50 142
Z5	418	61 584
Z6	360	122 595
Z10	300	483 996
Z7	270	370 439
Z9	250	730 494
Z8	225	5 000 000

Table 5.6: Number of cycles to failure for X-specimens

X-specimens loading		
Specimen ID	**Max stress (MPa)**	**N (Cycles)**
X4	360	147 027
X5	300	218 190
X9	270	346 930
X6	230	513 876
X7	210	893 273
X10	200	1 153 581
X8	190	5 000 000

© Central University of Technology, Free State

Table 5.7: Number of cycles to failure for Y-specimens

Y-specimens loading		
Specimen ID	**Max stress (MPa)**	**N (Cycles)**
Y4	360	132 859
Y5	300	304 007
Y9	270	434 787
Y8	250	538 903
Y6	230	598 800
Y10	200	1 002 143
Y7	190	5 000 000

The fatigue strength of 225 MPa for Z-specimens was found to be higher than that of X- and Y-specimens, which was 190 MPa. At the fatigue strength recorded, the specimens were able to attain more than 5 million cycles. In Figure 5.15, the SN curve is shown for X-, Y- and Z-specimens.

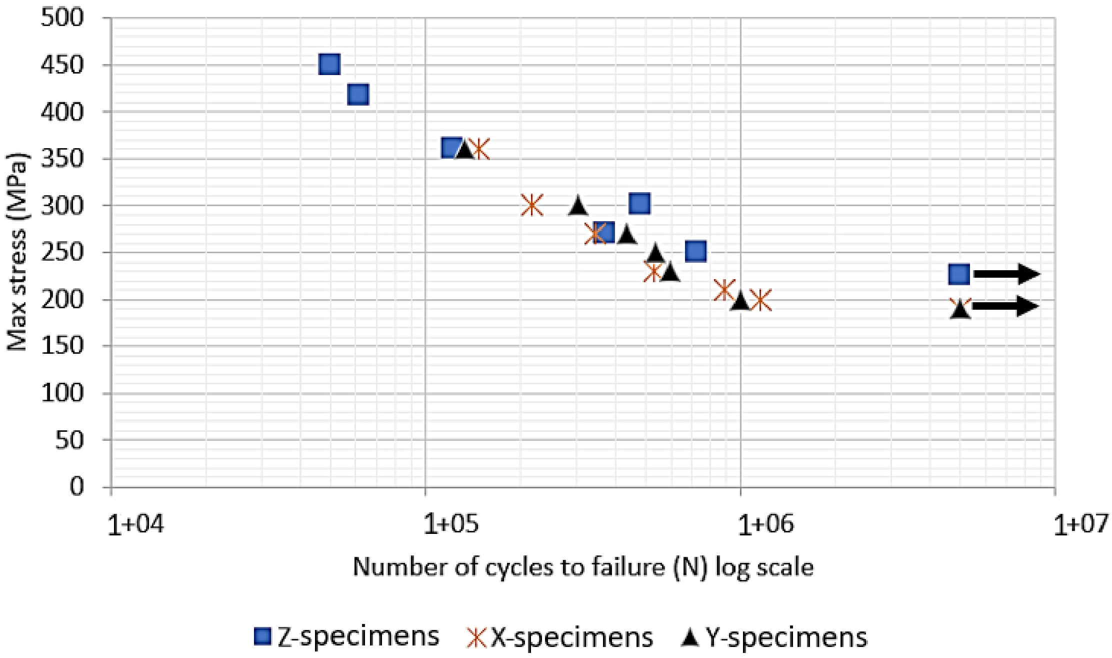

Figure 5:15: The SN curve of the L-PBF Ti6Al4V(ELI) specimen built with the inherent surface roughness along Z, X and Y

The fatigue strength measured in the current study for L-PBF Ti6Al4V(ELI) Z-specimens is 54% less than that reported by Malefane *et al.*, whereas for X and Y it is 57% less [136]. The surface roughness was found to be the only factor contributing towards the low level of fatigue strength since the specimens used in the current study were built using the same L-PBF machine parameter, same powder and heat treated following the same process as that of the previous study by Malefane *et al*. with the only difference being the surface roughness. It is important to note that the L-PBF post-process also has a direct impact on fatigue strength. For example, the as-built surface roughness Ti6Al4V(ELI) specimens that were submitted to stress-relief heat treatments at 750 ℃, furnace cooled to 540 ℃ and rapidly cooled to room temperature in an argon atmosphere have a fatigue strength of 120 to 360 MPa [191].

The high surface roughness observed on these X- and Y-specimens compared to that of Z-specimens was the root cause of the lower fatigue strength measured on these specimens. In Figure 5.16, the surface roughness of X- and Y-, and Z-specimens is illustrated.

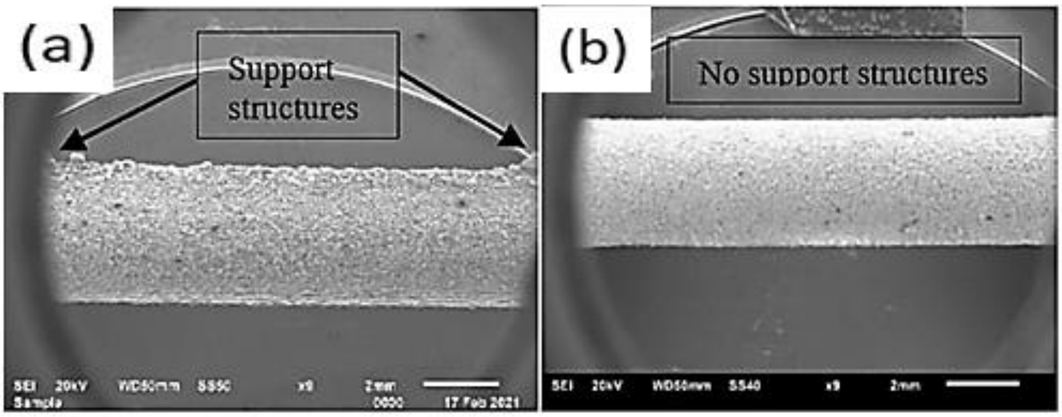

Figure 5:16: An illustration of the surface roughness on the SEM image (a) representing X- and Y- and (b) representing Z-specimens

When performing a visual inspection in the SEM, the surface roughness found in the X- and Y-specimens was similar, whereas the Z-specimens had lower surface roughness compared to both the X- and Y-specimens. This was attributed to the layer orientation on the specimens and the use of a pin support structure necessary for the L-PBF process. A previous study by Hartunian *et al.* also confirmed less surface roughness for L-PBF Ti6Al4V(ELI) Z-specimens compared to the X- and Y-specimens [192].

© Central University of Technology, Free State

The in-depth field of view provided by the SEM images in Figure 5.17, shows three stages of fatigue fracture of HFC specimens, namely crack initiation zone, propagation zones and final fracture.

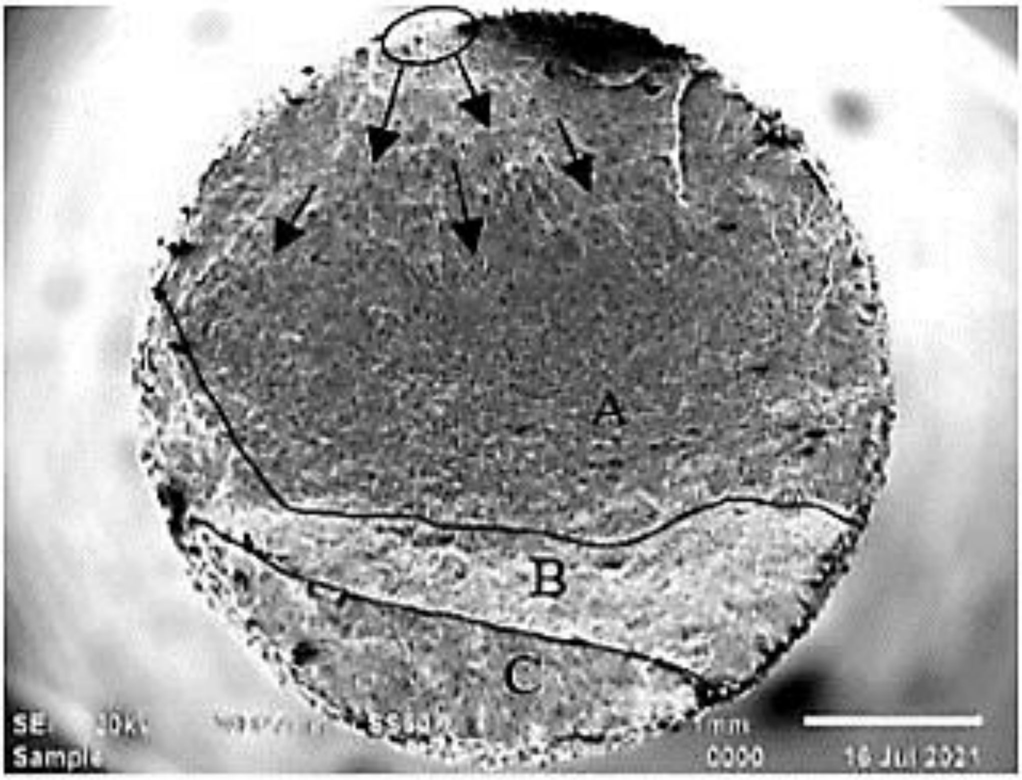

Figure 5:17: Overview of the fracture surface of the fatigue Z4 specimen. A, B and C represent stable crack propagation zone, propagation and final fracture, respectively

The crack initiates from the surface of the specimen and undergoes stable crack propagation, as shown by an ellipse and arrow in Figure 5.17. Moreover, Figure 5.18(a) confirms that the crack initiated due to the irregular surface of the specimen. Furthermore, two crack initiation zones are indicated with a ratchet mark between them. The depicted combination of ratchet mark in Figure 5.18(a) and small final fracture zone C in Figure 5.17 confirmed that the Z4 specimen was experiencing high stress concentration due to high surface roughness.

© Central University of Technology, Free State

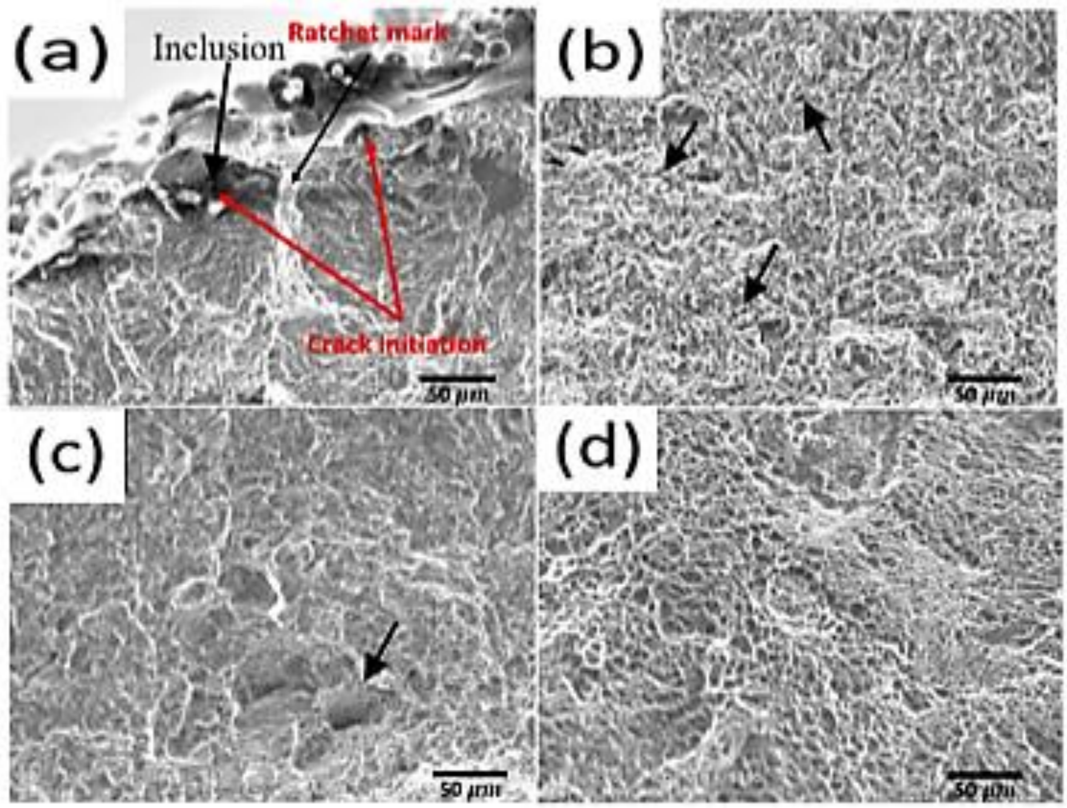

Figure 5:18: SEM image of the (a) crack initiation, (b) area A, slow crack propagation, (c) area B, faster crack propagation and area C, final fracture

In Figure 5.18(b), a high magnification of area A of Figure 5.17 is shown. This image depicts micro-cracks as indicated by the arrows and represents a slow crack propagation region. Figure 5.18(c) shows a high magnification of the faster crack propagation, area B in Figure 5.17. This region consists of micro-pores and shallow dimple fracture mode leading to the fibrous final fracture, as shown in Figure 5.18(d). Consequently, the Ti6Al4V(ELI) L-PBF Z4-specimen failed at low cycles of 50 142 cycles.

In Figure 5.19, the fracture regions of the Y10-specimen are shown. This includes crack initiation and final fracture.

© Central University of Technology, Free State

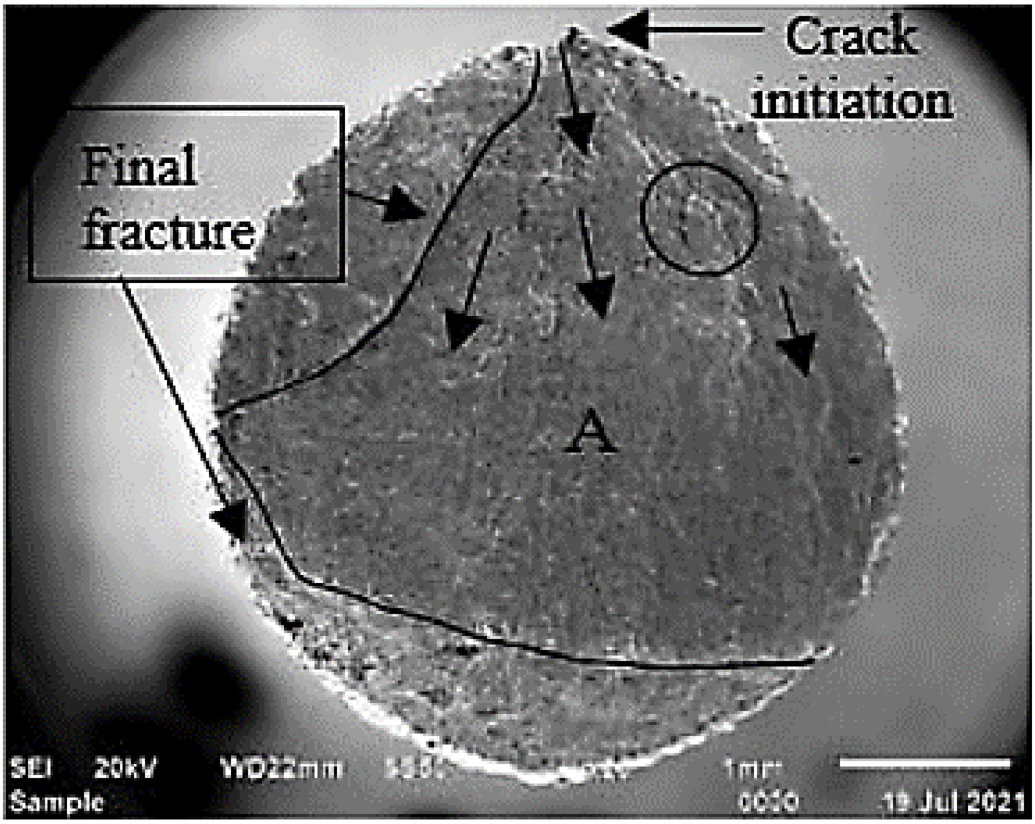

Figure 5:19: SEM image illustrating the fracture mode of the Y-10 specimen

The Y-specimen, which has the same fracture mode as the X-specimen, depicted crack initiation on the surface irregularities where the support structures had been removed. This uneven surface acted as a high-stress-concentration region leading to crack initiation. Subsequently, the crack propagated towards the centre of the specimen until reaching the final fracture after 1 002 143 cycles. This high number of cycles to failure is related to a maximum stress of 200 MPa.

In Figure 5.20, the in-depth views of the fracture surface of specimen Y10 shown in Figure 5.19 are presented. The high-magnification view in Figure 5.20(a) reveals that the cause of crack initiation is the surface roughness caused by a pin support structure. In addition, micro-cracks were also observed in the encircled area in Figure 5.19 and appeared to be linked to the tear ridges in the crack propagation area, see Figure 5.20(c). The circled area in Figure 5.20(c) depicted fatigue striation indicated in Figure 5.20(b) and magnified in Figure 5.20(d).

© Central University of Technology, Free State

Similar fatigue striations were presented in the previous study on the effect of defects on fatigue testing of the as-built SLM Ti6Al4V specimens [193].

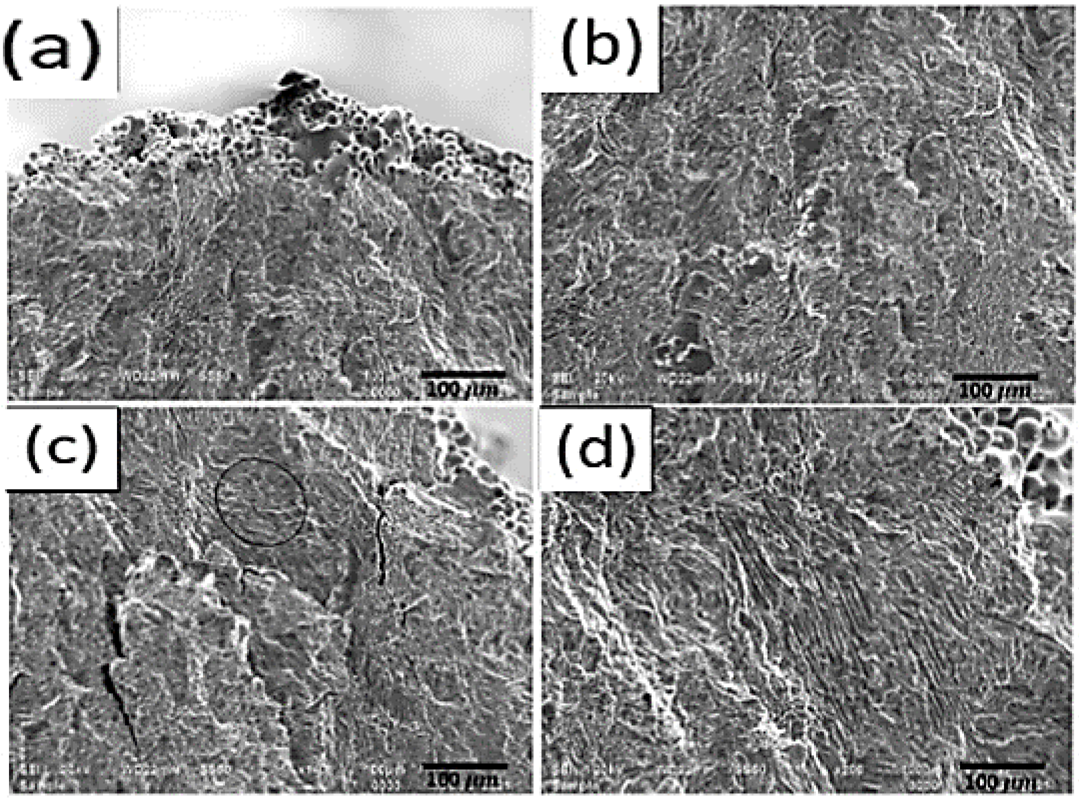

Figure 5:20: High-magnification SEM image of the Y10-specimen’s fracture surface, (a) crack initiation zone, (b) fatigue striation on the crack propagation zone A, (c) encircled area in Figure 5.19 and (d) high magnification of Figure 5.20(c)

Specimen Y10 had a larger crack propagation zone than the Z4, since their respective maximum stresses were 200 MPa and 450 MPa. These clearly demonstrated that the applied stress is proportional to the number of cycles to failure which were recorded as 1 002 143 and 50 142 for specimens Y10 and Z4, respectively. The previous study on the fatigue performance of the Ti6Al4V(ELI) L-PBF specimens that were machined and polished recorded a fatigue strength of 450 MPa [136]. Therefore, the combination of multiple crack initiation and the small final fracture that was observed in the fracture surface of the Z4-specimen confirmed that stress concentration due to surface roughness was the cause of failure. This phenomenon corresponds with what was reported in the previous study by Sachs *et al.* [171]. In addition, the inclusion found near the sub-surface

© Central University of Technology, Free State

of the Z4-specimens also contributed to shorter fatigue life, since it had initiated a crack. Several studies have demonstrated that internal defects can cause premature failure in the HCF specimens [172][194].

5.5. Summary

In this chapter, the microstructure of the L-PBF Ti6Al4V(ELI) specimens obtained after two-stage heat treatment was presented and discussed. The results underscored isotropic microstructure when observed in orthogonal planes. Additionally, the mechanical properties are directly dependent on the type of the microstructures and can be altered through the selected heat treatment. Therefore, the appropriate heat treatment carried out in the current study resulted in tensile, impact and fracture toughness accepted in the aviation industry for the production of the aircraft structural part in Ti6Al4V(ELI). Moreover, the mechanical properties obtained confirmed good built quality as they comply with ASTM F3001-14 standard. Finally, the 20% reduction in the impact toughness of the 3D-printed V-notch compared to wire cut V-notch was presented.

The fatigue properties of the L-PBF Ti6Al4V(ELI) specimens were also reported and discussed. They revealed improved fatigue crack growth resistance after the two-stage heat treatment and the effect of surface roughness on fatigue. Stress concentration resulting from surface roughness reduces the fatigue strength by 50%. This was due to the L-PBF defects such as the internal inclusion near the surface of the specimens, partially melted powder particles on the surface and high surface roughness, particularly on the area of the support structure, which were observed through the fractographic analysis.

CHAPTER 6: PERFORMANCE OF THE L-PBF Ti6Al4V(ELI) NOSE WHEEL FORK

Partial material contained in Chapter 6 was published in the peer-reviewed media stated below:

- L. F. Monaheng, W. B. du Preez, and C. Polese, “Failure analysis of a landing gear nose wheel fork produced in Ti6Al4V(ELI) through selective laser melting,” *Engineering Failure Analysis*, p. 107548, 2023, https://doi:10.1016/j.engfailanal.2023.107548

6.1. Introduction

In Chapter 6, the performance of the L-PBF Ti6Al4V(ELI) scaled-down nose wheel fork built, and heat treated as prescribed in sections 3.7 and 3.8 is discussed. This performance test included the experimental static and fatigue testing. Thereafter, the microstructure of the alloy and the fractographic features of the fatigue failure of the fork are presented. Subsequently, the experimentally validated FEA results obtained during static performance testing are presented. Finally, the finite-element-based simulation of the fatigue performance of the nose wheel fork is presented and compared with experimental results.

6.2. Experimental performance test results

6.2.1. Static test results

The static test results obtained, as prescribed in section 3.11.3, are presented in the current section, whereas the experimental strain values for the maximum static loading of 6 000 N and 8 300 N for X- and Z-load cases are presented in Appendix K. In Figure 6.1, experimental strain values for each strain gauge (SG) are plotted against time for the maximum static load of 6 000 N and 8 300 N acting in the X- and Z-direction, respectively. When the loads were gradually applied in the negative and positive X- and Z-directions, the strain gauges experienced compression and tensile strain, as expected, confirming the reliability of the strain measurements. During the X-load case, the SG3b gauge recorded the highest tensile strain values followed by the SG4a and SG2 gauges, whereas the SG3 and SG2b gauges measured the highest compressive strain. As for the Z-load

© Central University of Technology, Free State

case, SG 1 recorded the largest compressive strain, whereas SG 3a, recorded the largest tensile strain during negative Z-loading. No failure was depicted on the L-PBF Ti6Al4V(ELI) scaled-down nose wheel fork during the application of the maximum static X-, and Z-load case. Therefore, a topologically optimised Ti6Al4V(ELI) nose wheel fork produced through L-PBF technology can handle the static loads without any failure.

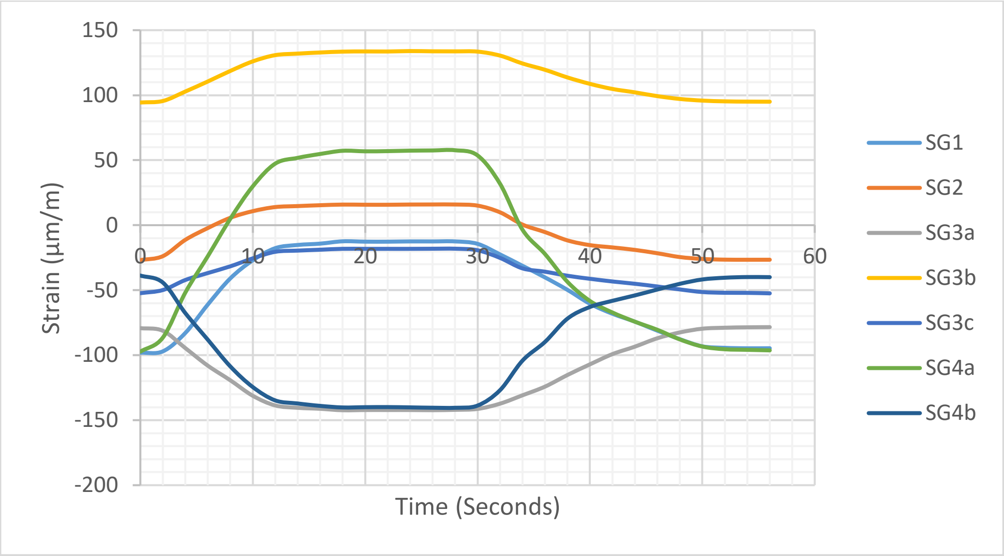

(a)

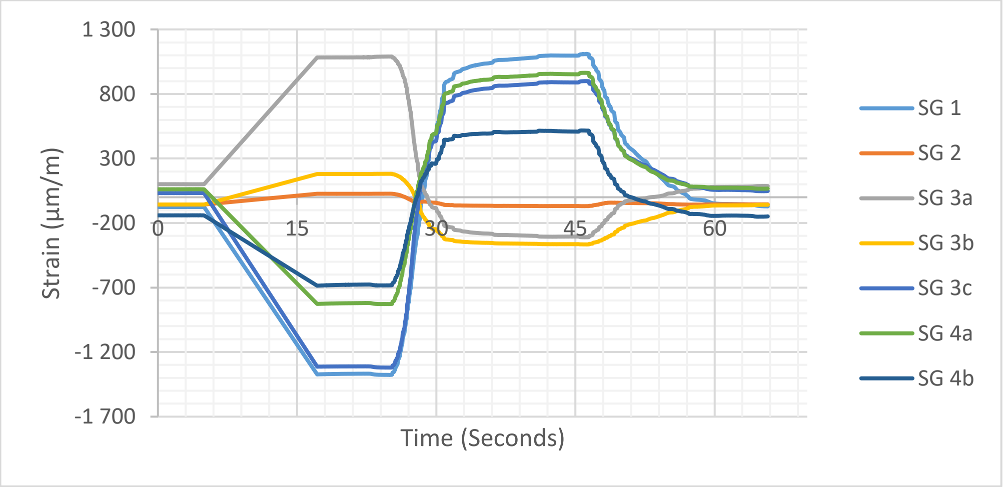

(b)

Figure 6:1: Experimental strain values against time for maximum static, (a) for X-load case and (b) Z-load case

© Central University of Technology, Free State

6.2.2. Fatigue test results

In the completely reversed (stress ratio R = -1) force-controlled fatigue tests, two experimental load cases were considered. The strain values recorded during X- and Z-load cases are shown in Figure 6.2(a) and (b), respectively, as well as in Appendix L. These results were obtained following the method that was presented in section 3.11.3.

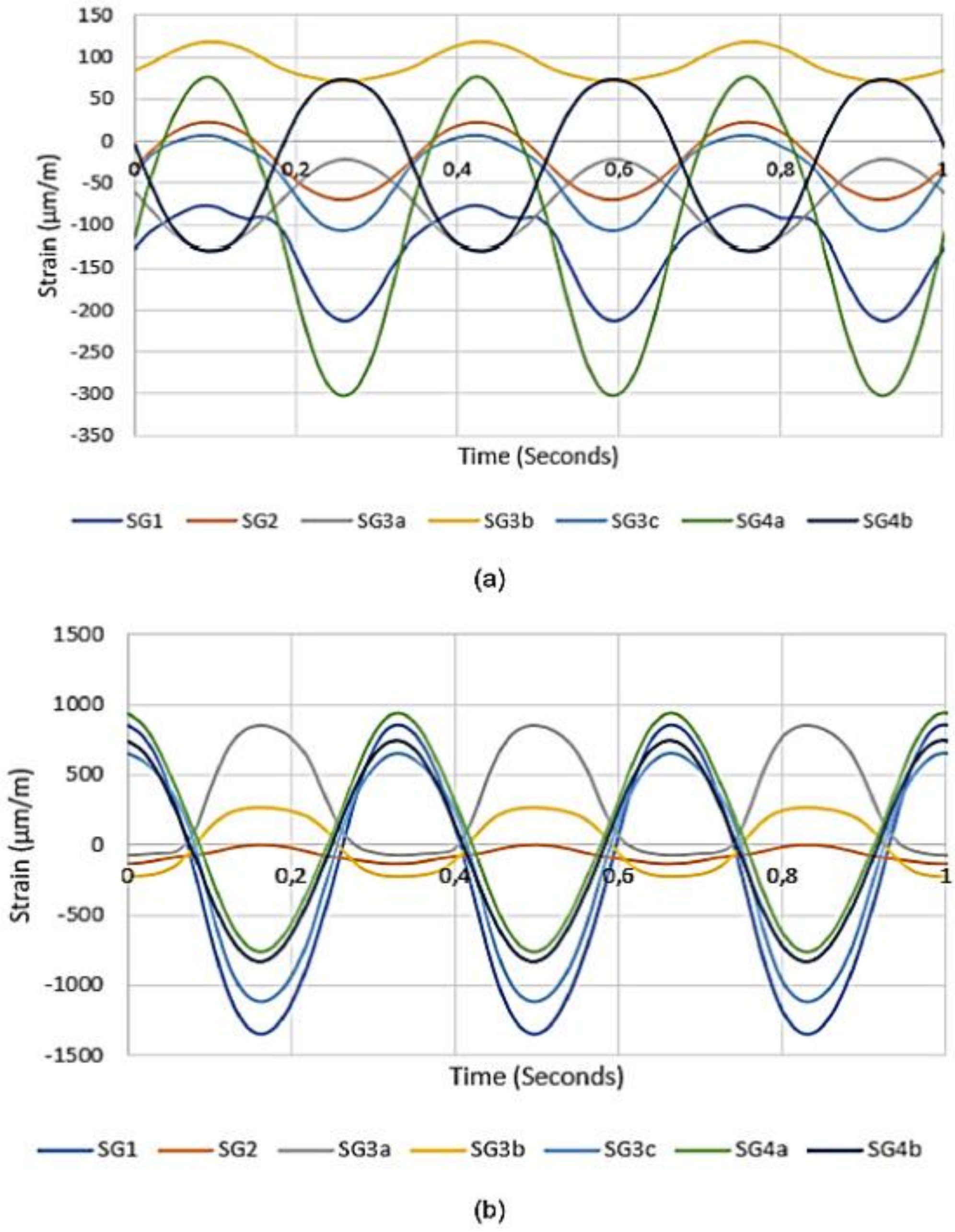

Figure 6:2: Strain values recorded during fatigue testing of (a) X- and (b) Z-experimental-load cases

© Central University of Technology, Free State

It is clear from Figure 6.2 that the Z-load case yielded a higher strain of the L-PBF scaled-down Ti6Al4V(ELI) nose wheel fork than the X-load case. The maximum strain values recorded during the X- and Z-load cases ranged from 120 to -304 μm/m and 1 089 to -1 366 μm/m, respectively. Consequently, the nose wheel fork failure occurred during fatigue testing with the Z-load case.

In Table 6.1, the number of cycles achieved by the fork without failure during fatigue testing with the X-load case and the number of cycles to failure under the Z-load case are given. During the X-load case of the force-controlled experimental fatigue testing no failure was observed, and the test was stopped after 101 609 cycles. No cracks were observed on the surface of the scaled-down nose wheel fork when it was investigated using 996 PB red dye penetrant. Although it was expected to obtain high cycles, when the Z-load case fatigue testing was performed, cracks were identified in the region of Crack 1 on the surface of the nose wheel fork after 15 000 cycles. This was attributed to the high surface roughness of the L-PBF Ti6Al4V(ELI) scaled-down nose wheel fork. This is discussed in detail in section 6.2.4 of the current chapter.

Table 6.1. Number of cycles achieved by the Ti6Al4V(ELI) nose wheel fork during force-controlled experimental fatigue testing with the X- and Z-load cases

Fatigue load case	**Applied load (N)**	**Frequency (Hz)**	**Number of cycles**
X	6 000	3	101 609→
Z	8 300	3	15 000

6.2.3. Microstructure of the experimental prototype

The fork was cut into two sections to create specimens for microstructure (Specimen 1) and fractographic analysis (Specimen 2) as shown in Figure 6.3(a). Specimen 1 was further sectioned into three portions, as shown in Figure 6.3(b), to allow the evaluation of microstructures on various planes of the nose wheel fork. In section 3.11 of Chapter 3, the metallographic preparations of these specimens were described.

© Central University of Technology, Free State

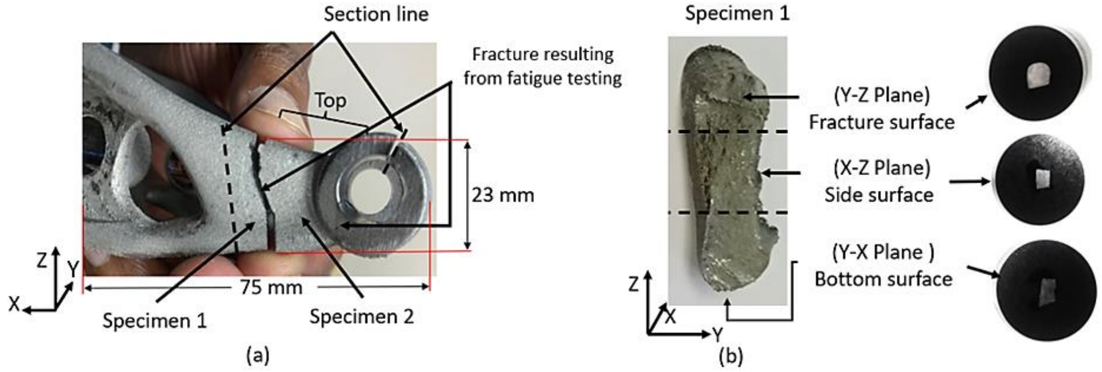

Figure 6:3: Images showing (a) the specimen sectioning from the nose wheel fork, (b) Specimen 1 sections for microstructure evaluation on various planes

These microstructures consisted of acicular *α* and a small amount of *β* with evidence of some *α* globalization, as indicated by the arrows in Figure 6.4.

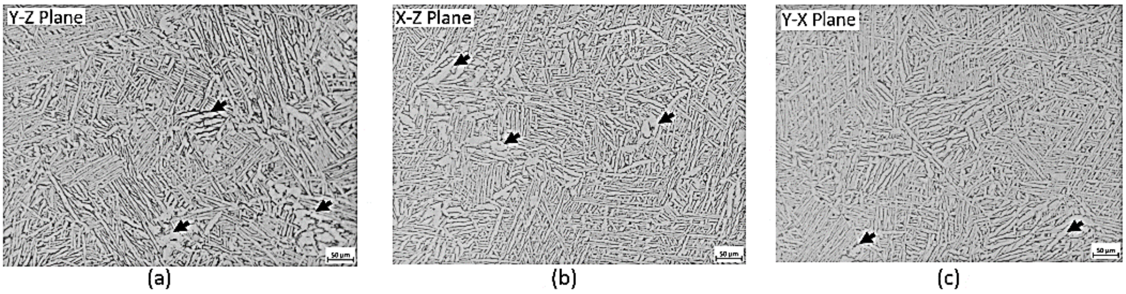

Figure 6:4: Optical micrographs of the near crack microstructure of the Ti6Al4V(ELI) nose wheel fork in (a) Y-Z plane (fracture surface plane), (b) X-Z plane (side surface), (c) Y-X plane (bottom surface)

Isotropic microstructures were observed near the fracture surface of the Ti6Al4V(ELI) nose wheel fork in the different cross-sectional planes of Specimen 1. These confirmed that the mechanical properties should also be isotropic. The tensile strength and elongation percentage measured from the specimens that were built and heat treated together with the nose wheel fork, with the microstructure shown in Figure 6.4, are 935 MPa and 20.8%, respectively. Becker *et al*. [47] observed similar microstructures in L-PBF Ti6Al4V(ELI) specimens submitted to the same heat treatment as the nose wheel fork. In their study, they reported tensile strength and elongation of 914 MPa and 10.3%, respectively. However, the specimens presented in Chapter 5 have the same microstructure

© Central University of Technology, Free State

but built without removing the inherent L-PBF surface roughness and had UTS and elongation of 890 MPa and 15%, respectively. These results confirm that the surface roughness had no significant impact on the tensile properties of the L-PBF Ti6Al4V(ELI) specimens. Finally, the reported tensile properties of the L-PBF Ti6Al4V(ELI) specimens that were submitted to two-stage heat treatment conformed to the ASTM F 3001-14 standard, since the UTS and elongation were higher than 860 and 10%, respectively, as required [147].

6.2.4. Fractographic features of the fatigue failure.

In Figure 6.5(a), fatigue cracks that were found on the L-PBF Ti6Al4V(ELI) nose wheel fork after testing under the Z-experimental-load case are shown. These fatigue crack surfaces were investigated following a method stated in section 3.12. The failure analysis focused on Crack 1 in Figure 6.5(a), since it occurred on the portion of the nose wheel fork that was optimised for light weight without compromising the required strength. The surface roughness in the area around the cracks is shown in Figure 6.5(b). The roughness on the side surface of the nose wheel fork, depicted in Figure 6.5(a), had a R_a value of 5.5 μm and was due to the attachment of unmelted powder particles on the surface of the fork. This was caused by the limited fusion of the powder particles located at the boundaries of the layers fused during the L-PBF process. However, the side surface of the nose wheel fork was less rough than the bottom surface, see Figure 6.5(b). The higher roughness on the bottom surface of the fork resulted from the manual removal of the support structure, but its R_a value could not be measured with the Surftest SJ-210 due to the sensing limitations of this tester. On the top contour of the nose wheel fork, a surface roughness value of R_a = 7.6 μm was measured. This is attributed to the staircase effect and resulted in micro-grooves shown in Figure 6.5(b). This effect was also reported in a study on the melt pool characterisation for L-PBF of Ti6Al4V powder [195].

© Central University of Technology, Free State

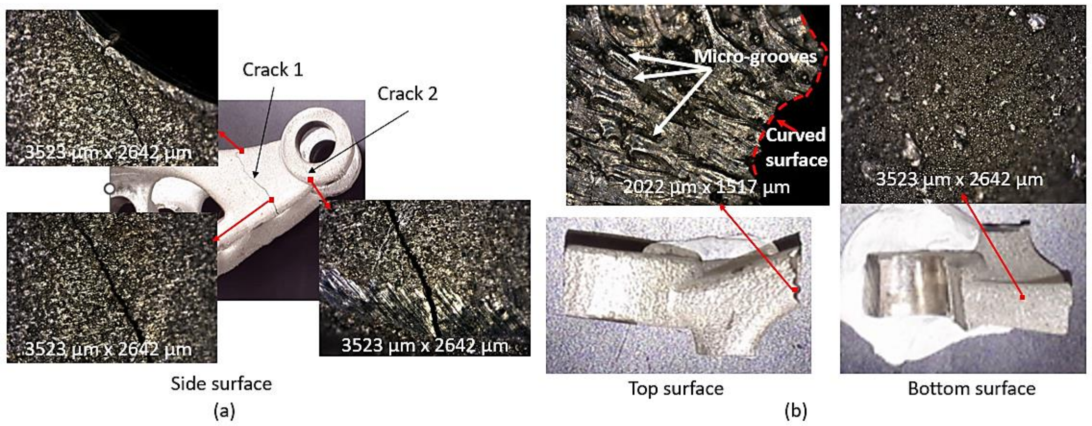

Figure 6:5: (a) Fatigue cracks and surface roughness on the side view of the fork, (b) near crack micro-grooves on the top surface and surface roughness on the bottom surface of the L-PBF Ti6Al4V(ELI) nose wheel fork

In Figure 6.6(a), the sectioning of the L-PBF Ti6Al4V(ELI) nose wheel fork for evaluation of Crack 1 from Specimen 2 is illustrated, whereas Figure 6.6(b) shows the total fracture surface of Specimen 2. The SEM image in Figure 6.6(c) shows the crack initiation at low magnification. The SEM image in Figure 6.6(d) depicts partially melted powder particles on the external surface of the nose wheel fork where the crack had initiated. The partially melted powder particles shown in Figure 6.6(d) resulted in high surface roughness, which caused a stress concentration area that was conducive to the initiation of the fatigue crack. This conforms to the low cycle fatigue performance presented in Table 6.1 under the Z-load case. The river marks depicted in Figure 6.6(d) show the direction of fatigue crack propagation.

© Central University of Technology, Free State

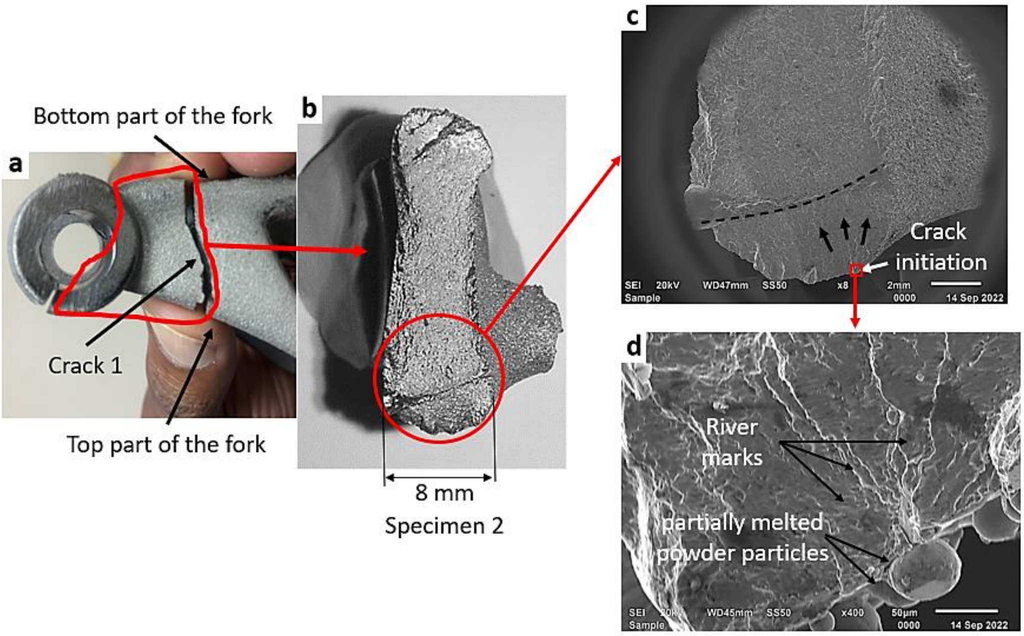

Figure 6:6: An illustration of the crack initiation zone, (a) sectioning of Specimen 2, (b) an overview of the fracture surface, (c) and (d) SEM images of the crack initiation zone

The crack propagated from the top part of the nose wheel fork where the crack initiated and propagated towards the bottom part of the fork. In Figure 6.7(a) and (b), the crack propagation direction is indicated by the arrows. Detailed features of the stable crack propagation zone are shown in Figure 6.7(c). In this zone, micro-cracks were observed and are indicated by arrows in Figure 6.7(c). At the side-end of the fracture surface, a shear lip was formed, as indicated in Figure 6.7(b) and (d). This is attributed to material rupture due to shear stress in a plane at about 45^o with respect to the direction of the applied stress. The final fracture occurred after 15 000 cycles during fatigue testing of the Z-experimental-load case. This occurred when the crack reached the point where the remaining material was overloaded. As a result, a flat-faced final fracture surface was depicted, as shown in Figure 6.7(e).

© Central University of Technology, Free State

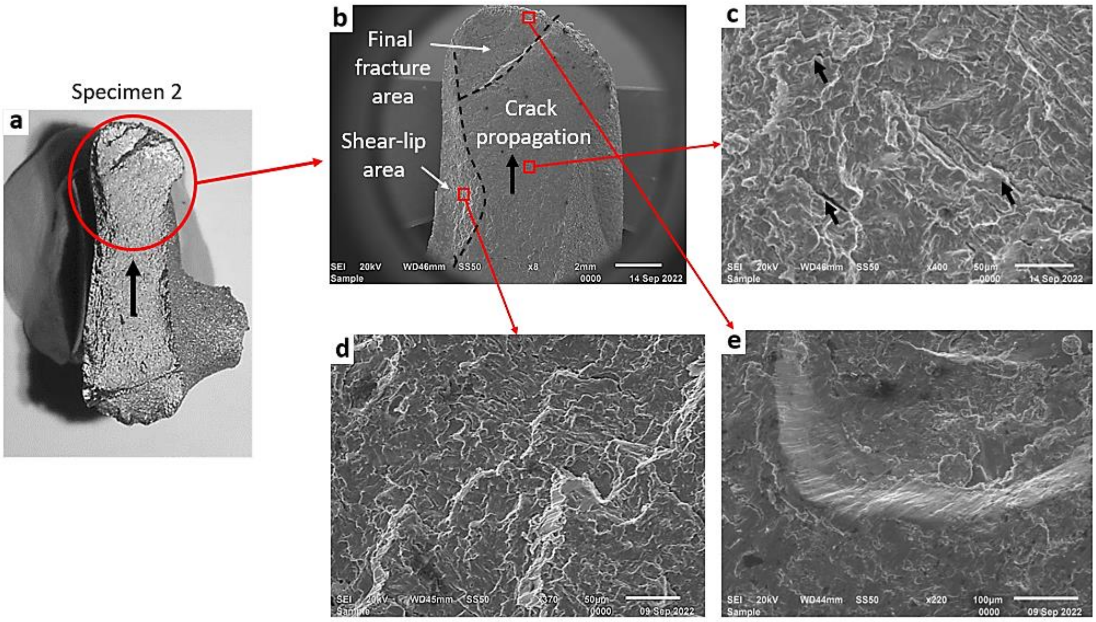

Figure 6:7: (a) Total fracture surface of Specimen 2, SEM images of (b) the fracture area encircled in (a), (c) micro-cracks indicated by arrows in the crack propagation area, (d) the shear-lip area and (e) the flat-faced final fracture area

6.3. Results of finite element analysis

FEA images in Figure 6.8 show the von Mises stress distribution on the surface of the L-PBF Ti6Al4V(ELI) nose wheel fork. These results were obtained following a method that was presented in section 3.11.5. The stresses resulted from the FEA simulation under a static Z-load case that was set at 24% higher than the design load acceptable by FAR.

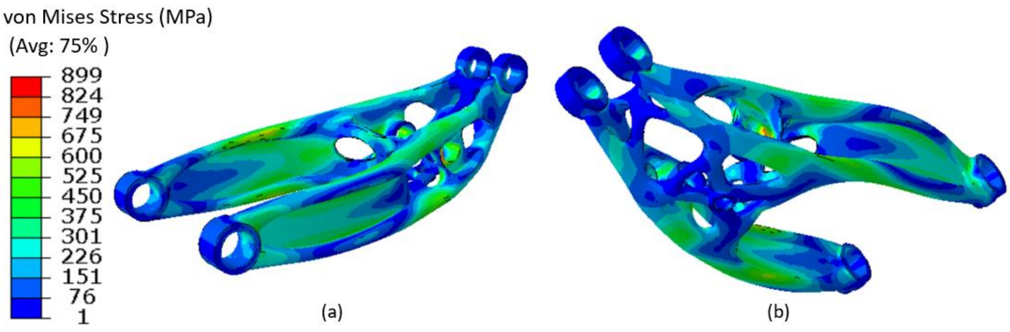

Figure 6:8: FEA map of the stress distribution on the surface of the L-PBF Ti6Al4V(ELI) nose wheel fork that was obtained under static Z-load case, (a) shows mainly the top side, while (b) illustrates mainly the bottom side

The maximum principal stress distribution for positive (vertically upwards) and negative (vertically downwards) Z-loads are also plotted in Figure 6.9. During positive Z-load, the top contour of the nose wheel fork experienced compressive stress whereas the bottom contour had tensile stress, see Figure 6.9(a) and (b). Inversely, the tensile and compressive stresses were experienced by the top and bottom contour of the nose wheel fork, respectively when the negative Z-load was applied, see Figure 6.9(c) and (d).

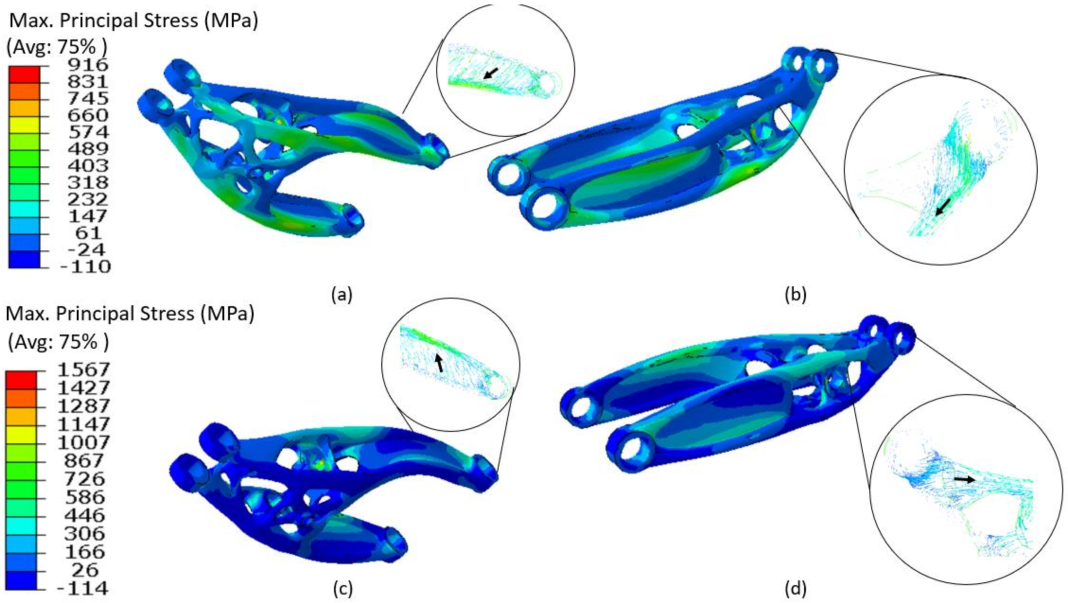

Figure 6:9: FEA map of the maximum principal stress distribution on the surface of the L-PBF Ti6Al4V(ELI) nose wheel fork, (a) and (b) represent vertically upwards Z-load, whereas (c) and (d) represent vertically downwards Z-load. The error shows principal stress distribution from low to high concentration

The maximum von Mises and principal stress were experienced by shock strut bushes of the L-PBF Ti6Al4V(ELI) nose wheel fork. In these images, the area of relatively high stress does not correspond with the area where cracks were observed on the nose wheel fork during experimental testing. The stress level on the primary crack initiation point shown in Figure 6.6(d) is only 226 MPa, indicating that stress overloading was not the main cause of fatigue crack initiation in this region. In Chapter 5, the HCF performance of standard L-PBF Ti6Al4V(ELI) specimens produced with inherent L-PBF surface roughness, had fatigue endurance limits ranging from 190 MPa to 225 MPa. This lower range was

© Central University of Technology, Free State

attributed to the impact of the surface roughness on the fatigue performance of the specimens.

6.4. Experimental validation of the FEA

The experimentally measured strain values were compared with the simulated strain values for five static Z-load divisions following the method prescribed in section 3.11.4. The static load levels were calculated by dividing the Z maximum landing load into five equal divisions. In Table 6.2, the experimentally measured and the FEA strain values are compared.

Table 6.2: Strain values as determined experimentally and through FEA (total strain values) for five static load divisions of the Z-load cases, where a positive and negative sign of Z-load represent vertically upward and downward loads, respectively

	Load	**Strain**	**Single grid**		**Rosette SG3**			**Rosette SG4**		
	(N)	**(μm/m)**	**SG1**	**SG2**	**SG3a**	**SG3b**	**SG3c**	**SG4a**	**SG4b**	**SG4c**
1	-8 300	Experimental	-1 196	77	901	216	-1 230	-822	-506	Invalid
		FEA	-1 310	91	740	168	-904	-1 060	-186	
		Deviation %	9%	15%	-22%	-29%	-36%	22%	-172%	
	+8 300	Experimental	1 079	-10	-357	-290	771	824	634	
		FEA	1 300	-56	-669	-108	843	1 060	188	
		Deviation %	-17%	-82%	-47%	168%	-9%	-22%	237%	
2	-6 640	Experimental	-1 001	63	754	189	-1 051	-710	-470	
		FEA	-1 050	73	589	134	-716	-848	-150	
		Deviation %	5%	-14%	28%	41%	47%	-16%	213%	
	+6 640	Experimental	866	-1	-295	-250	636	673	525	
		FEA	1 050	-45	-537	-86	677	852	151	
		Deviation %	18%	97%	45%	-189%	6%	21%	-248%	
3	-4 980	Experimental	-731	44	519	144	-716	-509	-335	
		FEA	-787	55	440	100	-535	-636	-422	
		Deviation %	7%	19%	-18%	-44%	-34%	20%	21%	
	+ 4980	Experimental	674	5	-229	-206	454	477	374	
		FEA	783	34	-403	-65	508	639	113	
		Error %	14%	86%	43%	-218%	11%	25%	-231%	
4	-3 320	Experimental	-481	27	335	104	-462	-342	-221	
		FEA	-524	37	293	66	-357	-424	-424	
		Deviation %	-8%	-28%	14%	57%	29%	-19%	-48%	
	+3 320	Experimental	399	11	-167	-150	323	312	303	
		FEA	522	23	-269	-43	339	426	76	
		Deviation %	24%	53%	38%	-247%	5%	27%	-302%	
5	-1 660	Experimental	-247	9	167	58	-212	-165	-118	

Load (N)	Strain (µm/m)	Single grid		Rosette SG3			Rosette SG4		
		SG1	SG2	SG3a	SG3b	SG3c	SG4a	SG4b	SG4c
	FEA	-262	18	147	33	-178	-212	75	
	Deviation %	-6%	-48%	13%	75%	19%	-22%	-257%	
+1 660	Experimental	156	11	-97	-84	177	147	190	
	FEA	261	11	-134	-22	169	213	38	
	Deviation %	40%	5%	28%	-290%	-5%	31%	-402%	

* For FEA strain: An average of the nodal total strain component values on the surface of the nose wheel fork along each strain gauge sensing grid were recorded for comparison with experimentally measured strain values. No plastic strain was measured and computed by the strain gauges and FEA, respectively.

The experimentally measured strain values for SG1, SG3c and SG4a vary between 5% and 28% from the values computed by FEA for almost all the load cases. The inconsistency in strain measurement of SG2 when a load was applied in the Z-direction is attributed to its orientation. When a load was applied in the Z-direction the sensing grid of SG2 experienced a moment of force in the Z-direction along its short axis, which impacted negatively on its sensitivity. For SG3b and SG4b, which were respectively positioned at 45^o from SG3a and SG4a on the rosette strain gauge, higher strain deviation between the experimental and FEA values was consistently found. A similar relatively high strain deviation between FEA and experimental data measured from Ti6Al4V(ELI) components was reported by Seabra *et al*. [26]. In Figure 6.10, the correlation between experimental and FEA data for SG1 and SG3c is illustrated graphically.

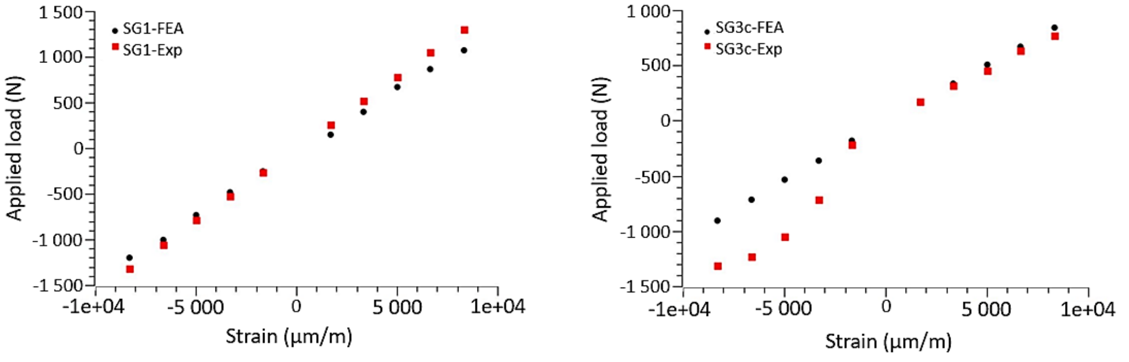

(a) (b)

Figure 6:10: Graphical correlation between experimental and FEM strain data for (a) SG1 and (b) SG3c illustrate no plastic strain was experienced by the nose wheel fork at the region of the strain gauges

© Central University of Technology, Free State

From Figure 6.10 it is clear that the deviation between the experimental and FEA data was related to the direction of the load applied. For SG1, the experimental and FEA data were not perfectly the same when a high positive z-load was applied, while more accurate results were obtained for a negative loading. In contrast, the SG3c strain gauge depicted larger deviations for negative applied Z-loads. However, at positive Z-loads good correlation between the experimental and FEA values was recorded. The percentage difference between experiment and FEA was found to be less than 10%. Other strain gauges also depicted good correlation between experiment and FEA, as shown in Table 6.2. Therefore, the bulk of the data used during validation depicted equivalence between experiment and FEA.

6.5. Simulated fatigue performance results

Based on the experimentally validated FEA, the fatigue performance for the two load cases was simulated following a method presented in section 3.11.5. The simulation predicted that the nose wheel fork would not fail under the X-load case. However, the simulated Z-load case resulted in 4 570 ($10^{3.66}$) cycles to failure. In Figure 6.11, the log life simulated for the Z-load case is shown.

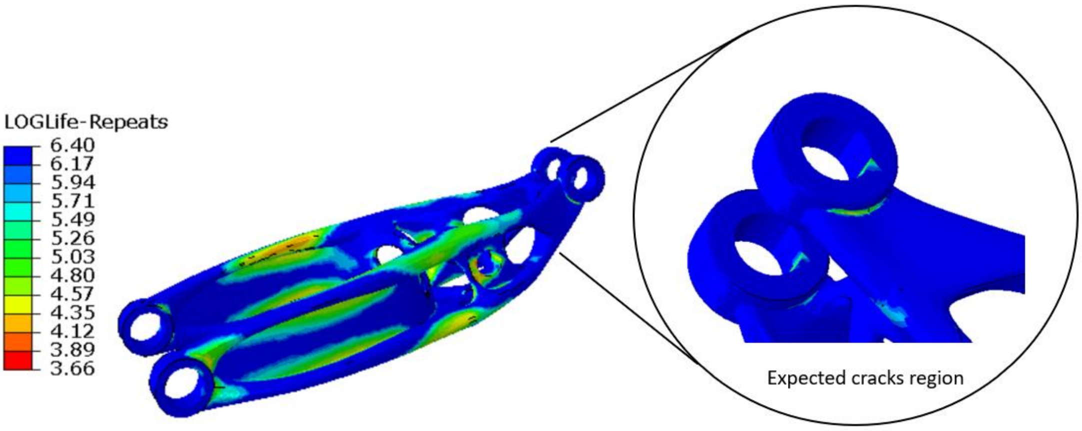

Figure 6:11: The FEA log life distribution on the L-PBF Ti6Al4V(ELI) nose wheel fork for the Z-load case

© Central University of Technology, Free State

It should be noted that the blue area on the plot represents $10^{6.40}$ cycles to failure and the red represents $10^{3.66}$ cycles to failure. The fatigue simulation depicts no cracks in the region of the L-PBF TI6Al4V(ELI) nose wheel fork where Crack 1 was identified during experimentation, see Figure 6.11. These results suggest that the fatigue life of the L-PBF Ti6Al4V(ELI) nose wheel fork with inherent surface roughness cannot be accurately predicted with the available FEA model. The quality of the L-PBF Ti6Al4V(ELI) nose wheel fork that was submitted to two-stage heat treatment was accepted because the microstructure and the mechanical properties conformed to the ASTM F 3001-14 standard. However, the fork had a low fatigue life for the Z-load case. This was due to its inherent surface roughness as was also confirmed through the fractographic analysis. The partially melted powder particles on the surface of the L-PBF Ti6Al4V(ELI) nose wheel fork and micro-grooves resulted in localised stress concentration and consequently low fatigue life. During HCF performance in Chapter 5, it was demonstrated that the inherent L-PBF surface roughness of Ti6Al4V(ELI) specimens reduces the fatigue life by 50%. As in the experimental fatigue testing, the prediction of fatigue life from the validated FEA model also confirmed that the L-PBF Ti6Al4V(ELI) nose wheel fork had high and low fatigue life under X- and Z-load cases, respectively.

6.6. Summary

In this chapter, it was demonstrated that the L-PBF Ti6Al4V(ELI) nose wheel fork can sustain the extreme static X- and Z-loads without any failure. Moreover, it did not fail due to X-fatigue loading. No cracks were observed after 101 609 cycles. Nonetheless, failure was observed after 15 000 cycles during Z-fatigue loading. This failure was caused by the stress concentration resulting from a partially melted powder particle on the surface of the nose wheel fork. A good correlation between FEA and experimental data was also presented and the deviation was below 10%. The predicted fatigue life for X-loading confirms no failure whereas for the Z-loading a failure is predicted to occur at $10^{3.66}$ cycles. This corresponds with the experimentally obtained fatigue performance. However, the area where

© Central University of Technology, Free State

failure was predicted does not correlate with the experimental result. This was attributed to random L-PBF defects on the Ti6Al4V(ELI) nose wheel fork. The facility of producing the nose wheel fork in Ti6Al4V(ELI) through L-PBF was confirmed.

© Central University of Technology, Free State

CHAPTER 7: HOLISTIC DISCUSSION

7.1. Introduction

In this chapter, a holistic discussion of the results obtained in this study is presented. It begins with a discussion of the topologically optimised design of the AHRLAC for production in Ti6Al4V(ELI) through L-PBF which was presented in Chapter 4. This is followed by the discussions of the various mechanical and fatigue results presented in Chapter 5. The results of the performance testing that were presented in Chapter 6 are discussed. Microstructure and failure mechanisms obtained through various fractographic analyses are also discussed. The failure mechanism of the Ti6Al4V(ELI) nose wheel fork which was investigated to characterise features of the fatigue fracture surface is reviewed. The FEA model that was validated using strain gauges and the fatigue simulation that was generated and compared with the experimental results are discussed.

7.2. L-PBF Ti6Al4V(ELI) optimal nose wheel fork

The redesign followed in the current study arrived at an optimal nose wheel fork of the AHRLAC which is 20% lighter in weight than the actual fork. This redesign process integrated the TO technology through the Altair SolidThinking Inspire® and MSC Patran-Nastran® software. The Inspire® was found to be a more appropriate suit for TO than the other software used, since it consists of various tools that allow a generation of completely new designs without the use of additional software. The most important tool is the PolyNurb function. A very complex and novel-shaped nose wheel fork was obtained, which cannot be produced through conventional methods, but is quite feasible through AM processes.

The success of building a component from Ti6Al4V(ELI) through a commercially available L-PBF system is based on the appropriate built orientation and support structures. This was confirmed by the scaled-down nose wheel fork produced in Ti6Al4V(ELI) through L-PBF. The best build orientation and the corresponding distortion of this fork were determined using Simufact Additive® software. Next, the predicted residual stress that caused the distortion informed the design of the

© Central University of Technology, Free State

supporting pins and normal support structures. The combination of normal and pins support structures minimises the distortion during the production of L-PBF Ti6Al4V(ELI) components.

7.3. Structural integrity of L-PBF Ti6Al4V(ELI) nose wheel fork

The study on the geometric deviation of the Ti6Al4V(ELI) nose wheel fork after L-PBF, followed by removal of support structure plus stress-releasing heat treatment (Scan A), and after additional HTA (Scan B) demonstrated the following:

A dimensionally accurate nose wheel fork of a light aircraft can be built through L-PBF in Ti6Al4V(ELI).

The maximum deviation was ~1.3 mm with the largest portion of the nose wheel fork being built within 0.2 mm. To gain dimensional accuracy on bushes of the nose wheel fork, machining was necessary. However, these features are also usually finished to the required tolerance in conventionally machined parts. Additional material must be provided on the fork bushes to allow machining after L-PBF and its post-processes. Finding the optimal build orientation is key to successfully building the fork with minimal geometric deviation and optimal surface roughness. The deviation recorded on a plane perpendicular to the build direction was found to be less than that found on a plane parallel to the build direction.

The L-PBF Ti6Al4V(ELI) nose wheel fork has a high surface roughness that varies with respect to the built orientation. The top surface (XY-plane) had a R_a value of 7.395 μm and the other sides were projected to have higher surface roughness than the top face. Specimens built with the fork had a varying surface roughness (R_a value) in planes XY, ZX and ZY of 4.86 μm,12.69 μm and 13.20 μm, respectively. The side of the nose wheel fork and specimens, where the support structure was attached, have the highest surface roughness. Nonetheless, the as-built surface roughness of Ti6Al4V(ELI) parts produced through L-PBF has an insignificant impact on geometric deviation, irrespective of mismatches in the surface roughness between the CAD model and the as-built part.

© Central University of Technology, Free State

The L-PBF Ti6Al4V(ELI) nose wheel fork and specimens had a built density of 99.997% since the measured maximum porosity was 0.0033%. It can be concluded that the machine parameters provided by the EOSINT M290 produce an acceptable L-PBF part from Ti6Al4V(ELI).

7.4. Mechanical properties of L-PBF Ti6Al4V(ELI) specimens

The tensile, impact toughness and fracture toughness of Ti6Al4V(ELI) specimens produced through L-PBF followed by two-stage heat treatment (stress-relieved at 650 °C for 3 hours and HTA at 950 °C for 2 hours) resulted in the following mechanical properties:

The tensile properties of the L-PBF Ti6Al4V specimens, such as the yield strength, UTS and elongation of 779 MPa, 892 MPa and 14%, respectively conform with the ASTM F3001-14. These confirmed a good metallographic bond between the L-PBF Ti6Al4V(ELI) layers of powder particles during the fabrication of the specimens. Moreover, the lowest tensile properties measured were still comparable to those of the wrought Ti6Al4V(ELI) alloy and complied with the specifications of the aircraft industry, which confirmed the quality of the L-PBF process [196][197].

Charpy impact testing specimens with wire-cut V-notches have a higher value of impact toughness compared to that of 3D-printed V-notches for all build orientations. Therefore, wire-cut V-notches resist impact energy better than the 3D-printed notches. The impact toughness determined for specimens with 3D-printed V-notches along the XY built orientation significantly differs from that measured for the wire-cut V-notch specimens. The percentage shear fracture area of the specimens with 3D-printed V-notches was larger than that of specimens with wire-cut V-notches. The presence of the 3D-printed V-notch can reduce the impact toughness by 3.5–20% compared to the wire-cut V-notch.

All build orientations of the specimens revealed acceptable impact energy after two-stage heat treatment when compared to the toughness required in the aircraft industry [186]. Two-stage heat treatment improved the impact toughness of the Ti6Al4V(ELI)

© Central University of Technology, Free State

specimens built through L-PBF by approximately 40%. Such improvement is 8% more than the requirement of the aerospace industry [186].

The microstructure obtained after two-stage heat treatment consists of acicular α and a small amount of β. The surface roughness in the root of the 3D-printed V-notches of the Ti6Al4V(ELI) specimens significantly reduced the impact toughness compared to the impact toughness value of the wire-cut V-notches. The Ti6Al4V(ELI) specimens consist of a ductile fracture mechanism, since it consists of tortuous fracture surfaces with dimples in the shear-lip region when subjected to impact load. The final fracture region of the Ti6Al4V(ELI) specimens subjected to impact load has a flat-face fracture surrounded by dimples, pointing towards a mixed fracture mode (ductile and brittle fracture).

Parts that were built using L-PBF have impact toughness acceptable to produce aircraft structural parts which operate at a low temperature of -50 °C. Isotropic conditional fracture toughness was obtained for the L-PBF Ti6Al4V(ELI) alloy by applying the two-stage heat treatment with soaking periods of 3 hours and 2 hours for stress relieving and HTA heat treatments, respectively. This two-stage heat treatment also improved the fracture toughness by 20% compared to the wrought ($\alpha + \beta$) Ti6Al4V(ELI) alloy with equiaxed microstructure.

7.5. Fatigue properties of L-PBF Ti6Al4V(ELI) specimens

An improvement in the FCG resistance of the Ti6Al4V(ELI) specimens produced by L-PBF in the current study was observed compared to previous studies. The critical crack size determined for these Ti6Al4V(ELI) specimens was 16 mm after ~ 55 000 cycles. Ti6Al4V(ELI) specimens produced through L-PBF have the ductility required by the aircraft industry [186]. From the current study, it is evident that L-PBF processes that are well controlled could produce mission-critical aircraft components.

The HCF testing confirmed that the inherent surface roughness had a negative impact on the fatigue strength of the L-PBF Ti6Al4V(ELI) specimens. The L-PBF defect reduced the fatigue strength by 50%. The fatigue strength of 225 MPa was recorded for the L-PBF Ti6Al4V(ELI) specimens built with inherent surface roughness along the

© Central University of Technology, Free State

Z-orientation, whereas 190 MPa was recorded for both X- and Y-specimens. This implied that surface finishing would be needed to improve the fatigue properties for application in the mission critical structural aircraft component.

The required support structure for maintaining the integrity of a component during L-PBF process, impacted the fatigue performance negatively. They acted as the stress concentration region which was conducive to crack initiation. Therefore, the support structure should not be placed on the critical load-bearing area when designing a structural component.

7.6. Performance of the L-PBF Ti6Al4V(ELI) nose wheel fork

Failure analysis of the L-PBF Ti6Al4V(ELI) scaled-down nose wheel fork was carried out in this study. Static and fatigue tests, as well as experimentally validated fatigue simulation of a nose wheel fork with an as-built surface roughness that was stress-relieved and annealed through two-stage heat treatment, resulted in the following conclusions:

The L-PBF Ti6Al4V(ELI) scaled-down nose wheel fork could handle the static loads without any failure.

Tensile strain values of 120 µm/m and 1 089 µm/m were measured by strain gauges SG3b and SG4a for X- and Z-loading, respectively. The potential to produce the full-scale nose wheel fork of the AHRLAC through L-PBF was confirmed. Fatigue failure was not recorded during X-loading of the scaled-down prototype. However, during Z-loading, a primary crack was identified after 15 000 cycles due to surface roughness resulting from the presence of partially melted powder particles on the nucleation surface. This confirmed that an unfinished L-PBF surface is not acceptable for structural components experiencing cyclic loading, since the inherent surface roughness was detrimental to the fatigue life of the nose wheel fork. The maximum principal stresses predicted through FEA in the region of the primary crack of the scaled-down nose wheel fork was 226 MPa. This is comparable with the fatigue strength of the as-built surface roughness L-PBF Ti6Al4V(ELI) specimens built along Z-orientation [144]. Therefore, stress overloading was not the main cause of crack initiation. Single crack initiation points depicted on the fracture surface region confirm that stress overloading was not the main cause of crack initiation. It can be concluded that surface treatment to remove the inherent surface roughness resulting from L-PBF is essential for mission-critical aircraft components. Experimentally validated FEA simulation carried out in the current study resulted in the maximum and minimum deviation of 48% and 5% for most of the SGs between FEA and experimental data. Therefore, an experimentally validated FEA can be used in the design of the L-PBF Ti6Al4V(ELI) nose wheel fork, provided the material data that were determined experimentally and the effects of inherent defects of the L-PBF process (surface roughness) are incorporated in the simulation model.

7.7. Summary

The L-PBF Ti6Al4V(ELI) nose wheel fork is 20% lighter in weight compared to the Al 7050 actual fork of the AHRLAC produced through a traditional milling machine. The production of the L-PBF fork requires the combination of normal and pin support structures to eliminate warpage and minimise distortion. A dimensionally accurate nose wheel fork can be built through L-PBF with a maximum deviation of 0.2 mm to 1.3 mm. The inherent L-PBF surface roughness of Ti6Al4V(ELI) components ranges from 5 µm to 13.5 µm. Moreover, the L-PBF is capable of building 99.997% density parts from Ti6Al4V(ELI) alloy.

Two-stage post-process heat treatments, first stress-relieved at 650 °C for 3 hours and HTA at 950 °C for 2 hours must be performed to obtain microstructure and mechanical properties accepted in the aircraft industry. This heat treatment results in acicular α and a small amount of β microstructure in orthogonal planes. Furthermore, the resulting microstructure achieves isotropic mechanical properties such as tensile, impact toughness and fracture toughness. Tensile strength, UTS and elongation are equal to 779 MPa, 892 MPa and 14%, respectively. The impact toughness of 3D-printed V-notch is less than that of wire-cut notch specimens. The values obtained for the 3D-printed and wire-cut V-notch specimens are 35 J/cm^2 and 38 J/cm^2, respectively. On the other hand, the conditional fracture toughness is equal to 80 MPa·m$^{0.5}$.

The L-PBF Ti6Al4V(ELI) specimens tested under fatigue for crack propagation attain a critical length of 16 mm after ~ 55 000 cycles. This was evident from high fatigue crack growth resistance at the Paris region with a slope of 2.78. Finally, the fatigue strength of Z-specimens is 225 MPa, whereas each X- and Y- L-PBF Ti6Al4V specimens has a strength of 190 MPa.

The L-PBF Ti6Al4V(ELI) nose wheel fork can handle static loads and fatigue X-loading without failure. However, it failed after 15 000 cycles during the Z fatigue load. The crack was initiated by the stress concentration which resulted from partially melted powder particles on the surface of the nose wheel fork. Therefore, surface treatment to remove the inherent surface roughness resulting from L-PBF is essential for mission-critical aircraft components.

Experimentally validated FEA can be applied to simulate the stress and strains of the nose wheel fork with a deviation of less than 10%. Such validated FEA can be applied in predicting fatigue performance, provided the material data that were determined experimentally and the effects of inherent defects of the L-PBF process (surface roughness) are incorporated in the simulation model.

© Central University of Technology, Free State

CHAPTER 8: CONCLUSION AND RECOMMENDATIONS

8.1. Introduction

In this research study, the redesign and characterisation of the nose wheel fork of a light aircraft for production in Ti6Al4V(ELI) through L-PBF was carried out. Firstly, a novel geometrically shaped nose wheel fork was designed using TO technology and its scaled-down version was produced through L-PBF from Ti6Al4V(ELI). This fork was characterised through NDT methods such as geometric accuracy, porosity and surface roughness testing. Thereafter, destructive testing using standard test specimens was performed. These included tensile, impact toughness, fracture toughness, FCGR and HCF testing. To assess the compliance and confirm the feasibility of producing the nose wheel fork of the AHRLAC, performance testing of the scaled-down L-PBF Ti6Al4V(ELI) fork was carried out. Finally, the microstructure and fracture surface of the L-PBF Ti6Al4V(ELI) component were also evaluated. The important conclusions, contributions and recommendations that were reached in this thesis are presented in this chapter.

8.2. Conclusions

The current study was a unique first attempt to redesign and characterise a mission-critical structural component of an actual aircraft for production in Ti6Al4V(ELI) through L-PBF technology and assess its compliance with the performance requirements of the component. It can be concluded that a structural component designed following TO for production in Ti6Al4V(ELI) through L-PBF is 20% lighter in weight compared to the one produced through traditional manufacturing methods. Moreover, it was confirmed that a digital design method that includes FEA can be used to design a unique intricately shaped L-PBF Ti6Al4V(ELI) nose wheel fork, provided experimentally determined mechanical properties, fatigue properties and inherent surface roughness were integrated into the model. The linear static FEA model of the nose wheel fork that incorporates the experimentally tested mechanical properties has a percentage deviation which is less than 10%. However, there were discrepancies in predictions of fatigue life which resulted from the inherent surface roughness of the L-PBF Ti6Al4V(ELI) component. A region where a crack occurred during the experimental test of the L-PBF Ti6Al4V(ELI) scaled-down nose wheel fork did not match with the predicted fatigue results irrespective of the incorporation of the experimentally tested mechanical and fatigue properties. This indicates that surface roughness is the main key to predicting fatigue performance accurately.

Based on static and fatigue performance testing, as well as standardised destructive and non-destructive testing, the potential to produce a dimensionally accurate full-scale nose wheel fork of the AHRLAC in Ti6Al4V(ELI) through L-PBF was confirmed. A 0.2 mm geometrically accurate nose wheel fork with a very low porosity level of 0.0033% can be built from Ti6Al4V(ELI) through L-PBF. These benefits are compromised by the inherent surface roughness that varies across the L-PBF Ti6Al4V(ELI) component. Although the tensile properties, impact and fracture toughness of the L-PBF Ti6Al4V(ELI) nose wheel fork complied with the requirement of the aviation industry, the inherent surface roughness is detrimental to the fatigue life. This high surface roughness diminished the fatigue strength by 50%. It was concluded that the improved fatigue performance of a full-scale L-PBF Ti6Al4V(ELI) nose wheel fork can be obtained through surface finishing.

8.3. Contributions

A methodology to redesign a novel topologically optimised nose wheel fork was contributed to the aviation industry by the current study. The conventional method of designing and fabricating the nose wheel fork of a light aircraft can now be replaced by design for L-PBF that includes TO and experimentally validated FEA. The study also contributed towards the qualification of L-PBF for production of mission-critical aircraft components through various standard testing methods which yield tensile properties, impact toughness, fracture toughness, fatigue crack growth resistance and fatigue strength.

© Central University of Technology, Free State

The reliability of L-PBF for production of aircraft components from Ti6Al4V(ELI) was assessed through performance testing of the nose wheel fork. Consequently, the failure mechanisms of the L-PBF Ti6Al4V(ELI) component are now understood. This provides confidence for application of L-PBF to produce mission-critical components of the aircraft. Moreover, L-PBF Ti6Al4V(ELI) data are available for comparison with failure mechanisms of components manufactured using traditional processes. Through this output, the research makes a valuable contribution towards qualification of metal AM for the production of mission-critical undercarriage structural components of a light aircraft.

8.4. Recommendations

Researchers and designers in the aviation industry can use the contents of this study as a framework towards TO DfAM and for qualifying mission-critical structural components of an aircraft for production through L-PBF from Ti6Al4V(ELI). When applying a digital design process presented in the current study for a different component, validation must be carried out since data provided are product specific.

Mechanical and fatigue properties presented in the current study can be used as reference data if the L-PBF machine parameters and post-process are the same. Determining the K_{IC} and FCGR of Ti6Al4V(ELI) specimens produced by L-PBF, followed by two-stage post-process heat treatment, through testing at low temperatures should be the focus of further research. Future research should also include investigation of hot isostatic pressing techniques of large structural components of aircraft.

As the prediction of fatigue life was based on the smooth CAD model of the L-PBF Ti6Al4V(ELI) scaled-down nose wheel fork, future studies must focus on physically scanned CAD models with representative inherent surface roughness. Moreover, the performance test of the full-scale L-PBF Ti6Al4V(ELI) nose wheel fork with inherent surface roughness must be carried out with a damping system and force applied simultaneously in three orthogonal directions through the wheel

© Central University of Technology, Free State

axle. Finally, the surface treatment technique of large L-PBF Ti6Al4V(ELI) components must be investigated to reduce the surface roughness, which will result in better fatigue performance.

© Central University of Technology, Free State

REFERENCES

[1] M. Intelligence, "Military aircraft recognition- growth, trends, covid-19 impact, and forecast," *Mordor intelligence*, 2021. https://www.mordorintelligence.com/industry-reports/military-aircraft-market# (accessed May 31, 2022).

[2] M. Oyesola, N. Mathe, K. Mpofu, and S. Fatoba, "Science direct sustainability of additive manufacturing for the South African aerospace industry : A business model for laser technology production, commercialization and market prospects," *Procedia CIRP*, vol. 00, pp. 1530–1535, 2018, doi: 10.1016/j.procir.2018.03.072.

[3] D. de Beer, W. B. du Preez, H. Greyling, F. Prinsloo, F. Sciammarella, N. Trollip, M. Vermeulen, T. Wohlers, "A South African additive manufacturing strategy," *Dep. Sci. Technol.*, pp. 1–92, 2016.

[4] P. Middleton, "Aeroswift : a large-scale powder bed fusion AM system," *Crown Publications*, pp. 20–21, 2018. [Online]. Available: https://www.crown.co.za/images/LatestNews/AfricanFusion/AF_June_2018_Aeroswift_PBF_AM_Laser_titanium_machine.pdf

[5] J. Katzenellenbogen, "Paramount's AHRLAC ramps up production - defenceWeb," *DefenceWeb*, 2017. https://www.defenceweb.co.za/aerospace/aerospace-aerospace/paramounts-ahrlac-ramps-up-production/ (accessed May 01, 2019).

[6] EDM On-line, "Paramount Aerospace: future of AHRLAC secured as business rescue nears completion," *European defence review*, 2020. [Online]. Available: https://www.edrmagazine.eu/paramount-aerospace-future-of-ahrlac-secured-as-business-rescue- nears-completion

[7] P. A. Kobryn, N. R. Ontko, L. P. Perkins, and J. S. Tiley, "Additive manufacturing of Aerospace alloys for Aircraft structures," *Cost Eff. Manuf. via Net-Shape Process. (pp. 3-1 – 3-14). Meet. Proc. RTO-MP-AVT-139,* vol. 139, no. 2006, pp. 1–14, 2006, [Online]. Available:

© Central University of Technology, Free State

http://oai.dtic.mil/oai/oai?verb=getRecord&metadataPrefix=html&identifier=ADA521726

[8] J. Allen, “An investigation into the comparative costs of additive manufacture vs machine from solid for aero engine parts,” in *Meeting Proceedings RTO-MP-AVT-139*, 2006, p. 17. [Online]. Available: http://www.rto.nato.int/abstracts.asp

[9] D. Olivier, “Paramount group’s AHRLAC makes first public flight.pdf,” *Defence Industry News, Featured*, 2014. https://www.africandefence.net/paramount-groups-ahrlac-makes-first-public-flight/ (accessed Jun. 30, 2023).

[10] V. Infante, L. Fernandes, M. Freitas, and R. Baptista, “Failure analysis of a nose landing gear fork,” *Eng. Fail. Anal.*, vol. 82, no. October 2016, pp. 554–565, 2017, doi: 10.1016/j.engfailanal.2017.04.020.

[11] M. Roth, M. Yanishevsky, and P. Beaudet, “Failure analysis of aircraft landing gear components,” in *Failure Analysis Techniques and Applications (Proceedings of the First International Conference on Failure Analysis)*, 2019, pp. 1–6. doi: https://doi.org/10.31399/asm.fach.aero.c9001504.

[12] L. A. L. Franco, N. J. Lourenço, M. L. A. Graça, O. M. M. Silva, P. P. de Campos, and C. F. A. von Dollinger, “Fatigue fracture of a nose landing gear in a military transport aircraft,” *Eng. Fail. Anal.*, vol. 13, no. 3 SPEC. ISS., pp. 474–479, 2006, doi: 10.1016/j.engfailanal.2004.12.025.

[13] H. K. Rafi, N. V. Karthik, H. Gong, T. L. Starr, B. E. Stucker, and A. A. Antonysamy, “Microstructure, texture and mechanical property evolution during additive manufacturing of Ti6Al4V alloy for aerospace applications,” 2012. doi: 10.1007/s11665-013-0658-0.

[14] S. Liu and Y. C. Shin, “Additive manufacturing of Ti6Al4V alloy : A review,” *Mater. Des.*, vol. 164, p. 107552, 2019, doi: 10.1016/j.matdes.2018.107552.

[15] M. Intelligence, “Titanium alloy market size & share analysis - growth trends & forecasts (2023 - 2028),” *Mordor intelligence*, 2022. https://www.mordorintelligence.com/industry-reports/titanium-alloy-market?gclid=EAIaIQobChMIgceRuufl_wIVs-HmCh3Cug-uEAAYASAAEgLcr_D_BwE (accessed Jun. 28, 2023).

© Central University of Technology, Free State

[16] I. Inagaki, T. Takechi, Y. Shirai, and N. Ariyasu, “Application and features of titanium for the aerospace industry,” *Nippon Steel Sumitomo Met. Tech. Rep.*, vol. 106, no. 105, pp. 22–27, 2014, [Online]. Available: https://www.nipponsteel.com/en/tech/report/nssmc/pdf/106-05.pdf

[17] A. Material, “Titanium alloys - Ti6Al4V grade 5,” *U.S. Titanium Industry Inc*, 2002. (accessed Jun. 29, 2023).

[18] P. T. Summers, Y. Chen, C. M. Rippe, B. Allen, A. P. Mouritz, S. W. Case, and B. Y. Lattimer, “Overview of aluminum alloy mechanical properties during and after fires,” *Fire Sci. Rev.*, vol. 4, no. 1, 2015, doi: 10.1186/s40038-015-0007-5.

[19] G. Lutjiering and J. C. Williams, *Titanium*. 2016. doi: 10.2134/agronmonogr9.2.c15.

[20] D. M. Engelbrecht, “Titanium beneficiation in South Africa: A product space and location-centric analysis,” 2021. [Online]. Available: https://scholar.sun.ac.za

[21] Department of Mineral Resources RSA, “A beneficiation strategy for the minerals industry of South Africa,” 2011.

[22] K. Salonitis and S. Al Zarban, “Redesign optimization for manufacturing using additive layer techniques,” *Procedia CIRP*, vol. 36, pp. 193–198, 2015, doi: 10.1016/j.procir.2015.01.058.

[23] F. P. Kader Mohideen and S. Verma, “Topology optimization of landing gear for additive manufacturing 2020-28-0389,” *SAE Int.*, no. 2020, p. 8, 2020, doi: 10.4271/2020-28-0389.

[24] M. G. Fanni, M., Shabara, M. N., Alkalla, “A comparison between different topology optimization methods,” *Eng. J.*, no. March 2019, 2013.

[25] M. Leary, L. Merli, F. Torti, M. Mazur, and M. Brandt, “Optimal topology for additive manufacture: A method for enabling additive manufacture of support-free optimal structures,” *Mater. Des.*, vol. 63, pp. 678–690, Nov. 2014, doi: 10.1016/j.matdes.2014.06.015.

[26] M. Seabra. J. Azevedo, A. Araujo, L. Reis, E. Pinto, N. Alves, R. Santos, and J.P. Mortagua, “Selective laser melting (SLM) and topology optimization for

© Central University of Technology, Free State

lighter aerospace components," *Procedia Struct. Integr.*, vol. 1, pp. 289–296, 2016, doi: 10.1016/j.prostr.2016.02.039.

[27] S. Rao, J Kiran, "Topology optimization of aircraft wing," *CEUR Workshop Proc.*, vol. 1542, no. 9, pp. 33–36, 2015, doi: 10.1017/CBO9781107415324.004.

[28] D. J. Munk, G. A. Vio, and J. E. Cooper, "Topology optimisation of aircraft structures for flutter suppression," *Proc. Int. Conf. Noise Vib. Eng. ISMA*, pp. 3111–3126, 2016, [Online]. Available: http://past.isma-isaac.be/downloads/isma2016/papers/isma2016_0479.pdf

[29] F. Chengwei, L. Haotian, Z. Zhengzheng, A. Liqiang, L. Shaolin, and L. Cheng, "Whole-process design and experimental validation of landing gear lower drag stay with global/local linked driven optimization strategy," *Chinese J. Aeronaut.*, vol. 34, no. 2, pp. 318–328, 2021, doi: 10.1016/j.cja.2020.07.035.

[30] B. Wu, Y. Shi, and Y. Yin, "Optimization design of landing gear structure based on fatigue life constraint," *J. Phys. Conf. Ser.*, vol. 2403, no. 1, pp. 1–7, 2022, doi: 10.1088/1742-6596/2403/1/012027.

[31] M. A. Cain, "Topology optimization of a landing gear assembly," 2016.

[32] C. B. Niutta, A Tridello, G. Barletta, N. Gallo, A. Baroni, and D.S. Paolino, "Defect-driven topology optimization for fatigue design of additive manufacturing structures: Application on a real industrial aerospace component," *Eng. Fail. Anal.*, vol. 142, no. July, p. 106737, 2022, doi: 10.1016/j.engfailanal.2022.106737.

[33] M. K. Thompson, G. Moroni, T. Vaneker, G. Fadel, R.I. Campbell, I. Gibson, A. Bernard, J. Schulz, P. Graf, B. Ahuja, and F. Matina, "Design for additive manufacturing : Trends, opportunities, considerations, and constraints," *CIRP Ann. - Manuf. Technol.*, vol. 65, no. 2, pp. 737–760, 2016, doi: 10.1016/j.cirp.2016.05.004.

[34] A. Mital, A. Desai, A. Subramanian, and A. Mital, "Product development: A structured approach to consumer product development, design, and manufacture, second edition," *Prod. Dev. A Struct. Approach to Consum. Prod. Dev. Des. Manuf. Second Ed.*, no. January 2014, pp. 1–522, 2014, doi:

© Central University of Technology, Free State

10.1016/B978-0-12-799945-6.00015-6.

[35] S. Graziosi, F. Rosa, R. Casati, P. Solarino, M. Vedani, and M. Bordegoni, “Designing for metal additive manufacturing: a case study in the professional sports equipment field,” *Procedia Manuf.*, vol. 11, no. June, pp. 1544–1551, 2017, doi: 10.1016/j.promfg.2017.07.288.

[36] A. Jiménez, P. Bidare, H. Hassanin, F. Tarlochan, S. Dimov, and K. Essa, “Powder-based laser hybrid additive manufacturing of metals: a review,” *Int. J. Adv. Manuf. Technol.*, vol. 114, pp. 63–96, 2021, doi: https://doi.org/10.1007/s00170-021-06855-4.

[37] M. D. Monzón, Z. Ortega, A. Martínez, and F. Ortega, “Standardization in additive manufacturing: activities carried out by international organizations and projects,” *Int. J. Adv. Manuf. Technol.*, vol. 76, no. 5–8, pp. 1111–1121, 2014, doi: 10.1007/s00170-014-6334-1.

[38] J. Gausemeier, N. Wchterhoff, M. Kokoschka, and M. Wall, *Thinking ahead the future of additive manufacturing – Analysis of promising industries*. Germany: Heinz Nixdorf Institute, 2011.

[39] Z. Doubrovski, J. C. Verlinden, and I. Horvath, “First steps towards collaboratively edited design for additive manufacturing knowledge,” no. May 2014, 2012.

[40] G. Survey, *The Use of Galerkin Finite-Element Methods to Solve Mass-Transport Equations Geological Survey, Denver, Colo Water Resources Div*. 1977.

[41] R. Singiresu, *The finite element method in engineering*, Fourth Edi. Butterworth-Heinemann, 2004.

[42] R. Jones, R. K. S. Raman, A. P. Iliopoulos, J. G. Michopoulos, N. Phan, and D. Peng, “Additively manufactured Ti-6Al-4V replacement parts for military aircraft,” *Int. J. Fatigue*, vol. 124, no. March, pp. 227–235, 2019, doi: 10.1016/j.ijfatigue.2019.02.041.

[43] N. Macallister, K. Vanmeensel, and T. Hermann, “Fatigue crack growth

© Central University of Technology, Free State

parameters of laser powder bed fusion produced Ti6A4V," *Int. J. Fatigue*, vol. 145, no. November 2020, p. 106100, 2021, doi: 10.1016/j.ijfatigue.2020.106100.

[44] Y. N. Hu, S.C. Wu, P.J. Withers, J. Zhang, H.Y.X. Bao, Y.N. Fu, and G.Z. Kang, "The effect of manufacturing defects on the fatigue life of selective laser melted Ti-6Al-4V structures," vol. 192, 2020, doi: 10.1016/j.matdes.2020.108708.

[45] I. van Zyl, I. Yadroitsava, and I. Yadroitsev, "Residual stress in TI6AL4V objects produced by direct metal laser sintering," *South African J. Ind. Eng.*, vol. 27, no. December, pp. 134–141, 2016, doi: https://doi.org/10.7166/27-4-1468.

[46] L. Mugwagwa, D. Dimitrov, S. Matope, and R. Muvunzi, "Residual stress and distortion in selective laser melting - A review," 2016.

[47] T. H. Becker, M. Beck, and C. Scheffer, "Microstructure and mechanical properties of direct metal laser sintered TI-6AL-4V," *South African J. Ind. Eng.*, vol. 26, no. May, p. 6, 2015, doi: https://doi.org/10.7166/26-1-1022.

[48] Y. Xu, Y. Lu, K. L. Sundberg, J. Liang, and R. D. Sisson, "Effect of annealing treatments on the microstructure, mechanical properties and corrosion behavior of direct metal laser sintered Ti6Al4V," *J. Mater. Eng. Perform.*, vol. 26, no. 6, pp. 2572–2582, 2017, doi: 10.1007/s11665-017-2710-y.

[49] M. Jurg, A. E. Medvedev, W. Yan, and A. Molotnikov, "Surface improvement of laser powder bed fusion processed Ti6Al4V for fatigue applications," *Addit. Manuf. Lett.*, vol. 3, no. June, p. 100070, 2022, doi: 10.1016/j.addlet.2022.100070.

[50] C. Dordlofva and P. Törlind, "Qualification challenges with additive manufacturing in space applications," in *Solid Freeform Fabrication*, 2017, pp. 2699–2712.

[51] C. A. Brice, "Unintended consequences: How qualification constrains innovation," *Proc. 1st World Congr. Integr. Comput. Mater. Eng. ICME*, pp. 241–246, 2011, [Online]. Available: http://www.scopus.com/inward/record.url?eid=2-s2.0-80051691114&partnerID=40&md5=ec6853cd343dd6b3d7db5026234bc419

© Central University of Technology, Free State

[52] D. W. Gibbons, J. P. L. Serfontein, and A. F. van der Merwe, "Mapping the path to certification of metal laser powder bed fusion for aerospace applications," *Rapid Prototyp. J.*, vol. 27, no. 2, pp. 355–361, 2021, doi: 10.1108/RPJ-07-2020-0154.

[53] L. Portolés, O. Jordá, L. Jordá, A. Uriondo, M. Esperon-Miguez, and S. Perinpanayagam, "A qualification procedure to manufacture and repair aerospace parts with electron beam melting," *J. Manuf. Syst.*, vol. 41, pp. 65–75, 2016, doi: 10.1016/j.jmsy.2016.07.002.

[54] T. Mauery, J. Alonso, A. Cary, V. Lee, R. Malecki, D. Mavriplis, G. Medic, J. Schaefer, and J. Slotnick, "A guide for aircraft certification by analysis," 2021. [Online]. Available: http://www.sti.nasa.gov

[55] R. Stolt and F. Elgh, "Introducing design for selective laser melting in aerospace industry," *J. Comput. Des. Eng.*, vol. 7, no. 4, pp. 489–497, 2020, doi: 10.1093/jcde/qwaa042.

[56] Federal Aviation Administration, *Code for federal regulation: Aeronautics and Space*, Special ed. The Office of the Federal Register National Archives and Record Administration, 1988.

[57] S. Gudmundsson, *The Anatomy of the Landing Gear*. 2014. doi: 10.1016/b978-0-12-397308-5.00013-1.

[58] *Aircr. Tire data B.*, vol. 02, no. 005357, p. 24, 2002, [Online]. Available: https://www.aps-aviation.com/wp-content/uploads/goodyear-aircarft-tire-data.pdf

[59] L. Pazmany, *Landing gear design for light aircraft*, vol. 1. 1986.

[60] E. K. Orhorhoro, I. A. Essienubong, and O. O. Joel, "Failure analysis and optimization of aircraft wheel hub for optimum landing scenario," *Int. J. Eng. Trends Technol.*, vol. 60, no. 2, pp. 135–141, 2018, doi: 10.14445/22315381/ijett-v60p219.

[61] Federal Aviation Administration, "Aircraft landing gear systems," in *Aviation Maintenance Technician Handbook Volume II*, 2012, pp. 13.1-13.96. [Online].

© Central University of Technology, Free State

Available: https://www.faa.gov/regulations_policies/handbooks_manuals/aircraft/amt_airframe_handbook/media/ama_Ch13.pdf

[62] P. W. Christensen and A. Klarbring, “An introduction to structural optimization,” *Solid Mech. its Appl.*, vol. 153, pp. 3–214, 2009.

[63] R. Larsson, “Methodology for topology and shape optimization: Application to a rear lower control arm,” 2016.

[64] J. Lógó and H. Ismail, “Milestones in the 150-Year history of topology optimization: A review,” *Comput. Assist. Methods Eng. Sci.*, vol. 27, no. 2–3, pp. 97–132, 2020, doi: 10.24423/cames.296.

[65] A. G. M. Michell, “The limits of economy of material in frame-structures,” *Philosophical Magazine*, vol. 8, pp. 589–597, 1904. doi: 10.1080/14786440409463229.

[66] D. J. Munk, G. A. Vio, N. F. Giannelis, and J. E. Cooper, “Topology optimisation of representative aircraft wing geometries with an experimental validation,” no. June, pp. 1–14, 2017.

[67] M. Langelaar, “Topology optimization of 3D self-supporting structures for additive manufacturing,” *Addit. Manuf.*, vol. 12, pp. 60–70, 2016, doi: 10.1016/j.addma.2016.06.010.

[68] K.-J. Bathe, *Finite element procedures. Second edition*. 2006. [Online]. Available: http://web.mit.edu/kjb/www/Books/FEP_2nd_Edition_4th_Printing.pdf

[69] ANSYS, “ME 304 Finite element analysis basic types of FEA elements,” 2013. [Online]. Available: https://faculty.up.edu/lulay/ME304/BeamElements.pdf

[70] D. E. Dobbs, M. Fontana, and S. Frisch, “Polynomial function,” 2009. doi: 10.1016/B978-0-12-259655-1.50007-X.

[71] D. W. Pepper and J. C. Heinrich, “The Finite Element Method: Basic Concepts and Applications.” pp. 1–24, 1992.

© Central University of Technology, Free State

[72] Abaqus, "Abaqus Version 6.5 documentation," 2009. https://classes.engineering.wustl.edu/2009/spring/mase5513/abaqus/docs/v6.5/books/gss/default.htm?startat=ch07s02.html

[73] A. Kaw, "Newton-Raphson method of solving a nonlinear equation," in *Nonlinear Equations*, no. 1, 2009, pp. 135–165. doi: 10.1007/978-3-030-83450-0_5.

[74] F. C. Campbell, *Element of metallurgy and engineering alloy*. 2008. [Online]. Available: www.asminternational.org

[75] J. H. Park and J. H. Song, "Detailed evaluation of methods for estimation of fatigue properties," *Int. J. Fatigue*, vol. 17, no. 5, pp. 365–373, 1995, doi: 10.1016/0142-1123(95)99737-U.

[76] M. M. Pedersen, "Introduction to metal fatigue," Denmark, 2018. [Online]. Available: http://www.eng.au.dk

[77] C. Plm, *SIMULIA fe - safe user guide*. Dassault Systemes, 2021. [Online]. Available: https://www.caecis.com/wp-content/uploads/2020/12/FesafeUser.pdf

[78] S. K. Lok, M. J. Paul, and V. Upendranath, "Prescience life of landing gear using multiaxial Fatigue numerical analysis," *Procedia Eng.*, vol. 86, no. i, pp. 775–779, 2014, doi: 10.1016/j.proeng.2014.11.097.

[79] Y. Lee, J. Pan, W. M. Hathaway, and M. E. Barkey, *Fatigue testing and analysis: theory and practice*, vol. 192, no. 3. Elsevier Butterworth–Heinemann, 2005.

[80] L. F. Monaheng, W. B. Du Preez, and T. H. Becker, "Validation through digital image correlation of finite element analysis used in the design of a Ti6Al4V mandibular implant," 2018.

[81] P. Frankovsky and F. Trebuna, "Application of photostress method in stress analysis of rotating disc," *Metalurgija*, vol. 53, no. 4, pp. 541–544, 2014.

[82] L. Monaheng, W. Du Preez, A. Olwagen, and P. Haupt, "Strain gauge validation of finite element analysis of a Ti6Al4V (ELI) mandibular implant produced through additive manufacturing," *Proc. 17th Annu. Int. Conf. Rapid Prod. Dev. Assoc. South Africa*, no. 978-0-620-72061–8, pp. 1–14, 2016.

© Central University of Technology, Free State

[83] P. Hewlett, *Practical strain gauge measurements*. 1981. [Online]. Available: http://www.omega.co.uk/techref/pdf/straingage_measurement.pdf%5Cn[Accessed 15.4.13]

[84] ASTM International, “F2792-12a - Standard terminology for additive manufacturing technologies,” 2013. doi: 10.1520/F2792-12A.2.

[85] S. Singamneni, Y. LV, A. Hewitt, R. Chalk, W. Thomas, and D. Jordison, “Additive manufacturing for the aircraft industry: A review,” *J. Aeronaut. Aerosp. Eng.*, vol. 08, no. 01, 2019, doi: 10.35248/2168-9792.19.8.215.

[86] EOS, “DMLS Technology for Metal 3D Printer.” https://www.eos.info/en/industrial-3d-printing/additive-manufacturing-how-it-works/dmls-metal-3d-printing

[87] A. Verma and R. Rai, “Energy efficient modeling and optimization of additive manufacturing processes,” no. 1, pp. 1–11.

[88] S. M. Yusuf, S. Cutler, and N. Gao, “Review: The impact of metal additive manufacturing on the aerospace industry,” *Metals (Basel).*, vol. 9, no. 12, 2019, doi: 10.3390/met9121286.

[89] A. E. Patterson, S. L. Messimer, and P. A. Farrington, “Overhanging features and the SLM/DMLS residual stresses problem: Review and future research need,” *Technologies*, vol. 5, no. 4, p. 15, 2017, doi: 10.3390/technologies5020015.

[90] Y. He, C. Montgomery, J. Beuth, and B. Webler, “Melt pool geometry and microstructure of Ti6Al4V with B additions processed by selective laser melting additive manufacturing,” *Materials and Design*, vol. 183. 2019. doi: 10.1016/j.matdes.2019.108126.

[91] M. Letenneur, V. Brailovski, A. Kreitcberg, V. Paserin, and I. Bailon-Poujol, “Laser powder bed fusion of water-atomized iron-based powders: Process Optimization,” *J. Manuf. Mater. Process.*, vol. 1, no. 2, p. 23, 2017, doi: 10.3390/jmmp1020023.

[92] A. M. Khorasani, I. Gibson, U. S. Awan, and A. Ghaderi, “The effect of SLM

© Central University of Technology, Free State

process parameters on density, hardness, tensile strength and surface quality of Ti-6Al-4V,” *Addit. Manuf.*, vol. 25, no. September 2018, pp. 176–186, 2019, doi: 10.1016/j.addma.2018.09.002.

[93] E. GMBH, “Technical description EOSINT M 280,” 2010.

[94] E. GMBH, “Metal solutions EOS M 290,” 2014.

[95] H. Rezaeifar and M. Elbestawi, “Porosity formation mitigation in laser powder bed fusion process using a control approach,” *Opt. Laser Technol.*, vol. 147, no. July 2021, p. 107611, 2022, doi: 10.1016/j.optlastec.2021.107611.

[96] A. Sola and A. Nouri, “Microstructural porosity in additive manufacturing: The formation and detection of pores in metal parts fabricated by powder bed fusion,” *J. Adv. Manuf. Process.*, vol. 1, no. 3, pp. 1–21, Jul. 2019, doi: 10.1002/amp2.10021.

[97] M. Abdelrahman, E. W. Reutzel, A. R. Nassar, and T. L. Starr, “Flaw detection in powder bed fusion using optical imaging,” *Addit. Manuf.*, vol. 15, pp. 1–11, 2017, doi: 10.1016/j.addma.2017.02.001.

[98] T. H. Becker and N. M. Dhansay, “Influence of porosity on the fatigue life of laser powder bed fusion–produced Ti6Al4V,” *Mater. Des. Process. Commun.*, vol. 3, no. 1, pp. 1–7, 2021, doi: 10.1002/mdp2.141.

[99] T. C. Lueth and W. Volk, “Compensation for geometrical deviations in additive manufacturing,” *Technologies*, vol. 7, no. 83, pp. 1–13, 2019, doi: 10.3390/technologies7040083.

[100] Z. Zhu, N. Anwer, and L. Mathieu, “Geometric deviation modeling with Statistical shape Analysis in Design for Additive Manufacturing,” *Procedia CIRP*, vol. 84, pp. 496–501, 2019, doi: 10.1016/j.procir.2019.04.251.

[101] R. K. Leach, D. Bourell, S. Carmignato, A. Donmez, N. Senin, and W. Dewulf, “Geometrical metrology for metal additive manufacturing,” *CIRP Ann.*, vol. 68, no. 2, pp. 677–700, 2019, doi: 10.1016/j.cirp.2019.05.004.

[102] C. Moriconi, “Simufact additive : Collaborative simultaneous engineering tool for additive manufacturing,” *Safran additive manufacturing*, vol. IX, pp. 27–29,

© Central University of Technology, Free State

2019.

[103] S. Tedia and C. B. Williams, “Manufacturability analysis tool for additive manufacturing using voxel-based geometric modeling,” in *27th Annual International Solid Freeform Fabrication Symposium - An Additive Manufacturing Conference*, 2016, pp. 3–22.

[104] N. Britz and J. L. Serfontein, “The development of a design cycle of additive manufactured prismatic and aerospace components,” in *Pre-conference seminar on design and additive manufacturing titanium parts*, 2019, pp. 149–162. doi: 10.1017/CBO9781107415324.004.

[105] M. B. Bauza, P. S. Moylan, R. M. Panas, S. C Burke, H. E. Martz, J.S, Taylor, P. Alexander, R. H. Knebel, R. Bhogaraju, M. T. Connel and J. D. Smokovitz, “Study of accuracy of parts produced using additive manufacturing,” in *Proceedings of the 2014 ASPE Spring Topical Meeting--Dimensional Accuracy and Surface Finish in Additive Manufacturing*, 2014, vol. 57, pp. 86–91.

[106] P. Rokicki, G. Budzik, K. Kubiak, and T. Dziubek, “The assessment of geometric accuracy of aircraft engine blades with the use of an optical coordinate scanner,” *Aircr. Eng. Aerosp. Technol.*, vol. 88, no. 3, pp. 374–381, 2016, doi: 10.1108/aeat-01-2015-0018.

[107] S. Carmignato, A. Voltan, and E. Savio, “Metrological performance of optical coordinate measuring machine under industrial conditions,” *CIRP Ann.*, vol. 59, no. 1, pp. 497–500, 2010, doi: 10.1016/j.cirp.2010.03.128.

[108] E. Sovio, L. De Chiffre, and R. Schmitt, “Metrology of freeform shaped parts,” *CIRP Ann.*, vol. 56, no. 2, pp. 810–835, 2007, doi: 10.1016/j.cirp.2007.10.008.

[109] P. I. Stavroulakis and R. K. Leach, “Invited Review Article: Review of post-process optical form metrology for industrial-grade metal additive,” *Rev. Sci. Instrum.*, vol. 87, no. 4, pp. 8704–1101, 2016, doi: 10.1063/1.4944983.

[110] Z. Zhu, S. Keimasi, N. Anwer, and L. Mathieu, “Review of shape deviation modeling for additive manufacturing,” *Springer Int. Publ.*, pp. 241–242, 2017, doi: 10.1007/978-3-319-45781-9.

© Central University of Technology, Free State

[111] J. Paul and J. Drake, *Dimensioning and tolerancing handbook*, no. Y14, 5. McGraw-Hill, 1973.

[112] G. Ameta, R. Lipman, S. Moylan, and P. Witherell, "Investigating the role of geometric dimensioning and tolerancing in additive manufacturing," *J. Mech. Des. Trans. ASME*, vol. 137, no. 11, p. 111401, 2015, doi: 10.1115/1.4031296.

[113] R. Wojtuszewski and A. Banaś, "Topology optimization for additive manufacturing," *Annu. Forum Proc. - AHS Int.*, pp. 1752–1759, 2011.

[114] E. Malekipour and H. El-Mounayri, "Common defects and contributing parameters in powder bed fusion AM process and their classification for online monitoring and control: a review," *Int. J. Adv. Manuf. Technol.*, no. 95, pp. 527–550, 2018, doi: 10.1007/s00170-017-1172-6.

[115] Y. Ning, Y. Wong, J. Y. Fuh, and H. Loh, "An approach to minimize build errors in direct metal laser sintering," *IEEE Trans. Autom. Sci. Engineering*, vol. 3, no. 1, pp. 73–80, 2006, doi: 10.1109/TASE.2005.857656.

[116] J. S.-S. Chen and H.-Y. Feng, "Optimal layer setup generation in layered manufacturing with a given error constraint," *J. Manuf. Syst.*, vol. 30, no. 3, pp. 166–174, 2011, doi: 10.1016/s0278-6125(98)90032-2.

[117] E. Yasa and J. Kruth, "Application of laser re-melting on selective laser melting parts," *Adv. Prod. Eng. Manag.*, vol. 6, no. 4, pp. 259–270, 2011.

[118] E. Yasa, O. Poyraz, E. U. Solakoglu, G. Akbulut, and S. Oren, "A study on the stair stepping effect in direct metal laser sintering of a nickel-based superalloy," *Procedia CIRP*, vol. 45, pp. 175–178, 2016, doi: 10.1016/j.procir.2016.02.068.

[119] Z. Zhu, N. Anwer, and L. Mathieu, "Shape transformation perspective for geometric deviation modeling in additive manufacturing," *Procedia CIRP*, vol. 75, pp. 75–80, 2018, doi: 10.1016/j.procir.2018.04.038.

[120] Q. Huang, "An analytical foundation for optimal compensation of three-dimensional shape deformation in additive manufacturing," *J. Manuf. Sci. Eng. Trans. ASME*, vol. 138, no. 6, 2016, doi: 10.1115/1.4032220.

[121] Y. Jin, S. J. Qin, and Q. Huang, "Offline predictive control of out-of-plane shape

deformation for additive manufacturing," *J. Manuf. Sci. Eng. Trans. ASME*, vol. 138, no. 12, 2016, doi: 10.1115/1.4033444.

[122] L. Zhang, S. Zhang, H. Zhu, Z. Hu, G. Wang, and X. Zeng, "Horizontal dimensional accuracy prediction of selective laser melting," *Mater. Des.*, vol. 160, pp. 9–20, 2018, doi: 10.1016/j.matdes.2018.08.059.

[123] A. Armillotta, M. Bellotti, and M. Cavallaro, "Warpage of FDM parts : Experimental tests and analytic model," *Robot. Comput. Manuf.*, vol. 000, no. May, pp. 4–6, 2017.

[124] J. Matthew and J. Donachie, *Titanium: A technical guide*, Second Edi. ASM International, 2000.

[125] D. Callister and J. William, *Materials science and engineering: An introduction*, Seventh. John Wiley & Sons, Inc, 2007.

[126] D. Banerjee and J. C. Williams, "Perspectives on titanium science and technology," *Acta Mater.*, vol. 61, no. 3, pp. 844–879, 2013, doi: 10.1016/j.actamat.2012.10.043.

[127] X. Yan, S. Yin, C. Chen, C. Huang, R. Bolot, and T. Eli, "Effect of heat treatment on the phase transformation and mechanical properties of Ti6AL4V fabricated by selective laser melting," *J. Alloys Compd.*, vol. 764, no. June, pp. 1056–1071, 2018, doi: 10.1016/j.jallcom.2018.06.076.

[128] R. Pederson, "Microstructure and phase transformation of Ti-6Al-4V, PhD thesis, Lulea University of Technology, Sweden," 2002.

[129] P. Manikandan, V.A. Kumar, P. I. Pradeep, R. Vivek, S. K. Manwatkar, G. S. Rao, S. V. S. Narayana Murty, D. Sivakumar, and P. R Narayanan, "On the anisotropy in room-temperature mechanical properties of laser powder bed fusion processed Ti6Al4V-ELI alloy for aerospace applications," *J. Mater. Sci.*, 2022, doi: 10.1007/s10853-022-07032-y.

[130] L. E. Murr, S.A. Quinones, S.M. Gaytan, M.I. Lopez, A Rdela, E.Y. Martinez, D.H. Hernandez, E. Martinez, F. Medina, and R.B. Wicker, "Microstructure and mechanical behavior of Ti-6Al-4V produced by rapid-layer manufacturing, for

© Central University of Technology, Free State

biomedical applications," *J. Mech. Behav. Biomed. Mater.*, vol. 2, no. 1, pp. 20–32, 2009, doi: 10.1016/j.jmbbm.2008.05.004.

[131] L. Thijs, F. Verhaeghe, T. Craeghs, J. Van Humbeeck, and J. P. Kruth, "A study of the microstructural evolution during selective laser melting of Ti-6Al-4V," *Acta Mater.*, vol. 58, no. 9, pp. 3303–3312, May 2010, doi: 10.1016/j.actamat.2010.02.004.

[132] E. Sallica-Leva, A. L. Jardini, and J. B. Fogagnolo, "Microstructure and mechanical behavior of porous Ti-6Al-4V parts obtained by selective laser melting," *J. Mech. Behav. Biomed. Mater.*, vol. 26, pp. 98–108, 2013, doi: 10.1016/j.jmbbm.2013.05.011.

[133] A. Muiruri, M. Maringa, W. du Preez, and L. Masu, "Effects of stress-relieving heat treatment on impact toughness of direct metal laser sintering (DMLS)-produced Ti6Al4V (ELI) parts," *JOM*, vol. 72, pp. 1175–1185, 2019, doi: https://doi.org/10.1007/s11837-019-03862-5.

[134] M. G. Moletsane, P. Krakhmalev, N. Kazantseva, A. du Plessis, I. Yadroitsava, and I. Yadroitsev, "Tensile properties and microstructure of direct metal laser-sintered Ti6Al4V (ELI) alloy," *South African J. Ind. Eng.*, vol. 27, pp. 110–121, 2016, doi: 10.7166/27-3-1667.

[135] ASTM International, "E8/E8M standard test methods for tension testing of metallic materials," 2010. doi: 10.1520/E0008.

[136] L. B. Malefane, W. B. du Preez, M. Maringa, and A. du Plessis, "Tensile and high cycle fatigue properties of annealed TI6AL4V (ELI) specimens produced by direct metal laser sintering," *South African J. Ind. Eng.*, vol. 29, no. 3 Special Edition, pp. 299–311, 2018, doi: 10.7166/29-3-2077.

[137] L. T. D. Louw, S.E. Hoosain, "Mechanical testing of Ti6Al4V produced on the Aeroswift platform," in *RAPDASA conference*, 2019, pp. 140–148.

[138] G. Kasperovich and J. Hausmann, "Improvement of fatigue resistance and ductility of TiAl6V4 processed by selective laser melting," *J. Mater. Process. Technol.*, vol. 220, pp. 202–214, 2015, doi: https://doi.org/10.1016/j.jmatprotec.2015.01.025.

© Central University of Technology, Free State

[139] P. Edwards and M. Ramulu, “Fatigue performance evaluation of selective laser melted Ti – 6Al – 4V,” *Mater. Sci. Eng. A*, vol. 598, pp. 327–337, 2014, doi: 10.1016/j.msea.2014.01.041.

[140] M. Koike, K. Martinez, L. Guo, G. Chahine, R. Kovacevic, and T. Okabe, “Evaluation of titanium alloy fabricated using electron beam melting system for dental applications,” *J. Mater. Process. Tech.*, vol. 211, no. 8, pp. 1400–1408, 2011, doi: 10.1016/j.jmatprotec.2011.03.013.

[141] T. Vilaro, C. Colin, and D. Bartout, “As-fabricated and heat-treated microstructures of the Ti-6Al-4V alloy processed by selective laser melting,” *Metall. Mater. Trans. A*, vol. 42, no. 10, pp. 3190–3199, 2011, doi: 10.1007/s11661-011-0731-y.

[142] B. Wysocki, P. Maj, R. Sitek, J. Buhagiar, K. J. Kurzydłowski, and W. Świeszkowski, “Laser and electron beam additive manufacturing methods of fabricating titanium bone implants,” *Appl. Sci.*, vol. 7, no. 7, pp. 1–20, 2017, doi: 10.3390/app7070657.

[143] M. Simonelli, Y. Tse, and C. J. Tuck, “The formation of α + β microstructure in as-fabricated selective laser melting of Ti–6Al–4V,” *J. Mater. Res.*, vol. 29, no. 17, pp. 2028–2035, 2014, doi: 10.1557/jmr.2014.166.

[144] H. P. Miya, W. B. du Preez, and L. F. Monaheng, “High cycle fatigue performance of Ti6Al4V(ELI) specimens produced with inherent laser powder bed fusion surface roughness,” *South African J. Ind. Eng.*, vol. 32, no. 3, pp. 248–257, 2021, doi: 10.7166/32-3-2659.

[145] Q. Huang, X. Liu, X. Yang, R. Zhang, Z. Shen, and Q. Feng, “Specific heat treatment of selective laser melted Ti–6Al–4V for biomedical applications,” *Front. Mater. Sci.*, vol. 9, no. 4, pp. 373–381, 2015, doi: 10.1007/s11706-015-0315-7.

[146] B. Vrancken, L. Thijs, J. P. Kruth, and J. Van Humbeeck, “Heat treatment of Ti6Al4V produced by selective laser melting: Microstructure and mechanical properties,” *J. Alloys Compd.*, vol. 541, pp. 177–185, 2012, doi: 10.1016/j.jallcom.2012.07.022.

© Central University of Technology, Free State

[147] ASTM International, “F2924-14 standard specification for additive manufacturing titanium-6 aluminum-4 vanadium with powder bed fusion,” vol. i, pp. 1–8, 2012, doi: 10.1520/F2924-12A.2.

[148] D. Roylance, *Mechanical properties of materials*, vol. 190. 2008. doi: 10.1007/978-94-007-4342-7.

[149] ASTM International, “E23 standard test methods for notched bar impact testing of metallic materials 1,” 2020. doi: 10.1520/E0023-18.

[150] A. Muiruri, M. Maringa, W. du Preez, and L. Masu, “Variation of impact toughness of as-built DMLS TI6Al4V (ELI) specimens with temperature,” *South African J. Ind. Eng.*, vol. 29, no. November, pp. 284–298, 2018.

[151] D. F. Louw, “Charpy impact toughness and prior β-grain size in Ti6Al4V manufactured by high speed, high-power (3kw) laser powder bed fusion,” *South African J. Ind. Eng.*, pp. 1–3, 2015.

[152] Y. Kim and J. Yu, “Effect of Heat Treatment on Microstructure and impact toughness of Ti-6Al- 4V manufactured by selective laser melting process,” *Arch. Metall. Mater.*, vol. 62, no. 2B, pp. 1341–1346, 2017, doi: 10.1515/amm-2017-0205.

[153] H. Bin Younis, K. Kamal, M. F. Sheikh, and A. Hamza, “Prediction of fatigue crack growth rate in aircraft aluminum alloys using optimized neural networks,” *Theor. Appl. Fract. Mech.*, vol. 117, no. July 2021, 2022, doi: 10.1016/j.tafmec.2021.103196.

[154] ASTM International, “E399 standard test method for linear-elastic plane-strain fracture toughness of metallic materials,” 2020. doi: 10.1520/E0399-20.2.

[155] ASTM International, “E399 standard test method for plane-strain fracture toughness of metallic materials 1,” *Configurations*, vol. 90, no. Reapproved, pp. 1–31, 1997, doi: 10.1520/E0399-09E02.2.

[156] V. E. M. Cain, L. Thijs, J. Van Humbeeck, B. Van Hooreweder, and R. Knutsen, “Crack propagation and fracture toughness of Ti6Al4V alloy produced by selective laser melting,” *Addit. Manuf.*, vol. 5, pp. 68–76, 2015, doi:

© Central University of Technology, Free State

10.1016/j.addma.2014.12.006.

[157] P. Kumar and U. Ramamurty, “Microstructural optimization through heat treatment for enhancing the fracture toughness and fatigue crack growth resistance of selective laser melted Ti6Al4V alloy,” *Acta Mater.*, vol. 169, pp. 45–59, 2019, doi: 10.1016/j.actamat.2019.03.003.

[158] ASTM International, “E647 standard test method for measurement of fatigue crack growth rates,” 2016. doi: 10.1520/E0647-15E01.2.

[159] L. Kunz, P. Pokorny, R. Konecana, and G. Nicoletto, “Propagation of long fatigue cracks in Ti6Al4V alloy produced by propagation of long direct fatigue cracks in sintering,” *Procedia Struct. Integr.*, vol. 17, pp. 222–229, 2019, doi: 10.1016/j.prostr.2019.08.030.

[160] A. K. Syed, .B Ahmad, H. Guo, T. Machry, D. Eatock, J. Meyer, M.E. Fitzpatrick, and X. Zhang, “An experimental study of residual stress and direction-dependence of fatigue crack growth behaviour in as-built and stress-relieved selective-laser-melted Ti6Al4V,” *Mater. Sci. Eng. A*, vol. 755, no. February, pp. 246–257, 2019, doi: 10.1016/j.msea.2019.04.023.

[161] T. H. Becker, P. Kumar, and U. Ramamurty, “Fracture and fatigue in additively manufactured metals,” *Acta Mater.*, vol. 219, p. 117240, 2021, doi: 10.1016/j.actamat.2021.117240.

[162] E. Amsterdam, J. Willem E. Wiegman, M. Nawijn, and J. T. M. De Hosson, “On the strain energy release rate and fatigue crack growth rate in metallic alloys,” *Eng. Fract. Mech.*, vol. 286, no. April, p. 109292, 2023, doi: 10.1016/j.engfracmech.2023.109292.

[163] S. Leuders, M. Thone, A. Riemer, T. Niendorf, T. Troster, H. A. Richrd, and H. J. Maier , “On the mechanical behaviour of titanium alloy TiAl6V4 manufactured by selective laser melting: Fatigue resistance and crack growth performance,” *International Journal of Fatigue*, vol. 48. pp. 300–307, 2013. doi: 10.1016/j.ijfatigue.2012.11.011.

[164] D. Agius, K. I. Kourousis, and C. Wallbrink, “A review of the as-built SLM Ti-6Al-4V mechanical properties towards achieving fatigue resistant designs,” *Metals*

© Central University of Technology, Free State

(Basel)., vol. 8, no. 1, 2018, doi: 10.3390/met8010075.

[165] N. M. Dhansay, “Fracture mechanics based fatigue and fracture toughness evaluation of SLM Ti-6Al-4V,” 2015. [Online]. Available: https://open.uct.ac.za/bitstream/handle/11427/24326/thesis_ebe_2015_dhansay_nur_mohamed.pdf?sequence=1

[166] L. Motibane, L. Tshabalala, N. Mathe, and R. Knutsen, “Dynamic mechanical properties of high speed selective laser melting at 4.5kw,” in *RAPDASA conference*, 2019, pp. 52–57.

[167] E. D. George, “Mechanical metallurgy” pp. 1–646, 1961.

[168] ASTM International, “E466 standard practice for conducting force controlled constant amplitude axial fatigue tests of metallic materials 1,” 2020. doi: 10.1520/E0466-15.2.

[169] F. C. Campbell, “Elements of metallurgy and engineering alloys,” in *Elements of Metallurgy and Engineering Alloys (#05224G)*, 2008.

[170] E. Wycisk, A. Solbach, S. Siddique, D. Herzog, and F. Walther, “Effects of Defects in Laser Additive Manufactured Ti-6Al-4V on Fatigue Properties,” *Phys. Procedia*, vol. 56, pp. 371–378, 2014, doi: 10.1016/j.phpro.2014.08.120.

[171] N. W. Sachs, “Understanding the surface features of fatigue fractures: How they describe the failure cause,” vol. 5, no. April, pp. 11–15, 2005, doi: 10.1361/15477020522924.

[172] E. Wycisk, A. Solbach, S. Siddique, D. Herzog, F. Walther, and C. Emmelmann, “Effects of defects in laser additive manufactured Ti-6Al-4V on fatigue effects of defects in laser additive manufactured Ti-6Al-4V on fatigue properties,” *Phys. Procedia*, vol. 56, no. October, pp. 371–378, 2014, doi: 10.1016/j.phpro.2014.08.120.

[173] R. H. Bossi, B. W. Knutson, J. L. Cline, R. J. Kruse, and G. E. Georgeson, “X-ray computed tomography for the aircraft/aerospace industry,” *Quant. Nondestruct. Eval.*, vol. 10B, pp. 2121–2122, 1991.

[174] Smiths, “7050 Aluminium,” 2017. [Online]. Available:

© Central University of Technology, Free State

https://www.smithmetal.com/pdf/aluminium/7xxx/7050.pdf

[175] E. Buckingham, *On physically similar systems: Illustrations of the use of dimensional equations*. 1914. [Online]. Available: https://empslocal.ex.ac.uk/people/staff/gv219/classics.d/Buckingham-Pi14.pdf

[176] A. M. Muiruri, M. Maringa, and W. du Preez, "Developing microstructure- and dislocation-based constitutive numerical models for predicting the mechanical behaviour of dmls Ti6Al4v(ELI) at various strain rates," 2021. [Online]. Available: http://ir.cut.ac.za/bitstream/handle/11462/2368/Muiruri%2C Amos Mwangi.pdf?sequence=1&isAllowed=y

[177] ASTM International, "F136-08, standard specification for wrought titanium-6 aluminum-4 vanadium ELI (extra low interstitial) alloy for surgical implant applications (UNS R56401), 2020. doi: 10.1520/F0136-08

[178] K. Thejane, S. Chikosha, and W. B. du Preez, "Characterisation and monitoring of Ti6Al4V (ELi) powder used in different selective laser melting systems," *South African J. Ind. Eng.*, vol. 28, no. November, pp. 161–171, 2017.

[179] 3D-Systems, "Geomagics Control X," *3D Syst.*, pp. 1–173, 2016.

[180] H. P. Miya, W. B. Du Preez, and L. F. Monaheng, "Performance assessment of a Ti6Al4V(ELI) light aircraft nose wheel fork produced through laser powder bed fusion," Master degree dissertation, Department of Mechanical and Mechatronics Engineering, Central University of Technology, Free State, Bloemfontein, South Africa, 2023.

[181] Simulia, "FE-Safe: Durability analysis software for finite element model," *Dassault System*. https://www.3ds.com/products-services/simulia/products/fe-safe/fe-safe/ (accessed Feb. 23, 2023).

[182] S. Ramadurga *et al.*, "A comprehensive review on laser powder bed fusion of steels : Processing, microstructure, defects and control methods, mechanical properties, current challenges and future trends," *J. Manuf. Process.*, vol. 75, no. January 2021, pp. 375–414, 2022, doi: 10.1016/j.jmapro.2021.12.033.

[183] A. Du Plessis, S. G. Le Roux, J. Els, G. Booysen, and D. C. Blaine, "Application

© Central University of Technology, Free State

of microCT to the non-destructive testing of an additive manufactured titanium component," *Case Stud. Nondestruct. Test. Eval.*, vol. 4, pp. 1–7, 2015, doi: 10.1016/j.csndt.2015.09.001.

[184] G. Lütjering, "Influence of processing on microstructure and mechanical properties of (α + β) titanium alloys," *Mater. Sci. Eng. A*, vol. 243, no. 1–2, pp. 32–45, 1998, doi: 10.1016/s0921-5093(97)00778-8.

[185] AZoM, "Grade 23 Ti 6Al 4V ELI Alloy (UNS R56401)," 2013. [Online]. Available: https://www.azom.com/article.aspx?ArticleID=9365

[186] ASM Aerospace Specification Metals Inc, "Titanium Ti-6Al-4V (Grade 5), ELI, Annealed." http://asm.matweb.com/search/SpecificMaterial.asp?bassnum=MTP643 (accessed Jun. 29, 2021).

[187] S. V. Panin, P. O. Maruschak, I. V. Vlasov, and B. B. Ovechkin, "Impact toughness of 12Cr1MoV steel. Part 1 - Influence of temperature on energy and deformation parameters of fracture," *Theor. Appl. Fract. Mech.*, vol. 83, pp. 105–113, 2016, doi: 10.1016/j.tafmec.2015.12.008.

[188] S. V. Panin, P. O. Maruschak, I. V. Vlasov, V. P. Sergeev, B. B. Ovechkin, and V. V. Neifeld, "Impact toughness of 12Cr1MoV steel. Part 2 - Influence of high intensity ion beam irradiation on energy and deformation parameters and mechanisms of fracture," *Theor. Appl. Fract. Mech.*, vol. 83, pp. 82–92, 2016, doi: 10.1016/j.tafmec.2015.12.009.

[189] J. W. Kysar, "Energy dissipation mechanisms in ductile fracture," *J. Mech. physic solid*, vol. 51, pp. 795–824, 2003, doi: 10.1016/S0022-5096(02)00141-2.

[190] L. Wu, Z. Jiao, and H. Yu, "Study on fatigue crack growth behavior of selective laser-melted Ti6Al4V under different build directions, stress ratios, and temperatures," *Fatigue Fract. Eng. Mater. Struct.*, vol. 45, no. 5, pp. 1421–1434, 2022, doi: 10.1111/ffe.13670.

[191] G. Nicoletto, R. Konečná, L. Kunz, and M. Frkáň, "Influence of as-built surface on fatigue strength and notch sensitivity of Ti6Al4V alloy produced by DMLS," *MATEC Web Conf.*, vol. 165, pp. 2–7, 2018, doi:

© Central University of Technology, Free State

10.1051/matecconf/201816502002.

[192] P. Hartunian and M. Eshraghi, “Effect of build orientation on the microstructure and mechanical properties of selective laser-melted Ti-6Al-4V Alloy,” *J. Manuf. Mater. Process.*, vol. 2, no. 4, 2018, doi: 10.3390/jmmp2040069.

[193] H. Gong, K. Rafi, T. Starr, and B. Stucker, “Effect of defects on fatigue tests of as-built TI-6AL-4V parts fabricated by selective laser melting,” *23rd Annu. Int. Solid Free. Fabr. Symp. - An Addit. Manuf. Conf. SFF 2012*, no. July 2015, pp. 499–506, 2012.

[194] K. S. R. Chandran, “Duality of fatigue failures of materials caused by Poisson defect statistics of competing failure modes,” *Nat. Mater.*, vol. 4, no. 4, pp. 303–308, 2005, doi: 10.1038/nmat1351.

[195] H. Gong, H. Gu, K. Zeng, J.J.S. Dilip, D. Pal, B. Strcker, D. Christiansen, J Beuth, J. J. Lewamdowski, “Melt pool characterization for selective laser melting of Ti-6Al-4V pre-alloyed powder,” in *University of Texas*, 2014, pp. 256–267. doi: http://dx.doi.org/10.26153/tsw/15682.

[196] Iternational Organisation of Satanarsation, “ISO 5832-3 metallic materials part 3: Wrought titanium 6-aluminium 4-vanadium alloy,” 1996.

[197] C. N. Sun and A. Adnan, *Mechanics of aircraft structure*, Third edit. Wiley, 2021. [Online]. Available: https://www.google.co.za/books/edition/Mechanics_of_Aircraft_Structures/bU9EEAAAQBAJ?hl=en&gbpv=1&dq=Characteristics+of+aircraft+structures+and+materials&printsec=frontcover

© Central University of Technology, Free State

APPENDIX A: ABOUT THE AUTHOR

Mr **Lehlohonolo Francis Monaheng** is a lecturer of Machine Mechanics in the Department of Mechanical and Mechatronics Engineering of the Faculty of Engineering, Built Environment and Information Technology (FEBIT) at Central University of Technology (CUT). He is registered with the Engineering Council of South Africa as a Candidate Professional Engineering Technologist. Besides lecturing undergraduate students, he co-supervised a Master of Engineering project which was titled "Performance assessment of a TI6Al4V(ELI) light aircraft nose wheel fork produced through laser powder bed fusion (L-PBF)". He started studying towards a Doctor of Engineering in Mechanical Engineering (D Eng) in 2019 after obtaining a Master of Engineering in Mechanical Engineering (Cum Laude) in 2017. His first registration of the D Eng topic stated on the cover page was in 2020 at CUT.

The D Eng of Mr Monaheng initiated multiple collaborations with an aircraft industry player. In 2019, a Non Disclosure Agreement between CUT and Paramount Aerospace Industries, which was called Advanced High-Performance Reconnaissance Light Aircraft (AHRLAC) company at that time, was signed. This was done to share technical information necessary to redesign the nose wheel fork of the AHRLAC for production in Ti6Al4V(ELI) through L-PBF. In the same year, a collaboration between CUT and the CSIR National Laser Centre (NLC) was enhanced. The Aeroswift machine of the NLS was identified for the production of the AHRLAC nose wheel fork. The collaboration with the University of Pretoria (UP) allowed the testing of the scaled-down nose wheel fork that was created as the experimental prototype. Finally, software such as MSC Patran-Nastran® plus Simufact Additive®, SolidThinking Inspire® and Abaqus were procured from SIMTEQ, Altair and FEAS, respectively. This was done to execute the redesign of the nose wheel fork with confidence while applying state-of-the-art technology.

Mr Monaheng presented several aspects of his D Eng studies at international and national conferences. In 2019, he presented "The topology optimisation design of light aircraft for production in Ti6Al4V(ELI) through L-PBF," at the 14th World Conference on Titanium (France, Nantes). This was followed by a virtual conference titled the ASTM International Conference on Additive Manufacturing (ASTM ICAM 2021)**,** where

© Central University of Technology, Free State

“Towards qualification: Fatigue crack growth rate of Ti6Al4V(ELI) specimens produced through Direct Metal Laser Sintering” was presented. His presentation on the failure analysis of the nose wheel fork at the CUT seminar of 2022 (FEBIT, Bloemfontein), received an award to the value of R2 000 for the 3rd best presenter. Other aspects of the failure analysis of the nose wheel fork for production in Ti6Al4V(ELI) through selective laser melting (SLM) were presented at the online 9th International Conference on Engineering Failure Analysis (ICEFA 2022). Moreover, the SLM process chain for the development of a Ti6Al4V(ELI) nose wheel fork of a light aircraft was presented at the 15th World Conference on Titanium in 2023 (Scotland, Edinburgh). The performance of the scaled-down landing gear nose wheel fork produced in Ti6Al4V(ELI) through L-PBF was presented at the Aeronautical Society of South Africa conference (AeSSA 2023, in CSIR Pretoria). Finally, a total of three research articles were published in high-impact journals and are listed in the research output section of this thesis.

To conclude, Mr Monaheng’s project, “Redesign and characterisation of the nose wheel fork of a light aircraft for production in TI6Al4V(ELI) through laser powder bed fusion” was accepted as the technology demonstrator by the director of the Innovation and Technology transfer at CUT. His achievements made him the best candidate to be awarded the Doctor of Engineering in Mechanical Engineering.

© Central University of Technology, Free State

APPENDIX B: TECHNOLOGY DEMONSTRATOR

Central University of
Technology, Free State

Innovation & Technology Transfer

27 March 2023

TO WHOM IT MAY CONCERN

TECHNOLOGY DEMONSTRATOR: REDESIGN AND CHARACTERISATION OF THE NOSE WHEEL FORK OF A LIGHT AIRCRAFT FOR PRODUCTION IN TI6AL4V(ELI) THROUGH LASER POWDER BED FUSION

This letter serves to confirm that the scaled-down nose wheel fork of the Advanced High-performance Reconnaissance Light Aircraft (AHRLAC) produced in Ti6Al4V(ELI) through Direct Metal Laser Sintering (DMLS) was recognised as a technology demonstrator by the Central University of Technology, Free State (CUT).

The acceptance of the development of the Ti6Al4V(ELI) nose wheel fork through DMLS by the aviation industry would significantly reduce the large amount of raw material wastage associated with the traditional manufacturing techniques. Later, the full-scale nose wheel fork will be produced using the High-speed Laser Powder Bed Fusion (HL-PBF) known as Aeroswift.

A Non-Disclosure Agreement (NDA) was signed between the CUT and the Aerospace Development Corporation Group on 23 January 2018 having their registered office at the AHRLAC manufacturing facility in Linvelt Road, Wonderboom Airport, Pretoria. The parties agreed to share information necessary for the redesign and development of a nose wheel fork of the AHRLAC produced through DMLS of Ti6Al4V(ELI). This was followed by registration of the Doctor of Engineering in Mechanical Engineering at the CUT in 2020 of Mr LF Monaheng.

The manufacturing of the DMLS Ti6Al4V(ELI) scaled-down nose wheel fork was carried out at the Centre for Rapid Prototyping and Manufacturing (CRPM) and performance testing of the prototype was done at the University of Pretoria (UP). The tests results demonstrated that the DMLS technology can be used to produce the Ti6Al4V(ELI) nose wheel fork of an aircraft provided post process surface finishing is applied to reduce defects such as surface roughness caused by the staircase effect and partially melted particles. The buy-to-fly ratio was significantly improved when DMLS was used to replace the conventional manufacturing process for production of the nose wheel fork. A weight saving of 20% was obtained without compromising the strength of the nose wheel fork.

The main funding of the project came from the Collaborative Program in Additive Manufacturing (CPAM).

CUT Innovation Services • Private Bag X20539 • Bloemfontein • SOUTH AFRICA • 9300 •
Tel: +27 051 507 4338 • **Fax:** +27 051 507 3835 • **E-mail:** fmatongo@cut.ac.za • **Website:** www.cut.ac.za

Yours truly,

Fredrick Matongo
Director: Innovation & Technology Transfer

APPENDIX C: NON-DISCLOSURE AGREEMENT

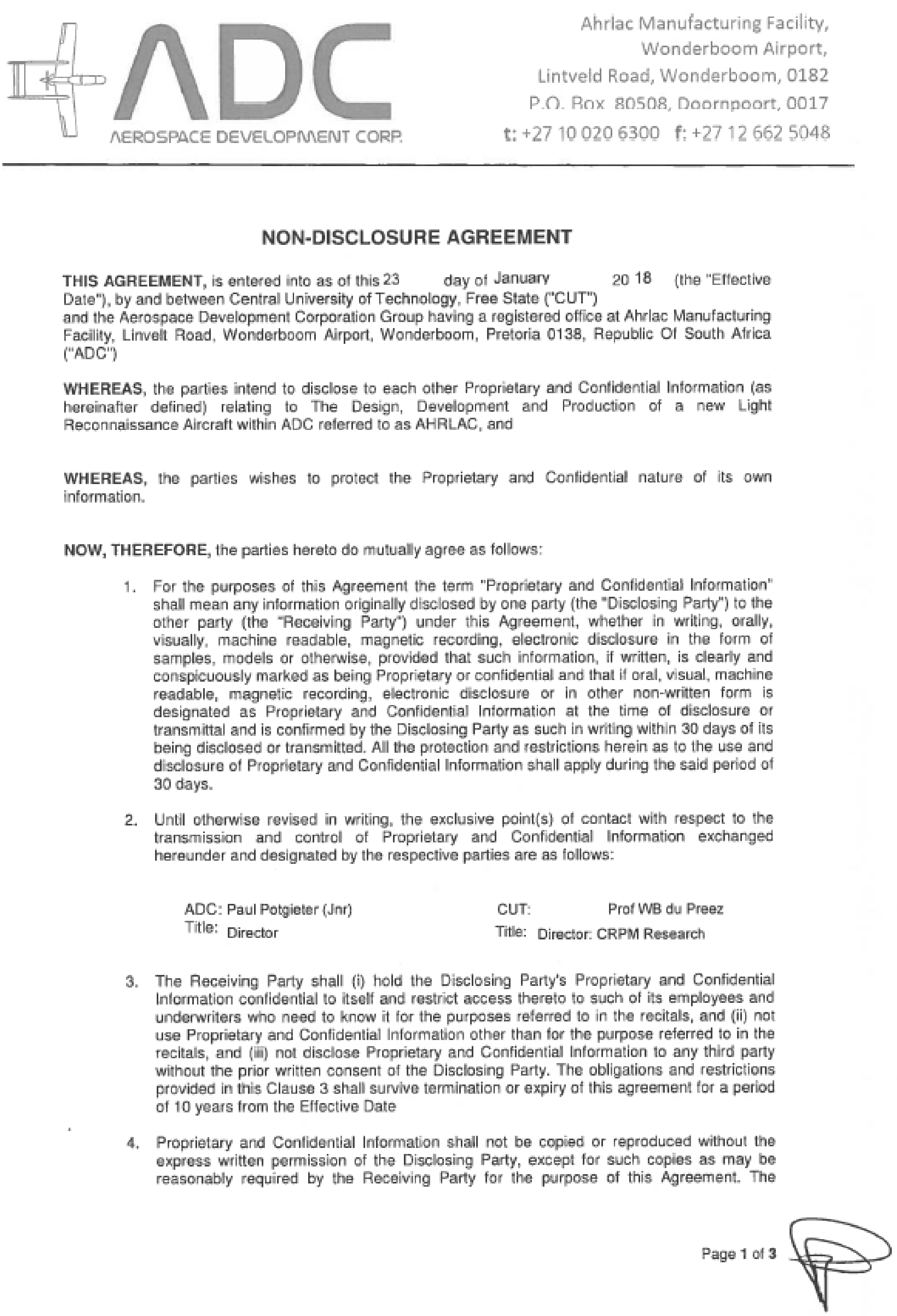

ADC
AEROSPACE DEVELOPMENT CORP.

Ahrlac Manufacturing Facility,
Wonderboom Airport,
Lintveld Road, Wonderboom, 0182
P.O. Box 80508, Doornpoort, 0017
t: +27 10 020 6300 f: +27 12 662 5048

NON-DISCLOSURE AGREEMENT

THIS AGREEMENT, is entered into as of this 23 day of January 20 18 (the "Effective Date"), by and between Central University of Technology, Free State ("CUT") and the Aerospace Development Corporation Group having a registered office at Ahrlac Manufacturing Facility, Linvelt Road, Wonderboom Airport, Wonderboom, Pretoria 0138, Republic Of South Africa ("ADC")

WHEREAS, the parties intend to disclose to each other Proprietary and Confidential Information (as hereinafter defined) relating to The Design, Development and Production of a new Light Reconnaissance Aircraft within ADC referred to as AHRLAC, and

WHEREAS, the parties wishes to protect the Proprietary and Confidential nature of its own information.

NOW, THEREFORE, the parties hereto do mutually agree as follows:

1. For the purposes of this Agreement the term "Proprietary and Confidential Information" shall mean any information originally disclosed by one party (the "Disclosing Party") to the other party (the "Receiving Party") under this Agreement, whether in writing, orally, visually, machine readable, magnetic recording, electronic disclosure in the form of samples, models or otherwise, provided that such information, if written, is clearly and conspicuously marked as being Proprietary or confidential and that if oral, visual, machine readable, magnetic recording, electronic disclosure or in other non-written form is designated as Proprietary and Confidential Information at the time of disclosure or transmittal and is confirmed by the Disclosing Party as such in writing within 30 days of its being disclosed or transmitted. All the protection and restrictions herein as to the use and disclosure of Proprietary and Confidential Information shall apply during the said period of 30 days.

2. Until otherwise revised in writing, the exclusive point(s) of contact with respect to the transmission and control of Proprietary and Confidential Information exchanged hereunder and designated by the respective parties are as follows:

ADC: Paul Potgieter (Jnr)	CUT: Prof WB du Preez
Title: Director	Title: Director: CRPM Research

3. The Receiving Party shall (i) hold the Disclosing Party's Proprietary and Confidential Information confidential to itself and restrict access thereto to such of its employees and underwriters who need to know it for the purposes referred to in the recitals, and (ii) not use Proprietary and Confidential Information other than for the purpose referred to in the recitals, and (iii) not disclose Proprietary and Confidential Information to any third party without the prior written consent of the Disclosing Party. The obligations and restrictions provided in this Clause 3 shall survive termination or expiry of this agreement for a period of 10 years from the Effective Date

4. Proprietary and Confidential Information shall not be copied or reproduced without the express written permission of the Disclosing Party, except for such copies as may be reasonably required by the Receiving Party for the purpose of this Agreement. The

Page 1 of 3

© Central University of Technology, Free State

Receiving Party will affix to all complete and partial copies the legends and notices appearing on the original provided by the Disclosing Party.

5. Neither party shall be liable for the inadvertent, accidental, unauthorized or mistaken disclosure or use by its employees of Proprietary and Confidential Information obtained pursuant to this Agreement provided that (a) the Receiving Party handles Proprietary and Confidential Information of the Disclosing Party which bears such a notice with the same degree of care normally used to protect its own Proprietary and Confidential Information within its own organization, but in no event anyless than reasonable care; (b) upon discovery of such disclosure or use, all reasonable steps are taken to retrieve the disclosed Proprietary and Confidential Information and to prevent any further inadvertent, accidental, unauthorized, or mistaken disclosure or use; and (c) such disclosure will not relieve the Receiving Party who disclosed the Proprietary and Confidential Information from its continuing obligation to adhere to the terms and conditions of this Agreement.

6. The obligations and restrictions provided in Clause 3 hereof shall not apply to information which the receiving Party can show:
   - (i) is in the unrestricted possession of the Receiving Party at the time of disclosure hereunder, or
   - (ii) is or becomes available in the public domain otherwise than by breach of this Agreement, or
   - (iii) to have been lawfully obtained from a third party without notice of such restrictions as to use and disclosure, or
   - (iv) is or has been developed independently by the Receiving Party without reliance upon Proprietary and Confidential Information disclosed hereunder, as evidenced by written records of the Receiving Party.

7 This Agreement does not obligate any party to disclose Proprietary and Confidential information to the other party. All Proprietary and Confidential Information, samples and models if any, exchanged hereunder shall remain the property of the Disclosing Party and shall be returned to it or destroyed within 30 days at the request of the Disclosing Party, or upon termination or expiration of this Agreement together with all copies made thereof. Upon request, the Receiving Party shall promptly send the Disclosing Party a destruction certificate.

8. No rights in or license under any present or future patents, data, drawings, plans, ideas or methods disclosed pursuant to this Agreement are granted or conveyed to the Receiving Party by the Disclosing Party's disclosing Proprietary and Confidential Information or other information.IN PROVIDING ANY PROPRIETARY AND CONFIDENTIAL INFORMATION HEREUNDER, NEITHER PARTY MAKES ANY REPRESENTATION, EITHER EXPRESSED OR IMPLIED, AS TO ITS ADEQUACY, ACCURACY, SUFFICIENCY OR FREEDOM FROM DEFECT OF ANY KIND, INCLUDING FREEDOM FROM ANY PATENT INFRINGEMENT THAT MAY RESULT FROM THE USE OF SUCH PROPRIETARY AND CONFIDENTIAL INFORMATION, NOR SHALL ANY PARTY INCUR ANY RESPONSIBILITY OR OBLIGATION WHATSOEVER BY REASON OF SUCH PROPRIETARY AND CONFIDENTIAL INFORMATION, EXCEPT AS PROVIDED UNDER THIS AGREEMENT.

9. No party shall assign or transfer its rights and/or obligations pursuant to this Agreement without the prior written consent of the other party. No exercise, or failure to exercise, or delay in exercising any right, power or remedy vested in any party under or pursuant hereto shall constitute a waiver by that party of that or any other right, power or remedy.

10. This Agreement shall apply in lieu of and notwithstanding the terms or conditions in any specific legend or restrictive statement associated with any information exchanged hereunder and the duties of the parties shall be determined exclusively by the terms and conditions of this Agreement.

© Central University of Technology, Free State

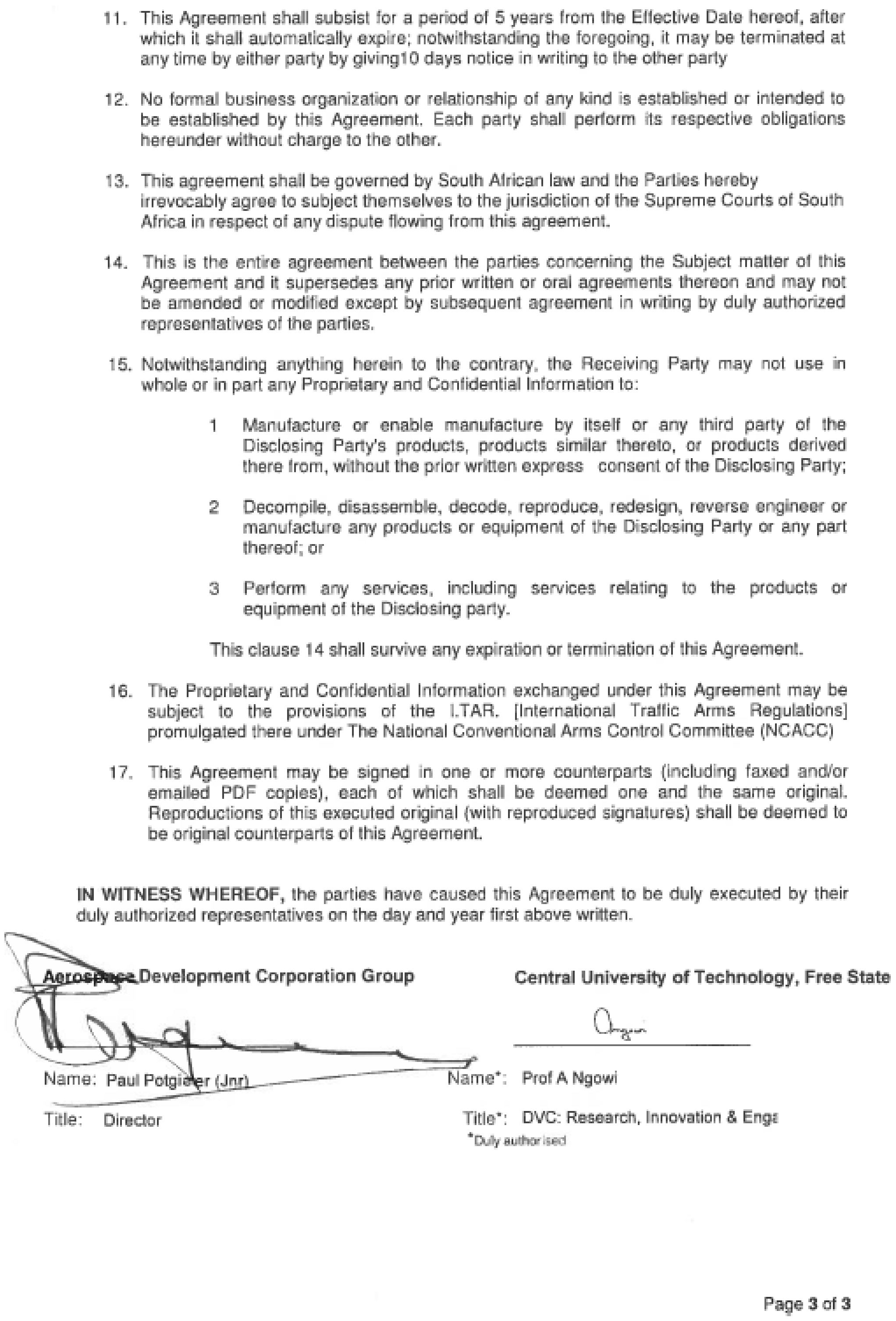

11. This Agreement shall subsist for a period of 5 years from the Effective Date hereof, after which it shall automatically expire; notwithstanding the foregoing, it may be terminated at any time by either party by giving10 days notice in writing to the other party

12. No formal business organization or relationship of any kind is established or intended to be established by this Agreement. Each party shall perform its respective obligations hereunder without charge to the other.

13. This agreement shall be governed by South African law and the Parties hereby irrevocably agree to subject themselves to the jurisdiction of the Supreme Courts of South Africa in respect of any dispute flowing from this agreement.

14. This is the entire agreement between the parties concerning the Subject matter of this Agreement and it supersedes any prior written or oral agreements thereon and may not be amended or modified except by subsequent agreement in writing by duly authorized representatives of the parties.

15. Notwithstanding anything herein to the contrary, the Receiving Party may not use in whole or in part any Proprietary and Confidential Information to:

    1 Manufacture or enable manufacture by itself or any third party of the Disclosing Party's products, products similar thereto, or products derived there from, without the prior written express consent of the Disclosing Party;

    2 Decompile, disassemble, decode, reproduce, redesign, reverse engineer or manufacture any products or equipment of the Disclosing Party or any part thereof; or

    3 Perform any services, including services relating to the products or equipment of the Disclosing party.

    This clause 14 shall survive any expiration or termination of this Agreement.

16. The Proprietary and Confidential Information exchanged under this Agreement may be subject to the provisions of the I.TAR. [International Traffic Arms Regulations] promulgated there under The National Conventional Arms Control Committee (NCACC)

17. This Agreement may be signed in one or more counterparts (including faxed and/or emailed PDF copies), each of which shall be deemed one and the same original. Reproductions of this executed original (with reproduced signatures) shall be deemed to be original counterparts of this Agreement.

IN WITNESS WHEREOF, the parties have caused this Agreement to be duly executed by their duly authorized representatives on the day and year first above written.

Aerospace Development Corporation Group	**Central University of Technology, Free State**
Name: Paul Potgieter (Jnr)	Name*: Prof A Ngowi
Title: Director	Title*: DVC: Research, Innovation & Eng
	*Duly authorised

Page **3** of **3**

© Central University of Technology, Free State

APPENDIX D: F-DISTRIBUTION TABLE

	F-table of Critical Values of α = 0.05 for F(df1, df2)																		
	DF1=1	**2**	**3**	**4**	**5**	**6**	**7**	**8**	**9**	**10**	**12**	**15**	**20**	**24**	**30**	**40**	**60**	**120**	**∞**
DF2=1	161.45	199.50	215.71	224.58	230.16	233.99	236.77	238.88	240.54	241.88	243.91	245.95	248.01	249.05	250.10	251.14	252.20	253.25	254.31
2	18.51	19.00	19.16	19.25	19.30	19.33	19.35	19.37	19.38	19.40	19.41	19.43	19.45	19.45	19.46	19.47	19.48	19.49	19.50
3	10.13	9.55	9.28	9.12	9.01	8.94	8.89	8.85	8.81	8.79	8.74	8.70	8.66	8.64	8.62	8.59	8.57	8.55	8.53
4	7.71	6.94	6.59	6.39	6.26	6.16	6.09	6.04	6.00	5.96	5.91	5.86	5.80	5.77	5.75	5.72	5.69	5.66	5.63
5	6.61	5.79	5.41	5.19	5.05	4.95	4.88	4.82	4.77	4.74	4.68	4.62	4.56	4.53	4.50	4.46	4.43	4.40	4.37
6	5.99	5.14	4.76	4.53	4.39	4.28	4.21	4.15	4.10	4.06	4.00	3.94	3.87	3.84	3.81	3.77	3.74	3.70	3.67
7	5.59	4.74	4.35	4.12	3.97	3.87	3.79	3.73	3.68	3.64	3.57	3.51	3.44	3.41	3.38	3.34	3.30	3.27	3.23
8	5.32	4.46	4.07	3.84	3.69	3.58	3.50	3.44	3.39	3.35	3.28	3.22	3.15	3.12	3.08	3.04	3.01	2.97	2.93
9	5.12	4.26	3.86	3.63	3.48	3.37	3.29	3.23	3.18	3.14	3.07	3.01	2.94	2.90	2.86	2.83	2.79	2.75	2.71
10	4.96	4.10	3.71	3.48	3.33	3.22	3.14	3.07	3.02	2.98	2.91	2.85	2.77	2.74	2.70	2.66	2.62	2.58	2.54
11	4.84	3.98	3.59	3.36	3.20	3.09	3.01	2.95	2.90	2.85	2.79	2.72	2.65	2.61	2.57	2.53	2.49	2.45	2.40
12	4.75	3.89	3.49	3.26	3.11	3.00	2.91	2.85	2.80	2.75	2.69	2.62	2.54	2.51	2.47	2.43	2.38	2.34	2.30
13	4.67	3.81	3.41	3.18	3.03	2.92	2.83	2.77	2.71	2.67	2.60	2.53	2.46	2.42	2.38	2.34	2.30	2.25	2.21
14	4.60	3.74	3.34	3.11	2.96	2.85	2.76	2.70	2.65	2.60	2.53	2.46	2.39	2.35	2.31	2.27	2.22	2.18	2.13
15	4.54	3.68	3.29	3.06	2.90	2.79	2.71	2.64	2.59	2.54	2.48	2.40	2.33	2.29	2.25	2.20	2.16	2.11	2.07
16	4.49	3.63	3.24	3.01	2.85	2.74	2.66	2.59	2.54	2.49	2.42	2.35	2.28	2.24	2.19	2.15	2.11	2.06	2.01
17	4.45	3.59	3.20	2.96	2.81	2.70	2.61	2.55	2.49	2.45	2.38	2.31	2.23	2.19	2.15	2.10	2.06	2.01	1.96
18	4.41	3.55	3.16	2.93	2.77	2.66	2.58	2.51	2.46	2.41	2.34	2.27	2.19	2.15	2.11	2.06	2.02	1.97	1.92
19	4.38	3.52	3.13	2.90	2.74	2.63	2.54	2.48	2.42	2.38	2.31	2.23	2.16	2.11	2.07	2.03	1.98	1.93	1.88
20	4.35	3.49	3.10	2.87	2.71	2.60	2.51	2.45	2.39	2.35	2.28	2.20	2.12	2.08	2.04	1.99	1.95	1.90	1.84
21	4.32	3.47	3.07	2.84	2.68	2.57	2.49	2.42	2.37	2.32	2.25	2.18	2.10	2.05	2.01	1.96	1.92	1.87	1.81
22	4.30	3.44	3.05	2.82	2.66	2.55	2.46	2.40	2.34	2.30	2.23	2.15	2.07	2.03	1.98	1.94	1.89	1.84	1.78
23	4.28	3.42	3.03	2.80	2.64	2.53	2.44	2.37	2.32	2.27	2.20	2.13	2.05	2.01	1.96	1.91	1.86	1.81	1.76
24	4.26	3.40	3.01	2.78	2.62	2.51	2.42	2.36	2.30	2.25	2.18	2.11	2.03	1.98	1.94	1.89	1.84	1.79	1.73
25	4.24	3.39	2.99	2.76	2.60	2.49	2.40	2.34	2.28	2.24	2.16	2.09	2.01	1.96	1.92	1.87	1.82	1.77	1.71
26	4.23	3.37	2.98	2.74	2.59	2.47	2.39	2.32	2.27	2.22	2.15	2.07	1.99	1.95	1.90	1.85	1.80	1.75	1.69
27	4.21	3.35	2.96	2.73	2.57	2.46	2.37	2.31	2.25	2.20	2.13	2.06	1.97	1.93	1.88	1.84	1.79	1.73	1.67
28	4.20	3.34	2.95	2.71	2.56	2.45	2.36	2.29	2.24	2.19	2.12	2.04	1.96	1.91	1.87	1.82	1.77	1.71	1.65
29	4.18	3.33	2.93	2.70	2.55	2.43	2.35	2.28	2.22	2.18	2.10	2.03	1.94	1.90	1.85	1.81	1.75	1.70	1.64
30	4.17	3.32	2.92	2.69	2.53	2.42	2.33	2.27	2.21	2.16	2.09	2.01	1.93	1.89	1.84	1.79	1.74	1.68	1.62
40	4.08	3.23	2.84	2.61	2.45	2.34	2.25	2.18	2.12	2.08	2.00	1.92	1.84	1.79	1.74	1.69	1.64	1.58	1.51
60	4.00	3.15	2.76	2.53	2.37	2.25	2.17	2.10	2.04	1.99	1.92	1.84	1.75	1.70	1.65	1.59	1.53	1.47	1.39
120	3.92	3.07	2.68	2.45	2.29	2.18	2.09	2.02	1.96	1.91	1.83	1.75	1.66	1.61	1.55	1.50	1.43	1.35	1.25
∞	3.84	3.00	2.60	2.37	2.21	2.10	2.01	1.94	1.88	1.83	1.75	1.67	1.57	1.52	1.46	1.39	1.32	1.22	1.00

APPENDIX E: GEOMETRIC DEVIATION REPORT OF SCAN A

E.1. Scan A results

technology innovation
AGENCY

PDTS

Product Development Technology Station

Product Name	Comparison Report
Part Name	Post Heat Treatment
Part Number	19-247 - Landing Gear Scan and Compare
Department	PDTS
Inspector	Let-Mari van Heerden
Date	Oct 16, 2019
Unit	mm

Disclaimer
The results of this analysis and forecastings are believed to be reliable but are not to be construed as providing a warranty, including any warranty of merchantability or fitness for purpose, or representation for which 3D Systems, Inc. assumes legal responsibility. Users should undertake sufficient verification and iterative testing to determine the suitability of any information presented. Nothing herein is to be taken as permission, inducement or recommendation by 3D Systems, Inc. to practice any patented invention without a license or to in any way infringe upon the intellectual property rights of any other party.

E.2. Reference data

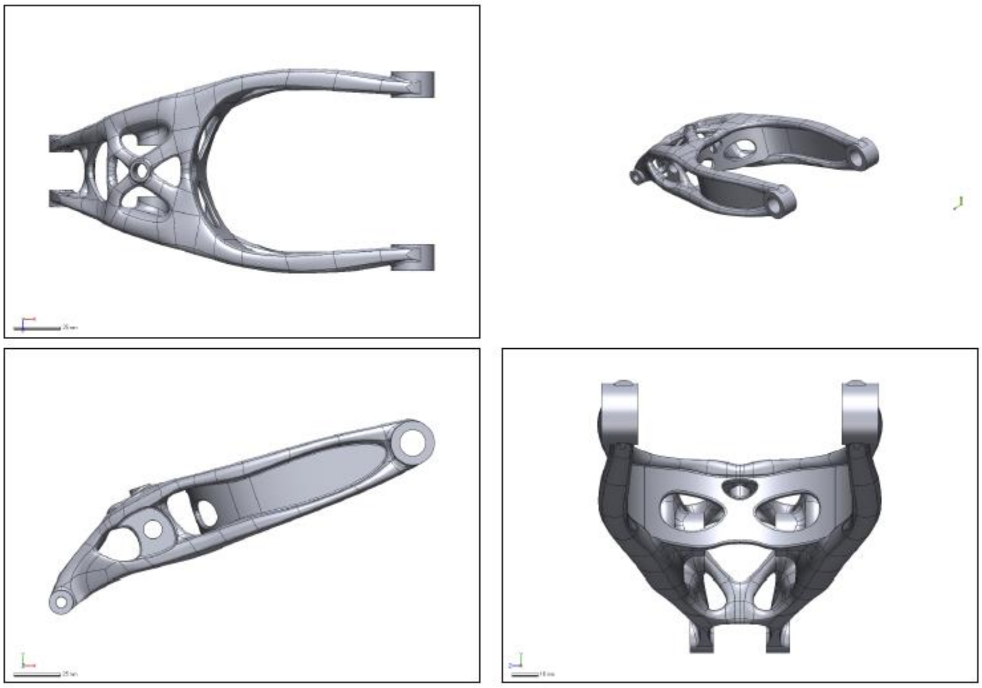

E.3. Data alignment

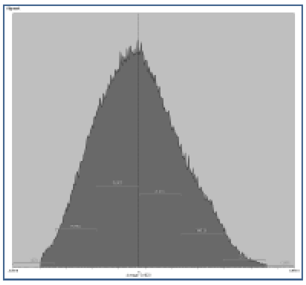

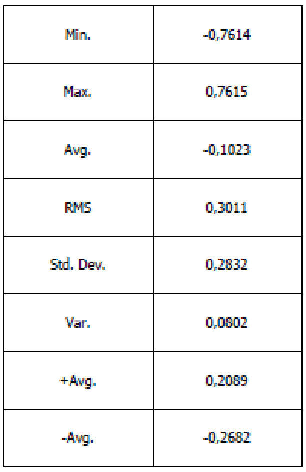

Min.	-0,7614
Max.	0,7615
Avg.	-0,1023
RMS	0,3011
Std. Dev.	0,2832
Var.	0,0802
+Avg.	0,2089
-Avg.	-0,2682

E.4. Results data

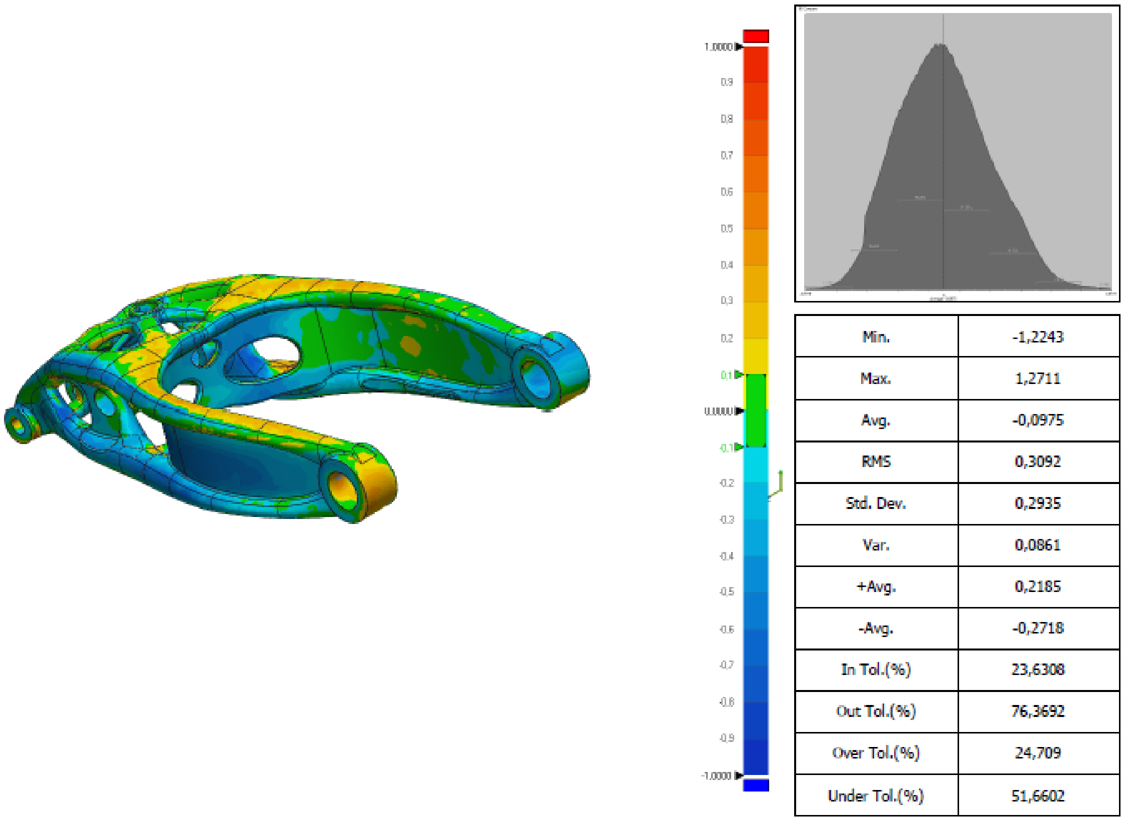

Min.	-1,2243
Max.	1,2711
Avg.	-0,0975
RMS	0,3092
Std. Dev.	0,2935
Var.	0,0861
+Avg.	0,2185
-Avg.	-0,2718
In Tol.(%)	23,6308
Out Tol.(%)	76,3692
Over Tol.(%)	24,709
Under Tol.(%)	51,6602

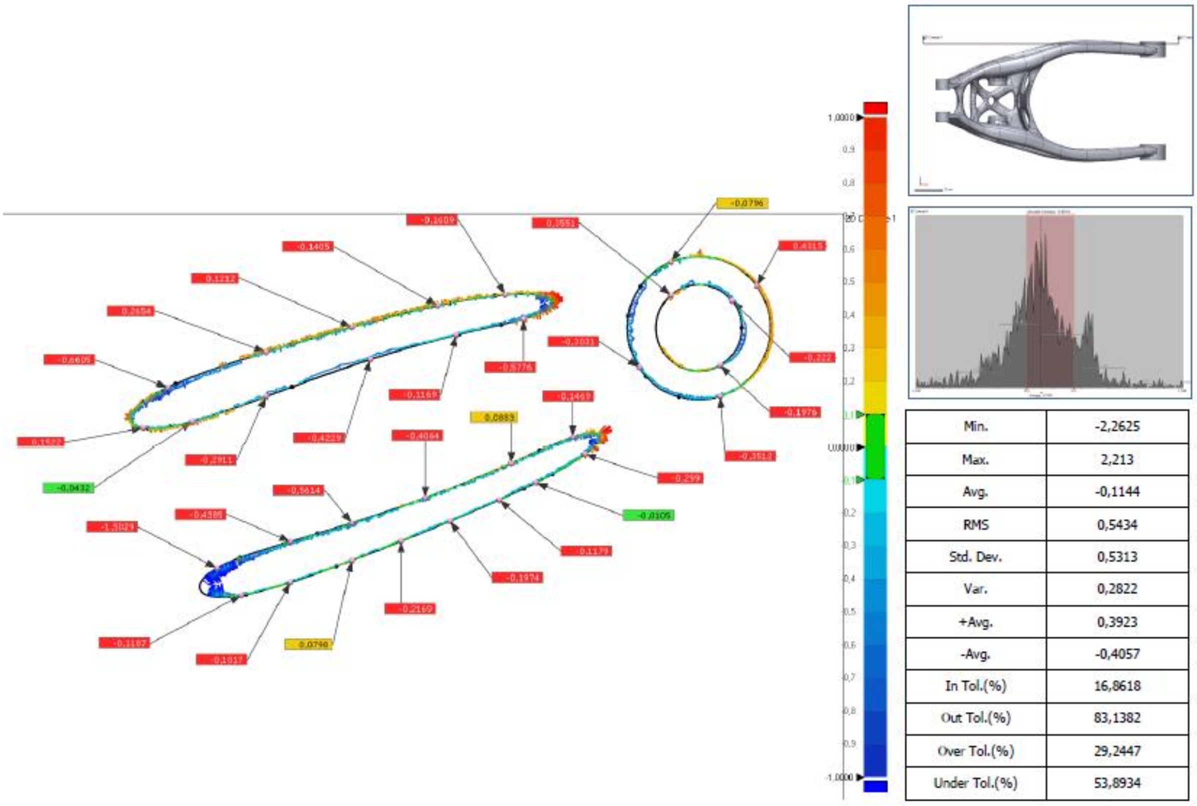

Min.	-2,2625
Max.	2,213
Avg.	-0,1144
RMS	0,5434
Std. Dev.	0,5313
Var.	0,2822
+Avg.	0,3923
-Avg.	-0,4057
In Tol.(%)	16,8618
Out Tol.(%)	83,1382
Over Tol.(%)	29,2447
Under Tol.(%)	53,8934

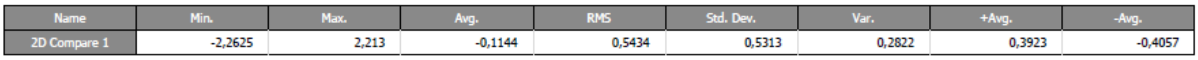

Name	Min.	Max.	Avg.	RMS	Std. Dev.	Var.	+Avg.	-Avg.
2D Compare 1	-2,2625	2,213	-0,1144	0,5434	0,5313	0,2822	0,3923	-0,4057

Name	Result Name	Tolerance	Gap Dist.	Reference Pos.		Measured Pos.	
				X	Y	X	Y
2D Compare 1: 1	Result Data - Landing Fork Gear	±0,1	-0,6605	-242	-61,2768	-241,7169	-61,8735
2D Compare 1: 2	Result Data - Landing Fork Gear	±0,1	0,2654	-226	-55,5326	-226,0776	-55,2788
2D Compare 1: 3	Result Data - Landing Fork Gear	±0,1	0,1212	-212	-51,4755	-212,0322	-51,3587
2D Compare 1: 4	Result Data - Landing Fork Gear	±0,1	-0,1405	-198	-47,9645	-197,9701	-48,1018
2D Compare 1: 5	Result Data - Landing Fork Gear	±0,1	-0,1609	-187	-46,1694	-186,9863	-46,3297
2D Compare 1: 6	Result Data - Landing Fork Gear	±0,1	-0,5776	-184	-50,1502	-184,1577	-49,5946
2D Compare 1: 7	Result Data - Landing Fork Gear	±0,1	-0,1169	-195	-52,7476	-195,0276	-52,634
2D Compare 1: 8	Result Data - Landing Fork Gear	±0,1	-0,4229	-209	-56,7268	-209,1296	-56,3242
2D Compare 1: 9	Result Data - Landing Fork Gear	±0,1	-0,2911	-226	-62,757	-226,1011	-62,484
2D Compare 1: 10	Result Data - Landing Fork Gear	±0,1	-0,0432	-238	-66,8347	-238,0119	-66,7932
2D Compare 1: 11	Result Data - Landing Fork Gear	±0,1	0,1522	-246	-67,8401	-246,0238	-67,9904
2D Compare 1: 12	Result Data - Landing Fork Gear	±0,1	-1,5029	-234	-90,7966	-233,2531	-92,1007
2D Compare 1: 13	Result Data - Landing Fork Gear	±0,1	-0,4385	-222	-86,4691	-221,8759	-86,8897
2D Compare 1: 14	Result Data - Landing Fork Gear	±0,1	-0,5614	-212	-83,4418	-211,8304	-83,977
2D Compare 1: 15	Result Data - Landing Fork Gear	±0,1	-0,4064	-200	-79,3645	-199,8606	-79,7463
2D Compare 1: 16	Result Data - Landing Fork Gear	±0,1	0,0883	-186	-73,7317	-186,0358	-73,6509
2D Compare 1: 17	Result Data - Landing Fork Gear	±0,1	-0,1469	-176	-69,3439	-175,9515	-69,4825
2D Compare 1: 18	Result Data - Landing Fork Gear	±0,1	-0,299	-174	-72,2249	-174,1812	-71,987

Name	Result Name	Tolerance	Gap Dist.	Reference Pos.		Measured Pos.	
				X	Y	X	Y
2D Compare 1: 19	Result Data - Landing Fork Gear	±0,1	-0,0105	-182	-76,8813	-182,0046	-76,8719
2D Compare 1: 20	Result Data - Landing Fork Gear	±0,1	-0,1179	-188	-79,6768	-188,048	-79,5692
2D Compare 1: 21	Result Data - Landing Fork Gear	±0,1	-0,1974	-196	-83,1202	-196,0761	-82,9381
2D Compare 1: 22	Result Data - Landing Fork Gear	±0,1	-0,2169	-204	-86,3952	-204,0807	-86,1939
2D Compare 1: 23	Result Data - Landing Fork Gear	±0,1	0,0798	-212	-89,5234	-211,9717	-89,598
2D Compare 1: 24	Result Data - Landing Fork Gear	±0,1	-0,1017	-222	-93,0864	-222,0313	-92,9896
2D Compare 1: 25	Result Data - Landing Fork Gear	±0,1	-0,1187	-230	-95,1772	-230,0198	-95,0601
2D Compare 1: 26	Result Data - Landing Fork Gear	±0,1	-0,3031	-165,163	-58	-164,9104	-57,8324
2D Compare 1: 27	Result Data - Landing Fork Gear	±0,1	-0,0796	-160	-40,8627	-159,9678	-40,9355
2D Compare 1: 28	Result Data - Landing Fork Gear	±0,1	0,4315	-146	-44,7554	-145,6503	-44,5026
2D Compare 1: 29	Result Data - Landing Fork Gear	±0,1	-0,3512	-152	-62,7137	-152,1024	-62,3778
2D Compare 1: 30	Result Data - Landing Fork Gear	±0,1	-0,222	-150	-47,1773	-149,8285	-47,0363
2D Compare 1: 31	Result Data - Landing Fork Gear	±0,1	-0,1976	-152	-57,6797	-151,9028	-57,8517
2D Compare 1: 32	Result Data - Landing Fork Gear	±0,1	0,3551	-160	-46,2724	-159,761	-46,535
Min.			-1,5029	-246,0000	-95,1772	-246,0238	-95,0601
Max.			0,4315	-146,0000	-40,8627	-145,6503	-40,9355
Avg.			-0,1935	-196,4426	-66,7553	-196,3931	-66,7778

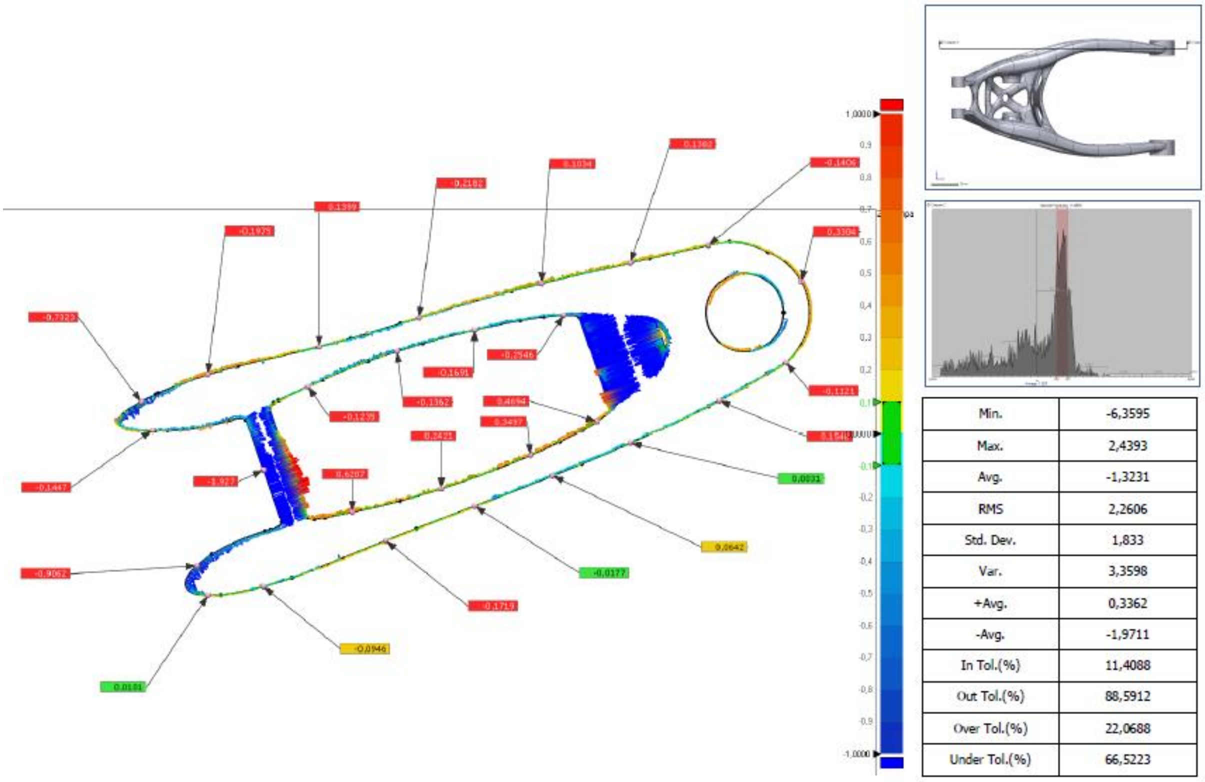

Min.	-6,3595
Max.	2,4393
Avg.	-1,3231
RMS	2,2606
Std. Dev.	1,833
Var.	3,3598
+Avg.	0,3362
-Avg.	-1,9711
In Tol.(%)	11,4088
Out Tol.(%)	88,5912
Over Tol.(%)	22,0688
Under Tol.(%)	66,5223

Name	Min.	Max.	Avg.	RMS	Std. Dev.	Var.	+Avg.	-Avg.
2D Compare 2	-6,3595	2,4393	-1,3231	2,2606	1,833	3,3598	0,3362	-1,9711

Name	Result Name	Tolerance	Gap Dist.	Reference Pos.		Measured Pos.	
				X	Y	X	Y
2D Compare 2: 1	Result Data - Landing Fork Gear	±0,1	-0,1235	-234	-64,8652	-234,052	-64,7532
2D Compare 2: 2	Result Data - Landing Fork Gear	±0,1	-0,1362	-218	-58,5425	-218,0413	-58,4127
2D Compare 2: 3	Result Data - Landing Fork Gear	±0,1	-0,1691	-204	-54,6913	-204,0388	-54,5267
2D Compare 2: 4	Result Data - Landing Fork Gear	±0,1	-0,2546	-188	-52,0546	-188,0064	-51,8001
2D Compare 2: 5	Result Data - Landing Fork Gear	±0,1	0,4694	-182	-71,1709	-182,2669	-70,7847
2D Compare 2: 6	Result Data - Landing Fork Gear	±0,1	0,3497	-194	-77,3555	-194,1387	-77,0345
2D Compare 2: 7	Result Data - Landing Fork Gear	±0,1	0,2421	-210	-83,3333	-210,0741	-83,1028
2D Compare 2: 8	Result Data - Landing Fork Gear	±0,1	0,6207	-226	-87,5378	-226,1258	-86,93
2D Compare 2: 9	Result Data - Landing Fork Gear	±0,1	-1,927	-241,9597	-80	-240,1408	-79,3638
2D Compare 2: 10	Result Data - Landing Fork Gear	±0,1	-0,1447	-262	-72,8435	-261,9978	-72,6988
2D Compare 2: 11	Result Data - Landing Fork Gear	±0,1	-0,9062	-254	-97,1732	-253,3927	-97,8457
2D Compare 2: 12	Result Data - Landing Fork Gear	±0,1	-0,7323	-264	-67,6084	-263,653	-68,2533
2D Compare 2: 13	Result Data - Landing Fork Gear	±0,1	-0,1975	-252	-62,6988	-251,9415	-62,8874
2D Compare 2: 14	Result Data - Landing Fork Gear	±0,1	0,1399	-232	-57,7205	-232,0338	-57,5847
2D Compare 2: 15	Result Data - Landing Fork Gear	±0,1	-0,2182	-214	-52,5128	-213,9355	-52,7212
2D Compare 2: 16	Result Data - Landing Fork Gear	±0,1	0,1034	-192	-46,3562	-192,0245	-46,2557
2D Compare 2: 17	Result Data - Landing Fork Gear	±0,1	0,1302	-176	-42,6443	-176,0287	-42,5173
2D Compare 2: 18	Result Data - Landing Fork Gear	±0,1	-0,1406	-162	-39,5252	-161,972	-39,663

© Central University of Technology, Free State

Name	Result Name	Tolerance	Gap Dist.	Reference Pos.		Measured Pos.	
				X	Y	X	Y
2D Compare 2: 19	Result Data - Landing Fork Gear	±0,1	0,3304	-145,2145	-46	-144,9245	-45,8417
2D Compare 2: 20	Result Data - Landing Fork Gear	±0,1	-0,1121	-148	-60,5483	-148,0717	-60,4621
2D Compare 2: 21	Result Data - Landing Fork Gear	±0,1	0,1548	-160	-67,3973	-159,9282	-67,5344
2D Compare 2: 22	Result Data - Landing Fork Gear	±0,1	0,0031	-176	-75,1421	-175,9987	-75,145
2D Compare 2: 23	Result Data - Landing Fork Gear	±0,1	0,0642	-190	-81,0225	-189,9761	-81,0821
2D Compare 2: 24	Result Data - Landing Fork Gear	±0,1	-0,0177	-204	-86,4927	-204,0064	-86,4762
2D Compare 2: 25	Result Data - Landing Fork Gear	±0,1	-0,1719	-220	-92,6887	-220,0638	-92,5291
2D Compare 2: 26	Result Data - Landing Fork Gear	±0,1	-0,0946	-242	-100,9116	-242,0245	-100,8203
2D Compare 2: 27	Result Data - Landing Fork Gear	±0,1	0,0101	-252	-102,5308	-252,0008	-102,5409
Min.			-1,9270	-264,0000	-102,5308	-263,6530	-102,5409
Max.			0,6207	-145,2145	-39,5252	-144,9245	-39,6630
Avg.			-0,1010	-209,0065	-69,6803	-208,9207	-69,6136

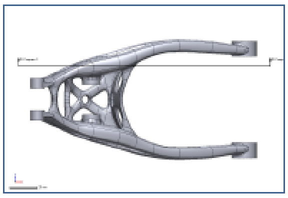

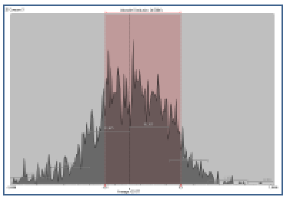

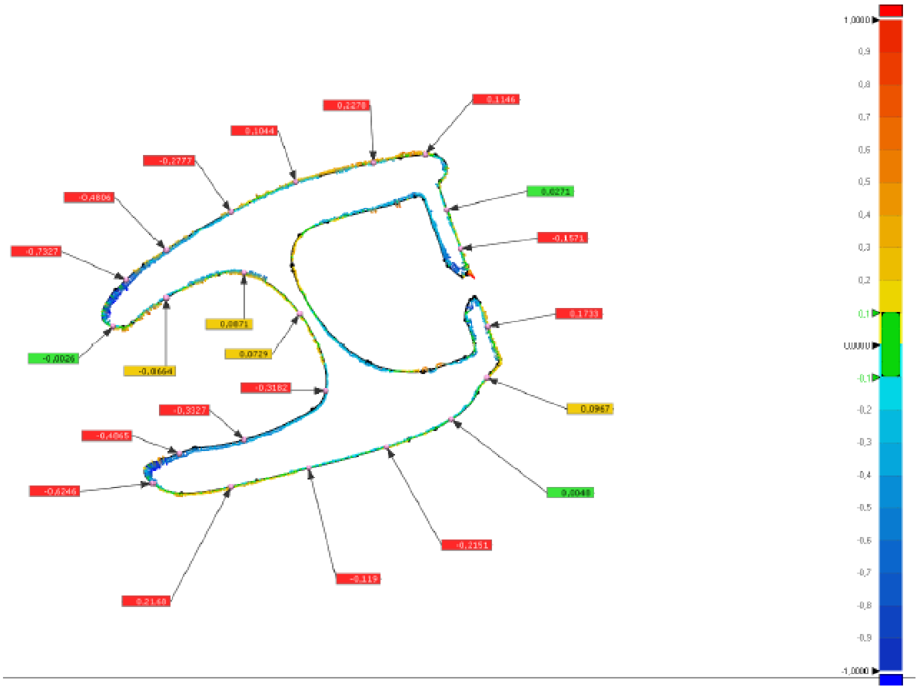

Min.	-1,3
Max.	1,343
Avg.	-0,1077
RMS	0,3319
Std. Dev.	0,314
Var.	0,0986
+Avg.	0,1964
-Avg.	-0,2938
In Tol.(%)	24,5604
Out Tol.(%)	75,4396
Over Tol.(%)	26,9242
Under Tol.(%)	48,5154

© Central University of Technology, Free State

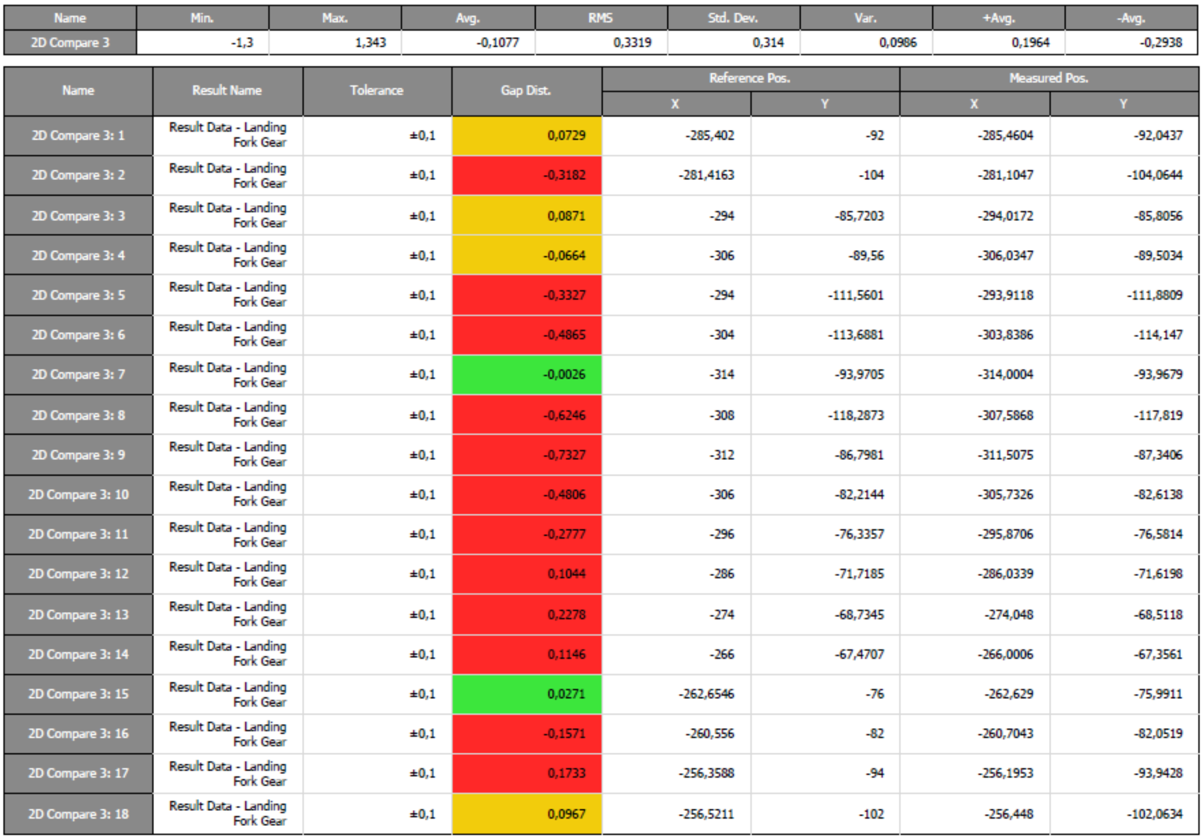

Name	Min.	Max.	Avg.	RMS	Std. Dev.	Var.	+Avg.	-Avg.
2D Compare 3	-1,3	1,343	-0,1077	0,3319	0,314	0,0986	0,1964	-0,2938

Name	Result Name	Tolerance	Gap Dist.	Reference Pos.		Measured Pos.	
				X	Y	X	Y
2D Compare 3: 1	Result Data - Landing Fork Gear	±0,1	0,0729	-285,402	-92	-285,4604	-92,0437
2D Compare 3: 2	Result Data - Landing Fork Gear	±0,1	-0,3182	-281,4163	-104	-281,1047	-104,0644
2D Compare 3: 3	Result Data - Landing Fork Gear	±0,1	0,0871	-294	-85,7203	-294,0172	-85,8056
2D Compare 3: 4	Result Data - Landing Fork Gear	±0,1	-0,0664	-306	-89,56	-306,0347	-89,5034
2D Compare 3: 5	Result Data - Landing Fork Gear	±0,1	-0,3327	-294	-111,5601	-293,9118	-111,8809
2D Compare 3: 6	Result Data - Landing Fork Gear	±0,1	-0,4865	-304	-113,6881	-303,8386	-114,147
2D Compare 3: 7	Result Data - Landing Fork Gear	±0,1	-0,0026	-314	-93,9705	-314,0004	-93,9679
2D Compare 3: 8	Result Data - Landing Fork Gear	±0,1	-0,6246	-308	-118,2873	-307,5868	-117,819
2D Compare 3: 9	Result Data - Landing Fork Gear	±0,1	-0,7327	-312	-86,7981	-311,5075	-87,3406
2D Compare 3: 10	Result Data - Landing Fork Gear	±0,1	-0,4806	-306	-82,2144	-305,7326	-82,6138
2D Compare 3: 11	Result Data - Landing Fork Gear	±0,1	-0,2777	-296	-76,3357	-295,8706	-76,5814
2D Compare 3: 12	Result Data - Landing Fork Gear	±0,1	0,1044	-286	-71,7185	-286,0339	-71,6198
2D Compare 3: 13	Result Data - Landing Fork Gear	±0,1	0,2278	-274	-68,7345	-274,048	-68,5118
2D Compare 3: 14	Result Data - Landing Fork Gear	±0,1	0,1146	-266	-67,4707	-266,0006	-67,3561
2D Compare 3: 15	Result Data - Landing Fork Gear	±0,1	0,0271	-262,6546	-76	-262,629	-75,9911
2D Compare 3: 16	Result Data - Landing Fork Gear	±0,1	-0,1571	-260,556	-82	-260,7043	-82,0519
2D Compare 3: 17	Result Data - Landing Fork Gear	±0,1	0,1733	-256,3588	-94	-256,1953	-93,9428
2D Compare 3: 18	Result Data - Landing Fork Gear	±0,1	0,0967	-256,5211	-102	-256,448	-102,0634

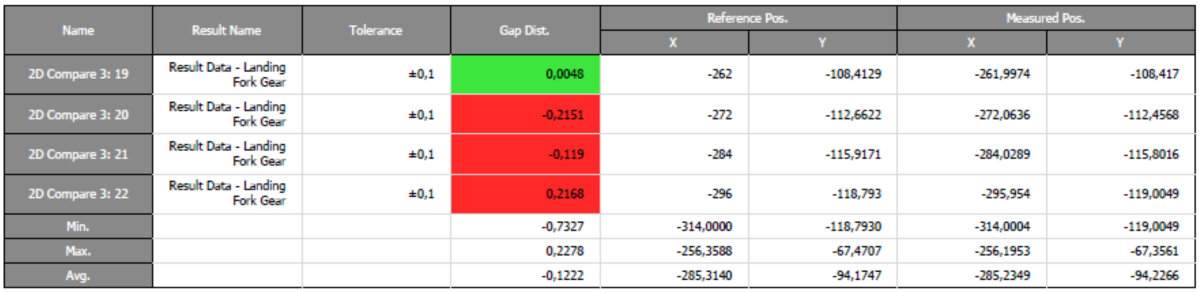

Name	Result Name	Tolerance	Gap Dist.	Reference Pos.		Measured Pos.	
				X	Y	X	Y
2D Compare 3: 19	Result Data - Landing Fork Gear	±0,1	0,0048	-262	-108,4129	-261,9974	-108,417
2D Compare 3: 20	Result Data - Landing Fork Gear	±0,1	-0,2151	-272	-112,6622	-272,0636	-112,4568
2D Compare 3: 21	Result Data - Landing Fork Gear	±0,1	-0,119	-284	-115,9171	-284,0289	-115,8016
2D Compare 3: 22	Result Data - Landing Fork Gear	±0,1	0,2168	-296	-118,793	-295,954	-119,0049
Min.			-0,7327	-314,0000	-118,7930	-314,0004	-119,0049
Max.			0,2278	-256,3588	-67,4707	-256,1953	-67,3561
Avg.			-0,1222	-285,3140	-94,1747	-285,2349	-94,2266

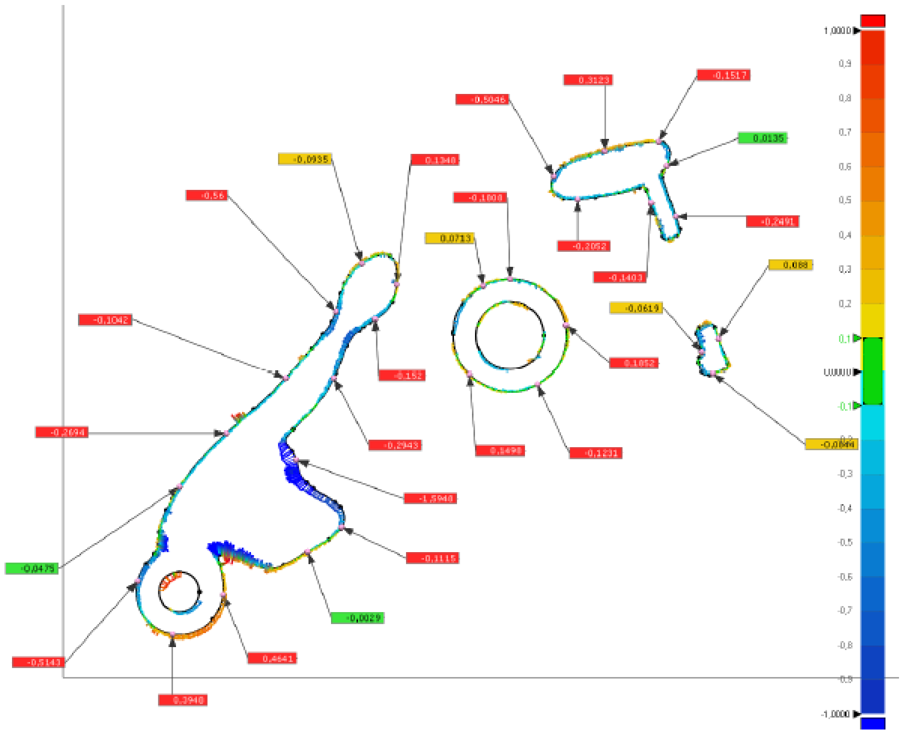

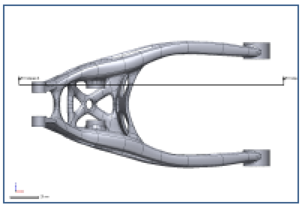

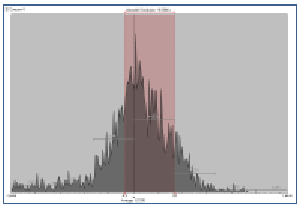

Min.	-2,2334
Max.	1,4743
Avg.	-0,1938
RMS	0,521
Std. Dev.	0,4836
Var.	0,2339
+Avg.	0,2477
-Avg.	-0,4217
In Tol.(%)	19,5094
Out Tol.(%)	80,4906
Over Tol.(%)	24,2458
Under Tol.(%)	56,2447

Name	Min.	Max.	Avg.	RMS	Std. Dev.	Var.	+Avg.	-Avg.
2D Compare 4	-2,2334	1,4743	-0,1938	0,521	0,4836	0,2339	0,2477	-0,4217

Name	Result Name	Tolerance	Gap Dist.	Reference Pos.		Measured Pos.	
				X	Y	X	Y
2D Compare 4: 1	Result Data - Landing Fork Gear	±0,1	0,4641	-336,5196	-136	-336,0586	-136,0535
2D Compare 4: 2	Result Data - Landing Fork Gear	±0,1	0,3948	-344	-141,8879	-344,063	-142,2777
2D Compare 4: 3	Result Data - Landing Fork Gear	±0,1	-0,5143	-349,1824	-134	-348,6836	-134,1253
2D Compare 4: 4	Result Data - Landing Fork Gear	±0,1	-0,0475	-342,942	-120	-342,9026	-120,0266
2D Compare 4: 5	Result Data - Landing Fork Gear	±0,1	-0,2694	-336	-112,1367	-335,8184	-112,3356
2D Compare 4: 6	Result Data - Landing Fork Gear	±0,1	-0,1042	-327,2183	-104	-327,1408	-104,0697
2D Compare 4: 7	Result Data - Landing Fork Gear	±0,1	-0,56	-319,793	-94	-319,2613	-94,1759
2D Compare 4: 8	Result Data - Landing Fork Gear	±0,1	-0,0935	-316	-86,8702	-315,9436	-86,9447
2D Compare 4: 9	Result Data - Landing Fork Gear	±0,1	0,1348	-310,8225	-90	-310,6885	-90,0151
2D Compare 4: 10	Result Data - Landing Fork Gear	±0,1	-0,152	-314	-95,1208	-314,0799	-94,9915
2D Compare 4: 11	Result Data - Landing Fork Gear	±0,1	-0,2943	-320,1284	-104	-320,3936	-103,8727
2D Compare 4: 12	Result Data - Landing Fork Gear	±0,1	-1,5948	-325,6165	-116	-327,1194	-116,5334
2D Compare 4: 13	Result Data - Landing Fork Gear	±0,1	-0,0029	-324	-129,6635	-324,0015	-129,6609
2D Compare 4: 14	Result Data - Landing Fork Gear	±0,1	-0,1115	-318,9716	-126	-319,068	-125,944
2D Compare 4: 15	Result Data - Landing Fork Gear	±0,1	0,1498	-300	-103,4576	-300,1069	-103,5626
2D Compare 4: 16	Result Data - Landing Fork Gear	±0,1	-0,1231	-290	-104,9534	-290,0575	-104,8446
2D Compare 4: 17	Result Data - Landing Fork Gear	±0,1	0,1852	-285,7559	-96	-285,574	-95,9652
2D Compare 4: 18	Result Data - Landing Fork Gear	±0,1	-0,1808	-294	-89,1711	-294,0002	-89,3519

© Central University of Technology, Free State

Name	Result Name	Tolerance	Gap Dist.	Reference Pos.		Measured Pos.	
				X	Y	X	Y
2D Compare 4: 19	Result Data - Landing Fork Gear	±0,1	0,0713	-298	-90,1805	-298,035	-90,1183
2D Compare 4: 20	Result Data - Landing Fork Gear	±0,1	-0,5046	-287,5762	-74	-287,1433	-74,2593
2D Compare 4: 21	Result Data - Landing Fork Gear	±0,1	0,3123	-280	-70,3202	-280,079	-70,018
2D Compare 4: 22	Result Data - Landing Fork Gear	±0,1	-0,1517	-272	-68,8914	-272,0149	-69,0424
2D Compare 4: 23	Result Data - Landing Fork Gear	±0,1	0,0135	-270,7714	-72,5	-270,7595	-72,5064
2D Compare 4: 24	Result Data - Landing Fork Gear	±0,1	0,088	-263,143	-98	-263,0599	-97,971
2D Compare 4: 25	Result Data - Landing Fork Gear	±0,1	-0,0844	-264	-103,3221	-264,0292	-103,2429
2D Compare 4: 26	Result Data - Landing Fork Gear	±0,1	-0,0619	-265,6053	-100	-265,5468	-100,0201
2D Compare 4: 27	Result Data - Landing Fork Gear	±0,1	-0,1403	-273,1141	-78	-272,9817	-77,9537
2D Compare 4: 28	Result Data - Landing Fork Gear	±0,1	-0,2052	-284	-77,4708	-284,0113	-77,266
2D Compare 4: 29	Result Data - Landing Fork Gear	±0,1	-0,2491	-269,4387	-80	-269,6739	-80,0822
Min.			-1,5948	-349,1824	-141,8879	-348,6836	-142,2777
Max.			0,4641	-263,1430	-68,8914	-263,0599	-69,0424
Avg.			-0,1252	-302,8482	-99,8602	-302,8378	-99,9045

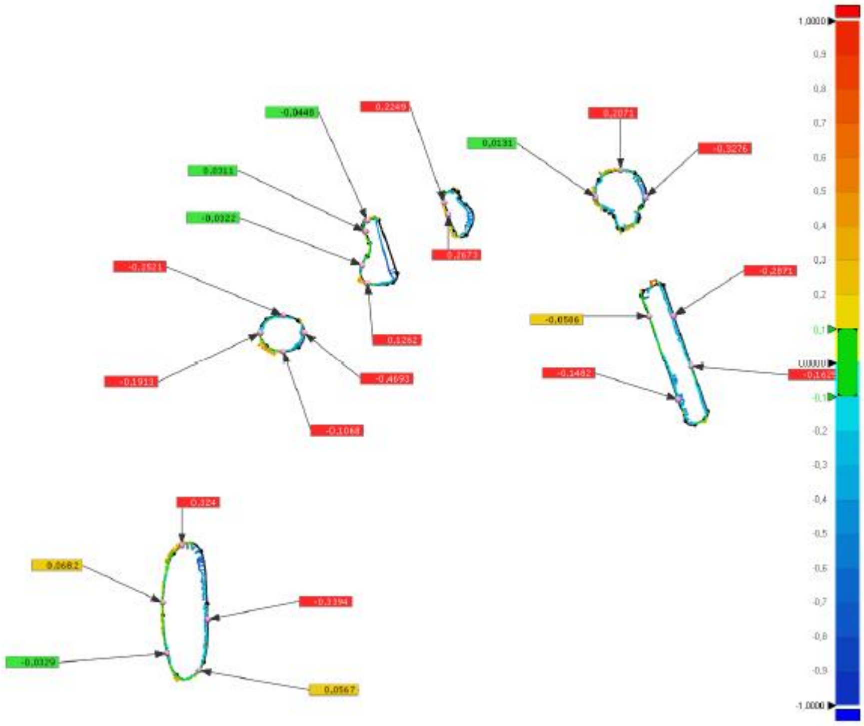

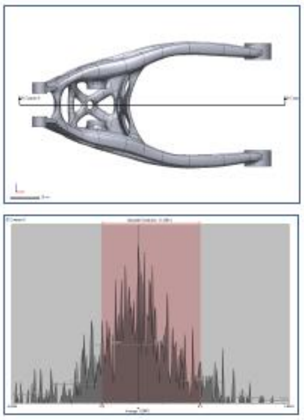

Min.	-0,8214
Max.	0,7411
Avg.	-0,0801
RMS	0,2683
Std. Dev.	0,2561
Var.	0,0656
+Avg.	0,1843
-Avg.	-0,2218
In Tol.(%)	31,2601
Out Tol.(%)	68,7399
Over Tol.(%)	21,8901
Under Tol.(%)	46,8498

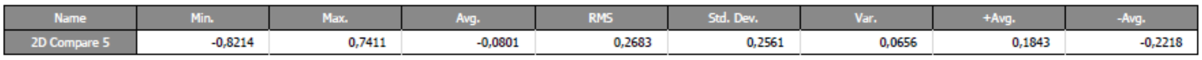

Name	Min.	Max.	Avg.	RMS	Std. Dev.	Var.	+Avg.	-Avg.
2D Compare 5	-0,8214	0,7411	-0,0801	0,2683	0,2561	0,0656	0,1843	-0,2218

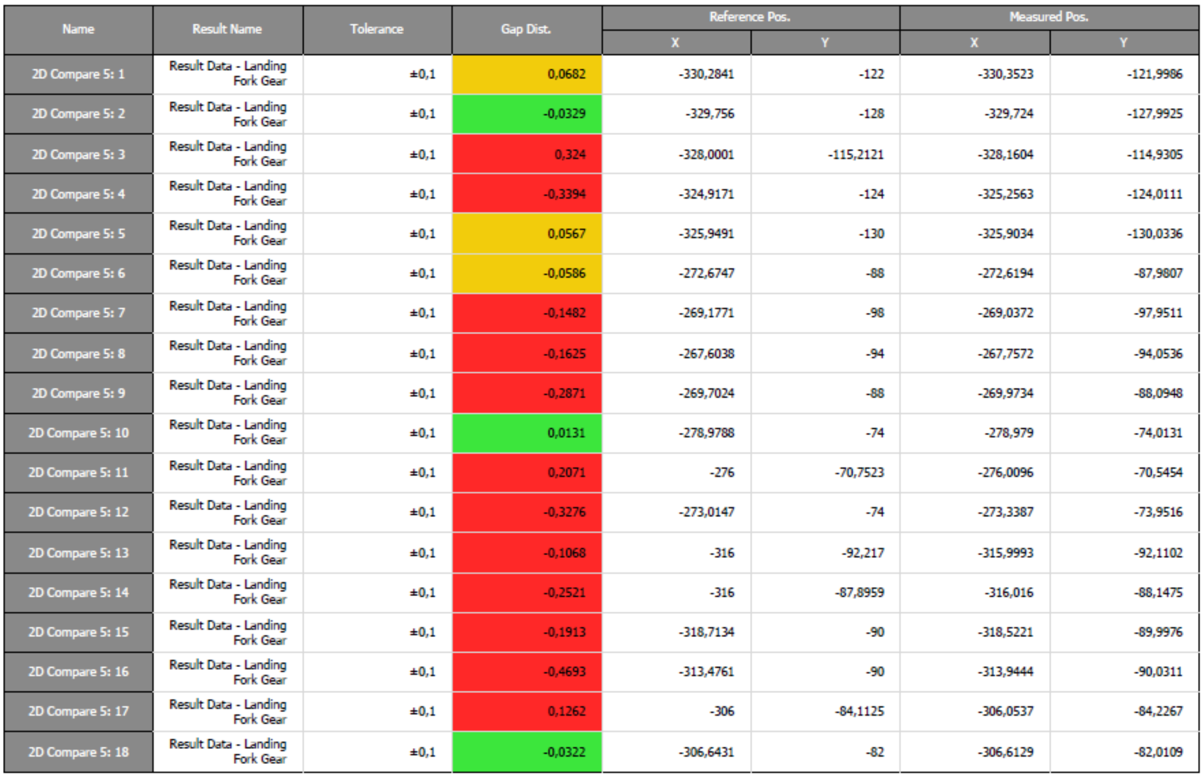

Name	Result Name	Tolerance	Gap Dist.	Reference Pos.		Measured Pos.	
				X	Y	X	Y
2D Compare 5: 1	Result Data - Landing Fork Gear	±0,1	0,0682	-330,2841	-122	-330,3523	-121,9986
2D Compare 5: 2	Result Data - Landing Fork Gear	±0,1	-0,0329	-329,756	-128	-329,724	-127,9925
2D Compare 5: 3	Result Data - Landing Fork Gear	±0,1	0,324	-328,0001	-115,2121	-328,1604	-114,9305
2D Compare 5: 4	Result Data - Landing Fork Gear	±0,1	-0,3394	-324,9171	-124	-325,2563	-124,0111
2D Compare 5: 5	Result Data - Landing Fork Gear	±0,1	0,0567	-325,9491	-130	-325,9034	-130,0336
2D Compare 5: 6	Result Data - Landing Fork Gear	±0,1	-0,0586	-272,6747	-88	-272,6194	-87,9807
2D Compare 5: 7	Result Data - Landing Fork Gear	±0,1	-0,1482	-269,1771	-98	-269,0372	-97,9511
2D Compare 5: 8	Result Data - Landing Fork Gear	±0,1	-0,1625	-267,6038	-94	-267,7572	-94,0536
2D Compare 5: 9	Result Data - Landing Fork Gear	±0,1	-0,2871	-269,7024	-88	-269,9734	-88,0948
2D Compare 5: 10	Result Data - Landing Fork Gear	±0,1	0,0131	-278,9788	-74	-278,979	-74,0131
2D Compare 5: 11	Result Data - Landing Fork Gear	±0,1	0,2071	-276	-70,7523	-276,0096	-70,5454
2D Compare 5: 12	Result Data - Landing Fork Gear	±0,1	-0,3276	-273,0147	-74	-273,3387	-73,9516
2D Compare 5: 13	Result Data - Landing Fork Gear	±0,1	-0,1068	-316	-92,217	-315,9993	-92,1102
2D Compare 5: 14	Result Data - Landing Fork Gear	±0,1	-0,2521	-316	-87,8959	-316,016	-88,1475
2D Compare 5: 15	Result Data - Landing Fork Gear	±0,1	-0,1913	-318,7134	-90	-318,5221	-89,9976
2D Compare 5: 16	Result Data - Landing Fork Gear	±0,1	-0,4693	-313,4761	-90	-313,9444	-90,0311
2D Compare 5: 17	Result Data - Landing Fork Gear	±0,1	0,1262	-306	-84,1125	-306,0537	-84,2267
2D Compare 5: 18	Result Data - Landing Fork Gear	±0,1	-0,0322	-306,6431	-82	-306,6129	-82,0109

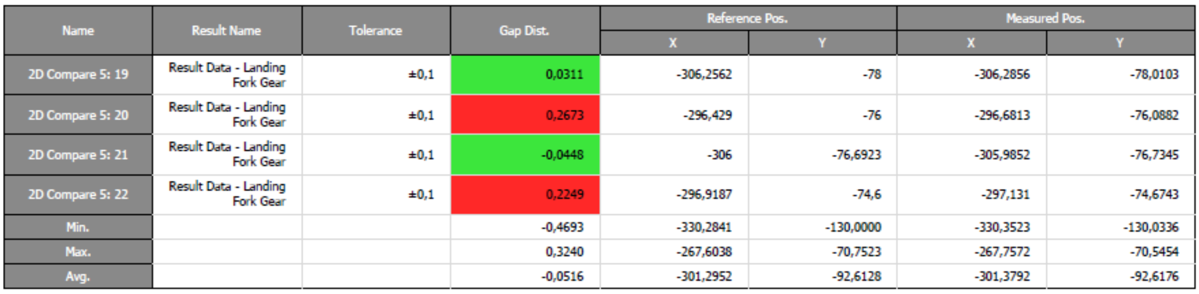

Name	Result Name	Tolerance	Gap Dist.	Reference Pos.		Measured Pos.	
				X	Y	X	Y
2D Compare 5: 19	Result Data - Landing Fork Gear	±0,1	0,0311	-306,2562	-78	-306,2856	-78,0103
2D Compare 5: 20	Result Data - Landing Fork Gear	±0,1	0,2673	-296,429	-76	-296,6813	-76,0882
2D Compare 5: 21	Result Data - Landing Fork Gear	±0,1	-0,0448	-306	-76,6923	-305,9852	-76,7345
2D Compare 5: 22	Result Data - Landing Fork Gear	±0,1	0,2249	-296,9187	-74,6	-297,131	-74,6743
Min.			-0,4693	-330,2841	-130,0000	-330,3523	-130,0336
Max.			0,3240	-267,6038	-70,7523	-267,7572	-70,5454
Avg.			-0,0516	-301,2952	-92,6128	-301,3792	-92,6176

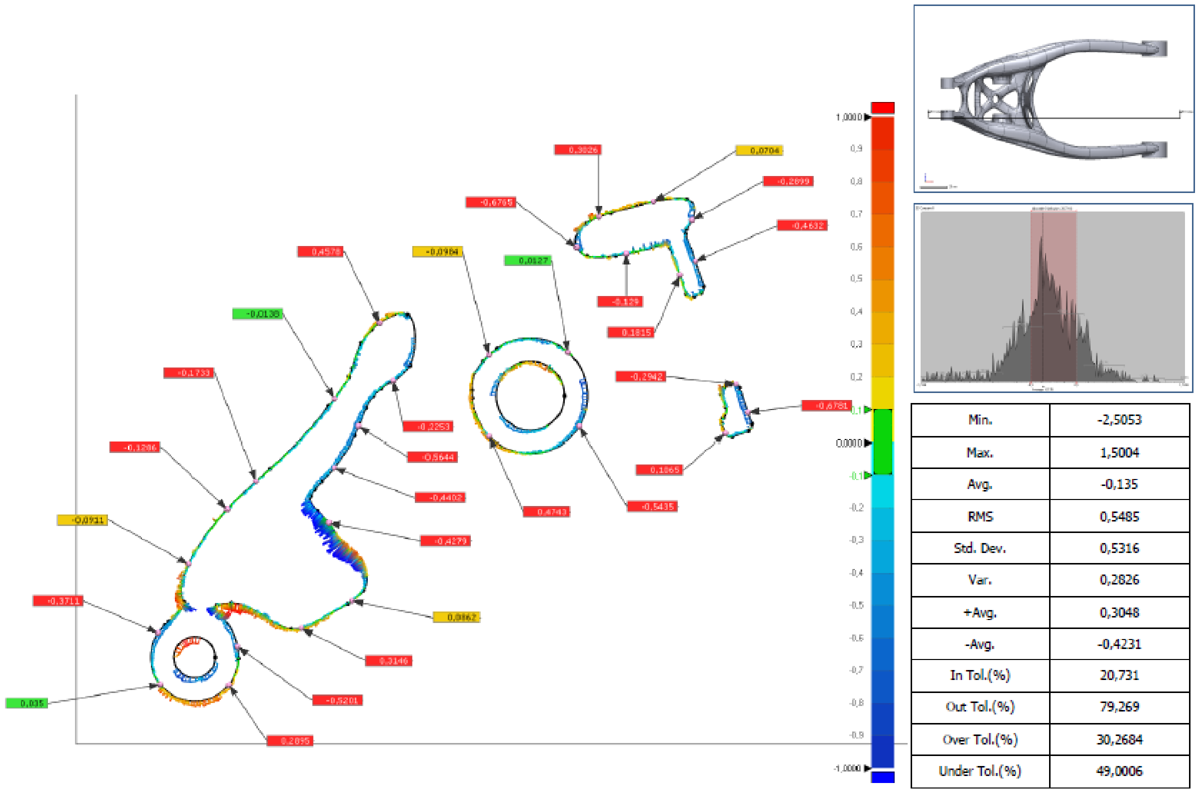

Min.	-2,5053
Max.	1,5004
Avg.	-0,135
RMS	0,5485
Std. Dev.	0,5316
Var.	0,2826
+Avg.	0,3048
-Avg.	-0,4231
In Tol.(%)	20,731
Out Tol.(%)	79,269
Over Tol.(%)	30,2684
Under Tol.(%)	49,0006

Name	Min.	Max.	Avg.	RMS	Std. Dev.	Var.	+Avg.	-Avg.
2D Compare 6	-2,5053	1,5004	-0,135	0,5485	0,5316	0,2826	0,3048	-0,4231

Name	Result Name	Tolerance	Gap Dist.	Reference Pos.		Measured Pos.	
				X	Y	X	Y
2D Compare 6: 1	Result Data - Landing Fork Gear	±0,1	0,4743	-300	-103,4576	-300,3383	-103,79
2D Compare 6: 2	Result Data - Landing Fork Gear	±0,1	-0,5435	-286,8701	-102	-287,332	-101,7136
2D Compare 6: 3	Result Data - Landing Fork Gear	±0,1	0,0127	-288,5	-91,2287	-288,4915	-91,2192
2D Compare 6: 4	Result Data - Landing Fork Gear	±0,1	-0,0984	-300	-91,6281	-299,934	-91,701
2D Compare 6: 5	Result Data - Landing Fork Gear	±0,1	-0,6765	-287,235	-76	-286,6307	-75,6959
2D Compare 6: 6	Result Data - Landing Fork Gear	±0,1	0,3026	-284	-71,507	-284,1078	-71,2242
2D Compare 6: 7	Result Data - Landing Fork Gear	±0,1	0,0704	-276	-69,3599	-276,0142	-69,291
2D Compare 6: 8	Result Data - Landing Fork Gear	±0,1	-0,2899	-270,3987	-72	-270,6658	-71,8874
2D Compare 6: 9	Result Data - Landing Fork Gear	±0,1	-0,4632	-269,9356	-78	-270,3728	-78,1529
2D Compare 6: 10	Result Data - Landing Fork Gear	±0,1	0,1815	-272,2122	-80	-272,3835	-80,0599
2D Compare 6: 11	Result Data - Landing Fork Gear	±0,1	-0,129	-280	-76,8978	-280,0221	-76,7707
2D Compare 6: 12	Result Data - Landing Fork Gear	±0,1	0,1065	-265,5492	-103,0413	-265,6488	-103,0789
2D Compare 6: 13	Result Data - Landing Fork Gear	±0,1	-0,6781	-262,2408	-100	-262,8808	-100,2239
2D Compare 6: 14	Result Data - Landing Fork Gear	±0,1	-0,2253	-314	-95,3531	-314,1143	-95,1589
2D Compare 6: 15	Result Data - Landing Fork Gear	±0,1	-0,5644	-319,0759	-102	-319,602	-101,7955
2D Compare 6: 16	Result Data - Landing Fork Gear	±0,1	-0,4402	-322,6349	-108	-322,9723	-107,7172
2D Compare 6: 17	Result Data - Landing Fork Gear	±0,1	-0,4279	-323,3794	-116	-323,7116	-116,2698
2D Compare 6: 18	Result Data - Landing Fork Gear	±0,1	0,0862	-320	-127,3229	-319,9511	-127,3939

© Central University of Technology, Free State

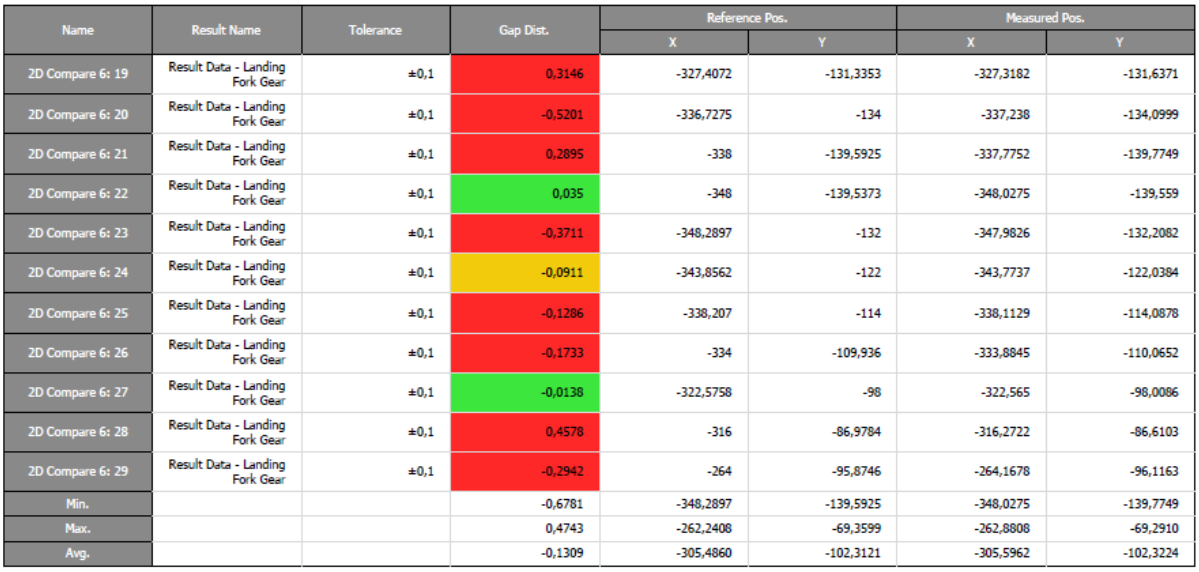

Name	Result Name	Tolerance	Gap Dist.	Reference Pos.		Measured Pos.	
				X	Y	X	Y
2D Compare 6: 19	Result Data - Landing Fork Gear	±0,1	0,3146	-327,4072	-131,3353	-327,3182	-131,6371
2D Compare 6: 20	Result Data - Landing Fork Gear	±0,1	-0,5201	-336,7275	-134	-337,238	-134,0999
2D Compare 6: 21	Result Data - Landing Fork Gear	±0,1	0,2895	-338	-139,5925	-337,7752	-139,7749
2D Compare 6: 22	Result Data - Landing Fork Gear	±0,1	0,035	-348	-139,5373	-348,0275	-139,559
2D Compare 6: 23	Result Data - Landing Fork Gear	±0,1	-0,3711	-348,2897	-132	-347,9826	-132,2082
2D Compare 6: 24	Result Data - Landing Fork Gear	±0,1	-0,0911	-343,8562	-122	-343,7737	-122,0384
2D Compare 6: 25	Result Data - Landing Fork Gear	±0,1	-0,1286	-338,207	-114	-338,1129	-114,0878
2D Compare 6: 26	Result Data - Landing Fork Gear	±0,1	-0,1733	-334	-109,936	-333,8845	-110,0652
2D Compare 6: 27	Result Data - Landing Fork Gear	±0,1	-0,0138	-322,5758	-98	-322,565	-98,0086
2D Compare 6: 28	Result Data - Landing Fork Gear	±0,1	0,4578	-316	-86,9784	-316,2722	-86,6103
2D Compare 6: 29	Result Data - Landing Fork Gear	±0,1	-0,2942	-264	-95,8746	-264,1678	-96,1163
Min.			-0,6781	-348,2897	-139,5925	-348,0275	-139,7749
Max.			0,4743	-262,2408	-69,3599	-262,8808	-69,2910
Avg.			-0,1309	-305,4860	-102,3121	-305,5962	-102,3224

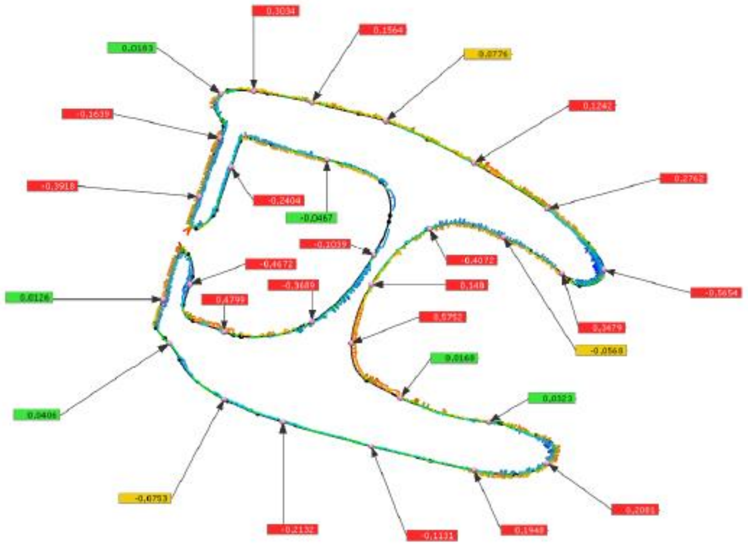

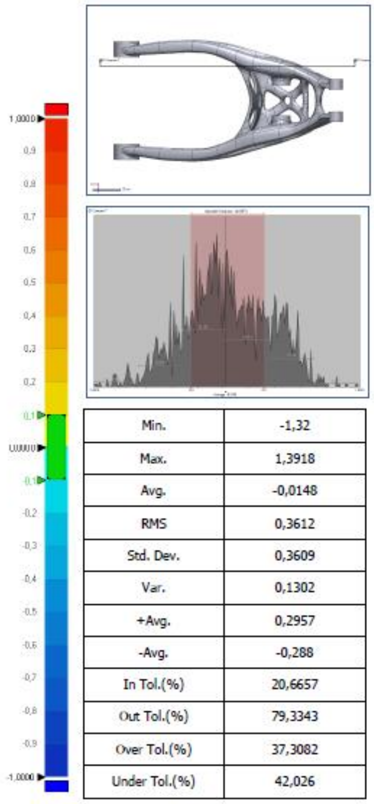

Min.	-1,32
Max.	1,3918
Avg.	-0,0148
RMS	0,3612
Std. Dev.	0,3609
Var.	0,1302
+Avg.	0,2957
-Avg.	-0,288
In Tol.(%)	20,6657
Out Tol.(%)	79,3343
Over Tol.(%)	37,3082
Under Tol.(%)	42,026

© Central University of Technology, Free State

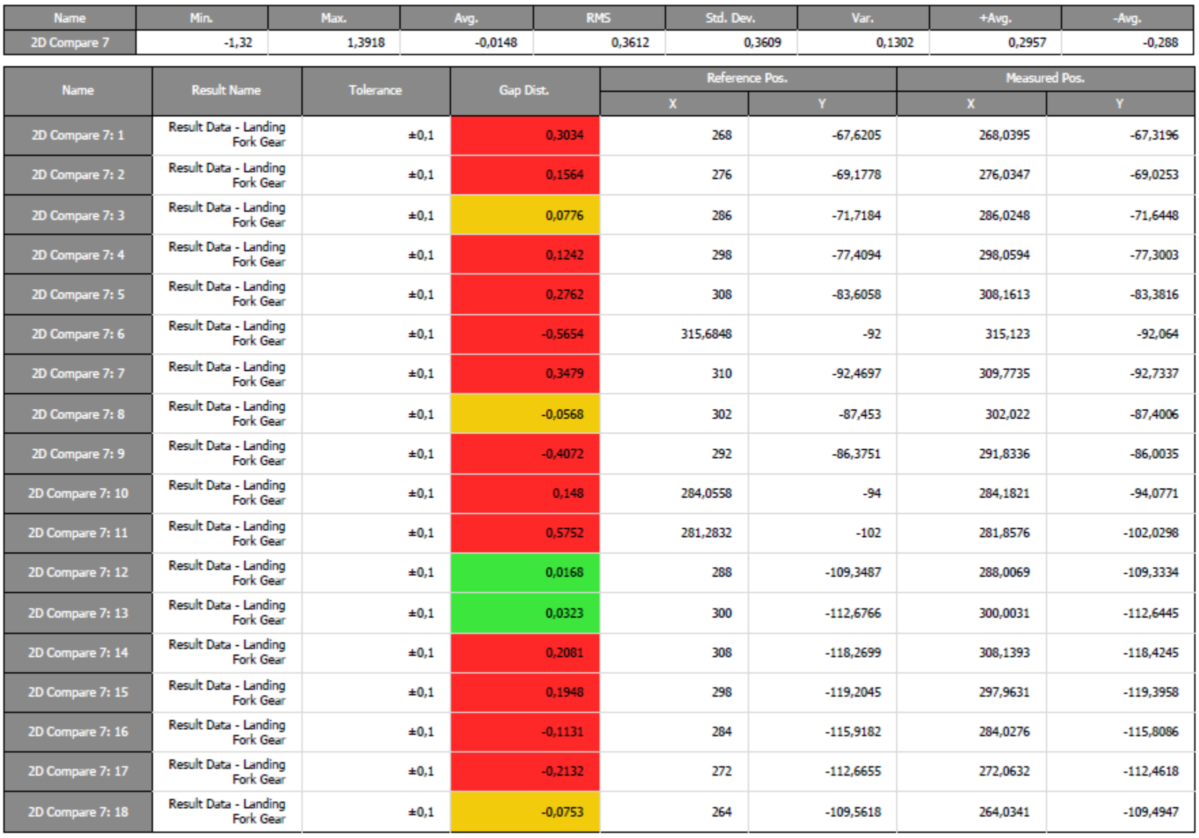

Name	Min.	Max.	Avg.	RMS	Std. Dev.	Var.	+Avg.	-Avg.
2D Compare 7	-1,32	1,3918	-0,0148	0,3612	0,3609	0,1302	0,2957	-0,288

Name	Result Name	Tolerance	Gap Dist.	Reference Pos.		Measured Pos.	
				X	Y	X	Y
2D Compare 7: 1	Result Data - Landing Fork Gear	±0,1	0,3034	268	-67,6205	268,0395	-67,3196
2D Compare 7: 2	Result Data - Landing Fork Gear	±0,1	0,1564	276	-69,1778	276,0347	-69,0253
2D Compare 7: 3	Result Data - Landing Fork Gear	±0,1	0,0776	286	-71,7184	286,0248	-71,6448
2D Compare 7: 4	Result Data - Landing Fork Gear	±0,1	0,1242	298	-77,4094	298,0594	-77,3003
2D Compare 7: 5	Result Data - Landing Fork Gear	±0,1	0,2762	308	-83,6058	308,1613	-83,3816
2D Compare 7: 6	Result Data - Landing Fork Gear	±0,1	-0,5654	315,6848	-92	315,123	-92,064
2D Compare 7: 7	Result Data - Landing Fork Gear	±0,1	0,3479	310	-92,4697	309,7735	-92,7337
2D Compare 7: 8	Result Data - Landing Fork Gear	±0,1	-0,0568	302	-87,453	302,022	-87,4006
2D Compare 7: 9	Result Data - Landing Fork Gear	±0,1	-0,4072	292	-86,3751	291,8336	-86,0035
2D Compare 7: 10	Result Data - Landing Fork Gear	±0,1	0,148	284,0558	-94	284,1821	-94,0771
2D Compare 7: 11	Result Data - Landing Fork Gear	±0,1	0,5752	281,2832	-102	281,8576	-102,0298
2D Compare 7: 12	Result Data - Landing Fork Gear	±0,1	0,0168	288	-109,3487	288,0069	-109,3334
2D Compare 7: 13	Result Data - Landing Fork Gear	±0,1	0,0323	300	-112,6766	300,0031	-112,6445
2D Compare 7: 14	Result Data - Landing Fork Gear	±0,1	0,2081	308	-118,2699	308,1393	-118,4245
2D Compare 7: 15	Result Data - Landing Fork Gear	±0,1	0,1948	298	-119,2045	297,9631	-119,3958
2D Compare 7: 16	Result Data - Landing Fork Gear	±0,1	-0,1131	284	-115,9182	284,0276	-115,8086
2D Compare 7: 17	Result Data - Landing Fork Gear	±0,1	-0,2132	272	-112,6655	272,0632	-112,4618
2D Compare 7: 18	Result Data - Landing Fork Gear	±0,1	-0,0753	264	-109,5618	264,0341	-109,4947

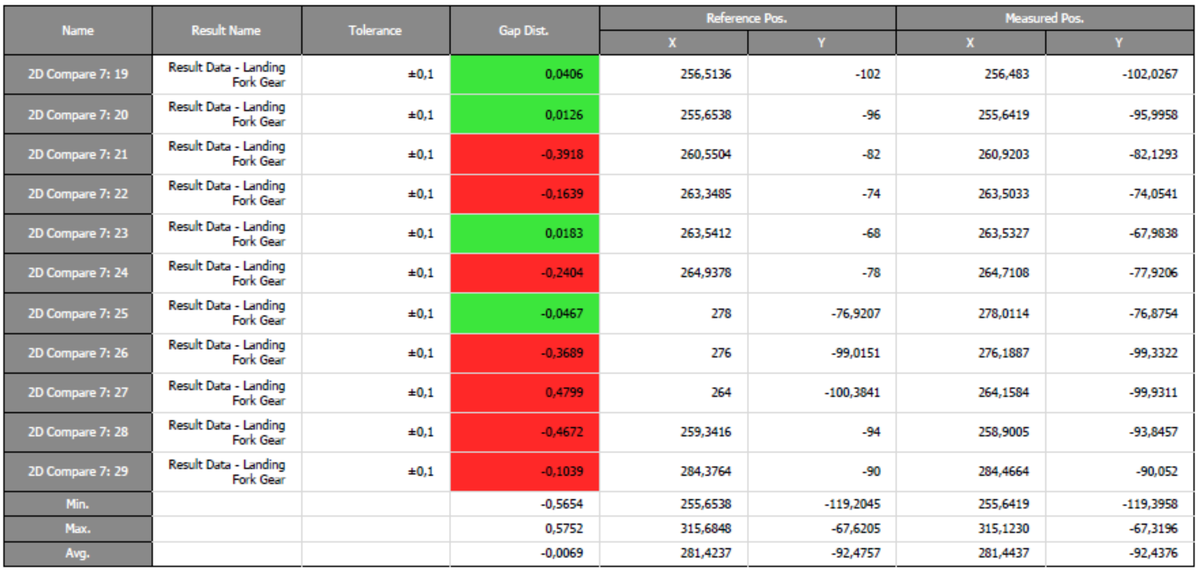

Name	Result Name	Tolerance	Gap Dist.	Reference Pos.		Measured Pos.	
				X	Y	X	Y
2D Compare 7: 19	Result Data - Landing Fork Gear	±0,1	0,0406	256,5136	-102	256,483	-102,0267
2D Compare 7: 20	Result Data - Landing Fork Gear	±0,1	0,0126	255,6538	-96	255,6419	-95,9958
2D Compare 7: 21	Result Data - Landing Fork Gear	±0,1	-0,3918	260,5504	-82	260,9203	-82,1293
2D Compare 7: 22	Result Data - Landing Fork Gear	±0,1	-0,1639	263,3485	-74	263,5033	-74,0541
2D Compare 7: 23	Result Data - Landing Fork Gear	±0,1	0,0183	263,5412	-68	263,5327	-67,9838
2D Compare 7: 24	Result Data - Landing Fork Gear	±0,1	-0,2404	264,9378	-78	264,7108	-77,9206
2D Compare 7: 25	Result Data - Landing Fork Gear	±0,1	-0,0467	278	-76,9207	278,0114	-76,8754
2D Compare 7: 26	Result Data - Landing Fork Gear	±0,1	-0,3689	276	-99,0151	276,1887	-99,3322
2D Compare 7: 27	Result Data - Landing Fork Gear	±0,1	0,4799	264	-100,3841	264,1584	-99,9311
2D Compare 7: 28	Result Data - Landing Fork Gear	±0,1	-0,4672	259,3416	-94	258,9005	-93,8457
2D Compare 7: 29	Result Data - Landing Fork Gear	±0,1	-0,1039	284,3764	-90	284,4664	-90,052
Min.			-0,5654	255,6538	-119,2045	255,6419	-119,3958
Max.			0,5752	315,6848	-67,6205	315,1230	-67,3196
Avg.			-0,0069	281,4237	-92,4757	281,4437	-92,4376

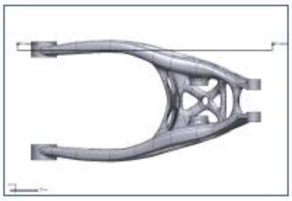

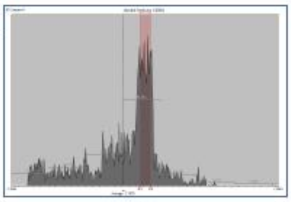

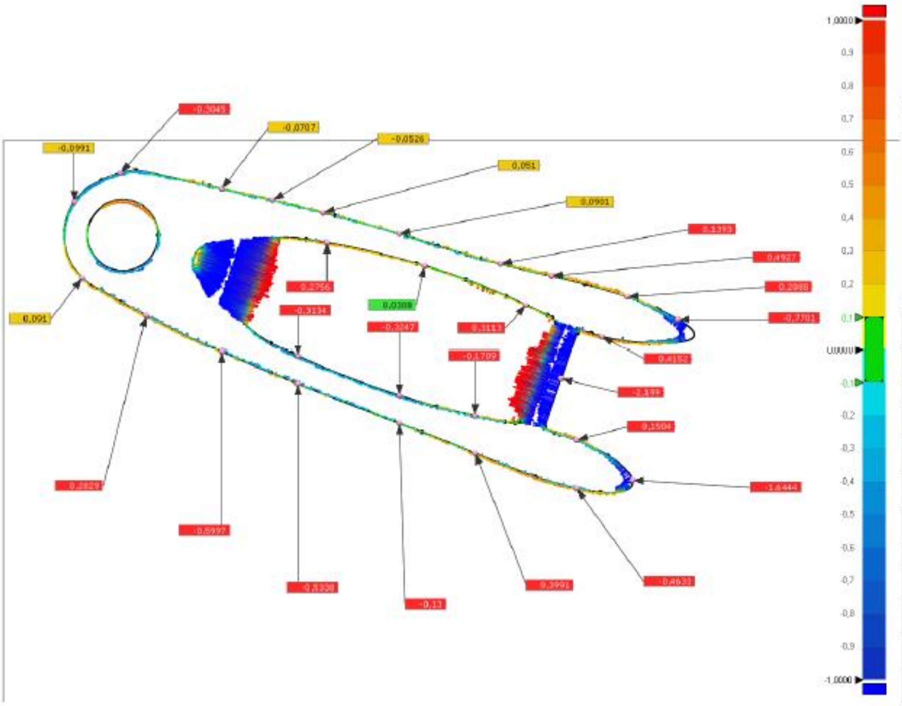

Min.	-6,3597
Max.	3,8452
Avg.	-1,1879
RMS	2,3544
Std. Dev.	2,0328
Var.	4,1322
+Avg.	0,6599
-Avg.	-2,0005
In Tol.(%)	8,8056
Out Tol.(%)	91,1944
Over Tol.(%)	26,6373
Under Tol.(%)	64,5571

Name	Min.	Max.	Avg.	RMS	Std. Dev.	Var.	+Avg.	-Avg.
2D Compare 8	-6,3597	3,8452	-1,1879	2,3544	2,0328	4,1322	0,6599	-2,0005

Name	Result Name	Tolerance	Gap Dist.	Reference Pos.		Measured Pos.	
				X	Y	X	Y
2D Compare 8: 1	Result Data - Landing Fork Gear	±0,1	-0,3045	155	-39,2993	155,0714	-39,5953
2D Compare 8: 2	Result Data - Landing Fork Gear	±0,1	-0,0991	145,8278	-45	145,9099	-45,0557
2D Compare 8: 3	Result Data - Landing Fork Gear	±0,1	0,091	147,385	-60	147,3221	-60,0658
2D Compare 8: 4	Result Data - Landing Fork Gear	±0,1	0,2829	160	-67,3968	159,8687	-67,6474
2D Compare 8: 5	Result Data - Landing Fork Gear	±0,1	-0,5997	175	-74,697	175,2451	-74,1496
2D Compare 8: 6	Result Data - Landing Fork Gear	±0,1	-0,5338	190	-81,0235	190,1989	-80,5281
2D Compare 8: 7	Result Data - Landing Fork Gear	±0,1	-0,13	210	-88,7905	210,0465	-88,6691
2D Compare 8: 8	Result Data - Landing Fork Gear	±0,1	0,3991	225	-94,7052	224,8498	-95,075
2D Compare 8: 9	Result Data - Landing Fork Gear	±0,1	-0,4633	245	-101,6542	245,1004	-101,2019
2D Compare 8: 10	Result Data - Landing Fork Gear	±0,1	0,1504	245	-92,0928	245,0548	-91,9527
2D Compare 8: 11	Result Data - Landing Fork Gear	±0,1	-1,6444	255,9933	-100	254,3823	-100,3301
2D Compare 8: 12	Result Data - Landing Fork Gear	±0,1	-2,199	241,9383	-80	239,8626	-79,274
2D Compare 8: 13	Result Data - Landing Fork Gear	±0,1	0,4152	250	-71,4787	249,894	-71,8802
2D Compare 8: 14	Result Data - Landing Fork Gear	±0,1	-0,7701	265	-68,1717	264,6146	-68,8384
2D Compare 8: 15	Result Data - Landing Fork Gear	±0,1	0,2088	255	-63,6946	255,0697	-63,4978
2D Compare 8: 16	Result Data - Landing Fork Gear	±0,1	0,4927	240	-59,6053	240,1111	-59,1253
2D Compare 8: 17	Result Data - Landing Fork Gear	±0,1	0,1393	230	-57,214	230,0349	-57,0792
2D Compare 8: 18	Result Data - Landing Fork Gear	±0,1	0,0901	210	-51,2834	210,0261	-51,1971

© Central University of Technology, Free State

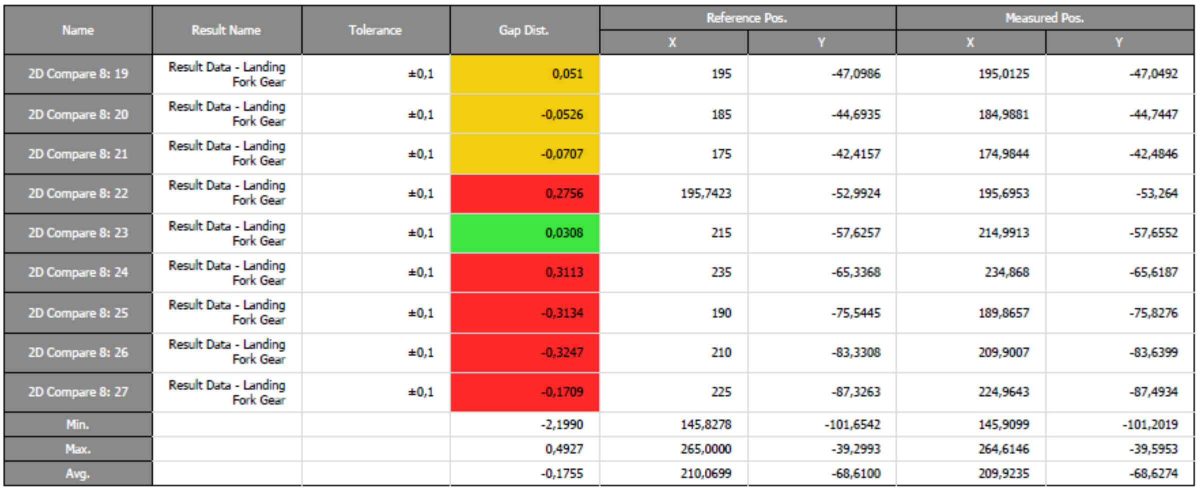

Name	Result Name	Tolerance	Gap Dist.	Reference Pos.		Measured Pos.	
				X	Y	X	Y
2D Compare 8: 19	Result Data - Landing Fork Gear	±0,1	0,051	195	-47,0986	195,0125	-47,0492
2D Compare 8: 20	Result Data - Landing Fork Gear	±0,1	-0,0526	185	-44,6935	184,9881	-44,7447
2D Compare 8: 21	Result Data - Landing Fork Gear	±0,1	-0,0707	175	-42,4157	174,9844	-42,4846
2D Compare 8: 22	Result Data - Landing Fork Gear	±0,1	0,2756	195,7423	-52,9924	195,6953	-53,264
2D Compare 8: 23	Result Data - Landing Fork Gear	±0,1	0,0308	215	-57,6257	214,9913	-57,6552
2D Compare 8: 24	Result Data - Landing Fork Gear	±0,1	0,3113	235	-65,3368	234,868	-65,6187
2D Compare 8: 25	Result Data - Landing Fork Gear	±0,1	-0,3134	190	-75,5445	189,8657	-75,8276
2D Compare 8: 26	Result Data - Landing Fork Gear	±0,1	-0,3247	210	-83,3308	209,9007	-83,6399
2D Compare 8: 27	Result Data - Landing Fork Gear	±0,1	-0,1709	225	-87,3263	224,9643	-87,4934
Min.			-2,1990	145,8278	-101,6542	145,9099	-101,2019
Max.			0,4927	265,0000	-39,2993	264,6146	-39,5953
Avg.			-0,1755	210,0699	-68,6100	209,9235	-68,6274

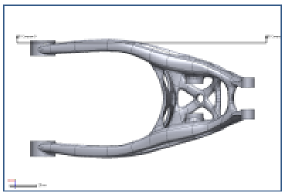

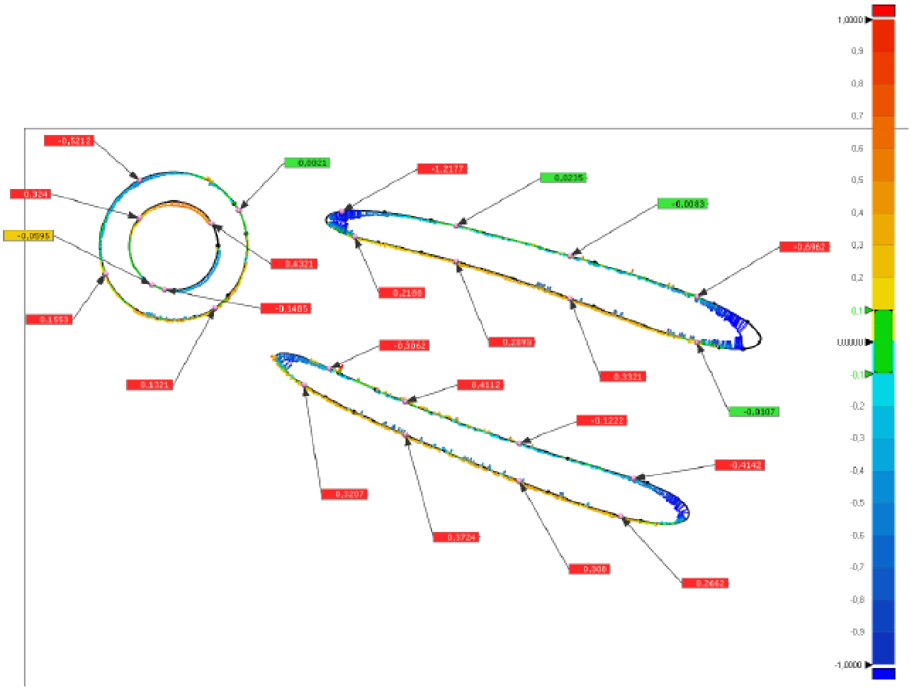

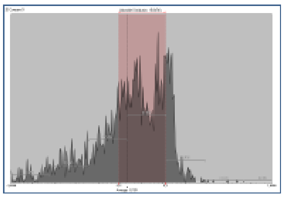

Min.	-2,1612
Max.	1,414
Avg.	-0,189
RMS	0,5338
Std. Dev.	0,4992
Var.	0,2492
+Avg.	0,2516
-Avg.	-0,485
In Tol.(%)	15,8474
Out Tol.(%)	84,1526
Over Tol.(%)	33,4135
Under Tol.(%)	50,7391

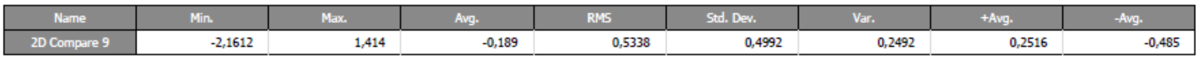

Name	Min.	Max.	Avg.	RMS	Std. Dev.	Var.	+Avg.	-Avg.
2D Compare 9	-2,1612	1,414	-0,189	0,5338	0,4992	0,2492	0,2516	-0,485

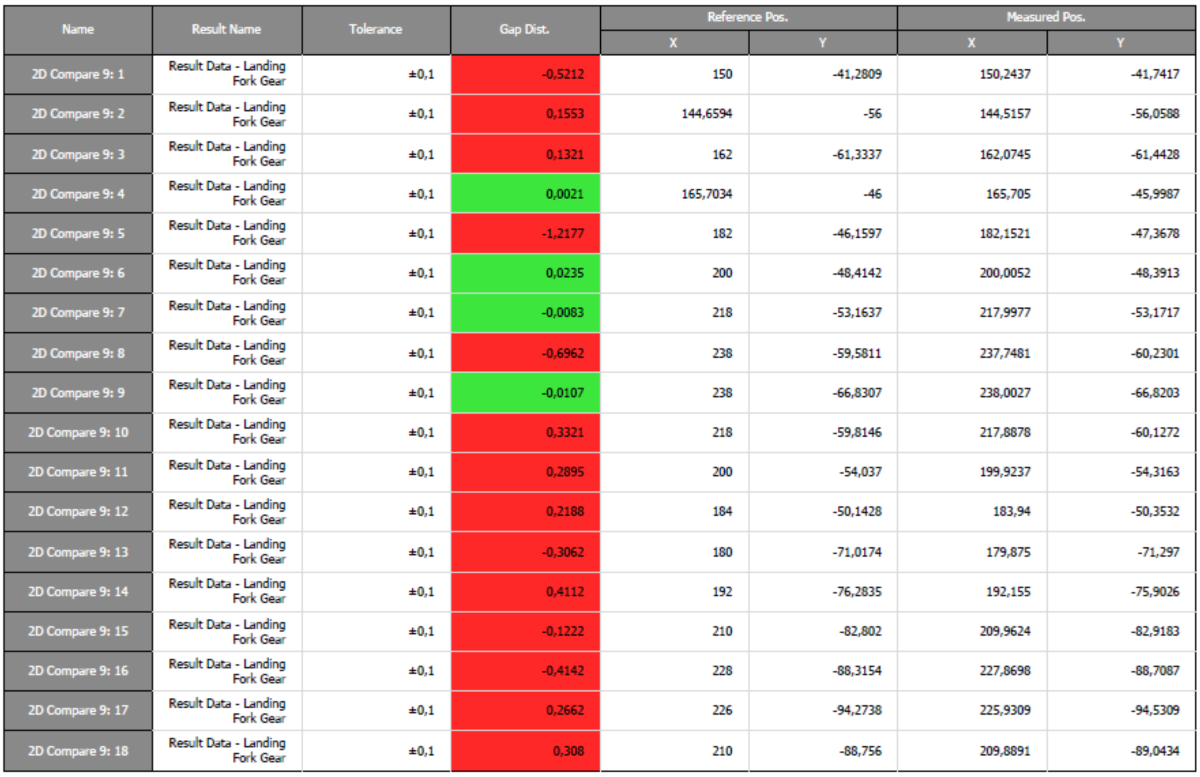

Name	Result Name	Tolerance	Gap Dist.	Reference Pos.		Measured Pos.	
				X	Y	X	Y
2D Compare 9: 1	Result Data - Landing Fork Gear	±0,1	-0,5212	150	-41,2809	150,2437	-41,7417
2D Compare 9: 2	Result Data - Landing Fork Gear	±0,1	0,1553	144,6594	-56	144,5157	-56,0588
2D Compare 9: 3	Result Data - Landing Fork Gear	±0,1	0,1321	162	-61,3337	162,0745	-61,4428
2D Compare 9: 4	Result Data - Landing Fork Gear	±0,1	0,0021	165,7034	-46	165,705	-45,9987
2D Compare 9: 5	Result Data - Landing Fork Gear	±0,1	-1,2177	182	-46,1597	182,1521	-47,3678
2D Compare 9: 6	Result Data - Landing Fork Gear	±0,1	0,0235	200	-48,4142	200,0052	-48,3913
2D Compare 9: 7	Result Data - Landing Fork Gear	±0,1	-0,0083	218	-53,1637	217,9977	-53,1717
2D Compare 9: 8	Result Data - Landing Fork Gear	±0,1	-0,6962	238	-59,5811	237,7481	-60,2301
2D Compare 9: 9	Result Data - Landing Fork Gear	±0,1	-0,0107	238	-66,8307	238,0027	-66,8203
2D Compare 9: 10	Result Data - Landing Fork Gear	±0,1	0,3321	218	-59,8146	217,8878	-60,1272
2D Compare 9: 11	Result Data - Landing Fork Gear	±0,1	0,2895	200	-54,037	199,9237	-54,3163
2D Compare 9: 12	Result Data - Landing Fork Gear	±0,1	0,2188	184	-50,1428	183,94	-50,3532
2D Compare 9: 13	Result Data - Landing Fork Gear	±0,1	-0,3062	180	-71,0174	179,875	-71,297
2D Compare 9: 14	Result Data - Landing Fork Gear	±0,1	0,4112	192	-76,2835	192,155	-75,9026
2D Compare 9: 15	Result Data - Landing Fork Gear	±0,1	-0,1222	210	-82,802	209,9624	-82,9183
2D Compare 9: 16	Result Data - Landing Fork Gear	±0,1	-0,4142	228	-88,3154	227,8698	-88,7087
2D Compare 9: 17	Result Data - Landing Fork Gear	±0,1	0,2662	226	-94,2738	225,9309	-94,5309
2D Compare 9: 18	Result Data - Landing Fork Gear	±0,1	0,308	210	-88,756	209,8891	-89,0434

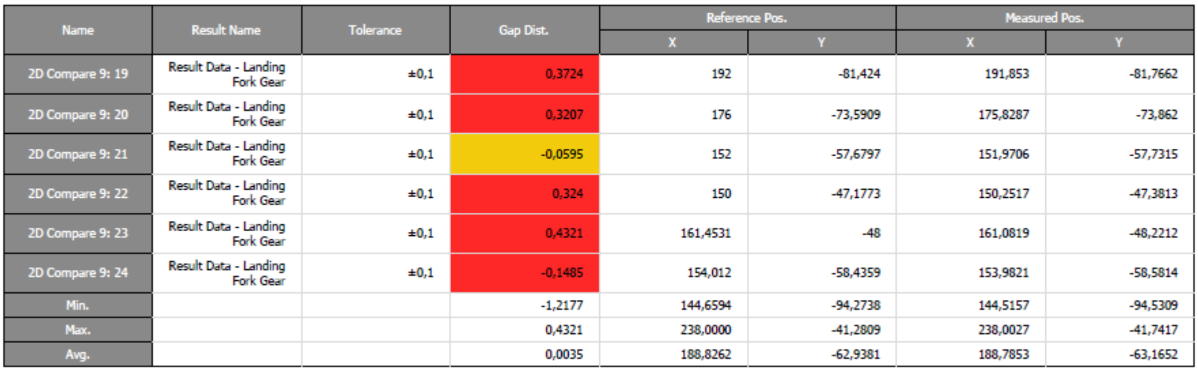

Name	Result Name	Tolerance	Gap Dist.	Reference Pos.		Measured Pos.	
				X	Y	X	Y
2D Compare 9: 19	Result Data - Landing Fork Gear	±0,1	0,3724	192	-81,424	191,853	-81,7662
2D Compare 9: 20	Result Data - Landing Fork Gear	±0,1	0,3207	176	-73,5909	175,8287	-73,862
2D Compare 9: 21	Result Data - Landing Fork Gear	±0,1	-0,0595	152	-57,6797	151,9706	-57,7315
2D Compare 9: 22	Result Data - Landing Fork Gear	±0,1	0,324	150	-47,1773	150,2517	-47,3813
2D Compare 9: 23	Result Data - Landing Fork Gear	±0,1	0,4321	161,4531	-48	161,0819	-48,2212
2D Compare 9: 24	Result Data - Landing Fork Gear	±0,1	-0,1485	154,012	-58,4359	153,9821	-58,5814
Min.			-1,2177	144,6594	-94,2738	144,5157	-94,5309
Max.			0,4321	238,0000	-41,2809	238,0027	-41,7417
Avg.			0,0035	188,8262	-62,9381	188,7853	-63,1652

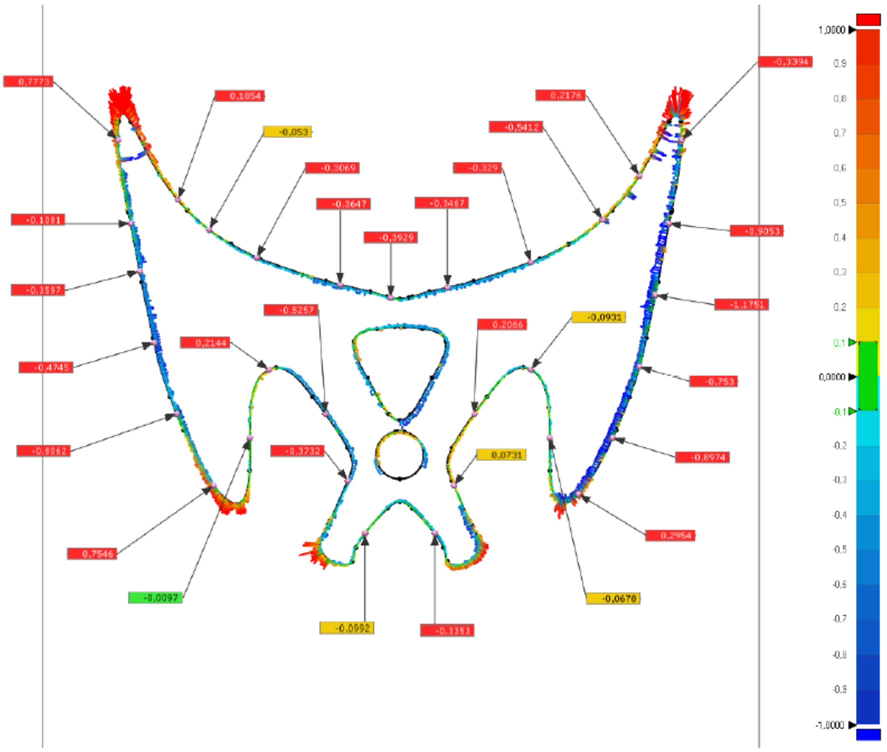

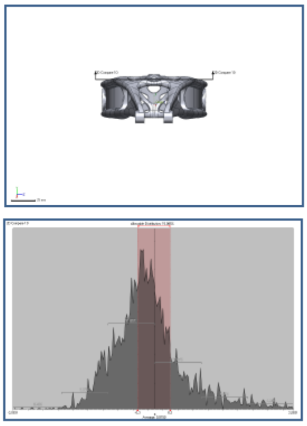

Min.	-2,4059
Max.	4,6196
Avg.	0,0159
RMS	0,8559
Std. Dev.	0,8557
Var.	0,7323
+Avg.	0,7254
-Avg.	-0,4587
In Tol.(%)	15,085
Out Tol.(%)	84,915
Over Tol.(%)	32,9521
Under Tol.(%)	51,9629

Name	Min.	Max.	Avg.	RMS	Std. Dev.	Var.	+Avg.	-Avg.
2D Compare 10	-2,4059	4,6196	0,0159	0,8559	0,8557	0,7323	0,7254	-0,4587

Name	Result Name	Tolerance	Gap Dist.	Reference Pos.		Measured Pos.	
				X	Y	X	Y
2D Compare 10: 1	Result Data - Landing Fork Gear	±0,1	0,1854	-37,2176	-266	-37,0757	-265,8806
2D Compare 10: 2	Result Data - Landing Fork Gear	±0,1	-0,3069	-24	-275,6847	-24,1275	-275,9638
2D Compare 10: 3	Result Data - Landing Fork Gear	±0,1	-0,3647	-10	-280,2427	-10,0847	-280,5974
2D Compare 10: 4	Result Data - Landing Fork Gear	±0,1	-0,3929	-1,5275	-282,4086	-1,6224	-282,7899
2D Compare 10: 5	Result Data - Landing Fork Gear	±0,1	-0,3467	8	-280,704	8,0765	-281,0421
2D Compare 10: 6	Result Data - Landing Fork Gear	±0,1	-0,329	22	-276,4711	22,1109	-276,7809
2D Compare 10: 7	Result Data - Landing Fork Gear	±0,1	0,2176	40,1722	-262	39,9895	-261,8818
2D Compare 10: 8	Result Data - Landing Fork Gear	±0,1	-0,053	-32	-271,0037	-32,032	-271,0459
2D Compare 10: 9	Result Data - Landing Fork Gear	±0,1	-0,5412	34	-269,3473	34,365	-269,7469
2D Compare 10: 10	Result Data - Landing Fork Gear	±0,1	-0,9053	45,1718	-270	44,2838	-269,8237
2D Compare 10: 11	Result Data - Landing Fork Gear	±0,1	-1,1751	42,8935	-282	41,7413	-281,769
2D Compare 10: 12	Result Data - Landing Fork Gear	±0,1	-0,753	40,2296	-294	39,5055	-293,7935
2D Compare 10: 13	Result Data - Landing Fork Gear	±0,1	-0,8974	35,7163	-306	34,901	-305,625
2D Compare 10: 14	Result Data - Landing Fork Gear	±0,1	0,2954	30	-315,4661	30,2136	-315,6702
2D Compare 10: 15	Result Data - Landing Fork Gear	±0,1	0,7773	-47,3089	-256	-48,0859	-256,0247
2D Compare 10: 16	Result Data - Landing Fork Gear	±0,1	-0,1081	-45,1653	-270	-45,0593	-269,979
2D Compare 10: 17	Result Data - Landing Fork Gear	±0,1	-0,3597	-43,6544	-278	-43,3007	-277,9345
2D Compare 10: 18	Result Data - Landing Fork Gear	±0,1	-0,4745	-41,1857	-290	-40,7214	-289,9018

Name	Result Name	Tolerance	Gap Dist.	Reference Pos.		Measured Pos.	
				X	Y	X	Y
2D Compare 10: 19	Result Data - Landing Fork Gear	±0,1	-0,8062	-37,4292	-302	-36,6813	-301,6991
2D Compare 10: 20	Result Data - Landing Fork Gear	±0,1	0,7546	-31,2154	-314	-31,8212	-314,45
2D Compare 10: 21	Result Data - Landing Fork Gear	±0,1	-0,0097	-25,1497	-306	-25,1594	-306,0001
2D Compare 10: 22	Result Data - Landing Fork Gear	±0,1	-0,0678	25,1563	-306	25,2241	-306,0001
2D Compare 10: 23	Result Data - Landing Fork Gear	±0,1	-0,0992	-5,8563	-322	-5,9348	-321,9394
2D Compare 10: 24	Result Data - Landing Fork Gear	±0,1	-0,3353	5,8629	-322	6,1283	-321,7951
2D Compare 10: 25	Result Data - Landing Fork Gear	±0,1	0,0731	9,0925	-314	9,1591	-313,97
2D Compare 10: 26	Result Data - Landing Fork Gear	±0,1	-0,3732	-8,7211	-313,194	-8,3799	-313,345
2D Compare 10: 27	Result Data - Landing Fork Gear	±0,1	-0,5257	-12,4599	-302	-12,0341	-301,6916
2D Compare 10: 28	Result Data - Landing Fork Gear	±0,1	0,2144	-22	-294,4988	-21,898	-294,6874
2D Compare 10: 29	Result Data - Landing Fork Gear	±0,1	0,2066	12,4664	-302	12,6337	-302,1212
2D Compare 10: 30	Result Data - Landing Fork Gear	±0,1	-0,0931	22	-294,4952	22,0425	-294,4124
2D Compare 10: 31	Result Data - Landing Fork Gear	±0,1	-0,3394	47,3155	-256	46,9763	-255,9892
Min.			-1,1751	-47,3089	-322,0000	-48,0859	-321,9394
Max.			0,7773	47,3155	-256,0000	46,9763	-255,9892
Avg.			-0,2236	-0,1553	-289,4683	-0,2151	-289,4952

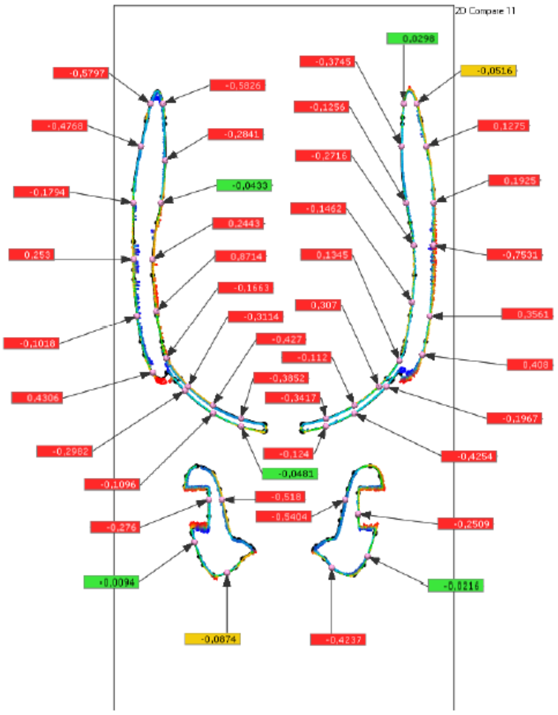

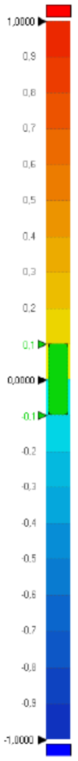

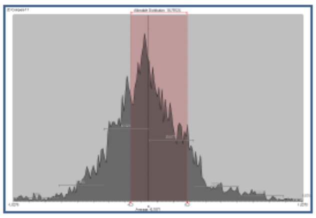

Statistic	Value
Min.	-2,1527
Max.	2,1414
Avg.	-0,1071
RMS	0,4854
Std. Dev.	0,4735
Var.	0,2242
+Avg.	0,3499
-Avg.	-0,358
In Tol.(%)	18,7912
Out Tol.(%)	81,2088
Over Tol.(%)	27,1302
Under Tol.(%)	54,0786

Name	Min.	Max.	Avg.	RMS	Std. Dev.	Var.	+Avg.	-Avg.
2D Compare 11	-2,1527	2,1414	-0,1071	0,4854	0,4735	0,2242	0,3499	-0,358

Name	Result Name	Tolerance	Gap Dist.	Reference Pos.		Measured Pos.	
				X	Y	X	Y
2D Compare 11: 1	Result Data - Landing Fork Gear	±0,1	-0,5797	-47,098	-170	-46,5379	-170,1491
2D Compare 11: 2	Result Data - Landing Fork Gear	±0,1	-0,4768	-50,4983	-185	-50,0331	-185,1046
2D Compare 11: 3	Result Data - Landing Fork Gear	±0,1	-0,1794	-53,1188	-205	-52,9394	-205,0031
2D Compare 11: 4	Result Data - Landing Fork Gear	±0,1	0,253	-53,0101	-225	-53,2631	-225,0021
2D Compare 11: 5	Result Data - Landing Fork Gear	±0,1	-0,1018	-51,7997	-245	-51,6987	-244,9873
2D Compare 11: 6	Result Data - Landing Fork Gear	±0,1	0,4306	-46,2658	-265	-46,6127	-265,2551
2D Compare 11: 7	Result Data - Landing Fork Gear	±0,1	-0,2982	-35	-271,5536	-34,7852	-271,3467
2D Compare 11: 8	Result Data - Landing Fork Gear	±0,1	-0,1096	-25	-279,5133	-24,9436	-279,4193
2D Compare 11: 9	Result Data - Landing Fork Gear	±0,1	-0,0481	-15	-284,0648	-14,9852	-284,019
2D Compare 11: 10	Result Data - Landing Fork Gear	±0,1	-0,124	15	-284,0669	14,9617	-283,9489
2D Compare 11: 11	Result Data - Landing Fork Gear	±0,1	-0,4254	25	-279,5173	24,7813	-279,1523
2D Compare 11: 12	Result Data - Landing Fork Gear	±0,1	-0,1967	36,4391	-270	36,2917	-269,8698
2D Compare 11: 13	Result Data - Landing Fork Gear	±0,1	-0,0516	47,1046	-170	47,0547	-170,0133
2D Compare 11: 14	Result Data - Landing Fork Gear	±0,1	0,1275	50,5048	-185	50,6293	-184,972
2D Compare 11: 15	Result Data - Landing Fork Gear	±0,1	0,1925	53,1254	-205	53,3178	-204,9968
2D Compare 11: 16	Result Data - Landing Fork Gear	±0,1	-0,7531	53,0471	-220	52,294	-219,9956
2D Compare 11: 17	Result Data - Landing Fork Gear	±0,1	0,3561	51,8063	-245	52,1596	-245,0445
2D Compare 11: 18	Result Data - Landing Fork Gear	±0,1	0,408	49,0904	-258,8289	49,4802	-258,9492
2D Compare 11: 19	Result Data - Landing Fork Gear	±0,1	0,0298	42,5923	-170	42,5629	-169,9956
2D Compare 11: 20	Result Data - Landing Fork Gear	±0,1	-0,3745	41,788	-185	42,1625	-185,0046
2D Compare 11: 21	Result Data - Landing Fork Gear	±0,1	-0,1256	43,3619	-205	43,4854	-204,9768
2D Compare 11: 22	Result Data - Landing Fork Gear	±0,1	-0,2716	46,0063	-220	46,2765	-219,972
2D Compare 11: 23	Result Data - Landing Fork Gear	±0,1	-0,1462	45,452	-240	45,5971	-240,0178
2D Compare 11: 24	Result Data - Landing Fork Gear	±0,1	0,1345	40,9904	-260,8523	40,8742	-260,7846
2D Compare 11: 25	Result Data - Landing Fork Gear	±0,1	0,307	33,7341	-270	33,5207	-269,7792
2D Compare 11: 26	Result Data - Landing Fork Gear	±0,1	-0,112	25	-276,7027	25,0578	-276,7986
2D Compare 11: 27	Result Data - Landing Fork Gear	±0,1	-0,3417	15	-281,2585	15,1056	-281,5835
2D Compare 11: 28	Result Data - Landing Fork Gear	±0,1	-0,3852	-15	-281,2564	-15,119	-281,6227
2D Compare 11: 29	Result Data - Landing Fork Gear	±0,1	-0,427	-25	-276,6987	-25,22	-277,0647
2D Compare 11: 30	Result Data - Landing Fork Gear	±0,1	-0,3114	-33,7275	-270	-33,944	-270,2238
2D Compare 11: 31	Result Data - Landing Fork Gear	±0,1	-0,1663	-41,4409	-260	-41,5895	-260,0748
2D Compare 11: 32	Result Data - Landing Fork Gear	±0,1	0,8714	-45	-243,3473	-44,1375	-243,2235
2D Compare 11: 33	Result Data - Landing Fork Gear	±0,1	0,2443	-46,3279	-225	-46,0837	-225,0069
2D Compare 11: 34	Result Data - Landing Fork Gear	±0,1	-0,0433	-43,3554	-205	-43,3979	-204,992
2D Compare 11: 35	Result Data - Landing Fork Gear	±0,1	-0,2841	-41,7917	-190	-42,0758	-189,9944
2D Compare 11: 36	Result Data - Landing Fork Gear	±0,1	-0,5826	-42,5858	-170	-43,1624	-170,0834
2D Compare 11: 37	Result Data - Landing Fork Gear	±0,1	-0,0874	-20	-335,8548	-20,0358	-335,775

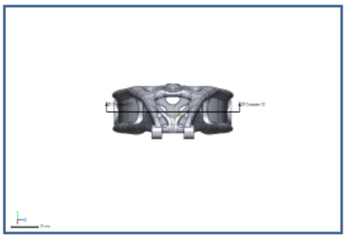

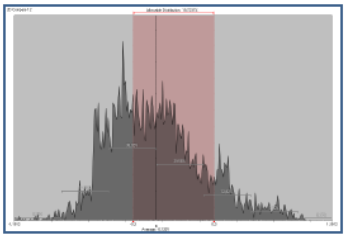

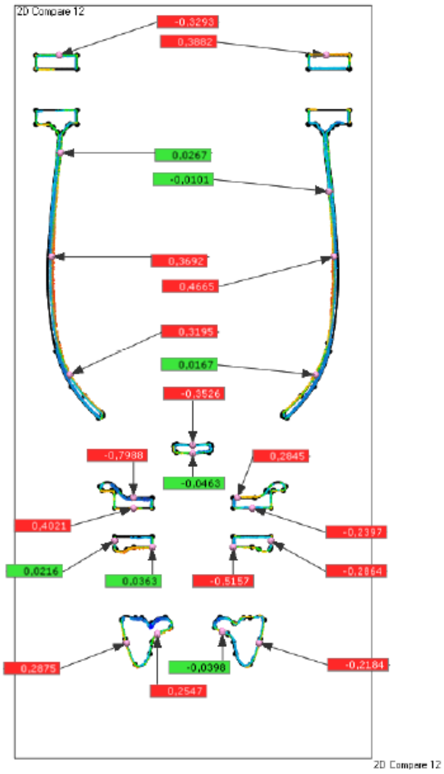

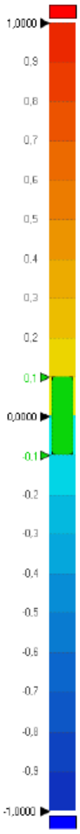

Min.	-1,3495
Max.	0,9944
Avg.	-0,1301
RMS	0,3737
Std. Dev.	0,3504
Var.	0,1227
+Avg.	0,2791
-Avg.	-0,3232
In Tol.(%)	19,7237
Out Tol.(%)	80,2763
Over Tol.(%)	23,3823
Under Tol.(%)	56,894

Name	Min.	Max.	Avg.	RMS	Std. Dev.	Var.	+Avg.	-Avg.
2D Compare 12	-1,3495	0,9944	-0,1301	0,3737	0,3504	0,1227	0,2791	-0,3232

Name	Result Name	Tolerance	Gap Dist.	Reference Pos.		Measured Pos.	
				X	Y	X	Y
2D Compare 12: 1	Result Data - Landing Fork Gear	±0,1	-0,3293	-45	-152,1475	-45	-152,4768
2D Compare 12: 2	Result Data - Landing Fork Gear	±0,1	0,3882	45	-152,1475	45	-151,7593
2D Compare 12: 3	Result Data - Landing Fork Gear	±0,1	0,0267	-44,5813	-185	-44,5548	-185,0025
2D Compare 12: 4	Result Data - Landing Fork Gear	±0,1	0,3692	-47,6246	-220	-47,2557	-220,0135
2D Compare 12: 5	Result Data - Landing Fork Gear	±0,1	0,3195	-41,466	-260	-41,1861	-259,8459
2D Compare 12: 6	Result Data - Landing Fork Gear	±0,1	0,0167	41,4726	-260	41,4579	-259,992
2D Compare 12: 7	Result Data - Landing Fork Gear	±0,1	-0,3526	0	-283,633	0	-283,9856
2D Compare 12: 8	Result Data - Landing Fork Gear	±0,1	-0,0463	0	-286,4386	0	-286,3923
2D Compare 12: 9	Result Data - Landing Fork Gear	±0,1	0,4021	-20	-304,9161	-20	-305,3183
2D Compare 12: 10	Result Data - Landing Fork Gear	±0,1	-0,7988	-20	-301,4417	-20	-302,2405
2D Compare 12: 11	Result Data - Landing Fork Gear	±0,1	0,2845	15	-301,4417	15	-301,1572
2D Compare 12: 12	Result Data - Landing Fork Gear	±0,1	-0,2397	20	-304,9161	20	-304,6764
2D Compare 12: 13	Result Data - Landing Fork Gear	±0,1	0,0363	-13,6167	-318,0289	-13,5805	-318,0323
2D Compare 12: 14	Result Data - Landing Fork Gear	±0,1	-0,5157	13,6233	-318,0289	14,0539	-317,7452
2D Compare 12: 15	Result Data - Landing Fork Gear	±0,1	-0,2184	22,3381	-350	22,1283	-349,9395
2D Compare 12: 16	Result Data - Landing Fork Gear	±0,1	0,2875	-22,33	-350	-22,6063	-350,0795
2D Compare 12: 17	Result Data - Landing Fork Gear	±0,1	0,2547	-11,8908	-347,2047	-11,7736	-347,4309
2D Compare 12: 18	Result Data - Landing Fork Gear	±0,1	-0,0398	10	-346,4238	10,0134	-346,3864
2D Compare 12: 19	Result Data - Landing Fork Gear	±0,1	0,4665	47,6312	-220	47,165	-220,0171
2D Compare 12: 20	Result Data - Landing Fork Gear	±0,1	-0,0101	45,906	-198	45,916	-197,999
2D Compare 12: 21	Result Data - Landing Fork Gear	±0,1	-0,2864	26,4233	-316	26,1369	-316
2D Compare 12: 22	Result Data - Landing Fork Gear	±0,1	0,0216	-26,4167	-316	-26,4384	-316
Min.			-0,7988	-47,6246	-350,0000	-47,2557	-350,0795
Max.			0,4665	47,6312	-152,1475	47,1650	-151,7593
Avg.			0,0017	-0,2514	-276,8986	-0,2511	-276,9314

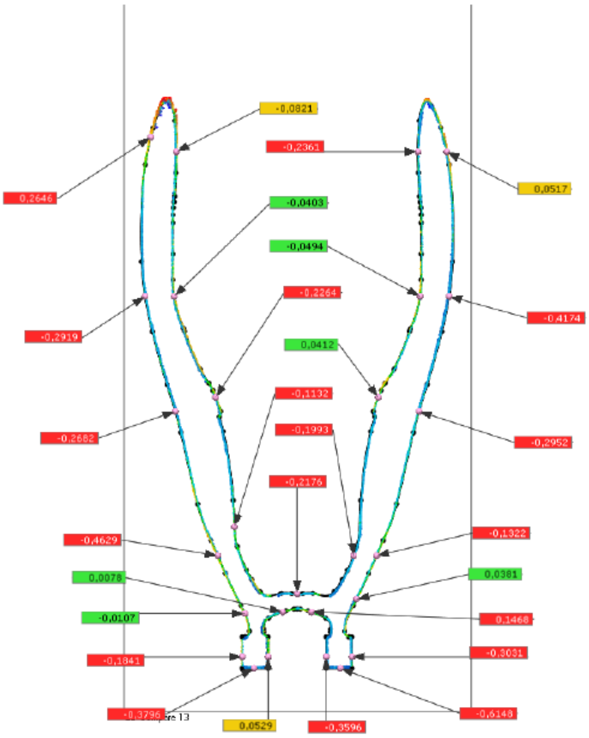

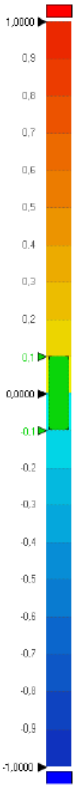

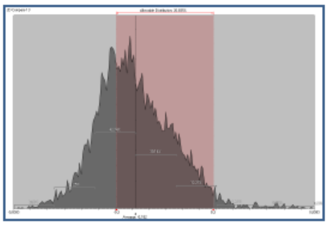

Min.	-1,3416
Max.	1,3438
Avg.	-0,182
RMS	0,3112
Std. Dev.	0,2524
Var.	0,0637
+Avg.	0,1717
-Avg.	-0,2802
In Tol.(%)	20,835
Out Tol.(%)	79,165
Over Tol.(%)	12,1452
Under Tol.(%)	67,0197

Name	Min.	Max.	Avg.	RMS	Std. Dev.	Var.	+Avg.	-Avg.
2D Compare 13	-1,3416	1,3438	-0,182	0,3112	0,2524	0,0637	0,1717	-0,2802

Name	Result Name	Tolerance	Gap Dist.	Reference Pos.		Measured Pos.	
				X	Y	X	Y
2D Compare 13: 1	Result Data - Landing Fork Gear	±0,1	0,2646	-50,6853	-190	-50,9416	-189,9343
2D Compare 13: 2	Result Data - Landing Fork Gear	±0,1	-0,2919	-52,6392	-245	-52,3507	-244,9552
2D Compare 13: 3	Result Data - Landing Fork Gear	±0,1	-0,2682	-42,211	-285	-41,9529	-284,9273
2D Compare 13: 4	Result Data - Landing Fork Gear	±0,1	-0,4629	-27,4878	-335	-27,0624	-334,8176
2D Compare 13: 5	Result Data - Landing Fork Gear	±0,1	-0,0107	-18,0551	-355	-18,0454	-354,9956
2D Compare 13: 6	Result Data - Landing Fork Gear	±0,1	-0,1841	-18,9967	-370	-18,8127	-370
2D Compare 13: 7	Result Data - Landing Fork Gear	±0,1	0,0529	-10,0167	-370	-9,9638	-370
2D Compare 13: 8	Result Data - Landing Fork Gear	±0,1	-0,3796	-15	-373,9472	-15	-373,5675
2D Compare 13: 9	Result Data - Landing Fork Gear	±0,1	-0,6148	15	-373,9472	15	-373,3323
2D Compare 13: 10	Result Data - Landing Fork Gear	±0,1	-0,3596	10,0233	-370	10,3829	-370
2D Compare 13: 11	Result Data - Landing Fork Gear	±0,1	0,0078	-5	-354,458	-4,9975	-354,4654
2D Compare 13: 12	Result Data - Landing Fork Gear	±0,1	0,1468	5	-354,4558	4,9527	-354,5948
2D Compare 13: 13	Result Data - Landing Fork Gear	±0,1	-0,2176	0,0033	-348,1733	0,0033	-348,3908
2D Compare 13: 14	Result Data - Landing Fork Gear	±0,1	-0,1132	-21,6907	-325	-21,8038	-325,0057
2D Compare 13: 15	Result Data - Landing Fork Gear	±0,1	-0,2264	-28,1604	-280	-28,3719	-280,0807
2D Compare 13: 16	Result Data - Landing Fork Gear	±0,1	-0,0403	-42,5842	-245	-42,6242	-245,0054
2D Compare 13: 17	Result Data - Landing Fork Gear	±0,1	-0,0821	-41,8004	-195	-41,8825	-195
2D Compare 13: 18	Result Data - Landing Fork Gear	±0,1	0,0517	51,8292	-195	51,88	-194,9902

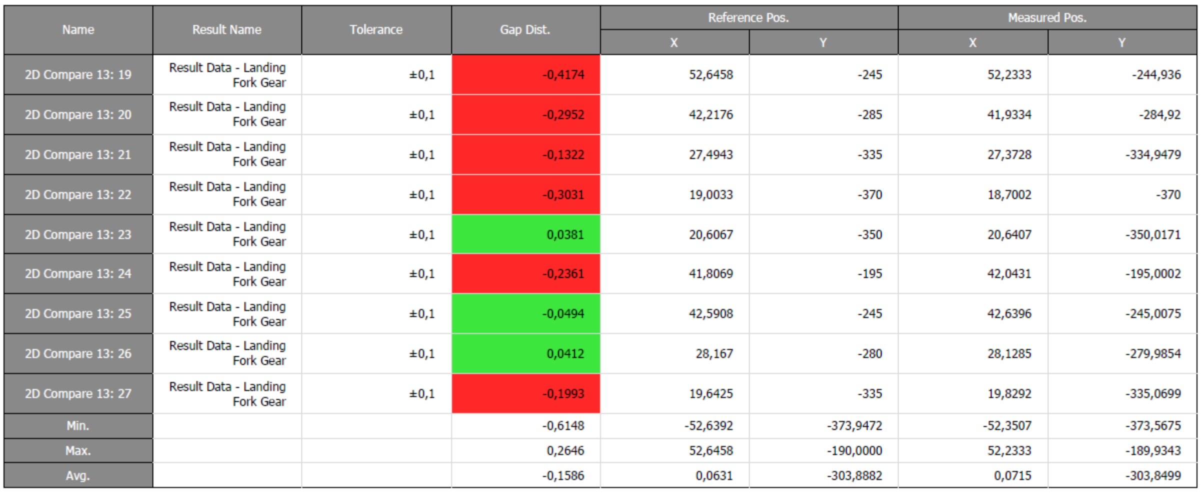

Name	Result Name	Tolerance	Gap Dist.	Reference Pos.		Measured Pos.	
				X	Y	X	Y
2D Compare 13: 19	Result Data - Landing Fork Gear	±0,1	-0,4174	52,6458	-245	52,2333	-244,936
2D Compare 13: 20	Result Data - Landing Fork Gear	±0,1	-0,2952	42,2176	-285	41,9334	-284,92
2D Compare 13: 21	Result Data - Landing Fork Gear	±0,1	-0,1322	27,4943	-335	27,3728	-334,9479
2D Compare 13: 22	Result Data - Landing Fork Gear	±0,1	-0,3031	19,0033	-370	18,7002	-370
2D Compare 13: 23	Result Data - Landing Fork Gear	±0,1	0,0381	20,6067	-350	20,6407	-350,0171
2D Compare 13: 24	Result Data - Landing Fork Gear	±0,1	-0,2361	41,8069	-195	42,0431	-195,0002
2D Compare 13: 25	Result Data - Landing Fork Gear	±0,1	-0,0494	42,5908	-245	42,6396	-245,0075
2D Compare 13: 26	Result Data - Landing Fork Gear	±0,1	0,0412	28,167	-280	28,1285	-279,9854
2D Compare 13: 27	Result Data - Landing Fork Gear	±0,1	-0,1993	19,6425	-335	19,8292	-335,0699
Min.			-0,6148	-52,6392	-373,9472	-52,3507	-373,5675
Max.			0,2646	52,6458	-190,0000	52,2333	-189,9343
Avg.			-0,1586	0,0631	-303,8882	0,0715	-303,8499

APPENDIX F: GEOMETRIC DEVIATION REPORT OF SCAN B

F.1. Scan B results

technology innovation
AGENCY

PDTS

Product Development Technology Station

Product Name	Comparison Report
Part Name	Phase 3
Part Number	19-247 - Landing Gear Scan and Compare
Department	PDTS
Inspector	Let-Mari van Heerden
Date	Oct 30, 2019
Unit	mm

Disclaimer
The results of this analysis and forecastings are believed to be reliable but are not to be construed as providing a warranty, including any warranty of merchantability or fitness for purpose, or representation for which 3D Systems, Inc. assumes legal responsibility. Users should undertake sufficient verification and iterative testing to determine the suitability of any information presented. Nothing herein is to be taken as permission, inducement or recommendation by 3D Systems, Inc. to practice any patented invention without a license or to in any way infringe upon the intellectual property rights of any other party.

© Central University of Technology, Free State

F.2. Reference data

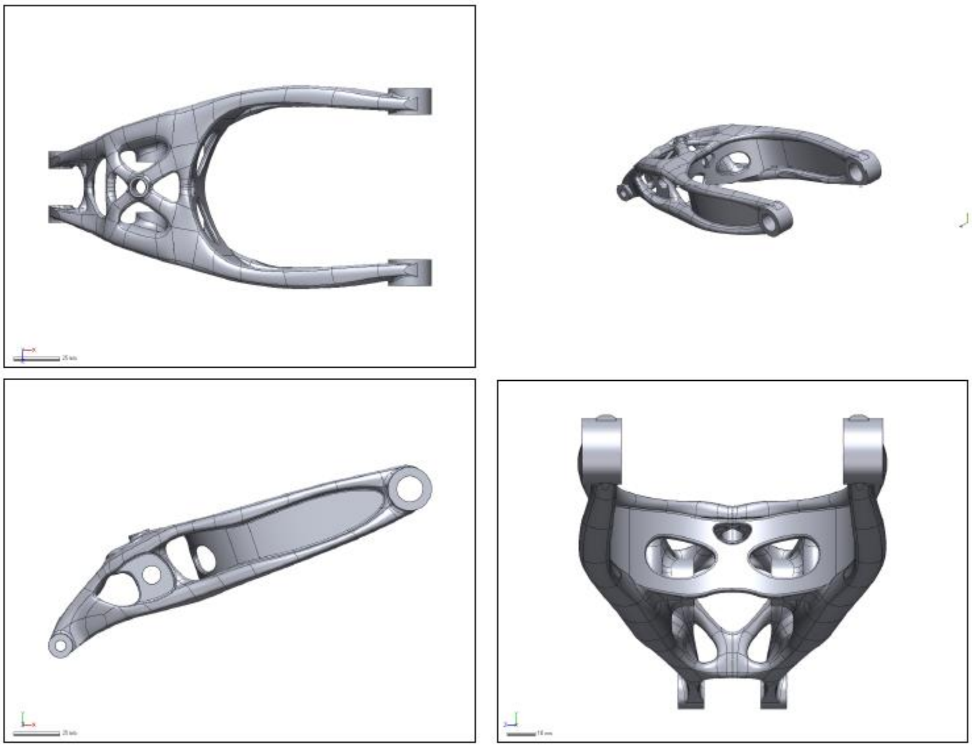

F.3. Data alignment

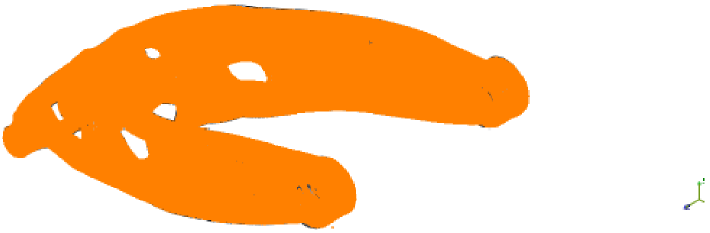

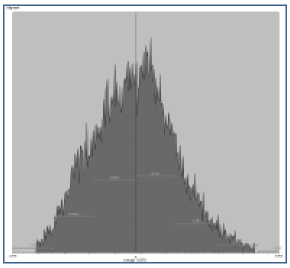

Min.	-0,74
Max.	0,7401
Avg.	-0,0753
RMS	0,2869
Std. Dev.	0,2769
Var.	0,0767
+Avg.	0,1952
-Avg.	-0,2549

F.4. Results data

© Central University of Technology, Free State

Name	Min.	Max.	Avg.	RMS	Std. Dev.	Var.	+Avg.	-Avg.
3D Compare	-1,2903	1,2795	-0,0774	0,3112	0,3014	0,0909	0,2087	-0,268

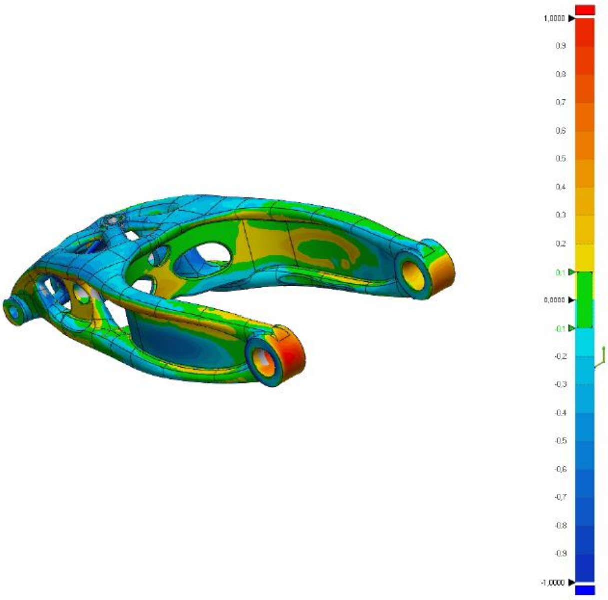

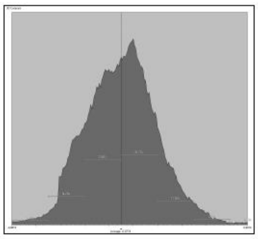

Min.	-1,2903
Max.	1,2795
Avg.	-0,0774
RMS	0,3112
Std. Dev.	0,3014
Var.	0,0909
+Avg.	0,2087
-Avg.	-0,268
In Tol.(%)	26,976
Out Tol.(%)	73,024
Over Tol.(%)	26,4846
Under Tol.(%)	46,5394

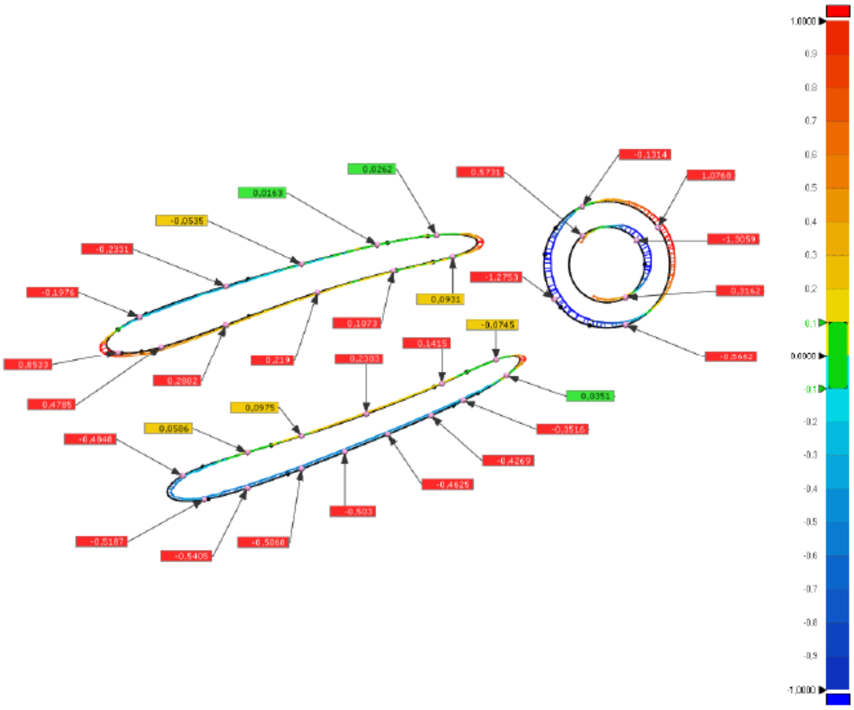

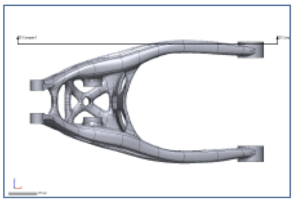

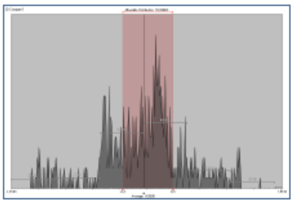

Min.	-1,3784
Max.	1,3534
Avg.	-0,0508
RMS	0,5253
Std. Dev.	0,5228
Var.	0,2733
+Avg.	0,3436
-Avg.	-0,4546
In Tol.(%)	18,4366
Out Tol.(%)	81,5634
Over Tol.(%)	40,413
Under Tol.(%)	41,1504

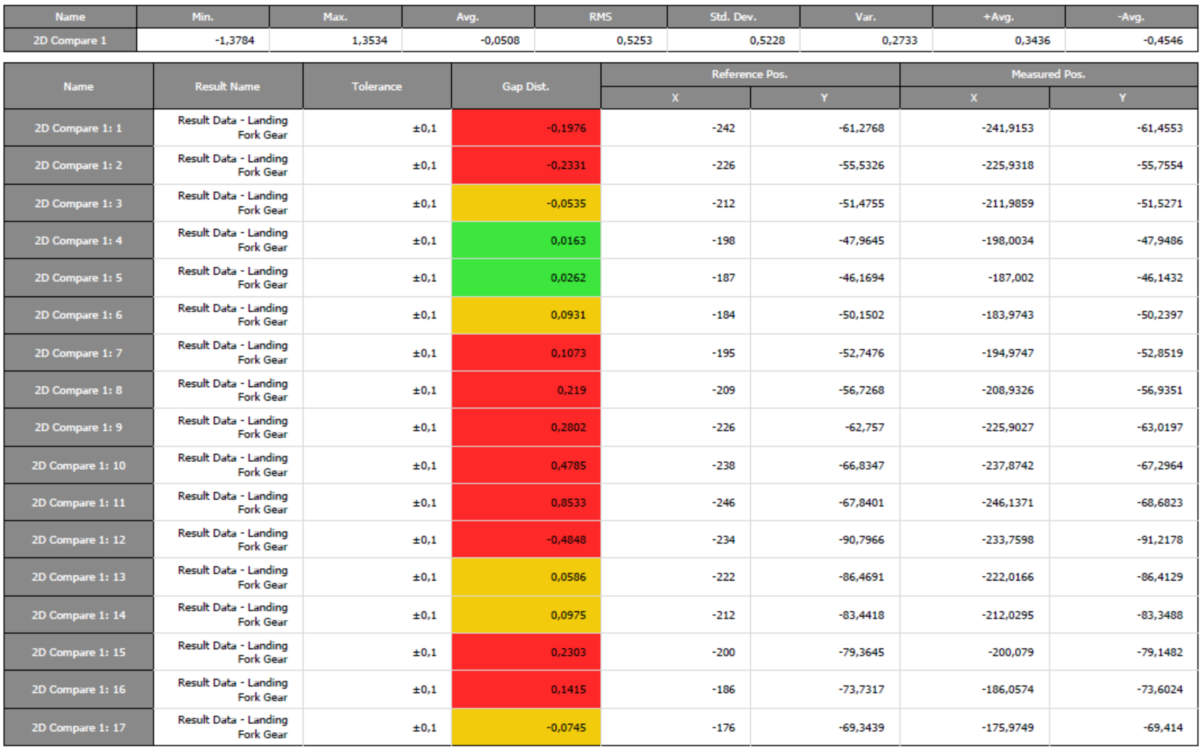

Name	Min.	Max.	Avg.	RMS	Std. Dev.	Var.	+Avg.	-Avg.
2D Compare 1	-1,3784	1,3534	-0,0508	0,5253	0,5228	0,2733	0,3436	-0,4546

Name	Result Name	Tolerance	Gap Dist.	Reference Pos.		Measured Pos.	
				X	Y	X	Y
2D Compare 1: 1	Result Data - Landing Fork Gear	±0,1	-0,1976	-242	-61,2768	-241,9153	-61,4553
2D Compare 1: 2	Result Data - Landing Fork Gear	±0,1	-0,2331	-226	-55,5326	-225,9318	-55,7554
2D Compare 1: 3	Result Data - Landing Fork Gear	±0,1	-0,0535	-212	-51,4755	-211,9859	-51,5271
2D Compare 1: 4	Result Data - Landing Fork Gear	±0,1	0,0163	-198	-47,9645	-198,0034	-47,9486
2D Compare 1: 5	Result Data - Landing Fork Gear	±0,1	0,0262	-187	-46,1694	-187,002	-46,1432
2D Compare 1: 6	Result Data - Landing Fork Gear	±0,1	0,0931	-184	-50,1502	-183,9743	-50,2397
2D Compare 1: 7	Result Data - Landing Fork Gear	±0,1	0,1073	-195	-52,7476	-194,9747	-52,8519
2D Compare 1: 8	Result Data - Landing Fork Gear	±0,1	0,219	-209	-56,7268	-208,9326	-56,9351
2D Compare 1: 9	Result Data - Landing Fork Gear	±0,1	0,2802	-226	-62,757	-225,9027	-63,0197
2D Compare 1: 10	Result Data - Landing Fork Gear	±0,1	0,4785	-238	-66,8347	-237,8742	-67,2964
2D Compare 1: 11	Result Data - Landing Fork Gear	±0,1	0,8533	-246	-67,8401	-246,1371	-68,6823
2D Compare 1: 12	Result Data - Landing Fork Gear	±0,1	-0,4848	-234	-90,7966	-233,7598	-91,2178
2D Compare 1: 13	Result Data - Landing Fork Gear	±0,1	0,0586	-222	-86,4691	-222,0166	-86,4129
2D Compare 1: 14	Result Data - Landing Fork Gear	±0,1	0,0975	-212	-83,4418	-212,0295	-83,3488
2D Compare 1: 15	Result Data - Landing Fork Gear	±0,1	0,2303	-200	-79,3645	-200,079	-79,1482
2D Compare 1: 16	Result Data - Landing Fork Gear	±0,1	0,1415	-186	-73,7317	-186,0574	-73,6024
2D Compare 1: 17	Result Data - Landing Fork Gear	±0,1	-0,0745	-176	-69,3439	-175,9749	-69,414

Name	Result Name	Tolerance	Gap Dist.	Reference Pos.		Measured Pos.	
				X	Y	X	Y
2D Compare 1: 18	Result Data - Landing Fork Gear	±0,1	0,0351	-174	-72,2249	-173,9797	-72,2535
2D Compare 1: 19	Result Data - Landing Fork Gear	±0,1	-0,3516	-182	-76,8813	-182,1554	-76,566
2D Compare 1: 20	Result Data - Landing Fork Gear	±0,1	-0,4269	-188	-79,6768	-188,1739	-79,287
2D Compare 1: 21	Result Data - Landing Fork Gear	±0,1	-0,4625	-196	-83,1202	-196,1784	-82,6935
2D Compare 1: 22	Result Data - Landing Fork Gear	±0,1	-0,503	-204	-86,3952	-204,1872	-85,9284
2D Compare 1: 23	Result Data - Landing Fork Gear	±0,1	-0,5068	-212	-89,5234	-212,1799	-89,0496
2D Compare 1: 24	Result Data - Landing Fork Gear	±0,1	-0,5405	-222	-93,0864	-222,1655	-92,5719
2D Compare 1: 25	Result Data - Landing Fork Gear	±0,1	-0,5187	-230	-95,1772	-230,085	-94,6655
2D Compare 1: 26	Result Data - Landing Fork Gear	±0,1	-1,2753	-165,163	-58	-164,0986	-57,2975
2D Compare 1: 27	Result Data - Landing Fork Gear	±0,1	-0,1314	-160	-40,8627	-159,9467	-40,9828
2D Compare 1: 28	Result Data - Landing Fork Gear	±0,1	1,0768	-146	-44,7554	-145,1274	-44,1245
2D Compare 1: 29	Result Data - Landing Fork Gear	±0,1	-0,5662	-152	-62,7137	-152,1664	-62,1725
2D Compare 1: 30	Result Data - Landing Fork Gear	±0,1	-1,3059	-150	-47,1773	-148,9848	-46,3558
2D Compare 1: 31	Result Data - Landing Fork Gear	±0,1	0,3162	-152	-57,6797	-152,1544	-57,4038
2D Compare 1: 32	Result Data - Landing Fork Gear	±0,1	0,5731	-160	-46,2724	-159,6171	-46,6989
Min.			-1,3059	-246,0000	-95,1772	-246,1371	-94,6655
Max.			1,0768	-146,0000	-40,8627	-145,1274	-40,9828
Avg.			-0,0947	-196,4426	-66,7553	-196,3672	-66,6578

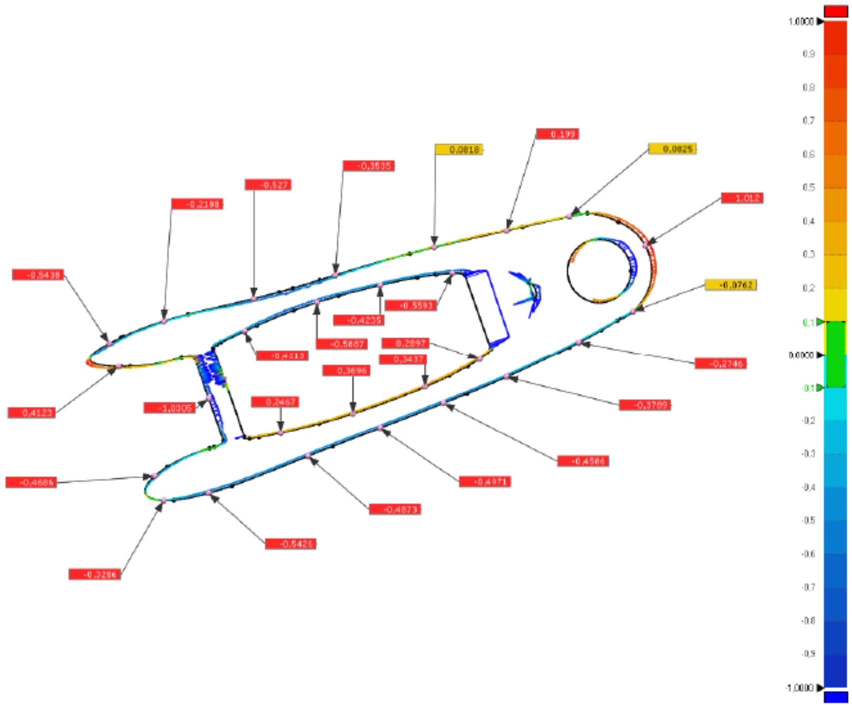

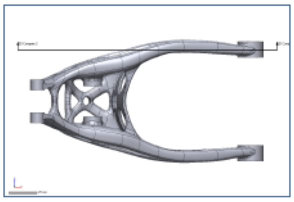

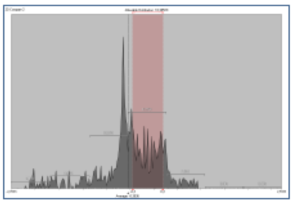

Min.	-4,9842
Max.	1,0262
Avg.	-0,3936
RMS	0,8647
Std. Dev.	0,7699
Var.	0,5927
+Avg.	0,3186
-Avg.	-0,6999
In Tol.(%)	10,3952
Out Tol.(%)	89,6048
Over Tol.(%)	25,2577
Under Tol.(%)	64,3471

Name	Min.	Max.	Avg.	RMS	Std. Dev.	Var.	+Avg.	-Avg.
2D Compare 2	-4,9842	1,0262	-0,3936	0,8647	0,7699	0,5927	0,3186	-0,6999

Name	Result Name	Tolerance	Gap Dist.	Reference Pos.		Measured Pos.	
				X	Y	X	Y
2D Compare 2: 1	Result Data - Landing Fork Gear	±0,1	-0,4213	-234	-64,8652	-234,1776	-64,4832
2D Compare 2: 2	Result Data - Landing Fork Gear	±0,1	-0,5887	-218	-58,5425	-218,1782	-57,9814
2D Compare 2: 3	Result Data - Landing Fork Gear	±0,1	-0,4235	-204	-54,6913	-204,0969	-54,279
2D Compare 2: 4	Result Data - Landing Fork Gear	±0,1	-0,5593	-188	-52,0546	-188,0141	-51,4955
2D Compare 2: 5	Result Data - Landing Fork Gear	±0,1	0,2897	-182	-71,1709	-182,1642	-70,9321
2D Compare 2: 6	Result Data - Landing Fork Gear	±0,1	0,3437	-194	-77,3555	-194,1363	-77,04
2D Compare 2: 7	Result Data - Landing Fork Gear	±0,1	0,3696	-210	-83,3333	-210,113	-82,9814
2D Compare 2: 8	Result Data - Landing Fork Gear	±0,1	0,2467	-226	-87,5378	-226,05	-87,2962
2D Compare 2: 9	Result Data - Landing Fork Gear	±0,1	-1,0305	-241,9597	-80	-240,987	-79,6598
2D Compare 2: 10	Result Data - Landing Fork Gear	±0,1	0,4123	-262	-72,8435	-262,0074	-73,2557
2D Compare 2: 11	Result Data - Landing Fork Gear	±0,1	-0,4686	-254	-97,1732	-253,6859	-97,5209
2D Compare 2: 12	Result Data - Landing Fork Gear	±0,1	-0,5438	-264	-67,6084	-263,7424	-68,0873
2D Compare 2: 13	Result Data - Landing Fork Gear	±0,1	-0,2188	-252	-62,6988	-251,9353	-62,9078
2D Compare 2: 14	Result Data - Landing Fork Gear	±0,1	-0,527	-232	-57,7205	-231,8729	-58,2319
2D Compare 2: 15	Result Data - Landing Fork Gear	±0,1	-0,3535	-214	-52,5128	-213,8954	-52,8504
2D Compare 2: 16	Result Data - Landing Fork Gear	±0,1	0,0818	-192	-46,3562	-192,0194	-46,2768
2D Compare 2: 17	Result Data - Landing Fork Gear	±0,1	0,199	-176	-42,6443	-176,0439	-42,4501

Name	Result Name	Tolerance	Gap Dist.	Reference Pos.		Measured Pos.	
				X	Y	X	Y
2D Compare 2: 18	Result Data - Landing Fork Gear	±0,1	0,0825	-162	-39,5252	-162,0164	-39,4443
2D Compare 2: 19	Result Data - Landing Fork Gear	±0,1	1,012	-145,2145	-46	-144,3263	-45,515
2D Compare 2: 20	Result Data - Landing Fork Gear	±0,1	-0,0762	-148	-60,5483	-148,0473	-60,4885
2D Compare 2: 21	Result Data - Landing Fork Gear	±0,1	-0,2746	-160	-67,3973	-160,1275	-67,1541
2D Compare 2: 22	Result Data - Landing Fork Gear	±0,1	-0,3789	-176	-75,1421	-176,1536	-74,7958
2D Compare 2: 23	Result Data - Landing Fork Gear	±0,1	-0,4586	-190	-81,0225	-190,1709	-80,5969
2D Compare 2: 24	Result Data - Landing Fork Gear	±0,1	-0,4971	-204	-86,4927	-204,1779	-86,0285
2D Compare 2: 25	Result Data - Landing Fork Gear	±0,1	-0,4873	-220	-92,6887	-220,1808	-92,2361
2D Compare 2: 26	Result Data - Landing Fork Gear	±0,1	-0,5426	-242	-100,9116	-242,143	-100,3882
2D Compare 2: 27	Result Data - Landing Fork Gear	±0,1	-0,3286	-252	-102,5308	-251,9894	-102,2024
Min.			-1,0305	-264,0000	-102,5308	-263,7424	-102,2024
Max.			1,0120	-145,2145	-39,5252	-144,3263	-39,4443
Avg.			-0,1904	-209,0065	-69,6803	-208,9797	-69,5029

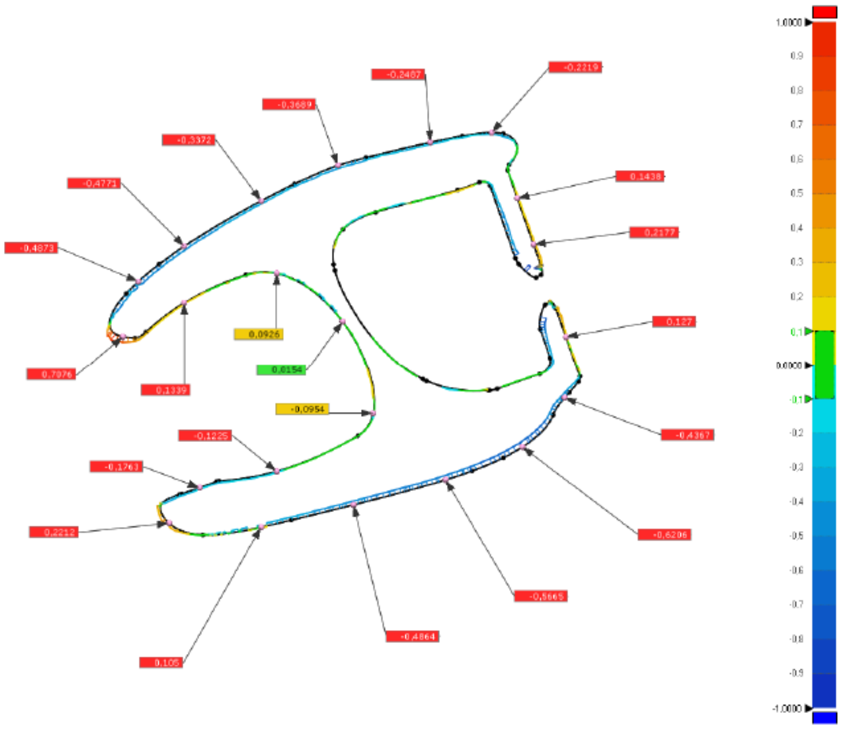

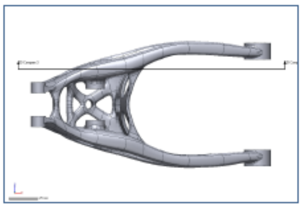

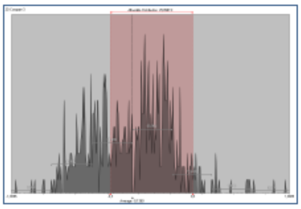

Min.	-0,978
Max.	0,9769
Avg.	-0,1399
RMS	0,3216
Std. Dev.	0,2896
Var.	0,0839
+Avg.	0,1655
-Avg.	-0,3007
In Tol.(%)	29,0941
Out Tol.(%)	70,9059
Over Tol.(%)	20,3833
Under Tol.(%)	50,5226

© Central University of Technology, Free State

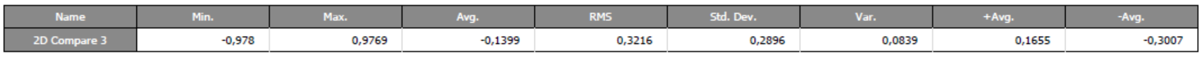

Name	Min.	Max.	Avg.	RMS	Std. Dev.	Var.	+Avg.	-Avg.
2D Compare 3	-0,978	0,9769	-0,1399	0,3216	0,2896	0,0839	0,1655	-0,3007

Name	Result Name	Tolerance	Gap Dist.	Reference Pos.		Measured Pos.	
				X	Y	X	Y
2D Compare 3: 1	Result Data - Landing Fork Gear	±0,1	0,0154	-285,402	-92	-285,4144	-92,0092
2D Compare 3: 2	Result Data - Landing Fork Gear	±0,1	-0,0954	-281,4163	-104	-281,3231	-104,0202
2D Compare 3: 3	Result Data - Landing Fork Gear	±0,1	0,0926	-294	-85,7203	-294,0187	-85,811
2D Compare 3: 4	Result Data - Landing Fork Gear	±0,1	0,1339	-306	-89,56	-305,9298	-89,6741
2D Compare 3: 5	Result Data - Landing Fork Gear	±0,1	-0,1225	-294	-111,5601	-293,9677	-111,6782
2D Compare 3: 6	Result Data - Landing Fork Gear	±0,1	-0,1763	-304	-113,6881	-303,9416	-113,8545
2D Compare 3: 7	Result Data - Landing Fork Gear	±0,1	0,7076	-314	-93,9705	-314,154	-94,6611
2D Compare 3: 8	Result Data - Landing Fork Gear	±0,1	0,2212	-308	-118,2873	-308,1474	-118,4522
2D Compare 3: 9	Result Data - Landing Fork Gear	±0,1	-0,4873	-312	-86,7981	-311,6732	-87,1595
2D Compare 3: 10	Result Data - Landing Fork Gear	±0,1	-0,4771	-306	-82,2144	-305,7345	-82,6108
2D Compare 3: 11	Result Data - Landing Fork Gear	±0,1	-0,3372	-296	-76,3357	-295,8428	-76,6341
2D Compare 3: 12	Result Data - Landing Fork Gear	±0,1	-0,3689	-286	-71,7185	-285,8826	-72,0681
2D Compare 3: 13	Result Data - Landing Fork Gear	±0,1	-0,2487	-274	-68,7345	-273,9477	-68,9776
2D Compare 3: 14	Result Data - Landing Fork Gear	±0,1	-0,2219	-266	-67,4707	-266,0005	-67,6926
2D Compare 3: 15	Result Data - Landing Fork Gear	±0,1	0,1438	-262,6546	-76	-262,5188	-75,9525
2D Compare 3: 16	Result Data - Landing Fork Gear	±0,1	0,2177	-260,556	-82	-260,3505	-81,9281
2D Compare 3: 17	Result Data - Landing Fork Gear	±0,1	0,127	-256,3588	-94	-256,239	-93,9581

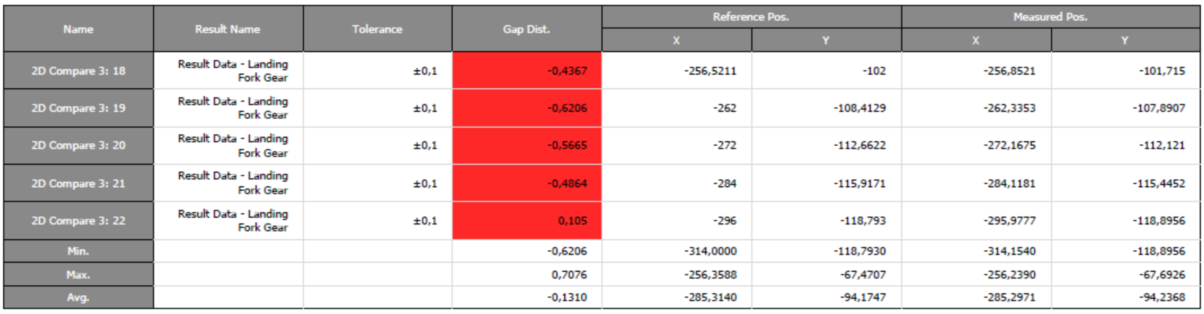

Name	Result Name	Tolerance	Gap Dist.	Reference Pos.		Measured Pos.	
				X	Y	X	Y
2D Compare 3: 18	Result Data - Landing Fork Gear	±0,1	-0,4367	-256,5211	-102	-256,8521	-101,715
2D Compare 3: 19	Result Data - Landing Fork Gear	±0,1	-0,6206	-262	-108,4129	-262,3353	-107,8907
2D Compare 3: 20	Result Data - Landing Fork Gear	±0,1	-0,5665	-272	-112,6622	-272,1675	-112,121
2D Compare 3: 21	Result Data - Landing Fork Gear	±0,1	-0,4864	-284	-115,9171	-284,1181	-115,4452
2D Compare 3: 22	Result Data - Landing Fork Gear	±0,1	0,105	-296	-118,793	-295,9777	-118,8956
Min.			-0,6206	-314,0000	-118,7930	-314,1540	-118,8956
Max.			0,7076	-256,3588	-67,4707	-256,2390	-67,6926
Avg.			-0,1310	-285,3140	-94,1747	-285,2971	-94,2368

© Central University of Technology, Free State

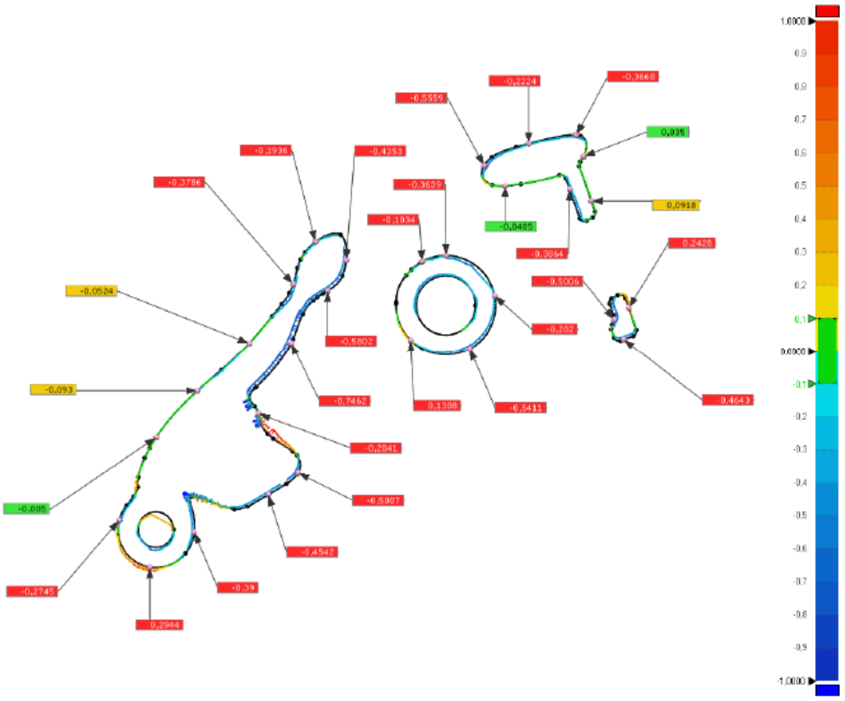

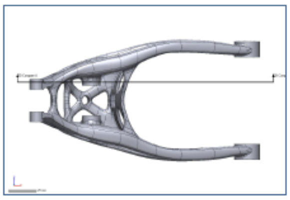

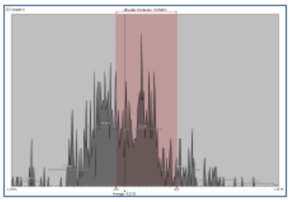

Min.	-1,4647
Max.	1,1747
Avg.	-0,2128
RMS	0,4252
Std. Dev.	0,3682
Var.	0,1356
+Avg.	0,238
-Avg.	-0,3719
In Tol.(%)	23,7681
Out Tol.(%)	76,2319
Over Tol.(%)	15,2174
Under Tol.(%)	61,0145

Name	Min.	Max.	Avg.	RMS	Std. Dev.	Var.	+Avg.	-Avg.
2D Compare 4	-1,4647	1,1747	-0,2128	0,4252	0,3682	0,1356	0,238	-0,3719

Name	Result Name	Tolerance	Gap Dist.	Reference Pos.		Measured Pos.	
				X	Y	X	Y
2D Compare 4: 1	Result Data - Landing Fork Gear	±0,1	-0,39	-336,5196	-136	-336,907	-135,9551
2D Compare 4: 2	Result Data - Landing Fork Gear	±0,1	0,2944	-344	-141,8879	-344,0467	-142,1786
2D Compare 4: 3	Result Data - Landing Fork Gear	±0,1	-0,2745	-349,1824	-134	-348,9163	-134,0674
2D Compare 4: 4	Result Data - Landing Fork Gear	±0,1	-0,005	-342,942	-120	-342,9377	-120,0027
2D Compare 4: 5	Result Data - Landing Fork Gear	±0,1	-0,093	-336	-112,1367	-335,9373	-112,2054
2D Compare 4: 6	Result Data - Landing Fork Gear	±0,1	-0,0524	-327,2183	-104	-327,1793	-104,0351
2D Compare 4: 7	Result Data - Landing Fork Gear	±0,1	-0,3786	-319,793	-94	-319,4336	-94,1191
2D Compare 4: 8	Result Data - Landing Fork Gear	±0,1	-0,1936	-316	-86,8702	-315,8825	-87,024
2D Compare 4: 9	Result Data - Landing Fork Gear	±0,1	-0,4353	-310,8225	-90	-311,2552	-89,9523
2D Compare 4: 10	Result Data - Landing Fork Gear	±0,1	-0,5802	-314	-95,1208	-314,3086	-94,6294
2D Compare 4: 11	Result Data - Landing Fork Gear	±0,1	-0,7462	-320,1284	-104	-320,8002	-103,6754
2D Compare 4: 12	Result Data - Landing Fork Gear	±0,1	-0,2041	-325,6165	-116	-325,8141	-116,0511
2D Compare 4: 13	Result Data - Landing Fork Gear	±0,1	-0,4542	-324	-129,6635	-324,2271	-129,2701
2D Compare 4: 14	Result Data - Landing Fork Gear	±0,1	-0,5007	-318,9716	-126	-319,4055	-125,7501
2D Compare 4: 15	Result Data - Landing Fork Gear	±0,1	0,1308	-300	-103,4576	-300,0922	-103,5504
2D Compare 4: 16	Result Data - Landing Fork Gear	±0,1	-0,5411	-290	-104,9534	-290,2581	-104,4778
2D Compare 4: 17	Result Data - Landing Fork Gear	±0,1	-0,202	-285,7559	-96	-285,9545	-96,0364

© Central University of Technology, Free State

Name	Result Name	Tolerance	Gap Dist.	Reference Pos.		Measured Pos.	
				X	Y	X	Y
2D Compare 4: 18	Result Data - Landing Fork Gear	±0,1	-0,3639	-294	-89,1711	-294,0037	-89,535
2D Compare 4: 19	Result Data - Landing Fork Gear	±0,1	-0,1034	-298	-90,1805	-297,9498	-90,2708
2D Compare 4: 20	Result Data - Landing Fork Gear	±0,1	-0,5559	-287,5762	-74	-287,0994	-74,2857
2D Compare 4: 21	Result Data - Landing Fork Gear	±0,1	-0,2224	-280	-70,3202	-279,9438	-70,5353
2D Compare 4: 22	Result Data - Landing Fork Gear	±0,1	-0,3668	-272	-68,8914	-272,0153	-69,2579
2D Compare 4: 23	Result Data - Landing Fork Gear	±0,1	0,035	-270,7714	-72,5	-270,7372	-72,5077
2D Compare 4: 24	Result Data - Landing Fork Gear	±0,1	0,2428	-263,143	-98	-262,9138	-97,9198
2D Compare 4: 25	Result Data - Landing Fork Gear	±0,1	-0,4643	-264	-103,3221	-264,1607	-102,8865
2D Compare 4: 26	Result Data - Landing Fork Gear	±0,1	-0,5006	-265,6053	-100	-265,1097	-100,0702
2D Compare 4: 27	Result Data - Landing Fork Gear	±0,1	-0,3864	-273,1141	-78	-272,7494	-77,8724
2D Compare 4: 28	Result Data - Landing Fork Gear	±0,1	-0,0485	-284	-77,4708	-284,0032	-77,4224
2D Compare 4: 29	Result Data - Landing Fork Gear	±0,1	0,0918	-269,4387	-80	-269,3521	-79,9697
Min.			-0,7462	-349,1824	-141,8879	-348,9163	-142,1786
Max.			0,2944	-263,1430	-68,8914	-262,9138	-69,2579
Avg.			-0,2506	-302,8482	-99,8602	-302,8757	-99,8453

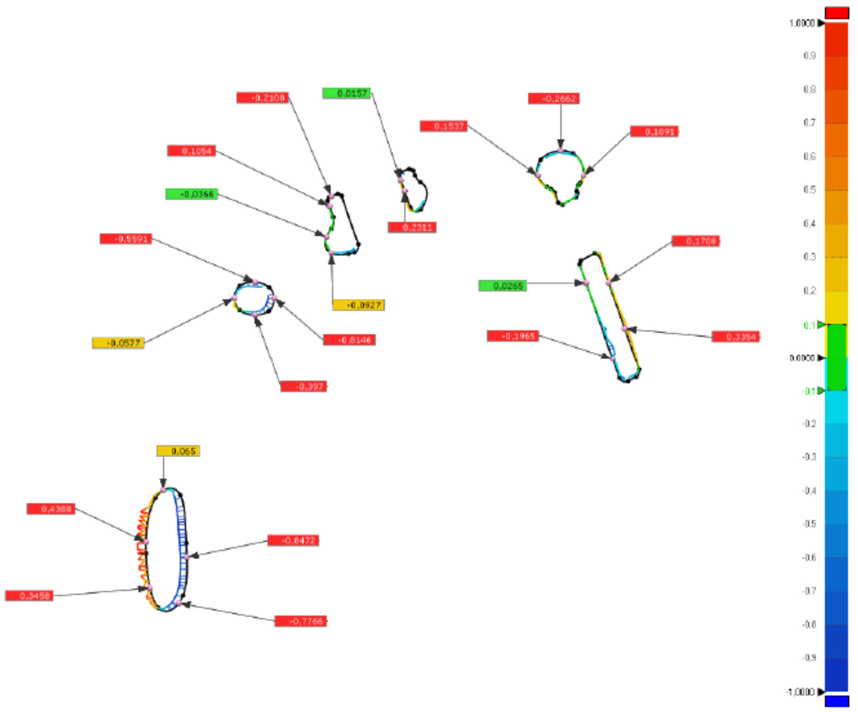

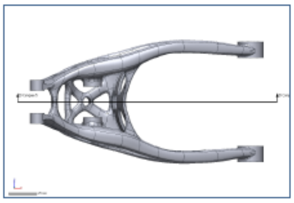

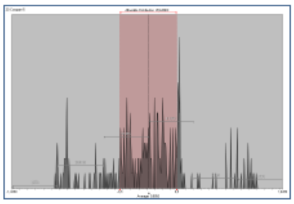

Min.	-0,9722
Max.	1,1499
Avg.	0,0053
RMS	0,4746
Std. Dev.	0,4746
Var.	0,2252
+Avg.	0,337
-Avg.	-0,3801
In Tol.(%)	20,6406
Out Tol.(%)	79,3594
Over Tol.(%)	42,3488
Under Tol.(%)	37,0107

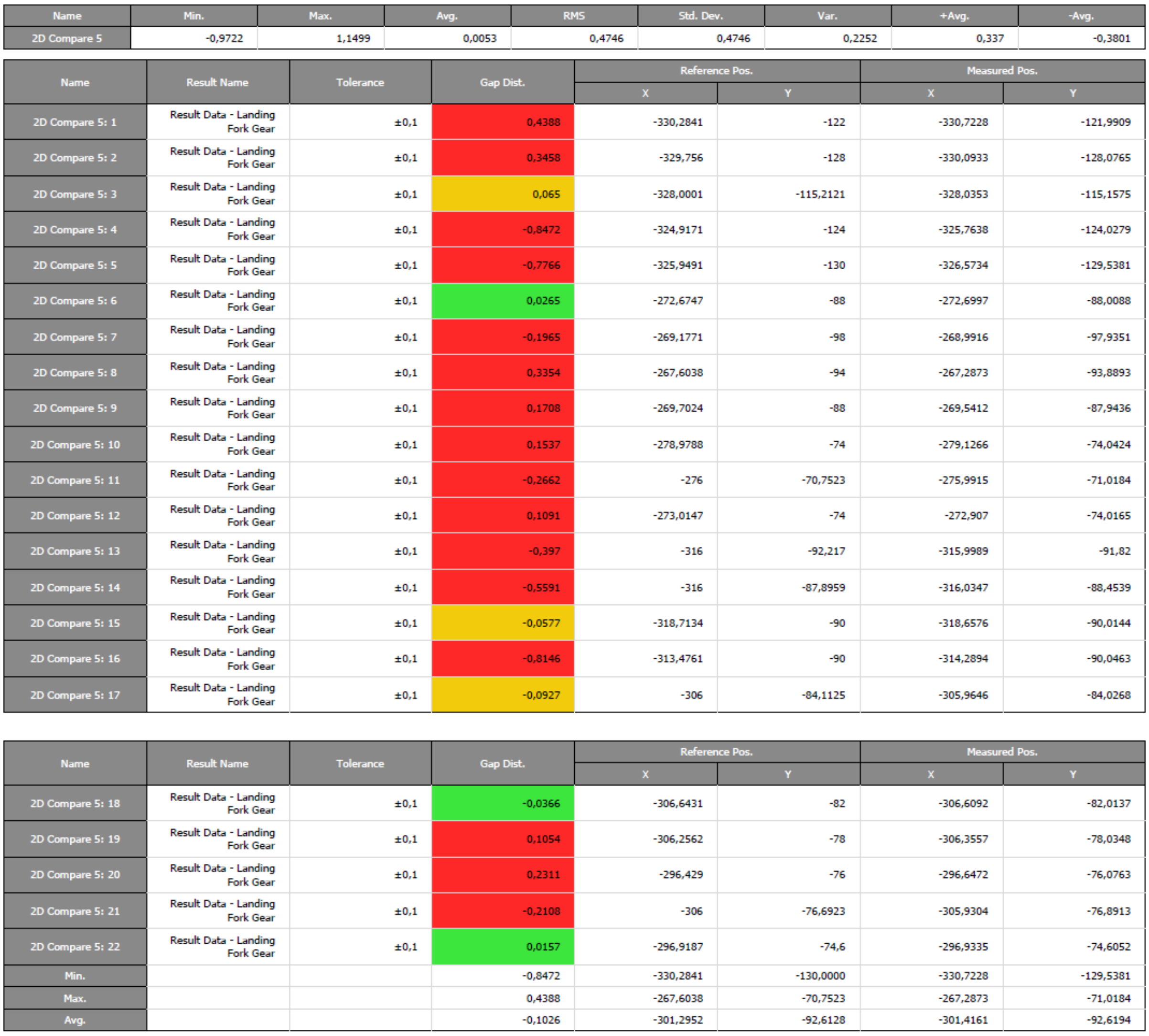

Name	Min.	Max.	Avg.	RMS	Std. Dev.	Var.	+Avg.	-Avg.
2D Compare 5	-0,9722	1,1499	0,0053	0,4746	0,4746	0,2252	0,337	-0,3801

Name	Result Name	Tolerance	Gap Dist.	Reference Pos.		Measured Pos.	
				X	Y	X	Y
2D Compare 5: 1	Result Data - Landing Fork Gear	±0,1	0,4388	-330,2841	-122	-330,7228	-121,9909
2D Compare 5: 2	Result Data - Landing Fork Gear	±0,1	0,3458	-329,756	-128	-330,0933	-128,0765
2D Compare 5: 3	Result Data - Landing Fork Gear	±0,1	0,065	-328,0001	-115,2121	-328,0353	-115,1575
2D Compare 5: 4	Result Data - Landing Fork Gear	±0,1	-0,8472	-324,9171	-124	-325,7638	-124,0279
2D Compare 5: 5	Result Data - Landing Fork Gear	±0,1	-0,7766	-325,9491	-130	-326,5734	-129,5381
2D Compare 5: 6	Result Data - Landing Fork Gear	±0,1	0,0265	-272,6747	-88	-272,6997	-88,0088
2D Compare 5: 7	Result Data - Landing Fork Gear	±0,1	-0,1965	-269,1771	-98	-268,9916	-97,9351
2D Compare 5: 8	Result Data - Landing Fork Gear	±0,1	0,3354	-267,6038	-94	-267,2873	-93,8893
2D Compare 5: 9	Result Data - Landing Fork Gear	±0,1	0,1708	-269,7024	-88	-269,5412	-87,9436
2D Compare 5: 10	Result Data - Landing Fork Gear	±0,1	0,1537	-278,9788	-74	-279,1266	-74,0424
2D Compare 5: 11	Result Data - Landing Fork Gear	±0,1	-0,2662	-276	-70,7523	-275,9915	-71,0184
2D Compare 5: 12	Result Data - Landing Fork Gear	±0,1	0,1091	-273,0147	-74	-272,907	-74,0165
2D Compare 5: 13	Result Data - Landing Fork Gear	±0,1	-0,397	-316	-92,217	-315,9989	-91,82
2D Compare 5: 14	Result Data - Landing Fork Gear	±0,1	-0,5591	-316	-87,8959	-316,0347	-88,4539
2D Compare 5: 15	Result Data - Landing Fork Gear	±0,1	-0,0577	-318,7134	-90	-318,6576	-90,0144
2D Compare 5: 16	Result Data - Landing Fork Gear	±0,1	-0,8146	-313,4761	-90	-314,2894	-90,0463
2D Compare 5: 17	Result Data - Landing Fork Gear	±0,1	-0,0927	-306	-84,1125	-305,9646	-84,0268
2D Compare 5: 18	Result Data - Landing Fork Gear	±0,1	-0,0366	-306,6431	-82	-306,6092	-82,0137
2D Compare 5: 19	Result Data - Landing Fork Gear	±0,1	0,1054	-306,2562	-78	-306,3557	-78,0348
2D Compare 5: 20	Result Data - Landing Fork Gear	±0,1	0,2311	-296,429	-76	-296,6472	-76,0763
2D Compare 5: 21	Result Data - Landing Fork Gear	±0,1	-0,2108	-306	-76,6923	-305,9304	-76,8913
2D Compare 5: 22	Result Data - Landing Fork Gear	±0,1	0,0157	-296,9187	-74,6	-296,9335	-74,6052
Min.			-0,8472	-330,2841	-130,0000	-330,7228	-129,5381
Max.			0,4388	-267,6038	-70,7523	-267,2873	-71,0184
Avg.			-0,1026	-301,2952	-92,6128	-301,4161	-92,6194

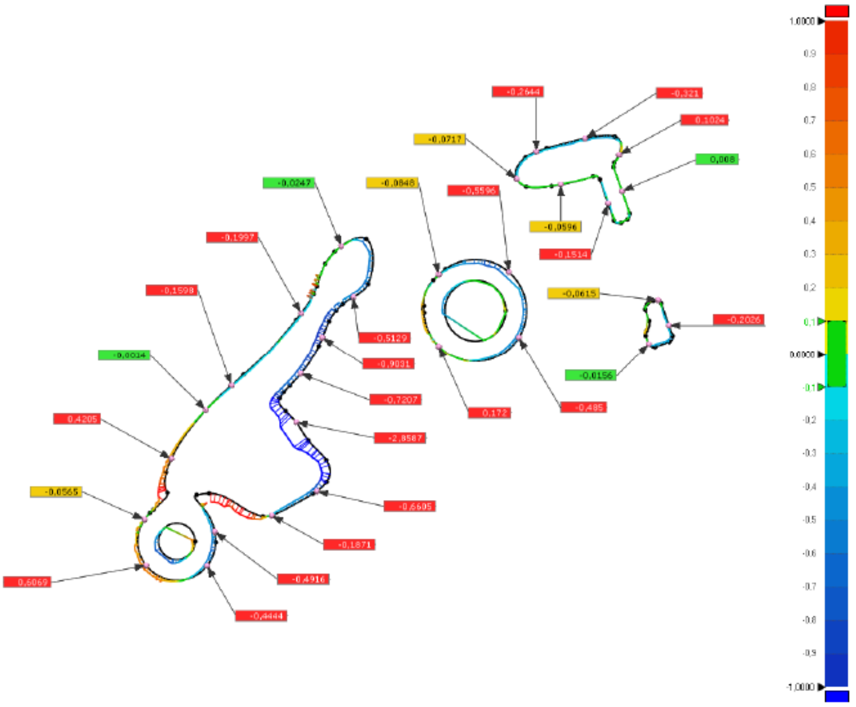

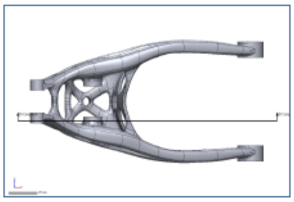

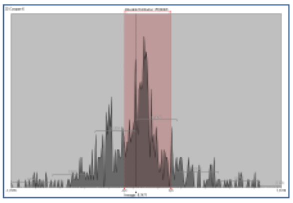

Min.	-2,4981
Max.	1,4508
Avg.	-0,1471
RMS	0,547
Std. Dev.	0,5269
Var.	0,2776
+Avg.	0,3794
-Avg.	-0,3883
In Tol.(%)	25,8446
Out Tol.(%)	74,1554
Over Tol.(%)	22,6351
Under Tol.(%)	51,5203

Name	Min.	Max.	Avg.	RMS	Std. Dev.	Var.	+Avg.	-Avg.
2D Compare 6	-2,4981	1,4508	-0,1471	0,547	0,5269	0,2776	0,3794	-0,3883

Name	Result Name	Tolerance	Gap Dist.	Reference Pos.		Measured Pos.	
				X	Y	X	Y
2D Compare 6: 1	Result Data - Landing Fork Gear	±0,1	0,172	-300	-103,4576	-300,1224	-103,5784
2D Compare 6: 2	Result Data - Landing Fork Gear	±0,1	-0,485	-286,8701	-102	-287,2826	-101,7448
2D Compare 6: 3	Result Data - Landing Fork Gear	±0,1	-0,5596	-288,5	-91,2287	-288,8386	-91,6742
2D Compare 6: 4	Result Data - Landing Fork Gear	±0,1	-0,0848	-300	-91,6281	-299,9443	-91,692
2D Compare 6: 5	Result Data - Landing Fork Gear	±0,1	-0,0717	-287,235	-76	-287,1705	-75,9688
2D Compare 6: 6	Result Data - Landing Fork Gear	±0,1	-0,2644	-284	-71,507	-283,9051	-71,7537
2D Compare 6: 7	Result Data - Landing Fork Gear	±0,1	-0,321	-276	-69,3599	-275,9341	-69,6741
2D Compare 6: 8	Result Data - Landing Fork Gear	±0,1	0,1024	-270,3987	-72	-270,3049	-72,0412
2D Compare 6: 9	Result Data - Landing Fork Gear	±0,1	0,008	-269,9356	-78	-269,928	-77,9974
2D Compare 6: 10	Result Data - Landing Fork Gear	±0,1	-0,1514	-272,2122	-80	-272,0693	-79,95
2D Compare 6: 11	Result Data - Landing Fork Gear	±0,1	-0,0596	-280	-76,8978	-280,0103	-76,8391
2D Compare 6: 12	Result Data - Landing Fork Gear	±0,1	-0,0156	-265,5492	-103,0413	-265,5379	-103,0306
2D Compare 6: 13	Result Data - Landing Fork Gear	±0,1	-0,2026	-262,2408	-100	-262,4321	-100,0669
2D Compare 6: 14	Result Data - Landing Fork Gear	±0,1	-0,5129	-314	-95,3531	-314,2613	-94,9117
2D Compare 6: 15	Result Data - Landing Fork Gear	±0,1	-0,9031	-319,0759	-102	-319,9176	-101,6728
2D Compare 6: 16	Result Data - Landing Fork Gear	±0,1	-0,7207	-322,6349	-108	-323,1877	-107,5375
2D Compare 6: 17	Result Data - Landing Fork Gear	±0,1	-2,8587	-323,3794	-116	-325,617	-117,7792

© Central University of Technology, Free State

Name	Result Name	Tolerance	Gap Dist.	Reference Pos.		Measured Pos.	
				X	Y	X	Y
2D Compare 6: 18	Result Data - Landing Fork Gear	±0,1	-0,6605	-320	-127,3229	-320,3746	-126,7788
2D Compare 6: 19	Result Data - Landing Fork Gear	±0,1	-0,1871	-327,4072	-131,3353	-327,4616	-131,1562
2D Compare 6: 20	Result Data - Landing Fork Gear	±0,1	-0,4916	-336,7275	-134	-337,21	-134,0944
2D Compare 6: 21	Result Data - Landing Fork Gear	±0,1	-0,4444	-338	-139,5925	-338,3462	-139,3138
2D Compare 6: 22	Result Data - Landing Fork Gear	±0,1	0,6069	-348	-139,5373	-348,4746	-139,9155
2D Compare 6: 23	Result Data - Landing Fork Gear	±0,1	-0,0565	-348,2897	-132	-348,2425	-132,0309
2D Compare 6: 24	Result Data - Landing Fork Gear	±0,1	0,4205	-343,8562	-122	-344,2385	-121,8248
2D Compare 6: 25	Result Data - Landing Fork Gear	±0,1	-0,0014	-338,207	-114	-338,206	-114,001
2D Compare 6: 26	Result Data - Landing Fork Gear	±0,1	-0,1598	-334	-109,936	-333,8935	-110,0552
2D Compare 6: 27	Result Data - Landing Fork Gear	±0,1	-0,1997	-322,5758	-98	-322,4171	-98,1213
2D Compare 6: 28	Result Data - Landing Fork Gear	±0,1	-0,0247	-316	-86,9784	-315,9855	-86,9983
2D Compare 6: 29	Result Data - Landing Fork Gear	±0,1	-0,0615	-264	-95,8746	-264,0249	-95,9308
Min.			-2,8587	-348,2897	-139,5925	-348,4746	-139,9155
Max.			0,6069	-262,2408	-69,3599	-262,4321	-69,6741
Avg.			-0,2824	-305,4860	-102,3121	-305,7013	-102,3494

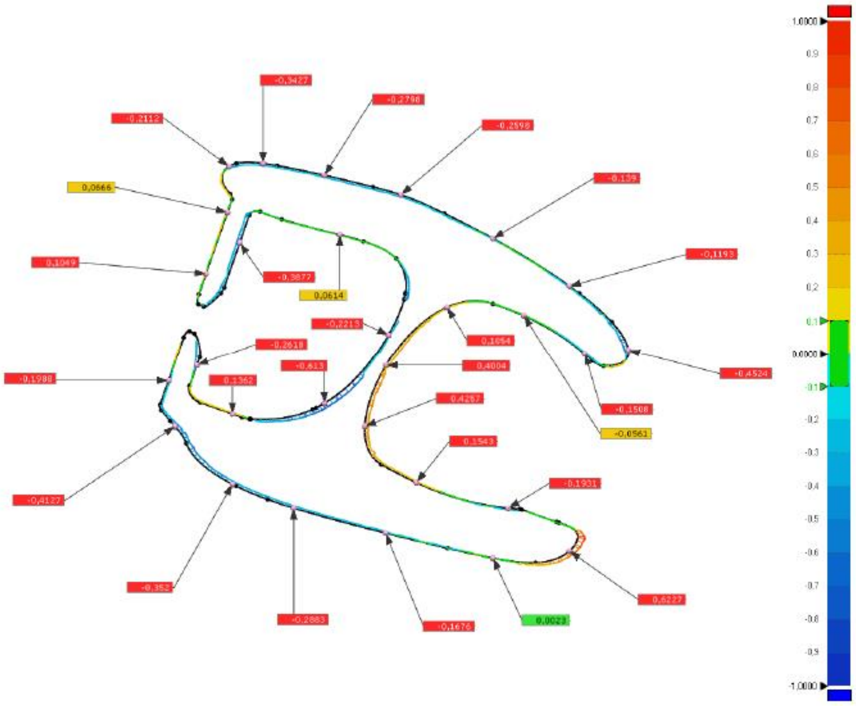

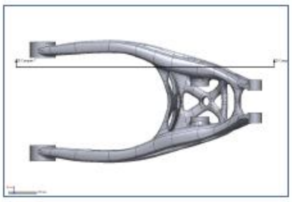

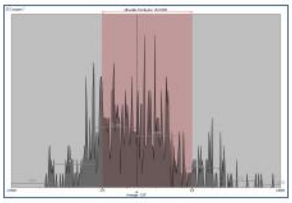

Min.	-0,6621
Max.	0,9624
Avg.	-0,07
RMS	0,2838
Std. Dev.	0,2751
Var.	0,0757
+Avg.	0,2093
-Avg.	-0,2433
In Tol.(%)	26,2238
Out Tol.(%)	73,7762
Over Tol.(%)	25
Under Tol.(%)	48,7762

Name	Min.	Max.	Avg.	RMS	Std. Dev.	Var.	+Avg.	-Avg.
2D Compare 7	-0,6621	0,9624	-0,07	0,2838	0,2751	0,0757	0,2093	-0,2433

Name	Result Name	Tolerance	Gap Dist.	Reference Pos.		Measured Pos.	
				X	Y	X	Y
2D Compare 7: 1	Result Data - Landing Fork Gear	±0,1	-0,3427	268	-67,6205	267,9557	-67,9603
2D Compare 7: 2	Result Data - Landing Fork Gear	±0,1	-0,2798	276	-69,1778	275,9379	-69,4505
2D Compare 7: 3	Result Data - Landing Fork Gear	±0,1	-0,2598	286	-71,7184	285,9175	-71,9648
2D Compare 7: 4	Result Data - Landing Fork Gear	±0,1	-0,139	298	-77,4094	297,9333	-77,5312
2D Compare 7: 5	Result Data - Landing Fork Gear	±0,1	-0,1193	308	-83,6058	307,9304	-83,7027
2D Compare 7: 6	Result Data - Landing Fork Gear	±0,1	-0,4524	315,6848	-92	315,2357	-92,0541
2D Compare 7: 7	Result Data - Landing Fork Gear	±0,1	-0,1508	310	-92,4697	310,0983	-92,3553
2D Compare 7: 8	Result Data - Landing Fork Gear	±0,1	-0,0561	302	-87,453	302,023	-87,4018
2D Compare 7: 9	Result Data - Landing Fork Gear	±0,1	0,1054	292	-86,3751	292,0429	-86,4713
2D Compare 7: 10	Result Data - Landing Fork Gear	±0,1	0,4004	284,0558	-94	284,3984	-94,2072
2D Compare 7: 11	Result Data - Landing Fork Gear	±0,1	0,4257	281,2832	-102	281,7084	-102,0201
2D Compare 7: 12	Result Data - Landing Fork Gear	±0,1	0,1543	288	-109,3487	288,0644	-109,2085
2D Compare 7: 13	Result Data - Landing Fork Gear	±0,1	-0,1931	300	-112,6766	299,9807	-112,8687
2D Compare 7: 14	Result Data - Landing Fork Gear	±0,1	0,6227	308	-118,2699	308,4151	-118,7341
2D Compare 7: 15	Result Data - Landing Fork Gear	±0,1	0,0023	298	-119,2045	297,9995	-119,2068
2D Compare 7: 16	Result Data - Landing Fork Gear	±0,1	-0,1676	284	-115,9182	284,0409	-115,7558
2D Compare 7: 17	Result Data - Landing Fork Gear	±0,1	-0,2883	272	-112,6655	272,0854	-112,3901
2D Compare 7: 18	Result Data - Landing Fork Gear	±0,1	-0,352	264	-109,5618	264,161	-109,2487
2D Compare 7: 19	Result Data - Landing Fork Gear	±0,1	-0,4127	256,5136	-102	256,8284	-101,7331
2D Compare 7: 20	Result Data - Landing Fork Gear	±0,1	-0,1988	255,6538	-96	255,8414	-96,0657
2D Compare 7: 21	Result Data - Landing Fork Gear	±0,1	0,1049	260,5504	-82	260,4514	-81,9654
2D Compare 7: 22	Result Data - Landing Fork Gear	±0,1	0,0666	263,3485	-74	263,2857	-73,978
2D Compare 7: 23	Result Data - Landing Fork Gear	±0,1	-0,2112	263,5412	-68	263,6518	-68,1799
2D Compare 7: 24	Result Data - Landing Fork Gear	±0,1	-0,3877	264,9378	-78	264,5717	-77,872
2D Compare 7: 25	Result Data - Landing Fork Gear	±0,1	0,0614	278	-76,9207	277,9851	-76,9803
2D Compare 7: 26	Result Data - Landing Fork Gear	±0,1	-0,613	276	-99,0151	276,3133	-99,542
2D Compare 7: 27	Result Data - Landing Fork Gear	±0,1	0,1362	264	-100,3841	264,045	-100,2555
2D Compare 7: 28	Result Data - Landing Fork Gear	±0,1	-0,2618	259,3416	-94	259,0944	-93,9136
2D Compare 7: 29	Result Data - Landing Fork Gear	±0,1	-0,2213	284,3764	-90	284,568	-90,1109
Min.			-0,6130	255,6538	-119,2045	255,8414	-119,2068
Max.			0,6227	315,6848	-67,6205	315,2357	-67,9603
Avg.			-0,1044	281,4237	-92,4757	281,4677	-92,5217

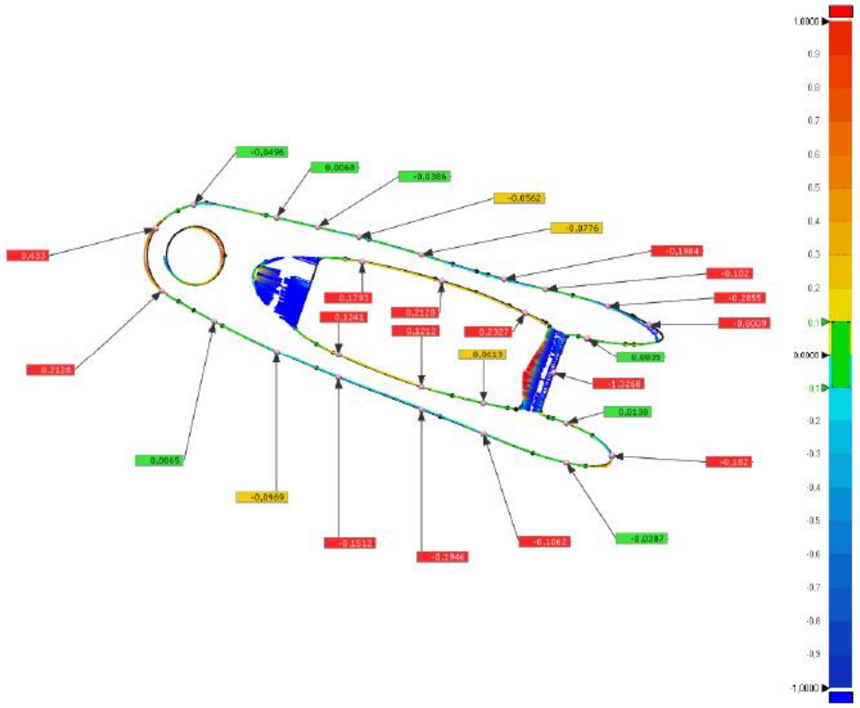

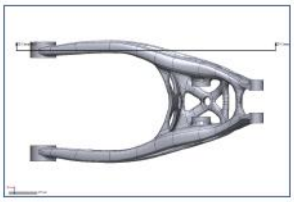

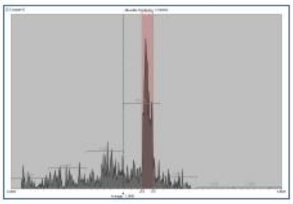

Min.	-6,3416
Max.	2,2053
Avg.	-1,2445
RMS	2,2546
Std. Dev.	1,8801
Var.	3,5347
+Avg.	0,4476
-Avg.	-1,9133
In Tol.(%)	17,9276
Out Tol.(%)	82,0724
Over Tol.(%)	20,9293
Under Tol.(%)	61,1431

Name	Min.	Max.	Avg.	RMS	Std. Dev.	Var.	+Avg.	-Avg.
2D Compare 8	-6,3416	2,2053	-1,2445	2,2546	1,8801	3,5347	0,4476	-1,9133

Name	Result Name	Tolerance	Gap Dist.	Reference Pos.		Measured Pos.	
				X	Y	X	Y
2D Compare 8: 1	Result Data - Landing Fork Gear	±0,1	-0,0496	155	-39,2993	155,0115	-39,3476
2D Compare 8: 2	Result Data - Landing Fork Gear	±0,1	0,433	145,8278	-45	145,4701	-44,7561
2D Compare 8: 3	Result Data - Landing Fork Gear	±0,1	0,2128	147,385	-60	147,2374	-60,1534
2D Compare 8: 4	Result Data - Landing Fork Gear	±0,1	0,0065	160	-67,3968	159,997	-67,4025
2D Compare 8: 5	Result Data - Landing Fork Gear	±0,1	-0,0969	175	-74,697	175,0396	-74,6086
2D Compare 8: 6	Result Data - Landing Fork Gear	±0,1	-0,1512	190	-81,0235	190,0564	-80,8832
2D Compare 8: 7	Result Data - Landing Fork Gear	±0,1	-0,1946	210	-88,7905	210,0696	-88,6087
2D Compare 8: 8	Result Data - Landing Fork Gear	±0,1	-0,1062	225	-94,7052	225,04	-94,6068
2D Compare 8: 9	Result Data - Landing Fork Gear	±0,1	-0,0387	245	-101,6542	245,0083	-101,6164
2D Compare 8: 10	Result Data - Landing Fork Gear	±0,1	0,0138	245	-92,0928	245,005	-92,0799
2D Compare 8: 11	Result Data - Landing Fork Gear	±0,1	-0,182	255,9933	-100	255,8171	-100,0456
2D Compare 8: 12	Result Data - Landing Fork Gear	±0,1	-1,3268	241,9383	-80	240,6859	-79,562
2D Compare 8: 13	Result Data - Landing Fork Gear	±0,1	0,0035	250	-71,4787	249,9991	-71,4821
2D Compare 8: 14	Result Data - Landing Fork Gear	±0,1	-0,8009	265	-68,1717	264,599	-68,865
2D Compare 8: 15	Result Data - Landing Fork Gear	±0,1	-0,2855	255	-63,6946	254,9046	-63,9636
2D Compare 8: 16	Result Data - Landing Fork Gear	±0,1	-0,102	240	-59,6053	239,977	-59,7047
2D Compare 8: 17	Result Data - Landing Fork Gear	±0,1	-0,1984	230	-57,214	229,9503	-57,4061

Name	Result Name	Tolerance	Gap Dist.	Reference Pos.		Measured Pos.	
				X	Y	X	Y
2D Compare 8: 18	Result Data - Landing Fork Gear	±0,1	-0,0776	210	-51,2834	209,9775	-51,3577
2D Compare 8: 19	Result Data - Landing Fork Gear	±0,1	-0,0562	195	-47,0986	194,9863	-47,1531
2D Compare 8: 20	Result Data - Landing Fork Gear	±0,1	-0,0386	185	-44,6935	184,9913	-44,7312
2D Compare 8: 21	Result Data - Landing Fork Gear	±0,1	0,0068	175	-42,4157	175,0015	-42,409
2D Compare 8: 22	Result Data - Landing Fork Gear	±0,1	0,1793	195,7423	-52,9924	195,7118	-53,1691
2D Compare 8: 23	Result Data - Landing Fork Gear	±0,1	0,2128	215	-57,6257	214,9393	-57,8297
2D Compare 8: 24	Result Data - Landing Fork Gear	±0,1	0,2327	235	-65,3368	234,9013	-65,5476
2D Compare 8: 25	Result Data - Landing Fork Gear	±0,1	0,1241	190	-75,5445	190,0532	-75,4323
2D Compare 8: 26	Result Data - Landing Fork Gear	±0,1	0,1212	210	-83,3308	210,0371	-83,2154
2D Compare 8: 27	Result Data - Landing Fork Gear	±0,1	0,0613	225	-87,3263	225,0127	-87,2663
Min.			-1,3268	145,8278	-101,6542	145,4701	-101,6164
Max.			0,4330	265,0000	-39,2993	264,5990	-39,3476
Avg.			-0,0777	210,0699	-68,6100	209,9807	-68,6372

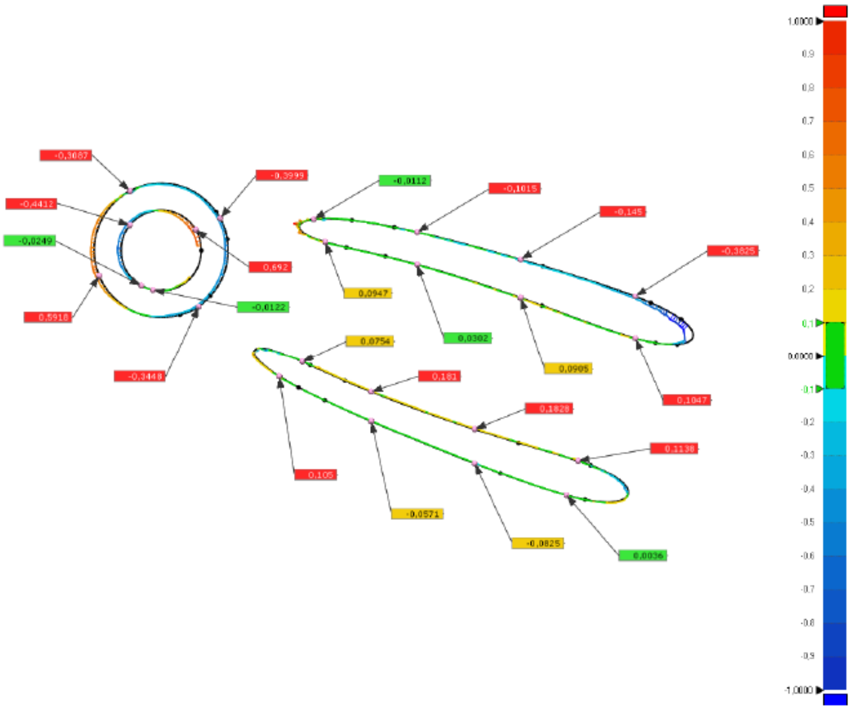

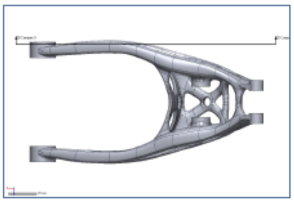

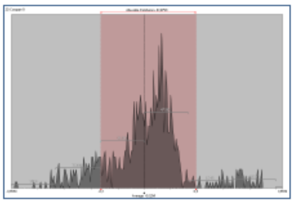

Min.	-1,0715
Max.	1,0458
Avg.	-0,0254
RMS	0,278
Std. Dev.	0,2768
Var.	0,0766
+Avg.	0,1631
-Avg.	-0,2272
In Tol.(%)	43,879
Out Tol.(%)	56,121
Over Tol.(%)	26,4099
Under Tol.(%)	29,7111

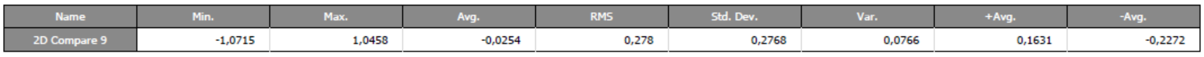

Name	Min.	Max.	Avg.	RMS	Std. Dev.	Var.	+Avg.	-Avg.
2D Compare 9	-1,0715	1,0458	-0,0254	0,278	0,2768	0,0766	0,1631	-0,2272

Name	Result Name	Tolerance	Gap Dist.	Reference Pos.		Measured Pos.	
				X	Y	X	Y
2D Compare 9: 1	Result Data - Landing Fork Gear	±0,1	-0,3087	150	-41,2809	150,1439	-41,5541
2D Compare 9: 2	Result Data - Landing Fork Gear	±0,1	0,5918	144,6594	-56	144,1117	-56,2243
2D Compare 9: 3	Result Data - Landing Fork Gear	±0,1	-0,3448	162	-61,3337	161,8034	-61,0505
2D Compare 9: 4	Result Data - Landing Fork Gear	±0,1	-0,3999	165,7034	-46	165,3557	-46,1975
2D Compare 9: 5	Result Data - Landing Fork Gear	±0,1	-0,0112	182	-46,1597	182,0021	-46,1707
2D Compare 9: 6	Result Data - Landing Fork Gear	±0,1	-0,1015	200	-48,4142	199,9772	-48,5131
2D Compare 9: 7	Result Data - Landing Fork Gear	±0,1	-0,145	218	-53,1637	217,9599	-53,3031
2D Compare 9: 8	Result Data - Landing Fork Gear	±0,1	-0,3825	238	-59,5811	237,8615	-59,9376
2D Compare 9: 9	Result Data - Landing Fork Gear	±0,1	0,1047	238	-66,8307	237,9724	-66,9316
2D Compare 9: 10	Result Data - Landing Fork Gear	±0,1	0,0905	218	-59,8146	217,9694	-59,8999
2D Compare 9: 11	Result Data - Landing Fork Gear	±0,1	0,0302	200	-54,037	199,992	-54,0661
2D Compare 9: 12	Result Data - Landing Fork Gear	±0,1	0,0947	184	-50,1428	183,9738	-50,2337
2D Compare 9: 13	Result Data - Landing Fork Gear	±0,1	0,0754	180	-71,0174	180,0307	-70,9486
2D Compare 9: 14	Result Data - Landing Fork Gear	±0,1	0,181	192	-76,2835	192,0682	-76,1158
2D Compare 9: 15	Result Data - Landing Fork Gear	±0,1	0,1828	210	-82,802	210,0563	-82,6281
2D Compare 9: 16	Result Data - Landing Fork Gear	±0,1	0,1138	228	-88,3154	228,0356	-88,2074
2D Compare 9: 17	Result Data - Landing Fork Gear	±0,1	0,0036	226	-94,2738	225,9991	-94,2773

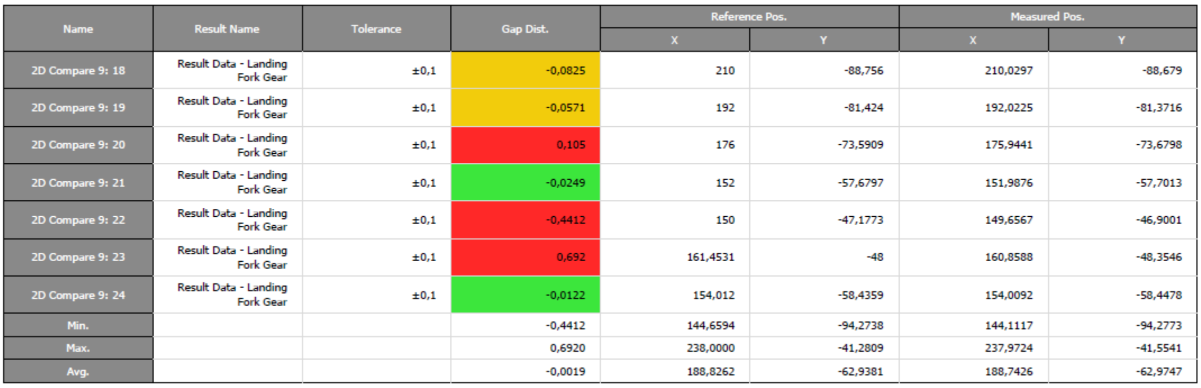

Name	Result Name	Tolerance	Gap Dist.	Reference Pos.		Measured Pos.	
				X	Y	X	Y
2D Compare 9: 18	Result Data - Landing Fork Gear	±0,1	-0,0825	210	-88,756	210,0297	-88,679
2D Compare 9: 19	Result Data - Landing Fork Gear	±0,1	-0,0571	192	-81,424	192,0225	-81,3716
2D Compare 9: 20	Result Data - Landing Fork Gear	±0,1	0,105	176	-73,5909	175,9441	-73,6798
2D Compare 9: 21	Result Data - Landing Fork Gear	±0,1	-0,0249	152	-57,6797	151,9876	-57,7013
2D Compare 9: 22	Result Data - Landing Fork Gear	±0,1	-0,4412	150	-47,1773	149,6567	-46,9001
2D Compare 9: 23	Result Data - Landing Fork Gear	±0,1	0,692	161,4531	-48	160,8588	-48,3546
2D Compare 9: 24	Result Data - Landing Fork Gear	±0,1	-0,0122	154,012	-58,4359	154,0092	-58,4478
Min.			-0,4412	144,6594	-94,2738	144,1117	-94,2773
Max.			0,6920	238,0000	-41,2809	237,9724	-41,5541
Avg.			-0,0019	188,8262	-62,9381	188,7426	-62,9747

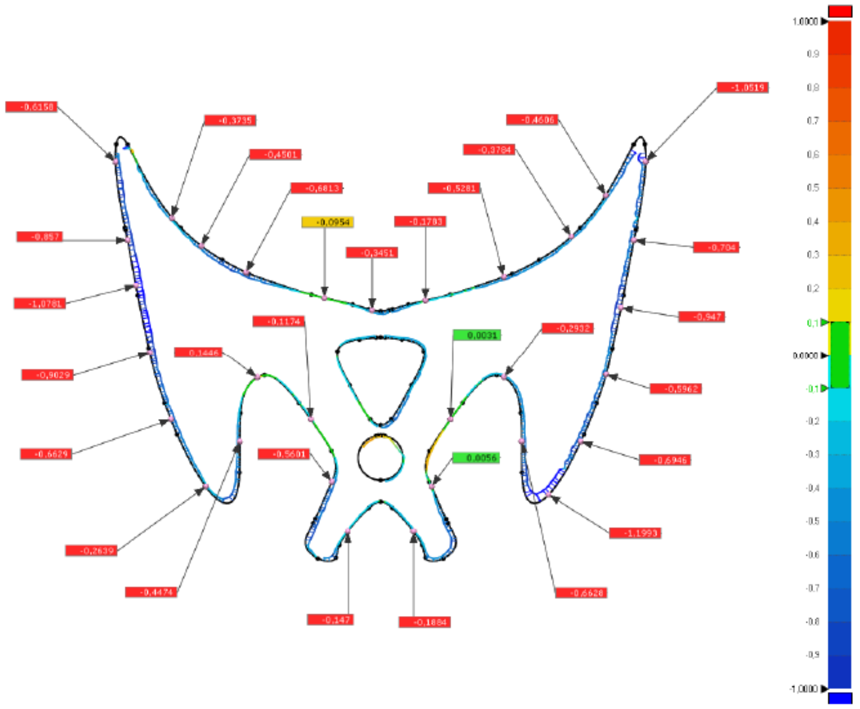

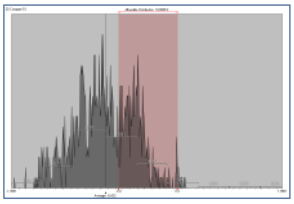

Min.	-1,5001
Max.	0,4127
Avg.	-0,433
RMS	0,5359
Std. Dev.	0,3157
Var.	0,0997
+Avg.	0,1653
-Avg.	-0,4724
In Tol.(%)	10,8901
Out Tol.(%)	89,1099
Over Tol.(%)	3,5602
Under Tol.(%)	85,5497

Name	Min.	Max.	Avg.	RMS	Std. Dev.	Var.	+Avg.	-Avg.
2D Compare 10	-1,5001	0,4127	-0,433	0,5359	0,3157	0,0997	0,1653	-0,4724

Name	Result Name	Tolerance	Gap Dist.	Reference Pos.		Measured Pos.	
				X	Y	X	Y
2D Compare 10: 1	Result Data - Landing Fork Gear	±0,1	-0,3735	-37,2176	-266	-37,5033	-266,2406
2D Compare 10: 2	Result Data - Landing Fork Gear	±0,1	-0,6813	-24	-275,6847	-24,2825	-276,3046
2D Compare 10: 3	Result Data - Landing Fork Gear	±0,1	-0,0954	-10	-280,2427	-10,0222	-280,3355
2D Compare 10: 4	Result Data - Landing Fork Gear	±0,1	-0,3451	-1,5275	-282,4086	-1,6087	-282,744
2D Compare 10: 5	Result Data - Landing Fork Gear	±0,1	-0,1783	8	-280,704	8,0393	-280,8778
2D Compare 10: 6	Result Data - Landing Fork Gear	±0,1	-0,5281	22	-276,4711	22,1784	-276,9682
2D Compare 10: 7	Result Data - Landing Fork Gear	±0,1	-0,4606	40,1722	-262	40,5591	-262,25
2D Compare 10: 8	Result Data - Landing Fork Gear	±0,1	-0,4501	-32	-271,0037	-32,2729	-271,3616
2D Compare 10: 9	Result Data - Landing Fork Gear	±0,1	-0,3784	34	-269,3473	34,2537	-269,6281
2D Compare 10: 10	Result Data - Landing Fork Gear	±0,1	-0,704	45,1718	-270	44,4813	-269,8629
2D Compare 10: 11	Result Data - Landing Fork Gear	±0,1	-0,947	42,8935	-282	41,965	-281,8138
2D Compare 10: 12	Result Data - Landing Fork Gear	±0,1	-0,5962	40,2296	-294	39,6562	-293,8366
2D Compare 10: 13	Result Data - Landing Fork Gear	±0,1	-0,6946	35,7163	-306	35,0853	-305,7097
2D Compare 10: 14	Result Data - Landing Fork Gear	±0,1	-1,1993	30	-315,4661	29,1368	-314,6335
2D Compare 10: 15	Result Data - Landing Fork Gear	±0,1	-0,6158	-47,3089	-256	-46,6934	-255,9802
2D Compare 10: 16	Result Data - Landing Fork Gear	±0,1	-0,857	-45,1653	-270	-44,3247	-269,8331
2D Compare 10: 17	Result Data - Landing Fork Gear	±0,1	-1,0781	-43,6544	-278	-42,5943	-277,8035

© Central University of Technology, Free State

Name	Result Name	Tolerance	Gap Dist.	Reference Pos.		Measured Pos.	
				X	Y	X	Y
2D Compare 10: 18	Result Data - Landing Fork Gear	±0,1	-0,9029	-41,1857	-290	-40,3024	-289,8131
2D Compare 10: 19	Result Data - Landing Fork Gear	±0,1	-0,6629	-37,4292	-302	-36,8142	-301,7527
2D Compare 10: 20	Result Data - Landing Fork Gear	±0,1	-0,2639	-31,2154	-314	-31,0034	-313,8428
2D Compare 10: 21	Result Data - Landing Fork Gear	±0,1	-0,4474	-25,1497	-306	-25,5972	-306,0005
2D Compare 10: 22	Result Data - Landing Fork Gear	±0,1	-0,6628	25,1563	-306	25,8191	-306,0002
2D Compare 10: 23	Result Data - Landing Fork Gear	±0,1	-0,147	-5,8563	-322	-5,9729	-321,9105
2D Compare 10: 24	Result Data - Landing Fork Gear	±0,1	-0,1884	5,8629	-322	6,012	-321,8848
2D Compare 10: 25	Result Data - Landing Fork Gear	±0,1	0,0056	9,0925	-314	9,0976	-313,9977
2D Compare 10: 26	Result Data - Landing Fork Gear	±0,1	-0,5601	-8,7211	-313,194	-8,2089	-313,4205
2D Compare 10: 27	Result Data - Landing Fork Gear	±0,1	-0,1174	-12,4599	-302	-12,3648	-301,9312
2D Compare 10: 28	Result Data - Landing Fork Gear	±0,1	0,1446	-22	-294,4988	-21,9317	-294,6262
2D Compare 10: 29	Result Data - Landing Fork Gear	±0,1	0,0031	12,4664	-302	12,4689	-302,0018
2D Compare 10: 30	Result Data - Landing Fork Gear	±0,1	-0,2932	22	-294,4952	22,1379	-294,2365
2D Compare 10: 31	Result Data - Landing Fork Gear	±0,1	-1,0519	47,3155	-256	46,264	-255,9687
Min.			-1,1993	-47,3089	-322,0000	-46,6934	-321,9105
Max.			0,1446	47,3155	-256,0000	46,2640	-255,9687
Avg.			-0,4944	-0,1553	-289,4683	-0,1401	-289,4700

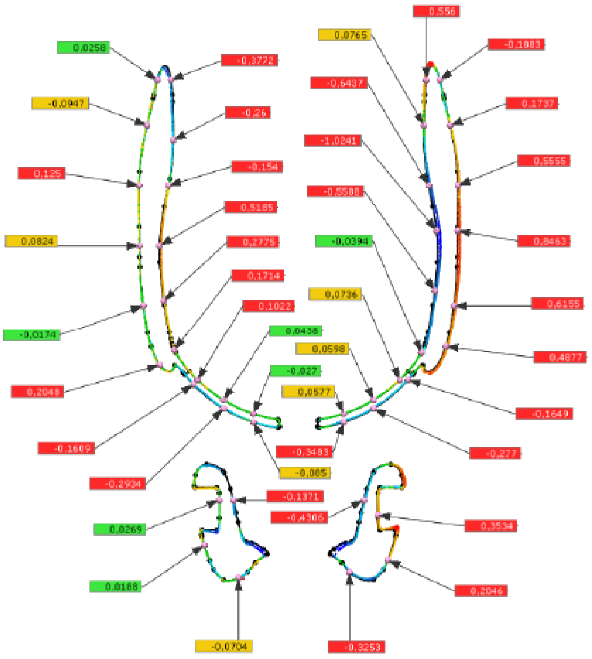

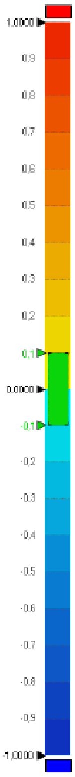

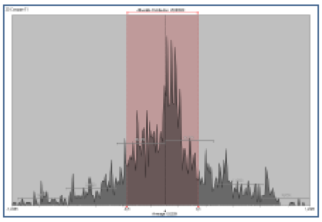

Min.	-1,4077
Max.	1,5246
Avg.	0,0209
RMS	0,4097
Std. Dev.	0,4091
Var.	0,1674
+Avg.	0,2909
-Avg.	-0,3148
In Tol.(%)	28,0094
Out Tol.(%)	71,9906
Over Tol.(%)	37,4633
Under Tol.(%)	34,5273

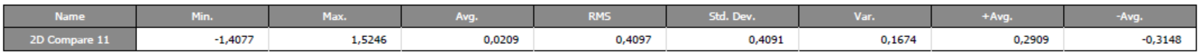

Name	Min.	Max.	Avg.	RMS	Std. Dev.	Var.	+Avg.	-Avg.
2D Compare 11	-1,4077	1,5246	0,0209	0,4097	0,4091	0,1674	0,2909	-0,3148

Name	Result Name	Tolerance	Gap Dist.	Reference Pos.		Measured Pos.	
				X	Y	X	Y
2D Compare 11: 1	Result Data - Landing Fork Gear	±0,1	0,0258	-47,098	-170	-47,1231	-169,9937
2D Compare 11: 2	Result Data - Landing Fork Gear	±0,1	-0,0947	-50,4983	-185	-50,4059	-185,0208
2D Compare 11: 3	Result Data - Landing Fork Gear	±0,1	0,125	-53,1188	-205	-53,2439	-204,9978
2D Compare 11: 4	Result Data - Landing Fork Gear	±0,1	0,0824	-53,0101	-225	-53,0926	-225,0007
2D Compare 11: 5	Result Data - Landing Fork Gear	±0,1	-0,0174	-51,7997	-245	-51,7825	-244,9979
2D Compare 11: 6	Result Data - Landing Fork Gear	±0,1	0,2048	-46,2658	-265	-46,4302	-265,1221
2D Compare 11: 7	Result Data - Landing Fork Gear	±0,1	-0,1609	-35	-271,5536	-34,8841	-271,442
2D Compare 11: 8	Result Data - Landing Fork Gear	±0,1	-0,2934	-25	-279,5133	-24,8491	-279,2617
2D Compare 11: 9	Result Data - Landing Fork Gear	±0,1	-0,085	-15	-284,0648	-14,9738	-283,9839
2D Compare 11: 10	Result Data - Landing Fork Gear	±0,1	-0,3483	15	-284,0669	14,8933	-283,7354
2D Compare 11: 11	Result Data - Landing Fork Gear	±0,1	-0,277	25	-279,5173	24,8575	-279,2797
2D Compare 11: 12	Result Data - Landing Fork Gear	±0,1	-0,1649	36,4391	-270	36,3154	-269,8909
2D Compare 11: 13	Result Data - Landing Fork Gear	±0,1	-0,1883	47,1046	-170	46,9226	-170,0484
2D Compare 11: 14	Result Data - Landing Fork Gear	±0,1	0,1737	50,5048	-185	50,6743	-184,9619
2D Compare 11: 15	Result Data - Landing Fork Gear	±0,1	0,5555	53,1254	-205	53,6808	-204,9903
2D Compare 11: 16	Result Data - Landing Fork Gear	±0,1	0,8463	53,0471	-220	53,8934	-220,005
2D Compare 11: 17	Result Data - Landing Fork Gear	±0,1	0,6155	51,8063	-245	52,417	-245,0768

Name	Result Name	Tolerance	Gap Dist.	Reference Pos.		Measured Pos.	
				X	Y	X	Y
2D Compare 11: 18	Result Data - Landing Fork Gear	±0,1	0,4877	49,0904	-258,8289	49,5563	-258,9731
2D Compare 11: 19	Result Data - Landing Fork Gear	±0,1	0,556	42,5923	-170	42,0421	-169,9199
2D Compare 11: 20	Result Data - Landing Fork Gear	±0,1	0,0765	41,788	-185	41,7115	-184,9991
2D Compare 11: 21	Result Data - Landing Fork Gear	±0,1	-0,6437	43,3619	-205	43,9944	-204,8808
2D Compare 11: 22	Result Data - Landing Fork Gear	±0,1	-1,0241	46,0063	-220	47,0249	-219,8937
2D Compare 11: 23	Result Data - Landing Fork Gear	±0,1	-0,5588	45,452	-240	46,0066	-240,068
2D Compare 11: 24	Result Data - Landing Fork Gear	±0,1	-0,0394	40,9904	-260,8523	41,0247	-260,8717
2D Compare 11: 25	Result Data - Landing Fork Gear	±0,1	0,0736	33,7341	-270	33,6831	-269,947
2D Compare 11: 26	Result Data - Landing Fork Gear	±0,1	0,0598	25	-276,7027	24,9692	-276,6514
2D Compare 11: 27	Result Data - Landing Fork Gear	±0,1	0,0577	15	-281,2585	14,9822	-281,2036
2D Compare 11: 28	Result Data - Landing Fork Gear	±0,1	-0,027	-15	-281,2564	-15,0083	-281,2821
2D Compare 11: 29	Result Data - Landing Fork Gear	±0,1	0,0438	-25	-276,6987	-24,9774	-276,6612
2D Compare 11: 30	Result Data - Landing Fork Gear	±0,1	0,1022	-33,7275	-270	-33,6565	-269,9265
2D Compare 11: 31	Result Data - Landing Fork Gear	±0,1	0,1714	-41,4409	-260	-41,2873	-259,9241
2D Compare 11: 32	Result Data - Landing Fork Gear	±0,1	0,2775	-45	-243,3473	-44,7253	-243,3079
2D Compare 11: 33	Result Data - Landing Fork Gear	±0,1	0,5185	-46,3279	-225	-45,8096	-225,0146
2D Compare 11: 34	Result Data - Landing Fork Gear	±0,1	-0,154	-43,3554	-205	-43,5067	-204,9715
2D Compare 11: 35	Result Data - Landing Fork Gear	±0,1	-0,26	-41,7917	-190	-42,0516	-189,995
2D Compare 11: 36	Result Data - Landing Fork Gear	±0,1	-0,3772	-42,5858	-170	-42,9591	-170,0545

© Central University of Technology, Free State

Name	Result Name	Tolerance	Gap Dist.	Reference Pos.		Measured Pos.	
				X	Y	X	Y
2D Compare 11: 37	Result Data - Landing Fork Gear	±0,1	-0,0704	-20	-335,8548	-20,0303	-335,7912
2D Compare 11: 38	Result Data - Landing Fork Gear	±0,1	0,0188	-31,4517	-325	-31,4696	-325,0056
2D Compare 11: 39	Result Data - Landing Fork Gear	±0,1	0,0269	-26,4167	-310	-26,4436	-310
2D Compare 11: 40	Result Data - Landing Fork Gear	±0,1	-0,1371	-21,7286	-310	-21,862	-310,0316
2D Compare 11: 41	Result Data - Landing Fork Gear	±0,1	-0,4306	21,7351	-310	22,1541	-310,0995
2D Compare 11: 42	Result Data - Landing Fork Gear	±0,1	-0,3253	17,0054	-334,0006	17,225	-333,7606
2D Compare 11: 43	Result Data - Landing Fork Gear	±0,1	0,2046	29,7313	-330	29,9218	-330,0746
2D Compare 11: 44	Result Data - Landing Fork Gear	±0,1	0,3534	26,4233	-315	26,7767	-315
Min.			-1,0241	-53,1188	-335,8548	-53,2439	-335,7912
Max.			0,8463	53,1254	-170,0000	53,8934	-169,9199
Avg.			-0,0005	-0,0154	-251,0799	0,0944	-251,0481

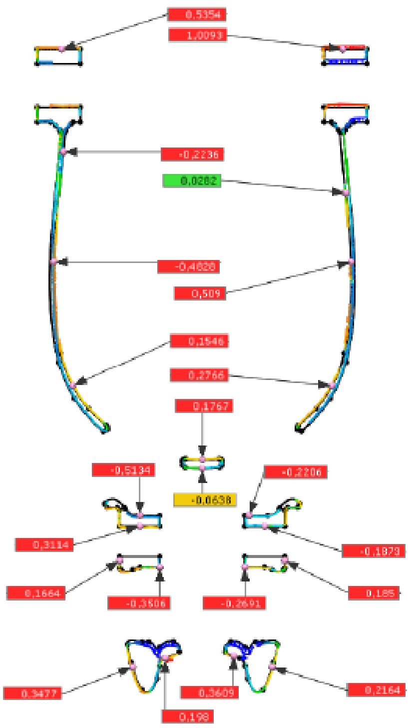

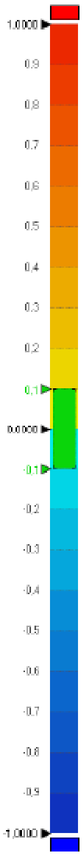

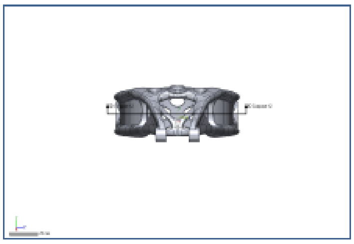

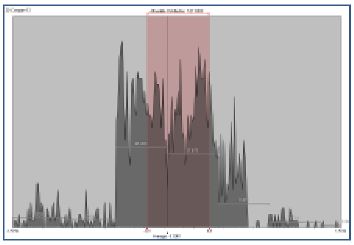

Min.	-2,0921
Max.	1,577
Avg.	-0,1061
RMS	0,5008
Std. Dev.	0,4894
Var.	0,2395
+Avg.	0,3189
-Avg.	-0,4337
In Tol.(%)	14,1336
Out Tol.(%)	85,8664
Over Tol.(%)	36,5464
Under Tol.(%)	49,3199

© Central University of Technology, Free State

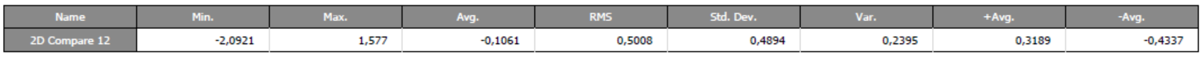

Name	Min.	Max.	Avg.	RMS	Std. Dev.	Var.	+Avg.	-Avg.
2D Compare 12	-2,0921	1,577	-0,1061	0,5008	0,4894	0,2395	0,3189	-0,4337

Name	Result Name	Tolerance	Gap Dist.	Reference Pos.		Measured Pos.	
				X	Y	X	Y
2D Compare 12: 1	Result Data - Landing Fork Gear	±0,1	0,5354	-45	-152,1475	-45	-151,6121
2D Compare 12: 2	Result Data - Landing Fork Gear	±0,1	1,0093	45	-152,1475	45	-151,1382
2D Compare 12: 3	Result Data - Landing Fork Gear	±0,1	-0,2236	-44,5813	-185	-44,8039	-184,9792
2D Compare 12: 4	Result Data - Landing Fork Gear	±0,1	-0,4828	-47,6246	-220	-48,1071	-219,9823
2D Compare 12: 5	Result Data - Landing Fork Gear	±0,1	0,1546	-41,466	-260	-41,3305	-259,9256
2D Compare 12: 6	Result Data - Landing Fork Gear	±0,1	0,2766	41,4726	-260	41,2302	-259,8668
2D Compare 12: 7	Result Data - Landing Fork Gear	±0,1	0,1767	0	-283,633	-0,0002	-283,4563
2D Compare 12: 8	Result Data - Landing Fork Gear	±0,1	-0,0638	0	-286,4386	0	-286,3748
2D Compare 12: 9	Result Data - Landing Fork Gear	±0,1	0,3114	-20	-304,9161	-20	-305,2275
2D Compare 12: 10	Result Data - Landing Fork Gear	±0,1	-0,5134	-20	-301,4417	-20	-301,9551
2D Compare 12: 11	Result Data - Landing Fork Gear	±0,1	-0,2206	15	-301,4417	15	-301,6622
2D Compare 12: 12	Result Data - Landing Fork Gear	±0,1	-0,1873	20	-304,9161	20	-304,7288
2D Compare 12: 13	Result Data - Landing Fork Gear	±0,1	-0,3506	-13,6167	-318,0289	-13,829	-317,7499
2D Compare 12: 14	Result Data - Landing Fork Gear	±0,1	-0,2691	13,6233	-318,0289	13,8551	-317,8923
2D Compare 12: 15	Result Data - Landing Fork Gear	±0,1	0,2164	22,3381	-350	22,546	-350,06
2D Compare 12: 16	Result Data - Landing Fork Gear	±0,1	0,3477	-22,33	-350	-22,6641	-350,0962
2D Compare 12: 17	Result Data - Landing Fork Gear	±0,1	0,198	-11,8908	-347,2047	-11,7992	-347,3802

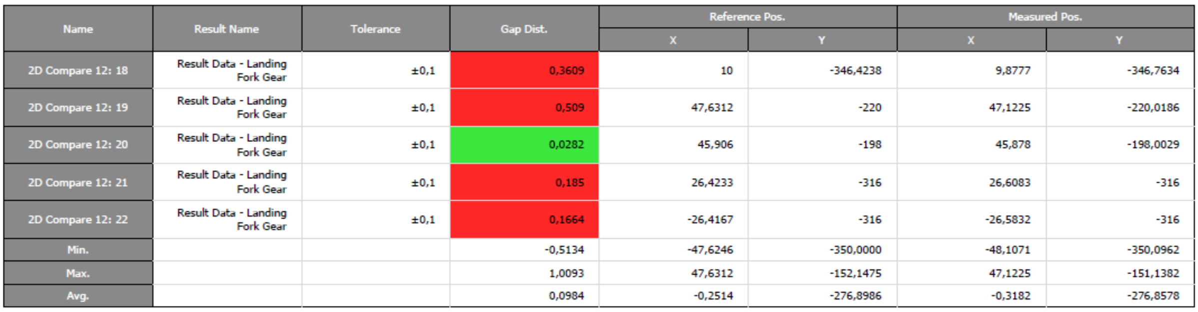

Name	Result Name	Tolerance	Gap Dist.	Reference Pos.		Measured Pos.	
				X	Y	X	Y
2D Compare 12: 18	Result Data - Landing Fork Gear	±0,1	0,3609	10	-346,4238	9,8777	-346,7634
2D Compare 12: 19	Result Data - Landing Fork Gear	±0,1	0,509	47,6312	-220	47,1225	-220,0186
2D Compare 12: 20	Result Data - Landing Fork Gear	±0,1	0,0282	45,906	-198	45,878	-198,0029
2D Compare 12: 21	Result Data - Landing Fork Gear	±0,1	0,185	26,4233	-316	26,6083	-316
2D Compare 12: 22	Result Data - Landing Fork Gear	±0,1	0,1664	-26,4167	-316	-26,5832	-316
Min.			-0,5134	-47,6246	-350,0000	-48,1071	-350,0962
Max.			1,0093	47,6312	-152,1475	47,1225	-151,1382
Avg.			0,0984	-0,2514	-276,8986	-0,3182	-276,8578

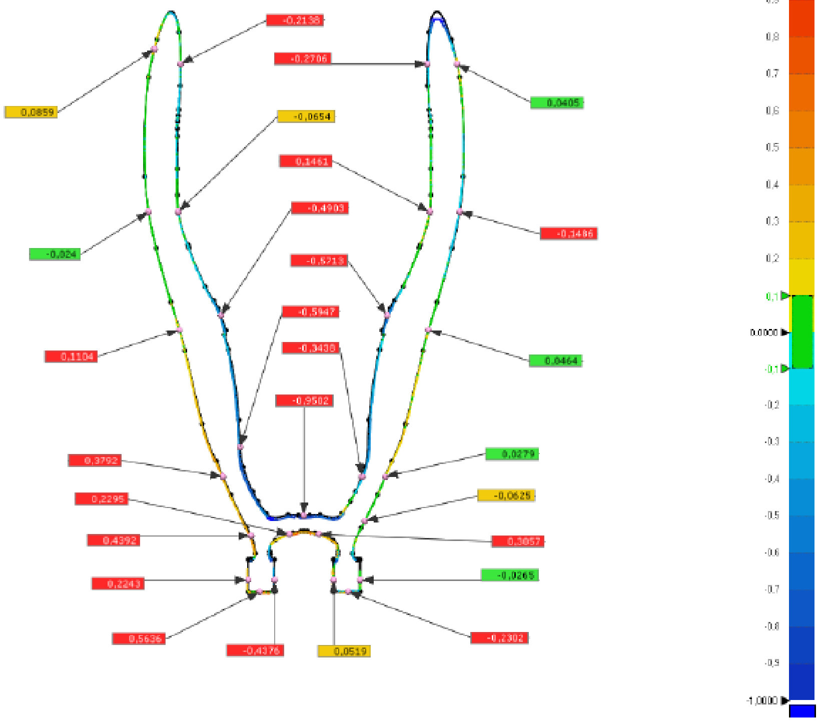

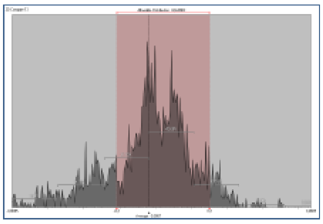

Min.	-1,1779
Max.	0,7857
Avg.	-0,0907
RMS	0,3057
Std. Dev.	0,292
Var.	0,0852
+Avg.	0,167
-Avg.	-0,2639
In Tol.(%)	34,6496
Out Tol.(%)	65,3504
Over Tol.(%)	23,4149
Under Tol.(%)	41,9355

Name	Min.	Max.	Avg.	RMS	Std. Dev.	Var.	+Avg.	-Avg.
2D Compare 13	-1,1779	0,7857	-0,0907	0,3057	0,292	0,0852	0,167	-0,2639

Name	Result Name	Tolerance	Gap Dist.	Reference Pos.		Measured Pos.	
				X	Y	X	Y
2D Compare 13: 1	Result Data - Landing Fork Gear	±0,1	0,0859	-50,6853	-190	-50,7685	-189,9787
2D Compare 13: 2	Result Data - Landing Fork Gear	±0,1	-0,024	-52,6392	-245	-52,6155	-244,9963
2D Compare 13: 3	Result Data - Landing Fork Gear	±0,1	0,1104	-42,211	-285	-42,3173	-285,0299
2D Compare 13: 4	Result Data - Landing Fork Gear	±0,1	0,3792	-27,4878	-335	-27,8363	-335,1494
2D Compare 13: 5	Result Data - Landing Fork Gear	±0,1	0,4392	-18,0551	-355	-18,4534	-355,185
2D Compare 13: 6	Result Data - Landing Fork Gear	±0,1	0,2243	-18,9967	-370	-19,221	-370
2D Compare 13: 7	Result Data - Landing Fork Gear	±0,1	-0,4376	-10,0167	-370	-10,4543	-370
2D Compare 13: 8	Result Data - Landing Fork Gear	±0,1	0,5636	-15	-373,9472	-15	-374,5107
2D Compare 13: 9	Result Data - Landing Fork Gear	±0,1	-0,2302	15	-373,9472	15	-373,717
2D Compare 13: 10	Result Data - Landing Fork Gear	±0,1	0,0519	10,0233	-370	9,9714	-370
2D Compare 13: 11	Result Data - Landing Fork Gear	±0,1	0,2295	-5	-354,458	-4,9261	-354,6753
2D Compare 13: 12	Result Data - Landing Fork Gear	±0,1	0,3057	5	-354,4558	4,9016	-354,7452
2D Compare 13: 13	Result Data - Landing Fork Gear	±0,1	-0,9502	0,0033	-348,1733	0,003	-349,1235
2D Compare 13: 14	Result Data - Landing Fork Gear	±0,1	-0,5947	-21,6907	-325	-22,2846	-325,0304
2D Compare 13: 15	Result Data - Landing Fork Gear	±0,1	-0,4903	-28,1604	-280	-28,6186	-280,1747
2D Compare 13: 16	Result Data - Landing Fork Gear	±0,1	-0,0654	-42,5842	-245	-42,6489	-245,0095
2D Compare 13: 17	Result Data - Landing Fork Gear	±0,1	-0,2138	-41,8004	-195	-42,0142	-195,0003

© Central University of Technology, Free State

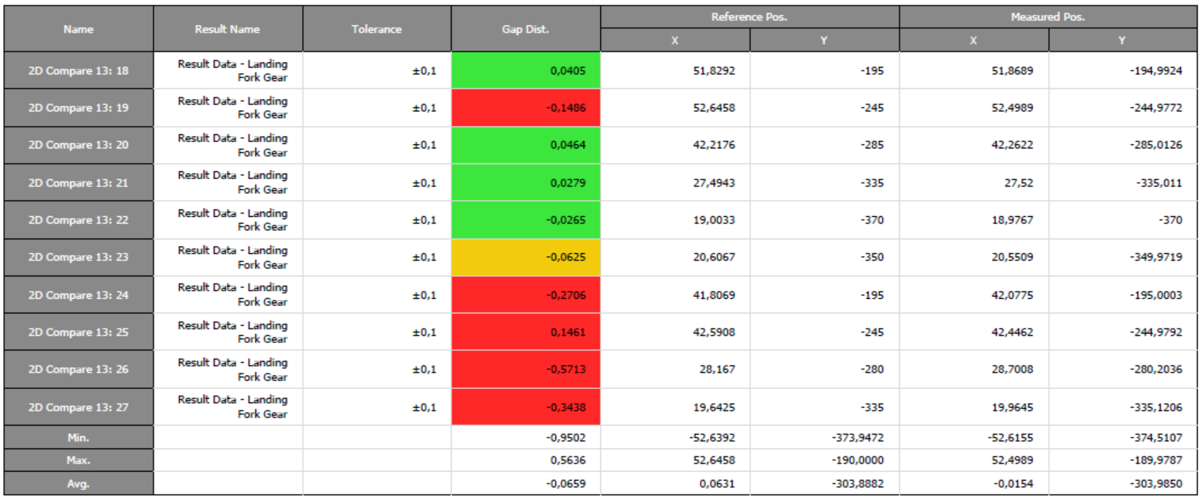

Name	Result Name	Tolerance	Gap Dist.	Reference Pos.		Measured Pos.	
				X	Y	X	Y
2D Compare 13: 18	Result Data - Landing Fork Gear	±0,1	0,0405	51,8292	-195	51,8689	-194,9924
2D Compare 13: 19	Result Data - Landing Fork Gear	±0,1	-0,1486	52,6458	-245	52,4989	-244,9772
2D Compare 13: 20	Result Data - Landing Fork Gear	±0,1	0,0464	42,2176	-285	42,2622	-285,0126
2D Compare 13: 21	Result Data - Landing Fork Gear	±0,1	0,0279	27,4943	-335	27,52	-335,011
2D Compare 13: 22	Result Data - Landing Fork Gear	±0,1	-0,0265	19,0033	-370	18,9767	-370
2D Compare 13: 23	Result Data - Landing Fork Gear	±0,1	-0,0625	20,6067	-350	20,5509	-349,9719
2D Compare 13: 24	Result Data - Landing Fork Gear	±0,1	-0,2706	41,8069	-195	42,0775	-195,0003
2D Compare 13: 25	Result Data - Landing Fork Gear	±0,1	0,1461	42,5908	-245	42,4462	-244,9792
2D Compare 13: 26	Result Data - Landing Fork Gear	±0,1	-0,5713	28,167	-280	28,7008	-280,2036
2D Compare 13: 27	Result Data - Landing Fork Gear	±0,1	-0,3438	19,6425	-335	19,9645	-335,1206
Min.			-0,9502	-52,6392	-373,9472	-52,6155	-374,5107
Max.			0,5636	52,6458	-190,0000	52,4989	-189,9787
Avg.			-0,0659	0,0631	-303,8882	-0,0154	-303,9850

APPENDIX G: TENSILE TEST REPORT

G.1. X specimens

T0381

Laboratory Name	CSIR Materials Testing Laboratory
Company	CUT Miya
Operator ID	203406
Method description	LM-WP-402 - ASTM E8 M
Sample description	Ti6Al4V
Test Date	22/02/2021

	Specimen label	Length (mm)	Area (mm^2)	Tensile stress at Yield (Offset 0.2 %) (MPa)	Modulus (Chord 150 MPa - 600 MPa) (GPa)	UTS (MPa)	% Elongation (4*D)	Reduction of Area (%)	Specimen note 1
1	X1	20.00	13.85	860.42	116.3	948.13	16.50	43.0	
2	X2	20.00	13.85	852.44	113.9	939.65	15.50	39.4	
3	X3	20.00	13.85	853.73	115.0	941.53	15.05	33.3	
Mean		20.00	13.85	855.53	115.1	943.10	15.68	38.6	
Coefficient of Variation		0.000	0.000	0.501	1.010	0.472	4.732	12.739	
Range		0.00	0.00	7.98	2.3	8.47	1.45	9.7	
Standard Deviation		0.000	0.000	4.285	1.162	4.450	0.742	4.914	
Minimum		20.00	13.85	852.44	113.9	939.65	15.05	33.3	
Maximum		20.00	13.85	860.42	116.3	948.13	16.50	43.0	
Median		20.00	13.85	853.73	115.0	941.53	15.50	39.4	

Specimen 1 to 3

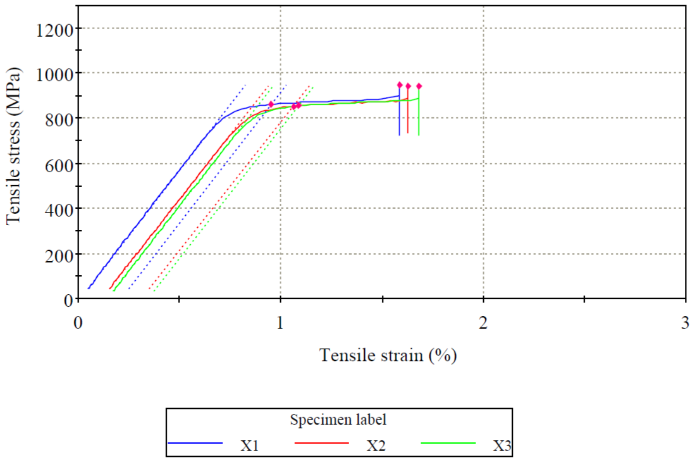

Specimen 1 to 3

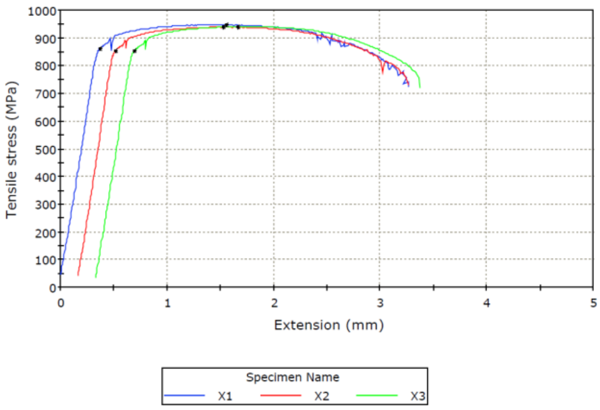

© Central University of Technology, Free State

G.2. Y specimens

Laboratory Name	CSIR Materials Testing Laboratory
Company	CUT Miya
Operator ID	203406
Method description	LM-WP-402 - ASTM E8 M
Sample description	Ti6Al4V
Test Date	22/02/2021

	Specimen label	Length (mm)	Area (mm^2)	Tensile stress at Yield (Offset 0.2 %) (MPa)	Modulus (Chord 150 MPa - 600 MPa) (GPa)	UTS (MPa)	% Elongation (4*D)	Reduction of Area (%)	Specimen note 1
1	Y1	20.00	13.85	863.94	118.1	947.64	13.25	30.6	
2	Y2	20.00	13.85	860.75	120.8	943.50	14.70	36.0	
3	Y3	20.00	13.85	856.71	114.6	941.14	15.05	41.2	
Mean		20.00	13.85	860.47	117.8	944.09	14.33	35.9	
Coefficient of Variation		0.000	0.000	0.421	2.622	0.348	6.658	14.846	
Range		0.00	0.00	7.23	6.2	6.50	1.80	10.7	
Standard Deviation		0.000	0.000	3.625	3.089	3.289	0.954	5.334	
Minimum		20.00	13.85	856.71	114.6	941.14	13.25	30.6	
Maximum		20.00	13.85	863.94	120.8	947.64	15.05	41.2	
Median		20.00	13.85	860.75	118.1	943.50	14.70	36.0	

Specimen 1 to 3

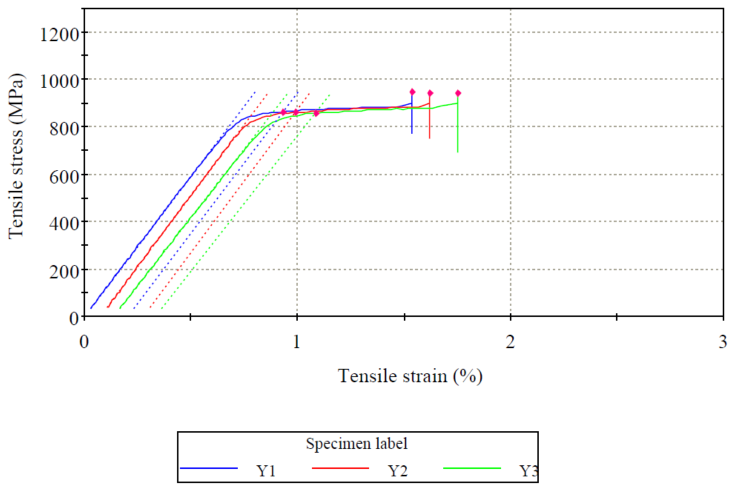

Specimen 1 to 3

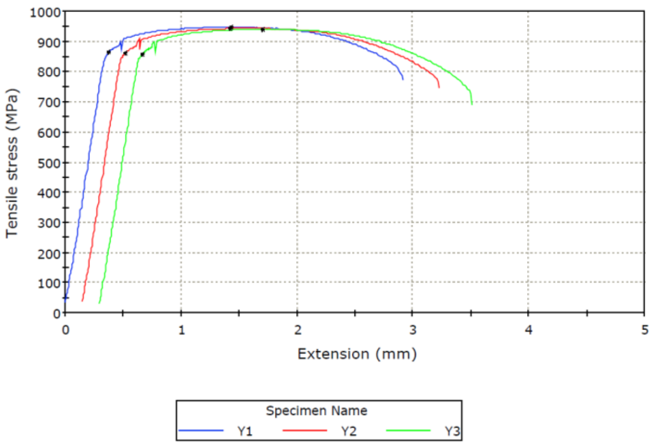

© Central University of Technology, Free State

G.3. Z specimens

T0381

Laboratory Name	CSIR Materials Testing Laboratory
Company	CUT Miya
Operator ID	203406
Method description	LM-WP-402 - ASTM E8 M
Sample description	Ti6Al4V
Test Date	22/02/2021

	Specimen label	Length (mm)	Area (mm^2)	Tensile stress at Yield (Offset 0.2 %) (MPa)	Modulus (Chord 150 MPa - 600 MPa) (GPa)	UTS (MPa)	% Elongation (4*D)	Reduction of Area (%)	Specimen note 1
1	Z1	20.00	14.32	774.78	110.0	888.52	15.75	50.3	
2	Z2	20.00	14.25	780.48	109.5	894.81	15.60	49.4	
3	Z3	20.00	14.25	781.33	108.5	891.61	16.15	50.4	
Mean		20.00	14.28	778.86	109.3	891.65	15.83	50.0	
Coefficient of Variation		0.000	0.271	0.457	0.703	0.353	1.796	1.098	
Range		0.00	0.07	6.55	1.5	6.29	0.55	1.0	
Standard Deviation		0.000	0.039	3.562	0.769	3.146	0.284	0.550	
Minimum		20.00	14.25	774.78	108.5	888.52	15.60	49.4	
Maximum		20.00	14.32	781.33	110.0	894.81	16.15	50.4	
Median		20.00	14.25	780.48	109.5	891.61	15.75	50.3	

Specimen 1 to 3

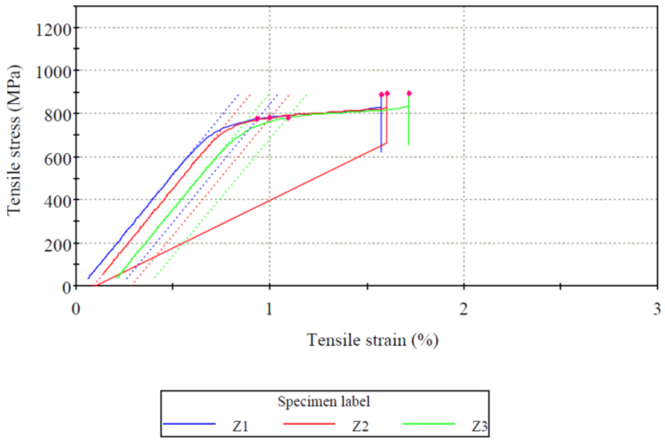

Specimen 1 to 3

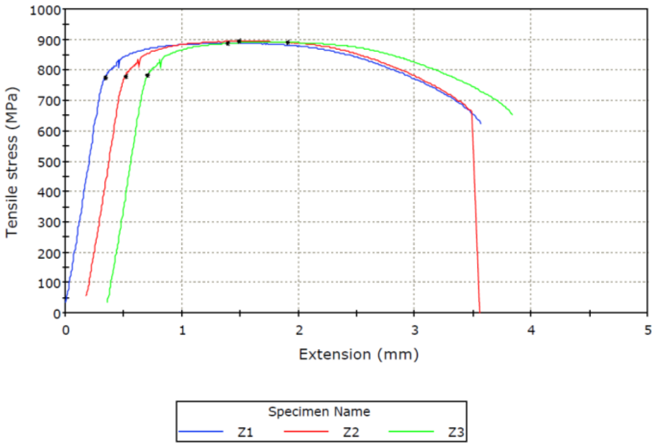

© Central University of Technology, Free State

APPENDIX H: CHARPY IMPACT TEST REPORT

SecMet (Pty) Ltd
A subsidiary of MegChem Holdings (Pty) Ltd

Secunda:
6 Bergius Street
Secunda
2302
+27 (0) 17 634-5555

Centurion:
55 Ireland Avenue
Eldoraigne
0157
+27 (0) 12 664-4680

P O Box 2040
Secunda
2302
doc.control@secmet.co.za
www.secmet.co.za

Form: BMS-7.5-012N R1

To: **Francis Monaheng**
Email: lmonaheng@cut.ac.za
Company: Central University of Technology
Your Ref. No: Signed quotation dated 6th May 2020

From: **Jaco Jonck**
Department: Materials and Forensic Engineering
Our Ref. No: MC4011853 Revision 2
Date: 2020-08-18 Pages: 2
Doc. History Rev. 1 Change: Original issue
2 Updated instrument details and test methodology

CVN impact testing of 3D printed Ti6Al4V material

1 SCOPE AND TESTING

SecMet was requested to assist with the Charpy V-Notch (CVN) impact testing of eighteen (18) 3D printed, grade Ti6Al4V samples in order to determine the impact toughness in accordance with ASTM E23[1].

The samples comprised of two sets of nine (9) samples each, with the first set having the notch machined by means of wire cutting (since conventional machining was not feasible) and for the second set the notch was included in the printed geometry.
Each set comprised of triplicate samples in three different printing orientations.

The impact tests were performed at -50°C using an Instron 450MP2-J1 impact testing machine with a maximum frame capacity of 300 Joule, in order to gauge the impact resistance of the samples.

The specimens were cooled to -50°C by immersion into an ethanol solution cooled to the appropriate temperature with liquid nitrogen.

2 RESULTS AND DISCUSSION

The results from the Charpy impact testing at -50°C is presented in Table 1. The impact energy values recorded were generally high considering the low test temperature. The impact toughness for the different orientations, printed notch and wire cut notch were comparable.

---

[1] American Society for Testing and Materials – ***Standard Test Methods for Notched Bar Impact Testing of Metallic Materials*** – ASTM E23 – 2007a.

© Central University of Technology, Free State

Table 1: Results from the impact testing at -50°C of the Ti6Al4V material.

Notch	Orientation	CVN Impact Toughness (Joules)			
		Values	Min	Max	Average
Printed	XY	26, 27, 26	26	27	26
	YX	28, 28, 27	27	28	28
	Z	29, 30, 31	29	31	30
Wire cut	XY	32, 33, 34	32	34	33
	YX	28, 29, 30	28	30	29
	Z	30, 30, 32	30	32	31

For and on behalf of SecMet
Materials and Forensic Engineering:

Author:

Digitally signed
by Jaco Jonck
Date: 2020.08.18
14:10:27 +02'00'

Jaco Jonck
(Senior Metallurgical Engineer)

Reviewer:

Digitally signed by
Ronald Koenis
Date: 2020.08.18
13:50:17 +02'00'

Ronald Koenis
(Principal Metallurgical Engineer and Group Leader)

APPENDIX I: FRACTURE TOUGHNESS REPORT

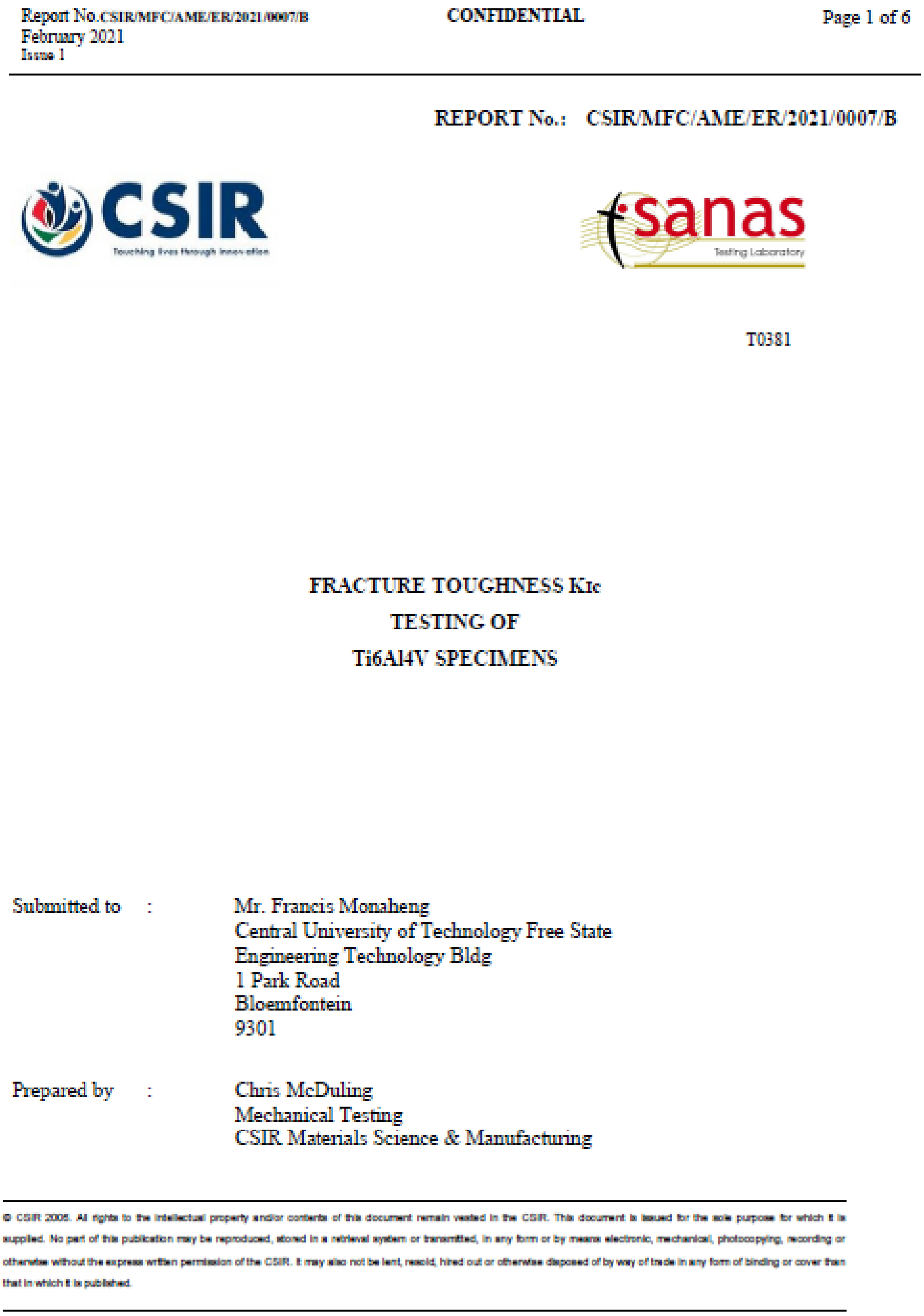

REPORT No.: CSIR/MFC/AME/ER/2021/0007/B

T0381

FRACTURE TOUGHNESS K$_{Ic}$ TESTING OF Ti6Al4V SPECIMENS

Submitted to : Mr. Francis Monaheng
Central University of Technology Free State
Engineering Technology Bldg
1 Park Road
Bloemfontein
9301

Prepared by : Chris McDuling
Mechanical Testing
CSIR Materials Science & Manufacturing

© CSIR 2006. All rights to the intellectual property and/or contents of this document remain vested in the CSIR. This document is issued for the sole purpose for which it is supplied. No part of this publication may be reproduced, stored in a retrieval system or transmitted, in any form or by means electronic, mechanical, photocopying, recording or otherwise without the express written permission of the CSIR. It may also not be lent, resold, hired out or otherwise disposed of by way of trade in any form of binding or cover than that in which it is published.

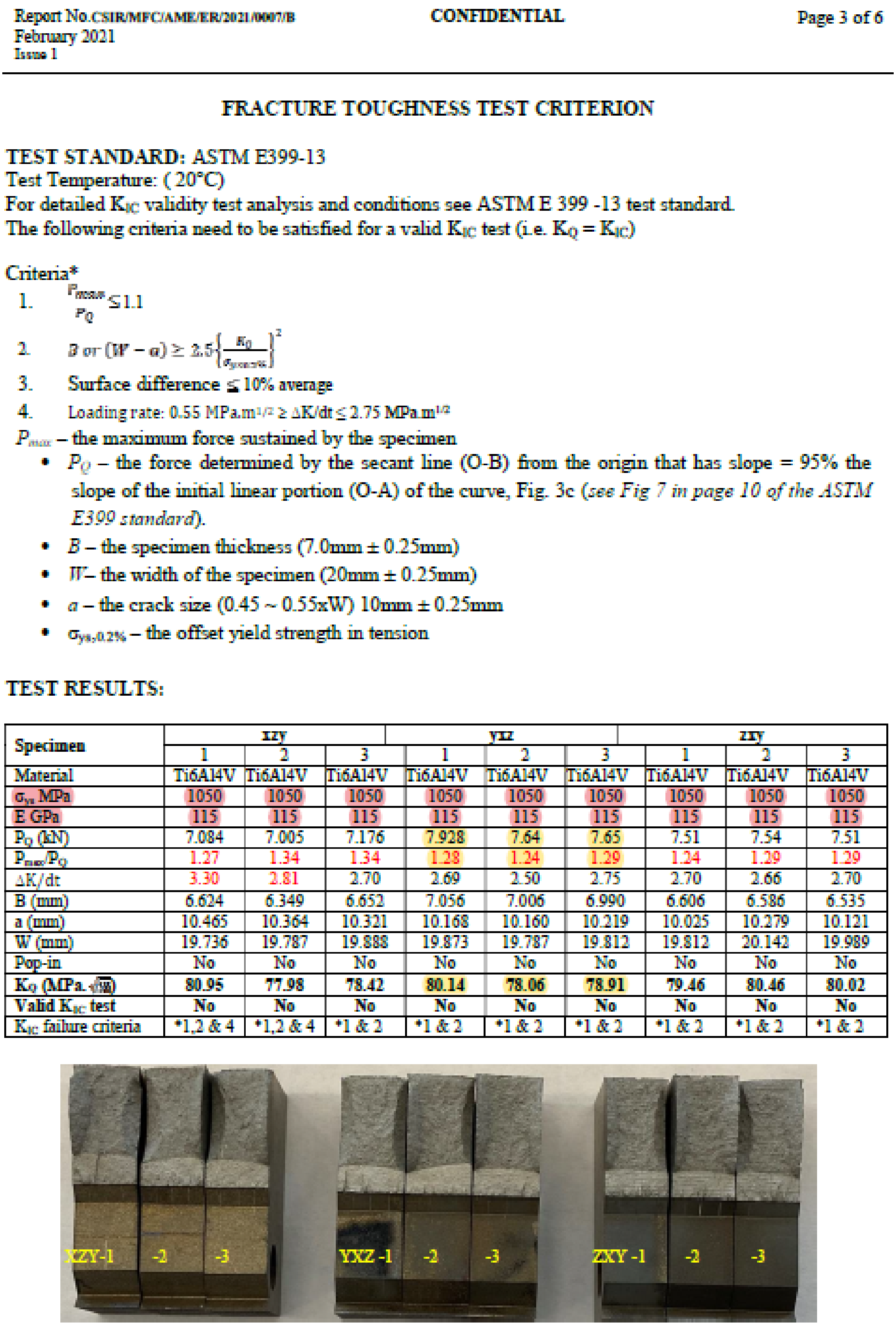

FRACTURE TOUGHNESS TEST CRITERION

TEST STANDARD: ASTM E399-13
Test Temperature: (20°C)
For detailed K_{IC} validity test analysis and conditions see ASTM E 399 -13 test standard.
The following criteria need to be satisfied for a valid K_{IC} test (i.e. $K_Q = K_{IC}$)

Criteria*

1. $\frac{P_{max}}{P_Q} \leq 1.1$
2. $B \text{ or } (W - a) \geq 2.5\left\{\frac{K_Q}{\sigma_{ys,0.2\%}}\right\}^2$
3. Surface difference $\leq$ 10% average
4. Loading rate: 0.55 MPa.m$^{1/2}$ ≥ ΔK/dt ≤ 2.75 MPa.m$^{1/2}$

P_{max} – the maximum force sustained by the specimen

- *P_Q* – the force determined by the secant line (O-B) from the origin that has slope = 95% the slope of the initial linear portion (O-A) of the curve, Fig. 3c (*see Fig 7 in page 10 of the ASTM E399 standard*).
- *B* – the specimen thickness (7.0mm ± 0.25mm)
- *W* – the width of the specimen (20mm ± 0.25mm)
- *a* – the crack size (0.45 ~ 0.55xW) 10mm ± 0.25mm
- $\sigma_{ys,0.2\%}$ – the offset yield strength in tension

TEST RESULTS:

Specimen	xzy			yxz			zxy		
	1	2	3	1	2	3	1	2	3
Material	Ti6Al4V	Ti6Al4V	Ti6Al4V	Ti6Al4V	Ti6Al4V	Ti6Al4V	Ti6Al4V	Ti6Al4V	Ti6Al4V
σ_{ys} MPa	1050	1050	1050	1050	1050	1050	1050	1050	1050
E GPa	115	115	115	115	115	115	115	115	115
P_Q (kN)	7.084	7.005	7.176	7.928	7.64	7.65	7.51	7.54	7.51
P_{max}/P_Q	1.27	1.34	1.34	1.28	1.24	1.29	1.24	1.29	1.29
ΔK/dt	3.30	2.81	2.70	2.69	2.50	2.75	2.70	2.66	2.70
B (mm)	6.624	6.349	6.652	7.056	7.006	6.990	6.606	6.586	6.535
a (mm)	10.465	10.364	10.321	10.168	10.160	10.219	10.025	10.279	10.121
W (mm)	19.736	19.787	19.888	19.873	19.787	19.812	19.812	20.142	19.989
Pop-in	No	No	No	No	No	No	No	No	No
K_Q (MPa.$\sqrt{m}$)	**80.95**	**77.98**	**78.42**	**80.14**	**78.06**	**78.91**	**79.46**	**80.46**	**80.02**
Valid K_{IC} test	**No**	**No**	**No**	**No**	**No**	**No**	**No**	**No**	**No**
K_{IC} failure criteria	*1,2 & 4	*1,2 & 4	*1 & 2	*1 & 2	*1 & 2	*1 & 2	*1 & 2	*1 & 2	*1 & 2

© Central University of Technology, Free State

LOAD/EXTENSION GRAPHS:

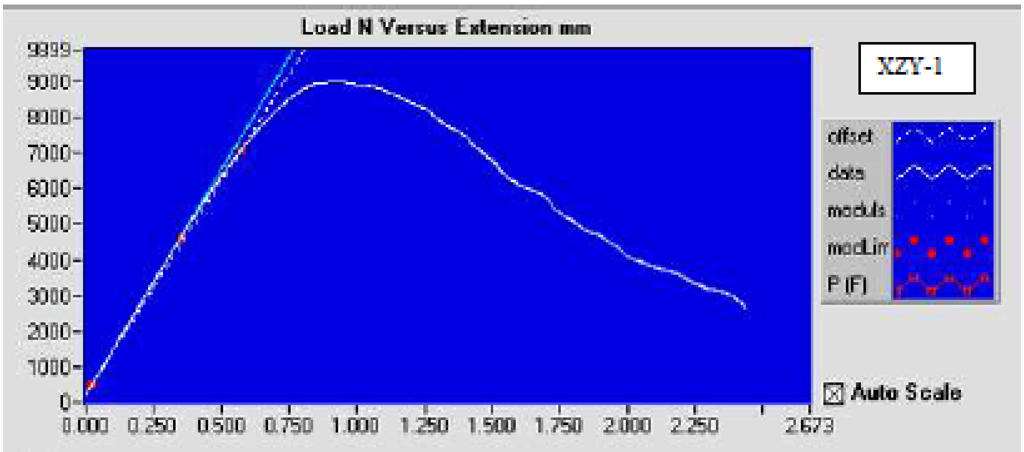

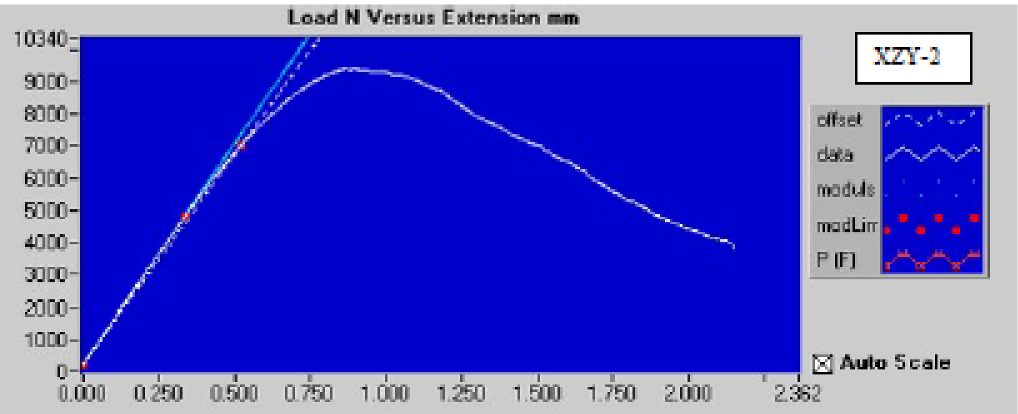

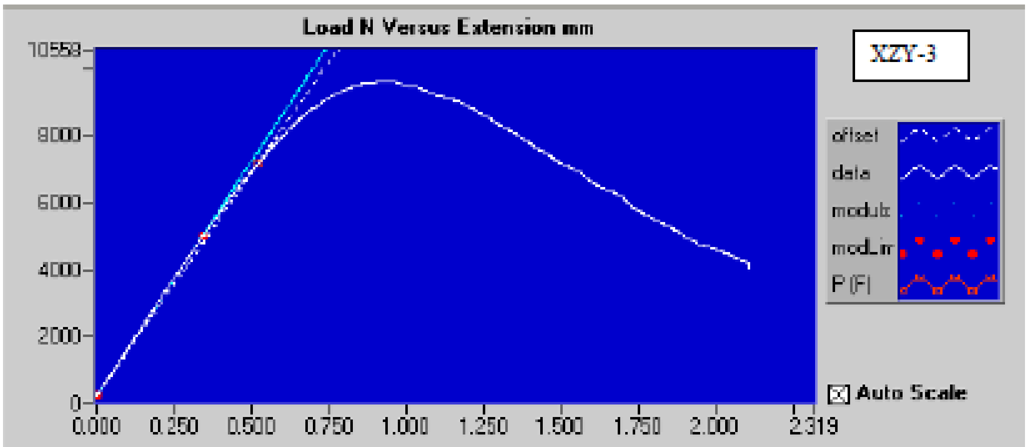

© Central University of Technology, Free State

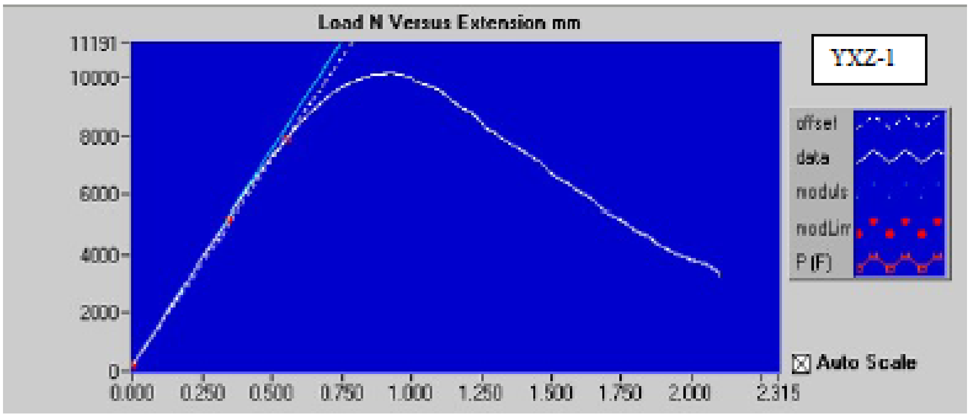

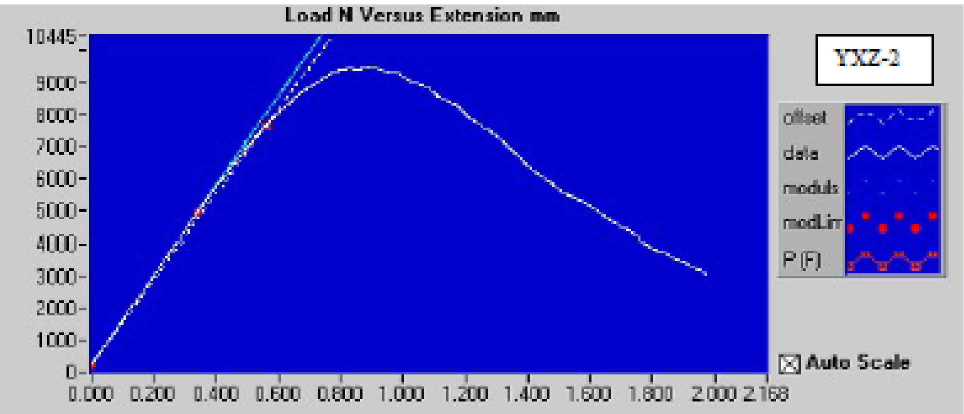

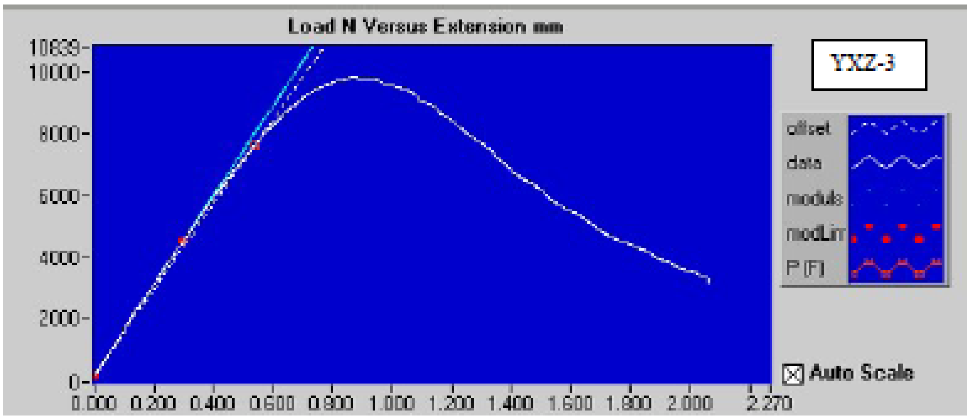

© Central University of Technology, Free State

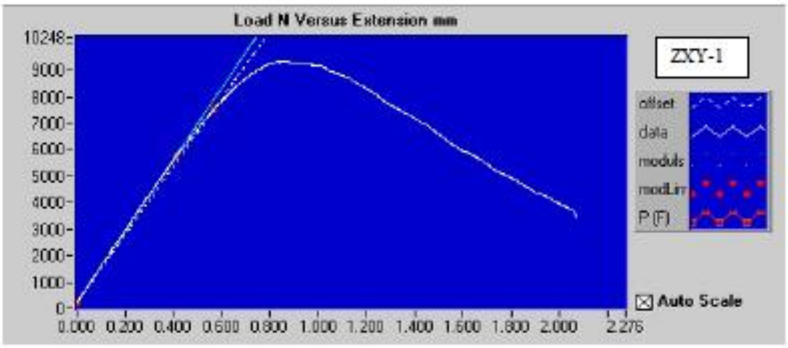

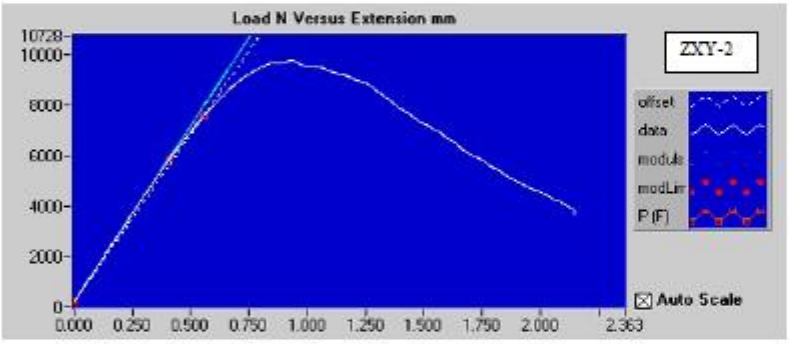

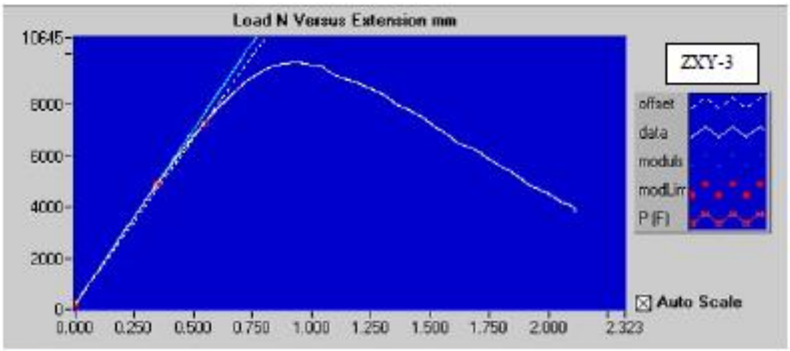

GENERAL REMARKS

These test results apply only to the samples supplied to the CSIR for testing and the CSIR accepts no responsibility for any product differences due to manufacturing variations.
The CSIR takes no responsibility for the applicability of the test results to real life operating conditions of the product.
The CSIR cannot be held responsible for any failure or consequential damage resulting from such failure.

END

© Central University of Technology, Free State

APPENDIX J: FATIGUE CRACK GROW RATE REPORT

REPORT No.: CSIR/MFC/AME/ER/2021/0006/B

CSIR
Touching lives through innovation

sanas
Testing Laboratory
T0381

FATIGUE CRACK GROWTH RATE TESTING OF Ti6Al4V SPECIMENS

Submitted to :
Mr. Francis Monaheng
Central University of Technology Free State
Engineering Technology Bldg
1 Park Road
Bloemfontein
9301

Prepared by :
Chris McDuling
Mechanical Testing Laboratory
CSIR Manufacturing Cluster

© CSIR 2006. All rights to the intellectual property and/or contents of this document remain vested in the CSIR. This document is issued for the sole purpose for which it is supplied. No part of this publication may be reproduced, stored in a retrieval system or transmitted, in any form or by means electronic, mechanical, photocopying, recording or otherwise without the express written permission of the CSIR. It may also not be lent, resold, hired out or otherwise disposed of by way of trade in any form of binding or cover than that in which it is published.

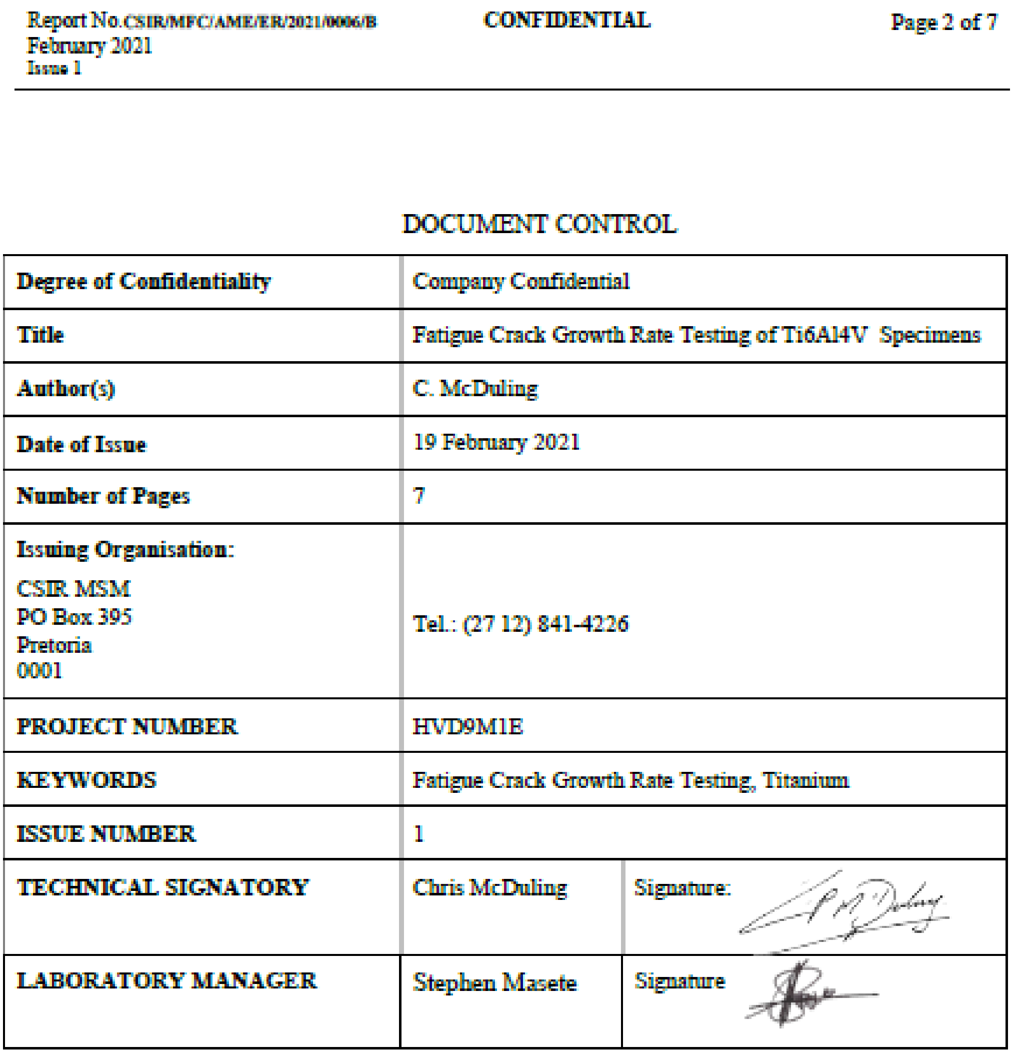

DOCUMENT CONTROL

Degree of Confidentiality	Company Confidential	
Title	Fatigue Crack Growth Rate Testing of Ti6Al4V Specimens	
Author(s)	C. McDuling	
Date of Issue	19 February 2021	
Number of Pages	7	
Issuing Organisation: CSIR MSM PO Box 395 Pretoria 0001	Tel.: (27 12) 841-4226	
PROJECT NUMBER	HVD9M1E	
KEYWORDS	Fatigue Crack Growth Rate Testing, Titanium	
ISSUE NUMBER	1	
TECHNICAL SIGNATORY	Chris McDuling	Signature:
LABORATORY MANAGER	Stephen Masete	Signature

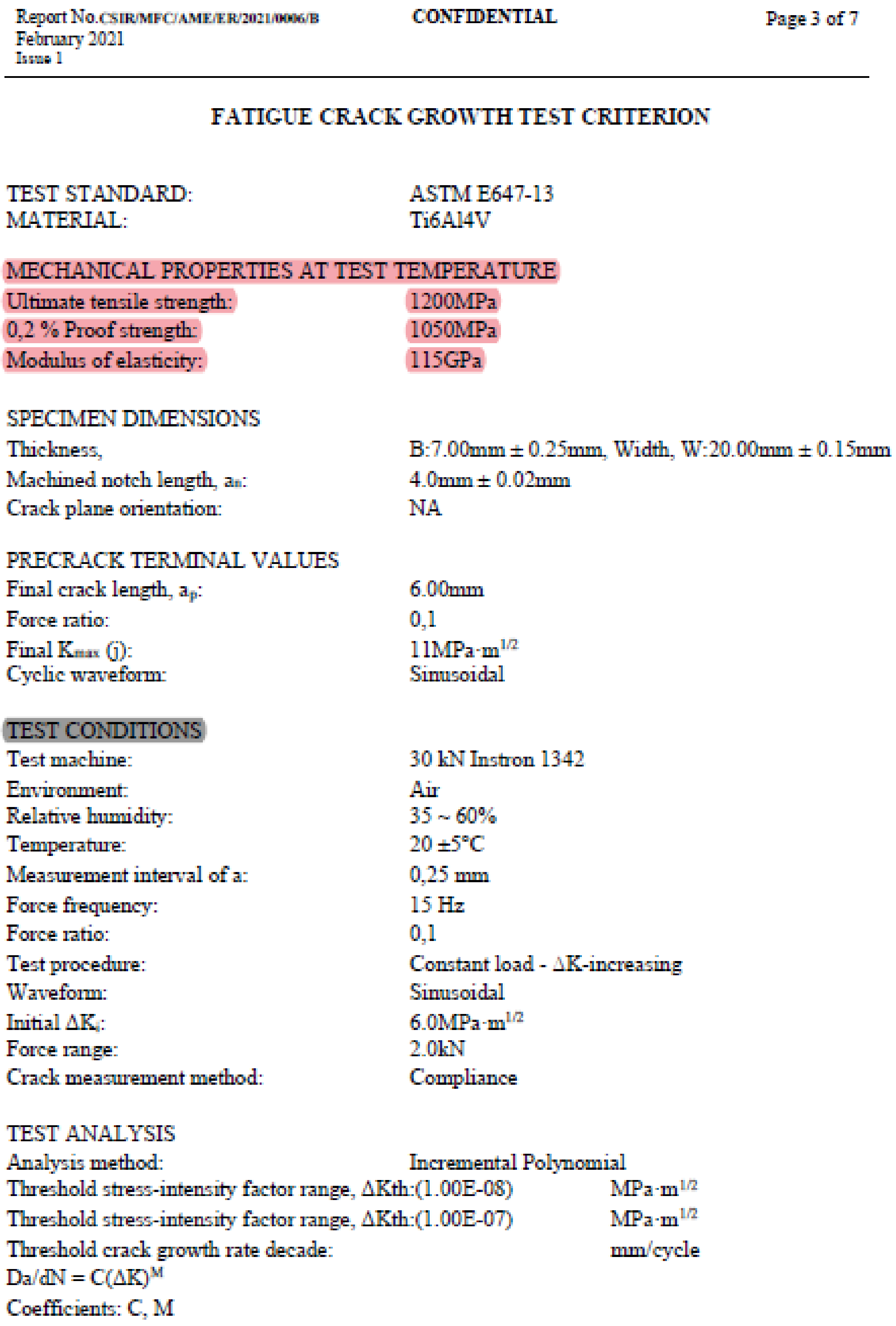

Report No.CSIR/MFC/AME/ER/2021/0006/B
February 2021
Issue 1

CONFIDENTIAL

Page 3 of 7

FATIGUE CRACK GROWTH TEST CRITERION

TEST STANDARD:	ASTM E647-13
MATERIAL:	Ti6Al4V

MECHANICAL PROPERTIES AT TEST TEMPERATURE

Ultimate tensile strength:	1200MPa
0,2 % Proof strength:	1050MPa
Modulus of elasticity:	115GPa

SPECIMEN DIMENSIONS

Thickness,	B:7.00mm ± 0.25mm, Width, W:20.00mm ± 0.15mm
Machined notch length, a_n:	4.0mm ± 0.02mm
Crack plane orientation:	NA

PRECRACK TERMINAL VALUES

Final crack length, a_p:	6.00mm
Force ratio:	0,1
Final K_{max} (j):	11MPa·m$^{1/2}$
Cyclic waveform:	Sinusoidal

TEST CONDITIONS

Test machine:	30 kN Instron 1342
Environment:	Air
Relative humidity:	35 ~ 60%
Temperature:	20 ±5°C
Measurement interval of a:	0,25 mm
Force frequency:	15 Hz
Force ratio:	0,1
Test procedure:	Constant load - ΔK-increasing
Waveform:	Sinusoidal
Initial ΔK_i:	6.0MPa·m$^{1/2}$
Force range:	2.0kN
Crack measurement method:	Compliance

TEST ANALYSIS

Analysis method:	Incremental Polynomial
Threshold stress-intensity factor range, ΔKth:(1.00E-08)	MPa·m$^{1/2}$
Threshold stress-intensity factor range, ΔKth:(1.00E-07)	MPa·m$^{1/2}$
Threshold crack growth rate decade:	mm/cycle

$Da/dN = C(\Delta K)^M$

Coefficients: C, M

© Central University of Technology, Free State

TEST RESULTS

Specimen ID:	ΔKth:(1.00E-08) MPa·m$^{1/2}$	ΔKth:(1.00E-07) MPa·m$^{1/2}$	Threshold crack growth rate decade: mm/cycle	Coefficients	
				C	M
XZY-4	0.653	1.465	$10^{-4} \sim 10^{-3}$	3.37E-08	2.85
XZY-5	0.661	1.477	$10^{-4} \sim 10^{-3}$	3.28E-08	2.86
XZY-6	0.761	1.661	$10^{-4} \sim 10^{-3}$	2.24E-08	2.95
YXZ-4	0.569	1.288	$10^{-4} \sim 10^{-3}$	4.98E-08	2.76
YXZ-5	0.463	1.111	$10^{-4} \sim 10^{-3}$	7.64E-08	2.65
YXZ-6	0.504	1.183	$10^{-4} \sim 10^{-3}$	6.36E-08	2.70
ZXY-4	0.539	1.261	$10^{-4} \sim 10^{-3}$	5.33E-08	2.71
ZXY-5	0.552	1.325	$10^{-4} \sim 10^{-3}$	4.55E-08	2.80
ZXY-6	0.577	1.325	$10^{-4} \sim 10^{-3}$	4.59E-08	2.77

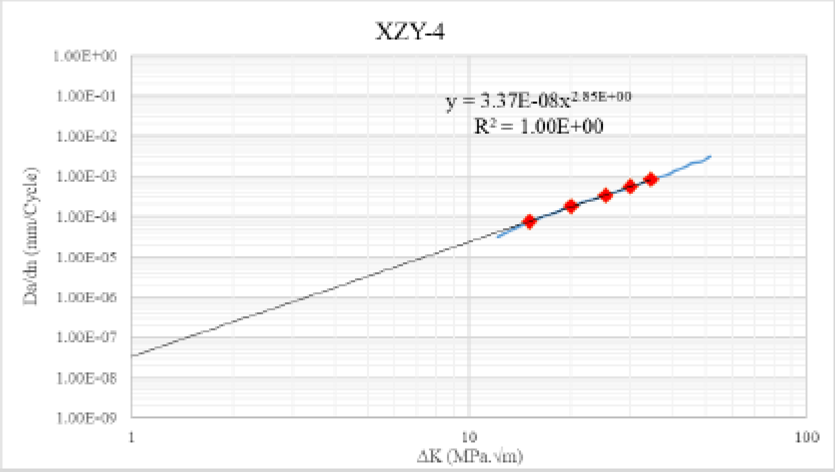

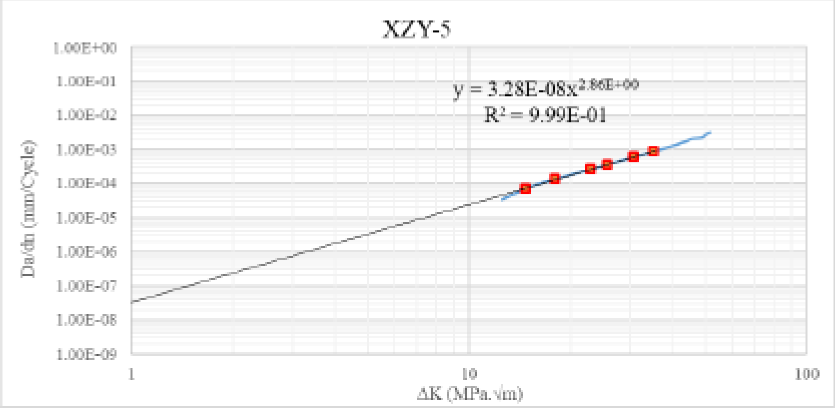

© Central University of Technology, Free State

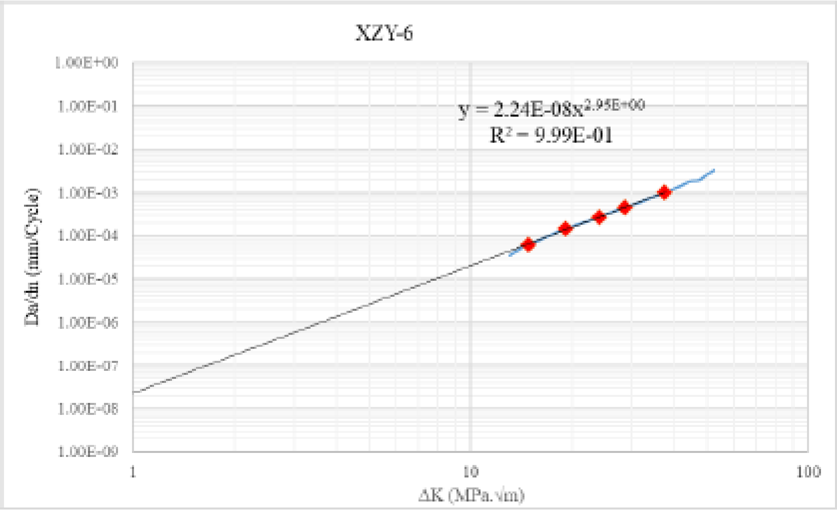

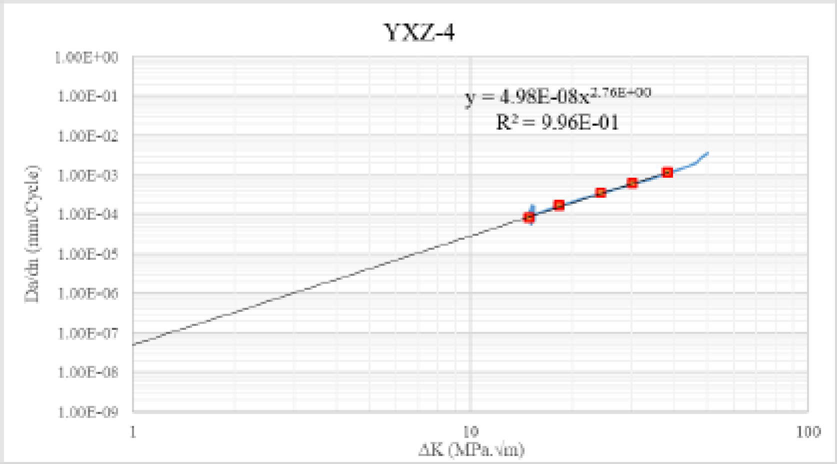

© Central University of Technology, Free State

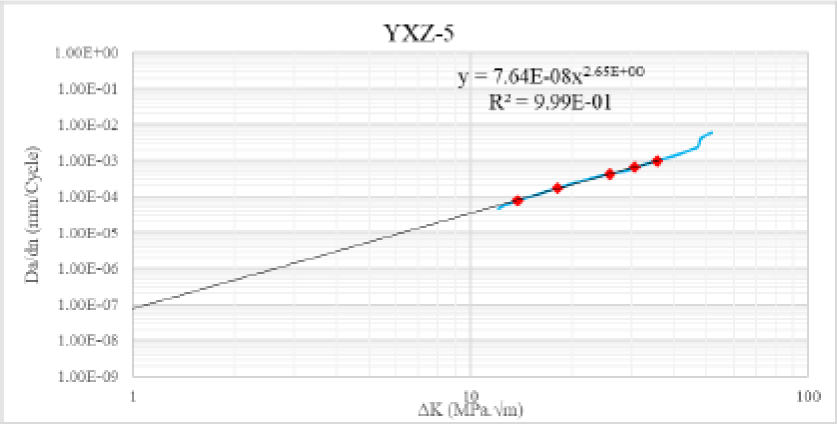

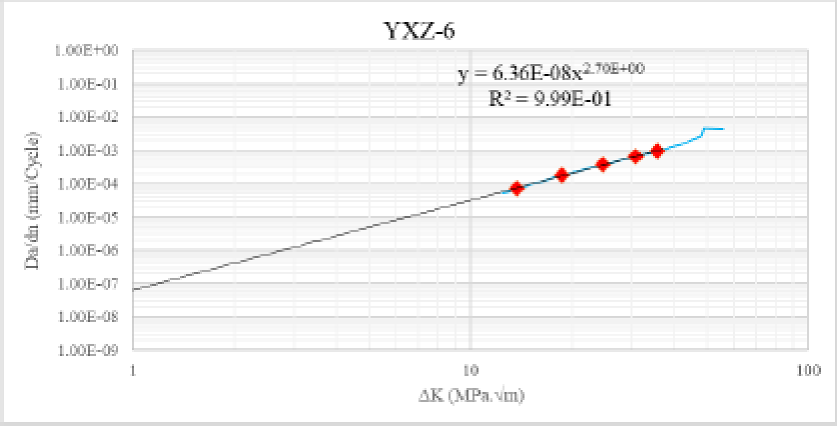

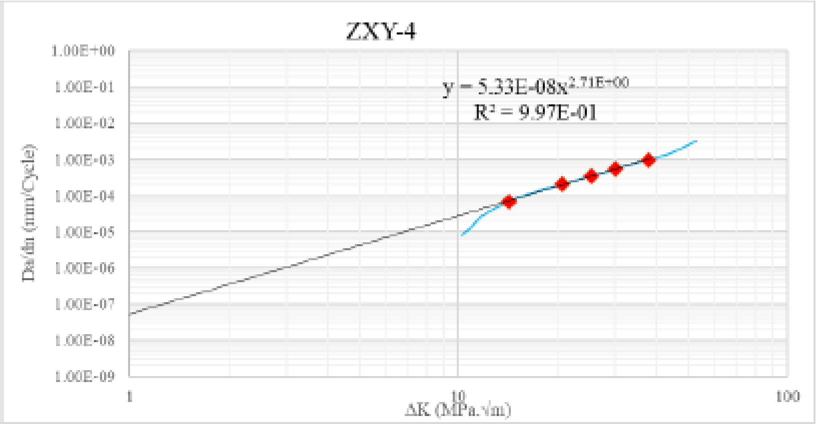

© Central University of Technology, Free State

Report No.CSIR/MFC/AME/ER/2021/0006/B
February 2021
Issue 1

CONFIDENTIAL

Page 7 of 7

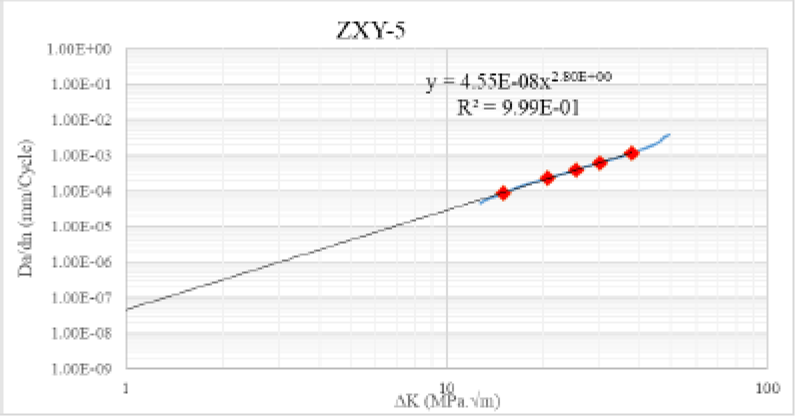

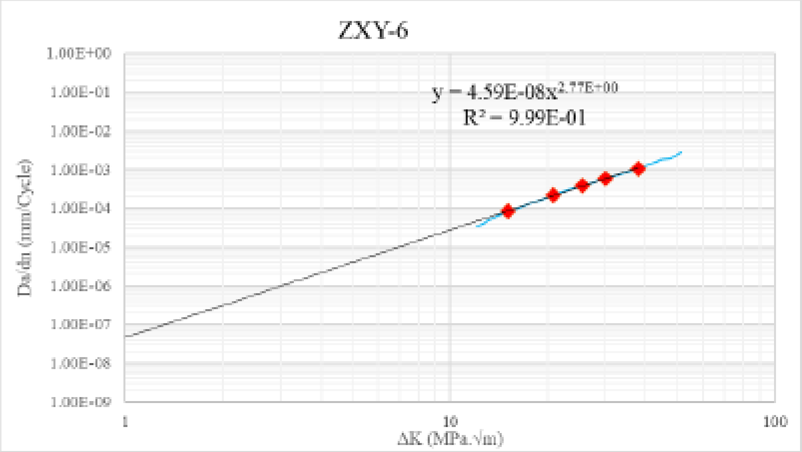

GENERAL REMARKS

These test results apply only to the samples supplied to the CSIR for testing and the CSIR accepts no responsibility for any product differences due to manufacturing variations.
The CSIR takes no responsibility for the applicability of the test results to real life operating conditions of the product.
The CSIR cannot be held responsible for any failure or consequential damage resulting from such failure.

END

© Central University of Technology, Free State

APPENDIX K: STATIC TEST RESULST DATA OF THE FORK

K.1. Strain data at X static loading of 6000 N.

Time	SG1	SG2	SG3a	SG3b	SG3c	SG4a	SG4b
0	-98,09	-26,85	-79,19	94,38	-52,3	-97,29	-38,72
2	-97,07	-23,83	-81,2	95,54	-49,89	-86,5	-44,11
4	-82,93	-11,28	-94,52	102,8	-42,17	-51,9	-67,59
6	-61,1	-2,232	-108,03	110,53	-36,82	-23,94	-88,05
8	-40,98	5,673	-119,25	118,64	-31,66	4,857	-108,58
10	-27,03	10,79	-131,18	126	-25,52	29,83	-124,48
12	-17,67	13,94	-138,66	130,8	-20,46	47,35	-134,78
14	-15,21	14,71	-140,48	131,98	-19,55	51,8	-137,14
16	-14,19	15,37	-141,24	132,85	-18,87	54,79	-139
18	-12,4	15,85	-142,35	133,51	-18,16	57,24	-140,2
20	-12,67	15,73	-142,17	133,67	-18,19	56,82	-140
22	-12,68	15,72	-142,18	133,6	-18,19	56,96	-139,91
24	-12,48	15,89	-142,17	133,94	-18,19	57,33	-140,15
26	-12,5	15,93	-142,29	133,74	-18,11	57,48	-140,41
28	-12,48	15,91	-142,03	133,7	-18,09	57,65	-140,45
30	-14,34	15,05	-141,32	133,52	-19,27	53,68	-138,77
32	-22,47	9,897	-137,28	130,46	-25,16	31,88	-126,92
34	-31,24	0,4466	-130,85	124,39	-33,23	-3,504	-104,16
36	-40,16	-5,301	-124,18	119,53	-35,77	-22,17	-89,8
38	-49,75	-11,7	-115,23	113,64	-38,88	-43,56	-71,88
40	-60,44	-15,34	-107,04	108,71	-41,22	-58,29	-62,91
42	-68,11	-17,1	-99,17	104,79	-43,3	-67,17	-58,17
44	-74,22	-19,01	-93,42	102,19	-45,06	-74,23	-54,01
46	-81,15	-21,6	-86,95	99,27	-47,15	-80,47	-49,49
48	-87,69	-24,51	-82,49	97,09	-49,43	-87,87	-45,09
50	-93,19	-25,97	-79,62	95,84	-51,42	-93,35	-41,74
52	-94,34	-26,5	-78,87	95,26	-51,98	-95,43	-40,41
54	-94,69	-26,58	-78,55	95,06	-52,04	-95,86	-39,89
56	-94,66	-26,56	-78,41	95	-52,42	-96,28	-39,97
Min	**-98,09**	**-26,85**	**-142,35**	**94,38**	**-52,42**	**-97,29**	**-140,45**
Mean	**-49,51**	**-3,57**	**-114,49**	**115,88**	**-34,22**	**-15,87**	**-92,65**
Max	**-12,40**	**15,93**	**-78,41**	**133,94**	**-18,09**	**57,65**	**-38,72**
SD	**33,81**	**17,51**	**25,96**	**15,99**	**13,56**	**63,14**	**41,87**

K.2. Strain data at Z static loading of 8300 N.

Time	SG1	SG2	SG3	SG4	SG5	SG6	SG7
16,42	-1,38E+03	26,99	1083	180,09	-1313,9	-830,28	-689,69
16,44	-1,38E+03	27,03	1083	180,05	-1314,1	-830,15	-689,67
16,46	-1,38E+03	27,04	1083,1	180,03	-1314,2	-830,08	-689,63
16,48	-1,38E+03	27,02	1083,2	179,97	-1314,2	-830,13	-689,49
16,50	-1,38E+03	26,98	1083,2	179,84	-1314,2	-830,1	-689,31
16,52	-1,38E+03	26,95	1083,3	179,86	-1314,1	-830,03	-689,19
16,54	-1,38E+03	26,93	1083,2	179,94	-1314,1	-830,02	-689,11
16,56	-1,38E+03	26,92	1083,3	179,91	-1314,1	-829,93	-689,07
16,58	-1,38E+03	26,92	1083,4	179,87	-1314,1	-829,61	-688,99
16,60	-1,38E+03	26,93	1083,4	179,93	-1314,1	-829,55	-688,9
16,62	-1,38E+03	26,97	1083,4	180,03	-1314,1	-829,49	-688,81
16,64	-1,38E+03	26,92	1083,4	179,95	-1313,9	-829,36	-688,73
16,66	-1,37E+03	26,9	1083,5	180	-1313,8	-829,27	-688,48
16,68	-1,37E+03	26,93	1083,5	180,09	-1313,8	-829,27	-688,23
16,70	-1,37E+03	26,98	1083,4	179,98	-1313,8	-829,21	-688,19
16,72	-1,37E+03	26,96	1083,4	179,92	-1313,8	-829,1	-688,23
16,74	-1,37E+03	26,95	1083,4	180,04	-1314	-828,95	-688,16
16,76	-1,37E+03	26,94	1083,4	180,1	-1313,9	-828,83	-687,93

© Central University of Technology, Free State

16,78	-1,37E+03	26,89	1083,4	179,99	-1313,7	-828,8	-687,8
16,80	-1,37E+03	26,88	1083,4	179,93	-1313,7	-828,72	-687,64
16,82	-1,37E+03	26,89	1083,4	179,94	-1313,6	-828,6	-687,46
16,84	-1,37E+03	26,9	1083,5	179,9	-1313,7	-828,6	-687,41
16,86	-1,37E+03	26,91	1083,5	179,85	-1313,6	-828,54	-687,34
16,88	-1,37E+03	26,88	1083,4	179,79	-1313,6	-828,46	-687,17
16,90	-1,37E+03	26,9	1083,3	179,82	-1313,6	-828,32	-687,08
16,92	-1,37E+03	26,96	1083,5	179,83	-1313,5	-828,24	-687,03
16,94	-1,37E+03	26,95	1083,5	179,79	-1313,5	-828,11	-686,89
16,96	-1,37E+03	26,9	1083,5	179,82	-1313,6	-827,98	-686,66
16,98	-1,37E+03	26,86	1083,6	179,86	-1313,5	-827,79	-686,63
17,00	-1,37E+03	26,81	1083,4	179,96	-1313,4	-827,62	-686,62
17,02	-1,37E+03	26,81	1083,4	179,98	-1313,3	-827,63	-686,56
17,04	-1,37E+03	26,86	1083,4	179,93	-1313,2	-827,79	-686,4
17,06	-1,37E+03	26,88	1083,4	179,93	-1313,3	-827,77	-686,29
17,08	-1,37E+03	26,85	1083,3	179,98	-1313,3	-827,57	-686,24
17,10	-1,37E+03	26,85	1083,2	179,84	-1313,4	-827,43	-686,15
17,12	-1,37E+03	26,83	1083,2	179,76	-1313,4	-827,31	-686,02
17,14	-1,37E+03	26,82	1083,3	179,77	-1313,3	-827,18	-685,93
17,16	-1,37E+03	26,84	1083,4	179,72	-1313,3	-827,04	-685,86
17,18	-1,37E+03	26,87	1083,3	179,8	-1313,3	-826,97	-685,8
17,20	-1,37E+03	26,84	1083,3	179,85	-1313,2	-826,95	-685,71
17,22	-1,37E+03	26,82	1083,3	179,86	-1313,1	-826,94	-685,63
17,24	-1,37E+03	26,83	1083,4	179,83	-1313,2	-826,92	-685,59
17,26	-1,37E+03	26,84	1083,4	179,88	-1313,3	-826,91	-685,47
17,28	-1,37E+03	26,84	1083,4	179,92	-1313,2	-826,89	-685,38
17,30	-1,37E+03	26,82	1083,4	179,89	-1313,2	-826,8	-685,23
17,32	-1,37E+03	26,81	1083,3	179,92	-1313	-826,7	-685,1
17,34	-1,37E+03	26,81	1083,3	180,11	-1312,9	-826,74	-685,07
17,36	-1,37E+03	26,82	1083,5	180,19	-1313	-826,76	-684,96
17,38	-1,37E+03	26,87	1083,5	180,08	-1313	-826,68	-684,86
17,40	-1,37E+03	26,83	1083,4	179,94	-1313	-826,49	-684,85
17,42	-1,37E+03	26,77	1083,5	180	-1312,8	-826,36	-684,84
17,44	-1,37E+03	26,78	1083,5	180,01	-1312,9	-826,28	-684,87
17,46	-1,37E+03	26,78	1083,4	180,01	-1312,9	-826,33	-684,93
17,48	-1,37E+03	26,79	1083,5	180	-1312,9	-826,44	-684,82
17,50	-1,37E+03	26,77	1083,5	179,97	-1312,9	-826,41	-684,66
17,52	-1,37E+03	26,77	1083,5	179,88	-1312,9	-826,27	-684,52
17,54	-1,37E+03	26,83	1083,6	179,8	-1313	-826,27	-684,43
17,56	-1,37E+03	26,86	1083,6	179,91	-1313	-826,28	-684,31
17,58	-1,37E+03	26,79	1083,7	179,91	-1313	-826,2	-684,18
17,60	-1,37E+03	26,72	1083,7	179,92	-1312,9	-826,06	-683,97
17,62	-1,37E+03	26,7	1083,6	180,01	-1312,9	-825,97	-683,91
17,64	-1,37E+03	26,71	1083,5	180,06	-1312,9	-825,94	-684,07
17,66	-1,37E+03	26,74	1083,5	179,93	-1312,9	-825,82	-684,2
17,68	-1,37E+03	26,76	1083,5	179,93	-1312,7	-825,81	-684,13
17,70	-1,37E+03	26,75	1083,6	179,96	-1312,7	-825,9	-684,04
17,72	-1,37E+03	26,74	1083,6	179,92	-1312,7	-825,87	-683,91
17,74	-1,37E+03	26,69	1083,5	179,88	-1312,8	-825,86	-683,84
17,76	-1,37E+03	26,74	1083,5	179,79	-1312,8	-825,83	-683,85
17,78	-1,37E+03	26,72	1083,5	179,82	-1312,7	-825,69	-683,85
17,80	-1,37E+03	26,67	1083,6	179,88	-1312,6	-825,61	-683,77
17,82	-1,37E+03	26,7	1083,8	179,89	-1312,5	-825,62	-683,64
17,84	-1,37E+03	26,74	1083,8	179,93	-1312,4	-825,64	-683,57
17,86	-1,37E+03	26,74	1083,7	179,92	-1312,5	-825,64	-683,6
17,88	-1,37E+03	26,74	1083,5	179,95	-1312,8	-825,62	-683,54
17,90	-1,37E+03	26,69	1083,5	180,03	-1312,8	-825,42	-683,42
17,92	-1,37E+03	26,7	1083,6	180,05	-1312,7	-825,23	-683,32
17,94	-1,37E+03	26,76	1083,6	180,08	-1312,5	-825,23	-683,27
17,96	-1,37E+03	26,74	1083,5	180,09	-1312,5	-825,33	-683,23
17,98	-1,37E+03	26,7	1083,5	180,04	-1312,6	-825,39	-683,23
18,00	-1,37E+03	26,7	1083,5	180,09	-1312,7	-825,34	-683,18
18,02	-1,37E+03	26,74	1083,7	180,09	-1312,7	-825,22	-682,94
18,04	-1,37E+03	26,76	1083,8	180,04	-1312,6	-825,12	-682,7
18,06	-1,37E+03	26,73	1083,7	179,98	-1312,5	-825,02	-682,59
18,08	-1,37E+03	26,72	1083,7	179,94	-1312,5	-824,98	-682,79

18,10	-1,37E+03	26,73	1083,8	179,92	-1312,5	-824,91	-682,89
18,12	-1,37E+03	26,73	1083,8	179,8	-1312,4	-824,82	-682,8
18,14	-1,37E+03	26,73	1083,8	179,77	-1312,4	-824,83	-683,7
18,16	-1,37E+03	26,72	1083,7	179,87	-1312,4	-824,9	-682,76
18,18	-1,37E+03	26,68	1083,7	179,93	-1312,5	-824,84	-682,76
18,20	-1,37E+03	26,69	1083,8	179,94	-1312,5	-824,76	-682,63
18,22	-1,37E+03	26,73	1083,7	179,94	-1312,5	-824,8	-682,5
18,24	-1,37E+03	26,67	1083,6	179,89	-1312,4	-824,76	-682,45
18,26	-1,37E+03	26,63	1083,7	179,99	-1312,4	-824,67	-682,45
18,28	-1,37E+03	26,64	1083,7	180,04	-1312,4	-824,61	-682,4
18,30	-1,37E+03	26,72	1083,7	180,03	-1312,3	-824,57	-682,32
18,32	-1,37E+03	26,76	1083,6	179,98	-1312,3	-824,58	-682,28
18,34	-1,37E+03	26,72	1083,5	179,96	-1312,3	-824,6	-682,23
18,36	-1,37E+03	26,67	1083,6	179,95	-1312,3	-824,61	-682,25
18,38	-1,37E+03	26,66	1083,7	179,92	-1312,4	-824,45	-682,22
18,40	-1,37E+03	26,7	1083,8	179,88	-1312,5	-824,39	-682,07
18,42	-1,37E+03	26,72	1083,8	179,84	-1312,3	-824,37	-681,88
18,44	-1,37E+03	26,68	1083,8	179,99	-1312,2	-824,28	-681,87
Min	**-1,38E+03**	**2,66E+01**	**1,08E+03**	**1,80E+02**	**-1,31E+03**	**-8,30E+02**	**-6,90E+02**
Mean	**-1,37E+03**	**2,68E+01**	**1,08E+03**	**1,80E+02**	**-1,31E+03**	**-8,27E+02**	**-6,85E+02**
Max	**-1,37E+03**	**2,70E+01**	**1,08E+03**	**1,80E+02**	**-1,31E+03**	**-8,24E+02**	**-6,82E+02**
SD	**1,37E+00**	**9,98E-02**	**1,80E-01**	**9,25E-02**	**5,75E-01**	**1,75E+00**	**2,27E+00**

© Central University of Technology, Free State

APPENDIX L: FATIGUE STRAIN VALUES

L.1. Strain data for X-loading during fatigue test

Time	SG1	SG2	SG3a	SG3b	SG3c	SG4a	SG4b
0	-126,9	-32,02	-60,47	84,47	-39,94	-115,69	-4,376
0,02	-107,31	-12,75	-81,25	93,06	-18	-44,74	-51,6
0,04	-94,79	4,561	-102,58	103,45	-5,268	10,27	-91,85
0,06	-84	16,45	-118,69	112,56	1,97	50,36	-117,21
0,08	-76,67	22,23	-127,03	117,83	5,826	73,06	-128,27
0,1	-77,59	22,43	-127,87	118,77	5,252	73,51	-129,84
0,12	-86,44	17,41	-121,9	115,71	-0,7036	50,67	-123,02
0,14	-92,23	6,624	-109,48	108,62	-10,12	10,01	-100,63
0,16	-90,11	-9,8	-92,11	98,17	-21,48	-41,52	-60,56
0,18	-102,31	-29,54	-72,27	87,71	-39,83	-105,66	-13,42
0,2	-136,46	-47,73	-53,06	80,28	-65,74	-180,34	27,74
0,22	-175,91	-61,01	-36,5	75,57	-89,46	-247,54	55,39
0,24	-203,45	-68,86	-25,2	72,49	-103,25	-290,37	69,38
0,26	-212,52	-71,02	-21,16	71,45	-106,61	-303,11	72,9
0,28	-203,98	-67,05	-24,4	72,86	-100,96	-286,19	68,06
0,3	-179,6	-57,77	-34,06	76,04	-84,85	-240	53,59
0,32	-146,86	-44	-48,61	80,51	-59,17	-169,64	24,79
0,34	-119,48	-26,1	-66,7	86,96	-32,25	-92,19	-19,1
0,36	-102,85	-6,94	-88,03	96,3	-13,36	-26,1	-65,55
0,38	-91,22	8,876	-108,32	106,59	-2,778	24,34	-101,44
0,4	-81,15	18,7	-122,21	114,65	3,475	59,61	-121,81
0,42	-75,95	22,69	-128,06	118,62	6,189	75,86	-129,47
0,44	-79,8	21,35	-126,6	118,16	4,005	68,82	-128,81
0,46	-89,36	14,66	-118,56	113,87	-3,379	39,53	-118,04
0,48	-91,61	2,046	-104,51	105,64	-13,31	-4,97	-89,58
0,5	-91,27	-15,75	-86,01	94,72	-26,32	-59,87	-45,95
0,52	-111,03	-35,54	-66,03	85,04	-47,62	-128,33	0,5638
0,54	-149,14	-52,39	-47,43	78,55	-73,91	-202,85	37,94
0,56	-186,33	-64	-32,18	74,29	-94,85	-263,91	60,99
0,58	-208,31	-70,14	-22,99	71,89	-105,33	-297,61	71,44
0,6	-211,48	-70,41	-21,3	71,74	-106,05	-300,74	72,43
0,62	-197,87	-64,69	-26,76	73,83	-97,44	-274,78	64,87
0,64	-169,58	-54,01	-38,23	77,22	-77,78	-220,1	46,43
0,66	-137,2	-38,87	-53,83	82,01	-50,44	-145,25	12,31
0,68	-113,31	-20,06	-73,14	89,51	-25,23	-69,84	-34,08
0,7	-99,04	-1,427	-94,95	99,58	-9,266	-8,7	-78,29
0,72	-87,81	12,68	-113,72	109,44	-0,4653	37,07	-109,35
0,74	-78,66	20,7	-125,03	116,32	4,701	66,88	-125,48
0,76	-75,97	23,02	-128,42	118,89	6,116	76,27	-130,25
0,78	-82,47	19,97	-124,94	117,26	2,235	61,98	-126,81
0,8	-91,29	11,39	-114,86	111,78	-6,325	26,85	-111,05
0,82	-90,61	-3,03	-99,09	102,29	-16,72	-20,96	-76,87
0,84	-94,77	-21,94	-79,7	91,32	-31,91	-79,7	-31,03
0,86	-121,65	-41,31	-59,99	82,65	-55,78	-151,64	13,58
0,88	-161,51	-56,6	-42,16	77,02	-81,39	-224,18	46,65
0,9	-195,03	-66,56	-28,47	73,35	-99,19	-277,64	65,43
0,92	-211,35	-70,93	-21,58	71,45	-106,54	-301,86	72,65
0,94	-209,2	-69,26	-22,19	71,91	-104,38	-295,87	71,04
0,96	-190,53	-61,87	-29,72	74,55	-92,31	-260,81	60,51

L.2. Strain data for Z-loading during fatigue test

Time	SG1	SG2	SG3a	SG3b	SG3c	SG4a	SG4b
0	853,84	-136,81	-72,83	-223,53	653,83	940,17	743,33
0,02	761,77	-126,6	-65,38	-217,12	595,27	847,8	658,01
0,04	556,39	-106,66	-57,09	-195,46	477,53	647,74	475,33
0,06	241,78	-88,8	-39,8	-134,92	309,57	384,92	220,49
0,08	-164,12	-79,68	92,63	-13,04	23,3	109,95	-63,45

© Central University of Technology, Free State

0,1	-630,02	-61,21	396,91	125,25	-419,73	-202,41	-359,57
0,12	-1022,7	-33,87	672,14	214,83	-814,12	-490,93	-610,2
0,14	-1262,4	-12	814,53	253,55	-1040,7	-682,59	-773,76
0,16	-1350,4	-3,038	855,96	264,07	-1117,3	-755,49	-834,94
0,18	-1298,2	-8,435	833,98	257,69	-1074,3	-705,86	-782,67
0,2	-1123,3	-26,57	760,95	236,58	-929,11	-548,5	-629,16
0,22	-845,47	-53,98	617,32	195,9	-677,61	-314,61	-404,14
0,24	-479,91	-81,35	357,82	111,42	-303,78	-45,38	-130,45
0,26	-53,2	-97,36	111,09	-22,74	82,07	238,57	167,07
0,28	377,97	-111,07	-9,358	-142,02	372,63	544,99	446,03
0,3	689,98	-126,26	-52,08	-203,12	554,65	795,53	644,29
0,32	840,22	-136,29	-70,02	-221,88	644,46	928,44	740,45
0,34	839,36	-134,96	-71,8	-222,4	643,51	925,37	728,78
0,36	709,85	-121,08	-62,31	-212,69	562,92	796,04	611,34
0,38	470,55	-100,02	-54,9	-182,31	431,4	569,98	402,15
0,4	125,45	-85,62	-19,44	-103,31	239,84	302,2	135,33
0,42	-308,82	-75,31	177,27	32,52	-106,26	15,64	-156,82
0,44	-767,42	-52,74	495,77	159,89	-558,83	-299,84	-445,67
0,46	-1115,5	-25,79	731,15	231,34	-904,2	-563,41	-671,86
0,48	-1306,2	-7,517	836,27	259,11	-1079,3	-718,71	-804,65
0,5	-1350,3	-2,956	855,46	263,99	-1116,8	-754,18	-832
0,52	-1257,5	-12,7	817,52	253,01	-1040,7	-668,58	-745,56
0,54	-1048,3	-34,29	727,1	226,86	-864,16	-483,03	-565,75
0,56	-738,49	-63,37	547,59	175,95	-571,33	-231,25	-321,74
0,58	-353,36	-87,43	270,3	72,98	-177,28	39,7	-38,9
0,6	87,8	-101,45	60,36	-65,07	186,1	335,01	260,4
0,62	492,52	-116,06	-27,48	-167,26	441,23	633,66	519,19
0,64	753,91	-130,45	-59,25	-212,09	593,11	851,06	685,76
0,66	854,81	-137,32	-72,19	-223,39	654,74	942,03	748,77
0,68	810,78	-131,82	-69,32	-220,51	626,1	897,14	703,03
0,7	646,26	-114,77	-59,49	-206,36	526,91	734,01	555,08
0,72	371,77	-94,16	-50,42	-164,17	380,1	486,73	321,94
0,74	-0,894	-83,17	18,42	-65,04	154,03	217,39	47
0,76	-456,59	-69,71	274,51	76,82	-246,6	-82,74	-249,91
0,78	-891,9	-44,09	583,95	188,23	-684,24	-391,42	-524,67
0,8	-1191,6	-18,72	776,53	243,47	-976,15	-624,71	-723,93
0,82	-1335,2	-4,466	850,03	262,52	-1104,6	-743,29	-825,16
0,84	-1335,3	-4,462	849,52	262,08	-1104,9	-739,95	-816,42
0,86	-1203,6	-18,18	795,65	246,4	-996,51	-619,61	-697,39
0,88	-962,9	-42,67	684,6	214,58	-787,84	-410,11	-495,49
0,9	-625,05	-72,11	465,99	150,41	-454,51	-146,96	-236,2
0,92	-220,15	-92,35	191,08	30,17	-55,34	127,73	54,65
0,94	225,99	-105,75	22,48	-103,91	278,04	433,01	349,76
0,96	593,27	-120,92	-40,77	-187,07	498,96	714,98	583,19